NASA Conference Publication 3257

LDEF Materials Results for Spacecraft Applications

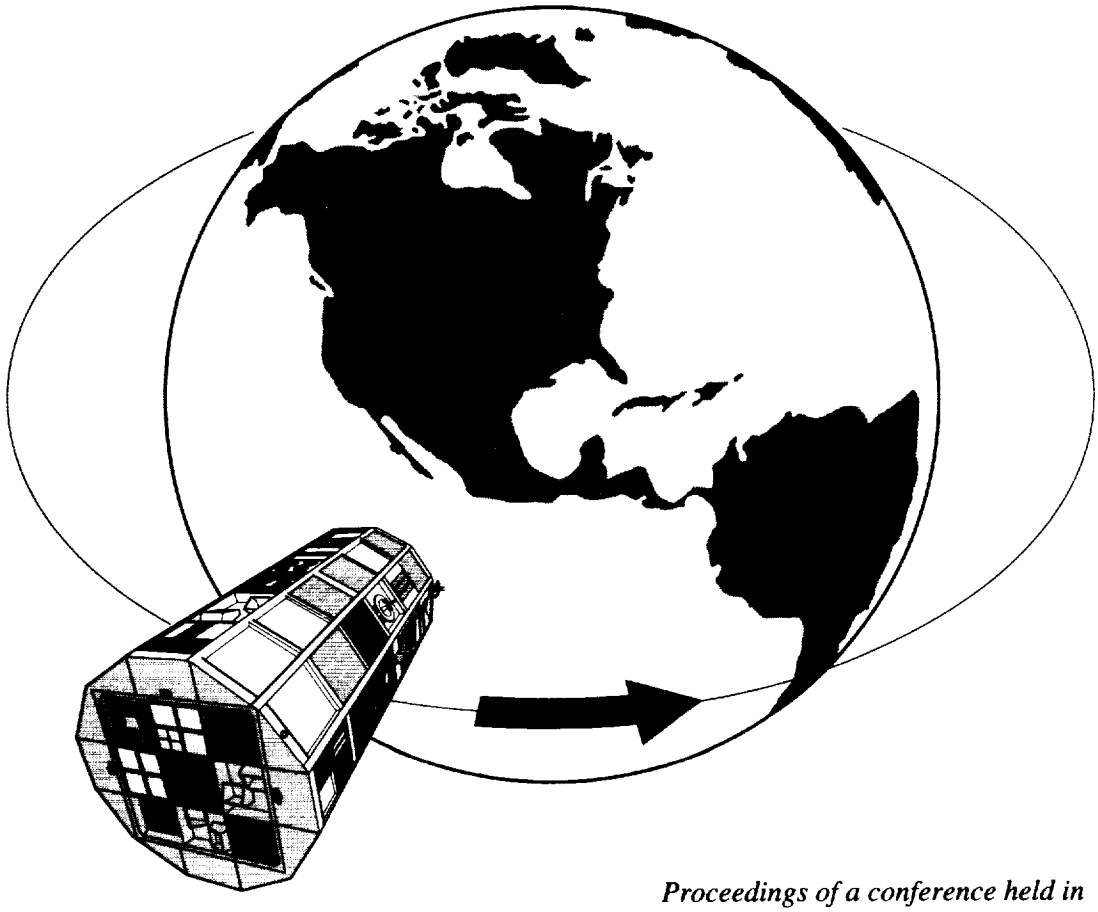

Proceedings of a conference held in Huntsville, Alabama October 27–28, 1992

NASA Conference Publication 3257

LDEF Materials Results for Spacecraft Applications

Compiled by
Dr. Ann F. Whitaker
NASA George C. Marshall Space Flight Center
Marshall Space Flight Center, Alabama

and

Dr. John Gregory
The University of Alabama
Huntsville, Alabama

Proceedings of a conference sponsored by the National Aeronautics and Space Administration, Washington, D C, The University of Alabama in Huntsville, The Alabama Space Grant Consortium, and the Society of Advanced Materials and Process Engineers, and held in Huntsville, Alabama October 27–28, 1992

NASA
National Aeronautics and Space Administration
Office of Management
Scientific and Technical Information Program
1994

TABLE OF CONTENTS

TABLE OF CONTENTS (Continued)

TABLE OF CONTENTS (Continued)

FOREWORD

The Long Duration Exposure Facility (LDEF) satellite was returned to the laboratory for analysis in early 1990 after nearly 6 years in space. It has proven to be by far the most comprehensive source of information ever obtained on the long-term performance of materials in the space environment. Much of this data has now been reported and published in the technical literature by the individual investigators.

The conference provided a forum for spacecraft designers, managers, material engineers, and scientists to review and critically assess the LDEF results from the standpoint of their relevance, significance, and impact on spacecraft design practice. The impact of the LDEF findings on materials selection, utilization, and qualification was addressed from the National Aeronautics and Space Administration, the Department of Defense, industry, and academic perspectives. Many timely and needed changes and modifications in external spacecraft materials selections have occurred as a result of LDEF investigations. A continuous need exists for current space environmental effects data on materials to ensure life and performance of spacecraft and payloads. Lack of high quality data on performance degradation of materials will continue to lead to costly overdesigns and/or severely degraded spacecraft performance. This conference clearly demonstrated the effectiveness of maintaining an access to space to verify ground test data which cannot completely provide the synergistic effects from the combined environments of space.

The format of the Proceedings follows that of the Conference itself, with sections in the principal areas of interest for spacecraft design:

- Thermal control coatings
- Spacecraft environment
- Materials erosion, radiation damage, and fluorescence
- Optical elements and materials
- Composites and structural materials
- Data bases
- Advanced approaches to spacecraft materials issues
- Material research, development, and program needs in space environmental effects.

The conference program was organized by a committee consisting of Ralph Carruth, John Gregory, Roger Linton, Ron Mize, Richard Sudduth, Ann Whitaker, Gary Workman, and James Zwiener. The session chairmen and organizers were:

Wayne Stuckey and James Zwiener

Dave Brinza and Ralph Carruth

Philip Young and Bruce Banks

Roger Linton and John Gregory

Gary Pippin and Rod Tennyson

Lubert Leger and Richard Sudduth

Paul Schuerer and Ann Whitaker

The papers underwent both technical and editorial review, and I wish to thank the many reviewers who assisted.

Finally, I want to thank the many people who helped make this conference such a success: Marshall Space Flight Center Director Jack Lee; MSFC's Materials and Processes Laboratory personnel; MSFC's sponsoring organizations— Space Station, Space Systems Projects, Payloads Projects, Program Development, and Safety and Mission Assurance; NASA Associate Administrator Richard Petersen; LDEF Project Office personnel; LDEF Chief Scientist William Kinard; The University of Alabama in Huntsville's Office of Conferences and Marketing; and all the government, industry, and academic investigators.

Additional copies of the Conference Proceedings may be obtained by contacting The NASA Center for Aerospace Information, P.O. Box 8757, Baltimore, MD 21240.

Ann F. Whitaker
Conference Chairman

THERMAL CONTROL MATERIALS

THE PERFORMANCE OF THERMAL CONTROL COATINGS ON LDEF AND IMPLICATIONS TO FUTURE SPACECRAFT

Donald R. Wilkes, Edgar R. Miller, Richard J. Mell, Paul S. LeMaster
AZ Technology, Inc.
3322 Memorial Parkway, SW
Building 600, Suite 93
Huntsville, AL 35801
Phone: 205/880–7481, Fax: 205/880–7483

James M. Zwiener
NASA/George C. Marshall Space Flight Center
Marshall Space Flight Center, AL 35812
Phone: 205/544–2528, Fax: 205/544–7329

SUMMARY

The stability of thermal control coatings over the lifetime of a satellite or space platform is crucial to the success of the mission. With increasing size, complexity, and duration of future missions, the stability of these materials becomes even more important. The Long Duration Exposure Facility (LDEF) offered an excellent testbed to study the stability and interaction of thermal control coatings in the low-Earth orbit (LEO) space environment. Several experiments on LDEF exposed thermal control coatings to the space environment. This paper provides an overview of the different materials flown and their stability during the extended LDEF mission. The exposure conditions, exposure environment, and measurements of materials properties (both in-space and postflight) are described. The relevance of the results and the implications to the design and operation of future space vehicles are also discussed.

INTRODUCTION

With the exception of the limited experimentation conducted aboard *Skylab*, LDEF has provided the only retrievable space exposure opportunity to test the long-term performance of thermal control coatings. Subsequent sample evaluation and data analysis has provided a wealth of information that is now being made available to aid in the design of future spacecraft. As an example of this, Space Station *Freedom* (S.S. *Freedom*) will employ the thermal control coating Z-93 extensively on large and complex structures. This is due in large part to the confidence generated by the stability Z-93 demonstrated on the LDEF mission.

This paper discusses the thermal control coatings tested on LDEF and the available data concerning the performance of these thermal control coatings on the LDEF mission. In addition, the implications for future spacecraft are discussed. It should be emphasized that the results presented here are not final and that in most cases analyses are continuing. Much of the data are not fully understood or explainable at this time.

Many of the 57 LDEF experiments exposed thermal control coatings to the LDEF environment either as test specimens or as operational coatings. In addition, several coatings were used as thermal control surfaces on LDEF itself. When the available data on these materials are evaluated along with the preparation, exposure, and measurement conditions, there will be several factors that complicate this analysis. In many cases there were no ground and/or flight control samples to establish a measurement baseline or to determine the effects of aging alone on these materials. Where there were control samples, many were either not stored under controlled conditions or were lost over the unanticipated 5-year delay in the recovery of LDEF. This long and uncertain mission duration also resulted in lost or incomplete preflight data and documentation. In addition, some test samples were prepared using different techniques, procedures, material batches, and sample thicknesses.

One of the most significant problems in comparing the different LDEF data on coatings is the difference in measurement instruments. Investigators used a number of different instruments that are difficult to compare. In many cases, the instruments used for preflight measurements have been replaced with new instruments or they have been upgraded or modified. Even with these complications, the LDEF experiments provide the most extensive data base on the performance of thermal control coatings in the space environment.

The available thermal control coatings data from the LDEF experiments and from the LDEF system have been reviewed. Data from selected experiments and samples have been analyzed and compared to compile this paper. Tables 1 and 2 list the experiments, their location on LDEF, and the coatings that are considered in this paper.

Table 1. Selected LDEF experiments with thermal control coatings.

Experiment No.	Ref. No.	LDEF Row	Title	PI	Organization
S0069	1,2,3 4	9	Thermal Control Surfaces Experiment	Wilkes Zwiener	AZ Technology NASA/MSFC
A0171	5	8	Solar Array Materials Passive LDEF Exposure (SAMPLE)	Whitaker	NASA/MSFC
A0114	2	3,9	Interaction of Atomic Oxygen with Solid Surfaces at Orbital Altitudes	Gregory Peters	Univ. of AL-HSV NASA/MSFC
M0003-5	6	3,9	Thermal Control Materials	Hurley	UDRI
M0003	7	3,4,8,9	DOD Materials Experiment	Jaggers Meshishnek	Aerospace Corp.
A0138-6	8	3	FRECOPA	Guillaumon Paillous	CERT
LDEF Components	9 10 11	----	LDEF Materials SIG Analysis	Golden Pippen Bourassa	The Boeing Co.
S1003	12	6	Ion Beam Textured and Coated Surfaces Experiment	Mirtich Rutledge	NASA/LeRC
S1001 A0076	13	1,9	Low Temperature Heat Pipe Experiment and Cascade Variable Conductance Heat Pipe Experiment	Kauder	NASA/GSFC

Table 2. Selected LDEF experiments with thermal control coatings.

Experiment Coating	S0069 (TCSE)	A0114 (UAH)	A0171 (SAMPLE)	S1003 (IBEX)	GSFC (Kauder)	M0003-5 (Dayton)	M0003 (Aerospace)	A0138-6 (FRECOPA)	MSIG
Z-93	X	X				X		X(6)	
S13G/LO	X	X	X	X	X	X	X	X(6)	X
A276	X	X	X			X	X	X	X
YB-71	X					X	X		
D111	X					X	X		
Z302	X	X	X			X		X	
Z306	X	X	X			X		X(7)	X
Chromic Acid Anodize	X					X			X
RTV 670/A276	X								
O1650/A276	X								

Notes for Table 2.

1. 401-C10 (Nextel) black, Z853 yellow, Tiodize K17 black, Tiodize K17 white
2. 401-C10 (Nextel) black, black chrome
3. SiO_x over Kapton™; 200, 500, 700, 1,000 Å
4. Acrylic/Urethane over Kapton™; silicone over Kapton™, RTV 615 white paint
5. NS43G; white silicone Eu 203 MeSi, a Al 203 MeSi, PV100, TiO_2 MeSi, DC 92-007
6. White paints similar to S13G and Z-93:
   PY100, 536, PSB, SG11, FD, PSG 120 FD, and conductive white paints PCB-2, PCB-T, PCB 119
7. Black paints similar to Z306:
   PU1, Cuvertin 306, VHT SP102, HT 650, Electrodag 501, L300, PNC, PUC.

The exposure environment for the test samples varied with the row location of the experiment on LDEF. Figure 1 shows the exposure environment by row number on LDEF (refs. 1,2).

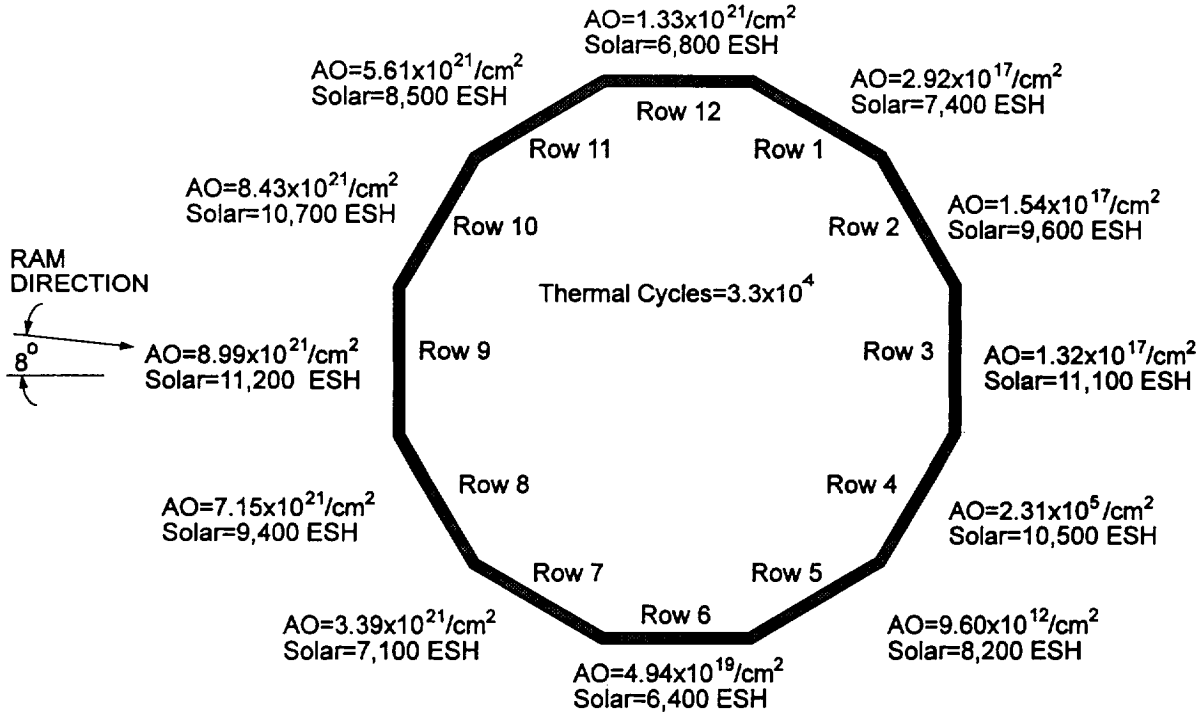

Figure 1. LDEF exposure environment.

The extended LDEF exposure caused significant changes in many coatings. These include optical as well as other surface physical changes. Surface changes include:

- The surfaces of silicones exposed to the RAM atomic oxygen were converted to SiO_x components and suffered microscopic cracking (ref. 3).
- There were trace contaminants on most LDEF surfaces (refs. 4–6):
  - Hydrocarbon contaminants were not present on RAM facing surfaces
  - Silicone contaminants were present in trace amounts on most surfaces
  - The effects of trace level contaminants were not significant for most thermal control coating applications.
- There was localized heavy contamination with significant optical degradation near contaminant sources and vents.
- The UV fluorescence of some coatings were changed (ref. 7).
- AO protective coatings suffered cracking, crazing, and peeling (ref. 8).
- Urethane and epoxy based coatings erode readily in AO (ref. 8).

OPTICAL EFFECTS

The material properties of a coating that are of the greatest concern are solar absorptance (α_s) and thermal emittance (ε_t). α_s and ε_t directly affect the thermal control of a spacecraft. The ε_t for all the materials presented here were basically unchanged by the LDEF exposure (ref. 8). Spectral reflectance measurements are the best method to determine α_s and provide the materials engineer with insight into the optical signature and stability of a material as a function of exposure environment and duration. Data are presented for a number of the more widely used and accepted thermal control coatings, illustrating the change in solar absorptance of these materials for the extended LDEF mission. Because of the difference in the stability of these materials, please note the scale change of the abscissa on graphs for different materials.

Z-93 Ceramic Nonspecular White Coating

The renewed interest in the white thermal control coating Z-93 (manufactured by the IIT Research Institute) is because it has been shown to be highly stable in the LEO environment. The results from LDEF, and in particular the Thermal Control Surfaces Experiment (TCSE-S0069), have demonstrated this stability through the in-flight optical data that are not subject to the uncertainties of data generated from pre- and postflight sample measurements alone. In addition to the LDEF demonstrated stability of Z-93 in LEO, it can be deposited onto large, complex structures with relative ease and with low weight and cost per square area. As a result of these characteristics, Z-93 has been baselined for use on the radiators and some of the antennas which will compose the critical and intricate structure of S.S. *Freedom.*

In Figures 2 and 3, Z-93 data from several experiments are plotted, both on the LDEF's leading and trailing edges. Change in solar absorptance is plotted against exposure time. The unique in-space optical measurements performed on experiment TCSE-S0069 provide a time history of changes in α_s. These in-space measurements also allowed investigations to develop a trend analysis and a prediction model for the material and to better understand the damage mechanisms affecting its optical stability (ref. 9). The data from the Z-93 samples indicate that it was very stable over

the LDEF mission, and data from three experiments corroborate these findings for both leading and trailing edge samples. The trend analysis studies also provide some insight into the small changes that were measured.

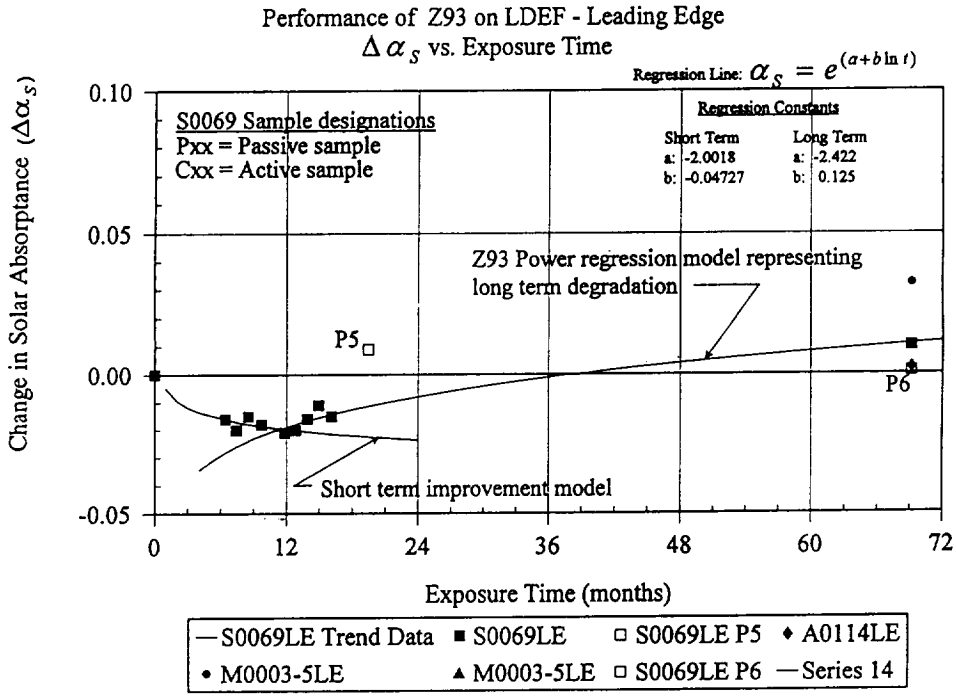

Figure 2. Performance of Z-93 on LDEF—leading edge.

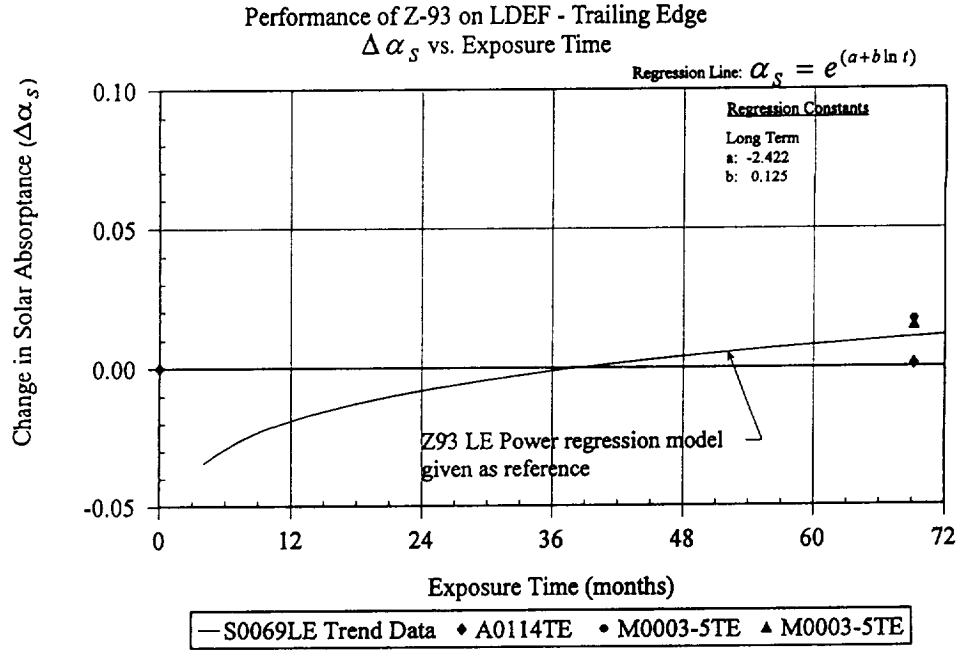

Figure 3. Performance of Z-93 on LDEF—trailing edge.

There appear to be at least two mechanisms affecting the Z-93 solar absorptance for the LDEF mission. The first is an improvement (decrease) in α_s typical of silicate coatings in thermal vacuum. This improvement is normally associated with loss of interstitial water from the ceramic matrix. Ground laboratory simulation tests have shown this process takes a much shorter time than the TCSE flight data suggests. This slower loss of water may be due to the cold temperature of the TCSE Z-93 sample mounted on a thermally isolated calorimeter. The temperature of the Z-93 sample ranged from approximately –55 °C to +6 °C but remained well below 0 °C most of the time. The short-term improvement is dominant for the first year of exposure after which a long term degradation becomes dominant.

This trend analysis is being expanded to include the TCSE spectral reflectance data shown in Figure 4, and to analyze how Z-93 changed at specific wavelengths. The increase in infrared reflectance early in the mission results in the improvement in α_s, while the decrease at shorter wavelengths is the long term degradation component for Z-93. This trend analysis is providing an analytical prediction model for specific materials and offering insight into the degradation mechanisms of Z-93. These data generated from the TCSE demonstrate the value of in-space optical measurements on materials.

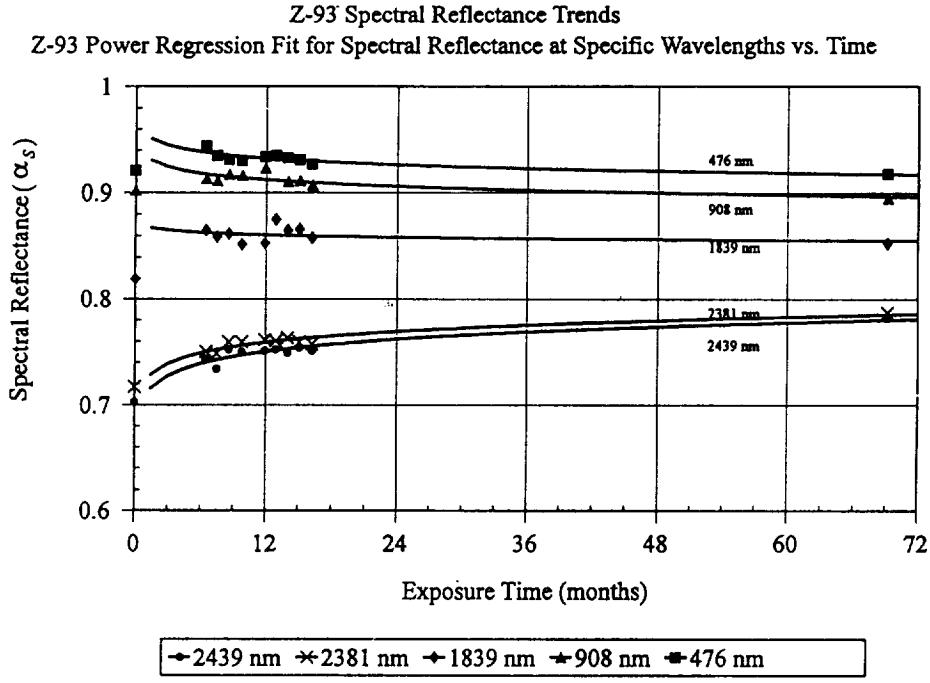

Figure 4. Z-93 spectral reflectance trends.

Z-93 IR Spectra

In Figure 5, the infrared spectra for both the exposed and unexposed areas of the Z-93 coating on flight sample C3-41 are plotted. The spectra was generated using a Fourier scanning infrared attenuated total reflectance microprobe system (SPECTRA TECH IRμs/SIRM system, technical assistance provided by Drs. J.A. Reffner and P.A. Martoglio). The system configuration used to analyze this sample has a beam spot area of approximately 53 microns. The shift in the silica

absorption band maximum from 1,019 to 1,026 cm^{-1} and the extinction of the 1378 cm^{-1} absorption band of the exposed Z-93 are thought to be accurate at this time. The trend to a general slight increase in reflectance of the exposed area of this sample may be caused from changes in its surface morphology rather than a chemical change. These changes to the samples surface may have affected the light scattering characteristics of the material resulting in the observed change in the IR reflectance. These are preliminary results and will require further investigation to determine their validity. However, it is thought that this is the first time such data and associated exposure effects have been reported for this spacecraft thermal control coating as such.

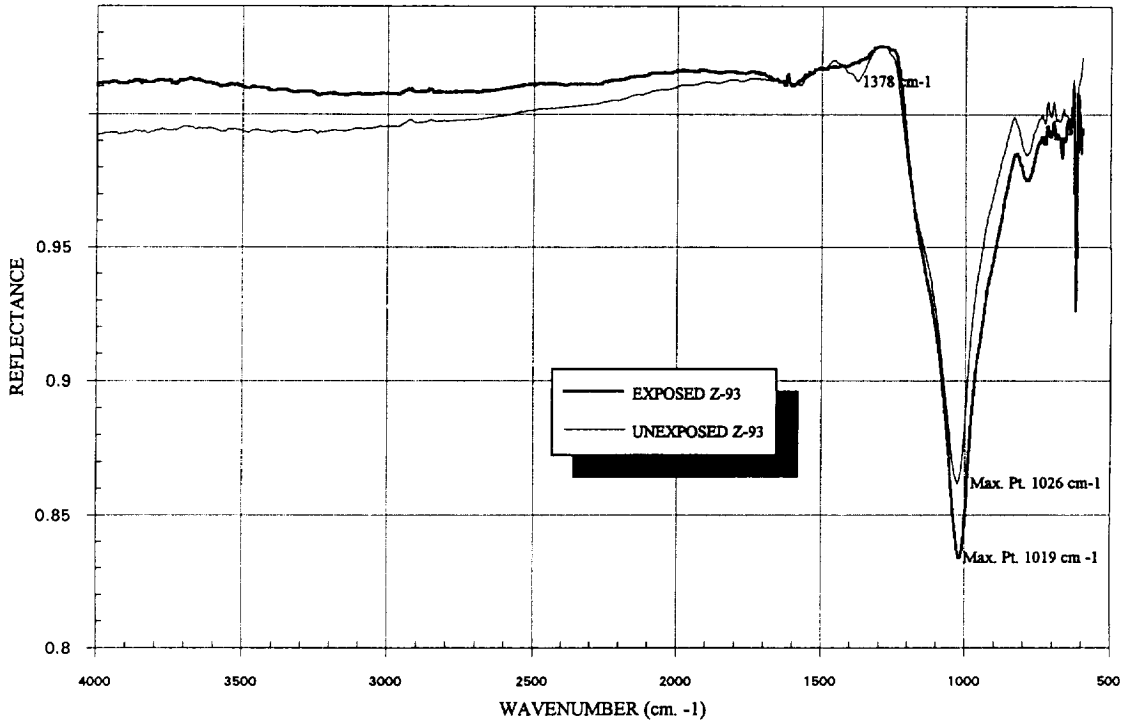

Figure 5. Exposed and unexposed Z-93 thermal control coating, sample C3-41, mode, microscopic attenuated total reflectance.

YB-71 and YB-71/Z-93 Ceramic Nonspecular White Coating

The YB-71 (manufactured by IIT Research Institute) coatings behaved similarly to the Z-93 samples. A small increase in the infrared reflectance early in the mission caused a decrease in α_s (Figures 6 and 7). This was offset by a slow long-term degradation resulting in a small overall increase in α_s. The samples with YB-71 applied over a primer coat of Z-93 had a somewhat lower initial α_s than the other YB-71 samples. YB-71 samples were flown on two experiments—the TCSE (S0069) and M0003. The TCSE samples were consistently more stable than the M0003 samples. The YB-71 samples were prepared for LDEF before the development of YB-71 was finalized. These differences could be due to batch variations of this new coating. There was no significant difference in the performance of leading and trailing edge samples on M0003. The M0003-5 YB-71 showed a slightly higher $\Delta\alpha_s$ than those samples on TCSE. The power regression model is shown for the TCSE data.

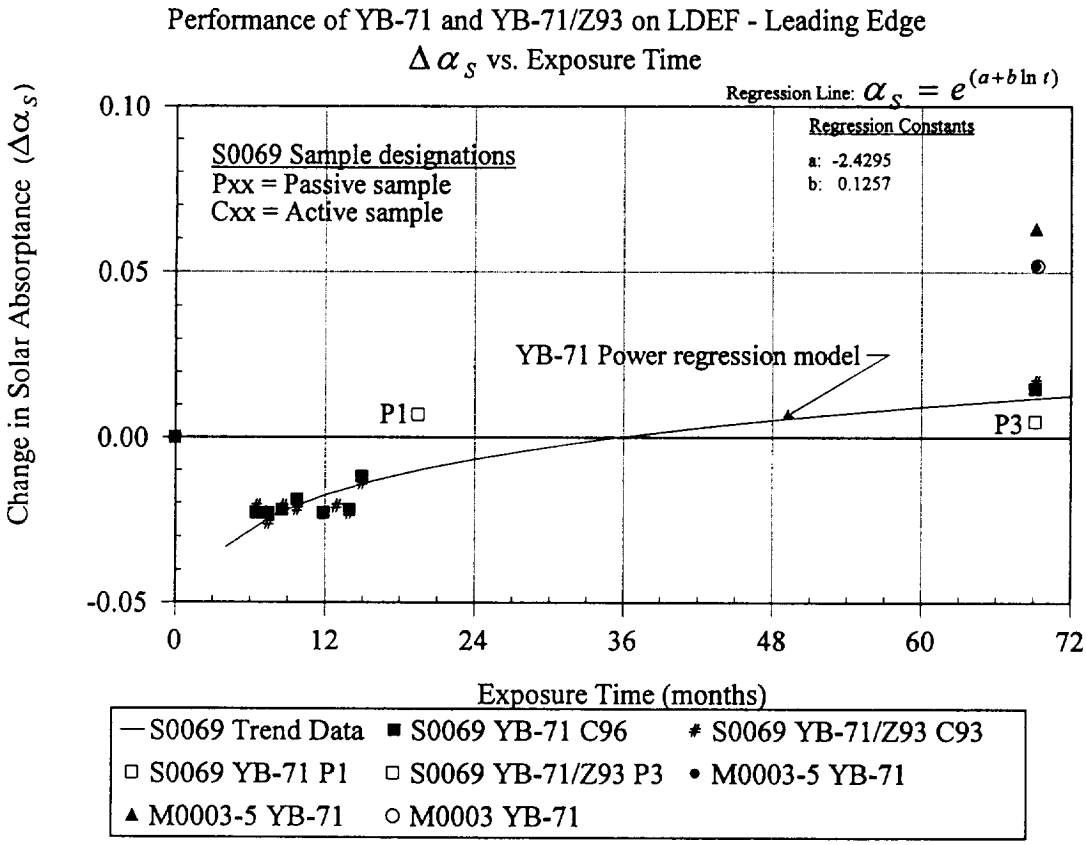

Figure 6. Performance of YB-71 and YB-71/Z-93 on LDEF—leading edge.

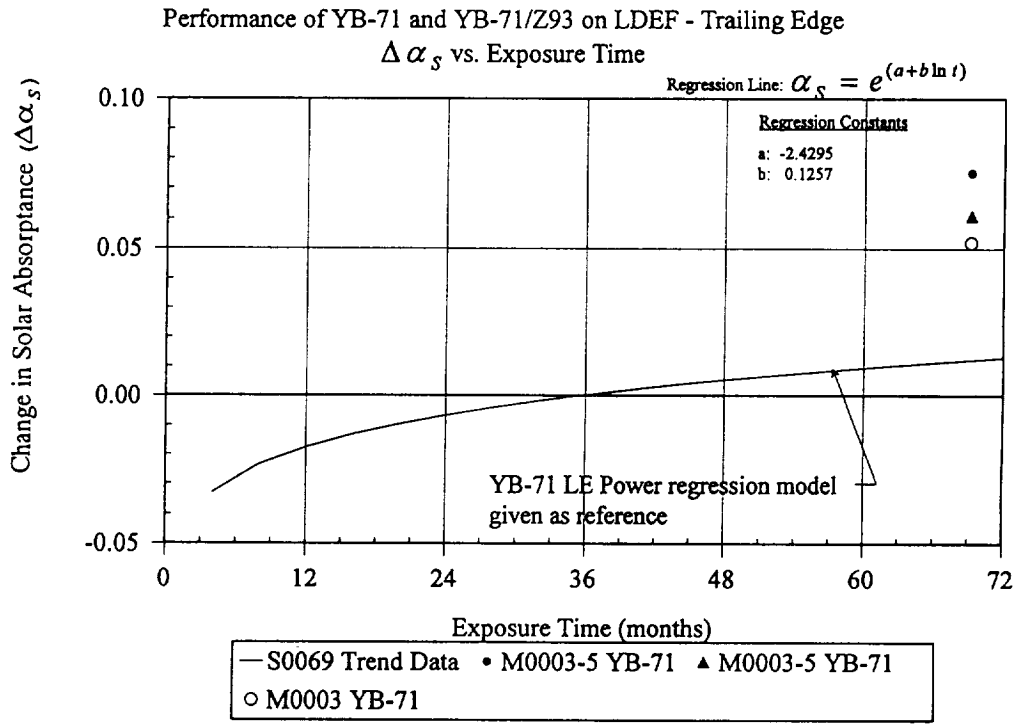

Figure 7. Performance of YB-71 and YB-71/Z-93 on LDEF—trailing edge.

S13G/LO Silicone Nonspecular White Coating

There is a wide variation in the results from the different LDEF experiments for S13G/LO (manufactured by the IIT Research Institute). These differences are unexplained at this time. Figures 8 and 9 show the change in α_s for the LDEF mission of several S13G/LO samples. There does not appear to be any clear correlation between ram and wake locations with respect to degradation in α_s of S13G/LO. The S0069 power regression model is shown and falls in the middle of the spread of data reported for the various experiments.

The interaction of the space environment with S13G/LO is very complex. However, from what is presently known about the LDEF environment and this type of material, material changes are likely to be the result of several factors or synergistic interactions. Some of components in this interaction which need to be considered are vacuum ultraviolet (VUV), ultraviolet (UV), atomic oxygen (AO), contamination, and material batch variability. The VUV, UV, and AO can combine to cause reaction (conversion) and ionization of the coating. This results in chain and aliphatic group scission and crosslinking of the polymer binder. Ultimately AO reaction with the silicone polymer causes glassification and trapping of residual carbon to produce color centers. The production of color centers is not only dependent on incident radiation and AO reaction, but also on material batch processing characteristics and contamination. Synergistics of these factors can exaggerate the observed change in solar absorptance of this and similar types of materials.

A276 White Specular Polyurethane Paint

The A276 (manufactured by Lord Chemical Co.) coating provides an excellent example of the synergistic effects of solar UV and AO impingement (Figures 10 and 11). Apparently, the oxidation and subsequent loss of the polyurethane binder prevented significant buildup of damaged material. When protected from AO the damaged, intact surface material and contaminants resulted in large increases in α_s. On LDEF, the majority of AO exposure occurred in the latter few months of the mission. This AO exposure may have eroded away the slight amount of degraded surfaces seen on the S0069 samples (ram) during the first part of the mission.

RTV670 and OI650 Silicone Overcoats on A276

An attempt was made to protect the A276 coating from AO erosion with overcoats of silicone. In Figure 10, the S0069 results of RTV670 (manufactured by General Electric, no longer being produced) and OI650 (manufactured by Owens Illinois, Television Products Division) over A276 are shown. The overcoat prevented material loss but allowed, presumably, solar UV damage of the A276 coating and possibly damage and darkening of the silicone protective layer. In addition, the silicone layer was cracked due to AO glassification and this may have resulted in shrinkage and loss of mass. Further investigations are ongoing to resolve these questions. There were no samples of the silicone coatings alone flown on LDEF.

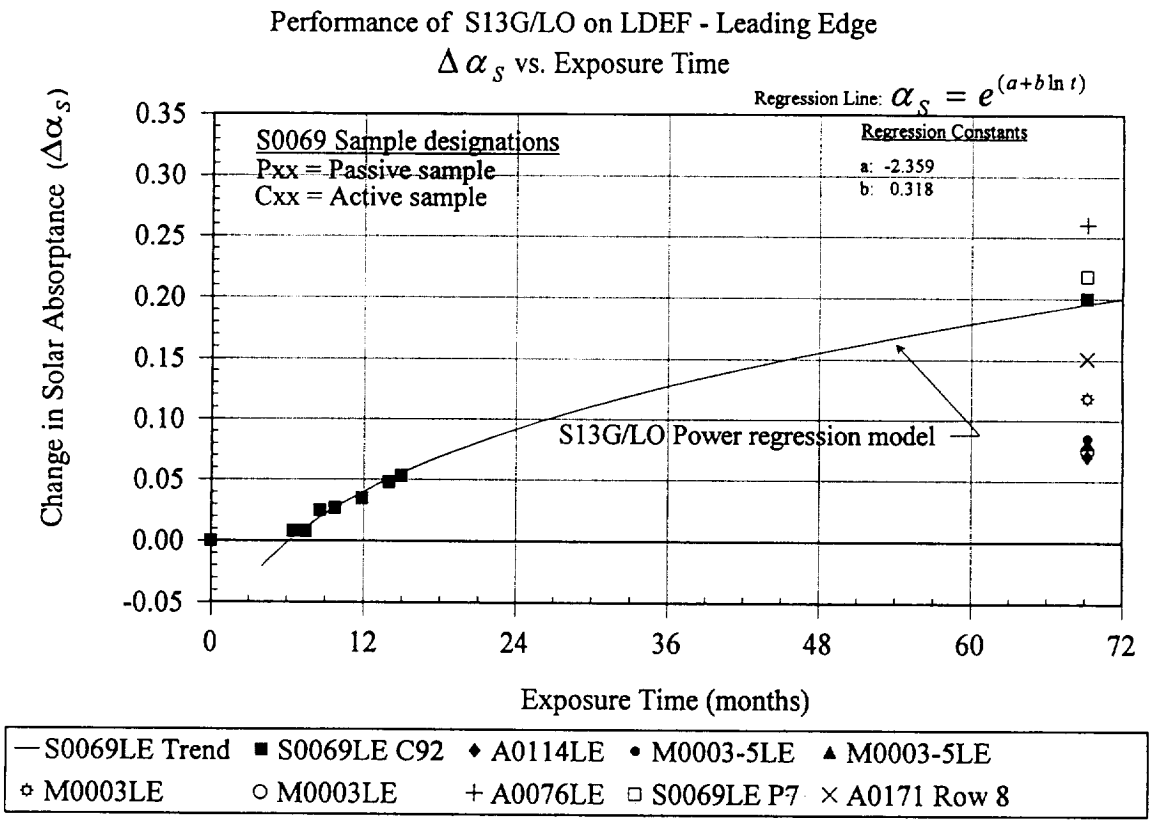

Figure 8. Performance of S13G/LO on LDEF—leading edge.

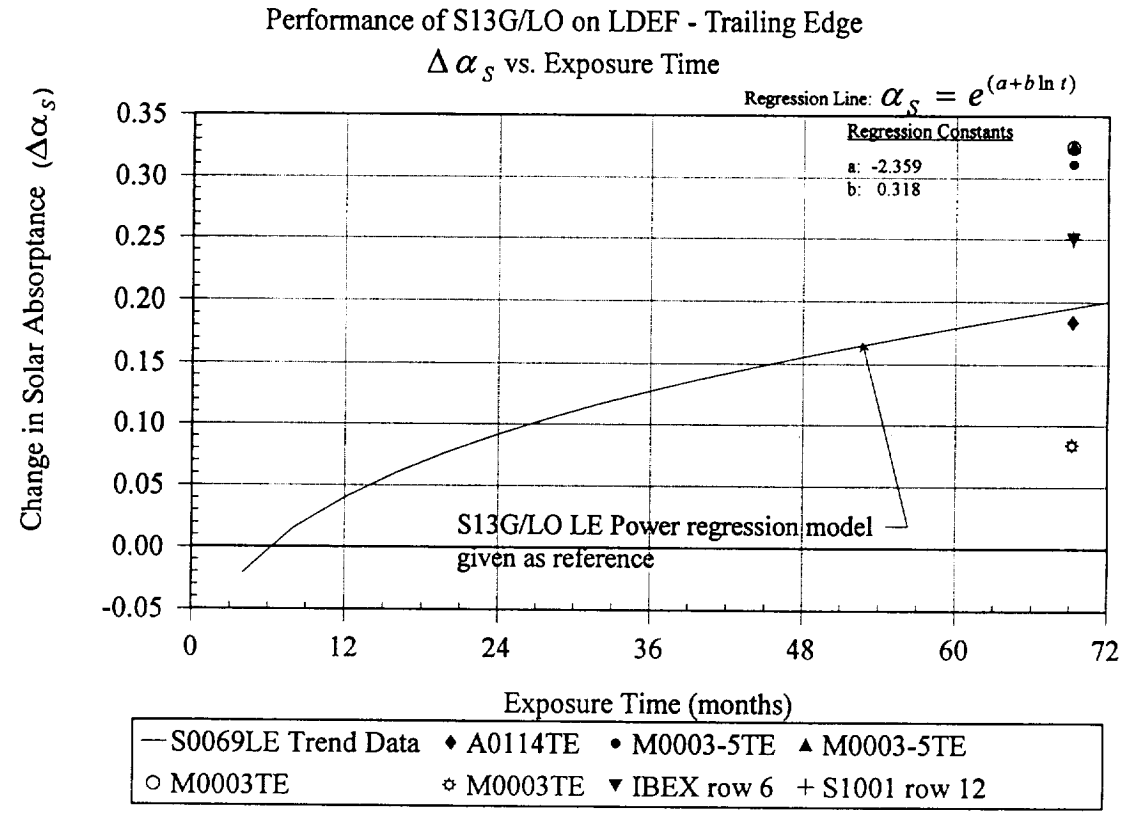

Figure 9. Performance of S13G/LO on LDEF—trailing edge.

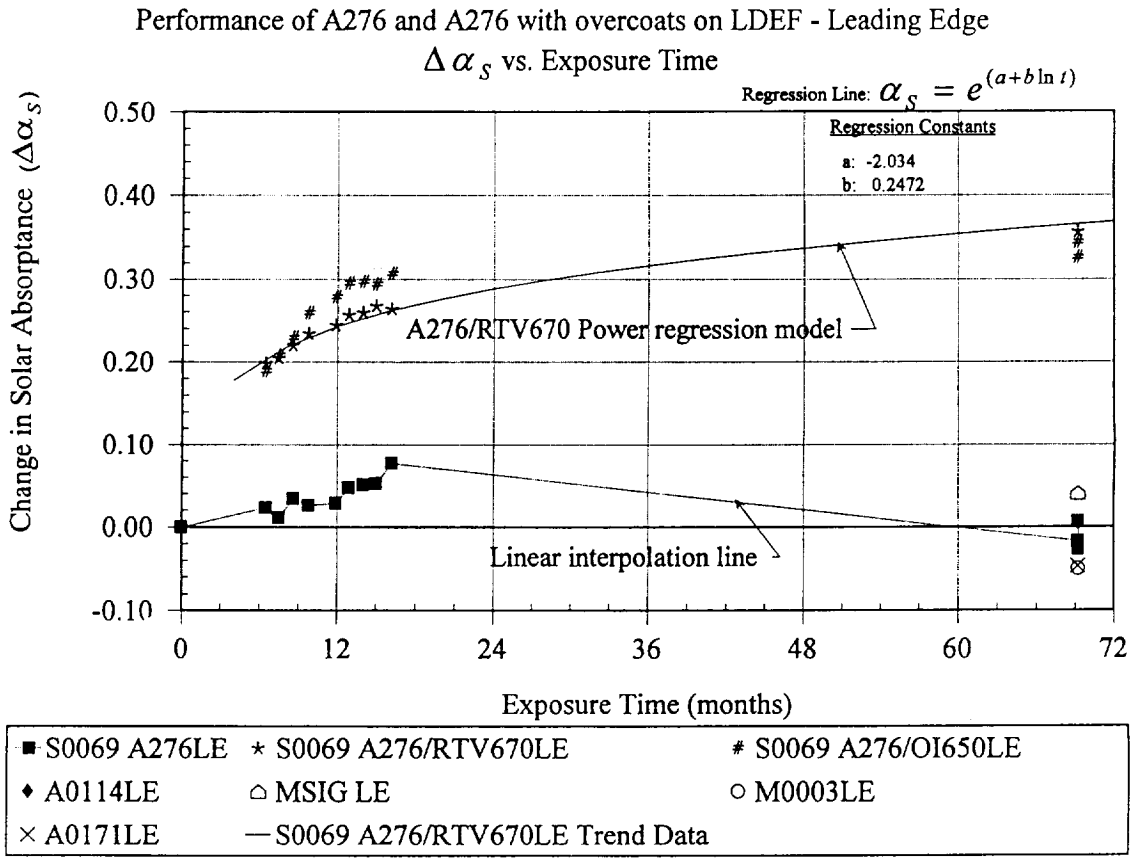

Figure 10. Performance of A276 and A206 with overcoats on LDEF—leading edge.

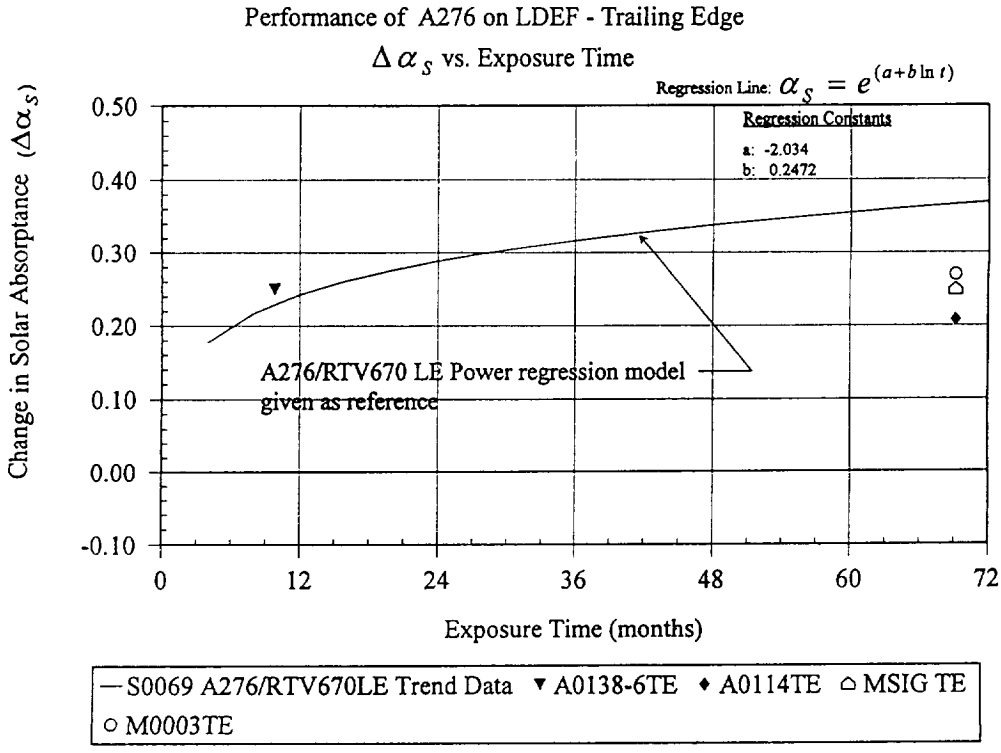

Figure 11. Performance of A276 on LDEF—trailing edge.

CHEMGLAZE Z302™ and Z306™ Polyurethane Black Paints

Z302 and Z306 (manufactured by Lord Chemical Company) are polyurethane-based gloss and flat black paints, respectively. They have been shown to be susceptible to AO interactions that result in erosion of the polyurethane binder and their carbon pigment when not protected from AO effectively. Several of the samples of Z302 exposed on the S0069 experiment (TCSE) had protective overcoats deposited onto their surfaces to evaluate the effectiveness of these materials. The samples with overcoats of either RTV670 or OI650 showed little change in solar absorptance (Figure 12). However, the surface of the silicone overcoatings have undergone some significant morphological changes. These changes are demonstrated primarily through the formation of fissures in the silicone likely resulting from the shrinkage of the overcoat material as it lost mass from AO, radiation, and general LEO space environmental exposure.

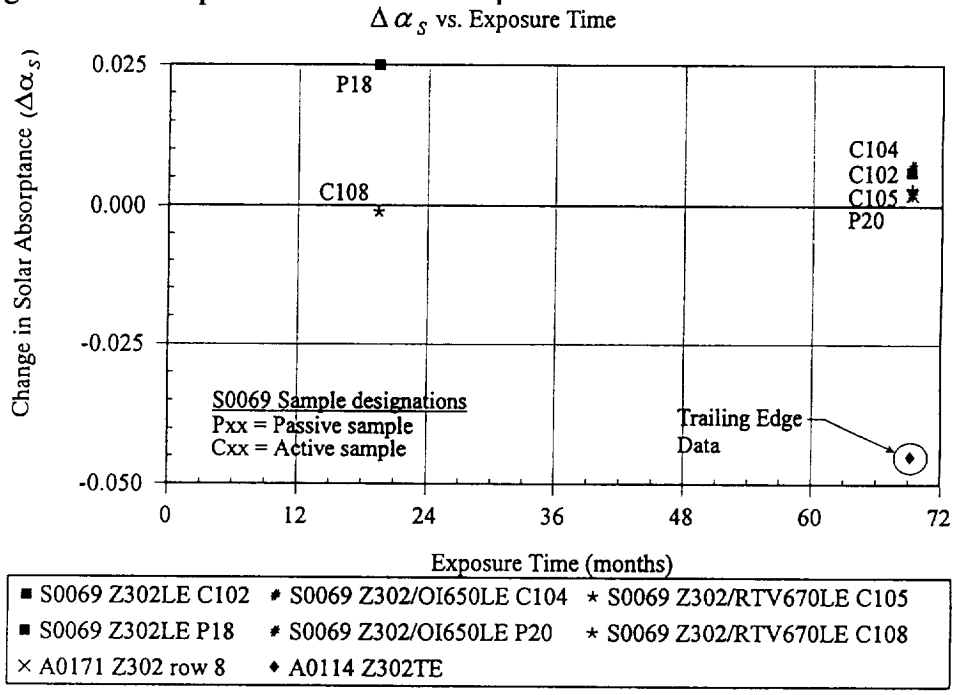

Figure 12. Performance of Z302 and Z302 with overcoats on LDEF—leading and trailing edge.

Visually these samples appear to have sustained no AO damage to the underlying polyurethane coating, but some mechanical damage has occurred. This damage is likely to have occurred as a result of the stresses that were developed in the laminated coatings as the silicone overcoat shrank and was exposed to the normal thermal cycling processes occurring on the experiment as it went in and out of solar exposure. As expected, unprotected Z302 was heavily eroded by the AO exposure. Two of the S0069 Z302 coatings were exposed to the environment for the total 5.8 years of the LDEF mission. These unprotected Z302 sample surfaces eroded down to the primer coat. Two other samples were exposed for only 19.5 months and, while they did erode somewhat, still possessed good solar absorptance (Figure 12). Uncoated samples of Z302 on A0114 showed considerable change (decrease) in α_s on the trailing edge sample, presumably due to a loss of material even with reduced AO exposure. The AO114 Z302 sample was completely eroded from the unprotected and uncovered area of the A0114 sample. Optically, Z306 was stable with the exception of an A0114 sample and an A0138-6 sample, both wake positioned, but showing $\Delta\alpha_s$ changes of about –0.04 (Figure 13). Physical and mechanical analysis of Z306 samples is planned for the future.

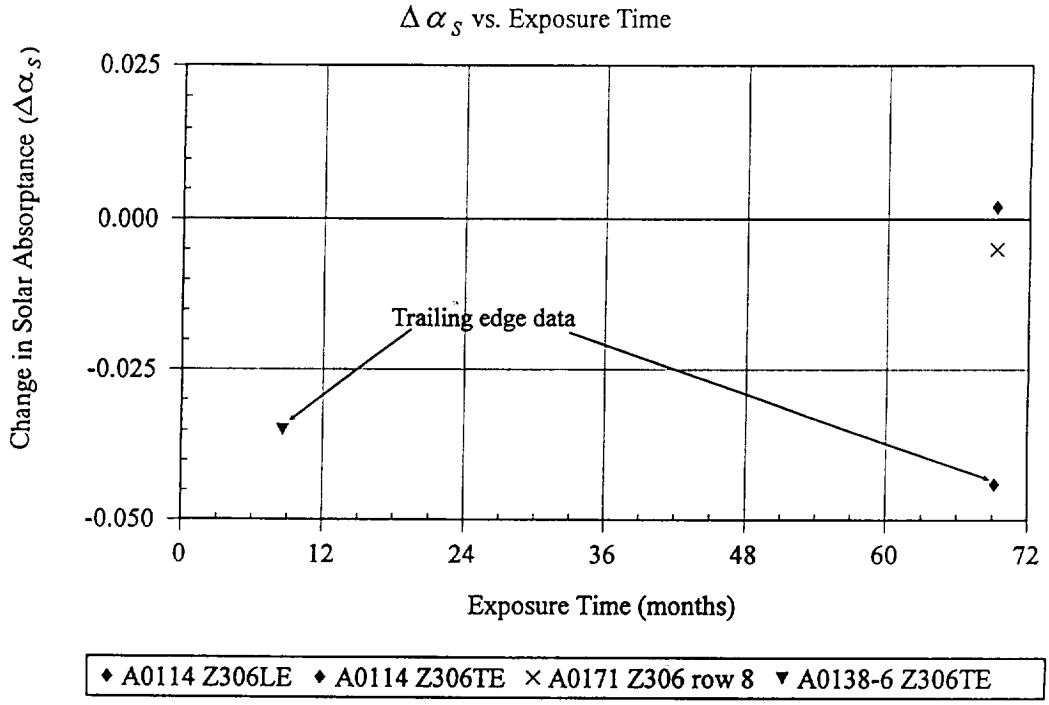

Figure 13. Performance of Z306 black paint on LDEF—leading and trailing edge.

D-111 Ceramic Nonspecular Black Coating

D-111 (manufactured by IIT Research Institute) black coating samples flown on LDEF demonstrated themselves to be relatively stable in LEO both in the ram and wake orientations (Figure 14). The D-111 coating was stable for both of these positions with the exception of the one M0003 trailing edge sample. This is curious since the pigment is a carbonous material and one may have expected some AO reaction with the pigment. However, it may be assumed that the glass binder effectively protected the pigment from AO interaction.

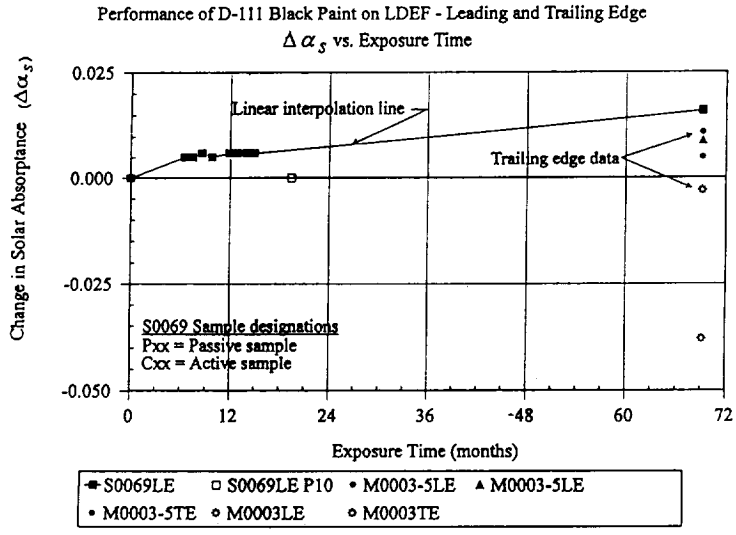

Figure 14. Performance of D-111 black paint on LDEF—leading and trailing edge.

IMPLICATIONS TO FUTURE SPACECRAFT

Spacecraft designers frequently need coatings with α_s and ε_t values tailored for a particular application. These requirements range from low α_s/high ε_t for many thermal radiator applications to many other combinations of low-to-high α_s and low-to-high ε_t. Figure 15 shows the range of coatings and films that can be prepared in the laboratory. However this range of available materials is more limited for space applications. Figure 16 shows that even though the selection is more limited there is still a wide range of coatings suitable for short-term applications. For long-term applications, this range of suitable materials is severely limited (Figure 17). The "LDEF test" validated only a few of these coatings for long-term applications. These include Z-93 and YB-71 white ceramic coatings, silver Teflon™ (when properly applied), thin chromic acid anodized aluminum and possibly D-111 black ceramic coating.

Because of the different combinations of space environment constituents, the range of coatings that are usable in geosynchronous earth orbit (GEO) are somewhat different than for LEO applications, but are also very limited (Figure 18).

With the limited range of proven coatings, designers of space hardware for long-term missions must accommodate the optical properties (α_s, ε_t) of these coatings. The behavior of coatings in the space environment is still not well understood, and conservative end-of-life estimates for coatings must be used. Until this materials/environment interaction is better understood and improved coatings are developed, the stability of coatings in the space environment will continue to be a limiting factor in the technology for long term missions.

CONCLUSION

The LDEF and its complement of experiments have provided unique data for the long-term effects of the space environment on thermal control materials. These data have already played a significant role in the selection of materials for S.S. *Freedom* and other space missions. While the "LDEF test" is currently the definitive data, there is significant spread in the data, and many questions remain about the synergistic effects of the space environment on materials. Additional flight experiments dedicated to materials effects are needed to better understand the response of materials to various environments. These experiments should include active experiments that perform optical and other measurements similar to those performed in ground laboratories. These experiments will provide the additional benefits for improved lifetime prediction models and better ground simulation testing. Many materials were badly degraded during the extended LDEF mission. Only a few thermal control coatings passed the "LDEF test." New materials are needed to broaden the range of stable coatings for long term applications.

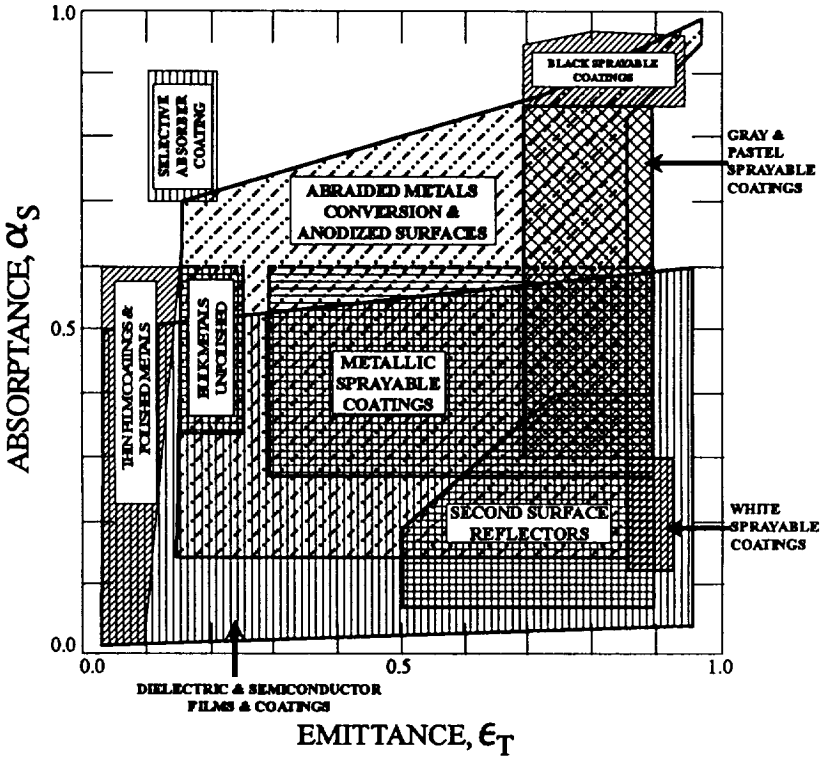

Figure 15. Available coatings and surfaces.

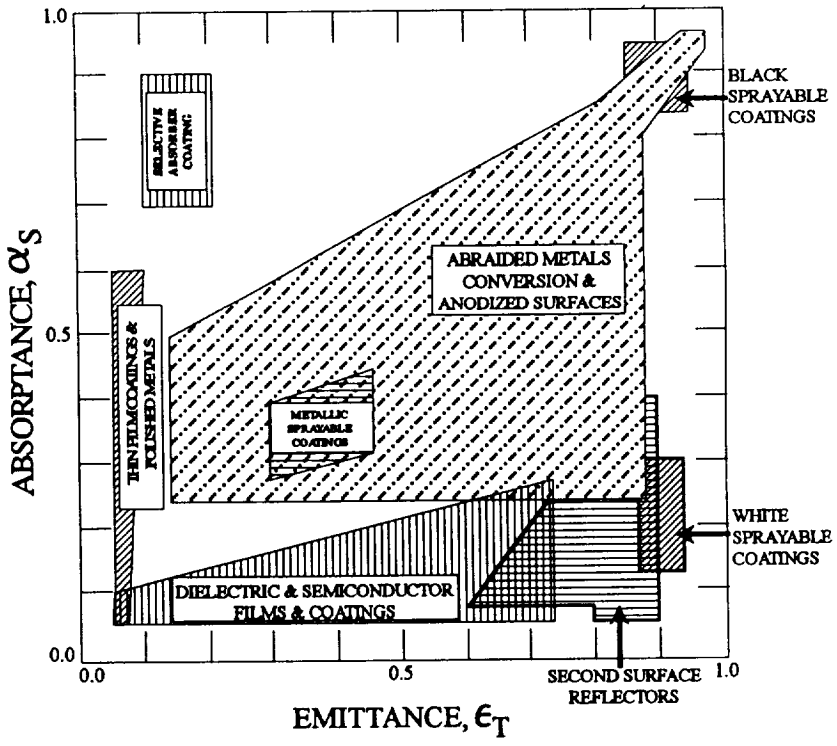

Figure 16. Usable coatings and surfaces—LEO short term.

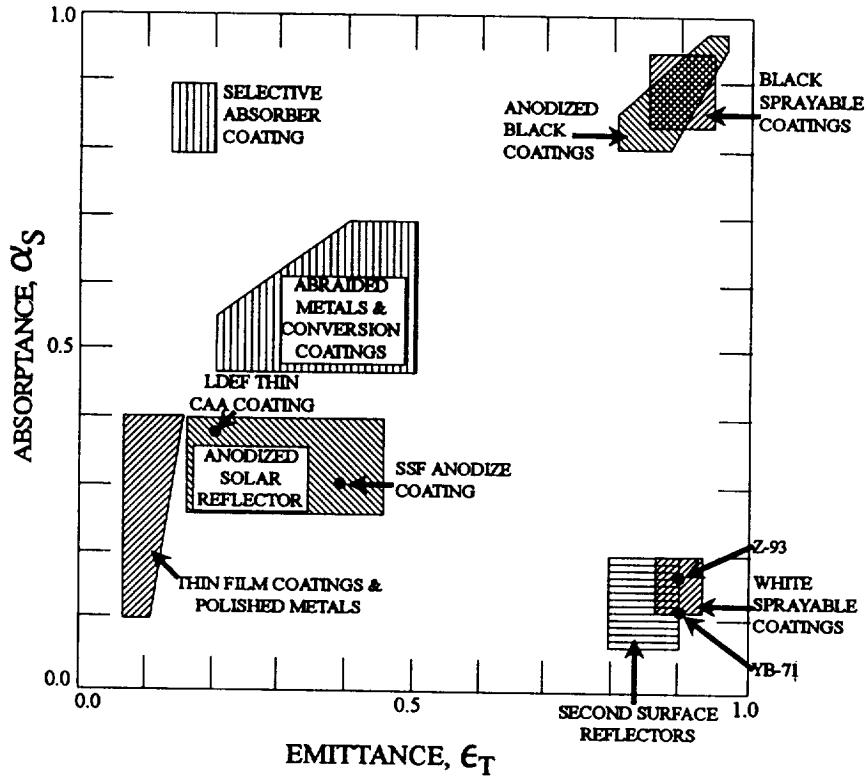

Figure 17. Usable coatings and surfaces—LEO >5 years.

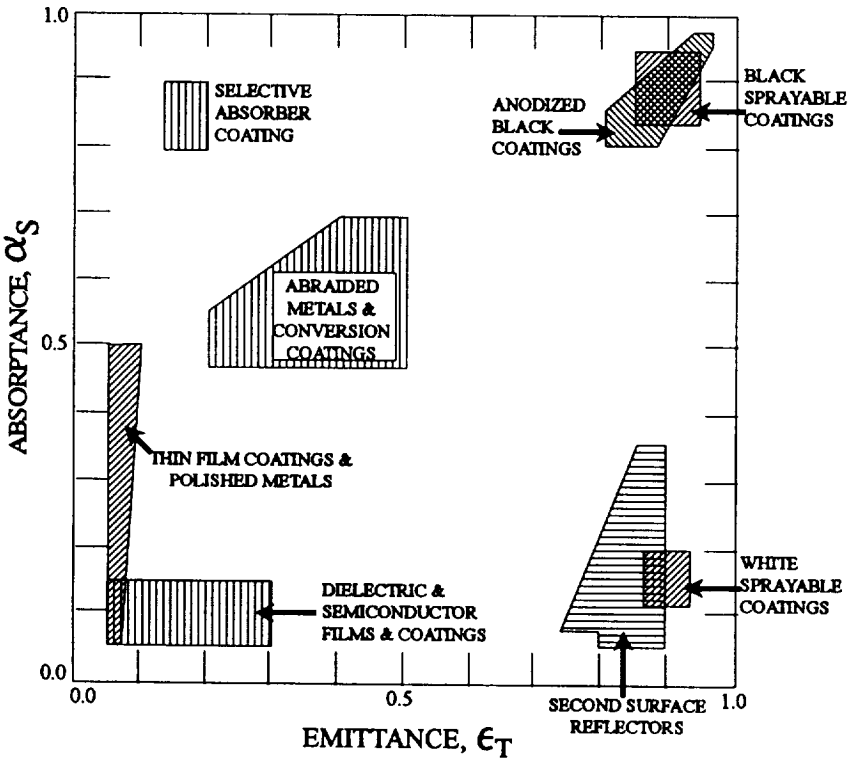

Figure 18. Usable coatings and surfaces—GEO 1 to 7 years.

REFERENCES

1. Bourassa, R.J., Gillis, J.R., and Rousslang, K.W.: "Atomic Oxygen and Ultraviolet Radiation Mission Total Exposures for LDEF Experiments." LDEF—69 Months in Space, First Post-Retrieval Symposium, NASA CP3134, June 2–8, 1991, pp. 643–661.

2. "LDEF Atomic Oxygen Fluence Update." NASA Conference Publication 3162, November 1991, pp. 59–69.

3. Banks, B., et.al.: "Atomic Oxygen Interactions with FEP Teflon™ and Silicones on LDEF." LDEF—69 Months in Space, First Post-Retrieval Symposium, NASA CP3134, June 2–8, 1991, pp. 801–816.

4. Pippin, H.G., and Crutcher, E.R.: "Contamination on LDEF Sources: Destruction and History." LDEF—69 Months in Space, Second Post-Retrieval Symposium, June 1–5, 1992.

5. Crutcher, E.R., et.al.: "Molecular Films Associated with LDEF." LDEF—69 Months in Space, First Post-Retrieval Symposium, NASA CP3134, June 2–8, 1991, pp. 155–177.

6. Harvey, G.A., et.al.: "Sources and Transport of Silicone NVR." NASA Conference Publication 3162, November 1991, pp. 175–184.

7. Zwiener, J., et.al.: "Unusual Materials Effects Observed on the Thermal Control Surfaces Experiment (S0069)." LDEF—69 Months in Space, First Post-Retrieval Symposium, NASA CP3134, June 2–8, 1991, pp. 919–934.

8. Wilkes, D.R., et.al.: "Thermal Control Surfaces Experiment Initial Flight Data Analysis Final Report." Report No. 90-1-100-2, June 1991.

9. Wilkes, D.R., et.al.: "The Continuing Materials Analysis of the Thermal Control Surfaces Experiment." LDEF—69 Months in Space, Second Post-Retrieval Symposium, June 1–5, 1992.

BIBLIOGRAPHY

Golden, J.: "Selected Results for LDEF Thermal Control Coatings, M0003-8." LDEF—69 Months in Space, Second Post-Retrieval Symposium, June 1–5, 1992.

Guillaumon, J.C., et.al.: "Spacecraft Thermal Control Coatings." LDEF—69 Months in Space, First Post-Retrieval Symposium, NASA CP3134, June 2–8, 1991, pp. 945–960.

Hurley, C.J.: "Long Duration Exposure Facility Experiment M0003-5 Thermal Control Materials." LDEF—69 Months in Space, First Post-Retrieval Symposium, NASA CP3134, June 2–8, 1991, pp. 961–974.

Jaggers, C., et.al.: "Thermal Control Paints on LDEF: Results of Sub-Experiment 802-18 M0003." LDEF—69 Months in Space, Second Post-Retrieval Symposium, June 1–5, 1992.

Kauder, L.: "Preliminary Results for the LDEF/HEPP Thermal Control Samples." LDEF—69 Months in Space, First Post-Retrieval Symposium, NASA CP3134, June 2–8, 1991, pp. 797–800.

Mirtich, M., et.al: "Ion Beam Textured and Coated Surfaces Experiment (IBEX)." LDEF—69 Months in Space, First Post-Retrieval Symposium, NASA CP3134, June 2–8, 1991, pp. 989–1004.

Pippin, H., et.al.: "Survey of Results from the Boeing Modules on the M0003 Experiment on LDEF." LDEF—69 Months in Space, First Post-Retrieval Symposium, NASA CP3134, June 2–8, 1991, pp. 1109–1114.

Whitaker, A.: Solar Array Materials and Passive LDEF Exposure, AO171, NASA, MSFC, private communication.

Wilkes, D.R., et.al.: "Thermal Control Surfaces on the MSFC LDEF Experiments." NASA Conference Publication 3162, November 1991, pp. 187–209.

PERFORMANCE OF SILVERED TEFLON™ THERMAL CONTROL BLANKETS ON SPACECRAFT

Gary Pippin
Boeing Defense & Space Group
Seattle, WA 98124-2499
Telephone: (206) 773-2846

Wayne Stuckey
Carol Hemminger
The Aerospace Corporation
Los Angeles, CA 90009-2957
Telephone: (310) 336-7389/(310) 336-1619

INTRODUCTION

Silverized Teflon™ (Ag/FEP) is a widely used passive thermal control material for space applications. The material has a very low α/e ratio (<0.1) for low operating temperatures and is fabricated with various FEP thicknesses (as the Teflon™ thickness increases, the emittance increases). It is low outgassing and, because of its flexibility, can be applied around complex, curved shapes. Ag/FEP has achieved multiyear lifetimes under a variety of exposure conditions, as demonstrated by the Long Duration Exposure Facility (LDEF) (ref. 1), Solar Max (ref. 2), Spacecraft Charging at High Altitudes (SCATHA) (ref. 3), and other flight experiments (refs. 4, 5). Ag/FEP material has been held in place on spacecraft by a variety of methods: mechanical clamping, direct adhesive bonding of tapes and sheets, and by Velcro™ tape adhesively bonded to back surfaces. On LDEF, for example, 5-mil blankets held by Velcro™ and clamping were used for thermal control over 3- by 4-ft areas on each of 17 trays. Adhesively bonded 2- and 5-mil sheets were used on other LDEF experiments, both for thermal control and as tape to hold other thermal control blankets in place.

Performance data over extended time periods are available from a number of flights. The observed effects on optical properties, mechanical properties, and surface chemistry will be summarized in this paper. This leads to a discussion of performance life estimates and other design lessons for Ag/FEP thermal control material.

LDEF RESULTS SUMMARY

The LDEF flight has provided the opportunity to substantially increase our knowledge of the performance of Ag/FEP in low Earth orbit (LEO), improving our understanding of both the expected performance and the limitations of this material. Specimens on the leading edge (rows 7 to 11) of the LDEF were exposed to both atomic oxygen (AO) and solar ultraviolet (UV). Those specimens located toward the trailing edge (rows 1 to 5 and 12) received only the solar exposure. Row 6 was a transition region, with some exposure to AO, but at reduced levels relative to the leading edge rows.

Optical Properties

A variety of visible changes were observed in the Ag/FEP surfaces on both leading- and trailing-edge samples. The exposed leading-edge blanket surfaces appeared uniformly foggy or clouded. The exposed trailing-edge blanket FEP surfaces were "patterned" in some areas with alternating transparent and clouded bands. Clouded areas were observed on many blanket edges, particularly near the bends between exposed and masked material ("transition zone"). Areas of orange/brown discoloration were notable near some of the keyhole-shaped vent slots along the edges of the Ag/FEP blankets.

A large number of optical property measurements were made on LDEF blankets (ref. 6). For the baseline measurement, areas not visibly contaminated and with no visible impacts and/or delaminations were chosen. Figures 1 and 2 show the distribution of end-of-mission absorption and emittance values around the LDEF. Solar absorptance remained constant to within experimental uncertainty, except for small areas where contaminant films were deposited or impacts had occurred. Locations that were adhesively bonded to an aluminum substrate were darkened in areas where cracking of the silver and Inconel™ layers allowed the underlying adhesive to bleed through over time and be exposed to solar radiation (ref. 7). This process led to increases in absorptance up to 0.25-in small areas. Data from both Boeing Defense & Space Group and the European Space Research and Technology Centre (ESTEC) show the expected decrease in emissivity as the thickness is decreased. The thickness change observed from leading-edge blankets was a consequence of atomic oxygen reaction with the FEP surface after the polymer structure was altered by vacuum ultraviolet (VUV) photons. Most blanket areas from the trailing-edge side, exposed only to solar UV, remained specular. The diffuse reflectance increased for those areas toward the leading edge roughened by exposure to both atomic oxygen and solar UV, giving rise to the uniformly clouded appearance.

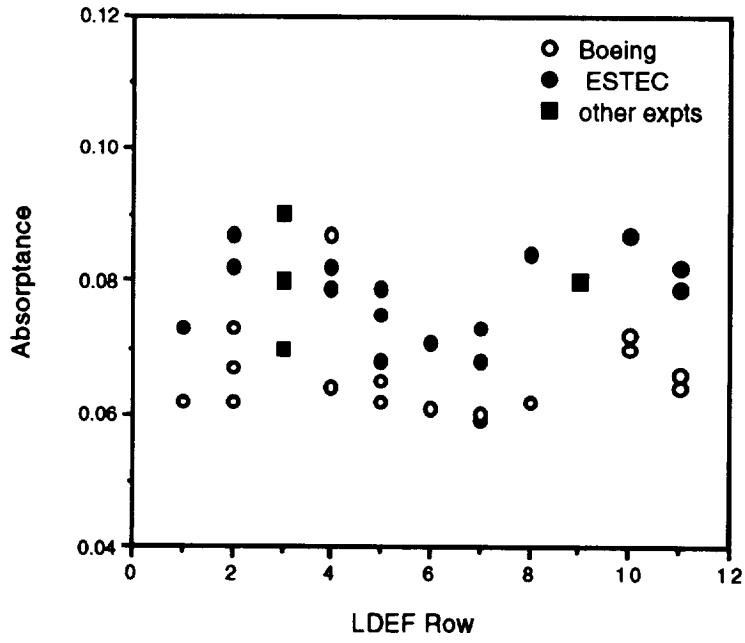

Figure 1. Absorptance of Ag/FEP versus location on LDEF.

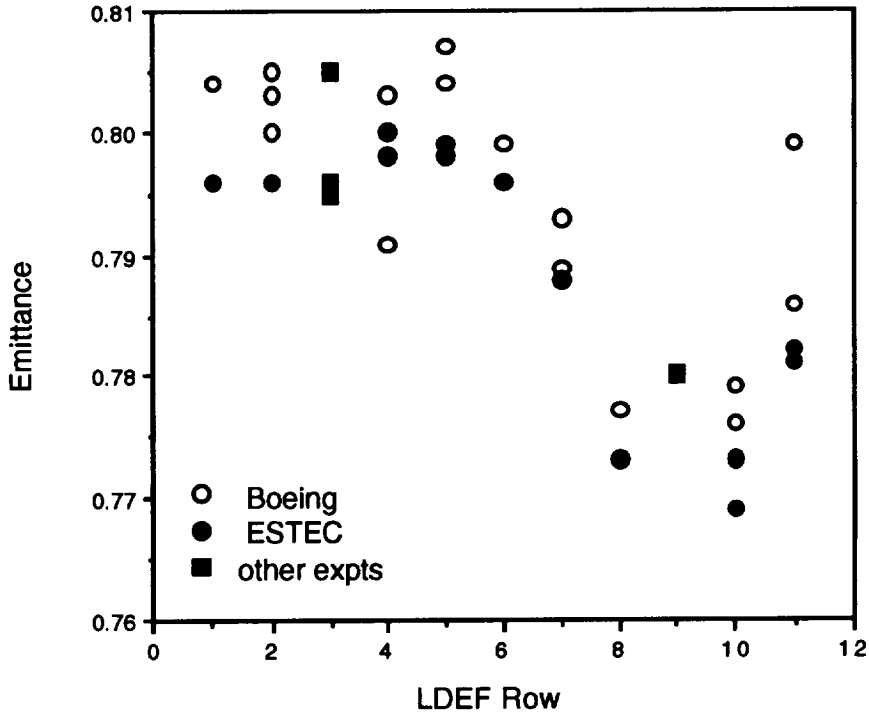

Figure 2. Emittance of Ag/FEP versus location on LDEF.

Mechanical Properties

Mechanical property changes that occurred in 5-mil Ag/FEP on LDEF (ref. 8) are indicated by the property data in Table 1. FEP from the trailing edge that was embrittled due to solar exposure had ultimate tensile values decreased by about one-third relative to controls. The percent-elongation to failure of the solar UV embrittled material also decreased by about 20 percent, while the recessed FEP from the leading edge was still flexible with percent-elongation to failure values only slightly decreased relative to controls. The leading-edge mechanical properties are not significantly different, although thinning of the Teflon™ would ultimately lead to reduced mechanical properties.

Comparisons between specimens from the leading edge and trailing edge, which had each been flexed over a 90° corner, showed that the FEP from the leading edge was still intact, and no cracking was visible under a × 100 microscope. FEP from the trailing edge, which showed no cracking prior to flexure, showed a large number of parallel cracks in the area of the specimen flexed around the radius. These cracks did not extend completely through the FEP layer, leading to the conclusion that only the UV-damaged portion of the FEP was cracking. This observation, together with the tensile measurements and the observation that up to about 20 percent of the thickness was recessed from the leading-edge specimens, suggests that significant UV damage extended about one-quarter of the way through the material.

Table 1. Mechanical properties changes of FEP with exposure on LDEF.

FEP From Ag/FEP Blankets	Percent Elongation to Failure (±40 percent)	Ultimate Tensile Strength, N/mm^2 (±3 N/mm^2)
Trailing Edge, Rows 1 to 6		
Exposed	230	14
Masked	300	21
Leading Edge, Rows 7 to 11		
Exposed	290	19
Masked	310	20

The Ag/FEP tapes holding the thermal control blankets for the Naval Research Laboratory cosmic-ray detection experiment (M0001) failed along at least two sides of every blanket. The most likely cause was shrinking and stretching due to thermal cycling. Some aluminum-backed FEP specimens from The Aerospace Corporation Space Environmental Effects on Materials Experiment (M0003) also failed mechanically during flight. This failure has been attributed to stress induced by thermal cycling and not to any significant material property change. The Ag/FEP blankets mounted with Velcro™ from the back, with large areas free to stretch during solar exposure, did not fail. Ag/FEP material adhesively bonded to aluminum substrates also remained intact mechanically. Cracking of the silver and Inconel™ layers of adhesively bonded Ag/FEP films have been attributed to flexing/stretching during preflight application to hardware (refs. 7, 9), and not to on-orbit stresses.

Surface and Chemical Analyses

The leading-edge samples of Ag/FEP from rows 7 to 11 all had roughened surfaces typical of high-velocity atomic oxygen erosion of polymers. The highly textured surfaces gave rise to diffuse light scattering and the consequent cloudy appearance. The FEP reaction efficiency on the leading edge was measured at 0.34×10^{-24} cm^3/O atom (ref. 10). Analysis by x-ray photoelectron spectroscopy (XPS) of the exposed surfaces showed that the surface composition and chemistry of the FEP remaining after erosion was indistinguishable from the control FEP, except for trace amounts of some contaminants, including oxygen (refs. 11, 12). Most deposited contaminants and damaged polymer were removed during atomic oxygen erosion.

The FEP surfaces exposed on the trailing edge of LDEF underwent changes that were observed both by scanning electron microscopy (SEM) and XPS. Within short distances on some trailing-edge samples, both the surface morphology and surface contamination levels were observed to change dramatically (refs. 11,12). The FEP surfaces nearest to row 3 were moderately to heavily contaminated, and the blanket surface areas that appear fogged or cloudy had become sufficiently diffuse to be observed visibly. Further from row 3, FEP surfaces showed little texture development and no significant contamination except oxygen, possibly from postflight exposure to moisture.

XPS data for the trailing-edge surfaces fell into two categories. The first was characterized by low contamination levels (Si < 1 percent) and a carbon 1s spectrum that arises from degradation

of the FEP surface. The spectral changes were consistent with damage to the carbon backbone of the Teflon™ polymer, resulting in molecular weight degradation, new chain terminations, branching, and crosslinking through free-radical reactions. The solar UV radiation exposure of the LDEF surfaces caused this FEP surface degradation. The FEP surfaces were also exposed to the stress of about 34,000 thermal cycles with calculated minimum temperatures of about –54 °C, but the maximum temperatures calculated for Ag/FEP blankets on LDEF were less than 0 °C and not sufficient to break chemical bonds. The second category of trailing-edge surfaces was characterized by moderate to high levels of surface contamination (Si, O, C, N, and S, and sometimes Cl). Contaminant carbon, thought to build up on the trailing-edge surfaces from decomposition products of outgassed silicones and hydrocarbons, was distinguished from FEP and degraded FEP carbon by binding energy, and was measured at $\leq$ 20 percent of the total surface composition. The predominant chemical state of Si identified on the trailing-edge FEP surfaces was SiO_2. The contaminant film was probably patchy on a submicron scale, with significant areas covered by <100 Å of deposited contamination.

COMPARISON WITH OTHER FLIGHT EXPERIENCE WITH AG/FEP

Prior to shuttle operations, a number of spacecraft flew with either Ag/FEP or Al/FEP material as test specimens on thermal control coating experiments (refs. 3–5,13,14). Thermal data from each of these experiments were telemetered to the ground, and the optical properties data were deduced indirectly from the calorimetry, as shown in Table 2. Spacecraft at altitudes ranging from tens to hundreds of thousands of kilometers showed rather large changes in absorptance over time. Among spacecraft flown at altitudes less than 1,000 km, specimens on both 0S0-H (ref. 13) and ML-101 (ref. 14) experiments showed rapid changes of about 0.02-in absorptance during the first month in orbit, followed by very slow, small changes over the following months and years. A likely cause of the early changes was contamination due to rapid outgassing and initial venting of the spacecraft.

The Solar Max repair mission, conducted on STS-41-C after the deployment of LDEF in 1984, returned 5-mil Ag/FEP surfaces that had been in orbit from February 1980 until April 1984 at altitudes that decreased from 574 to 491 km. Postflight measurements of solar absorptance (α_S) were made in many areas with values of 0.06 to 0.11 representing 80 to 90 percent of the Ag/FEP area (ref. 2). As was observed on LDEF, these areas show minimal degradation compared to typical values of 0.05 to 0.07 for unflown Ag/FEP. In the remaining area, the solar absorptance had increased to values ranging from 0.28 to 0.4, but in these regions, the silver Teflon™ either had been visibly contaminated or had environmental exposure on both sides of the film, resulting in severe degradation of the inconel and silver metallization layers. The tensile strength and elongation were also measured on the returned Solar Max samples with results similar to the changes observed on the LDEF samples. The thermal control performance of Ag/FEP in the LEO environment has generally been stable unless erosion of the Teflon™ on the leading edge by atomic oxygen erosion occurs, which can obviously result in emissivity changes. The more recent shuttle flights were too short in duration to cause large changes in the Ag/FEP (ref. 15).

Table 2. Flight experience with metalized Teflon™.

Altitude (Inclination)	Spacecraft	Thermal Property Changes
235,639 × 201,599 km(17°)	IMP-H	$\Delta\alpha_s \geq 0.07$ over 12,000 ESH
237,056 × 370 - 1600 km (29°)	IMP-1	Large $\Delta\alpha_s$ over time
43,288 × 27,578 km (7.9°)	P78-2 (SCATHA)	$\Delta\alpha_s > 0.2$ over 10 years (~27,800 ESH)
778 × 737 km (98°)	ML-101	$\Delta\alpha_s < 0.02$ initial ;then low $\Delta\alpha_s$ over time
574 - 491 km (28.5°)	Solar Max	$\Delta\alpha_s \leq 0.04$ typical; some areas 0.28 to 0.4 (~4 years)
560 × 327 km (33°)	OSO-H	Rapid $\Delta\alpha_s$ /e ~0.02, then constant (~8,000 ESH)
480 - 330 km (28.5°)	LDEF	$\Delta\alpha_s \leq 0.01$ typical; some areas >0.24 (~5.8 years)
270 km (28.5°)	STS-41G Shuttle Flight (EOIM-II)	Slight Changes (<100 ESH)
220 km (28.5°)	STS-8 Shuttle Flight (EOIM-I)	Slight Changes (<100 ESH)

Results from SCATHA are now available that cover 10 years of on-orbit performance of thermal control materials at geosynchronous altitudes (ref. 3). In 5 years, both 5-mil and 2-mil Ag/FEP had degraded to α_S values of greater than 0.24 due to electron and proton radiation. Contamination on SCATHA was probably not significant in these measurements, and these data should represent the material performance at geosynchronous altitudes. The Interplanetary Explorer missions IMP-H and IMP-1 (ref. 13) were flown at even higher altitudes, which have a similar UV and solar wind environment as geosynchronous altitudes, but are beyond the trapped-radiation, charged-particle belt. The Ag/FEP samples showed less degradation than observed on SCATHA.

The flight recession rate data for Ag/FEP shown in Table 3 comes from essentially three sources: shuttle flights (ref. 15), results from a Lockheed Missiles & Space Company, Inc. experiment published in 1985 (ref. 16), and the LDEF exposures (ref. 10). The Effects of Oxygen Interaction with Materials (EOIM) experiments were based on a well-documented exposure on orbit and measurements of the returned flight samples. Due to the short mission, which limited oxygen atom fluence and also the UV exposure, the erosion of the Teflon™ was too low on EOIM I and II to make an accurate measurement. A limit for the erosion rate was determined to be ≤0.05 cm^3/O atom. FEP exposed to atomic oxygen for the first 2 months on the Lockheed flight experiment showed little recession. After 2 months and ~100 ESH UV, the optical properties of the Ag/FEP on the Lockheed flight began to change in a manner suggesting material recession. For the last few days of exposure on the Lockheed experiment, the calculated recession rate was only about 0.13×10^{-24} cm^3/O atom, barely one-third of the average LDEF rate. The Teflon™ surfaces returned from the Solar Max Repair Mission did show evidence of the characteristic texture of an oxygen atom-eroded surface, but measurements of material loss were not reported.

The well-documented erosion observed for silver Teflon™ on the leading edge of LDEF results in a higher reaction efficiency for FEP Teflon™ than observed previously. This indicates that a synergistic effect exists with the atomic oxygen and UV. In contrast, linear relationships were observed for polymers such as Kapton, and there is good agreement on reaction efficiency between

these same missions. The UV degradation, clearly indicated in the studies of the trailing-edge Teflon™ surface from LDEF, is undoubtedly responsible for the higher erosion observed on LDEF (ref. 11). The LDEF mission had a high UV exposure followed by an increasing atomic oxygen fluence during the flight, which resulted in nearly an order of magnitude higher reaction efficiency than observed on earlier flights. These data confirm that atomic oxygen-induced recession of FEP in LEO is also a function of UV exposure level.

Table 3. Flight measurements of FEP Teflon™ reaction efficiency.

Flight	Atomic Oxygen Fluence (Atoms/cm^2)	Ultraviolet (Hr)	Reaction Efficiency (cm^3/O atom)
STS-8 Shuttle Flight (EOIM-I)	8.58×10^{19}	≤50	Not measured
STS-41G Shuttle Flight (EOIM-II)	3.5×10^{20}	≤50	$<0.05\times10^{-24}$
Solar Max	$\sim7\times10^{20}$	Unknown	Not measured
Lockheed Experiment	1.85×10^{22}	300	0.075 to 0.13×10^{-24}
LDEF	3.3 to 9.0×10^{21}	6,000 to 11,000	0.34×10^{-24}

PERFORMANCE LIFE ESTIMATES

Materials performance lifetime limits can be determined by several factors: increases in the α/ε ratio, causing increases in temperature above the allowed performance values; mechanical failure of the material; tearing due to thermal-cycling-induced stresses; embrittlement by solar VUV radiation, causing subsequent cracking; impact damage, creating punctures and associated damage and/or darkening of a portion of the blanket; and redeposition of outgassed contaminant materials that darken and change the absorptance characteristics of the material. Combined information from shuttle flights (ref. 15), LDEF (refs. 8, 10), Solar Max (ref. 2), and other flights (ref. 16) demonstrates that the recession rate of the Ag/FEP increases under combined UV and AO exposure. LDEF results provide the highest measured recession rates for this material seen to date.

An estimate of the expected environmental degradation for a specified mission can be made from the mission profile, which establishes the orbit and required lifetime. End-of-life requirements for the optical properties must be established. At geosynchronous altitude, the SCATHA degradation curves could be used to estimate the performance life with exposure to the trapped radiation charged particle belt. In LEO orbits, the atomic oxygen flux is strongly dependent upon altitude and solar activity. The atomic oxygen and solar UV fluences are determined based on the mission profile, and the total recession over the life of the mission is predicted. The minimum required thickness of the Ag/FEP material at end-of-life is based on the well established values for emittance of FEP as a function of thickness. The actual recession rate used will depend on the expected duration of

the mission. For short periods of time in LEO, recession rates of 0.15×10^{-24} cm^3/O atom will be sufficient to establish recession. For missions of greater length, the LDEF value $0.34 \times 10^{-24} cm^3/O$ atom is clearly more appropriate. In practice, the known reaction efficiency and expected oxygen fluence are used to predict the expected life of a film with a given initial thickness.

Lifetime predictions should also include consideration of the fraction of the blanket surface that will likely be darkened or destroyed by impacts and potential absorptance increases due to contaminant films over a fraction of the surface. These considerations were minor for LDEF. Impacts darkened 2 percent or less of the surface area of each LDEF blanket and delaminated <5 percent of the area on each blanket. Contaminant films caused absorptance values as high as about 0.25, but only for relatively small surface areas. The minimum area required for a given radiator would need to be scaled up by only 5 percent to 10 percent to compensate for these effects.

DESIGN AND PERFORMANCE LESSONS

In summary, the cumulative space environmental effects on Ag/FEP were a function of location and exposure orientation. The LDEF results for silver Teflon™ indicate that the thermal performance shows minimal degradation from the solar UV exposures of up to 11,000 ESH. The charged-particle environment at these LEO altitudes is too low to cause degradation, but at higher altitudes, up to geosynchronous altitudes, the Teflon™ is susceptible to degradation. Above geosynchronous altitudes, Teflon™ may have longer lifetimes due to the lower charged-particle environment. At the lower LEO altitudes, atomic oxygen erosion may result in degraded properties, depending on total fluence levels. The leading edge of LDEF was dominated by the effect of the atomic oxygen, resulting in erosion of the Teflon™. The resulting surfaces were highly textured and not significantly contaminated. Contaminants and UV-degraded FEP were removed by the AO-induced surface erosion. The trailing-edge samples had a wide variety of surface morphologies, and extensive contamination was present. The chemical structure of the FEP that remained on leading-edge blankets was essentially identical to ground control specimens. On trailing-edge surface areas where contamination was relatively low (particularly at larger angles to the trailing edge), degraded FEP, caused by UV exposure, was detected using XPS measurements. This degradation appears to result from damage to the carbon backbone of the Teflon™ polymer, resulting in molecular weight degradation, new chain terminations, branching, and crosslinking through free-radical reactions. The UV degradation could have occurred at a relatively constant rate during the entire mission. Any increases in the rate would have occurred toward the end of the mission as the increased solar activity produced more energy in the VUV. Teflon™ erosion occurred more rapidly near the end of the mission as the altitude dropped and the atomic oxygen flux rapidly increased.

The problem of delamination of Ag/FEP thermal control material at the metal/polymer interface must still be addressed. This interface strength may degrade during Earth storage of Ag/FEP, and deterioration was accelerated in the space environment. Delamination of the Ag/FEP has the potential for catastrophic failure of the material's thermal control properties when unsupported; this was deterred on the LDEF blankets by the presence of the paint on the back surfaces. There is also interest in the effects of adhesive bonding on Ag/FEP performance. Discoloration and streaking was observed at the metal/polymer interface of adhesively bonded Ag/FEP on LDEF, with some degradation of thermal control properties. This was due to diffusion of adhesive components through cracks in the metalization layer, which were caused by improper application and/or handling.

Ag/FEP has demonstrated good performance over long-term exposures in selected environments. For a given design, the acceptability of metalized Teflon™, either silver or aluminum, will depend on assessing degradation due to the charged-particle or atomic-oxygen environment expected for the planned orbit and lifetime.

REFERENCES

1. Stein, B.A., and Pippin. H.G.: "Preliminary Findings of the LDEF Materials Special Investigation Group." LDEF—69 Months in Space First Post-Retrieval Symposium, ed. A.S. Levine, NASA Conference Publication 3134, 1992, pp. 617–641.

2. Park, J.J.: "Results of Examination of Materials from the Solar Maximum Recovery Mission." Proceedings of the SMRM Degradation Study Workshop, NASA Publication 408-SMRM-79-0001, pp. 211–225.

3. Hall, D.F., and Fote, A.A.: "Thermal Control Coatings Performance at Near Geosynchronous Altitude." AIAA J. Thermophysics and Heat Transfer, vol. 6, No. 4, October–December 1992, pp. 665–671.

4. Hoffman, R.H.: "Spaceflight Performance of Silver Coated FEP Teflon™ as a Thermal Control Surface on the IMP-1 Spacecraft." NASA GSFC X-762-73-113, April 1973.

5. Lehn, W.L., and Hurley, C.J.: "Skylab D024 Thermal Control Coatings and Polymeric Films Experiment." AIAA/AGU Conference on Scientific Experiment of Skylab, Huntsville, AL, October 30–November 1, 1974 (AIAA 74-1228).

6. Dursch, H.W., Spear, W.S., Miller, E.A., Bohnhoff-Hlavacek, G.L., and Edelman, J.: "Analysis of Systems Hardware Flown on LDEF—Results of the Systems Special Investigation Group." NASA Contractor Report 189628, 1992.

7. Zwiener, J.M., Herren, K.A., Wilkes, D.R., Hummer, L., and Miller, E.R.: "Unusual Materials Effects Observed on the Thermal Control Surfaces Experiment (S0069)." LDEF-69 Months in Space First Post-Retrieval Symposium, ed. A.S. Levine, NASA Conference Publication 3134, 1992, pp. 919–933.

8. Levadou, F., and Pippin, G.: "Effects of the LDEF Environment on the Ag/FEP Thermal Blankets." LDEF Materials Workshop '91, eds. B.A. Stein and P.R. Young, NASA Conference Publication 3162, 1992, pp. 311–344.

9. Hemminger, C.S.: "Investigation of Edge Discoloration of Silvered Teflon™ Thermal Control Tape on GPS Satellite Hardware." Aerospace Report No. TOR-009(5470-02)-1, July 15, 1991.

10. Banks, Bruce A., Gebauer, L., and Hill, C.H.: "Atomic Oxygen Interactions with FEP Teflon™ and Silicones on LDEF." LDEF—69 Months in Space First Post-Retrieval Symposium, ed. A.S. Levine, NASA Conference Publication 3134, 1992, pp. 801–815.

11. Hemminger, C.S., Stuckey, W.K., and Uht, J.C.: "Space Environmental Effects on Silvered Teflon™ Thermal Control Surfaces." LDEF—69 Months in Space First Post-Retrieval Symposium, ed. A.S. Levine, NASA Conference Publication 3134, 1992, pp. 831–845.

12. Hemminger, C.S.: "Surface Contamination on LDEF Exposed Materials." LDEF Materials Workshop '91, eds. B.A. Stein and P.R. Young, NASA Conference Publication 3162, 1992, pp. 159–174.

13. Triolo, J.J., Heaney, J.B., and Hass, G.: "Coatings In Space Environment." Optics in Adverse Environments, SPIE Vol. 121, 1977, pp. 46–66.

14. Prince, D.E.: "ML-101 Thermal Control Coating Spaceflight Experiment." AFML-TR-75-17, August 1975, and R.A. Winn, "ML-101 Thermal Control Coating Spaceflight Experiment." AFML-TR-78-99, July 1978.

15. "Atomic Oxygen Effects Measurements for Shuttle Missions STS-8 and 41-G," vols. I–III, J. Visentine, ed., NASA Technical Memorandum 100459, September 1988.

16. Knopf, P.W., Martin, R.J., Damman, R.E., and McCargo, M.: "Correlation of Laboratory and Flight Data for the Effects of Atomic Oxygen on Polymeric Materials." AIAA 20th Thermophysics Conference, Williamsburg, VA, June 19–21, 1985.

SPACE ENVIRONMENT DURABILITY OF BETA CLOTH IN LDEF THERMAL BLANKETS

Roger C. Linton, Ann F. Whitaker, and Miria M. Finckenor
NASA George C. Marshall Space Flight Center
Marshall Space Flight Center, AL 35812

INTRODUCTION

Beta cloth performance for use on long-term space vehicles such as Space Station *Freedom* (S.S. *Freedom*) requires resistance to the degrading effects of the space environment. The major issues are retention of thermal insulating properties through maintaining optical properties, preserving mechanical integrity, and generating minimal particulates for contamination-sensitive spacecraft surfaces and payloads. The longest in-flight test of beta cloth's durability was on the Long Duration Exposure Facility (LDEF), where it was exposed to the space environment for 68 months.

The LDEF contained 57 experiments which further defined the space environment and its effects on spacecraft materials. It was deployed into low-Earth orbit (LEO) in April 1984 and retrieved January 1990 by the space shuttle. Among the 10,000 plus material constituents and samples onboard were thermal control blankets of multilayer insulation with a beta cloth outer cover and Velcro™ attachments. These blankets were exposed to hard vacuum, thermal cycling, charged particles, meteoroid/debris impacts, ultraviolet (UV) radiation, and atomic oxygen (AO). Of these space environmental exposure elements, AO appears to have had the greatest effect on the beta cloth.

The beta cloth analyzed in this report came from the MSFC Experiment S1005 (Transverse Flat-Plate Heat Pipe) tray oriented approximately 22° from the leading edge vector of the LDEF satellite (ref. 1). Figure 1 shows the location of the tray on LDEF and the placement of the beta cloth thermal blankets. The specific space environment exposure conditions for this material are listed in table 1.

The beta cloth in this study was impregnated with TFE Teflon™. Similar blankets are used as a static-free fabric liner in the shuttle cargo bay and are proposed for use on S.S. *Freedom*. Specifications for this cloth are a weave count of 87 by 62 with an uncoated areal weight of 5.5 to 6.7 oz/yd^2 (186.5 to 227.2 g/m^2). The finished cloth contains 17 to 23 percent resin by weight.

Analyses were made on multiple specimens taken from various locations on the blanket including areas subject to AO and UV radiation impingement, areas shielded from incident AO, areas shielded from both AO and UV radiation, and control samples. Areas containing meteoroid/debris impacts were also removed and analyzed.

This report includes photographic evidence of changes in the beta cloth due to the space environment, thickness loss of the Teflon™, particulate contamination analysis, and evaluation of thermal properties. The Velcro™ and Dacron™ thread used to attach the beta cloth thermal blankets to the experiment tray are also analyzed.

PHOTOGRAPHIC OBSERVATIONS

The beta cloth blanket was relatively well preserved as noted during the postflight inspection. Further inspection using a black light for enhanced contrast provided some indication of space exposure effects. Under this illumination, the samples exposed to solar UV and only indirect AO were slightly darker than the control sample, and the AO-exposed samples were somewhat darker than these. This change is probably due to increased light absorption of the textured surface of eroded Teflon™ surface and of the exposed glass fiber matrix, rather than alteration of fluorescent properties.

Photographs taken with a scanning electron microscope indicate the change in beta cloth caused by space environment exposure. Figure 2 is of beta cloth removed from the folded underside of the blanket, protected from AO, radiation, and thermal cycling. The sample is intact. For comparison, Figure 3 is of beta cloth exposed to the leading edge environment, where Teflon™ erosion by impinging AO was most severe. However, the Teflon™ erosion did not release the embedded glass fibers. Teflon™ is visible between the fibers in areas shielded from direct impingement of AO. Erosion is evident to the extent seen. Figure 4 shows the fine erosion peaks typical of AO-eroded polymeric material at high magnification. Figure 5 is a still higher magnification SEM photo showing the remaining Teflon™ in the glass fiber weave. The AO erosion seemed to be limited to the first layer of glass fibers. The glass fibers prevented further erosion by staying in place and protecting the remaining Teflon™. Also, areas impacted by meteoroid and debris particles have pulled-up fibers, but these fibers remained in the matrix (Figures 6, 7).

After photographing the AO erosion, samples of beta cloth from the most heavily eroded areas were then turned upside down and photographed again. Figure 8 is of flight beta cloth, showing the underside that was protected from AO and UV radiation. Teflon™ in this matrix shows no erosion, which would only occur if AO were able to completely penetrate the beta cloth. Figure 9 is of beta cloth from the folded underside of the entire thermal blanket. This beta cloth looks very much like the original received from the manufacturer (Figure 10), with no cracking or loss of Teflon™. These photographs are of representative areas found on the beta cloth samples.

BETA CLOTH PROPERTY CHANGES

In beta cloth, the glass fibers are bonded with TFE Teflon™ to prevent fiber-to-fiber abrasion. AO erosion of the Teflon™ might result in the exposure of any loose glass fibers, lending to the generation of particulate contamination, and loss of thermal performance in the blanket. AO erosion data for TFE Teflon™ from LDEF Experiment A0171 (ref. 2), located at 38° off-RAM angle of incidence, provided a reactivity value of 2.0×10^{-25} cm^3/atom from a thickness loss of 0.55 mils (14.0 microns). Based on these results and the estimated AO fluence incident on the beta cloth from LDEF Experiment S1005[3] of 8.43×10^{21} atoms/cm^2, the predicted loss of TFE Teflon™ from the S1005 beta cloth is approximately 0.61 mils (15.5 microns).

Thickness measurements were taken on each of the four blanket samples using a micrometer. Samples taken from areas exposed to the leading edge space environment, areas shielded from direct AO, areas shielded from both AO and UV radiation, and control samples all had thicknesses in the range of 7.70 to 7.73 mils with no discernible systematic differences between the samples. This indicates that the fiberglass mat was not significantly affected by space exposure and that the actual

thickness loss of TFE Teflon™ cannot be measured directly. However, the thickness loss can be reasonably determined through weight change.

Samples of the same surface area were taken from various locations of the exposed area and the folded underside of the blanket and weighed. Assuming that the glass fiber particulate loss during flight is negligible and the density of TFE Teflon™ is consistent, the calculated average thickness loss of TFE Teflon™ is 0.24 mils (6.1 microns). This is in general agreement with the estimates based on SEM observations of apparent erosion and the remaining Teflon™ shielded by the glass fibers at the 22° off-RAM angle of AO incidence.

The beta cloth was also evaluated for sloughing. The samples were flushed with Freon™ over a Millipore filter collector. A soft brush was then used to wipe the beta cloth surface directly above another collector. The results from the sloughing are presented in Figures 9 to 12. These graphs show the number of particles of a particular size collected after the Freon™ flush and brushing. The largest dimension of the particle is counted. Control material from the manufacturer, beta cloth from the folded underside of the thermal blanket, and beta cloth fully exposed to AO and UV radiation were evaluated. SEM photos of similar samples with particulate contamination (Figures 2 and 3) agree with the sloughing results. The beta cloth exposed to AO had the least amount of particulate contamination, most likely due to erosion. The beta cloth from the folded underside of the thermal blanket was cleaner than the control sample, presumably as a result of preflight preparation.

Optical property measurements of the beta cloth were made using a Gier-Dunkle portable reflectometer model DB100 for infrared thermal emittance (ε) and portable reflectometer model MS251 for solar absorptance (α). The beta cloth manufacturer specifications require a nominal 0.8 minimum emissivity. Table 2 lists the sample exposure conditions and the optical property measurements taken. The measured variation in absorptivity and emissivity are considered to indicate no significant degradation in thermal performance.

VELCRO™ PROPERTY CHANGES

One problem that did occur with the thermal blankets was the degradation of the Dacron™ threads attaching the Velcro™ bonding strips to the blankets. Figure 13 reveals the deterioration of the Dacron™ exposed to AO. Although the blanket did not detach during flight, it came apart easily at this seam during deintegration of the experiment tray. For long-term LEO space use, this problem must be remedied with a change in thread to one that is not susceptible to AO erosion or a change in configuration to shield against AO attack. Figure 14 shows an intact seam which was shielded from direct AO by a heat pipe.

Figure 15 is of the observed bleaching effect of AO on the Velcro™. SEM photos of unexposed and exposed Velcro™ hooks (Figures 16 and 17) show the AO erosion. In some places, only nubs of nylon were left (Figure 18). The loops were similarly affected. In addition, the mechanical strength of the Velcro™ was degraded by space exposure. Peel tests on uneroded Velcro™ indicated a peel strength of 2.0 to 2.5 lb/in. Velcro™ that had been eroded and bleached had a peel strength of 1.2 to 1.7 lb/in.

CONCLUSION

Microphotographs indicate that the Teflon™ is removed by erosion from the outer surface of the beta cloth. The eroded Teflon™ surface has the characteristic morphology of polymeric materials exposed to orbital AO. However, evidence shows that the Teflon™ remained underneath the first layer of glass fibers, and the glass fibers remain in the matrix, protecting the underlying Teflon™. Minimal particulate generation and maintenance of thermal insulating properties were documented during this investigation.

While beta cloth's performance over a 30-year S.S. *Freedom* mission remains unqualified, beta cloth's performance in the near 6-year exposure on the LDEF provides the evidence for satisfactory retention of properties for extended space exposure. Beta cloth overlap of the Velcro™ is being recommended, and new materials and configurations are under consideration for replacement of Dacron™ as a result of degradation of these blanket elements. It is anticipated that with these changes, beta cloth thermal blankets will endure space environment exposure well beyond 6 years.

REFERENCES

1. NASA Conference Proceedings, First LDEF Post-Retrieval Symposium, Orlando, FL, June 2–8, 1991, presentation by David Shular, MSFC.

2. Whitaker, A.F., Finckenor, M.M., Kamenetzky, R.R.: "Property Changes Induced by the Space Environment in Polymeric Materials on LDEF." Submitted for publication to AIAA.

Table 1. Space environment exposure conditions of LDEF beta cloth.

• High Vacuum	- 10^{-6} to 10^{-7} Torr (estimated)
• UV Radiation	- 8,680 ESH (Estimated Sun Hours)
• Proton Fluence	- 10^{9} p+/cm^2 (0.05 to 200 MeV)
• Electron Fluence	- Range of 10^{12} e-/cm^2 at 50 keV energy to 10^{8} e-/cm^2 at 3.0 MeV energy
• AO	- 8.17×10^{21} atoms/cm^2
• Micrometeoroid/ Space Debris	- 424 impacts >0.1 mm diameter craters per square meter
• Thermal Cycles	- ~32,000 cycles

Table 2. Beta cloth optical property measurements uncertainty ±0.02.

	Vacuum Only	AO + UV	UV Only
Absorptivity	0.22	0.22	0.23
Emissivity	0.89	0.89	0.89

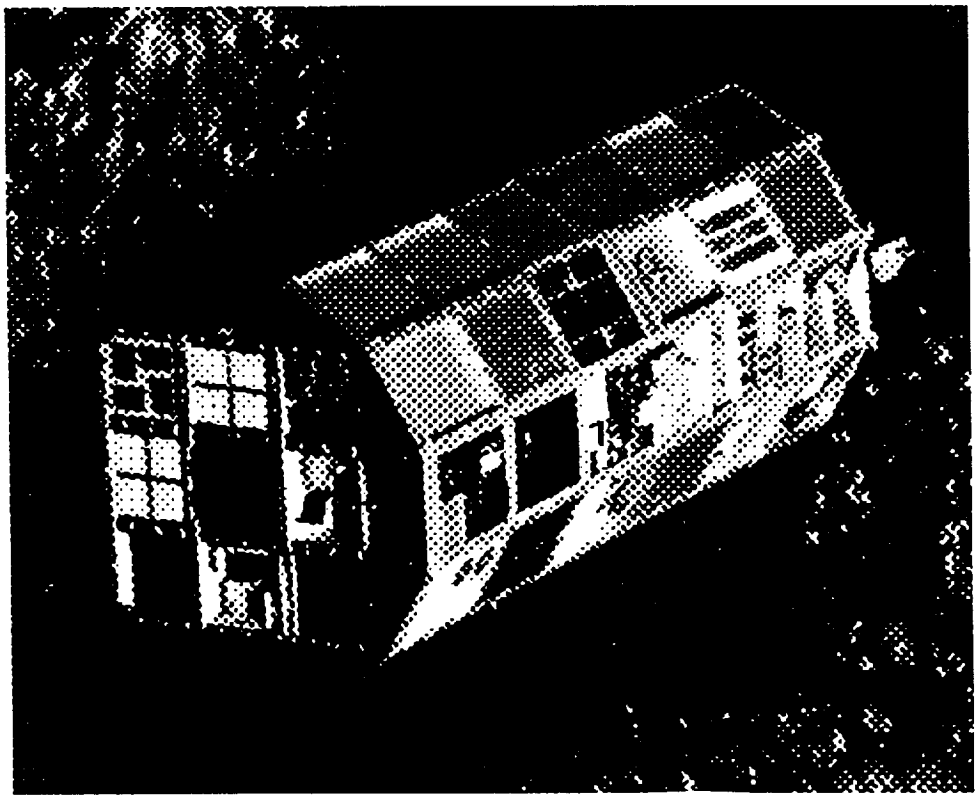

Figure 1. The LDEF.

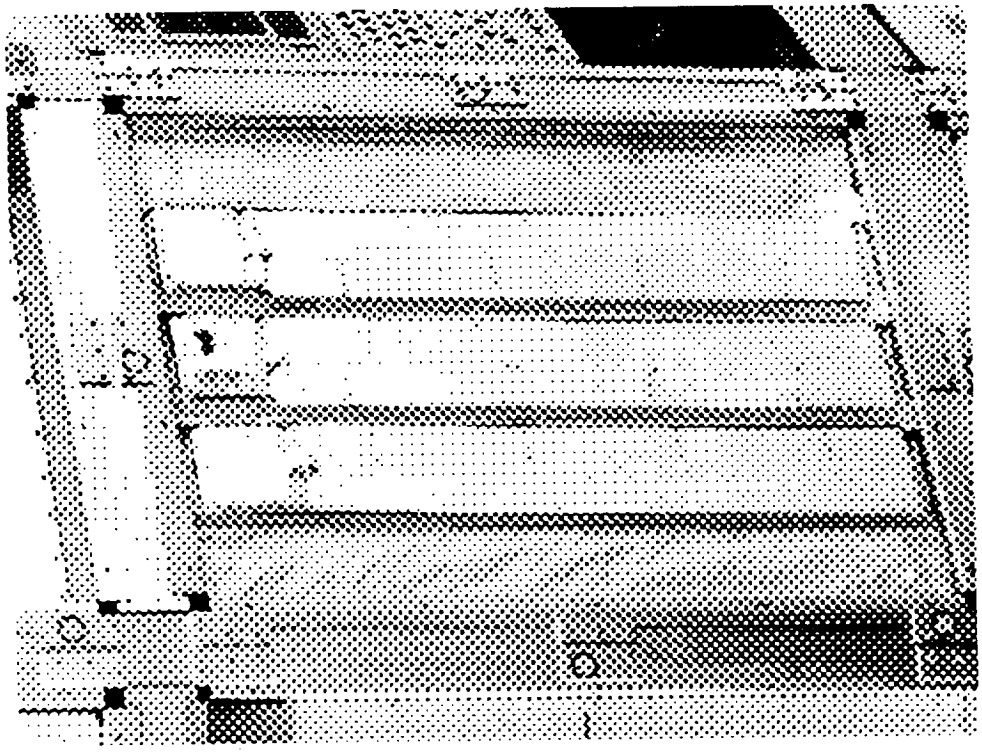

S1005 experiment, Tray B10, transverse flat plate heat pipe experiment.

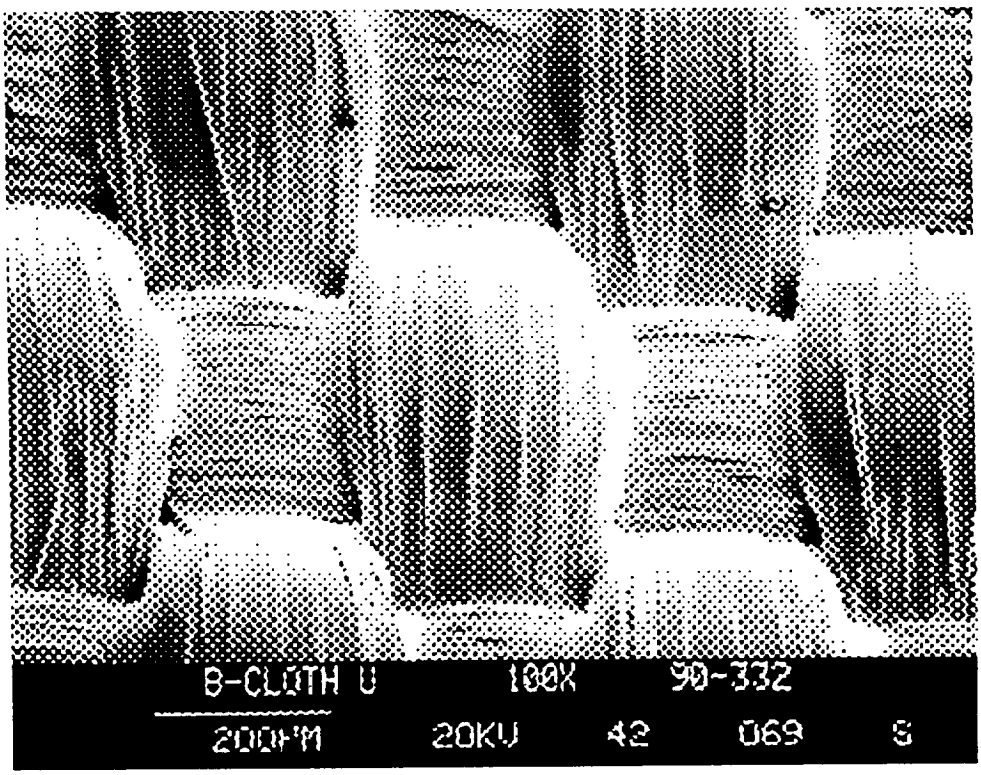

Figure 2. Beta cloth from folded underside of thermal blanket, protected from AO erosion.

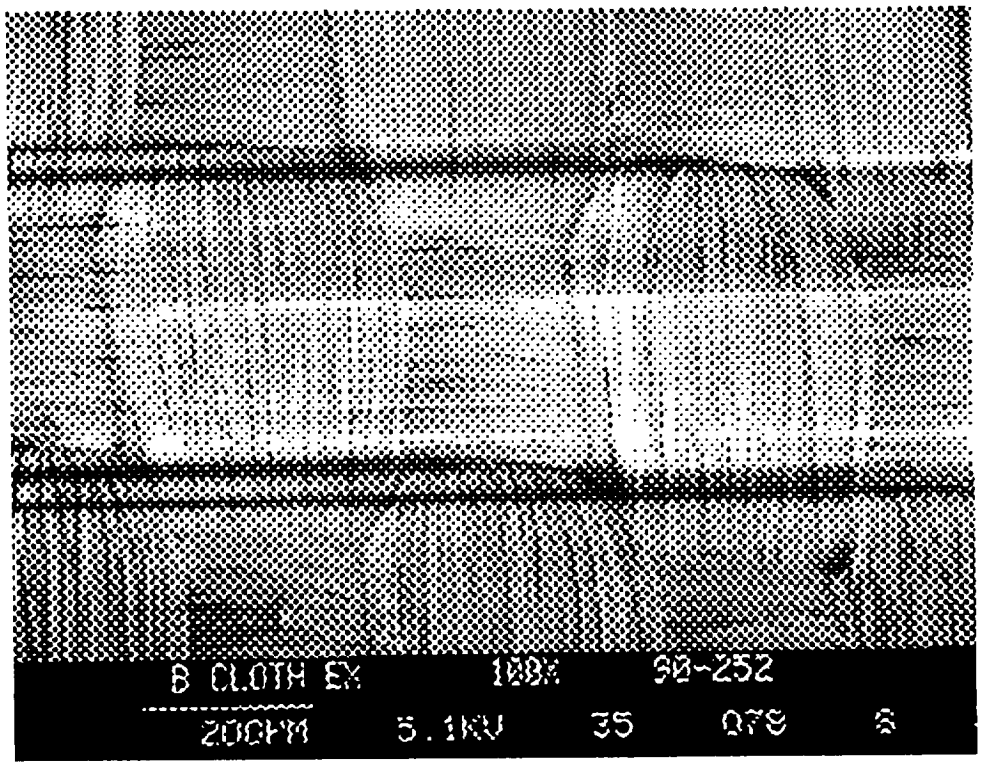

Figure 3. Beta cloth exposed to RAM environment.

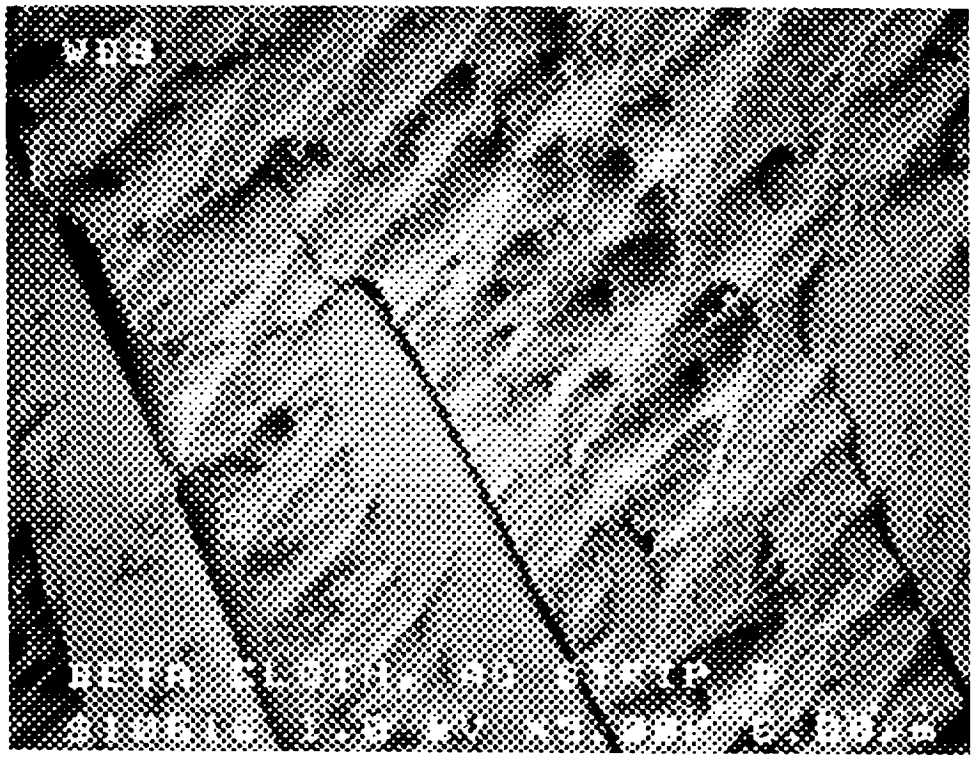

Figure 4. AO erosion peaks typical of Teflon™.

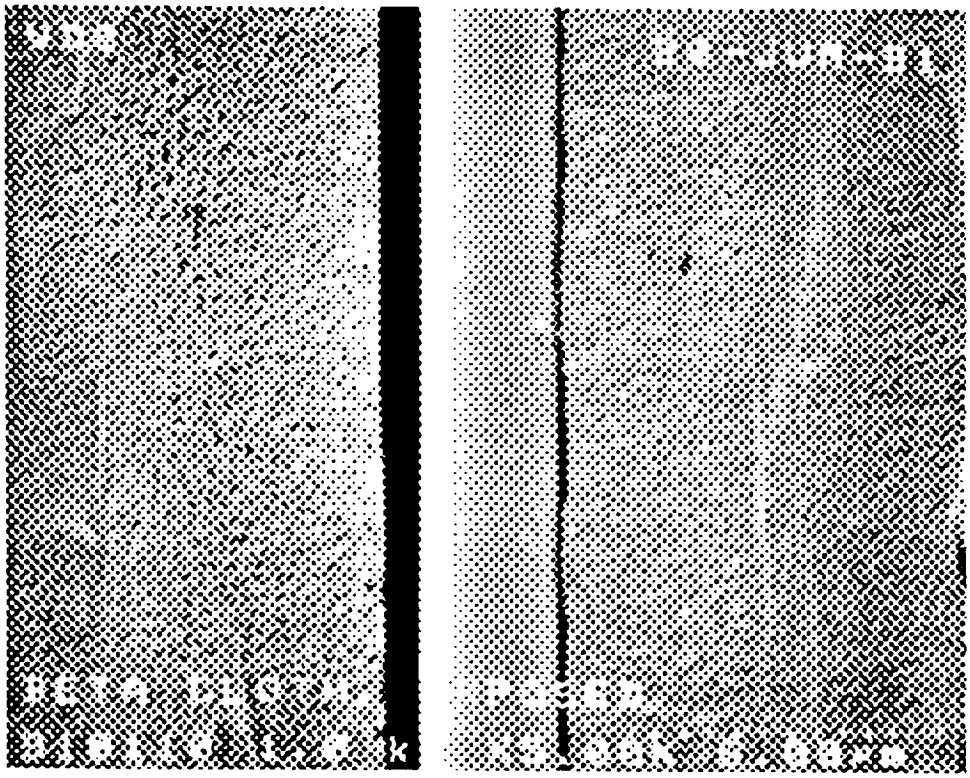

Figure 5. Remaining Teflon™ in glass fiber weave.

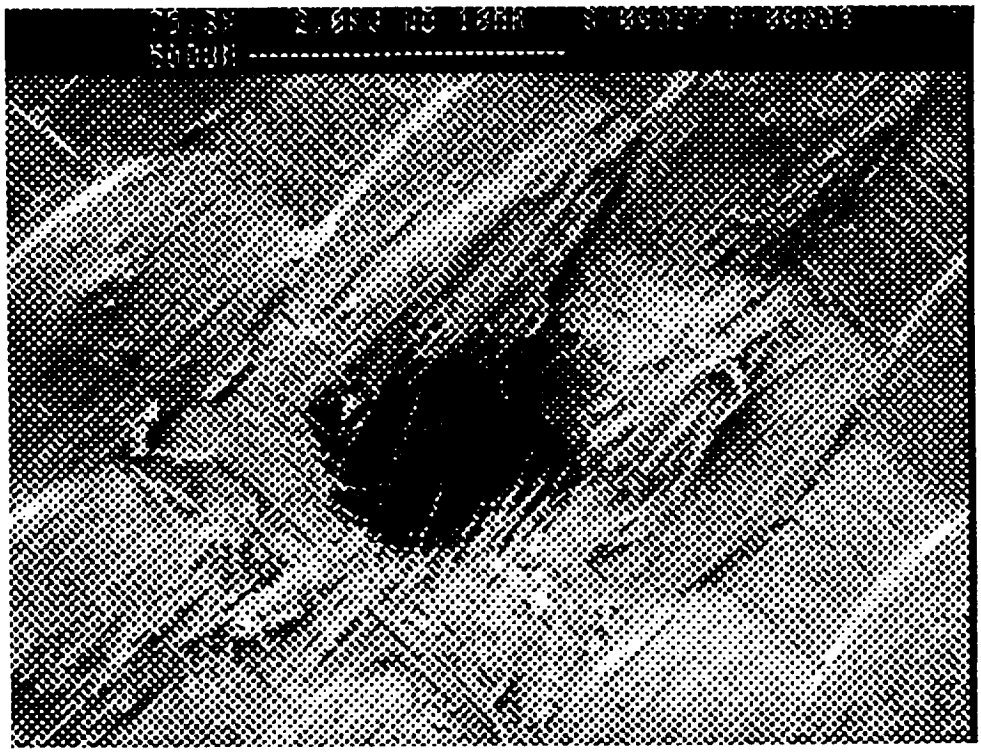

Figure 6. Meteoroid/debris impact in beta cloth.

Figure 7. Meteoroid/debris impact.

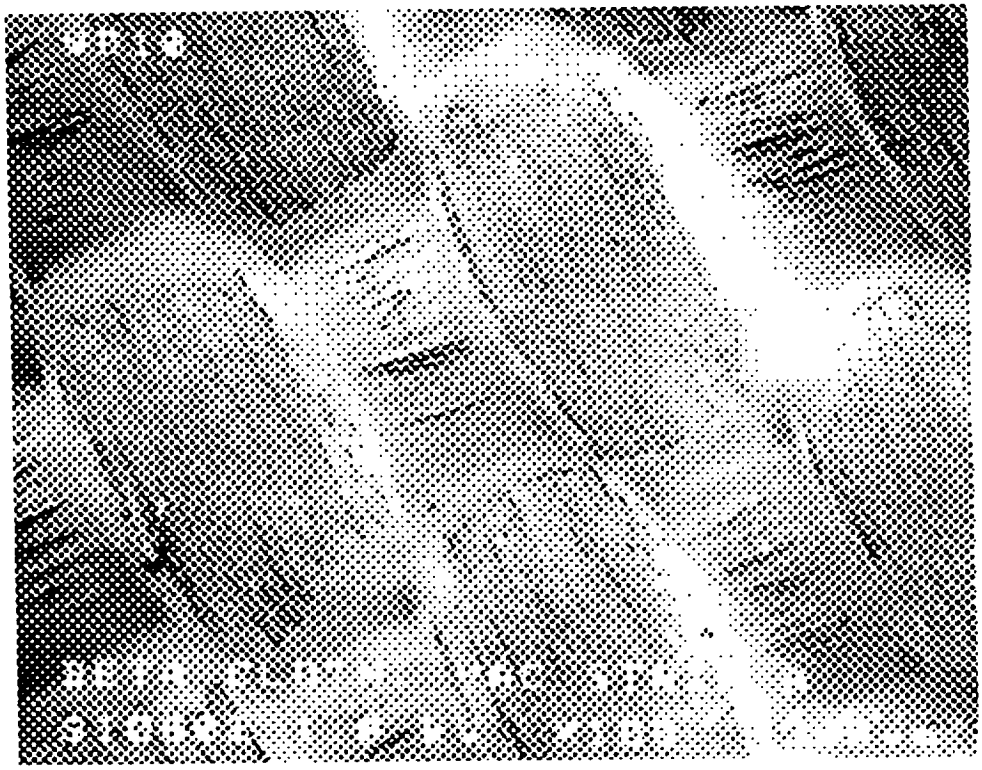

Figure 8. Underside of exposed beta cloth. No AO perforation visible.

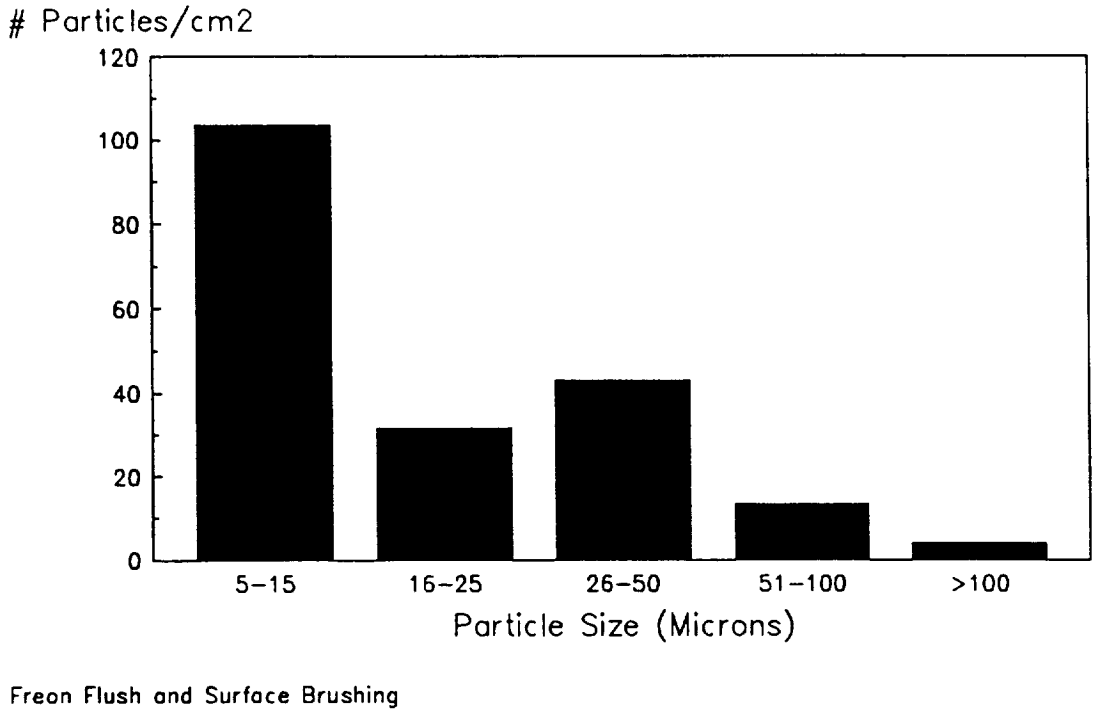

Figure 9. Beta cloth sloughing evaluation, AO and UV exposure.

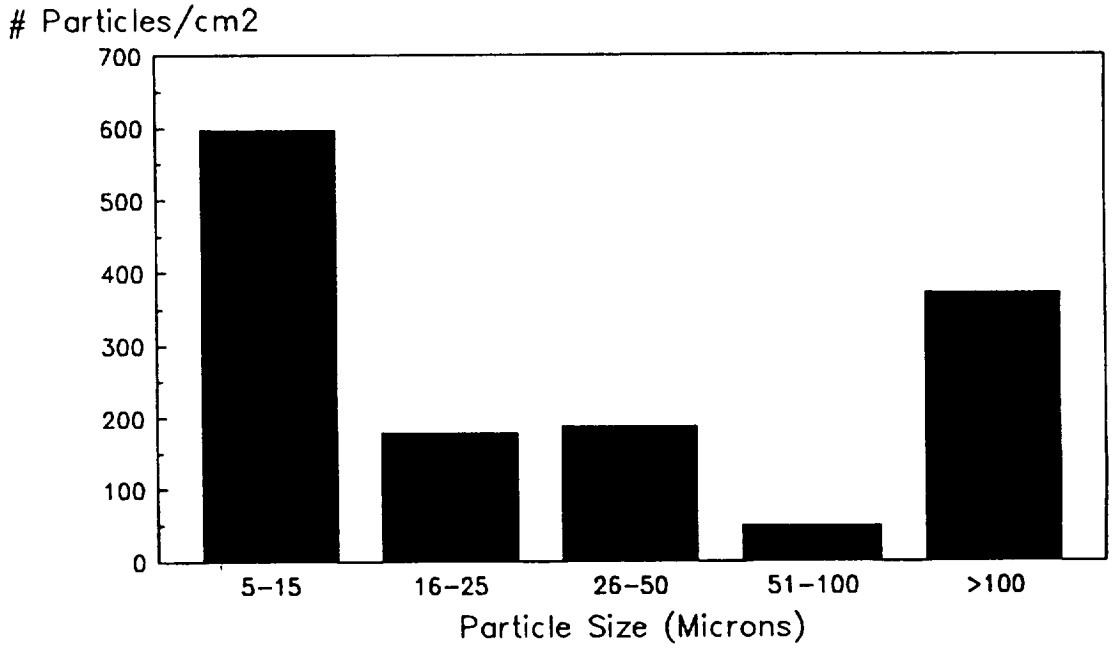

Freon Flush and Surface Brushing

Figure 10. Beta cloth sloughing evaluation, flight beta cloth, not exposed.

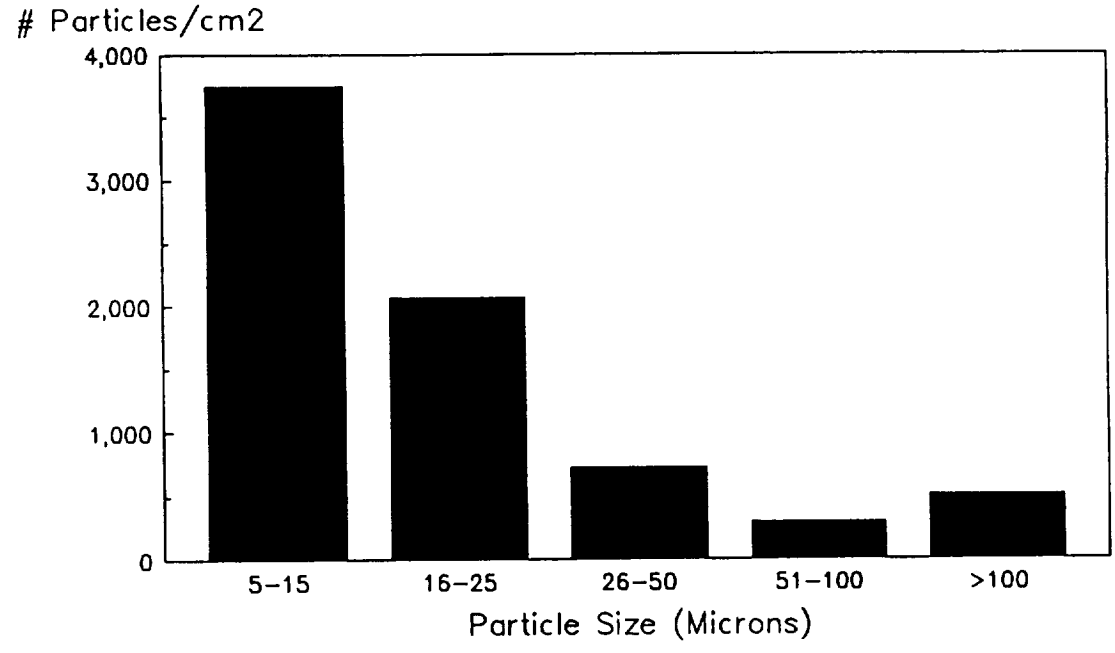

Freon Flush and Surface Brushing

Figure 11. Beta cloth sloughing evaluation, nonflight beta cloth.

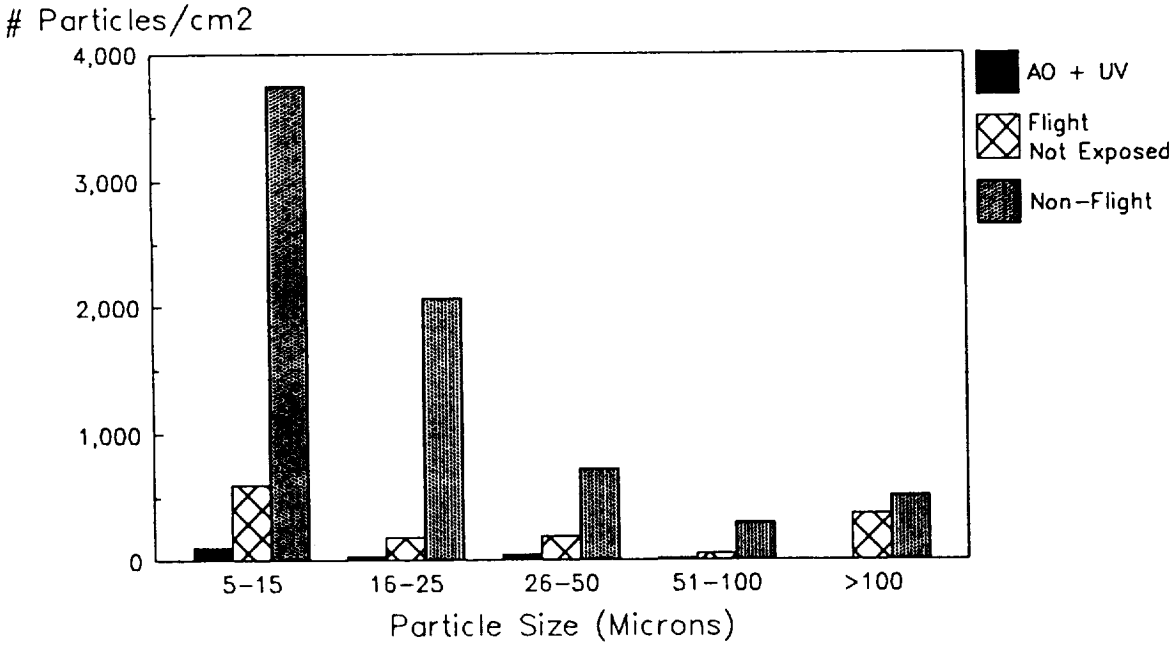

Figure 12. Beta cloth sloughing evaluation, comparison chart.

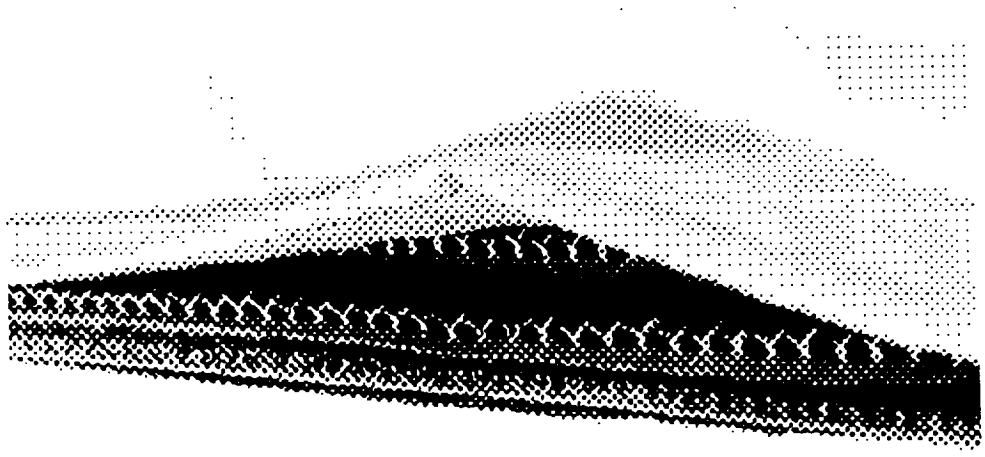

Figure 13. Velcro™ seam with failed Dacron™ thread.

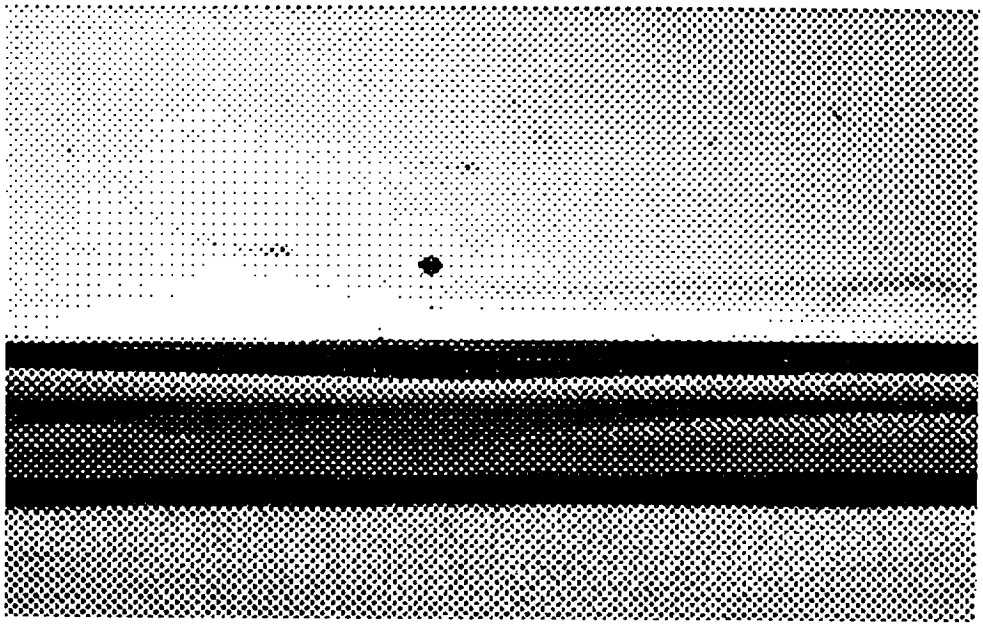

Figure 14. Intact seam shielded from AO.

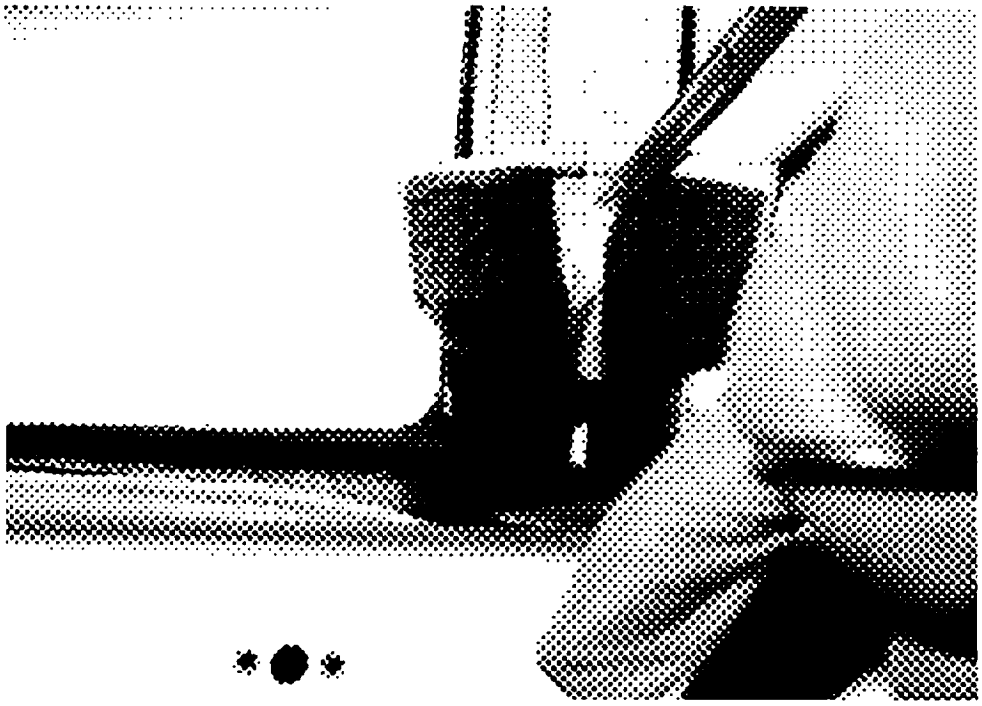

Figure 15. AO bleaching of Velcro™.

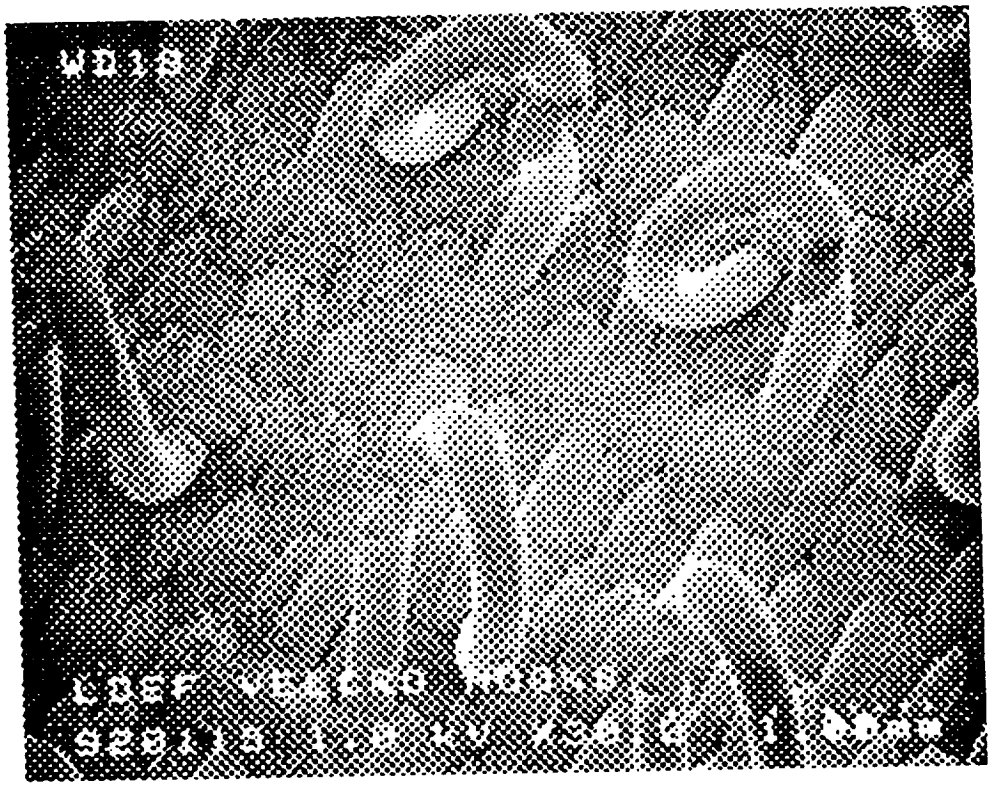

Figure 16. Unexposed Velcro™ hooks.

Figure 17. Velcro™ hooks eroded by AO.

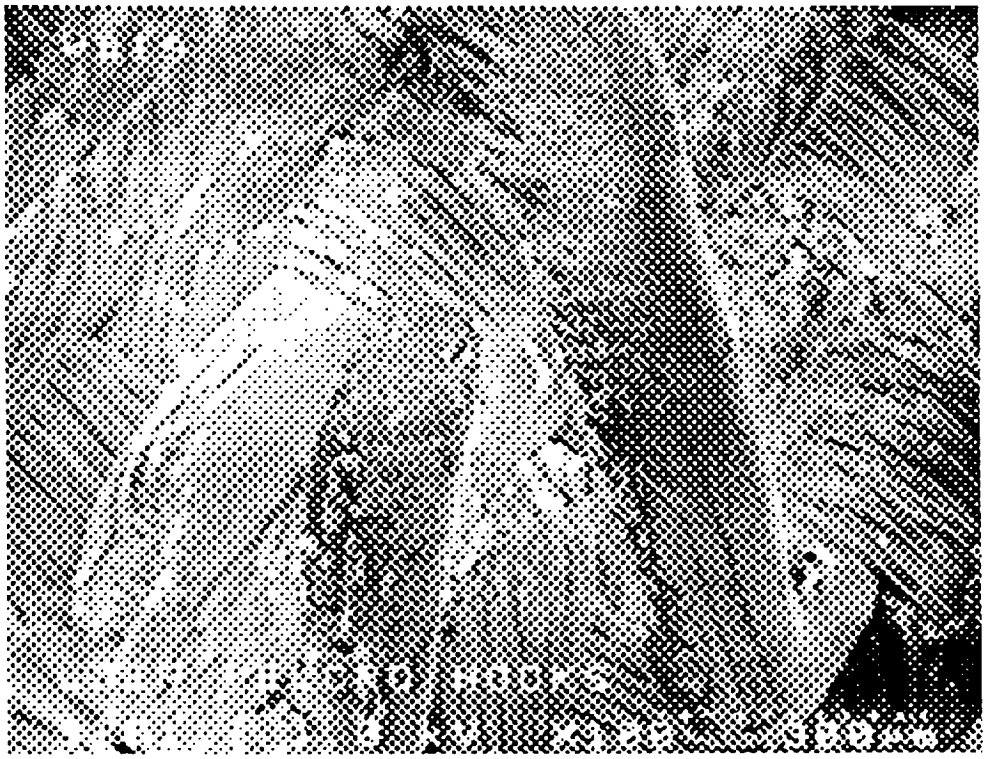

Figure 18. Higher magnification of eroded Velcro™.

SPACE STATION WP-2 APPLICATION OF LDEF MLI RESULTS

Charles A. Smith, Mark M. Hasegawa, and Cherie A. Jones
McDonnell Douglas Aerospace
5301 Bolsa, M. S. 17-4
Huntington Beach, CA 92647-2048
Phone (714) 896-9780, Fax (714) 896-5034

SUMMARY

The Cascaded Variable Conductance Heat Pipe Experiment, which was developed by Michael Grote of McDonnell Douglas Electronic Systems Company, was located in Tray F-9 of the Long Duration Exposure Facility (LDEF), where it received atomic oxygen almost normal to its surface. The majority of the tray was covered by aluminized Kapton® polyimide multilayer insulation (MLI), which showed substantial changes from atomic oxygen erosion. Most of the outermost Kapton layer of the MLI and the polyester scrim cloth under it were lost, and there was evidence of contaminant deposition which discolored the edges of the MLI blanket. Micrometeoroid and orbital debris (MM/OD) hits caused small rips in the MLI layers, and in some cases left cloudy areas where the vapor plume caused by a hit condensed on the next layer. The MLI was bent gradually through 90° at the edges to enclose the experiment, and the Kapton that survived along the curved portion showed the effects of atomic oxygen erosion at oblique angles. In spite of space environment effects over the period of the LDEF mission, the MLI blanket remained functional.

The results of the analysis of LDEF MLI were used in developing the standard MLI blanket for Space Station Work Package-2 (WP-2). This blanket is expected to last 30 years when exposed to the low Earth orbit (LEO) environment constituents of atomic oxygen and MM/OD, which are the most damaging to MLI materials. The WP-2 standard blanket consists of an outer cover made from Beta®-cloth glass fiber fabric which is aluminized on the interior surface, and an inner cover of 0.076-mm (0.003-in) double-side-aluminized perforated Kapton. The inner reflector layers are 0.0076-mm (0.0003-in) double-side aluminized, perforated Kapton separated by layers of Dacron® polyester fabric. The outer cover was selected to be resistant to the LEO environment and durable enough to survive in orbit for 30 years.

This paper describes the analyses of the LDEF MLI results, and how these results contributed to the selection of the WP-2 MLI blanket materials and configuration.

INTRODUCTION

Multilayer insulation (MLI) blankets, consisting of loose layers of flexible, highly reflective material, provide effective, light-weight thermal insulation for spacecraft systems operating in vacuum. They will be used on the propellant tanks and on many fluid lines of the Space Station *Freedom* (S.S. *Freedom*), where the design of the MLI blankets was based to a large part on post-flight characteristics of MLI on the LDEF satellite, in particular the heat pipe experiment No. A0076. This paper describes the effects on MLI of 6 years of exposure to the LEO environment on LDEF, and the development of an MLI blanket suitable for thirty years exposure on the space station.

In addition to the LEO effects on blanket materials seen on the LDEF, requirements for Work Package 2 MLI blankets include thermal cycling, deep temperature excursions, particle radiation exposure, plasma and sputtering interactions, outgassing, and flammability requirements. The blankets must also survive handling on orbit and on ground during installation. Materials must meet NASA requirements which specify that mass loss must not exceed 1 percent of total mass and volatile condensable materials must be less than 0.1 percent during prolonged vacuum exposure. Materials must also pass a vertical burn test per NASA NHB 8060.1 (ref. 1)

LDEF EXPERIMENT DESCRIPTION AND RESULTS

The LDEF Cascaded Variable Conductance Heat Pipe Experiment No. A0076 was covered on all sides by MLI, which was critical to the proper functioning of the experiment. The experiment was developed by McDonnell Douglas Electronic Systems Company to demonstrate precise temperature control of systems in space with no power consumption, using variable conductance heat pipes. Variable conductance heat pipes carry more or less heat to a radiator as the temperature of the heat producing equipment increases or decreases (ref. 2). Each heat pipe used ammonia as the working fluid. Nitrogen was the control gas, and was contained in a reservoir separated from the heat pipe by a long capillary tube which prevented the ammonia from transferring to the reservoir. For this experiment the temperature of a black chrome solar absorber was regulated by two cascaded heat pipes which transferred heat to a silver-Teflon® radiator. The experiment was successful, with temperature control within 0.3 °C of the set point being achieved over a period of at least 45 days (the length of data recording), despite widely varying thermal loads on the solar absorber. Testing after retrieval of LDEF showed that the temperature control band width was the same as in preflight tests, although the temperature set-point of the heat pipes had shifted slightly as expected.

The experiment was located in Tray F-9 of LDEF, where it received an atomic oxygen (AO) flux of 8.32×10^{21} atoms/cm^2 almost normal to its surface, and 11,100 equivalent sun hours (ref. 3). The majority of the tray was covered by aluminized Kapton® polyimide MLI blankets, which also covered the inner sides and bottom of the tray. The outermost layer of the MLI was a 0.076-mm (0.003-in) unperforated Kapton light block, aluminized only on the inner side, and all other layers were 0.0076-mm (0.0003-in), double aluminized, perforated Kapton. There was a total of 15 layers of 0.0003-in Kapton under the 0.003-in layer. All were separated by polyester scrim cloth to minimize heat leaks between layers. The MLI blankets were attached to the sides of the experiment tray using Velcro® tape.

Results of LDEF Space Exposure

The exposed MLI showed substantial changes caused by atomic oxygen erosion and debris particle impact. The appearance of the experiment changed from the bronze color of the outer Kapton layer to the shiny metallic finish of the exposed aluminizing. Most of the exposed outermost Kapton layer of the 0.076-mm (0.003-in) MLI and the polyester scrim cloth under it were lost, and there was evidence of contaminant deposition which discolored the edges of the MLI blanket. Some of the aluminizing on the back of the Kapton remained in place after the Kapton was eroded. This aluminizing shielded sections of the scrim cloth during the remainder of the exposure and accounted for the survival of some areas of the scrim cloth. During recovery and after landing, the extremely thin aluminum drifted away from the experiment. The aluminizing on the underlying double aluminized Kapton layers remained firmly attached and protected the Kapton from the space environment.

Meteoroid and debris hits caused small penetrations and rips in the MLI layers, and in some cases left cloudy areas where the vapor plume caused by a hit condensed on the next layer. An example of this is shown in Figures 1 to 7. A particle struck the 0.076-mm (0.003-in) thick outer layer of the MLI before that layer was completely eroded away by the atomic oxygen, and it produced a debris plume which hit the next 0.0076-mm (0.0003-in) thick Kapton layer, causing rips and perforations. These are shown in Figures 1 to 3. Most of the plume was stopped by the first 0.0076-mm (0.0003-in) layer, and the only place where the plume reached the second 0.0076-mm (0.0003-in) layer was at the vent hole, where the impact of the plume ripped and perforated it. Figure 4 shows the vent hole and the impact area, with the shadow of the scrim cloth. Figures 5 to 7 show higher magnifications of the impact area and of the rips and perforations caused by the debris plume.

Because the MLI was bent gradually through 90° at the edges in order to attach it to the Velcro strips on the side of the tray, the Kapton which survived along the curved portion showed the effects of atomic oxygen erosion at oblique angles, as shown in the scanning electron microscope photograph, Figure 8.

There were no visible changes in the MLI blanket which was underneath the experiment. It was shielded from solar radiation, atomic oxygen, and debris by the exposed MLI layer and by the parts of the experiment.

Effects of MLI Degradation on Spacecraft Systems

The aluminum flakes from the experiment could have degraded the performance of any optical experiments if they drifted into the field of view. The flakes had a large area for their mass and would have drifted away from a spacecraft in low earth orbit fairly rapidly because of the drag of the residual atmosphere, but there would be a possibility of interference until that time. All of the Kapton lost by erosion is converted to volatile products, adding to the density of released gases around the spacecraft and possibly interfering with some experiments requiring unobstructed viewing in the infrared spectral region. The effects of the debris hits on the thermal insulation effectiveness of the MLI was minimal, since it simply added a few more venting perforations to the MLI. In spite of space environment effects over the period of the LDEF mission, the MLI remained functional, and all except the top layer (the light block) survived.

Space Station WP-2 Blanket Requirements

LDEF results have shown that careful selection of blanket materials is required to meet the thirty year lifetime requirements of the S.S. *Freedom*. MLI materials exposed to LEO must be resistant to AO, micrometeoroid and orbital debris impacts (MM/OD), temperature cycling, excursions outside the normal operating temperature range, ultraviolet (UV) radiation, vacuum, and low levels of particle radiation (ref. 4). MLI materials must remain durable and flexible in order to resist damage from flexure due to thermal cycling, astronaut handling on EVA, thruster plume impingement, or physical abrasion, and must not create significant contamination in the form of particulates or outgassing products.

Atomic Oxygen Effects on WP-2 Blankets

LDEF has shown that exposed organic materials commonly used in the design of MLI are susceptible to AO erosion. LDEF also confirmed that AO is primarily a "line-of-sight" phe-

nomenon, and that providing some type of protective cover over susceptible materials will be sufficient to shield them from significant AO exposure. LDEF showed that erosion of organic layers can have a secondary contamination effect as evidenced by the erosion of Kapton from the single sided aluminized Kapton, releasing aluminum particles that could pose a contamination concern for the space station.

LDEF also showed the need to prevent any organic thread, commonly used in the manufacturing of MLI blankets, from exposure to the LEO environment. Organic thread will be eroded in a similar manner to that of the polyester separator scrim between reflector layers of the LDEF MLI blankets. The loss of the thread along the seam will cause the blanket to lose its structural stability and could allow layers of the blanket to drift away.

Thermal Cycling

The space station will be exposed to 100,000 day-night cycles during its 30-year lifetime. These cyclic solar exposures may cause significant temperature excursions during the cycling of the materials with low thermal mass, which will cause stresses in the materials especially when there is a difference in the thermal coefficient of expansion between materials. This stress may cause fatigue and resulting structural failure and shedding of particulates. Also, in materials such as ceramic fabrics, thermal contraction and expansion of the fabric could cause the fibers to abrade against each other and lead to fiber breakage and particle shedding.

Plasma Interactions

Plasma interactions with the material must also be considered. Because the S.S. *Freedom* truss structure is at a different potential than the surrounding plasma, sputtering and arcing of the exterior materials is possible. NASA tests using artificially created plasma have shown that chromic acid anodized aluminum coatings exhibit a breakdown voltage of as little as 80 V, depending on coating thickness. A potential difference greater than the breakdown voltage may cause local areas to be removed by sputtering due to arcing between the structure and the plasma (ref. 5). Depending on the final design of the S.S. *Freedom*, there could be a potential difference of as much as 120 V between the S.S. *Freedom* and the surrounding plasma. To prevent the sputtering of materials, coatings susceptible to plasma interactions are restricted from direct exposure to the LEO environment.

SPACE STATION WP-2 BLANKET DEVELOPMENT

MDA has developed an MLI blanket design which is expected to be compatible for 30 years in the S.S. *Freedom* LEO. This design is based on our understanding of material interactions which we gained from the LDEF experiment and from thermal system requirements. The blanket includes a 0.2-mm (0.008-in) thick polytetrafluoro-ethylene (PTFE) impregnated, single aluminized Beta™ glass cloth with the aluminized side facing inward, 20 layers of a light weight separator scrim alternating with 19 layers of a 0.008-mm (0.0003-in) double aluminized polyimide film, and a 0.076-mm (0.003-in) thick scrim reinforced double aluminized polyimide. The general blanket layout is shown in Figure 9.

Outer Cover

The purpose of the outer cover is to provide a durable surface which can be safely handled by astronauts on EVA and which will prevent damage to the internal layers of the blanket. The outer cover also shields the internal materials of the blanket from ultraviolet radiation, atomic oxygen, and plasma. The small penetrations through the outer cover from MM/OD, as seen on the LDEF blankets, are expected to affect a small percentage of the blanket surface area, and will not significantly affect the thermal performance or structural integrity of the blanket.

The industry standard for a durable, EVA compatible outer cover on MLI has been PTFE impregnated Beta glass cloth. At MDA, Beta™ cloth has been used on a number of different programs on Delta and Titan III launch vehicles and the Payload Assist Module. A PTFE impregnated Beta glass cloth has also been the standard outer cover material for the Orbiter blankets. Flight experience has shown few problems. Orbiter Beta glass cloth has turned yellow after prolonged exposure to UV radiation (ref. 6). This was primarily attributed to the methylsiloxane sizing used during the weaving of the Beta glass fabric. The methylsiloxane sizing may be removed by a high temperature exposure which burns off the silicone resin leaving only the woven glass fabric. Also, the fabric may be woven with or without Teflon sizing.

Testing at NASA-JSC by Dr. Steve Koontz indicates that Beta glass cloth is acceptable for 30 years use as the MLI outer cover. Mechanical testing on the Beta glass cloth included flexing for over 100,000 cycles after atomic oxygen exposure to simulate thermal stresses and fiber-fiber abrasion caused by 30 years of day-night cycle exposures, tear resistance test, and a dart drop impact resistance test. No particulate generation or significant loss in durability of the cover was seen. Analysis of satellite data has shown that atomic oxygen does not penetrate through the fiber bundles of the Beta glass cloth.

Beta glass cloth, while providing a barrier for atomic oxygen, allows approximately 25 percent through transmittance of solar radiation to the underlying layer. Previous MLI designs incorporated the use of a light block layer, and the feasibility of using a traditional light block in the WP-2 MLI blankets was investigated. The traditional light block is a single aluminized Kapton or Mylar layer that serves as a second surface mirror, with a much higher infrared emittance facing away from the blanket than toward it. It prevents an increase in temperature in the reflector layers by preventing solar radiation from striking the reflector layers and by radiating infrared radiation away from the blanket. This improves the thermal efficiency of the blanket.

The primary concern with using an organic material is erosion from atomic oxygen. While the light block is situated beneath the Beta glass outer cover, small penetrations from micrometeorites and debris will occur, allowing atomic oxygen into the lower layers. Although these penetrations represent a small fraction of the total surface area of the blanket, erosion would still occur to the underlying organic layer. As the orientation of the blanket changes with respect to the AO ram direction during the various flight modes, the area exposed to the atomic oxygen flux increases and will cause considerably more degradation to the underlying layers.

The effort to develop an outer cover that was AO resistant, opaque to solar radiation, flexible, and durable, and that was compatible with the LEO environment started with a commercially available, lightweight aluminized glass fabric. This lightweight glass fabric is constructed with large open weaves which are impregnated with Teflon on which a continuous aluminum film can be deposited. The cloth has been used on the Payload Assist Module (PAM) manufactured at MDA, which places satellites into geosynchronous transfer orbits. Testing for LEO compatibility was performed by

NASA-JSC, and showed that this cloth was unacceptable for use because prolonged AO exposure would result in the loss of the impregnated Teflon and the aluminized backing.

The use of an aluminized layer on Beta cloth was explored, since AO asher tests had shown that the tight weave of the Beta cloth might block AO penetration. In addition, McDonnell Douglas Electronic Systems Company (MDESC-St. Louis) has used an aluminized Beta glass on several space applications. These materials utilize a plasma etch pretreatment of the PTFE impregnated Beta cloth to increase the adhesion of the vapor deposited aluminum to the Teflon impregnate. A pretreatment in which a silica based material was incorporated into the Teflon impregnate to provide a more stable and adhesion promoting surface for the aluminum was also investigated. Beta cloth with silica, aluminized with 1,000 A of aluminum, was evaluated by NASA-JSC for compatibility with the LEO environment. The NASA-JSC evaluation reached the conclusion that the material would withstand thirty years of LEO, and it was chosen for the space station MLI blankets (ref. 6).

Separator Layers

The material selection for the separator layers depends on the expected service temperature of the blanket and on minimizing blanket weight. The current baselined material is a lightweight polyester netting (Dacron®) which has been used on Delta for low to moderate temperature applications. The netting is known to shrink and melt at temperatures above 177 °C (350 °F). MDA tests have shown that after 48 hours at 350 °F, blankets made with Dacron separators shrink up to 4 percent, and the separator layers have shown some adhesion to the reflector layers. The shrinkage of the separators may result from stress relief of the netting, which is created from denser, heavier netting which is heat stretched to form a lower areal density netting. To insure that the Dacron shrinkage does not affect the blanket performance or dimensions, the maximum use temperature for the separator layers is 121 °C (250 °F). For higher temperature applications, a lightweight weave of Nomex® (polyamide) thread has been selected for use as the separator layers.

Reflector layers

Two of the most common materials used in the aerospace industry for reflector layers in MLI are aluminized Mylar® and aluminized Kapton®. Past spacecraft programs at MDA have considered the upper temperature limit of aluminized Mylar to be 200 °F, depending on how sensitive the design is to blanket shrinkage. Present calculations of S.S. *Freedom* Propulsion Module temperatures have indicated that insulation which is used to control the temperature of the hydrazine fuel tanks on the module could be exposed to temperatures in excess of 149 °C (300 °F) during reboost thruster operation.

A comparison of Mylar and Kapton properties from the MAPTIS data base (ref. 7) is shown in Table 1.

Table 1. Mylar and Kapton property comparison.

PROPERTY	MYLAR	KAPTON
Transition Temperature	80 °C (176 °F)	360 °C (680 °F)
MAPTIS Flammability Rating Notes: "A" - passes NHB8060.1 Test 1 "X" - fails NHB8060.1 Test 1	"X" at 0.091 mm (0.006 in) thick, 25.9% and at 30.0% oxygen	"A" at 0.051 mm (0.002 in) thick, 25.9% oxygen, "A" at 0.076 (0.003 in) thick, 30.0% oxygen
Residual Shrinkage at 300 °F	1.5 %	0.2 %

MDA plans to use Kapton in the MLI blankets because Mylar does not meet temperature requirements in applications where the blankets may be exposed to the high temperatures previously noted and because the use of Kapton will prevent potential on-orbit fit problems due to material shrinkage. From a thermal standpoint, excessive blanket shrinkage is undesirable because of movement in the blanket assembly in joint and penetration areas, decreasing overlaps and area coverage, and stressing blanket attachments. The use of Kapton also allows vacuum baking of the MLI materials and assemblies at 121 °C (250 °F) to meet outgassing requirements.

Neither Kapton nor Mylar meet flame propagation requirements for the Orbiter Cargo Bay at the thicknesses used for reflector layers, 0.0076 mm (0.0003 in). Both films must be encapsulated and tested in configuration. Generally, inner and outer blanket covers (usually 0.0051- to 0.0076-mm thick Kapton or Beta cloth) meet flammability requirements, and the blanket, when tested as an assembly, meets the flammability requirement.

The number of reflector layers was selected to be 19 layers for WP-2. This number was based on previous MDA experience that blanket thermal performance starts to level out around 10 to 12 layers and reaches a maximum performance around 15 layers. The additional four layers allows some damage due to small MM/OD impacts without affecting blanket performance.

Inner Cover

The inner cover of the blanket will face the hardware, and like the outer cover, it must be durable to prevent damage to the inner layers caused by handling during ground installation and on-orbit. A number of different materials such as glass cloths and aluminized Mylar or Kapton layers have been used by MDA on previous programs. To meet the thermal optical and durability requirements, 0.076-mm (0.003-in) double aluminized Kapton was selected. The aluminized Kapton will be reinforced with a Nomex scrim to provide added strength and tear resistance to the film. The maximum infrared (IR) hemispherical emittance of the aluminized inner cover is expected to be 0.04, so that the majority of the radiation will be radiated to space rather than to the interior of the blanket.

Thread

LDEF results have shown that organic thread material such as Nomex will be eroded when exposed to atomic oxygen. To prevent seams and sewn joints from degrading and coming apart, the thread used must to sew blankets must be either compatible with atomic oxygen or protected from it. The thread must be strong enough to endure the sewing process, tend not to easily shred and generate particulates, and be compatible with the low earth orbit environment if exposed. Thread must

also be manageable for easy manufacturing. For applications where thread will be protected from atomic oxygen, Nomex will be used.

For those applications where thread may be exposed to atomic oxygen there are several possibilities. While a number of different materials such as quartz or aluminum borosilicate (Nextel™) are resistant to atomic oxygen and UV radiation, MDA has found that the they are difficult to use to sew seams. The quartz and Nextel threads tend to wear away the needles of the sewing machines, causing the thread to snag and break. This thread breakage is unacceptable on a manufacturing scale in which many blankets must be fabricated. MDA plans to use a polyamide coated Beta glass thread to sew high temperature MLI blankets that reach temperatures above the maximum use temperature of the Nomex threads. The thread is less flexible than the Nomex, but does not tend to shred and break as much as the quartz or Nextel threads. This thread is atomic oxygen resistant, although the coating will erode, and is expected to provide an adequate seam over the 30-year exposure to the LEO environment.

Fasteners

Hook and loop fasteners have been identified as an EVA compatible method to fasten MLI blankets to other surfaces. MIL-F-21840 type 2, class 1 hook and loop fasteners are the primary method for attaching blankets to underlying surfaces or to each other. The material meets outgassing requirements; however, it must be used in limited amounts to meet the flammability requirements. The current limitation on use of the material is two square inches of fastener separated by a minimum of two linear inches from other fastener material.

The MIL-F-21840 fastener is constructed from a 0.127-mm (0.005-in) thick nylon loop. Since nylon is eroded by atomic oxygen, precautions must be taken to insure that the fastener is not exposed to atomic oxygen. It was arbitrarily decided that the fastener could be exposed to atomic oxygen for a total or two weeks, while the blankets were opened for servicing, tests, or component replacement, before its peel strength and use life was shortened extensively. This period represents the amount of time required for atomic oxygen in direct ram orientation to erode one half of the thickness of the hook or loop section.

Fasteners may be attached to the blanket by either stitching or adhesively bonded, and may either be adhesively bonded or riveted to the underlying structure. Continuous temperature cycling between the lower and upper limits of the touch temperatures –118 °C (–180 °F) and +113 °C (235 °F) is not expected to degrade the mechanical performance of the MIL-F-21380 hook and loop fasteners.

Metallic hook and loop fasteners are commercially available and are resistant to atomic oxygen. They were not seriously considered because they begin to lose their mechanical properties after a limited number of cycle lives, and they would be a safety concern for extravehicular activity (EVA) because they may rip or abrade the outer layer of the astronaut's suit.

CONCLUSION

The results of MLI exposure to the LEO environment on LDEF, combined with the experience on other space programs at MDA and other companies, have been used to develop a light weight MLI blanket which gives excellent thermal performance and provides confidence that the blanket will last for 30 years in LEO on the space station.

REFERENCES

1. NASA NHB 8060.1: "Flammability, Odor, and Offgassing Requirements and Test Procedures for Materials in Environments that Support Combustion."

2. Grote, M.G., "Results from the LDEF/A0076 Cascaded Variable Conductance Heatpipe Experiment." LDEF–69 Months in Space, NASA Conference Publication No. 3134, pp 1455–1466, 1991.

3. "LDEF Spacecraft Environmental Effects Newsletter," vol. 2, No. 3, June 15, 1991.

4. Babel, H.W., Simpson, K.E., and Jones, C.A., "Material Considerations for Space Station *Freedom*." IAF-90-278. Presented at the 41st Congress of the International Astronautical Federation, October 6–12, Dresden, GDR.

5. Pfitzer, K.A., personal communication, August 10, 1992.

6. Koontz, S.L., Jacobs, S., and Le, J., "Beta Cloth Durability Assessment for Space Station Freedom (SSF) Multi-layer Insulation (MLI) Blanket Covers." NASA Technical Memorandum, NASA Johnson Space Center, January, 1992.

7. "Material and Process Technical Information System (MAPTIS)." Marshall Space Flight Center. For information contact Rene Hitson, (205) 544-6972.

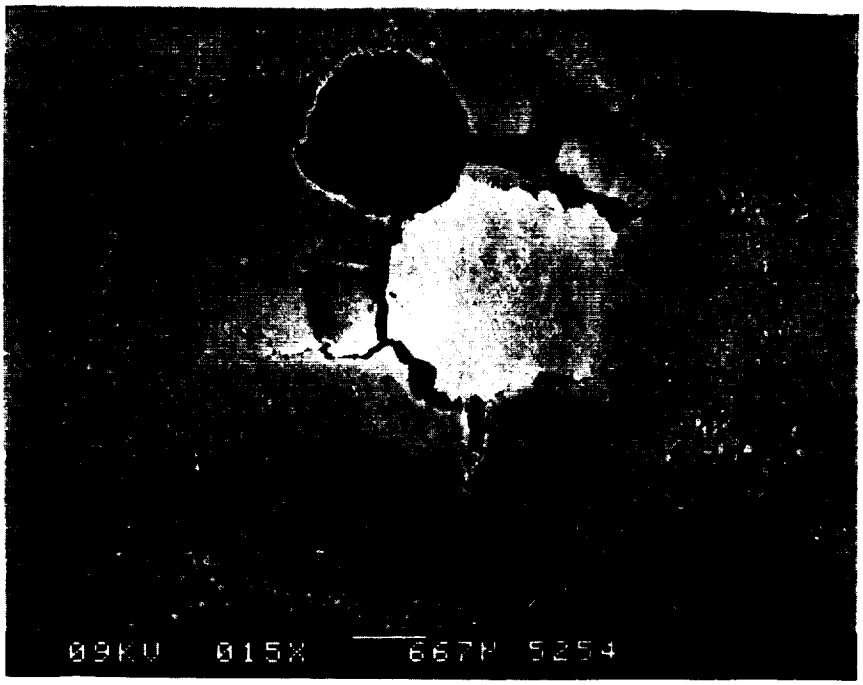

Figure 1. Debris impact area of second Kapton layer, SEM, × 15.

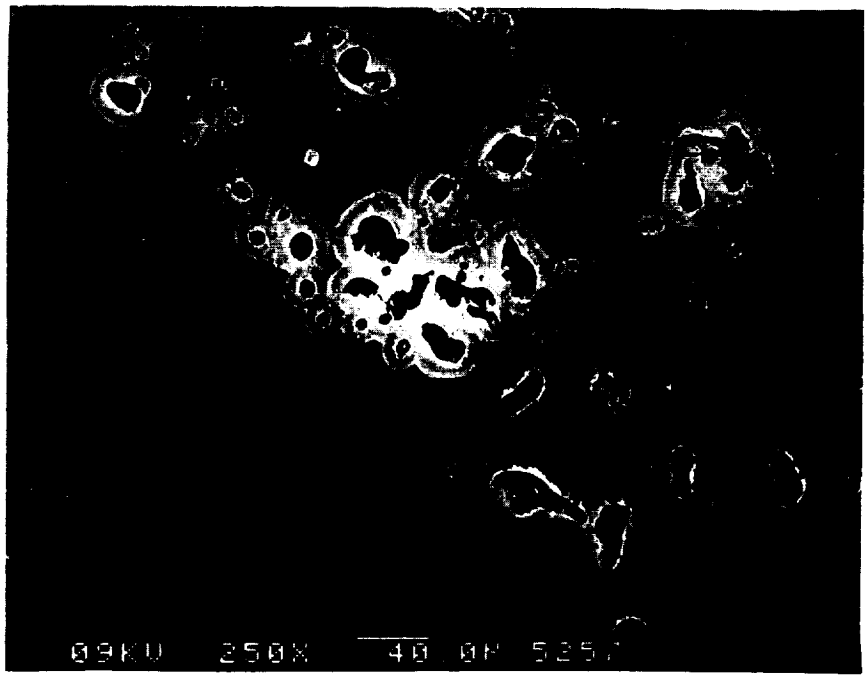

Figure 2. Debris impact area of second Kapton layer, showing perforations, SEM, × 250.

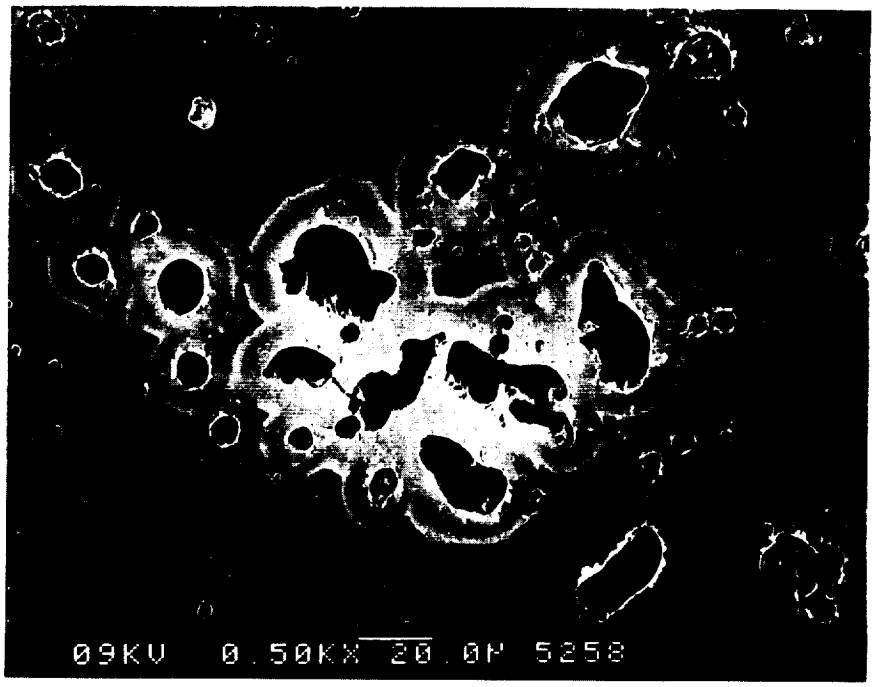

Figure 3. Debris impact area of second Kapton layer, showing undercutting, SEM, × 500.

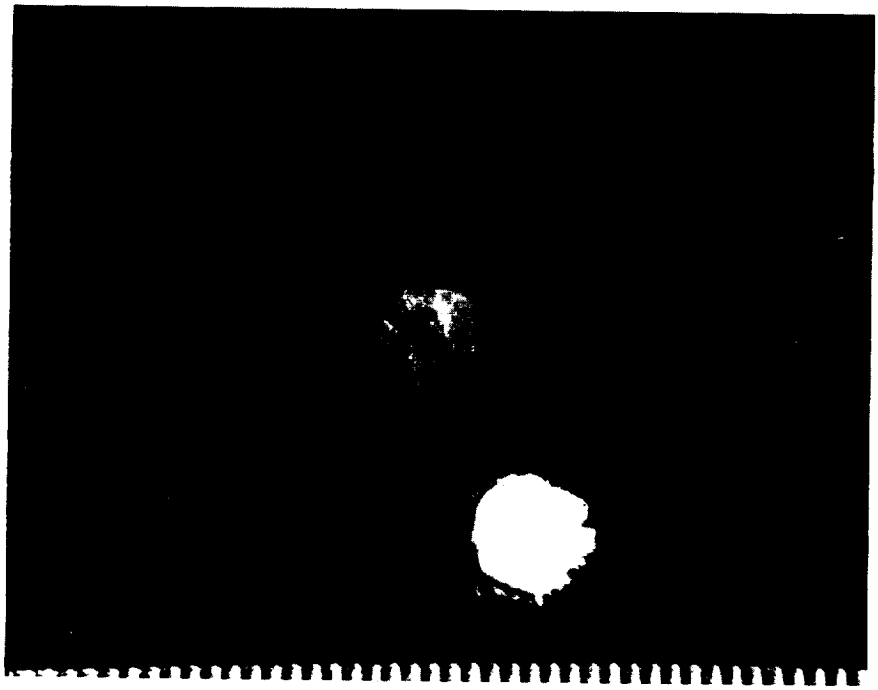

Figure 4. Third Kapton layer, showing impact of plume through vent hole of second layer, optical photograph, × 10.

Figure 5. Same area of third Kapton layer, SEM, × 100.

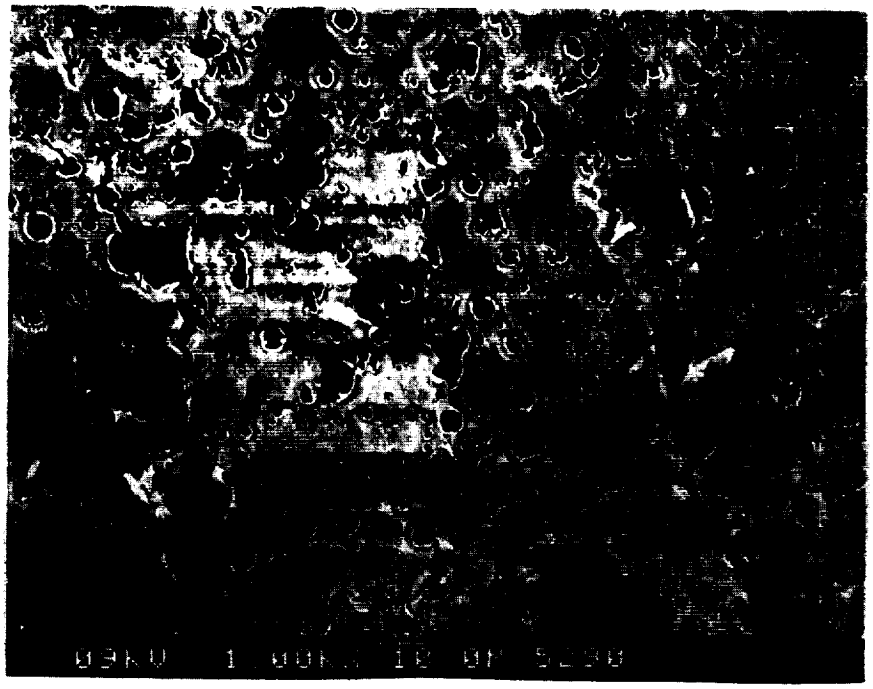

Figure 6. Same area of third Kapton layer, showing rips and perforations, SEM, × 1,000.

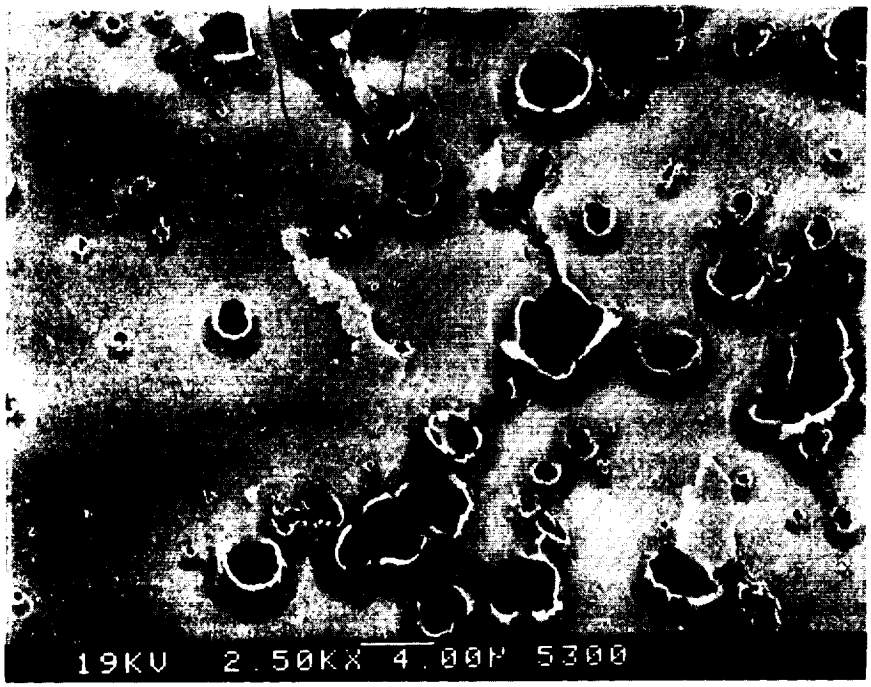

Figure 7. Third Kapton layer, showing a small particle with high titanium, possibly paint, SEM, × 2,500.

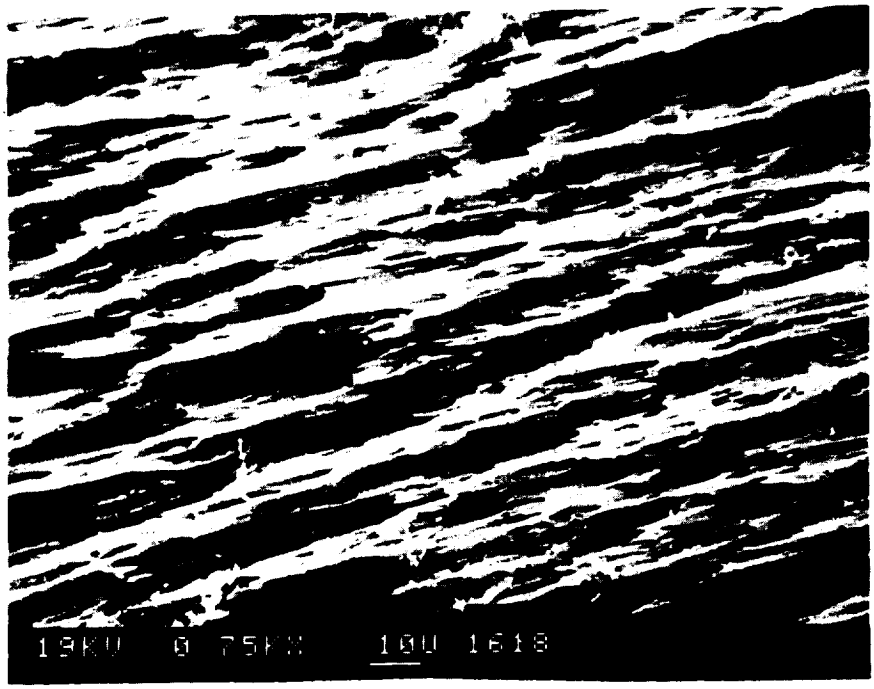

Figure 8. SEM photograph of the aluminized Kapton lightblock exposed to AO at a very oblique angle, SEM, × 750.

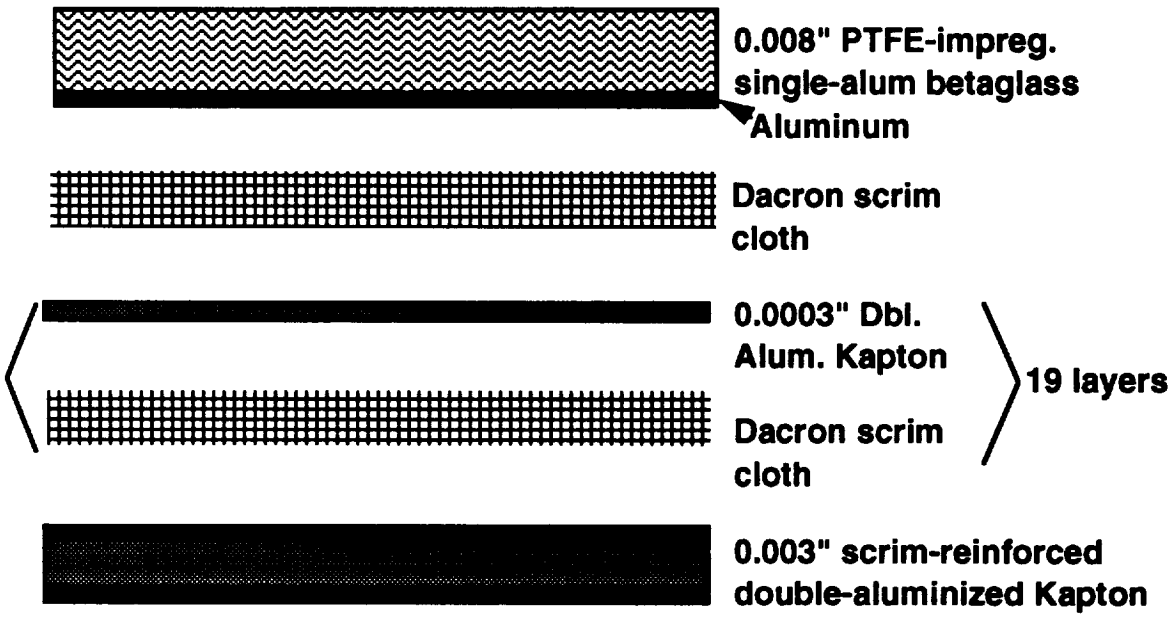

Figure 9. Layers of the space station MLI blanket and their arrangement.

ANODIZED ALUMINUM ON LDEF*

Johnny L. Golden
Boeing Defense & Space Group
P.O. Box 3999 M/S 82-32
Seattle, WA 98214-2499
Phone: (206) 773-2055, Fax: (206) 773-4946

SUMMARY

A compilation of reported analyses and results obtained for anodized aluminum flown on the Long Duration Exposure Facility (LDEF) has been prepared. Chromic acid, sulfuric acid, and dyed sulfuric acid anodized surfaces were exposed to the space environment. The vast majority of the anodized surface on LDEF was chromic acid anodize because of its selection as a thermal control coating for use on the spacecraft primary structure, trays, tray clamps, and space end thermal covers. Reports indicate that the chromic acid anodize was stable in solar absorptance and thermal emittance, but that contamination effects caused increases in absorptance on surfaces exposed to low atomic oxygen fluences. There were some discrepancies, however, in that some chromic acid anodized specimens exhibited significant increases in absorptance. Sulfuric acid anodized surfaces also appeared stable, although very little surface area was available for evaluation. One type of dyed sulfuric acid anodize was assessed as an optical baffle coating and was observed to have improved infrared absorptance characteristics with exposure on LDEF.

INTRODUCTION

The anodize process is an electrolytic oxidation of metal, essentially a controlled corrosion process, which yields a uniform and adherent oxide coating. It is typically used in the aerospace industry for corrosion protection, wear resistance, and/or as a base for subsequent organic finishes. In the context of this paper, however, anodized aluminum is utilized with regard to its ability to function as a thermal control coating for spacecraft use. In this capacity, anodized aluminum offers significant advantages including terrestrial durability, light weight, processing simplicity, and some tailorability of optical properties. The LDEF mission has provided a basis for evaluating the impact of the space environment on the ability of anodized aluminum to act as a predictable thermal control coating.

Aluminum anodizing as a process begins with a thorough cleaning of the aluminum part after all machining and heat treatment has been completed. The aluminum is then deoxidized to provide a uniform surface for anodizing. Sometimes a chemical polishing, or a bright dip, is performed at this point to establish a high initial reflectivity for the surface. Next, the part is placed in an electrolyte, and an electrical potential is established with the aluminum part as the anode. An oxide layer forms from the surface aluminum with a density and thickness principally controlled by the electrolyte composition and temperature, and by the voltage and time (total current) specified for the particular anodizing process.

*Work done under NAS1-19247 and NAS1-18224.

This as-anodized surface is highly porous on a submicron level. Finally, the electrolytically formed aluminum oxide coating is hydrated or sealed to close the porosity, bringing the surface to an equilibrium which is stable in the terrestrial environment and protective to the substrate material. Coloration of the anodize can be achieved through the occlusion of dyes in the pore structure prior to hydration or sealing.

Three types of anodized aluminum were flown on LDEF, for which results have been published. The types are chromic acid anodize, sulfuric acid anodize, and dyed sulfuric acid anodize. This paper is a compilation of results for these finishes.

RESULTS AND DISCUSSION

Chromic Acid Anodize

Chromic acid anodize was used as part of the passive thermal management system for LDEF. The anodize process used for LDEF structures was actually a modification of the standard chromic acid anodize process, as specified by MIL-STD-8625, Anodic Coatings for Aluminum and Aluminum Alloys, Type I. The modified process used for LDEF was developed by NASA Langley Research Center (LaRC), and permits tailoring of solar absorptance and thermal emittance through the selection and control of anodizing voltage and time (ref. 1). LDEF structural components were constructed of 6061 aluminum alloy and were anodized using the modified chromic acid process to achieve an average absorptance/emittance ratio of 0.32/0.16.

Postflight optical property measurements for LDEF longerons, intercostals, and thermal panels have been reported (ref. 2). Average emissivity readings taken on exposed LDEF structures indicated that there were no measurable changes when compared to preflight conditions ($\varepsilon = 0.15 \pm 0.03$), regardless of location. However, surfaces protected from atomic oxygen (AO) or ultraviolet (UV) radiation by overlapping structures exhibited a slight increase in average emissivity ($e = 0.18 \pm 0.04$). The cause of the slight emissivity increase for unexposed surfaces has not been determined.

Solar absorptance measurements for space-end thermal panels indicated an average increase of 0.03 from preflight conditions. Absorptance measurements made for intercostals and longerons indicated a more complex situation, and have been plotted versus row location in Figure 1. Data in Figure 1 for intercostals are located on the row numbers, and longerons data are between row numbers. For structures subjected to significant AO fluences (leading edge row locations 6.5 through 11.5), measurements indicated absorptances comparable to those made preflight ($\Delta\alpha < 0.02$). The longerons contributed most to the differences observed between preflight and postflight solar absorptance measurements on the leading edge structures. Structures subjected to low AO fluences (trailing edge row locations 12 and 0.5 through 6), however, exhibited significant increases in absorptance ($\Delta\alpha = 0.07$). Some indication of trends in the preflight solar absorptance measurements were still apparent in the postflight measurements on trailing edge row structures, such as was observed on the longeron between rows 2 and 3.

In an attempt to further investigate the cause(s) of absorptance changes for chromic acid anodize on the LDEF structure, solar absorptance has also been plotted as functions of UV radiation exposure and AO fluence in Figures 2 and 3, respectively. The UV exposure and AO fluence numbers were taken from the LDEF environmental exposure models (ref. 3). Figure 2 indicated that the influence of UV

exposure on solar absorptance was not strong. However, Figure 3 indicated that AO fluence does have a significant effect on solar absorptance, but that the effect was not a gradual one even when represented on a log-scale. Once a "threshold" AO fluence was reached, the average solar absorptance rapidly returned to preflight values. Recognizing this strong effect of AO above the threshold fluence, solar absorptance versus UV exposure was replotted using only data from structures which received an AO fluence below the threshold ($<10^{20}$ atoms/cm^2), as shown in Figure 4. A weak effect of UV exposure on solar absorptance was revealed, indicating an absorptance increase of approximately 0.008 per 1,000 equivalent Sun hours (ESH) of UV exposure.

Thermal control properties were also measured for the tray clamps used to hold experiment trays to the LDEF framework. Reported results (ref. 4) have been summarized in Table 1. No significant changes in emissivity were observed for the exposed surfaces of tray clamps, as compared to preflight data. Tray clamps exposed to fluences of atomic oxygen greater than 10^{20} atoms/cm^2, reported in Table 1 as ram side surfaces, did not indicate significant changes in solar absorptance. Tray clamps with less than the threshold AO fluence (wake side, Earth end, and space end surfaces) did have measurable but slight increases in average absorptance ($\Delta\alpha = 0.03$). Note that averages for flight tray clamps, regardless of their exposure conditions, exhibited optical properties closer to preflight measurements than did tray clamps held in uncontrolled storage during the LDEF mission. Anodize thickness measurements were also made, indicating that an emissivity of 0.16 corresponds to an anodize layer thickness of between 0.4 and 0.6 μm (about 0.00002 inch).

Table 1. Solar absorptance and thermal emittance measurement averages for 6061 aluminum tray clamps (including standard deviations, σ).

Measurements on Flight Tray Clamps						Measurements on Unused Clamps
Protected Surfaces	Ram Side Surfaces	Wake Side Surfaces	Space End Surfaces	Earth End Surfaces	Preflight (ref. 1)	
$\alpha = 0.34$ [$\sigma = 0.01$]	$\alpha = 0.33$ [$\sigma = 0.01$]	$\alpha = 0.35$ [$\sigma = 0.02$]	$\alpha = 0.35$ [$\sigma = 0.02$]	$\alpha = 0.35$ [$\sigma = 0.01$]	$\alpha = 0.32$	$\alpha = 0.36$
$\varepsilon = 0.16$ [$\sigma = 0.01$]	$\varepsilon = 0.15$ [$\sigma = 0.01$]	$\varepsilon = 0.15$ [$\sigma = 0.01$]	$\varepsilon = 0.16$ [$\sigma = 0.02$]	$\varepsilon = 0.17$ [$\sigma = 0.01$]	$\varepsilon = 0.16$ [$\sigma = 0.01$]	$\varepsilon = 0.18$ [$\sigma = 0.01$]
$\alpha/\varepsilon = 2.1$	$\alpha/\varepsilon = 2.2$	$\alpha/\varepsilon = 2.3$	$\alpha/\varepsilon = 2.2$	$\alpha/\varepsilon = 2.1$	$\alpha/\varepsilon = 2.0$	$\alpha/\varepsilon = 2.0$

Chromic acid anodized flight specimens of 6061 aluminum were flown as part of LDEF experiment S0010 (refs. 5, 6). The thermo-optical property measurements, shown in Table 2, indicate that the chromic acid anodize specimens were not significantly affected by either short-term (10 months, 1,600 ESH UV, and $<10^{17}$ AO atoms/cm^2) or long-term (5.8 years, 11,200 ESH UV and 9×10^{21} AO atoms/cm^2) exposure.

Another example of chromic acid anodize involved the surface of environment exposure control canisters (EECC) used on several LDEF experiments. Measurements of thermo-optical properties on the surfaces of these 6061 aluminum canisters have been reported for Experiment S1002 (ref. 7) and obtained from Experiment M0003 investigators (M. Meshishnek), shown in Table 3. The results in Table 3 are consistent with those observed for chromic acid anodize on the other LDEF structures.

Emissivity was not affected by the LDEF exposure conditions. Solar absorptance was not significantly affected in high AO fluence regions but increased by approximately 0.07 on low AO fluence surfaces.

Table 2. Solar absorptance and thermal emittance measurements for 6061 aluminum chromic acid anodize test specimens on LDEF experiment S0010 (ref. 5).

Coating	Preflight		10-Month Exposure		5.8-Year Exposure	
	α	ε	α	ε	α	ε
Thin chromic acid anodize	0.295	0.16	0.299	0.17	–	–
	0.288	0.18	–	–	0.296	0.19
Medium chromic acid anodize	0.292	0.43	0.287	0.43	–	–
	0.396	0.45	–	–	0.311	0.46
Thick chromic acid anodize	0.330	0.71	0.337	0.71	–	–
	0.341	0.75	–	–	0.354	0.75

Table 3. Solar absorptance and thermal emittance of 6061 aluminum EECC chromic acid anodized surfaces.

Experiment Number	Tray Location	UV (ESH)	AO (atoms/cm^2)	Preflight		Postflight	
				α	ε	α	ε
S1002	E3	11,100	10^{17}	0.29	0.19	0.36	0.20
M0003	D4	10,500	10^{5}	–	–	0.40	–
	D8	9,400	7×10^{21}	–	–	0.32	–

Results from Experiment S0069 (ref. 8) were not consistent with other results reported here for chromic acid anodized 6061 aluminum surfaces. Two specimens of chromic acid anodized 6061 aluminum were flown on tray A9, but when battery power failed for this active experiment (due to the unplanned extension of the LDEF mission) one specimen (C61) was exposed for the entire mission, and the other specimen (C63) was exposed for only the initial 19 months. The solar absorptance data for these two specimens were measured in situ, and are shown in Figure 5 as a function of estimated UV exposure. The last measurement for specimen C63 was actually made postflight, but is plotted on Figure 5 at the exposure it would have received for 19 months. These measurements indicated that the S0069 specimens degraded (increased) in solar absorptance at a rate of 0.04 per 1,000 ESH of UV exposure. The solar absorptance of specimen C61, however, recovered significantly due to the AO fluence received in the latter stages of the LDEF mission (from 0.50 to 0.47). The preflight and postflight emissivity for both of these two specimens was 0.84, unchanged with exposure as has been observed with other anodized surfaces. The emissivity measured for the two specimens on Experiment S0069 was surprisingly high for chromic acid anodized aluminum. The maximum emissivity for chromic acid anodize has been 0.70 to 0.75.

Chromic acid anodized 2024 aluminum alloy was also flown on LDEF. Investigators for Experiment A0034 used this material and finish combination for top cover plates (ref. 9). The thermal control coatings evaluated in Experiment A0138-6 (ref. 10) included a test specimen of chromic acid anodized 2024 aluminum (specific designation was alloy AU4G1, specimen E7). Results of absorptance

Table 4. Solar absorptance and thermal emittance of 2024 aluminum chromic acid anodized surfaces.

Experiment Number	Tray Location	UV (ESH)	AO (atoms/cm^2)	Unexposed Back		Exposed Front	
				α	ε	α	ε
A0034	C9	11,200	9×10^{21}	0.42	0.15	0.38	0.13
	C3	11,100	10^{17}	0.45	0.14	0.47	0.13
				Preflight		Postflight	
A0138-6	B3	1,582	negligible	0.48	0.34	0.54	0.34

and emittance measurements are shown in Table 4. The results for Experiment A0034 are somewhat difficult to interpret without preflight data. However, it was apparent to the investigators that a high AO fluence "cleaned" the tray C9 exposed cover plate surface. If it is assumed that this cleaned surface mimics the original absorptance of that surface, as has been observed for other LDEF chromic acid anodized surfaces, then that absorptance could be used as an indication of the cover plate preflight condition. Using this assumption, the cover plate for tray C3, with a low AO fluence, exhibited an absorptance increase of 0.09. Such an absorptance degradation is slightly higher than but comparable to that observed for the anodize on LDEF structures.

The test specimen flown on Experiment A0138-6 indicated significant degradation in solar absorptance considering its limited exposure (see Table 4). Since this test specimen was in an open canister during the initial 10 months of the LDEF mission, it received limited UV radiation and a negligible AO fluence (estimated at $<10^3$ atoms/cm^2). The absorptance increase was measured as $\Delta\alpha = 0.06$, or 0.04 per 1,000 ESH. This degradation rate was comparable to that observed for specimens on Experiment S0069.

As a comparison to LDEF flight data, ground-based testing data for chromic acid anodize (ref. 11) has been included here. Figure 6 shows how solar absorptance was affected by UV exposure for a chromic acid anodized 1145 aluminum alloy foil. An increase in solar absorptance of from 0.32 to 0.34 was observed in the initial 500 ESH of exposure. The test specimen then held at a constant solar absorptance of 0.34 for the next 4,500 ESH exposure tested. The thermal emittance of the specimen from this test was measured as 0.67, indicating a relatively thick oxide layer.

Sulfuric Acid Anodize

Experiment S1002 included both experimental and nonexperimental surfaces finished with sulfuric acid anodize (ref. 7). The experimental surface was an optical solar reflector (OSR), described as a 5-μm sulfuric acid anodize coating on an aluminum substrate. The OSR received a controlled environmental exposure due to its position in an EECC, amounting to 1,440 ESH of UV exposure and negligible atomic oxygen. Thermal control characteristics changes were minimal, with a postflight solar absorptance of 0.09 ($\Delta\alpha = 0.01$) and emissivity of 0.79 ($\Delta\varepsilon = 0.01$). The calorimeter support of Experiment S1002 was also sulfuric acid anodized and received the full mission experimental environmental exposure for tray E3 (11,100 ESH UV exposure and 10^{17} AO atoms/cm^2). Emissivity on this nonexperimental surface was 0.76, whether measured on exposed or protected areas. Solar absorptance had increased

slightly from 0.38 to 0.40 when moving from protected to exposed surfaces. The investigator cited contamination as the cause of the absorptance increase, with contamination enhanced by the coating porosity.

A disk of 6061 aluminum was sulfuric acid anodized for exposure on Experiment M0003 (ref. 12). The specimen was anodized to specification coating weight requirements of 1,500 to 2,000 mg/ft^2, and it received a chromate seal. After receiving 11,100 ESH UV exposure and 10^{17} atoms/cm^2 AO fluence, the postflight solar absorptance had increased only slightly, from 0.40 to 0.42. However, emissivity apparently increased significantly, from 0.75 to 0.84. This is the only example of a significant emissivity change for anodize that has been reported for LDEF. However, based on the established coating weight requirement, the preflight emissivity measurement is considered questionable, and it is suspected that there was no actual change in emissivity for this sulfuric acid anodized test specimen.

Dyed Sulfuric Acid Anodizing

Only one example of a dyed anodize coating has been reported from LDEF. Experiment S0050 involved a number of optical baffle coatings for low infrared reflectance (ref. 13). One of the coatings evaluated was a sample described as "Martin Black Anodize." This coating was a sulfuric acid anodize which had been permeated with a complex organic dye, and sealed in hot water. (Martin Black Anodize is prepared by Martin Marietta Astronautics Group.) Analysis of the black anodize coating was conducted after exposure to approximately 4,000 ESH of UV radiation and minimal atomic oxygen, due to location and test substrate orientation for experiment S0050. Postflight results indicated that the black anodize had increased its absorptance of wavelengths less than 150 microns. In this application, such an effect is a desirable consequence of space environmental exposure. The black anodize was, of the materials tested, alone in exhibiting this effect. Experiment investigators have postulated that this effect was the result of an increased density of absorption sites, formed as a result of vacuum and UV exposure.

CONCLUSIONS

For dyed anodize, there has been only one reported example from LDEF. The Martin Black Anodize improved in infrared absorptance with vacuum and moderate UV radiation exposure, but low AO fluence. The coating was evaluated for use as an optical baffle finish.

Performance results from sulfuric acid anodize looked very good. The available test surface area was limited, and no results were obtained for high AO fluence environment. However, the specimens flown indicated good solar absorptance stability to the UV radiation environment. Emissivity is considered stable. Although one specimen indicated a significant emissivity increase with exposure, the cause is thought to be preflight measurement error, based on the specified coating weight (thickness) of the oxide film.

A very large surface area of chromic acid anodize was exposed to all of the environmental conditions available from the LDEF mission. When considering the majority of measurements made from available surfaces, chromic acid anodize is stable in both solar absorptance and thermal emittance. Over 500 measurements have been made on structures, EECC's, and cover plates, with minimal changes

observed in absorptance for areas of high AO fluence. The solar absorptance changes observed for low AO fluence areas have been attributed to contamination processes occurring early in the LDEF mission. Emissivity on structural components was low (~0.2) and not significantly changed by the environment.

Inconsistencies have been observed, however, for chromic acid anodize. Test specimens having higher emissivities, or thicker anodize coatings, have not indicated any changes in thermal emittance with exposure. But solar absorptance for one set of specimens indicated excellent stability over a broad range of exposure conditions, whereas another set of specimens indicated a trend in solar absorptance degradation increasing at a rate of about 0.04 per 1,000 ESH. A failure analysis on the degraded chromic acid anodize specimens is needed to bring higher confidence to the assertion based on measurements from the vast majority of surface evaluated, that chromic acid anodize is stable in the low Earth orbital environment.

The central issue affecting absorptance stability for chromic acid anodize is likely one of contamination. Several authors have indicated that solar absorptance increase on anodize was associated with contamination. It was also apparent that AO fluences above the "threshold" of 10^{20} atoms/cm^2 reversed or removed the absorptance degradation effects. The primary concern does not appear to be one of inherent instability in the oxide produced through chromic acid anodize, but that the porosity of the anodize could act as a "sink" for molecular contamination.

REFERENCES

1. Duckett, R.J., and Gilliland, C.S.: "Variable Anodic Thermal Control Coating on Aluminum." AIAA-83-1492, 18th Thermophysical Conference, June 1–3, 1983.

2. Sampair, T.R., and Berrios, W.M.: "Effects of Low Earth Orbit Environment on the Long Duration Exposure Facility Thermal Control Coatings." First LDEF Post-Retrieval Symposium, NASA CP-3134, Part 2, 1991, p. 935.

3. Bourassa, R.J., and Pippin, H.G.: "Model of Spacecraft Atomic Oxygen and Solar Exposure Microenvironments." Third LDEF Post-Retrieval Symposium (Proceedings), in press.

4. Plagemann, W.L.: "Space Environmental Effects on the Integrity of Chromic Acid Anodized Coatings." First LDEF Post-Retrieval Symposium, NASA CP-3134, Part 2, 1991, p. 1023.

5. Slemp, W.S., and Young, P.R.: "LDEF Thermal Control Coatings Post-Flight Analysis." Second LDEF Post-Retrieval Symposium, NASA CP-3194, Part 3, p. 1093.

6. Golden, J.L.: "Anodized Aluminum on LDEF—A Current Status of Measurements on Chromic Acid Anodized Aluminum." LDEF Materials Workshop '91, NASA CP-3162, Part 1, 1992, p. 211.

7. Preuss, L.: "Evaluation of LDEF Experiment S1002." First LDEF Post-Retrieval Symposium, NASA CP-3134, Part 3, 1991, p. 1405.

8. Wilkes, D.R., Miller, E.R., Zwiener, J.M., and Mell, R.J.: "Thermal Control Surfaces Experiment (TSCE) Materials Analysis." Second LDEF Post-Retrieval Symposium, NASA CP-3194, 1993.

9. Linton, R.C., Kamenetzky, R.R., Reynolds, J.M., and Burris, C.L.: "LDEF Experiment A0034: Atomic Oxygen Stimulated Outgassing." First LDEF Post-Retrieval Symposium, NASA CP-3134, Part 2, 1991, p. 763.

10. Guillaumon, J., and Paillous, A.: "Spacecraft Thermal Control Coatings." First LDEF Post-Retrieval Symposium, NASA CP-3134, Part 2, 1991, p. 945.

11. Teichman, L.A., Slemp, W.S., and Witte, W.G., Jr.: "Evaluation of Selected Thermal Control Coatings for Long-Life Space Structures." NASA TM-4319, 1992.

12. Pippin, H.G., Mulkey, O., Verzemnieks, J., Miller, E., Hill, S., and Dursch, H.: "Survey of Results From the Boeing Modules on the M0003 Experiment on LDEF." First LDEF Post-Retrieval Symposium, NASA CP-3134, Part 2, 1991, p. 1109.

13. Blue, M.D., and Perkowitz, S.: "Space-Exposure Effects on Optical-Baffle Coatings at Far-Infrared Wavelengths." Applied Optics, vol. 31, No. 21, July 20, 1992, p. 4305.

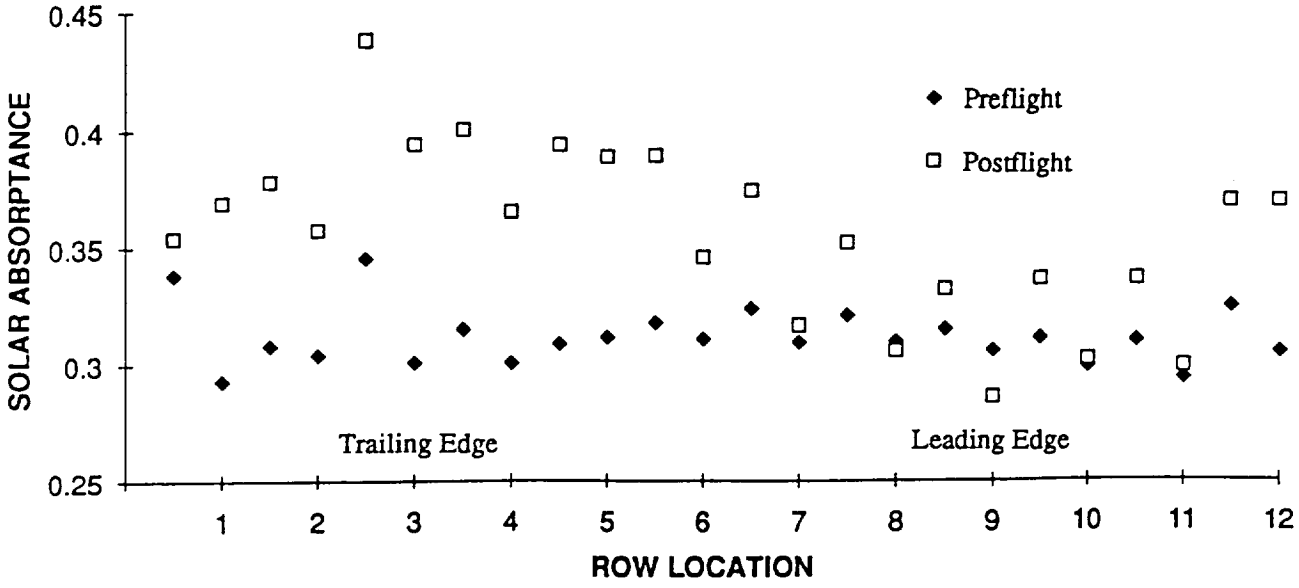

Figure 1. LDEF chromic acid anodize on longerons and intercostals, preflight and postflight absorptance versus row location.

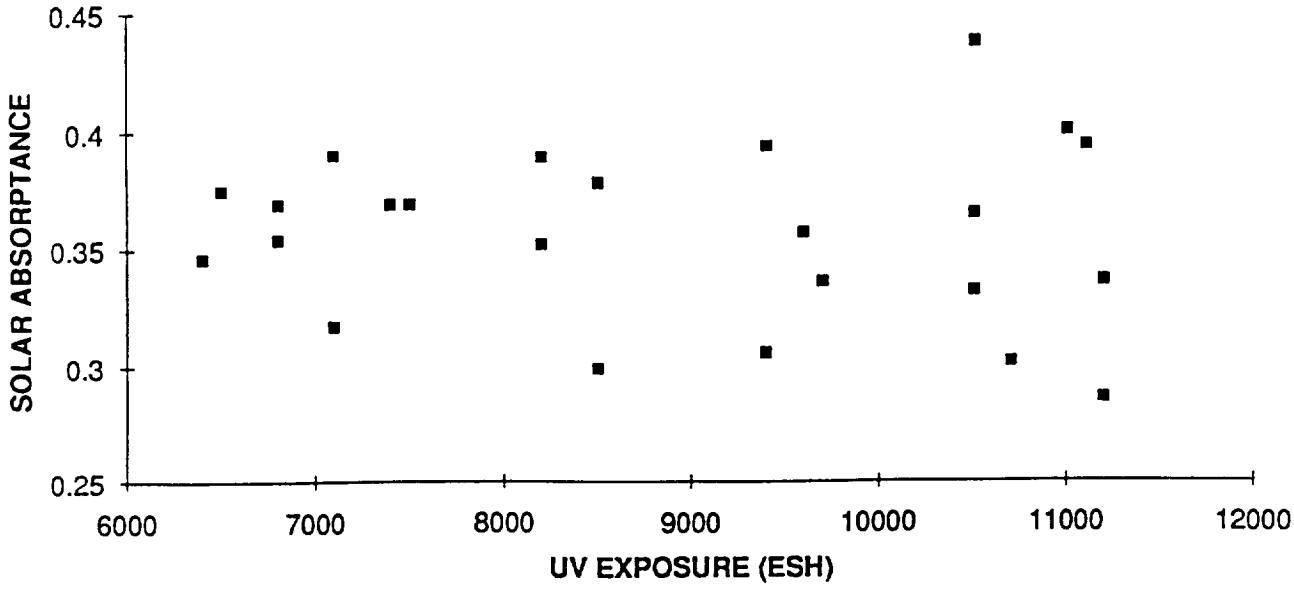

Figure 2. LDEF chromic acid anodize on longerons and intercostals, absorptance versus UV exposure.

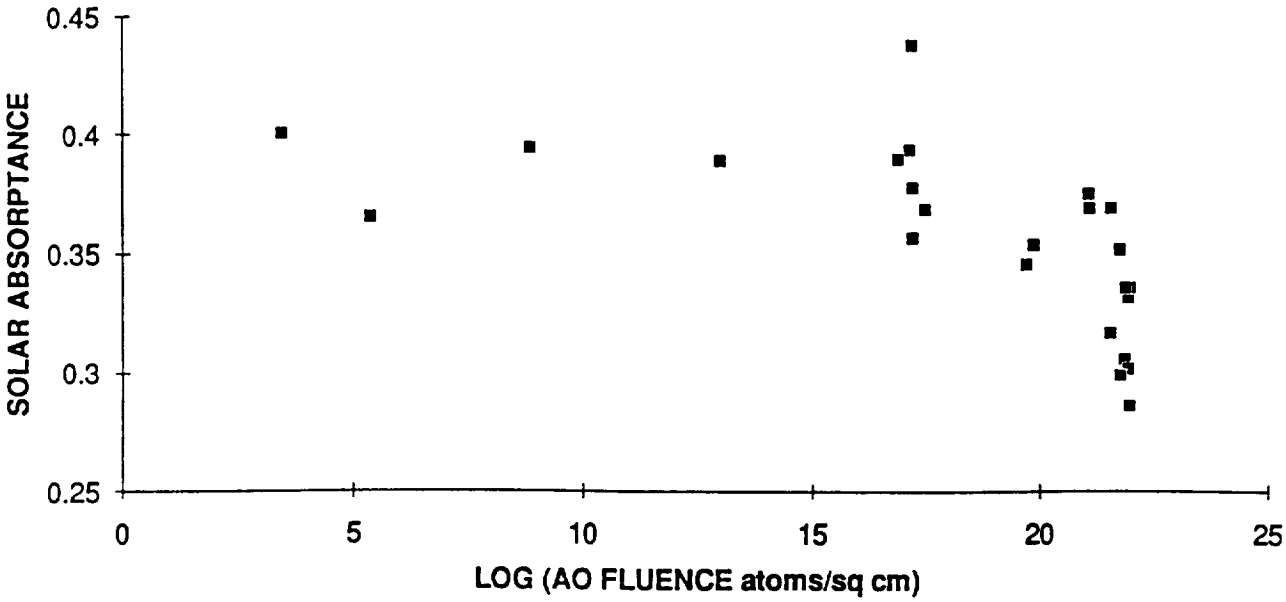

Figure 3. LDEF chromic acid anodize on longerons and intercostals, absorptance versus AO fluence.

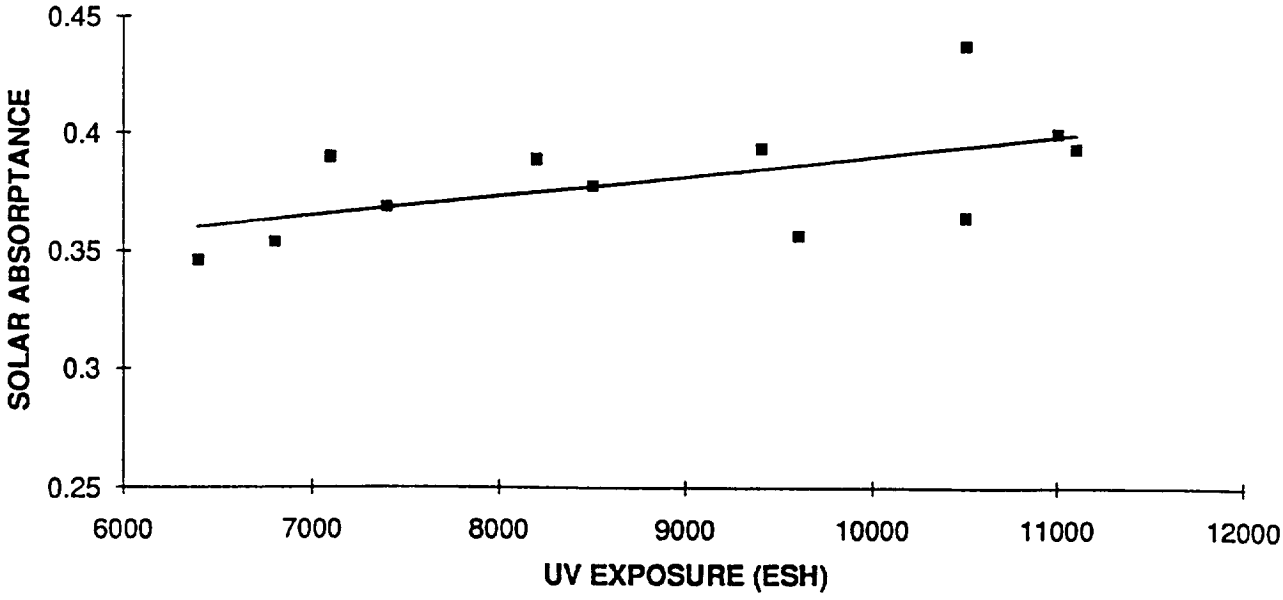

Figure 4. LDEF chromic acid anodize on low AO exposure longerons and intercostals, absorptance versus UV exposure.

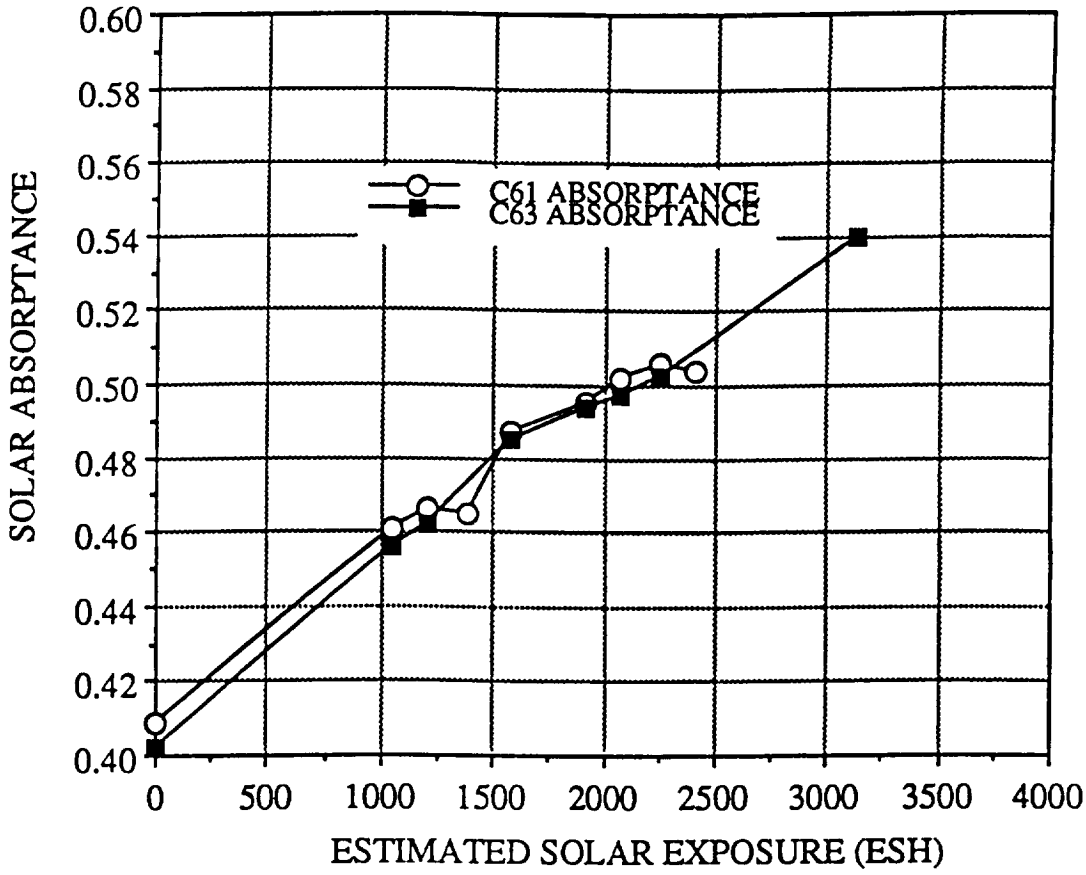

Figure 5. Experiment S0069 chromic acid anodize on 6061 aluminum, absorptance versus UV exposure.

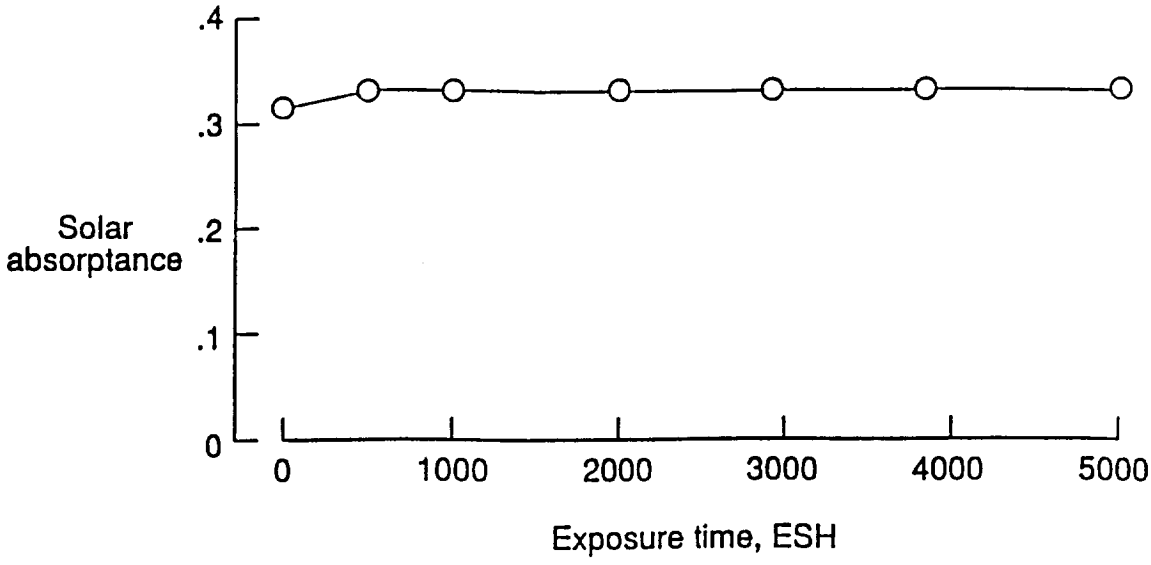

Figure 6. Chromic acid anodized 1145 aluminum foil, effects of groundbased UV exposure on absorptance (Ref. 11).

FOLLOW-UP ON THE EFFECTS OF THE SPACE ENVIRONMENT ON UHCRE THERMAL BLANKETS

François Levadou and Marc van Eesbeek
ESA/European Space Research and Technology Centre
Noordwijk, The Netherlands
Phone: (31)1719-83915, Fax: (31)1719-84992

SUMMARY

An overview of the effects of the space environment on the thermal blanket of the UHCRE experiment is presented with an emphasis on atomic oxygen (AO) erosion.

A more accurate value for FEP Teflon™ reaction efficiency is given and corresponds, at normal incidence, to 3.24 10^{-25} cm^3/atom, therefore, the FEP Teflon™ erosion corresponding to the Long Duration Exposure Facility (LDEF) total mission is 29.5 μm. A power 1.44 of the cosine of the incident angle of the oxygen atoms is found. It is shown that this value is not far from the power found using Fergusson's relationship between efficiency and energy of the O-atoms.

An hypothesis concerning the effect of oxygen ions (O^+) is also presented. The presence of oxygen ions may explain the different results obtained from different flights and from laboratory tests.

Finally an XPS analysis of Chemglaze Z306™ black paint demonstrates the presence of silicone in the paint which may explain part of the contamination found on LDEF.

FEP TEFLON™ EROSION

It has already been shown in previous papers (refs. 1,2) that the thickness of the FEP Teflon™ used for the UHCRE experiment (A0178) is not known with an accuracy better than ±6 μm for a total thickness of 127 μm (5 mils). Such an inaccuracy may give an error of 50 percent on the reaction efficiency (R_E) estimation of FEP Teflon™. To improve this accuracy, the only way is to increase the number of samples used to evaluate R_E.

Therefore, three more samples were cut from each tray from rows 7, 8, 10 and 11 to reach a total of at least six measurements by tray. The total number of measurements is 77 samples for the spare blankets, giving a mean value of the thickness of 126.5 μm and a standard deviation of 3.35 μm, and 45 eroded samples. Figure 1 shows the thickness decrease versus the AO fluence for each row.

Remark : The AO fluences at end of mission for all rows were changed, taking into account the revised data dated from September 29, 1992, which are mentioned in LDEF Newsletter vol. III No. 6 (November 15, 1992).

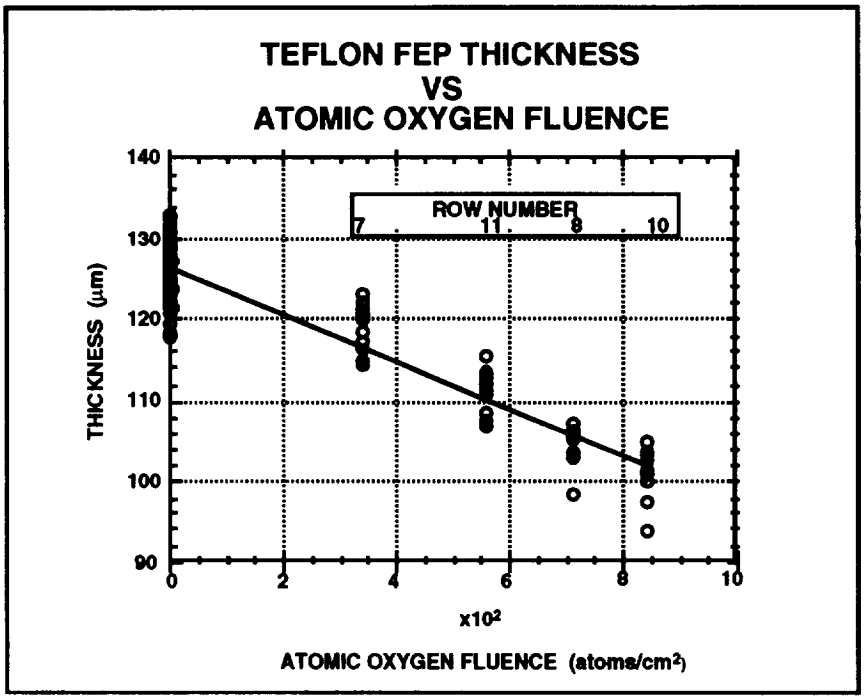

Figure 1

Each tray having received a different fluence, the thickness erosion of the film could be plotted versus the angle at which the oxygen atoms strike the thermal blanket and, to be more precise, versus the cosine of this angle (Figure 2). A power law regression curve could be calculated by the software used (Kaleidagraph from Synergy Software). An erosion of 29.5 µm is found for at normal incident angle and a power 1.44 of the cosine. This value is not far from the value of 1.5 found for the Kapton™ from previous flights and mentioned by Bruce Banks.

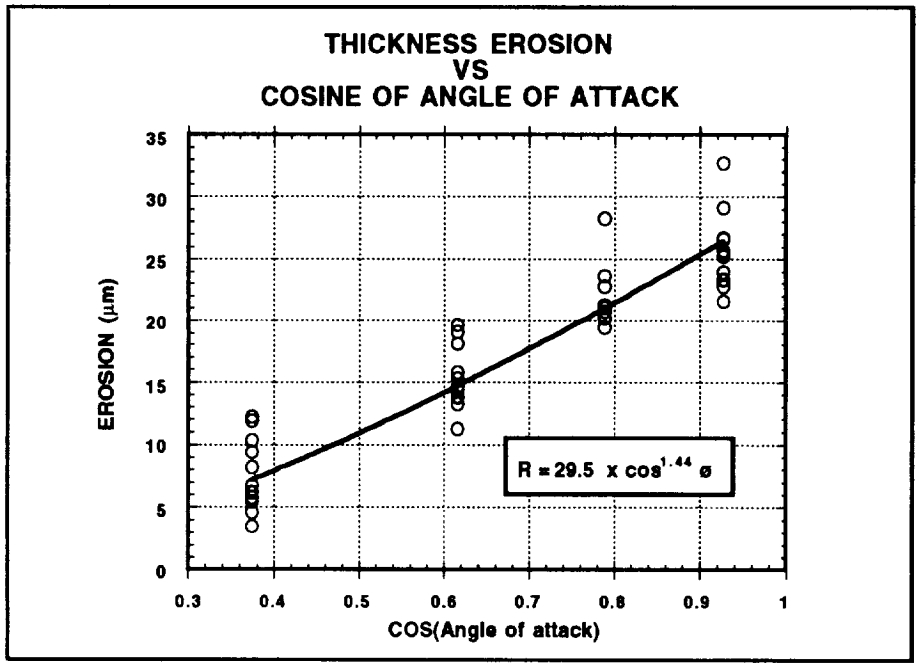

Figure 2

If the reaction efficiency is plotted instead of the recession (Figure 3), a value of 3.24×10^{-25} is found at normal incidence. For the other angles a law in $\cos^{0.44}$ applies. As the atomic oxygen fluence for each row is practically a cosine law of the incident angle of the atoms, it is quite normal to find a power 0.44.

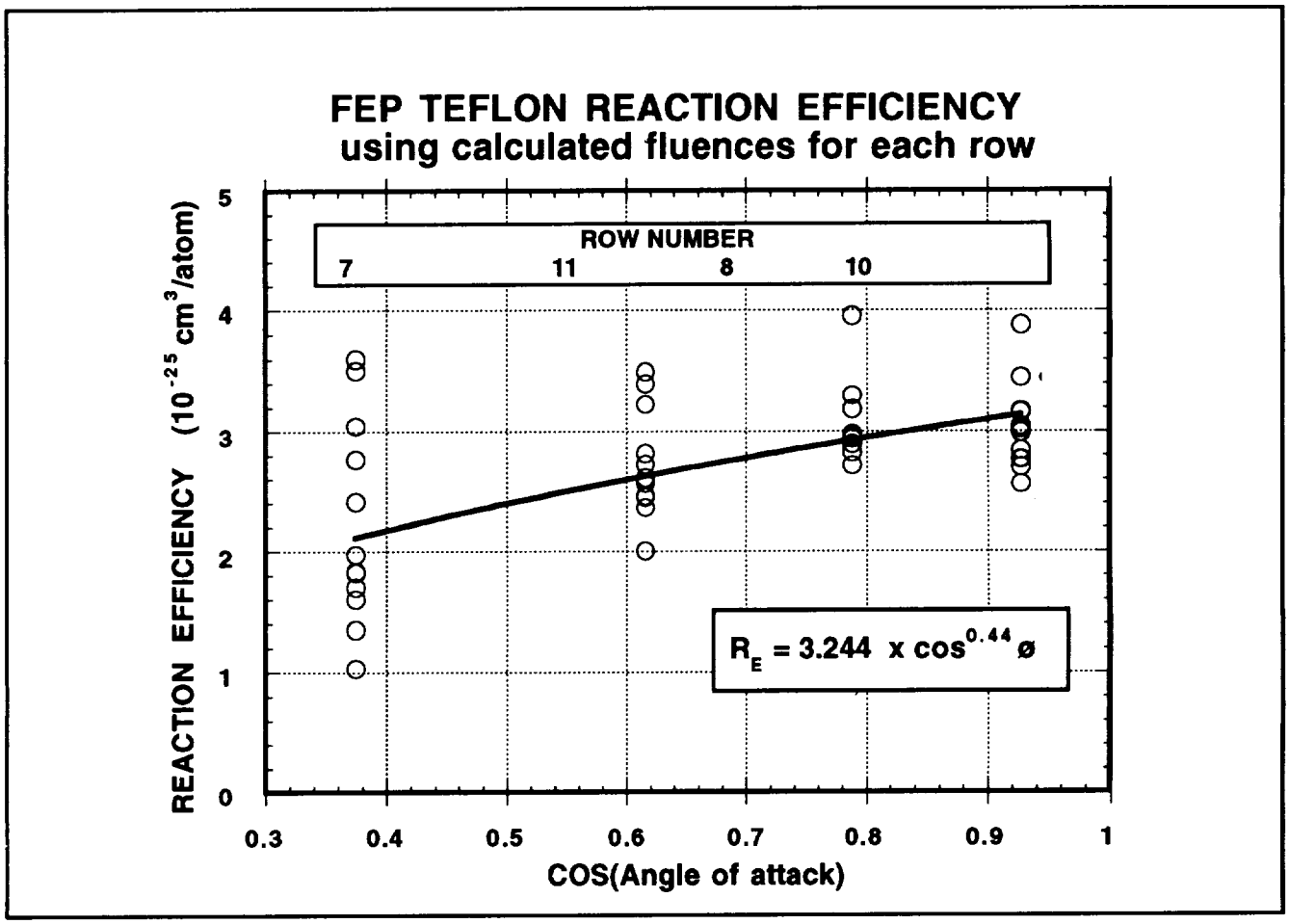

Figure 3

In addition, if the reaction efficiency is plotted versus the cosine of the angle of attack but, this time, when R_E is computed using only the fluence at normal incidence, i.e., 9.09×10^{21} atoms/cm^2, (Figure 4), the results obtained for the FEP Teflon™ film show an angular effect on the rate given by :

$$R_\theta = R_\perp \cos^{1.44}\theta$$

where R_θ is the erosion yield for the incidence angle θ, and $R_\perp$ the erosion yield at normal incidence.

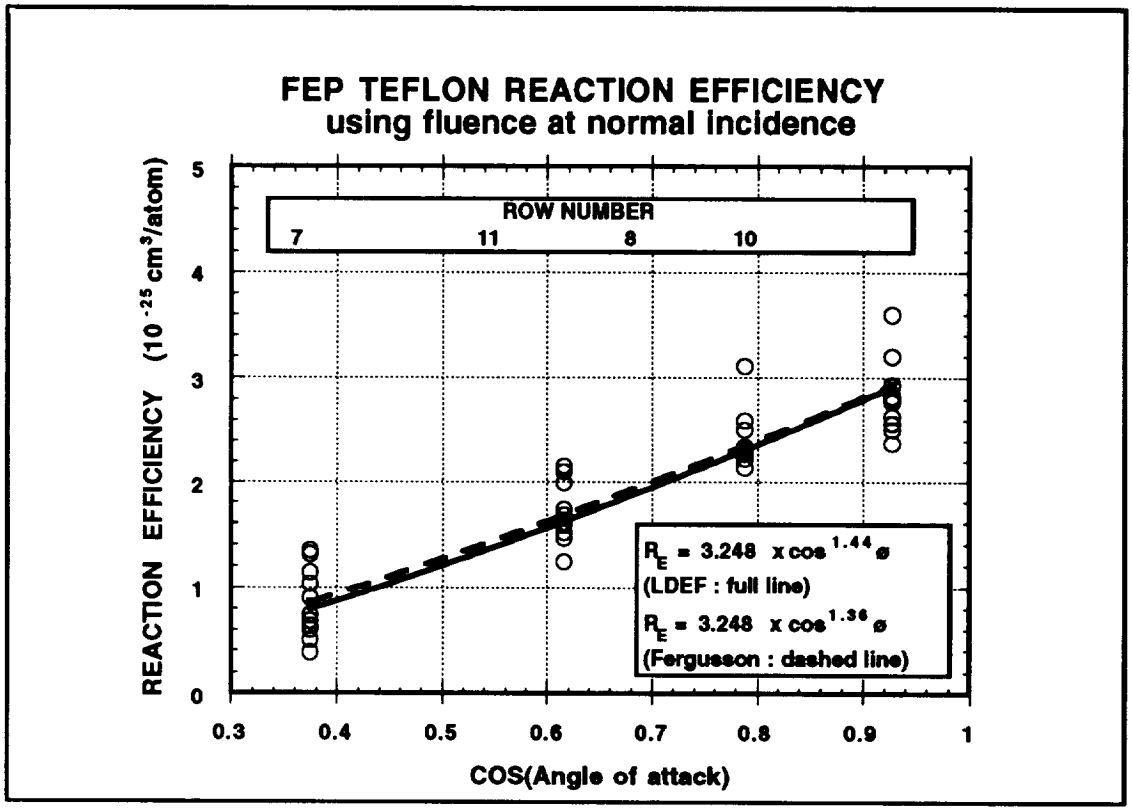

Figure 4

The effective energy of an oxygen atom is:

$$E_\theta = \frac{1}{2} m v_\perp^2 = \frac{1}{2} m (v_0 \cdot \cos\theta)^2 ,$$

for a normal incidence attack this energy would be:

$$E_\perp = \frac{1}{2} m v_0^2 .$$

Then :

$$E_\theta = E_\perp \cdot \cos^2\theta .$$

For Kapton™, the reactivity as function of energy was given by Fergusson as:

$$R \approx E^{0.68} .$$

Therefore, assuming this empirical law is also valid for FEP Teflon, we would expect a reactivity:

$$R_\theta \approx E_\theta^{0.68} = (E_\perp \cdot \cos^2\theta)^{0.68} ,$$

$$R_\theta \approx E_\perp^{0.68} \cdot \cos^{1.36}\theta ,$$

$$\boxed{R_\theta = R_\perp \cos^{1.36}\theta} .$$

The experimental value 1.44 found is not far from 1.36. For comparison the curve with cosine to the power 1.36 is plotted on the same Figure 4 assuming an identical reactivity at normal incidence.

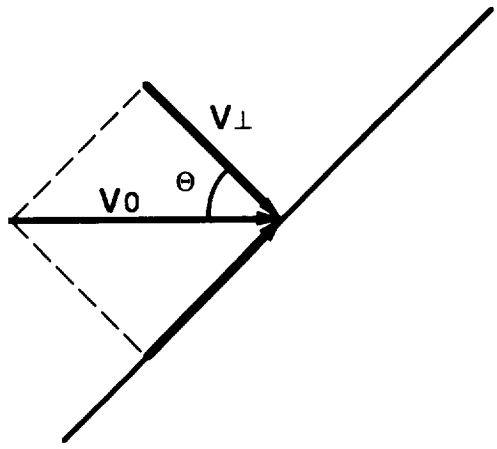

COMPARISON BETWEEN FLIGHT DATA AND TEST DATA

Figure 5 shows the erosion yield of FEP Teflon™ as a function of AO fluence for several environments as well as during onground simulations and in-flight. Even flight data seems to give different results between shuttle flights STS-8, STS-41G, EOIM-3, and LDEF. The synergism between the reaction due to oxygen atoms and the ultraviolet (UV) irradiation, particularly the far UV below 2,000 Å, is often mentioned as an explanation. It is true that in all facilities used to simulate oxygen atoms there is a wide variation in the flux of the far UV that is present along with the oxygen atom beam. The wavelength range and the spectral energy of this UV is generally unknown.

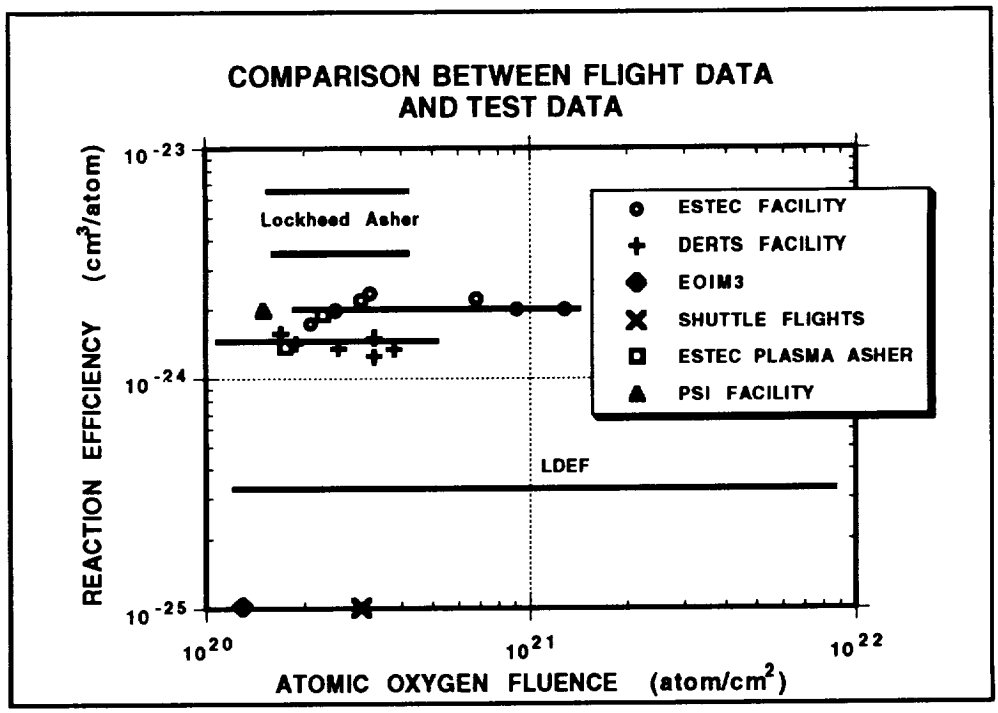

Figure 5

Another possible explanation, although somewhat speculative due to the lack of more exact data on ion concentration, is the presence of different ratios of oxygen ions and oxygen atoms as a function of altitude and the possibility that oxygen ions have a higher reactivity than neutral atoms. This hypothesis was mentioned a few years ago by D.G. Zimcik (ref. 3) to explain the differences between STS-41G and Solar Max Satellite.

The density of O^+ and O as function of altitude for minimum solar activity is given in Figure 6. This figure also shows that, for the given interval, the O^+/O_{tot} ratio between both species is increasing with altitude ($O_{tot} = O^+ + O$).

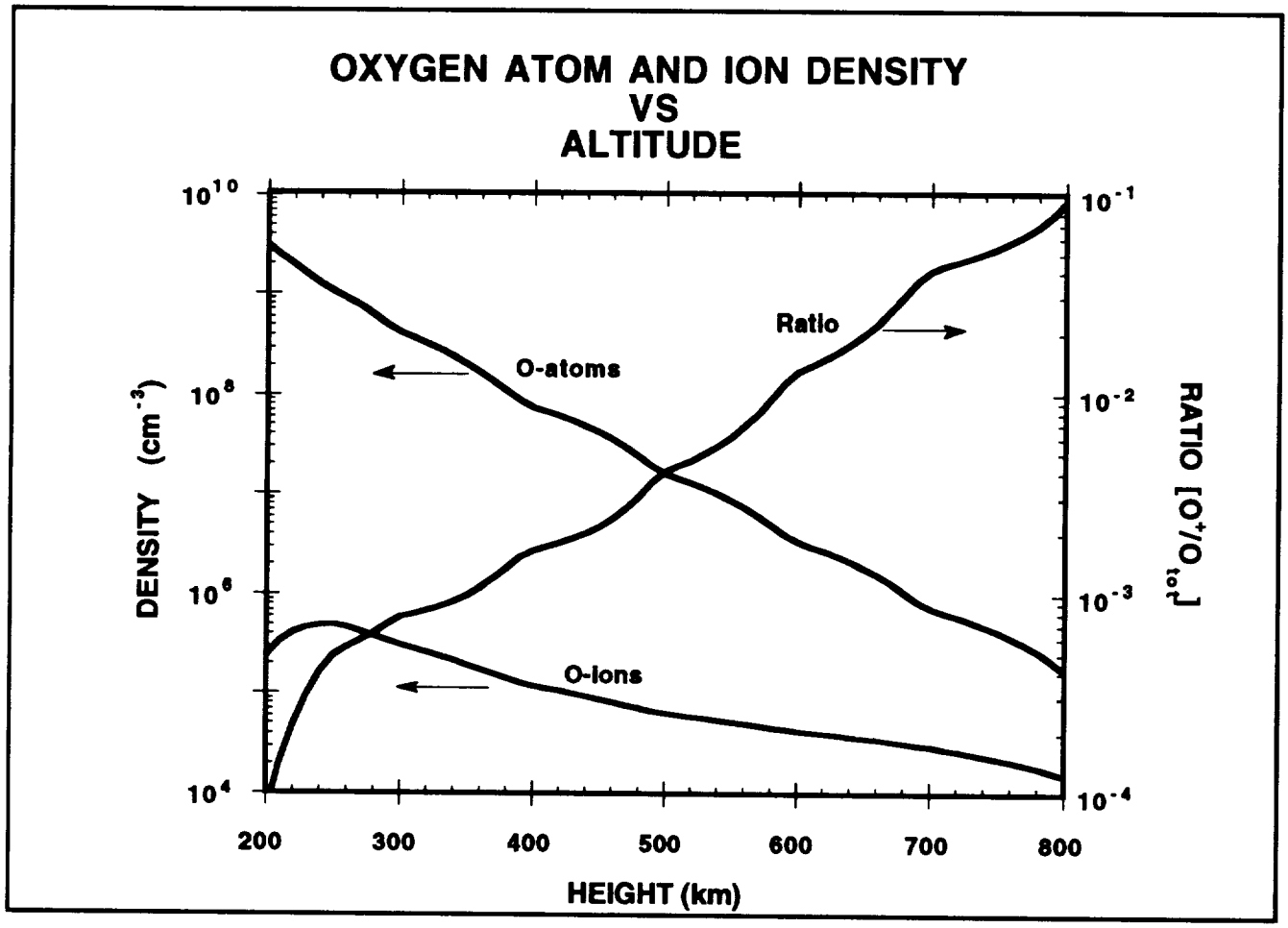

Figure 6

Although the nominal LDEF orbit for most of its lifetime was above 450 km, 50 percent of all fluence was accumulated in the last year, when the satellite orbit was decaying rapidly. Over this period, the height corresponding to the average flux was some 400 km, resulting in a O^+/O_{tot} ratio of 0.0016. The measured reaction efficiency was three times higher than what was found after STS-8, EOIM-3, and other exposures to the lower ratios (near 0.00025) encountered in the orbit of 225 km.

Onground simulations in Fast Atom Beam Facilities, such as the ones at PSI, CERT/DERTS and ESTEC, with an O^+/O_{tot} ratio of 0.01 or the Ion Beam Facility at Culham ($O^+/O_{tot} = 1$), show a further increase in yield.

From Figure 7, it appears that the relation between the yield and the O^+/O_{tot} ratio can be approached by a power function :

$$R = 6.2\ 10^{-23} \times C^{0.78}$$

with R = reaction efficiency in cm^3/O-atom and C = ratio O^+/O_{tot} .

The effects of ions could also explain why during Solar Max Mission (mean altitude 515 km, $O^+/O_{tot} = 0.0045$) the FEP Teflon™ deteriorated more dramatically than would be expected from shuttle flights or even LDEF results.

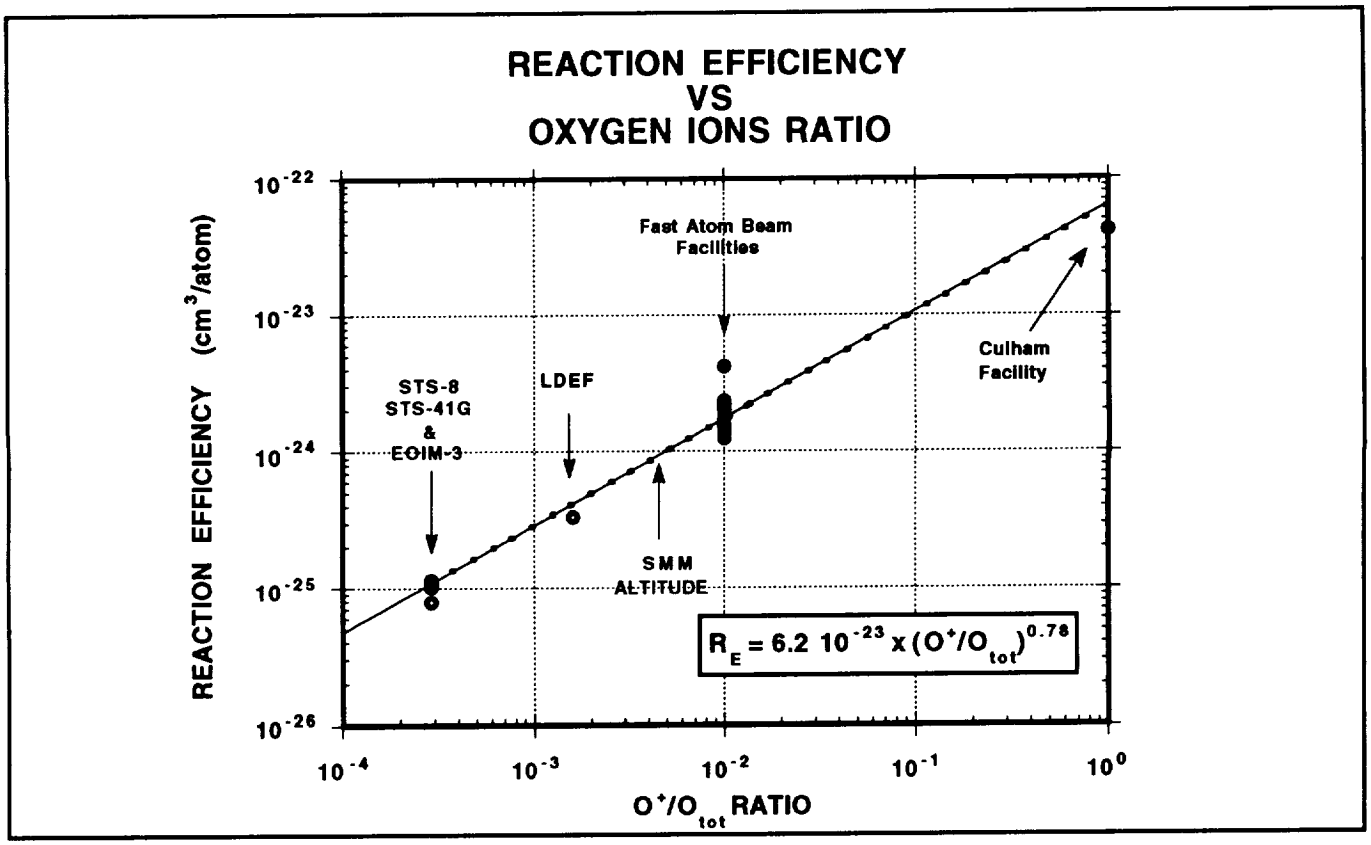

Figure 7

XPS ANALYSIS OF CHEMGLAZE Z306™

Purpose of this study

Since the beginning of the studies on LDEF contamination, the Chemglaze Z306™ was suspected to have been, among others, a source of silicone contaminant. In particular, the brown contamination which can be observed on leading trays, where oxygen atoms could penetrate inside LDEF, was strongly suspected to be due to this paint which covers the whole internal structure and some parts of the trays.

In the first instance, this assumption was based on information obtained from the British representative of the manufacturer, which confirmed the presence of a silicone fluid in the paint. Later on, the U.S. manufacturer denied that any silicone was present in the paint formulation, but the "Z306 formulation includes a fumed silica used as a flatting agent" (3.27 percent by weight). Therefore the presence of silica may explain the silicon peak found in all SEM/EDX analysis.

The study performed by Dr J. Golden (ref. 4), based on chemical extraction of silicone, has concluded that there is no silicone in the Z306. A similar measurement done for ESTEC by the TNO (ref. 5) (Delft, The Netherlands) has also given a negative answer.

In May 1992, the Max-Planck Institut Für Aeronomie sent to ESTEC an alert concerning the possible presence of siloxanes in Cab-O-Sil™ (American manufacturer) and Aerosil™ (German manufacturer). Consequently, to confirm or not the silicone content in Z306 formulation, XPS analysis were performed.

Experimental Technique

The analyses performed by CRPHT (ref. 6) (Orléans, France) were obtained using the ESCALAB Mark II from V.G. Instrument. The x-ray source line used is the Ka of magnesium at energy 1253,6 eV and width 0.75 eV. For nonconductive samples, the power is limited to 10 kV by 20 mA. During the measurements, the vacuum was 10^{-6} Pa and the samples were at room temperature. Acquisition time was 20 s, and the number of records for the different peaks were 50 scans for C1s, 30 scans for O1s, 200 scans for Si2p and 10 for another measurement of C1s at the end to verify that the sample did not charge during the acquisition.

Standard positions of the main peaks of chemical compounds are given by D. Briggs and M.P. Seah (ref 7).

Samples description

Table 1 lists the samples submitted to XPS analysis.

A1. The PS-7 silicate paint was submitted to analysis to determine the binding energy of the Si2p peak of silicate compared to silicone.

A2. This sample of Chemglaze Z306™ was cut from a spare flight blanket. It is therefore the formulation of the paint as manufactured circa 1981.

A3. The silicone adhesive C6-1104 was the one used to fix the Velcro™ on the thermal blanket and the frame of UHCRE as well as the Kapton™ sheets used to close the bottom of the trays.

A4. An unexposed sample of UHCRE thermal blanket cut from tray C11 on which a slight brown contamination can be seen.

The two following samples A5 and A6 are collected volatile condensable materials (CVCM), from Chemglaze Z306™ and Dow Corning C6 1104, obtained from recent lots of these materials. CVCM were obtained following ESA PSS-01-702 Specification (ref. 8) identical to ASTM E-695. If the black paint contains only fumed silica, then no silicon peak must be found in the CVCM.

Table 1

Sample	Description
A1	Silicate PS-7 Paint from Silvana
A2	Chemglaze Z306™ Paint from Lord (on UHCRE Spare blanket)
A3	C6 1104 Silicone Adhesive from Dow Corning
A4	Flight UHCRE blanket slightly contaminated (yellow stain)
A5	CVCM of Chemglaze Z306™ (recent lot)
A6	CVCM of C6 1104

Results

Table 2 gives the binding energies of the main peaks obtained for each sample. Tables 3 and 4 give these peaks for Chemglaze Z306™ (sample A2) and CVCM sample of Chemglaze Z306™ (sample A5).

Only results for Chemglaze are presented.

The analysis confirms the presence of silicone in the paint: for both samples, A2 and A5, the oxygen peak has its main component corresponding to the oxygen in silicone. The silicon peak is simple and corresponds to the bonding for silicones. Therefore, it is concluded in view of these results that there is silicone in the Chemglaze Z306™.

Table 2

Sample	A1	A2	A3	A4	A5	A6
C1s	284.6	284.6 286.1	284.6	284.6 286.6	284.6 285.9	284.6
O1s	530.5 532.3	532.2	532.1	532.8	532.0 533.3	532.5
Si2p	101.7	101.7	102.1	103.6	102.0	102.1
K2p3/2	292.3					
N1s		399.4				
F1s				687.4		

Table 3

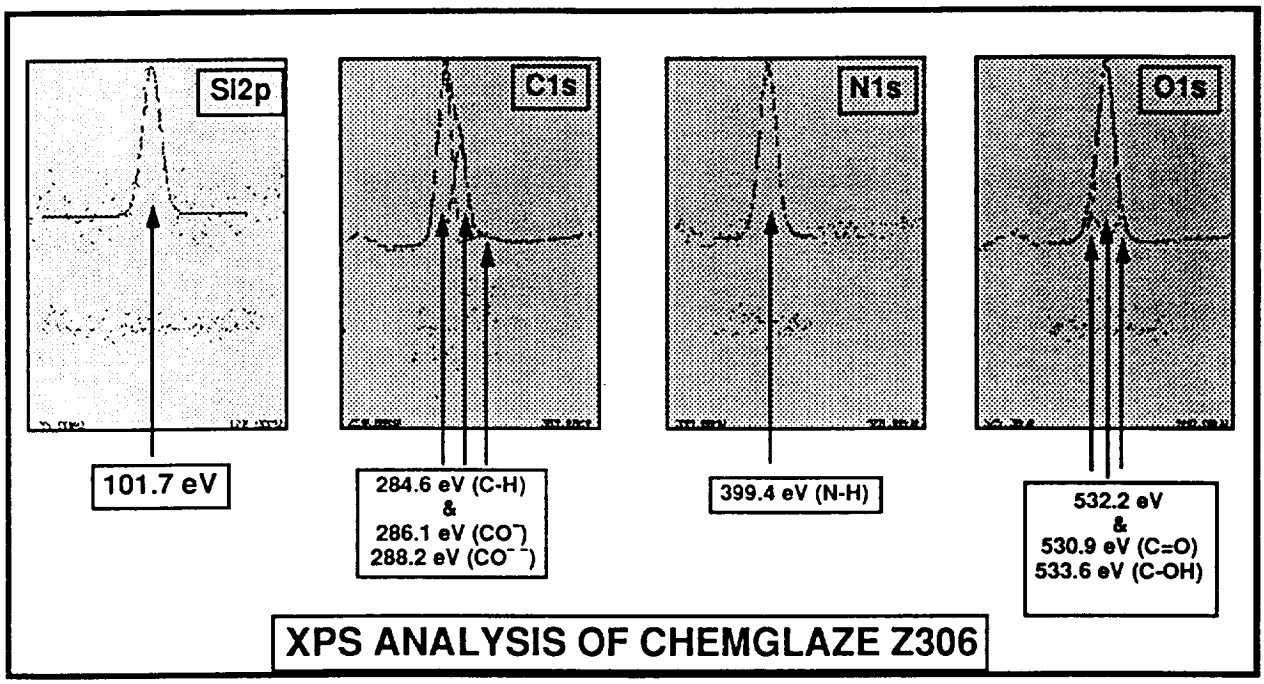

Table 4

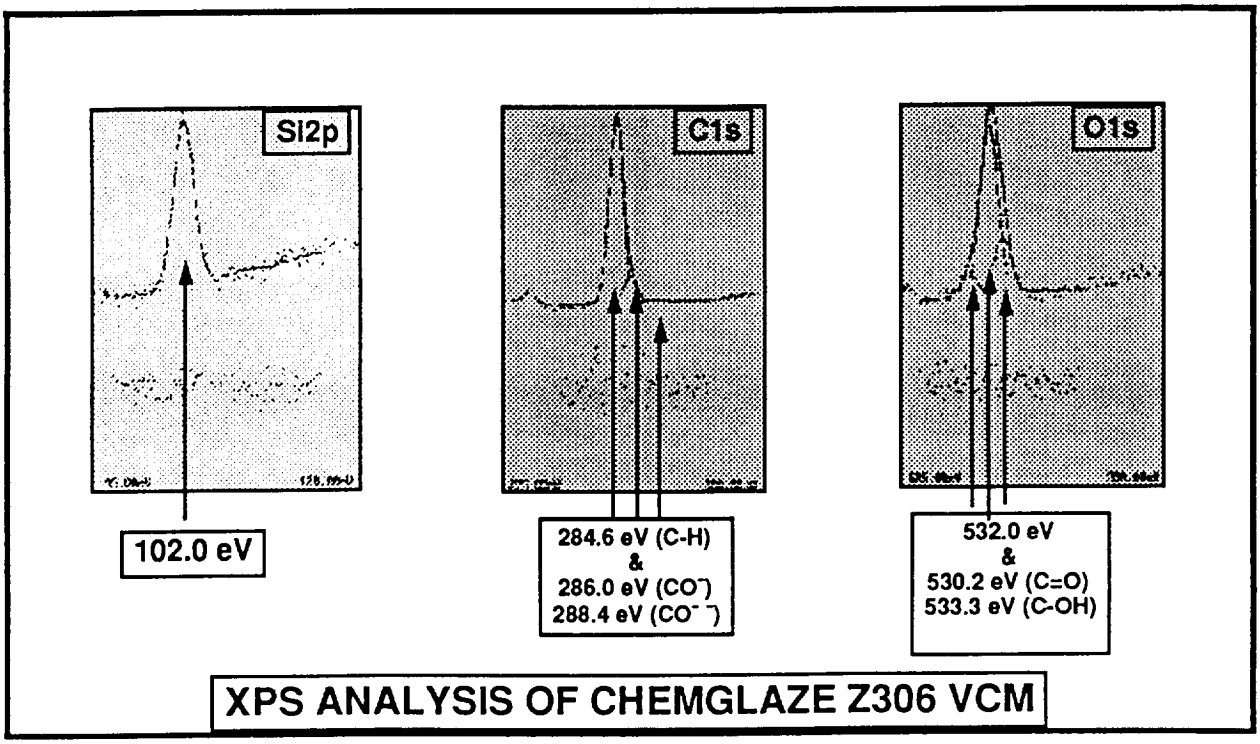
Si2p
102.0 eV
C1s
284.6 eV (C-H)
&
286.0 eV (CO)
288.4 eV (CO)
O1s
532.0 eV
&
530.2 eV (C=O)
533.3 eV (C-OH)
XPS ANALYSIS OF CHEMGLAZE Z306 VCM

REFERENCES

1. Levadou, F., Froggatt, M., Rott, M., and Schneider, E.: "Preliminary Investigations Into UHCRE Thermal Control Materials." LDEF First Retrieval Symposium, June 2–8, 1991, NASA CP3134, part 2, pp. 875–898.

2. Levadou, F., and Pippin, G.: "Effects of the LDEF Environment on the Ag/FEP Thermal Blankets." Materials Workshop '91, November 1991, NASA CP3162, part 1, pp. 311–344.

3. Zimcik, D.G.: "Effect of Long-Term Exposure to LEO Space Environment on Spacecraft Materials." Canadian Aeronautics and Space Journal, vol. 33, No. 1, March 1987, pp. 4–10.

4. Golden, J.L.: "Z306 Molecular Contamination—Ad Hoc Committee Results." LDEF Materials Workshop '91, November 1991, NASA CP3162, part 1, pp. 115–140.

5. Van der Meer, A.J.: "Silicone Compound in Chemglaze Z306." TNO Report No. 421/92.

6. Landron, C., Coutures, J.P., and Erre, R.: "Etude par XPS du silicium dans une série de six échantillons." ESTEC Purchase Order 120114, January 1992.

7. Wagner, C.D.: "Auger and Photoelectron Energies and the Auger Parameter in Practical Surface Analysis by Auger and X-Ray Photoelectron Spectroscopy." Edited by D. Briggs and M.P. Seah, John Wiley and Sons, 1983.

8. ESA PS-01-702, "A Thermal Vacuum Test for the Screening of Space Materials."

SPACECRAFT ENVIRONMENT

MODELING OF LDEF CONTAMINATION ENVIRONMENT

M. Ralph Carruth, Jr.
NASA Marshall Space Flight Center
Huntsville, AL 35812

Dr. Ray Rantanen
ROR Enterprises
Castle Rock, CO 80104

Tim Gordon
Applied Science Technologies
Littleton, CO 80162

SUMMARY

The Long Duration Exposure Facility (LDEF) satellite was unique in many ways. It was a large structure that was in space for an extended period of time and was stable in orientation relative to the velocity vector. There are obvious and well documented effects of contamination and space environment effects on the LDEF satellite. In order to examine the interaction of LDEF with its environment and the resulting effect on the satellite, the Integrated Spacecraft Environments Model (ISEM) was used to model the LDEF-induced neutral environment at several different times and altitudes during the mission.

INTRODUCTION

The LDEF satellite was placed in orbit to study the long-term effects of the space environment on materials and systems. It remained in orbit for almost 6 years, with its orbit decaying during the mission so that the environment experienced by the satellite changed with time. The LDEF satellite was a large structure which was stable in orientation relative to its velocity vector.

The large size, long duration of exposure, and orientation stability provided a unique opportunity for modeling the global neutral molecular environment induced by the satellite's motion in the ambient environment. Also, modeling of select local phenomena on the satellite was accomplished.

The intensity of outgassing was obviously maximum during the early part of the mission. This would be true also for the outgassing of the interior of the spacecraft which would be able to exit through vent holes around the experiments. The satellite face whose normal was into the velocity vector experienced the effect of the 5 eV atomic oxygen atoms. The opposite face experienced very little atomic oxygen exposure except for a small amount during retrieval and scattered atoms. More outgassing products could potentially be scattered back to the surface on the ram facing side of the vehicle.

Very noticeable brown deposits were present on the interior surfaces of the experiment trays. Modeling of a single vent was performed in order to compare the results with observed data.

C-2

INTEGRATED SPACECRAFT ENVIRONMENTS MODEL (ISEM)

ISEM is a collisional molecular transport code which computes the molecular density and flux in a three-dimensional modeling volume for any number of user-defined molecular species. The LDEF geometry used for this modeling study is shown in Figure 1 and Figure 2.

MODELING PARAMETERS

Three different periods in the LDEF mission were modeled to obtain representative results over the mission lifetime. These periods were representative of the beginning, middle, and end of the mission timeline and corresponded to orbital altitudes of 463 km, 417 km, and 333 km, respectively. Table 1 shows the ambient values for the six different molecular species modeled at the beginning and ending periods. The values were obtained using the atmosphere predicting model MSIS86 and represent annual and orbital position averaged values for the periods modeled.

Table 1. Average ambient atmosphere density values (MSIS86).

Species	Date	
#/cm^3	4/84	1/90
O	2.59×10^{7}	9.03×10^{8}
O_2	7.52×10^{3}	6.06×10^{6}
N	6.65×10^{5}	3.28×10^{7}
N_2	4.23×10^{5}	2.03×10^{8}
He	3.47×10^{6}	5.07×10^{6}
H	1.63×10^{5}	2.66×10^{4}

Table 2 shows the outgassing and erosion rates used for the modeling. External surfaces were modeled as having an average uniform outgassing rate which decreased with time. The initial outgassing rates were based on test data and the percentages of various materials present. Outgassing from internal surfaces was allowed to escape to the external environment via the numerous holes around the experiment trays. The external outgassing rate was assumed to decrease with an e folding time of 6,000 h. The internal outgassing rate was assumed to decrease with an e folding time of 7,000 h. The e folding times were based on Skylab measurements, taking into account differences in materials and materials control between the two programs. The average erosion rate was

Table 2. Outgassing and erosion rates.

Rate	463 km	333 km
g/cm^2/s	4/84	1/90
External	2.0×10^{-9}	1.4×10^{-12}
Internal	2.0×10^{-10}	4.8×10^{-13}
Erosion	6.3×10^{-11}	2.2×10^{-9}

assumed to be 15 percent of Kapton for all the surfaces. The erosion rate given in Table 2 is for a surface normal to ram, a cosine dependence (relative to the velocity vector) was assumed for non-normal surfaces.

GENERAL MODELING RESULTS

ISEM was used to compute the density of every tracked species throughout the three-dimensional modeling volume for the mission beginning, middle, and end cases described previously. Figures 3 and 4 show the iso-density contours for a plane of values from the three-dimensional modeling volume. The total density value is the sum of ambient species, surface reemitted ambient species, internal and external outgassed species, and the scatter portions of all species. The contour values have been normalized to the total undisturbed ambient density at the respective altitude. Figure 3 shows the total iso-density contours for the early mission case at an altitude of 463 km. A slight ram buildup can be seen in front of the vehicle (velocity vector from left to right), but the density around the vehicle is dominated by the outgassing. Figure 4 shows the total iso-density contours for the late mission case at an altitude of 333 km. There is a strong density buildup in front of the vehicle due to ambient and erosion products. The wake is very well defined, and although the densities are much less than on the ram side, the density in the wake region is still dominated by the outgassed species.

From the standpoint of surface materials interaction with the molecular environment, molecular flux of the different species is much more important than density. Flux of each tracked species was computed to each of the LDEF facets. Figures 5 through 8 show the surface incident flux at the highest and lowest modeled altitudes for atomic oxygen and molecular nitrogen. In the figures, the surface incident flux is plotted as a function of incident angle as measured from the ram direction. The term "direct" on figures refer to flux of molecules which have not had a collision. They still retain the kinetic energy of the orbital velocity (in the spacecraft reference frame). Figures 9 and 10 show the flux of outgassed and erosion products at the highest and lowest modeled altitudes, respectively. Note that there is no direct flux in these figures because only transport via scattering can produce the return flux of these species to the external surface. This may not be true on the scale of individual experiment trays. These figures illustrate, as expected, that the ram surfaces are dominated by the direct flux and that the wake surfaces are dominated by scattered flux. The calculations do show that a scatter flux exists even at nearly 180°. Also, the return flux in the wake regions is always dominated by outgassing products, even late in the mission when outgassing is lowest.

SMALL SCALE MODELING RESULTS

A modeling effort was undertaken to examine the molecular flux through a small aperture and the resulting incident flux on an internal surface, namely, the side of an experiment tray. Figure 11 shows the geometrical relationship of the aperture and the internal surface. Incident atomic oxygen was modeled as entering the aperture and then allowed to expand due to its thermal distribution. The atomic oxygen pattern incident on the side of the experiment tray was consistent with the deposition pattern observed on the side of the tray. Also, rivets and bolt heads shadowed portions of the experiment tray from atomic oxygen impingement and no deposition was observed. The modeling results are consistent with the view that outgassing products from inside the LDEF were adsorbed onto surfaces. Where atomic oxygen was able to flow through vents and apertures and impinge on these surfaces, resulting chemical interaction caused a permanent deposit to form.

CONCLUSIONS

Both large-scale and small-scale modeling of LDEF and its environment was accomplished for specific missions times, early and late in the mission. The modeling results were consistent with observations on LDEF and do provide some insight into important processes ongoing in determining the overall environment and contamination potential. Early in the mission, the environment was dominated by outgassing of the LDEF itself. Outgassing dominated the wake region density for the entire mission. For later times in the mission, the ram side density was many times that of the ambient. This was caused by a combination of accommodation and emission of oxygen, emission of reaction products and scattered molecules. The flux to the surface is dominated by direct atomic oxygen impingement, but a significant flux of scattered molecules exists. Even on the wake side, the scattered flux can be observed at angles up to 180°. The return flux of erosion species near the end of the mission was an order of magnitude greater than the return flux of outgassed products early in the mission.

Internal deposition has been observed on LDEF around vents and near apertures where atomic oxygen could flow unobstructed to the interior. Modeling of this flow indicated that the observed patterns were consistent with the thermally distributed flux of ambient atomic oxygen. The atomic oxygen must be reacting with internally outgassed contaminants on the internal surfaces to leave the observed deposits.

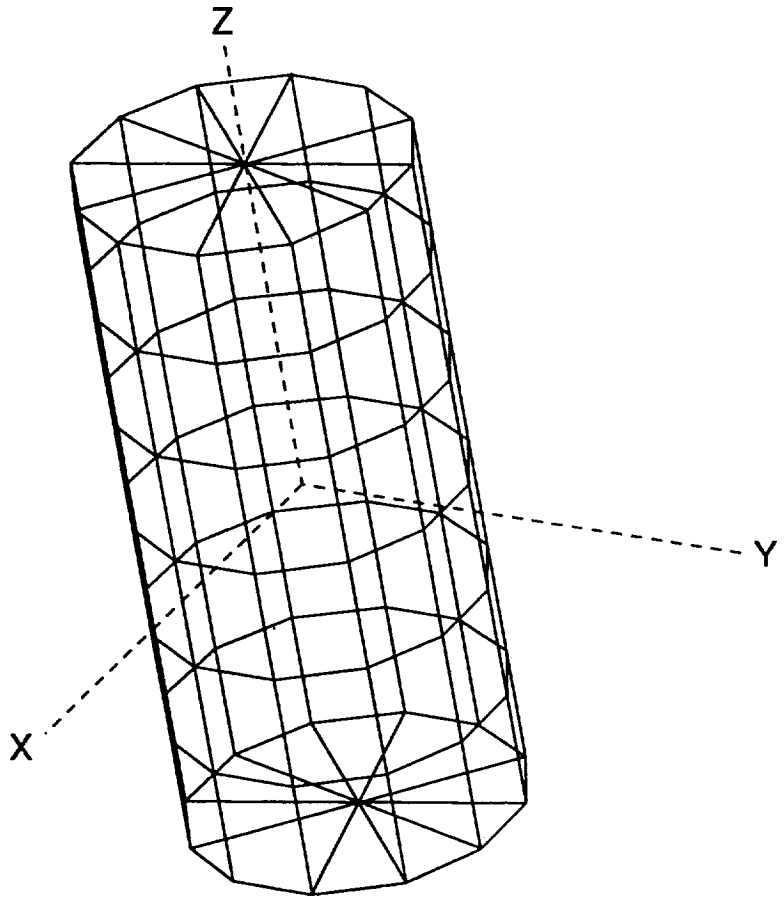

Figure 1. Geometry of LDEF model.

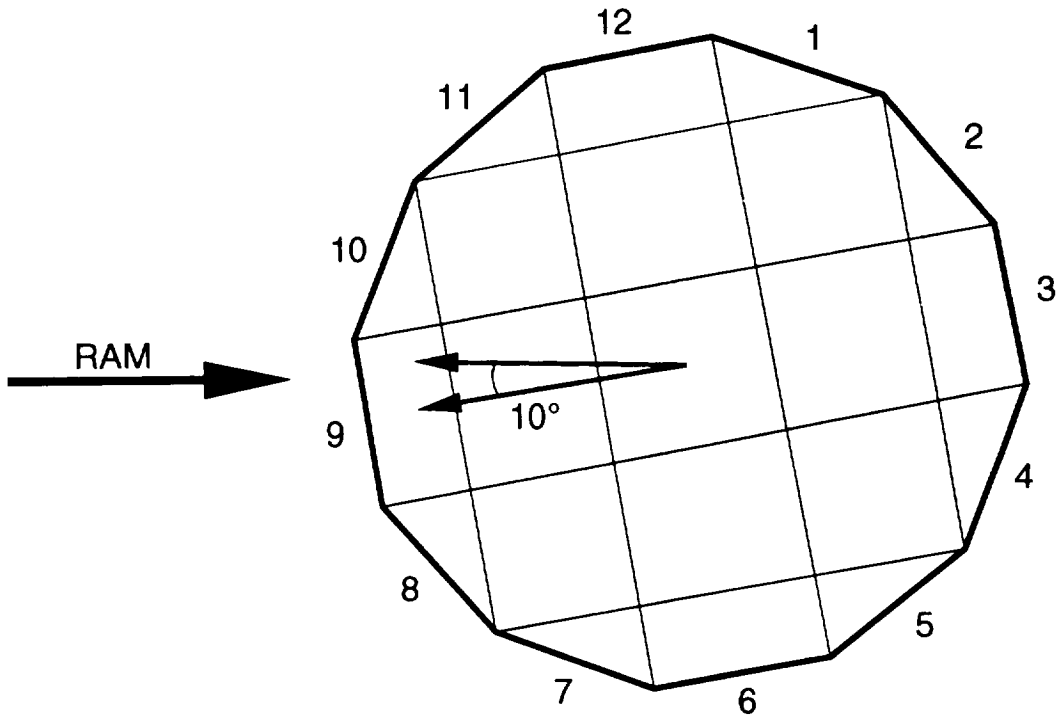

Figure 2. Ram direction orientation used in model.

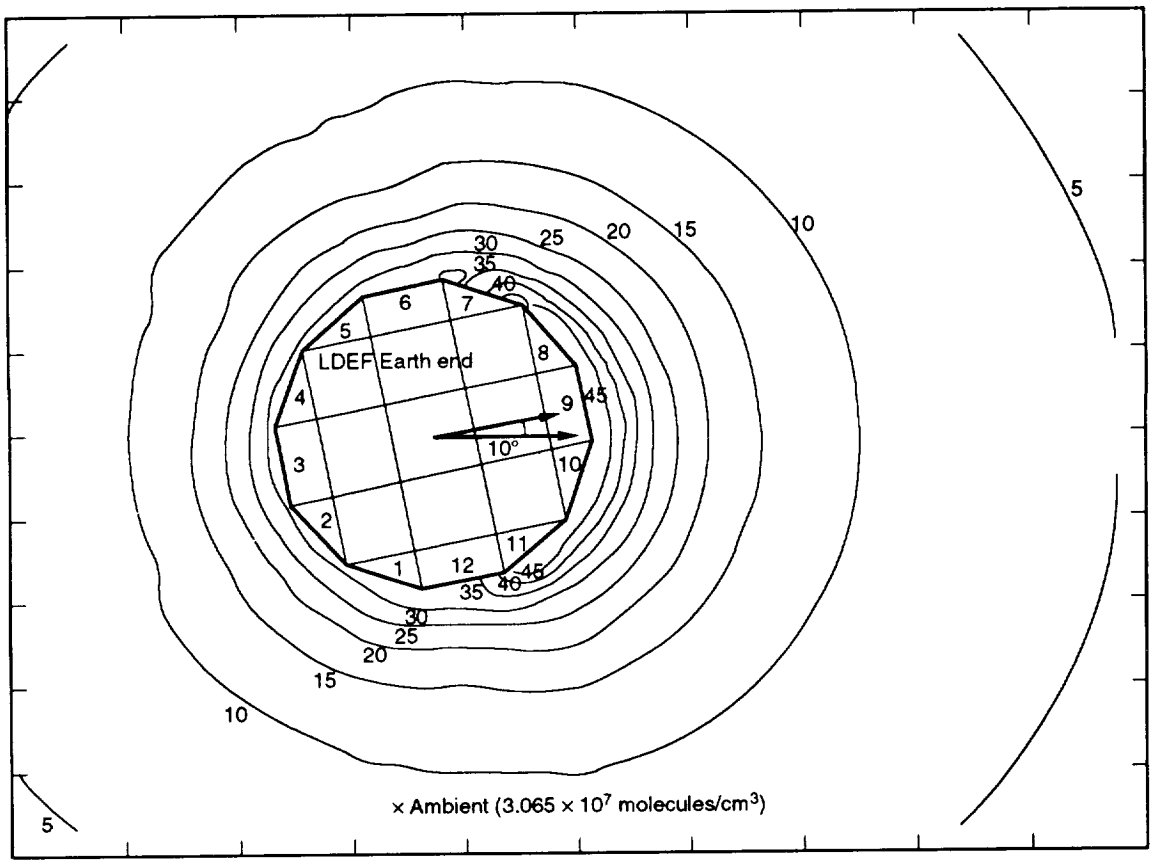

Figure 3. Total density at 463 km.

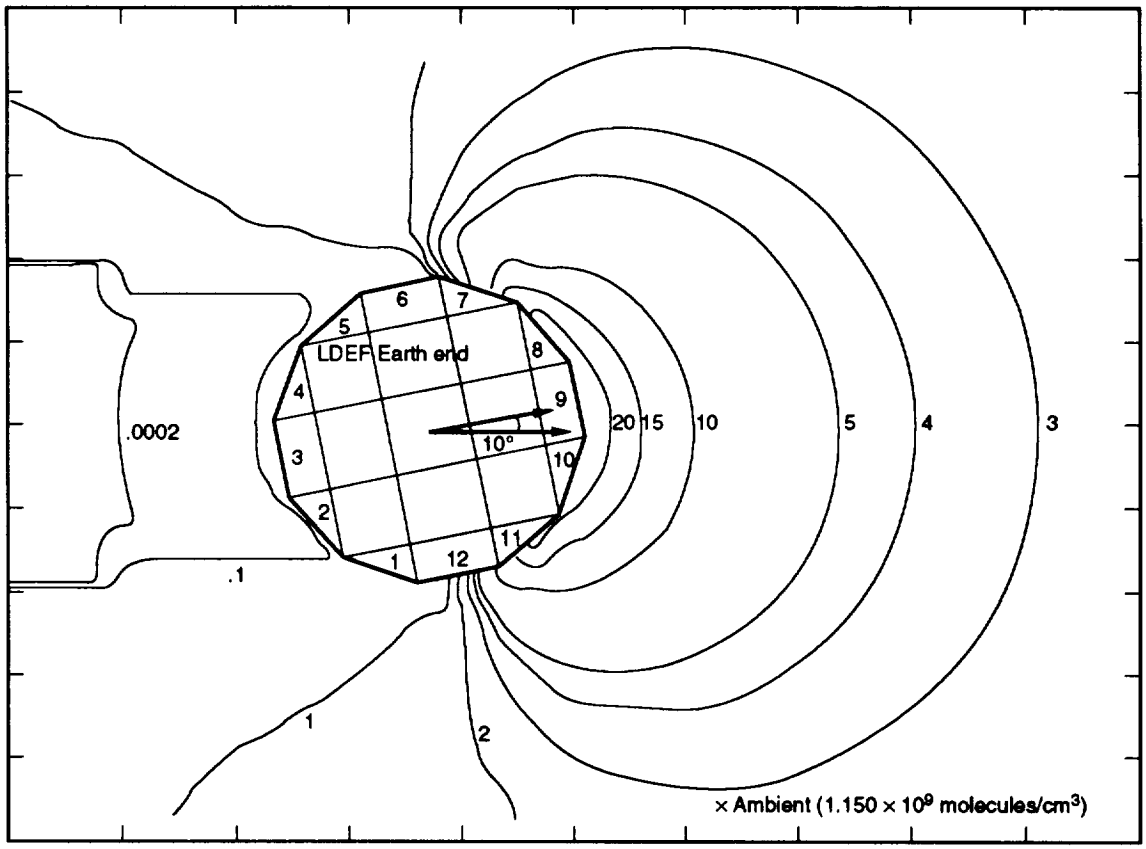

Figure 4. Total density at 333 km.

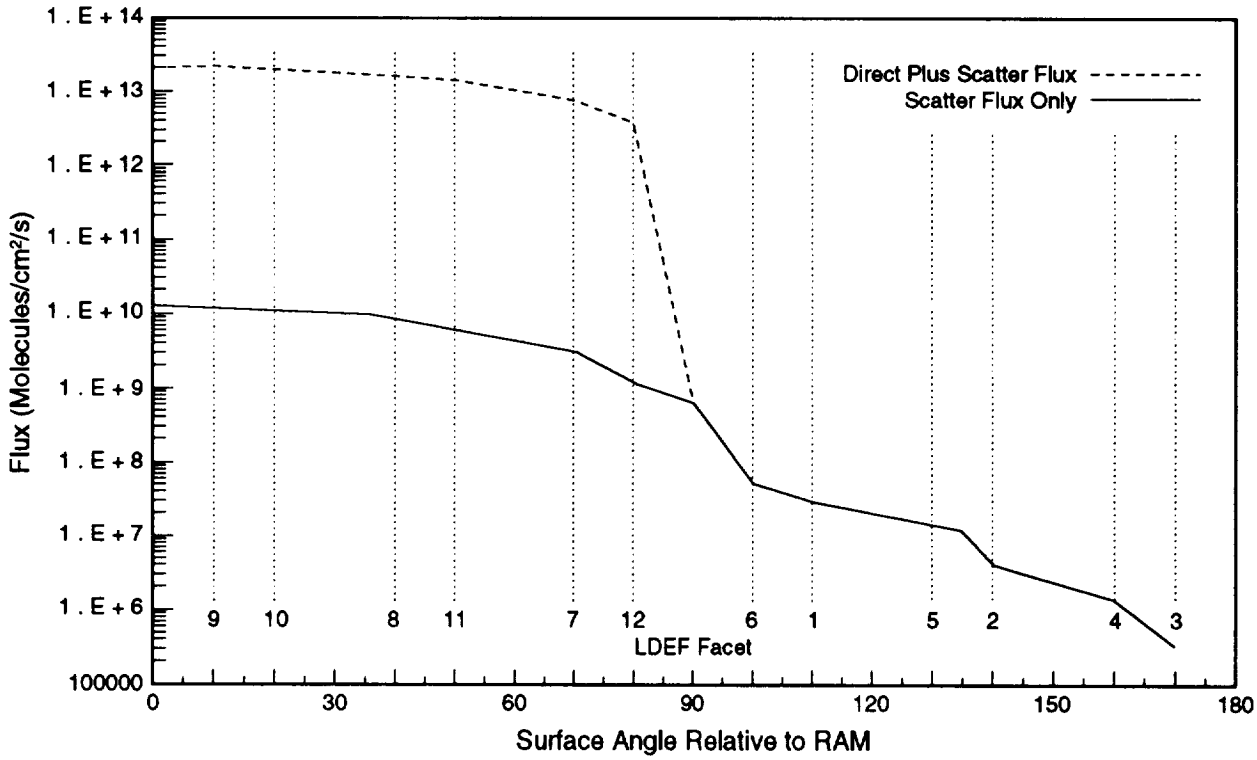

Figure 5. Atomic oxygen flux on LDEF surfaces at 463 km.

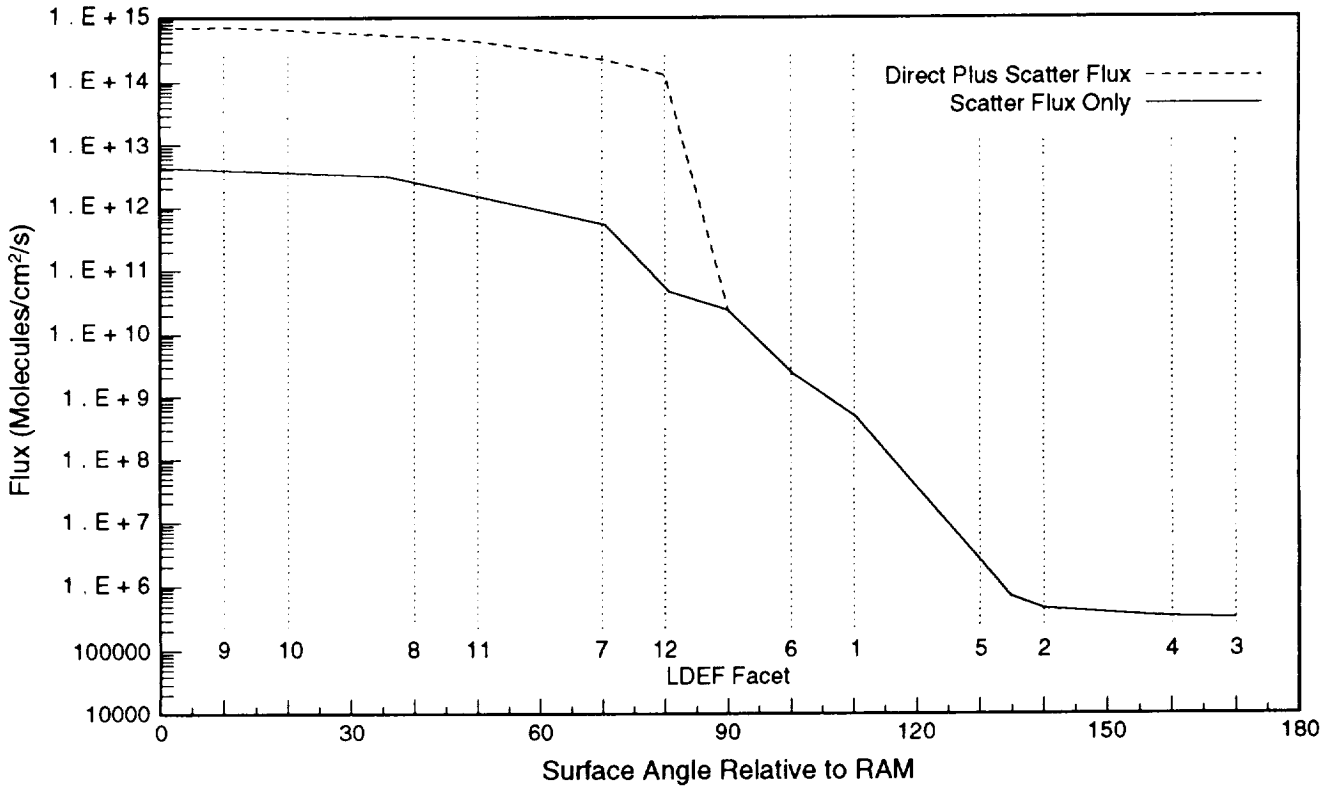

Figure 6. Atomic oxygen flux on LDEF surfaces at 333 km.

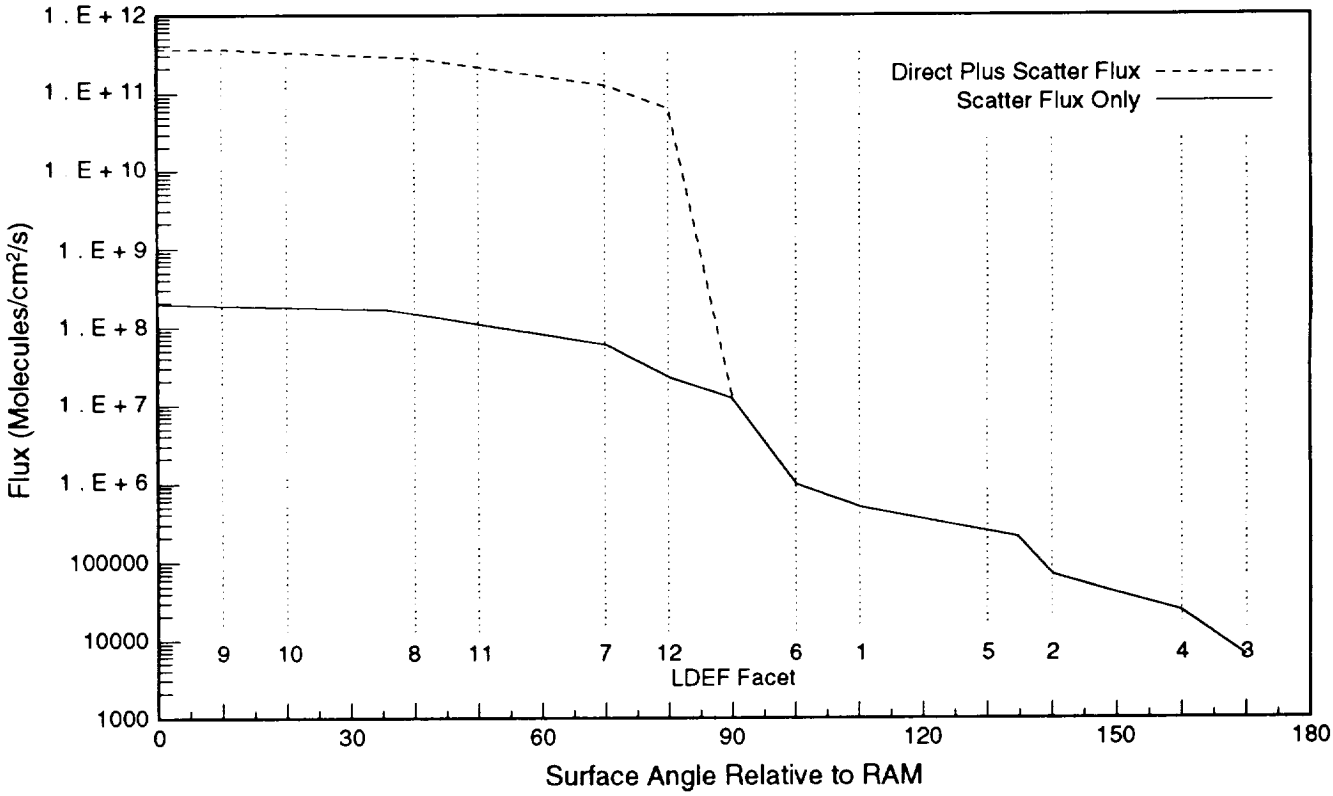

Figure 7. Molecular nitrogen flux at 463 km.

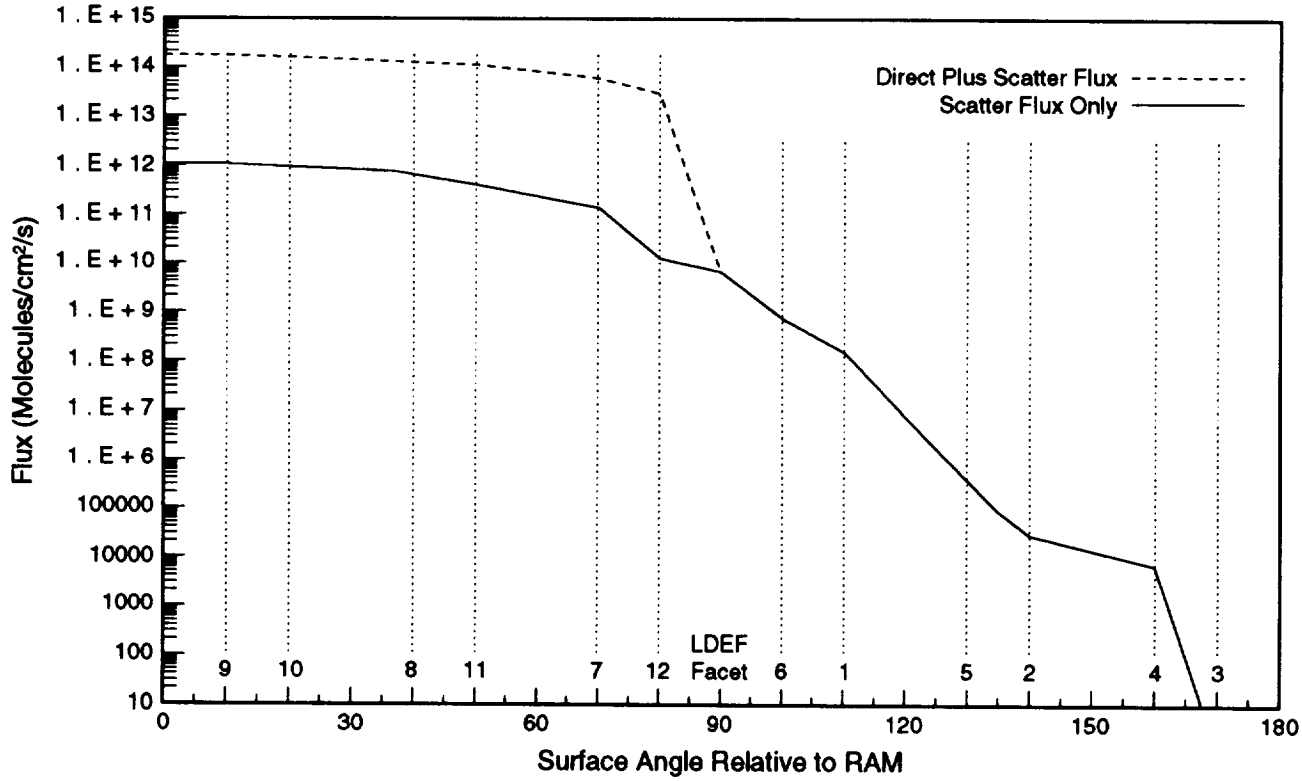

Figure 8. Molecular nitrogen flux at 333 km.

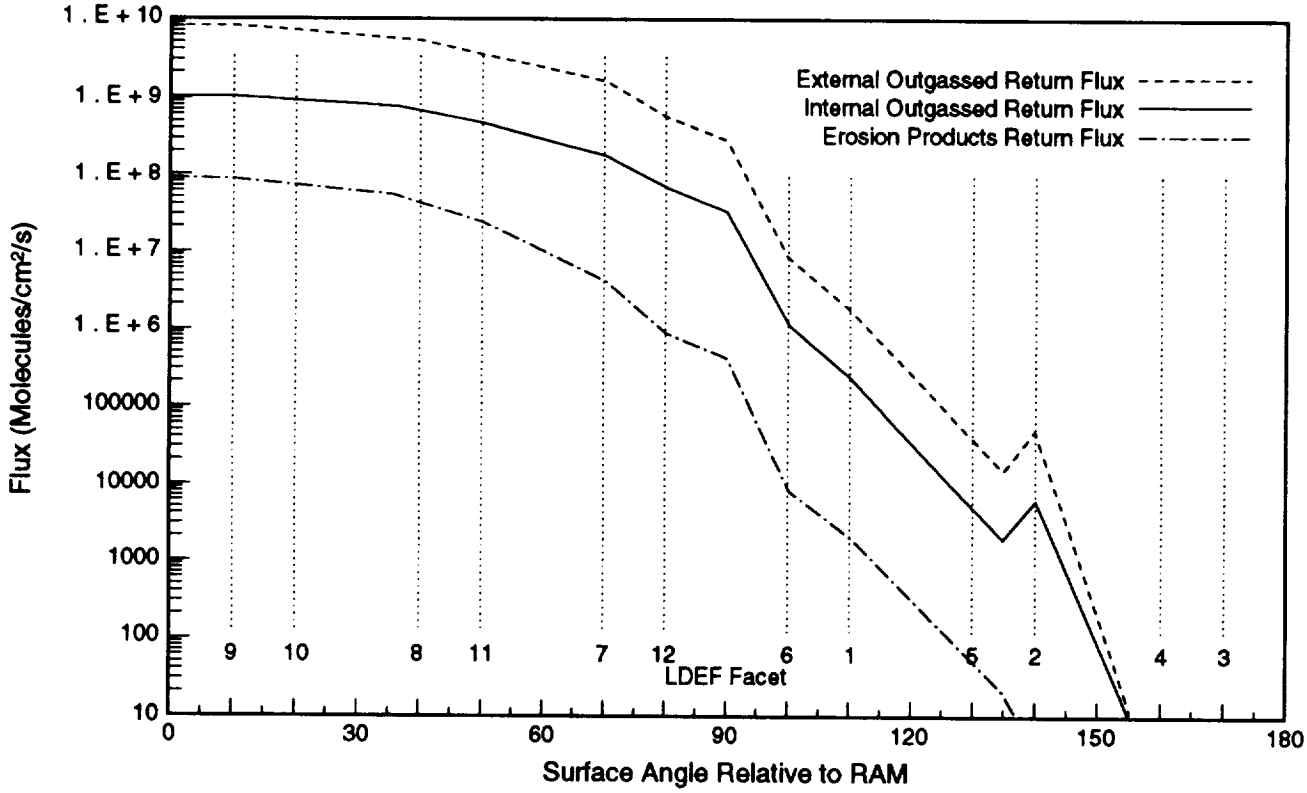

Figure 9. Outgas and erosion product flux at 463 km.

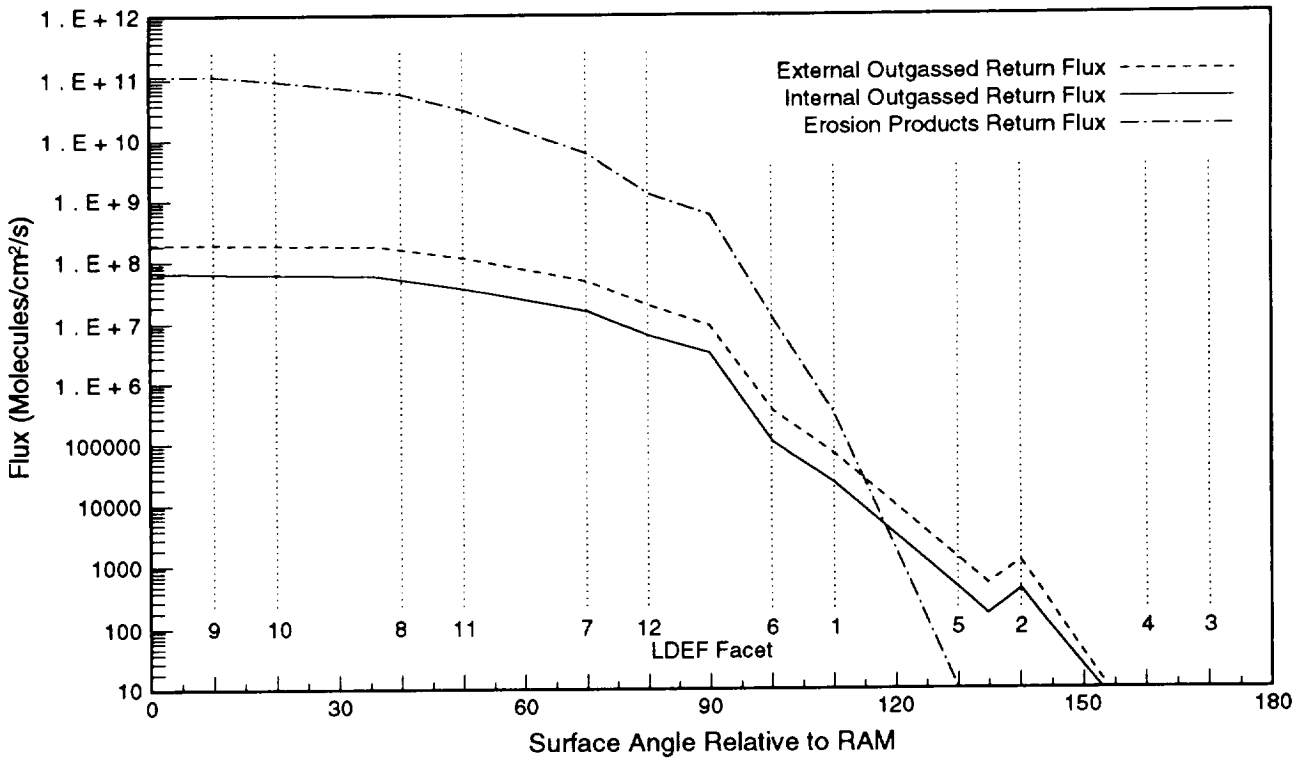

Figure 10. Outgas and erosion product flux at 333 km.

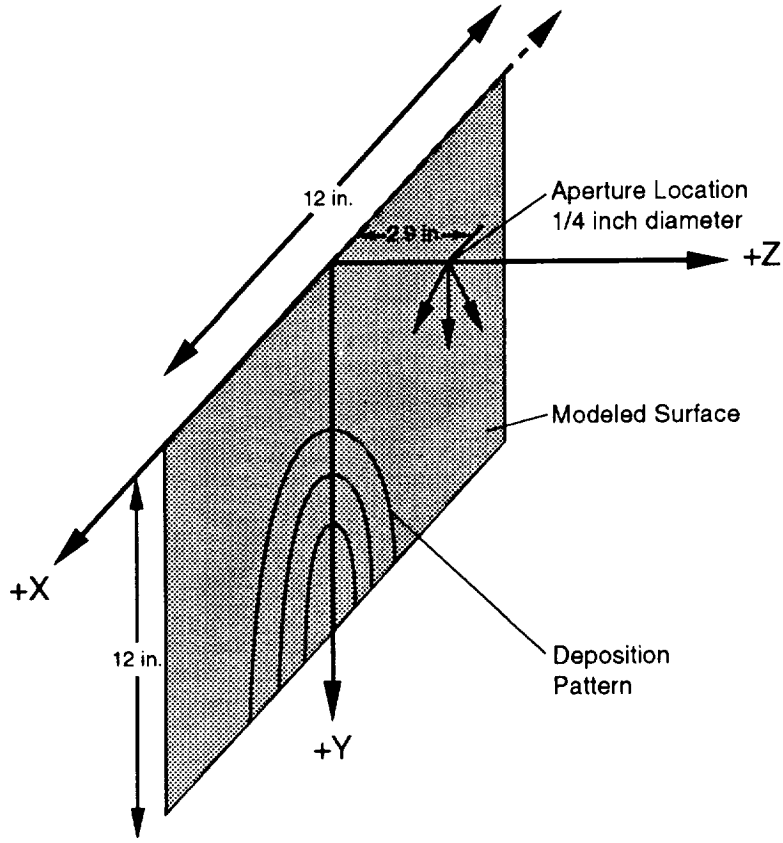

Figure 11. Geometry of atomic oxygen flux to interior.

SPACECRAFT CONTAMINATION ISSUES FROM LDEF: ISSUES FOR DESIGN*

Gary Pippin and Russ Crutcher
Boeing Defense & Space Group
P.O. Box 3999
Seattle, WA 98124–2499
Telephone: (206) 773–2846

INTRODUCTION

Many contamination sources have been identified on the Long Duration Exposure Facility (LDEF). Effects of contamination from these sources are being quantified and have been reported on in several papers (refs. 1 and 2).

For a designer, the essential question is how much contamination from all sources can be tolerated without causing a given spacecraft system to degrade below a critical performance level, or fail altogether. Even a rudimentary knowledge of the mechanisms by which molecular and particulate contamination can occur will allow simple design options to be chosen to circumvent potential contamination problems and reduce contamination levels.

Because of the varied nature and condition of hardware used on LDEF experiments, examples of many types of contamination were seen and these provide a useful guide to expected performance of many types of materials in space environments.

DESIGN CONSIDERATIONS

The central step in any contamination process is the transport of material from one location to another. For a designer, the choices are either to minimize the quantity of source materials or to physically block the materials from the source so it cannot redeposit on a surface which must remain clean. Low outgassing materials are chosen for space applications for various reasons, but for the long-term missions even materials which are low outgassing can build up substantial deposits over mission life. Vacuum thermal bakeout of hardware can help, but even baked out hardware will be subject to moisture reabsorption unless special (and expensive) precautions are taken.

For longer duration missions, the potential for "unexpected" events to occur increases. For such missions, designs will need to be more "fault tolerant" and provide capabilities for recovering from contamination events brought on by failure or degradation of a material by ultraviolet (UV), proton, and electron radiation, atomic oxygen (AO), vacuum, thermal cycling, and/or impact damage.

For example, cleaning a hydrocarbon from an optical sensor surface could be achieved by turning the surface to the ram direction. However other materials which also react with AO could

* Work done under NAS1-19247 and NAS1-18224.

be present. If siloxane-based films are present, these materials can be converted to nonvolatile silica type (SiO_x) species, trapping other contaminant films and leading to permanent performance degradation. Orientation of surfaces toward the Sun to increase volatility by temperature increases would also run the risk of photo-induced deposition.

Contaminant species on a spacecraft surface are likely to undergo changes in their structure and composition over time. Those products which remain on a surface for substantial amounts of time will be the more thermodynamically stable species.

LDEF RESULTS

On LDEF, two general sets of source conditions were present. At a number of leading edge sites, deterioration and/or outright failure of materials led to creation of a number of particle sources. Erosion of organic based materials by AO tended to leave these surfaces molecularly "clean."

Trailing edge conditions allowed creation of thin films as materials outgassed and redeposited. Without AO to remove these contaminants, they remain in place and may be altered by the UV exposure.

PARTICULATES

On-orbit generation of particles may be an issue for sensitive optics components. Particulate contaminants can physically obscure sensor lenses, block light from entering a detector and/or simply increase the amount of scattered light entering a camera or other detector, thereby degrading the quality of an image. Particles could interfere with moving parts, increase friction or wear on surfaces, even block the motion of a surface in a worst case. Particles could also abrade or scratch surfaces, leaving damaged areas even if the particle is dislodged.

In general, those materials which failed were largely toward the leading edge, where recession under the combined AO and UV exposure, coupled with thermal cycling, caused some materials to lose mechanical integrity and essentially disintegrate. Thus, some leading edge locations were sources of particulate contaminants. In contrast, trailing edge conditions allowed formation of thin molecular contaminant films from outgassing and redeposition processes. There was no evidence of particle generation from failed materials at trailing edge (no AO exposure) conditions.

NASA's video downlink during the recovery process showed a collection of highly reflective, thin particles had gathered in the LDEF wake. These particles were observed prior to the grappling procedure. The presence of such material traveling within the LDEF wake means, whatever the mechanism of transport, it has to explain how particles from the leading edge locations leave the surface, travel around the spacecraft, and collect again in the wake. The recovery operation approach represents a "snapshot" taken over a relatively short time. The particles may have some small momentum relative to the LDEF and actually be drifting through the wake over a period of weeks or months.

Particles such as those observed in the LDEF wake represent potential artifacts for telescopes, cameras, and/or other imaging equipment. Satellites which rotate intermittently or are reboosted periodically could have significant interactions with such contaminant particles. These motions could also be a significant source of additional particles.

FILMS

In general, contaminant films can lower the apparent AO induced material recession rate because they consume AO which would otherwise react with the material in question.

Both organic- and organic silicone-based films need to be considered. Organic-based film can be cleaned by oxidation because these processes create volatile products. Organic film may also be fixed in place by exposure to solar radiation. Silicones will be at least partially fixed in place by oxidation to SiO_x species, potentially trapping otherwise volatile species and allowing the opportunity for darkening of surfaces by radiation.

On LDEF specifically, there were many sources of both types of material producing contaminants. Organic-based potential film sources included paint solvents, polymeric thin films, and composite materials. Potential sources of silicon were adhesives, coatings for specimens, and support hardware, paints, and solar cells. Particulate sources from preflight conditions include dust, pollen, and fibers. On-orbit degradation of materials created new sources.

Thin film deposition on LDEF can be explained by line-of-sight deposition from many individual sources and with a smaller contribution from material reflecting from one surface to another. The grounding strap for blanket D11 shows a variety of contamination and environmentally induced changes. The adhesive release paper had a siloxane coating which left silicon-containing species on the copper. The silicone room temperature vulcanized (RTV) adhesive used to bond Velcro™ strips to the underside of thermal control blankets and to tray frames outgassed through vent holes at the edge of the blanket materials onto the portions of the copper grounding strap tucked down along the tray edge. Figure 1 shows a schematic of the strap with key areas of differing silicone deposition intensity shown. Areas of the copper strap exposed to significant AO show levels of silicone decreased from the levels on shielded areas and ground control specimens.

Optical properties of material were altered drastically in selected localized areas. Overall effects on anodized aluminum, which covered 60 percent of the LDEF external surface, and on silverized Teflon™ (Ag/FEP) which covered 18 percent of the surface, were minimal. Total absorptance changes on the chromic acid anodized aluminum ranged from 0 percent to about 8 percent. There was virtually no change in absorptance and very slight changes (<5 percent) in emissivity of Ag/FEP for exposed portions of these blankets. Averaged over all the blankets, the effect on thermal control performance due to contamination is at most 2 to 3 percent. This decrease shows that some oxidation processes were removing silicon containing species as well as creating nonvolatile SiO_x films.

OUTGASSING

Contamination on LDEF was extensive. Film deposits were produced in many locations. However, the molecular contamination was site specific; that is, produced by many different sources, redepositing or reflecting from surfaces until deposited on a "fixing" surface. The final redeposition of outgassed material was mostly on surfaces in the line of sight of the venting volume.

Some materials may outgas at a significant rate for an extremely long time. For these materials, short-term (24 h) outgassing tests may not be appropriate for characterizing their performance. Some materials may slowly decompose under vacuum conditions, in which case the material will outgas until it is gone. Under these conditions, the total amount of material becomes a significant consideration because the material never appears to "bake out."

Outgassed and redeposited material can undergo considerable subsequent changes under exposure to the space environment. Oxygen atoms can clean surfaces and also make nonvolatile oxide films.

Venting and outgassing of substantial amounts of material occurs early in a mission. Heavy deposits around selected vent paths from the interior of LDEF demonstrate the need for careful consideration of the location and orientation of vents relative to spacecraft surfaces. Venting should be directed normal to spacecraft surfaces. In addition, vent paths normal to the direction of motion should also minimize return flux.

One method is to minimize outgassed species contact with surfaces, where they could become attached and fixed in place by solar UV photons. Materials which outgas, such as paints, composites, thin polymeric films, or adhesives which are organic based, will likely outgas over a long period of time. Sixteen specimens of DC 6-1104 RTV silicone adhesive used to attach the Velcro™ strips on AO178 showed an average total mass loss (TML) of 0.34 wt%, as determined by ASTM E595, compared with original ground control measurements of 0.14 wt%. Specimens taken from the exposed bond line and from under the center portion of the Velcro™ showed no essential difference in the TML measurements. The conclusion is that, left indefinitely, this material will continue to outgas very slowly until it is gone. However, this process would take longer than the lifetime of any space hardware currently under design.

Similarly, heat shrink tubing used on aluminum clamps holding the wire barriers on the interior of LDEF outgassed at about 65 to 75 percent the rate of ground-based specimens. For this material the outgassing as measured by TML varies significantly with location; leading and trailing edge locations outgassing at a greater rate than all other locations. Table 1 shows the results of the outgassing measurements on the heat shrink tubing.

Fiberglass shims used between the heat shrink tubing and the aluminum wire harness clamps show outgassing rates slightly lower (85 to 95 percent) than the rates of ground control specimens.

SUMMARY

Observations made postflight on the LDEF hardware lead to the conclusion that there were significant interactions between contaminant materials and the low-Earth orbit (LEO) environmental factors during the 69 months of flight. Thermal cycling induced contaminant thin film with distinct layers were produced in some areas. Materials deposited on surfaces exposed to solar radiation were likely fixed in place by UV-assisted processes. These attached species are subject to changes over time brought about by energetic solar vacuum UV photons. AO may remove selected contaminant materials either directly or by removing the underlying substrate.

Potential consequences from exposure to contamination include degradation of optics by thin films which change the transmission characteristics and light scattering from particles which collect on detector lenses and physically block portions of the detector. Performance of thermal control surfaces may be degraded as films with increased absorptance are deposited. Contaminate films may also change surface electrostatic conditions. This subject has not been well studied during examination of LDEF. The most likely effect would be to convert conducting surfaces to insulators and allow charge buildup and create potential differences for one surface relative to another.

The particulate species produced by materials degradation on-orbit have the potential to interfere with scientific measurements being made around a spacecraft or by instruments on the spacecraft. Even if particulates do not attach to the lens, they may travel through the field-of-view and even remain in the field-of-view for long periods of time. The video downlinks showing particles collected in the LDEF wake and evidence of contamination from shuttle material dumps, obtained by postretrieval analysis, are examples of this concern.

Planned spacecraft orientation and temperature are two methods of passive contamination control. The higher the surface temperatures of the spacecraft can be maintained early in the mission, and without damaging essential components, the less opportunity for material redeposition. In LEO, ram and near-ram surfaces will be "cleaned" by exposure to AO. However, such exposure can damage the substrate, so this "cleaning" is limited in practice. Physically blocking sensitive locations from the line-of-sight of any potentially significant outgassing source is the most direct method of minimizing contamination. This solution is best considered in the design phase.

There are practical limits to cleanliness achievable at any large facilities, such as Kennedy Space Center (KSC). Improvements in methods of delivering clean hardware to KSC might be more effective, in both technical and cost terms, than seeking increased cleanliness levels at KSC.

Hardware should be cleaned prior to delivery at KSC and protected as much as possible prior to launch. Critical components should be designed so that they may be shielded until the hardware is in orbit. Maintaining the covers in place for a period of time in orbit would allow initial venting and outgassing to subside. This period might range from a day to up to a month, depending on requirements.

Contamination films on LDEF had a minimal effect on the overall thermal status of the satellite. Contaminant films did interfere with surface elemental analysis of test materials. Determination of average material recession rates must also consider the presence of contaminant films which react at different rates and/or even block recession for a period of time.

REFERENCES

1. "LDEF-69 Months in Space, First Post-Retrieval Symposium," NASA Conference Publication 3134, Part 1, Kissimmee, FL, June 2–8, 1991, section on LDEF Mission and Induced Environments.

2. "LDEF Materials Workshop '91," NASA Conference Publication 3162 Part 2, NASA LaRC, November 19–22, 1991, and contamination references therein.

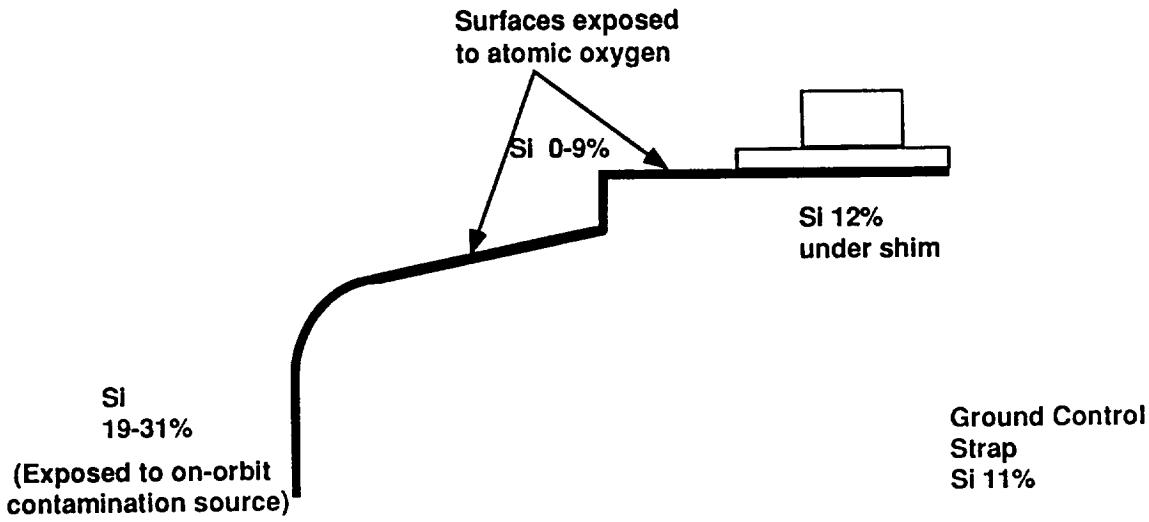

Figure 1. Cross section view of copper grounding strap, Tray D11, showing Mol% silicon on surface in different areas. (The value for the ground control strap is shown for comparison.)

Table 1. Total mass loss of heat shrink tubing as determined by ASTM E595.

Location on LDEF Bay and Longeron Between Rows	TML (Percent)
A,3-4	0.113
B,3-4	0.130
C,3-4	0.122
B,8-9	0.137
B,8-9	0.123
B,5-6	0.100
D-8, D-E	0.103
B,9-10	0.132
F,9-10	0.113
C,10-11	0.115
Space End	0.111
E,2-3	0.136
E,12-1	0.114
Earth End	0.102
F,8-9	0.126
B,3-4	0.139
Ground Control	0.170

MODEL OF SPACECRAFT ATOMIC OXYGEN AND SOLAR EXPOSURE MICROENVIRONMENTS*

R. J. Bourassa, and Dr. H. G. Pippin
Boeing Defense & Space Group
P. O. Box 3999, MS 82-32
Seattle, WA 98124
Phone: 206/773-8437; Fax: 206/773-4946

INTRODUCTION

Computer models of environmental conditions in Earth orbit are needed for the following reasons: (1) derivation of material performance parameters from orbital test data, (2) evaluation of spacecraft hardware designs, (3) prediction of material service life, and (4) scheduling spacecraft maintenance. To meet these needs, Boeing has developed programs for modeling atomic oxygen (AO) and solar radiation exposures. The models allow determination of AO and solar ultraviolet (UV) radiation exposures for spacecraft surfaces (1) in arbitrary orientations with respect to the direction of spacecraft motion, (2) over all ranges of solar conditions, and (3) for any mission duration. The models have been successfully applied to prediction of experiment environments on the Long Duration Exposure Facility (LDEF) and for analysis of selected hardware designs for deployment on other spacecraft.

The work on these models has been reported at previous LDEF conferences (refs. 1 through 5). Since publication of these reports, a revision has been made to the AO calculation for LDEF, and further work has been done on the microenvironments model for solar exposure.

OBJECTIVE

The objective of this report is to present the results of a revised calculation for AO exposure of LDEF experiments and to describe a newly developed microenvironments model for predicting solar exposure of spacecraft.

ATOMIC OXYGEN EXPOSURE

Primary Atomic Oxygen Model

Since 1986 Boeing has been developing predictive models for determining the exposure of a spacecraft surface to AO. The first program developed is referred to as the primary AO exposure

* Includes work done under NAS 1-19247, Task 8.

model. The primary model is used to determine the AO flux (atom/cm^2-s) and fluence (atoms/cm^2) to flat surfaces. The model includes the effects of thermal motion of ambient AO atoms and co-rotation of the atmosphere in addition to the ambient atmospheric density and the velocity of the spacecraft. The model treats noninterfering surfaces at arbitrary, but definite, orientations with respect to the direction of spacecraft motion. Orbit parameters and mission duration are defined by the user. The NASA MSIS-86 Model Atmosphere (ref. 6) is used to establish atmospheric densities as a function of time. Solar conditions required by the model atmosphere are input as functions of time.

Details of the primary model were presented at the First LDEF Post-Retrieval Symposium and at the LDEF Materials Workshop '91 (refs. 1,2) and its application to LDEF is reported in NASA CR 189627 (ref. 3). Following publication of reference 3, a revised prediction of AO fluences to LDEF experiments was completed. Results of the revised calculation are shown in Figure 1. The revision calculation differs from that given in reference 3 because of a correction made to the atmospheric co-rotation programming code. The actual differences between the two calculations is not large (3 to 4 percent) for leading surfaces of the spacecraft (rows 7, 8, 9, 10, and 11). For rows 12 and 1 on the side of the vehicle, the revised calculation shows an increase of about 25 percent relative to the previous calculation. A greater relative increase was seen on trailing edge rows 4 and 5, but the total fluence values for these rows are still very low. The total fluence values for rows 1, 2, and 3 are unchanged because fluence to these rows was dominated by the brief unplanned AO exposure during retrieval of the LDEF.

Atomic Oxygen Microenvironments Model

A second, more detailed AO exposure model has been developed over the last 2 years to account for interference, or shadowing of surfaces, by the three-dimensional structure of a spacecraft. This model, termed the "AO microenvironments model," also accounts for specular and diffuse reflectance from surfaces exposed to either primary or secondary impacts, and accounts for the potential of individual atoms to recombine on, or react with, the impacted surface. The secondary scattering processes are determined by a Monte Carlo routine which follows an individual particle until it either reacts on a surface or is scattered back into the ambient environment.

The microenvironments model is described in the proceedings of the LDEF Materials Workshop '91 (ref. 2) and the proceedings of the Second LDEF Post-Retrieval Symposium (ref. 4). Comparisons of observed effects of AO on materials flown on LDEF with results predicted by the microenvironments model are presented in references 4 and 5. The AO microenvironments model predicted exposure effects to within the uncertainty of the corresponding experimental measurements.

The model predictions are sensitive to the relative contribution of specular and diffuse scattering and to recombination efficiency. The surface property data we have used are estimates. We have made preliminary determinations of recombination efficiency for copper, silver oxide, gold, and anodized aluminum in the laboratory using calorimetric measurements. Further research is needed to establish the methodology for laboratory measurement of molecular reflective properties and recombination efficiency of spacecraft materials.

SOLAR RADIATION EXPOSURE

Solar radiation exposure of LDEF is reported in reference 7 which gives exposure in equivalent Sun hours for each surface of the LDEF vehicle. Like the AO exposure shown in Figure 1, the solar exposure data reported in reference 7 are limited to flat or convex, noninterfering surfaces. To overcome these limitations, Boeing has developed a "solar exposure microenvironments model" to account for shadowing and scattering of solar radiation caused by complex surface geometry. The model is similar to the "AO microenvironments model." The effects on solar exposure caused by any arbitrary surface size or shape may be modeled, including protrusions, indentations, and curvature. Figure 2 illustrates the effects on shadowing, specular reflection, and diffuse reflection of solar exposure of an indented surface.

The "solar microenvironments model" accounts for both direct and for Earth-reflected solar radiation. Entry times are randomly selected for solar ephemeral calculations. Satellite positions are determined using an orbital mechanics routine. For the selected position of the Sun, rays are traced to nodes on the spacecraft surface. The Monte Carlo routine follows individual rays as they reflect from surface to surface. Once a ray is either absorbed on a surface or is scattered back into the ambient environment, the process is repeated for another Sun position. Earth-reflected radiation is handled in a similar manner except that the source of Earth-reflected radiation is taken as a location on Earth determined by weighted-random selection. The attributes of the solar microenvironments model are summarized in Table 1.

Equivalent Sun hours exposure calculated by the Monte Carlo solar microenvironments model are shown on Table 2 compared with results reported for LDEF in reference 7. The results reported in reference 7 are based on a deterministic analysis. Deterministic analyses of solar exposure are limited in application to simple geometries and generally do not account for reflected radiation and shadowing. The data reported in reference 7 are valid for exposure of noninterfering, flat planar surfaces. The Monte Carlo calculation was applied to the same geometry. Even though the procedures used for the two calculations are totally different, results are in satisfactory agreement for the six locations on LDEF for which comparisons were made. However, the comparison is for the flat surfaces. Routines in the microenvironments program for shadowing and for scattering of radiation between surfaces must be verified by other means.

The solar microenvironments model has been used to predict solar exposure at the edge fold of a silverized/fluorinated ethylene propylene (FEP) thermal control blanket. The fold analyzed was at the trailing edge of Experiment tray D1. The blanket edge is identified in Figure 3. The most frequent azimuth of the Sun, visible from the experiment, tends to be west of the vehicle. This point is important in understanding the results calculated by the microenvironments program for exposure of the blanket edge.

The geometry of the blanket edge attachment is shown in Figure 4. Figure 5 shows how distance is defined. Distances shown in Figure 5 are measured first along the surface of the blanket and then continue along the aluminum frame of the experiment tray. The edge of the FEP blanket was designated as 45 millimeters. The origin (zero distance) for the measurements is a point on the flat, FEP-covered surface of the experiment tray. Points along the surface of the aluminum frame are at distances greater than 45 mm from the origin. The Sun at any randomly chosen time can be in any direction from an examined point (node) on the experiment surface as determined by solar ephemeral calculations. The Sun may not be visible from a node position. For aft-facing trays, the most

frequently observed Sun directions tend to be aft (to the right for tray D1 as shown in Figure 4) of the tray surface normal because the path of the Sun tends to be overhead and is not always visible from the side of the vehicle. This causes the radius between distances of 20 to 30 mm along the FEP blanket to be the most directly exposed surface of the blanket. Also, reflections from the FEP side of the attachment notch would be directed toward the aluminum. Much less reflection from the aluminum to the FEP would be expected than from the FEP to the aluminum.

These expectations are verified by the results shown in Figure 6. The area of highest solar exposure corresponds to the radius of the blanket fold (from 20 to 30 mm). The area of highest incidence of reflected radiation is on the aluminum side of the edge notch (from 45 to 60 mm). Exposure of the surface between 0 and 20 mm is the same as between 74 and 100 mm as would be expected because these surfaces are flat and parallel, thus they always make the same angle with a ray from the Sun.

Figure 6 shows that the plotted results of the Monte Carlo calculation are jagged. This may be due in part to statistical variations. The selection of node spacing and the number of Sun positions for the test case may not have been optimum. Overall, the calculated exposures behave as expected. Even with the variations noted, the results would be accurate enough for many engineering uses. The model is new and improvements will be incorporated as they are identified. The test calculation shown in Figure 6 does not provide verification between observed and predicted exposure of the materials on LDEF because the effects of solar exposure on FEP materials are not readily quantified.

Another factor in estimating solar exposure effects should be noted. The model yields equivalent Sun hours of exposure, the same as the deterministic model (ref. 7). It is radiation in the vacuum UV range that significantly affects exposed materials. The intensity of UV radiation at wavelengths shorter than 1,800 Å in the solar spectrum is a function of solar activity (ref. 8). This variation can be taken into account in future versions of the Monte Carlo model.

Applications of the environmental models are listed in Table 3. The primary AO program has been the most widely used thus far. The new microenvironments programs will greatly extend the application range of the modeling work in the future. We are now working on more flexible spacecraft orientation routines which will facilitate the determination of materials exposures on spinning and maneuvering satellites.

CONCLUSIONS

The latest revision of the AO exposure calculation reported herein should be used for analysis of LDEF results. The newly developed solar exposure microenvironments model produces results that are consistent with the deterministic model for flat surfaces exposed in orbit. Solar exposures calculated for surfaces of complex geometry using the microenvironments model are consistent with expected radiation intensity and reflection patterns.

REFERENCES

1. Bourassa, R.J., Gillis, J.R., and Rousslang, K.W.: "Atomic Oxygen and Ultraviolet Radiation Mission Total Exposures for LDEF Experiments." LDEF 69 Months in Space, First Post-Retrieval Symposium, NASA Conference Publication 3134, 1991.

2. Bourassa, R.J. and Gillis, J.R.: "LDEF Atomic Oxygen Fluence Update." LDEF Materials Workshop '91, NASA Conference Publication 3162, 1991.

3. Bourassa, R.J. and Gillis, J.R.: "Atomic Oxygen Exposure of LDEF Experiment Trays." NASA Contractor Report 189627, 1992.

4. Bourassa, R.J., Pippin, H.G., and Gillis, J.R.: "LDEF Microenvironments Observed and Predicted." Presented at the Second LDEF Post-Retrieval Symposium, San Diego, CA, June 1992.

5. Pippin, H.G., and Crutcher, E.R.: "LDEF Materials Data Analysis: Representative Examples." Presented at the Second LDEF Post-Retrieval Symposium, San Diego, CA, June 1992.

6. Hedin, A.E.: "MSIS-86 Thermospheric Model." Journal of Geophysical Research, vol. 92, No. A5, May 1, 1987, pp. 4649–4662.

7. Bourassa, R.J., and Gillis, J.R.: "Solar Exposure of LDEF Experiment Trays." NASA Contractor Report 189554, 1992.

8. Jursa, A.S., Scientific Ed.: "Handbook of Geophysics and the Space Environment." Air Force Geophysics Laboratory, 1985, pp. 2–19.

Table 1. Solar exposure microenvironments model.

Monte Carlo calculation of solar exposure to complex spacecraft surfaces.

- Includes direct-solar and Earth-reflected radiation.
- Multiple scattering of radiation from surface to surface.
- Weighted-random selection of specular reflection, diffuse reflection, or absorption with probabilities dependent on surface properties.
- Flexible input allows modeling for long or short missions.

Precision proportional to square root of number of Sun and satellite position pairs.

Code is computationally intensive.

Table 2. Comparison of Monte Carlo and deterministic models for solar exposure.

Surface	Monte Carlo, Sun Hours	NASA CR-189554, Sun Hours	Difference, Percent
Space End	14,200	14,547	–2.4
Earth End	4,400	4,472	–1.6
Row 3	11,900	11,100	+7.2
Row 6	6,690	6,400	+4.5
Row 9	10,900	11,200	–2.7
Row 12	6,900	6,800	+1.5
			Standard Deviation 4.1

LDEF Mission
1,000 Sun Positions
Earth Albedo = 0.246
Surface Grid: 10×10

Table 3. Applications of the environment models.

Atomic Oxygen Exposure

LDEF

- Fluence as a function of time by tray.
- Thermal control blanket edge attachment, trays B7 and D11.
- Angle bracket, tray F9.
- Copper grounding straps.
- Specimen cover plate for Experiment A0171.
- Space-end tray clamp.

Space Station *Freedom*

- Fluence as a function of time and incidence angle.

EOIM-3 Orbital Test

- Indirect exposure experiment.

TRMM—Tropical Rain Forest Measurement Mission

- AO fluence for mission.

Solar Exposure

LDEF

- Comparison of Monte Carlo model with analysis by Berrios and Sampair.
- Thermal control blanket edge attachment, trays D1 and C5.

TRMM—Tropical Rain Forest Measurement Mission

- UV exposure for mission.

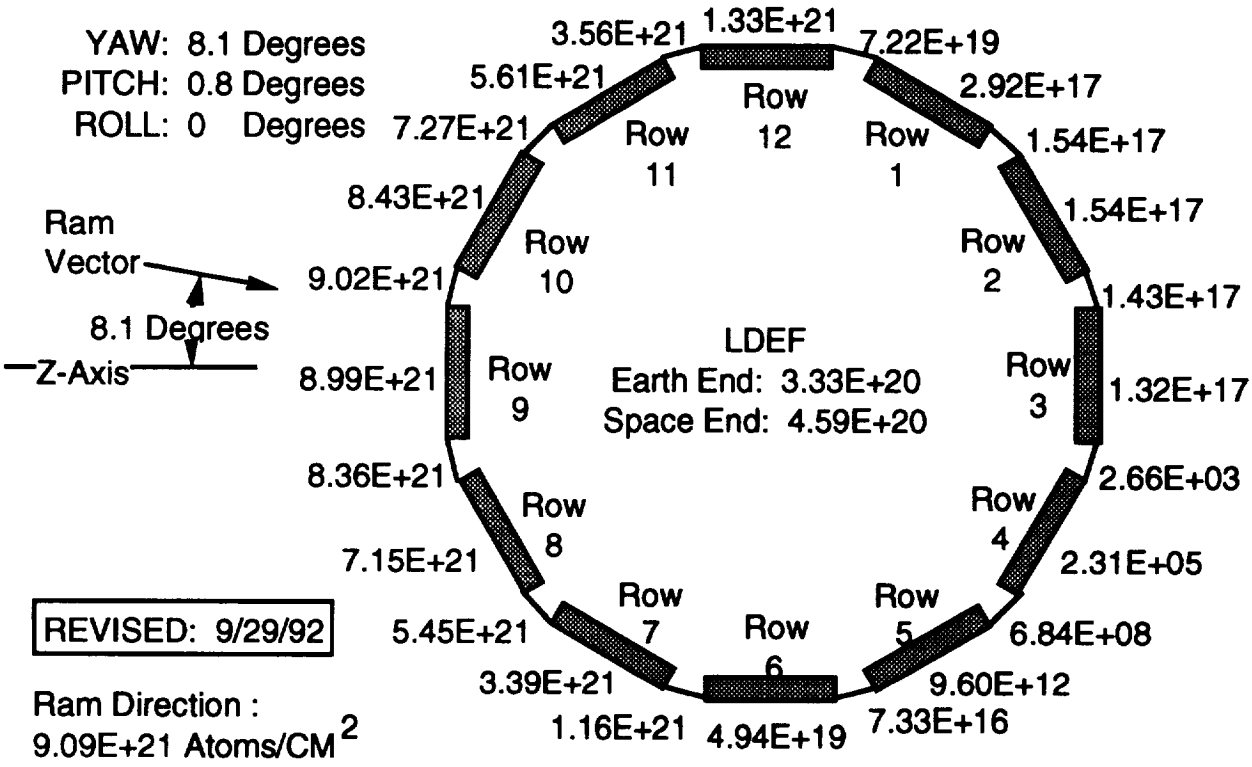

Figure 1. AO fluences at end of mission for all LDEF row, longeron, and end-bay locations including the fluence received during the retrieval altitude excursion.

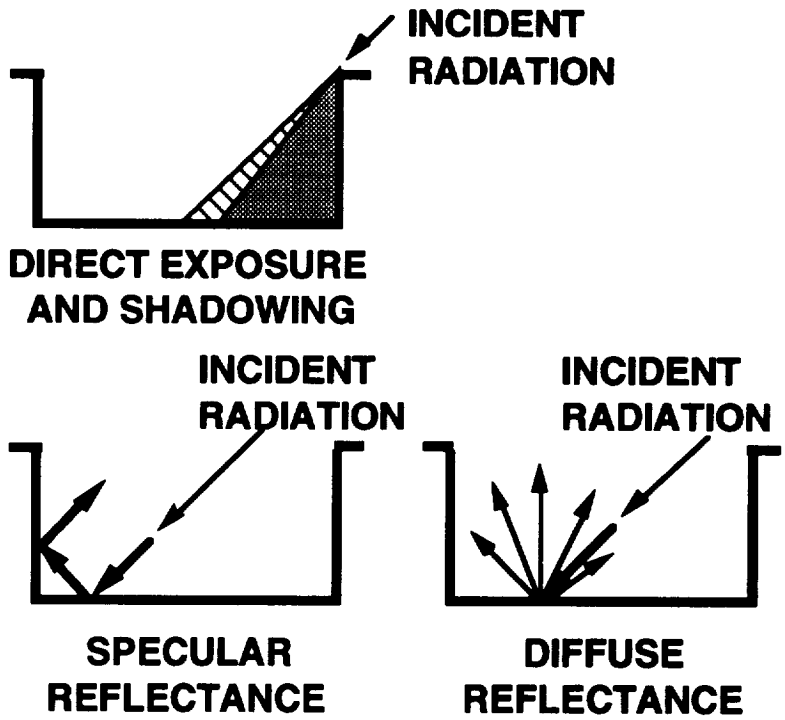

Figure 2. Effects of local geometry on solar exposure of spacecraft surfaces.

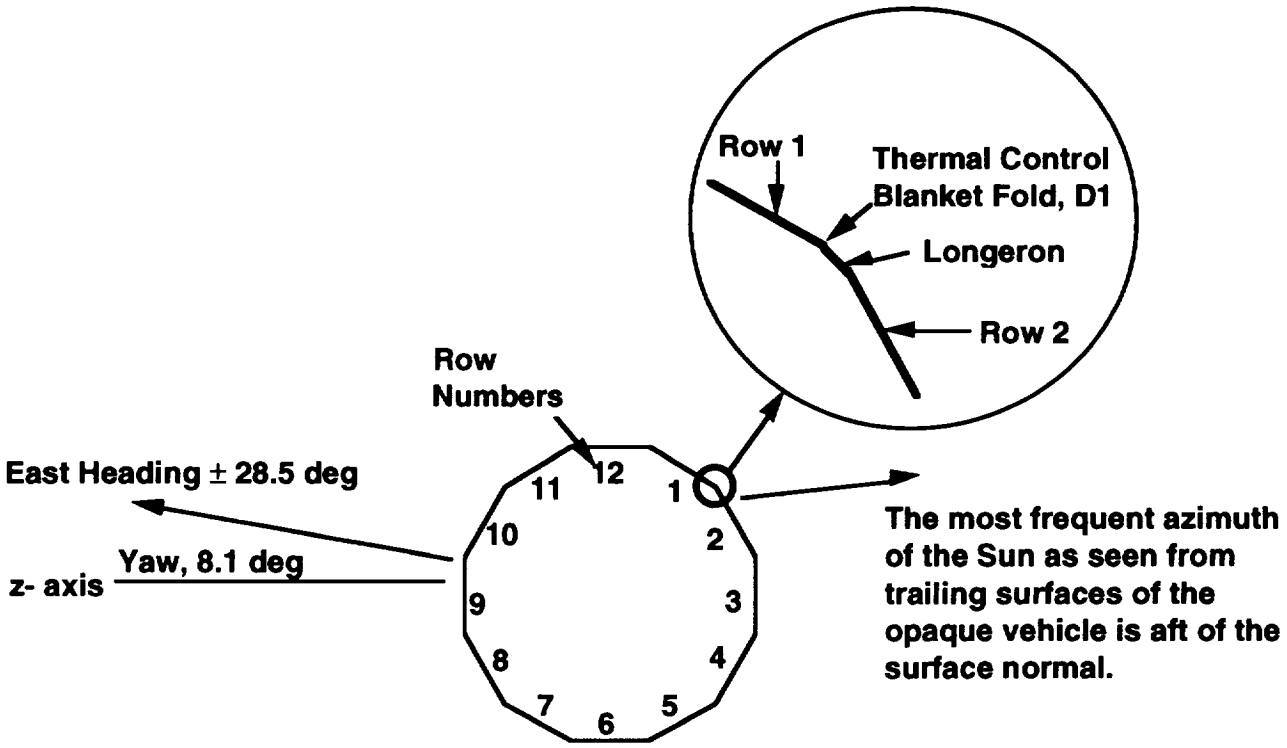

Figure 3. Location of the trailing side of LDEF Experiment tray D1.

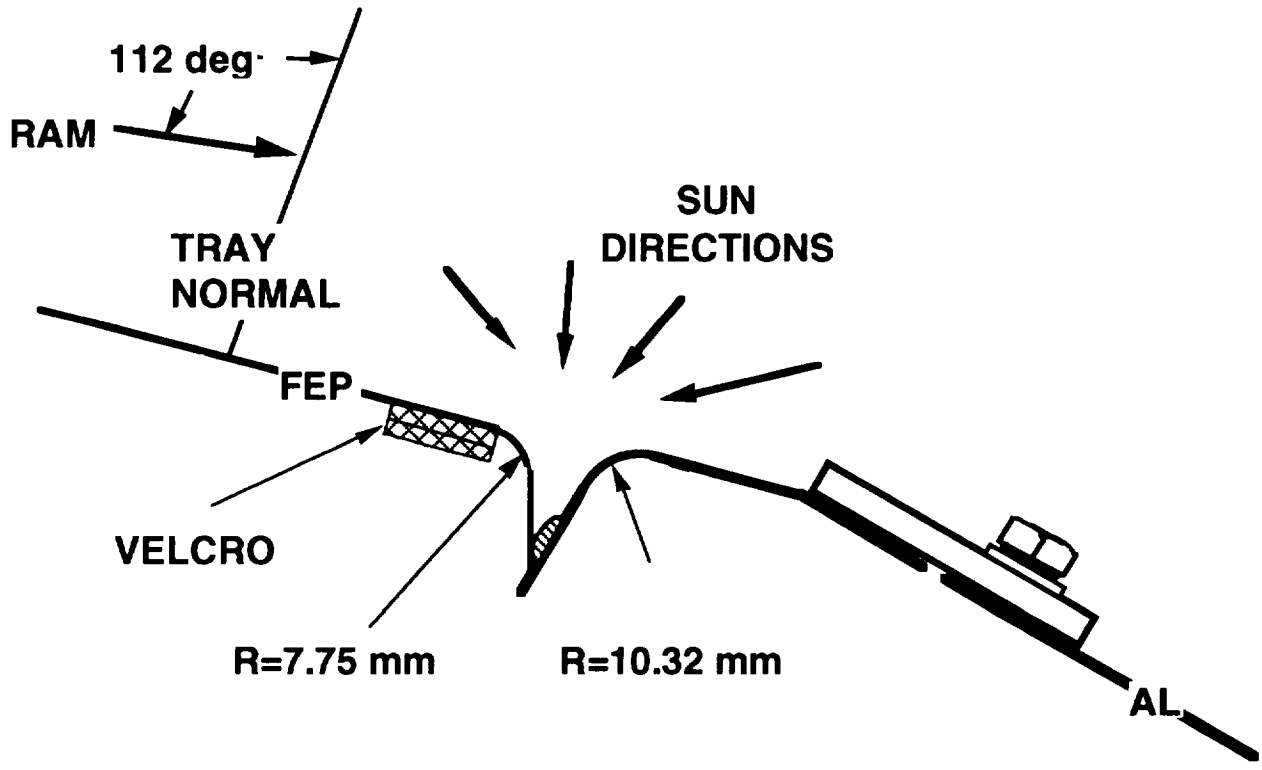

Figure 4. LDEF Experiment tray D1 thermal control blanket showing the blanket edge folded into a notch next to the experiment tray frame.

		Surface Properties		
		Specular	Diffuse	Absorption
D1 near row 2 edge	FEP Blanket	83%	10%	7%
	Aluminum	6%	60%	34%

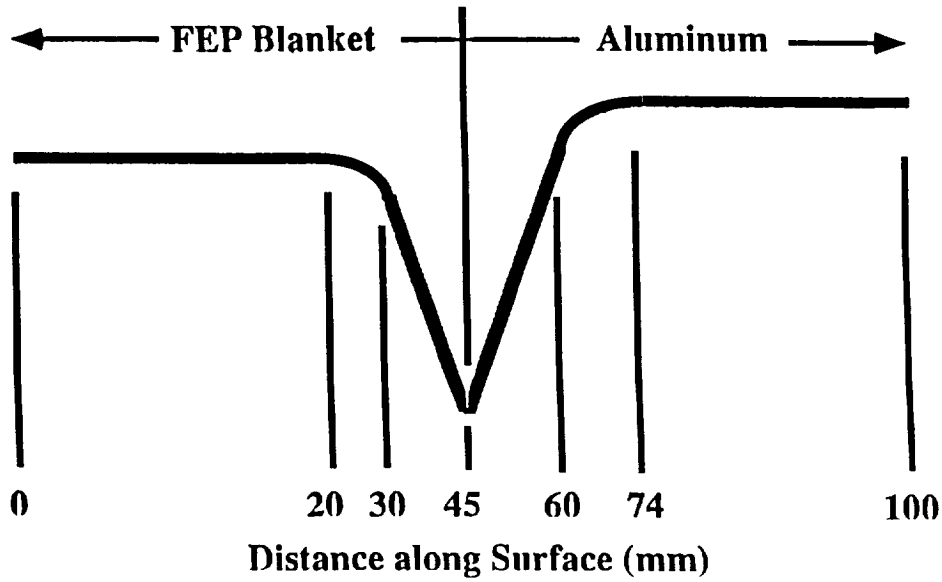

Figure 5. Definition of distance measurements for the microenvironments model study of the thermal control blanket edge fold, Experiment tray D1.

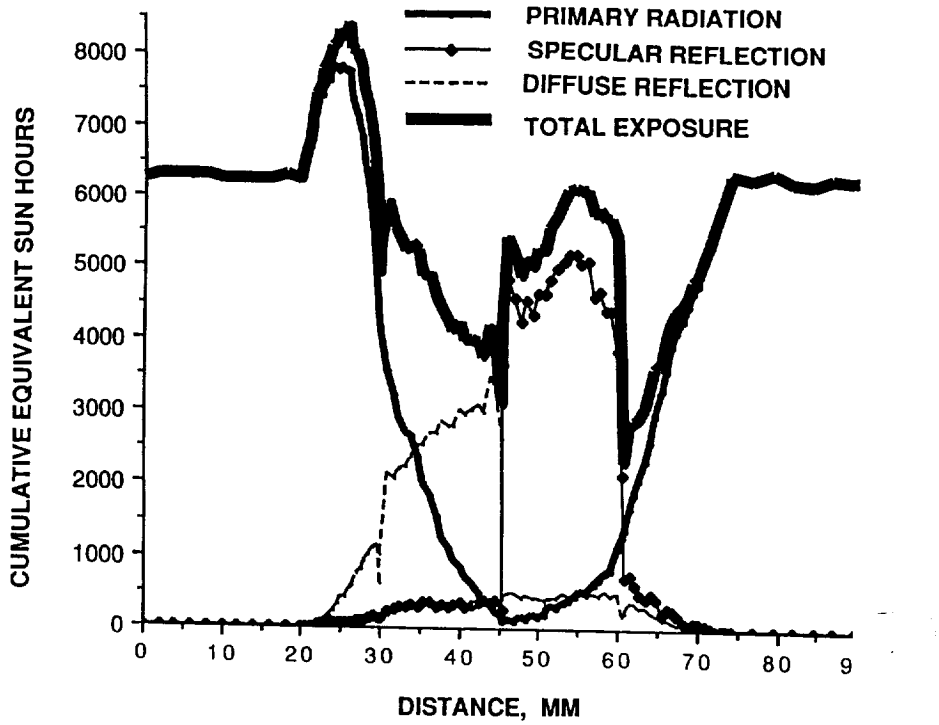

Figure 6. Calculated solar exposure for the Experiment tray D1, thermal control blanket fold.

POLYMER EROSION, RADIATION DAMAGE, AND FLUORESCENCE

N94-31022

ATOMIC OXYGEN EROSION CONSIDERATIONS FOR SPACECRAFT MATERIALS SELECTION

Ann F. Whitaker and Rachel R. Kamenetzky
NASA/Marshall Space Flight Center
Huntsville, Alabama

INTRODUCTION

The Long Duration Exposure Facility (LDEF) satellite carried 57 experiments that were designed to define the low-Earth orbit (LEO) space environment and to evaluate the impact of this environment on potential engineering materials and material processes. Deployed by the Shuttle *Challenger* in April of 1984, LDEF made over 32,000 orbits before being retrieved nearly 6 years later by the Shuttle *Columbia* in January of 1990.

The Solar Array Passive LDEF Experiment (SAMPLE) AO171 contained approximately 300 specimens, representing numerous material classes and material processes (ref. 1). AO171 was located on LDEF in position A8 at a yaw of 38.1° from the ram direction and was subjected to an atomic oxygen (AO) fluence of 6.93×10^{21} atoms/cm^2. LDEF AO171 data, as well as short-term shuttle data, will be discussed in this paper as it applies to engineering design applications of composites, bulk and thin film polymers, glassy ceramics, thermal control paints, and metals subjected to AO erosion.

DEFINITIONS

The terms associated with AO erosion as set forth in this paper need to be clearly defined in order to provide nonambiguous data for the design engineer. AO *fluence* is defined in terms of the ratio of the number of oxygen atoms incident to sample surface exposed area. A particular material's *reactivity* is defined in terms of a change in material thickness per AO fluence. Some materials react with AO in a manner such that long-term AO effects can not be linearly predicted from short-term data. These materials are often described in terms of a *nonlinear reactivity* which is defined as the ratio of a material's change in mass to the AO fluence. *Accommodation*, which is a term used particularly for oxidizing metals, is defined in terms of the number of atoms of AO reacted to the number of incident atoms of AO.

COMPOSITES

LDEF experiment AO171 included 33 composites (Table 1), 27 of which were carbon fiber composites configured in various layups in order to provide a potentially more complete analysis of both fiber and matrix strengths. These composites were the most promising types in the 1978 to 1980 timeframe when samples were chosen for this flight experiment. These samples included both

high strength (HMS series) and high modulus (HMF series) composites as well as the P75S/934 composites, which were used for the focal plane structure of the Hubble space telescope. Also included in the sample list were six "S" glass epoxy composites, three of which were covered with a protective aluminum thermal control tape.

Table 1. Experiment A0171 composites fiber/matrix/layup (number of samples).

• HMF 322 / P1700 / ±45° (5)
• HMS / 934 / 0° (5)
• HMS / 934 / 90° (6)
• P75S / 934 / 90° (6)
• P75S / 934 / 0° (5)
• "S" Glass Epoxy (3)
• "S" Glass Epoxy with Aluminum Thermal Control Tape (3)

Exposure to the LEO environment tended to darken the exposed composite surfaces and make them more optically diffuse. For the carbon fiber composites, matrix erosion was greater than that of the carbon fibers. Reactivity data based on erosion of the carbon fiber was approximately half that which was generated for short-term shuttle flight data where sample erosion is confined to the matrix rich top surface of the composite. The epoxy resin in the "S" glass composites was generally protected from AO attack by the glass fibers, but ultraviolet (UV) radiation degraded the thermal/optical properties of the composite. Composites covered with the aluminum thermal control tape were completely protected from AO erosion in the taped area (ref. 2), though a slight amount of AO undercutting along the unprotected edges of the sample was evident. Table 2 contains AO reactivity and percentage change in the ratio of absorptivity to emissivity generated for the space exposure of all the AO171 composites.

Table 2. Experiment A0171 composite space environmental exposure data.

Sample	AO Reactivity (cm^3/atom)	Percentage Change in (α/ε)
Graphite/Epoxy	1.0×10^{-24} *	–3 to 8 percent
"S" Glass Epoxy	0.13×10^{-24}	+9 %
"S" Glass Epoxy with Aluminum Thermal Control Tape	Tape Protected Composite	–8 percent (Aluminum Tape)

* Based on erosion of carbon fiber.

AO171 polymers (ref. 3) consisted of thin films of 5-mil Kapton™, 1-mil black Kapton™, 0.5-mil FEP Teflon™, and 1-mil white Tedlar™, of which only a residual film of the white Tedlar™ survived the space exposure. Bulk polymers included various configurations of Halar™, polyetherether ketone (PEEK), and RTV 511. In addition, TFE Teflon™ washers, which were used to secure flight samples to the experiment tray, were also evaluated for AO erosion effects. AO171 polymers also included samples of Kevlar 29™ and Kevlar 49™ configured in the form of woven fabrics, and polysulfone, which served as the matrix for the HMF 322 composites.

Unlike the Kapton™, black Kapton™, and FEP Teflon™ thin films, white Tedlar™ contains self-shielding inert particles which served to protect the film from complete AO erosion. Table 3 contains the reactivity values generated for the AO171 polymers along with reactivity values from previous shuttle flight data where available. Though no reactivity values were generated for RTV 511 due to outgassing of the specimens, SEM evaluation of the exposed surfaces clearly showed features characteristic of AO erosion. Although previous short-term shuttle data could not clearly distinguish TFE and FEP reactivity values, TFE data from LDEF experiment AO171 and FEP data from LDEF experiment SOO69 indicate a clear and definitive AO erosion difference between the two Teflons™, with FEP being the more reactive. LDEF reactivity values for the Halar™ and polysulfone specimens agree well with short-term shuttle values, indicating that these pure polymers erode linearly with AO fluence. The larger reactivity values for Kevlar 49™, a higher stressed state material than Kevlar™ 29, suggests a connection between stress and AO reactivity. This possible connection between stress state and AO reactivity has also been seen in data generated for other material types.

Table 3. Polymers AO reactivity data.

Polymer	AO Reactivity (10^{-24} cm^3/atom)		Comments
	AO171	Shuttle Flights	
White Tedlar™	0.29	- - - -	Inert particles retarded erosion.
TFE Teflon™	0.20	< 0.05 (estimated)	Data taken from AO171 washers.
FEP Teflon™	0.35	<0.05	Data from S0069.
PEEK	2.3	3.7 ± 1.0	Shuttle flight material was thin film with low emittance.
Halar™	2.1	2.0	
Kevlar™ 29	1.5±0.5	1.1 ± 0.2	Shuttle data based on STS-8 tether mass loss.
Kevlar™ 49	4.0	- - - -	Shuttle data based on STS-8 tether mass loss.
Polysulfone	2.3	2.4	

GLASSY CERAMICS

Approximately 30 silver and aluminum solar reflectors with thin coatings of various glassy ceramics were flown on this experiment. Many of these samples were configured so that only half of the sample surface was exposed to the environment.

Table 4 summarizes sample changes in solar reflectance and film thickness for the solar reflectors induced by exposure to the LEO. In general, all exposed sample surfaces experienced a small decrease in reflectivity. Angstrometer data revealed a general decrease of up to 160 Å in film thickness in the exposed region with corroborating evidence from low energy Rutherford back-scattering indicating a densification of the exposed film. In addition, a conversion of SiO to SiO_2 was identified for many of the specimens. Reactivity values, based on the assumption that the observed effects were the result of AO attack and that no other mechanism was involved, ranged from 0.40 to 2.3×10^{-28} cm^3/atom.

Table 4. Property changes in glassy ceramics.

Coating/Solar Reflector	Percentage Change in Solar Reflectance (%)	Decrease in Film Thickness (Å)
SiO_2/Ag	– <1	40
SiO_2/Al	– <1	50
SiO – SiO_2/Enhanced Al	– 2.0	125
SiO/Al	– 1.5	150
MgF_2 – Sapphire/ Enhanced Al	+ 1.5	25
MgF_2 – Sapphire/Ag	–5 to –10	150
Dielectric/Ag Alloy	–1 to –5	160

PAINTS

Experiment AO171 contained eight different paint specimens including several different polyurethane specimens, a black epoxy specimen, two tiodized specimens and a S13GLO specimen. All the paint samples were configured such that only half of the sample surface was exposed to the environment. Table 5 summarizes visual observations made for both the unexposed and exposed regions.

All the paints except the S13GLO lost mass as a result of the space exposure. Table 6 summarizes the thermal property changes and reactivity values (based on mass loss) for the AO171 paints and compares these values to data generated, where available, from previous shuttle flights. As evident from the data, AO reactivity is clearly nonlinear, with the implication that long-term reactivities cannot be predicted from short-term exposures. From a positive standpoint, the nonlinear erosion, coupled with a slight increase in emittance, indicates that the paints will remain effective as a thermal control coating longer than previously suggested by short-term shuttle data.

Table 5. A0171 summary visual observations on exposed paints.

Paint	AO171 - Visual Observations	
	Unexposed Region	Exposed Region
Z306	Diffuse, Black	More Diffuse
Z302	Specular, Black	Diffuse, Light Gray (Substrate)
Z853	Specular, Dark Yellow	Diffuse, Light Yellow
A276	Specular, White	Diffuse, Bright White
401-C10	Diffuse, Black	More Diffuse
Tiodized K17 Black	Diffuse, Black	Diffuse, Gold/Brown
Tiodized K17 White	Diffuse, White	Diffuse, White
S13GLO	Diffuse, White	Diffuse, Light Tan (UV Degradation)

Table 6. A0171 and shuttle flight paint thermal properties and reactivities.

Paint	Absolute Change in Absorptivity		Absolute Change in Emissivity	AO Reactivity (Nonlinear) (mg/incident atom)	
	Shuttle Flight	LDEF AO171	LDEF AO171	Shuttle Flight	LDEF AO171
Z306	–0.02	–0.01	+0.02	1.0×10^{-21}	2.3×10^{-22}
Z302	+0.04	~0.00	+0.02	5.8×10^{-21}	5.7×10^{-22}
Z853	+0.04	–0.07	+0.04	0.90×10^{-21}	1.4×10^{-22}
A276	~0.00	–0.05	+0.03	1.0×10^{-21}	1.4×10^{-22}
401-C10	+1.5 ±0.5	+0.01	+0.00	0.86×10^{-21}	1.6×10^{-22}
Tiodized K17 Black	Unavailable	+0.03	–	No Data	Unavailable
Tiodized K17 White	Unavailable	–0.15	–	No Data	Unavailable
S13GLO	+1.1 ± 2	+0.14	–0.04	Negligible	Negligible

METALS

AO171 metal specimens included 1-in diameter bulk pure metals, metal alloys in both the as-received and preoxidized condition, and cold-rolled silver ribbon both thermally heat sunk and thermally isolated configured with and without a stress loop. All the bulk metal specimens were well heat-sunk to the less than 100 °F flight structure.

All nonpreoxidized metals gained mass as a result of the nearly 6 years of exposure to the LEO environment. Macroscopic oxidation effects were observed on both the bulk copper and bulk

silver specimens. SEM photographs of the exposed silver specimens indicated a surface morphology which varied radically with sample microstructure and thermal configuration. Reactivity and accommodation numbers for all the metals as well as thermal properties are shown in Table 7. Although metals oxidize in a nonlinear process, all reactivity values calculated were based on a linear oxidation process in order to provide a relative means of comparison. In general, reactivity values for all but the silver specimens were less than 1×10^{-26} cm^3/atom. Accommodation numbers (calculated based on the assumption that the mass gain was due to the formation of the most thermodynamically favorable oxide) for all but the cold rolled silver ribbon stress loop were less than 10 oxygen atoms reacted per 10^4 incident. Reactivity and accommodation values for the cold rolled, stressed, thermally isolated silver were an order of magnitude greater than that for the same material which had no applied stress and were well heat sunk to the LDEF tray, suggesting that AO effects are more dependent on temperature and microstructure than on total incident AO.

Table 7. Thermal/optical property changes and AO reactivity and accommodation values for A0171 metals.

Metal	Thermal/Optical Properties		AO Reactivity (10^{-26} cm^3/atom)	AO Accommodation, (AO/10^4 incident atoms)*
	Change in Absorptivity, (%)	Change in Emissivity, (%)		
Copper	+57.1	+11.4	0.87	3.6
Molybdenum	+20.4	+ 1.89	0.14	2.8
Tungsten	+ 3.08	+ 9.09	0.04	~1.0
HOS 875	+ 6.92	- 2.90	0.29	2.5
Pre-Ox HOS 875	+ 0.39	+16.0	TBD	TBD
Tophet 30	+33.2	- 3.33	0.55	5.0
Pre-Ox Tophet 30	- 0.22	+ 0.69	–	–
Ni-Cr-Al-Zr Alloy	+10.8	+51.0	TBD	TBD
Pre-Ox Ni-Cr-Al-Zr Alloy	+ 2.93	+ 1.86	–	–
Tantalum	- 0.87	- 5.98	0.60	8.3
Titanium 75A	+ 5.17	- 2.97	0.39	4.4
Mg AZ31B	- 5.26	+ 1.54	0.45	2.0
Niobium	+ 2.58	+ 0.94	0.14	2.0
Silver disk-fine grain	+247.0	+262.0	2.90	8.4
Silver-cold rolled ribbon in stress loop	–	–	27.5	80.0

* Accommodation strongly dependent on temperature and stress; numbers are tentative pending confirmation of oxide identity.

CONCLUSIONS

The LDEF satellite proved to be a valuable source of information on the durability of potential engineering materials exposed to the LEO environment for an extended period of time. Coupled with

short-term shuttle data, material degradation due to AO attack can be predicted with a greater level of confidence.

Data from experiment AO171 indicated that long term AO erosion of carbon composites can be predicted from carbon reactivity. Glass fiber composites tend to become self-protecting and would thus perform well in an AO environment. In addition, AO171 data indicated that thermal control tapes worked well in protecting the underlying composite from AO attack. Data on the AO171 polymers, coupled with short-term shuttle polymer data, indicated that the unfilled "pure" polymers react linearly with AO such that long-term AO erosion can be predicted from short-term shuttle data. AO171 glass ceramics underwent a densification accompanied by a decrease in film thickness of less than a few hundred angstroms as a result of the space exposure. The role of AO in this densification process is not clearly understood. Data on the AO171 paints indicated that the AO erosion process is nonlinear. However, thermal/optical property data, in which emissivity values increased slightly while solar absorptivity values generally decreased slightly, indicates that the paints would last longer than previously predicted from short-term shuttle data. AO interactions with AO171 metals clearly showed a nonlinear relationship which is strongly dependent on temperature, stress, and material microstructure.

REFERENCES

1. Whitaker, A.F., and Young, L.E.: "An Overview of the First Results on the Solar Array Passive LDEF Experiment (SAMPLE), AO171." First LDEF Post-Retrieval Symposium, Orlando, FL, June 1991.

2. Kamenetzky, R.R. and Whitaker, A.F.: "Performance of Thermal Control Tape in the Protection of Composite Materials to Space Environmental Exposure." NASA TM-103582.

3. Whitaker, A.F., Finckenor, M.M., and Kamenetzky, R.R.: "Property Changes Induced by the Space Environment in Polymeric Materials on LDEF." AIAA 30th Aerospace Sciences Meeting, Reno, NV, January 1992.

4. Whitaker, A.F., Kamenetzky, R.R., Finckenor, M.M., and Norwood, J.K.: "Atomic Oxygen Effects on LDEF Experiment AO171." Second Post-Retrieval Symposium, San Diego, CA., June 1992.

PERFORMANCE OF SELECTED POLYMERIC MATERIALS ON LDEF

Philip R. Young, Wayne S. Slemp, and Bland A. Stein
NASA Langley Research Center
Hampton, VA 23681-0001

SUMMARY

The NASA Long Duration Exposure Facility (LDEF) provided a unique environmental exposure of a wide variety of materials for potential advanced spacecraft application. This paper examines the molecular level response of selected polymeric materials which flew onboard this vehicle. Polymers include polyimide, polysulfone, and polystyrene film and polyimide, polysulfone, and epoxy matrix resin/graphite fiber reinforced composites. Several promising experimental films were also studied. Most specimens received 5.8 years of low Earth orbital (LEO) exposure on LDEF. Several samples received only 10 months of exposure.

Chemical characterization techniques included ultraviolet-visible and infrared spectroscopy, thermal analysis, x-ray photoelectron spectroscopy, and selected solution property measurements. Results suggest that many molecular level effects present during the first 10 months of exposure were not present after 5.8 years of exposure for specimens on or near Row 9. Increased AO fluence near the end of the mission likely eroded away much environmentally induced surface phenomena. The objective of this work is to provide fundamental information for use in improving the performance of polymeric materials for LEO application. A secondary objective is to gain an appreciation for the constraints and limitations of results from LDEF polymeric materials experiments.

INTRODUCTION

The longer missions envisioned for the U.S. Space Program have placed increased demands on materials, particularly polymeric materials. Until now, most spacecraft have been launched with relatively short life expectancy, from a few days to a few years. Confidence has developed in materials which support these short-term missions. However, the 25 to 30 year Space Station *Freedom* mission and other planned space programs with long-term LEO exposures are driving additional concerns and challenges. Quite simply, we don't know how all nonmetallic materials are going to perform in space for extended periods of time.

Polymeric materials offer a number of electrical resistivity, thermal expansion, weight, and strength to weight advantages over metallic materials. Figure 1 compares several physical and mechanical properties of metals and nonmetals. The figure was extracted from an article written 30 years ago (ref. 1). The two extremes in relative properties have widened considerably in the intervening years with the development of space-age polymers. The application of these materials is critical to the success of long-term space activities.

Fortunately, the NASA LDEF is filling much of the data void concerning long-term space environmental effects. The LDEF story is continuing to unfold through a series of conferences, workshops, technical sessions and discussions, and journal articles (refs. 2–5). The present paper is an

effort to increase the body of knowledge on space environmental effects on materials resulting from the LDEF mission by summarizing the performance of selected polymeric materials which flew on that vehicle.

Through the cooperation of the Environmental Effects on Materials Special Investigation Group (MSIG) and several LDEF experiment Principal Investigators, a representative number of nonmetallic specimens have been assembled for examination at the Langley Research Center. Table I summarizes these materials, identifies their source, and gives respective LDEF tray and row locations in the footnotes.

The chemical characterization of most of these specimens is now complete. The objective of this effort has been to assess the molecular level response of a broad variety of experimental and commercially available polymers to the extended LEO exposure provided by LDEF. A secondary objective is to gain an appreciation for the limitations and constraints of LDEF polymer experimental results. The benefit is intended to be fundamental knowledge for use in developing new and improved space-stable materials and for enhancing our understanding of ground-based simulation of LEO environmental effects.

EXPERIMENTAL

Materials used in study were contributed by several Principal Investigators and are summarized in Table 1. The fabrication of Langley Research Center composite materials has been previously discussed (ref. 6). PMR-15/C6000 polyimide matrix composite was fabricated by Rockwell International, Tulsa, OK. Films were obtained from commercial sources or synthesized in-house at Langley. The LDEF location of specimens is included with information in Table 1. Environmental exposure conditions for specimens at these locations may be obtained from several sources familiar to the LDEF community (refs. 2,7,8).

Characterization. Several analytical techniques were used to characterize specimens. Ultraviolet–Visible (UV–VIS) spectra were recorded on a Perkin-Elmer Lambda 5 spectrometer. Infrared spectra were obtained on a Nicolet 60SX Fourier Transform Infrared System (FTIR) in the transmission or diffuse reflectance modes. Glass transition (Tg) determinations were conducted on a DuPont 9900 Computer/Thermal Analyzer-Model 943 Thermomechanical Analyzer (TMA).

The approach used to make solution property measurements has been previously reported (ref. 9). Gel Permeation Chromatography (GPC) was performed on a Waters Associates GPC interfaced with a Viscotek Model 100 Differential Viscometer (DV). A standard $10^6/10^5/10^4/10^3$ Å microstyragel column bank was used. Solvents for polysulfone, polyimide, and polystyrene specimens were chloroform, 0.0075M LiBr/DMAC, and toluene, respectively.

X-Ray Photoelectron Spectroscopy (XPS) measurements were conducted at the Virginia Tech Surface Analysis Laboratory, Department of Chemistry, VPI & SU, Blacksburg, VA (ref. 10). A Cambridge StereoScan 150 was used for Scanning Electron Microscopy (SEM).

RESULTS AND DISCUSSION

Much of the value of materials exposure on LDEF emanates from the remarkable attitude stability of the vehicle in orbit. As documented in several sources (refs. 2,11), one end of the spacecraft always faced space, one end faced Earth, and one row (Row 9) flew nominally in the leading edge or RAM direction for the duration of the 5.8-year flight. This orbital orientation dictated that most of the environmental exposure a specimen received depended on where it was located on the vehicle.

Figure 2 is an expanded version of a contribution to the LDEF Materials Workshop '91 held at the Langley Research Center (ref. 12). The figure identifies the same polymer matrix composite material at different LDEF locations. It also lists various environmental parameters at those locations and gives a sketch of the vehicle. In some instances, a particular material has been identified at five different LDEF locations. Thus, these specimens received several orders of magnitude difference in atomic oxygen (AO) fluence as well as different vacuum ultraviolet (VUV) exposures. A remarkable opportunity exists for LDEF investigators to compare the response of the same polymer to varying LEO environmental parameters.

Figure 3 clearly illustrates this directionality for Kapton film from three different LDEF locations. UV-VIS spectra are given for thin film which received 5.8 years of exposure on Tray C, Row 3 or C3, 5.8 years of exposure on the space end at H7, and 10 months of exposure at B9. Environmental effects are quite different for the three specimens. The C3 film, probably saw primarily VUV. The UV-VIS transmission spectrum for that sample did not change significantly from that of the control. The H7 specimen experienced considerable AO in addition to VUV. A significant change in transmission was noted for that film. A change was also noted in the spectrum of the film after 10 months of exposure of B9. Thus, materials test results reported by LDEF investigators will be influenced by where those materials were located on the vehicle. Even with this restriction, many results reported to date have been remarkably consistent. Figure 3 makes an additional point about information being derived from LDEF. We may have an orbit for a spacecraft, but where a particular material is located on that spacecraft may become critical.

Composite Materials. The characterization of 934/T300 and 5208/T300 epoxy/graphite, PMR-15/C6000 polyimide/graphite, and P1700/C6000 polysulfone/graphite composites has been discussed in a series of articles (refs. 6,13–16). While details of that characterization may be found in the referenced publications, several more significant results are summarized here. Uncoated composites protected or shielded from direct exposure exhibited no detectable weight loss or change in measured mechanical properties. In contrast, uncoated composites which received direct LEO exposure exhibited significant loss of both resin and fiber. Essentially one ply of the four ply composites was lost after 5.8 years in LEO. A proportional reduction of 25 percent in tensile strength and tensile modulus was noted with these specimens.

No real differences were noted at the molecular level for composites exposed for 5.8 years on or near Row 9. Figure 4 summarizes data obtained for polysulfone composites. Infrared spectra of exposed and protected surfaces were essentially identical. The subtraction of exposed from control spectra resulted in a straight line in many instances. This also suggested little difference between the specimens. No changes were noted in the glass transition temperature with exposure. A detailed molecular weight characterization of control, flight protected, and flight exposed polysulfone composite specimens resulted in identical molecular weight distributions for all samples. One conclusion of this assessment of 5.8-year exposed composites was that molecular level effects resulting from UV exposure in the LEO environment were apparently lost in the surface material eroded away by AO.

Thin silicon dioxide, metal, and metal oxide coatings appeared to protect composite surfaces from effects of the harsh LEO environment. No significant erosion or weight loss was noted for several coated specimens. Figure 5 shows SEM photomicrographs at two magnifications for 934/T300 specimens coated with 1,000 Å of nickel followed by 600 Å of SiO_2. A 10-month exposed specimen is included in the figure for comparison with a 5.8-year exposed specimen. Minimal evidence of AO erosion was noted for these coated composites.

As noted in several Langley publications (refs. 6,13,14), stripes developed in some exposed composite specimens. These white to charcoal-colored stripes run in the fiber direction and are probably a row wide. Further research needs to be done to adequately explain this phenomenon.

Films. An assessment of selected films on LDEF has also been reported. Silvered FEP Teflon thermal blanket material, which provided thermal protection for 17 LDEF experiments, is probably the most studied material on LDEF. Since FEP Teflon has been the subject of numerous publications within the LDEF community (refs. 2–4, for example), it will not be addressed in the present paper.

No films survived 5.8 years of exposure on Langley's Row 9 experiment. However, films which received 10 months of exposure in the experiment exposure control canister (EECC) did survive and have been extensively characterized (refs. 4,16,17). One EECC specimen, P1700 polysulfone, was subjected to in-depth analysis (ref. 16). Figure 6 summarizes pertinent results from that study.

The upper left side of Figure 6 shows an SEM photomicrograph of 10-month exposed polysulfone film. Partial surface contamination apparently protected underlying resin from AO, resulting in the relief pattern visible in the micrograph. As with 5.8-year exposed polysulfone composite specimens, no change in Tg was noted with exposure. The lower left portion of Figure 6 gives the result of subtracting the FTIR spectrum of exposed film from that of unexposed film. A downward inflection in the difference spectrum means more of a particular component in the exposed film. A large –OH band which resulted from exposure is noted around 3,400 cm^{-1}.

Solution property measurements also revealed changes at the molecular level for 10-month exposed specimens. The GPC-DV molecular weight distributions for polysulfone control, protected edge, and exposed specimens are included in Figure 6. The distribution broadened with exposure, indicative of both chain scission and crosslinking. Various molecular weight parameters for LDEF-exposed polysulfone specimens are given in Table 2. Film values were calculated from the GPC-DV distribution given in Figure 6. Note the decrease in film solubility with exposure, decrease in number average molecular weight (M_n), and increase in weight (M_w) and z-average (M_z) molecular weights. This is clear evidence for both chain scission and crosslinking. VUV likely played a major role in these processes. Data for control and 5.8-year exposed composite specimens showed no change in molecular weight, as discussed earlier with Figure 4. However, the analysis of a 10-month exposed composite specimen suggested the same molecular weight trends as the 10-month exposed film, as it should.

An indisputable result of comparing 10 month polysulfone data with 5.8 year data is that many molecular level effects are present after 10 months of LEO exposure but not after 5.8 years of LEO exposure. This potentially contradictory result is best understood by considering the orbit of the spacecraft. LDEF was deployed into an essentially circular 257 nautical mile orbit in April 1984 (ref. 18). It was retrieved 69 months later at an altitude of 179 nautical miles. Atomic oxygen fluence differs greatly at these two altitudes. EECC samples were exposed for 10 months early in the mission when AO levels were at a minimum and then sealed inside the vacuum canister. Specimens outside the EECC received significant AO exposure near the end of the mission after the orbit had decayed.

Approximately 50 percent of the total AO exposure was received during the last 6 months of flight. Thus, molecular level effects observed after 10 months of exposure, primarily related to changes in surface chemistry, were most likely eroded away by the time the spacecraft was retrieved. An earlier retrieval from a higher orbit may have provided different results.

Polyimide-polysiloxane Copolymers. The chemical characterization of a series of polyimide-polysiloxane copolymer films flown inside the EECC also provided insight into molecular level effects of LEO exposure. Preliminary results obtained on these experimental materials have been given in previous reports (refs. 15,17). In general, they discolored somewhat but did not exhibit significant weight loss. SEM, scanning tunneling microscopy (STM), and limited XPS data may be found in the referenced articles.

Table 3 gives detailed XPS results for three different siloxane-containing copolymers. Data for both control and exposed film is included in the table. Several points are made concerning these data. Note the decrease in surface carbon content with exposure and subsequent increase in surface oxygen content. Note also the increase in silicon and that the silicon to oxygen ratio is about 1:2 after exposure. Finally, note the increase in the silicon 2p electron binding energy with exposure from approximately 102 electron volts (eV) to 103 eV. This data is consistent with the following interpretation. Upon AO exposure, the surface of these siloxane-containing copolymers is eroded to expose silicon atoms. These atoms are initially present as an organic silicone, as evidenced by the 102 eV binding energy. Upon exposure to AO, organic silicone (102 eV B.E.) is oxidized to inorganic silicon (103 eV B.E.), most likely, an SiO_2 type of silicate. At this point, further AO erosion is retarded. Inorganic silicates are known to be effective barriers to AO erosion. These observations suggest an exciting potential for designing AO protection into the backbone of certain polymers. This protection could likely be achieved by periodic incorporation of siloxane groups into the molecular structure of the host polymer.

High Performance Films. Several experimental high performance polymer films which received 10 months of exposure on Langley's Row 9 experiment have also been characterized. Since these films are the subject of a future publication, only limited results will be presented in the current paper. Table 4 gives the molecular structure and color for five of the polyimide films. Commercially available Kapton film was included in this study as a reference material. The films were synthesized as part of a broad program to develop polymeric materials for a variety of potential space applications.

UV-VIS transmission properties were affected by the 10-month LEO exposure. Figure 7 gives spectra from 200 to 600 nm for the six films. As described in earlier research, 6F-$DDSO_2$ and 6F-BDAF were developed in an effort to obtain essentially transparent films and coatings (refs. 19–21). These two films exhibit a shorter UV cutoff than other films in Figure 7 and, thus, possess less color. Figure 8 gives corresponding spectra for LDEF-exposed film. While some UV and AO degradation of the polymer backbone no doubt occurred, the dramatic decrease in transmission with exposure is considered due to AO-induced roughening of the film surface. The roughened, diffuse-appearing surface reflected much of the impinging radiation and, thus, less light was transmitted.

Only the 6F-BDAF and 6F-$DDSO_2$ films were potentially soluble in non-degrading solvents. Solution property measurements were performed only on these two materials. Table 5 summarizes molecular weight data determined by GPC-DV. Analyses were conducted on control film, the edge of a flight specimen shielded from direct exposure, and a 10-month exposed specimen cut from the center of the film. All samples contained residual insoluble material. The insoluble gel was recovered by filtration and dried to constant weight. Analyzed concentrations were then adjusted to account for the insoluble portion.

An inspection of data for 6F-BDAF suggests that various molecular weight parameters were not effected by the 10-month LEO exposure provided by LDEF. In contrast, 6F-DDSO$_2$ exhibited significant changes at the molecular level. Solubility decreased from 94.5 to 60.9 percent with exposure. The number average molecular weight (M_n) remained fairly constant while the z-average molecular weight (M_z) doubled. Changes in the polydispersity ratio (M_w/M_n) are also noted for this material. These observations, particularly solubility and M_z behavior, are considered evidence that the 6F-DDSO$_2$ structure crosslinked during exposure. Hill noted that M_z is the neglected parameter for evaluating crosslinking in environmentally exposed polymers (ref. 22). The molecular weight change for 6F-DDSO$_2$ is considered primarily a result of VUV damage to the -SO$_2$-group in the backbone of the polymer. Previous research has shown this material to be affected by exposure to UV in the laboratory (refs. 20,21). Sulfur and, thus, the -SO$_2$-group was the suspected weak link in those earlier studies.

Traditional Polymers. The chemical characterization of more traditional polymers listed in Table 1 has also been completed. The results of this study will also be the subject of a future publication. However, pertinent data obtained for polystyrene and polyvinyl toluene is summarized in Figure 9 as examples of the type of information obtained. The specimens in Figure 9 flew on Row 3 and saw significant VUV for the duration of the LDEF flight.

The decrease in UV-VIS transmission with exposure for polystyrene on Row 3 was not nearly as dramatic as that observed for films obtained from other LDEF locations, for example, Row 9. Significant changes in transmission probably reflect considerable AO erosion. The decrease in transmission observed for polystyrene is considered primarily due to VUV damage. The result obtained by subtracting the FTIR spectrum of exposed polystyrene from that of unexposed polystyrene is also given in Figure 9. Bands centered around 3545, 3365, and 2084 cm are indicative of degradation in the exposed specimen. However, the origin of these bands has not been established.

The molecular weight and molecular weight distribution for both polystyrene and poly-vinyl toluene are included in Figure 9. The decrease in M_n and increase in M_w and M_z for polystyrene is consistent with chain scission and crosslinking. The solubility of polyvinyl toluene decreased from 90.1 to 56.5 percent with exposure. That observation, coupled with a decrease in M_n, is also considered as evidence for chain scission and crosslinking.

Contamination and Post Exposure Effects. As documented in numerous LDEF publications, much of the vehicle surface was coated with varying amounts of a molecular contamination film commonly referred to as the "nicotine stain." This stain was often found to contain silicon, either in the form of organic silicone or inorganic silicate. This layer of contamination likely had an effect on how various polymeric materials behaved. UV probably contributed to the discoloration of some contaminated specimens. Upon exposure to AO, the resultant silica/silicate layer probably affected the manner in which the material was eroded. We consider that contaminated samples probably performed differently than had they not been contaminated.

The possibility that some LDEF polymeric materials have changed or degraded after the spacecraft was returned to Earth has been raised on several occasions. At the first post retrieval conference, we reported that two thin films flown on STS-8 in 1983 had changed significantly in appearance since they were initially examined (ref. 14). We gave additional information on these two specimens at the LDEF Materials Workshop '91 (ref. 15). One of these films, an experimental polyimide designated PMDA-DAF, also flew on LDEF. It too has continued to change after deintegration in Spring 1990.

Some environmentally exposed thermal control paints are known to partially recover their deteriorated optical properties upon return to ambient laboratory conditions. The authors first observed this phenomenon with selected white paints associated with the Lunar Orbiter program in the 1960's. Alain Paillous made an effective argument for caution in the use of LDEF data obtained after deintegration during the LDEF Results for Spacecraft Application Workshop held October 27–28, 1992, in Huntsville (ref. 23). His observations spawned additional comment on this subject (ref. 24). For practical, logistical, and budget considerations, the chemical characterization of all LDEF polymeric materials could not be completed immediately after deintegration. Although analytical work proceeded with deliberate speed, many analyses were delayed for months for various reasons. Thus, we must be aware and appreciate the possibility that certain characterized effects may have occurred in the laboratory while the specimen awaited analysis and did not occur in space.

A Perspective. Lessons being learned from the LDEF mission concerning space environmental effects on materials are continuing to be refined. Panel sessions at the LDEF Materials Workshop '91 concerning several materials themes provided an excellent summary of finding to that date (ref. 3). Two expanded summary articles have also focused on LDEF materials results (refs. 25,26). Confirmed results, confusing or unexplained results, and new ground simulation testing requirements may be found in the cited references. The present article restricts the discussion to expectations and limitations of LDEF results as they apply to polymeric materials only.

As a result of work on LDEF polymers, several opportunities have been identified for the development of new space-stable polymers. LDEF has shown that flexible AO-resistant coatings and noncontaminating AO and UV resistant materials are needed. LDEF has also provided guidance for the chemistry and syntheses of such materials. They may originate as copolymers with mainchain or pendant siloxane groups, siloxane-modified polyimides, and thermoset siloxane resins, all of which are potentially intrinsically stable to AO. Highly fluorinated polymers and colorless polyimides hold promise as being potentially stable to UV. New polymeric materials developed after LDEF was flown should also be examined. These include various phosphorus-containing polymers as well as inorganic polymers.

Several points should be kept in mind when interpreting or applying LDEF results. Anticipated molecular level effects are present in many 10-month exposed specimens that are not apparent after 5.8 years. The relative intensity of AO versus VUV is a key to the resulting effects. The performance of polymeric materials on or near Row 9 is heavily biased by increased AO fluence near the end of the mission. In some instances, an earlier retrieval from a higher altitude may have provided different results.

An interfacial layer of a silicon-containing contaminant was often being exposed to the LEO environment. Was this layer degraded by VUV or oxidized by AO to affect the performance of the underlying polymer? Many questions concerning synergistic effects remain unanswered. Did one environmental parameter generate a lesser or greater response to another environmental parameter? Finally, which specimens have changed since retrieval? An appreciation for limitations of polymeric materials studies from LDEF exposures is necessary for their successful application.

A significant amount of fundamental information has been generated on several polymers which received 10 months or 5.8 years of LEO exposure. For example, Figure 6 gives molecular weight data for P1700 polysulfone after 10 months of exposure. Table V gives similar data for 6F-BDAF and 6F-$DDSO_2$ polyimides. Figure 9 gives solution property data for polystyrene and polyvinyl toluene after 5.8 years on Row 3. The latter specimens are two very well understood polymers. UV-VIS and IR data are available for all these samples. Can this information be used as a benchmark to calibrate the

ground-based simulation of LEO space environmental effects? If effects on materials described in this report can be duplicated, then the same conditions can be used to simulate the effects of LEO exposure on other polymers having more immediate potential for space application. Synergistic and accelerated effects may also then be better understood.

CONCLUDING REMARKS

Current studies indicate LDEF to be the definitive source for long-term exposure verification of LEO environmental effects on polymeric materials. A wide variety of materials have been characterized. No significant change at the molecular level has been noted in many 5.8-year exposed polymers. However, changes have been noted in the chemistry of selected polymeric films which received 10 months of exposure. Environmental effects for these specimens are primarily surface phenomena. That surface was eroded away by AO for many 5.8-year specimens on or near Row 9.

The performance of polymeric materials on LDEF may be biased by contamination, increased AO fluence near the end of the mission, and by post exposure effects. A unique opportunity exists for using LDEF data as a baseline or a "sanity check" on the ability of ground tests to adequately simulate LEO effects on polymeric materials. The ultimate benefit of data derived from the LDEF program will be its influence on future spacecraft design and new materials development.

ACKNOWLEDGMENTS

This work was not possible without the assistance of a number of talented individuals. The authors thank Carol R. Kalil, A.C. Chang, Judith R.J. Davis, Emilie J. Siochi, Karen S. Whitley, and D. Scott Warrington. The contribution of specimens by James B. Whiteside, Richard F. Vyhnal, John C. Gregory, Ann F. Whitaker, and Anne K. St. Clair is gratefully acknowledged. The cooperation of members of the Environmental Effects on Materials Special Investigation Group contributed significantly to the content of this report. The continued support of Darrel R. Tenney is also acknowledged.

REFERENCES

1. Pezdirtz, G.F.: "Polymers for Spacecraft." *Modern Plastics*, vol. 40, No.12, August 1963, pp. 123–128.

2. Levine, A.S., ed.: "LDEF-69 Months in Space, First Post Retrieval Symposium." NASA CP-3134, Parts 1, 2, and 3, 1991.

3. Stein, B.A., and Young, P.R., comp.: "LDEF Materials Workshop '91." NASA CP-3162, Parts 1 and 2, 1992.

4. Levine, A.S., ed.: "LDEF-69 Months in Space." NASA CP-3194, 1993.

5. Gregory, J.C., ed.: LDEF Materials for Spacecraft Applications Conference, Huntsville, AL, Oct. 27–28, 1992, NASA CP-XXXX.

6. Young, P.R., Slemp, W.S., Witte, W.G., and Shen, J.Y.: "Characterization of Selected LDEF Polymer Matrix Resin Composite Materials." SAMPE International Symposium, vol. 36, No. 1, 1991, pp. 403–416.

7. Bourassa, R.J., and Gillis, J.R.: "Atomic Oxygen Exposure of LDEF Experiment Trays." NASA CR 189627, Contracts NASI-18224 and NASI-19247, May 1992.

8. Bourassa, R.J., and Gillis, J.R.: "Solar Exposure of LDEF Experiment Trays." NASA CR 189554, Contract NASI-18224, February 1992.

9. Young, P.R., Davis, J.R., and Chang, A.C.: "Molecular Weight Characterization of Advanced Thermoplastic Resins." SAMPE International Symposium, vol. 34, No. 2, 1989, pp. 1450–1461.

10. NASA Grant NAG-1-1186, Virginia Polytechnic Institute and State University, Blacksburg, VA.

11. Clark, L.G., Kinard, W.H., Carter, D.J., and Jones, J.L., ed.: "The Long Duration Exposure Facility (LDEF)." NASA SP-473, 1984.

12. Tennyson, R.C., George, P., Steckel, G., and Zimicik, D.G.: "Proposed Test Program and Data Base For LDEF Polymer Matrix Composites." LDEF Materials Workshop '91, NASA CP-3162, Part 2, 1992, pp. 593–600.

13. Slemp, W.S., Young, P.R., Witte, W.G., and Chen, J.Y.: "Effects of LDEF Flight Exposure on Selected Polymer Matrix Resin Composite Materials." LDEF-69 Months in Space, NASA CP-3134, Part 2, 1991, pp. 1149–1162.

14. Young, P.R., and Slemp, W.S.: "Chemical Characterization of Selected LDEF Polymeric Materials." LDEF-69 Months in Space, NASA CP-3134, Part 2, 1991, pp. 687–703.

15. Young, P.R., and Slemp, W.S.: "Characterization of Selected LDEF-Exposed Polymer Films and Resins." LDEF Materials Workshop '91, NASA CP-3162, Part 1, 1992, pp. 357–389.

16. Young, P.R., Slemp, W.S., Siochi, E.J., and Davis, J.R.J.: "Analysis of a Space-Exposed Thermoplastic Resin." Intl. SAMPE Tech. Conf., vol. 24, 1992, pp. T174–185.

17. Young, P.R., Slemp, W.S., and Gautreaux, C.R.: "Characterization of Selected LDEF Exposed Polymer Films." SAMPE International Symposium, vol. 37, 1992, pp. 159–171.

18. O'Neal, R.L., and Lightner, E.B.: "Long Duration Exposure Facility." LDEF-69 Months in Space, Part 1, 1991, pp. 3–48.

19. St. Clair, A.K., St. Clair, T.L., and Shevket, K.J.: "Synthesis and Characterization of Essentially Colorless Polyimide Films." Proceeding of the ACS Division on Polymeric Materials Science and Engineering, vol. 51, 1984, pp. 62–66.

20. St. Clair, A.K., Slemp, W.S.: "Evaluation of Colorless Polyimide Film for Thermal Control Coating Applications." SAMPE Journal, vol. 21, No. 4, 1985, pp. 28–33.

21. St. Clair, A.K., St. Clair, T.L., and Slemp, W.S.: "Optically Transparent/Colorless Polyimides." *Recent Advances in Polyimide Science and Technology*, W. Weber and M. Gupta, ed., SPE, Poughkeepsie, N.Y., Chapter 2, 1987, pp. 16–36.

22. Hill, D.J.T., Lewis, D.A., O'Donnell, J.H., Pomery, P.J., Winzor, C.L., Winzor, D.J., and Whittaker, A.K.: "Recent Advances in the Radiation Chemistry of Polymers." First Pacific Polymer Conference, Maui, Hawaii, December 12–15, 1989. Pacific Polymer Preprints, vol. 1, 1989, pp. 67–68.

23. LDEF Spaceflight Environmental Effects Newsletter, vol. III, No. 6, November 15, 1992, p. 11.

24. LDEF Spaceflight Environmental Effects Newsletter, vol. III, No. 7, December 30, 1992, p. 3

25. Stein, B.A.: "LDEF Materials: An Overview of the Interim Findings." LDEF Materials Workshop '91, NASA CP-3162, Part 1, 1992, pp. 1–56.

26. Stein, B.A.: "LDEF Materials Overview." LDEF-69 Months in Space, Second Post Retrieval Symposium, NASA-CP XXXX.

Table 1. Polymeric materials.

Characterization Complete

[a]Composites:
- P1700/C6000 Polysulfone
- 934/T300 Epoxy
- 5208/T300 Epoxy
- PMR-15/C6000 Polyimide

[a]Films:
- FEP Teflon
- Silvered FEP Teflon
- Kynar Fluorocarbon
- P1700 Polysulfone
- Kapton Polyimide

[b]High Performance Polymers:
- Polyimide-Polysiloxane Copolymer
- BTDA-ODA Polyimide
- BTDA-ODA-Al^{3+} Doped polyimide
- 6F-$DDSO_2$ Soluble polyimide
- 6F-BDAF Soluble polyimide
- PMDA-DAF Polyimide

[c]Traditional Polymers:
- Polystyrene
- Polyvinyl toluene
- Polytetrafluoroethylene
- Polymethylmethacrylate
- Nylon
- Polyethylene terephthalate

[d]Characterization Pending
- Polyurethane
- Various Silicones
- Polyethylene terephthalate
- Kevlar Aromatic polyamide
- Teflon PTFE
- Kapton Polyimide

Source: [a] W. Slemp, PI, Expts. A0134/S0010 (B9) and LDEF MSIG (various LDEF locations).
[b] W. Slemp and A. St. Clair, PI, Expt. S0010 (B9).
[c] J. Gregory, PI, Expt. A0114 (C9/C3).
[d] A. Whitaker, PI, Expt. A0171 (A8).

Table 2. Molecular weight of LDEF-exposed P1700 specimens.

Film	% Soluble	[a]M_n	[a]M_w	[a]M_z	M_w/M_n	[b]IV
Control	100	18,100	53,600	92,600	2.97	0.48
10 month, edge	96	12,700	73,500	183,000	5.77	0.47
10 month, center	87	12,500	90,900	326,000	7.27	0.49
Composite	**% Resin**					
Control, top ply	30.3	15,800	57,400	100,600	3.62	0.43
10 month, top ply	27.5	14,300	61,200	115,600	4.28	0.39
5.8 year, top ply	32.9	15,400	57,300	99,800	3.71	0.45

[a] Molecular weight average, grams/mole.
[b] Intrinsic viscosity, dL/g.

Table 3. XPS analysis of 10-month LDEF-exposed polyimide-polysiloxane copolymers.

	PIPSX-6		PIPSX-9		PIPSX-11	
PHOTOPEAK	CONTROL	EXPOSED	CONTROL	EXPOSED	CONTROL	EXPOSED
C 1s B.E.[a] (eV)	285.0/287.6/288.7	285.0/286.1	284.7	284.6	285.0/286.5/288.6	283.7 ... 287.8[c]
A.C.[b] (%)	57.5	15.5	54.4	16.8	69.2	19.0
O 1s B.E. (eV)	532.6	532.9/533.8	532.5	533.0	532.2/533.7	532.7/533.8
A.C. (%)	23.4	53.8	23.7	52.4	19.2	53.0
N 1s B.E. (eV)	400.1	—	—	—	400.4	—
A.C. (%)	1.6	NSP[d]	NSP	NSP	2.5	NSP
Si 2p B.E. (eV)	102.6	103.8	102.2	103.4	102.2	103.6
A.C. (%)	17.6	27.1	21.6	30.8	9.2	28.0
F 1s B.E. (eV)	—				—	—
A.C. (%)	NSP				NSP	NSP
Na 1s B.E. (eV)		1073.1				
A.C. (%)		2.1				
Cl 2p B.E. (eV)		200.1				
A.C. (%)		1.3				

[a] Binding Energy [b] Atomic Concentration [c] Multiple Peaks [d] No Significant Peak

Table 4. High performance polyimide films.

SAMPLE	STRUCTURE	COLOR
6F-BDAF	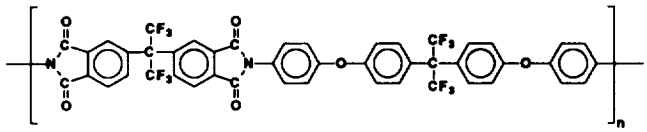	pale yellow
6F-DDSO$_2$	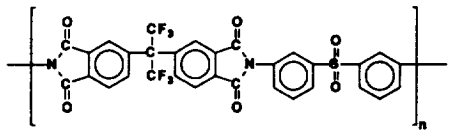	colorless
PMDA-DAF	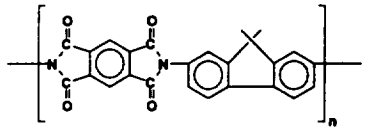	reddish-yellow
BTDA-ODA	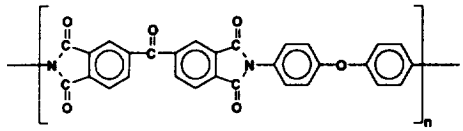	yellow
BTDA-ODA-Al^{3+}	BTDA-ODA + Al(acac)$_3$	brownish-yellow
KAPTON	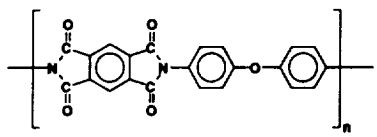	yellow

Table 5. Molecular weight of LDEF-exposed polyimide films.

SAMPLE	% SOLUBLE	[a]M_n ($\times 10^{-4}$)	M_w ($\times 10^{-5}$)	M_z ($\times 10^{-5}$)	M_w/M_n	I.V.[b]
6F-BDAF						
Control	98.8	8.56	2.18	7.10	2.54	0.829
		8.75	2.18	6.59	2.49	0.816
Edge[c]	98.7	7.65	2.12	7.67	2.77	0.846
		8.40	2.25	8.00	2.68	0.805
Center[d]	96.8	8.05	2.19	6.51	2.72	0.824
6F-$DDSO_2$						
Control	94.5	6.69	1.81	4.38	2.70	0.715
		4.65	1.76	4.07	3.79	0.732
Edge[c]	86.8	8.07	3.02	9.04	3.74	1.048
		7.62	3.09	9.66	4.06	1.042
Center[d]	60.9	4.18	3.06	11.10	7.32	0.619
		5.22	2.74	8.02	5.25	0.598

[a] Molecular weight average, grams/mole
[b] Intrinsic Viscosity, dL/g
[c] Shielded from direct exposure
[d] 10-month direct exposure

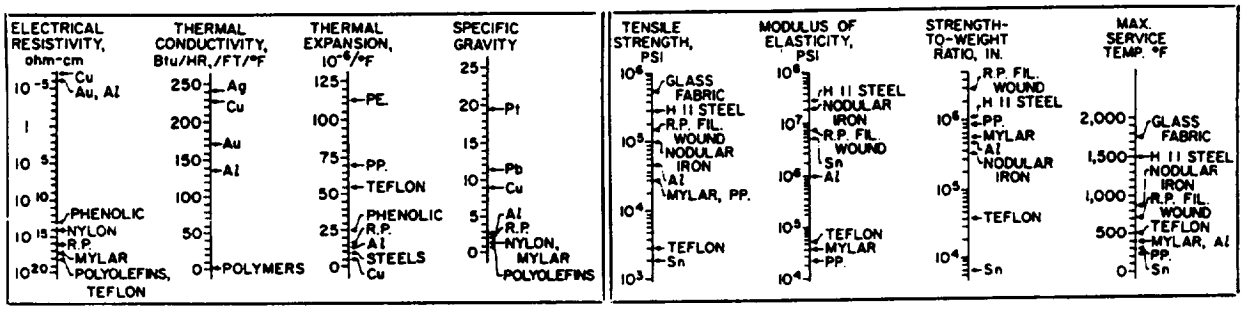

AEROSPACE APPLICATIONS

- Filament wound structures
- Thermal control surfaces
- Erectable structures
- Reduction of satellite weight

Figure 1. Some relative physical and mechanical properties of metals and nonmetals (ref. 1).

Row no.	Angle off RAM (°)	AO fluence (10^{21} a/cm^2)	VUV (ESH x 10^3)	Epoxy				Polyimide		Bismaleimide	Polysulfone
				934/T300	934/P75	CE339/GY70	5208/T300	PMR/C6000	LARC/C6000	F178A/T300	P1700/T300
9	8	8.72	11.1	✓	✓	✓	✓	✓			✓
8	-38	6.93	9.4	✓	✓	✓	✓	✓			
7	-68	3.28	7.2					✓		✓	
12	82	1.28	6.9	✓			✓				
1	112	0.0002	7.5	✓					✓		✓
3	172	0.0001	11.1	✓	✓	✓	✓	✓			

Additional Environmental Parameters

Thermal Cycles: ~34,000 (-20 to 160°F,±20°)

Particulate Radiation:

e- and p+: 2.5 x 10^5 rad

Cosmic: <10 rad

Vacuum: 10^{-6} - 10^{-7} torr

Micrometeoroid and Debris: 34,336 impacts (0.5mm - 5.25mm)

Altitude/Orbital Inclination: 255-180 nm/28.5°

LDEF Sketch and Orbital Orientation

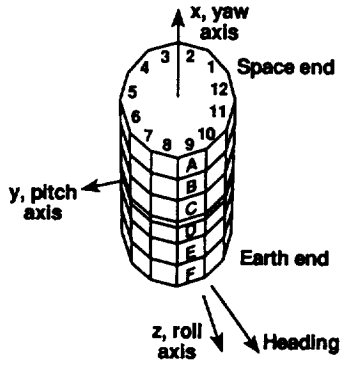

Figure 2. Selected LDEF-exposed composite materials.

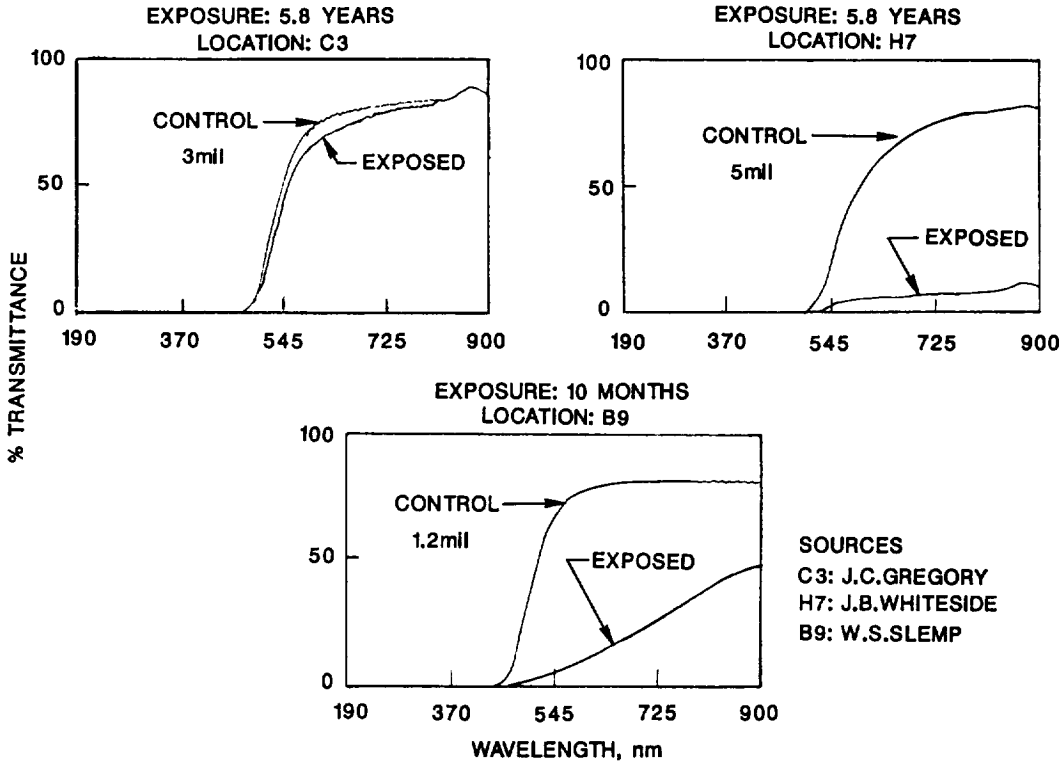

Figure 3. UV-VIS spectra of LDEF-exposed Kapton film.

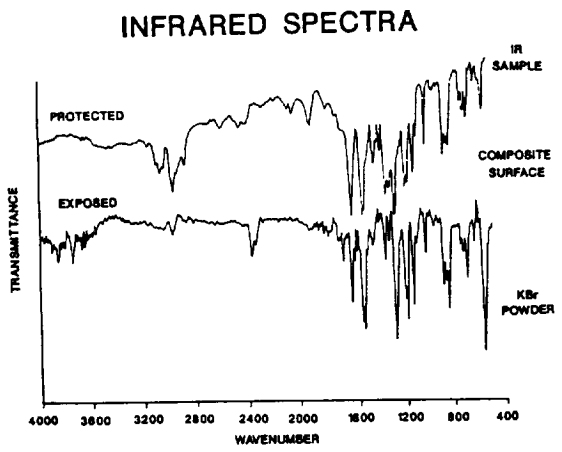

GLASS TRANSITION TEMPERATURE

Sample	Tg (°C)	Contacted side
Langley Control	167°	Random
	167°	
	170°	
	166°	
Flight Protected	164°	Side A
	166°	Side B
Flight Exposed	170°	Exposed side
	171°	
	169°	Nonexposed side
	171°	

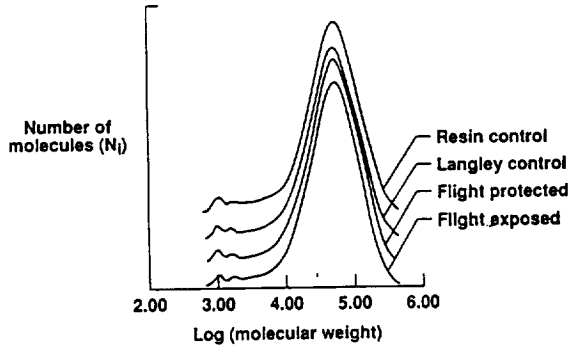

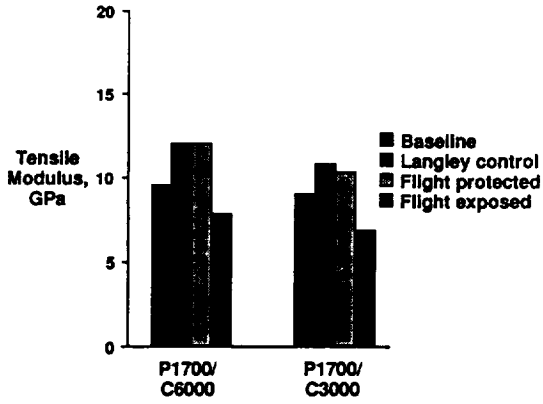

Figure 4. A summary of polysulfone composite characterization results; 5.8 years of Row 9 exposure.

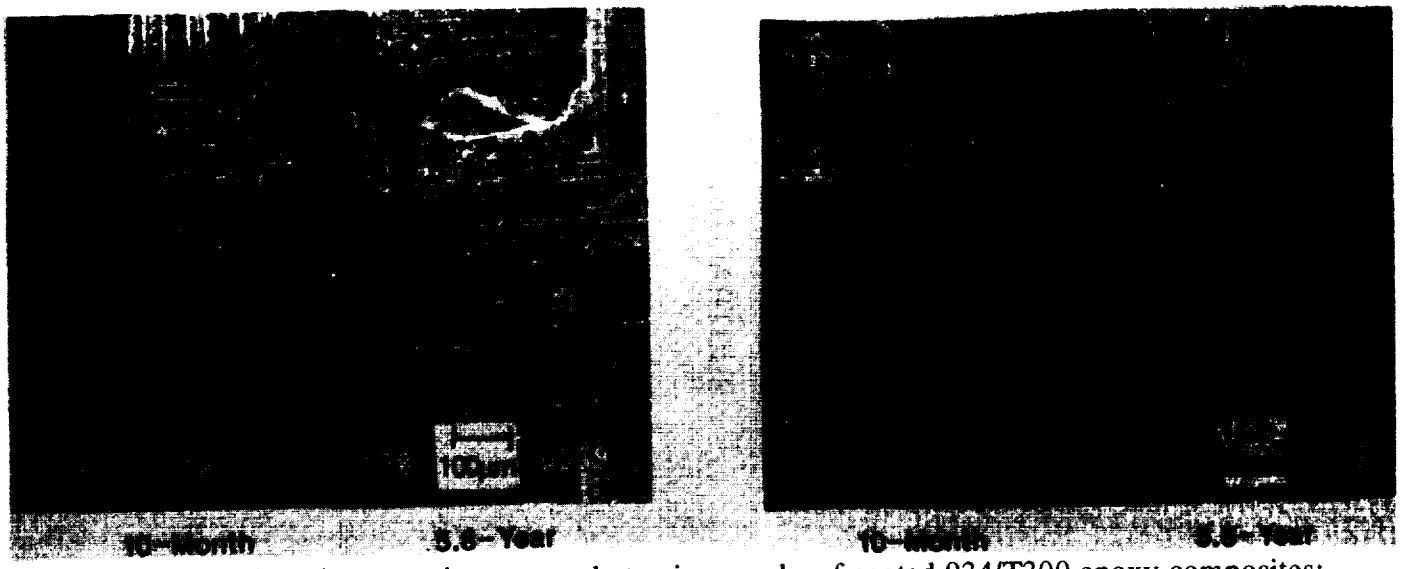

Figure 5. Scanning electron microscopy photomicrographs of coated 934/T300 epoxy composites; 600 Å SiO_2/1,000 Å nickel/composite.

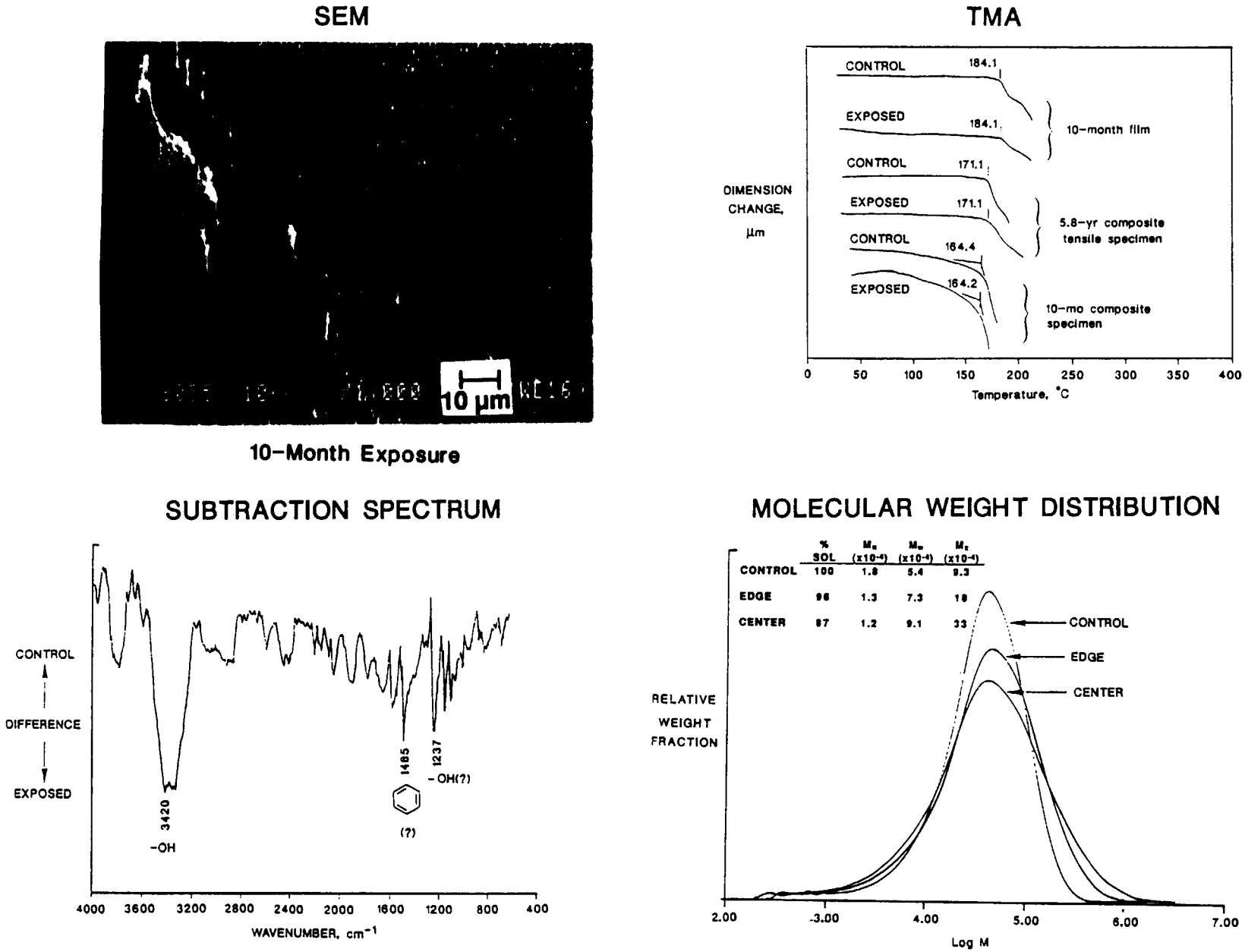

Figure 6. A summary of polysulfone film characterization results; 10 months of Row 9 exposure.

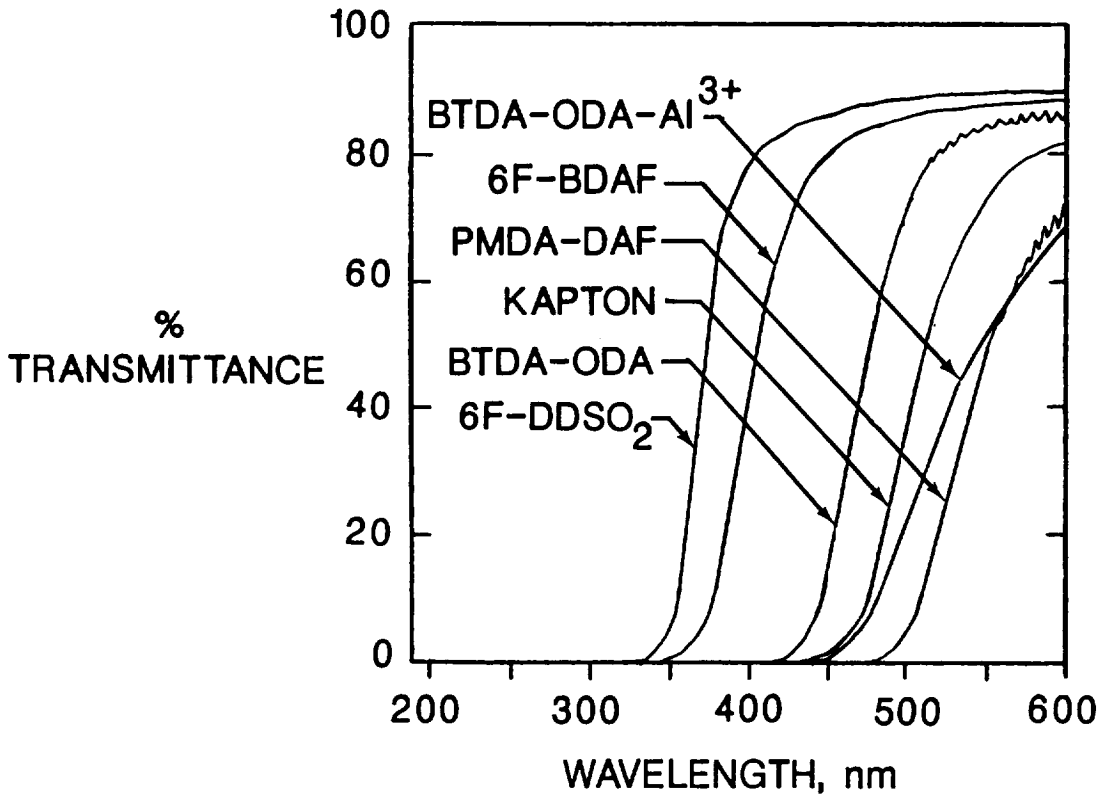

Figure 7. UV-VIS spectra of unexposed polyimide films.

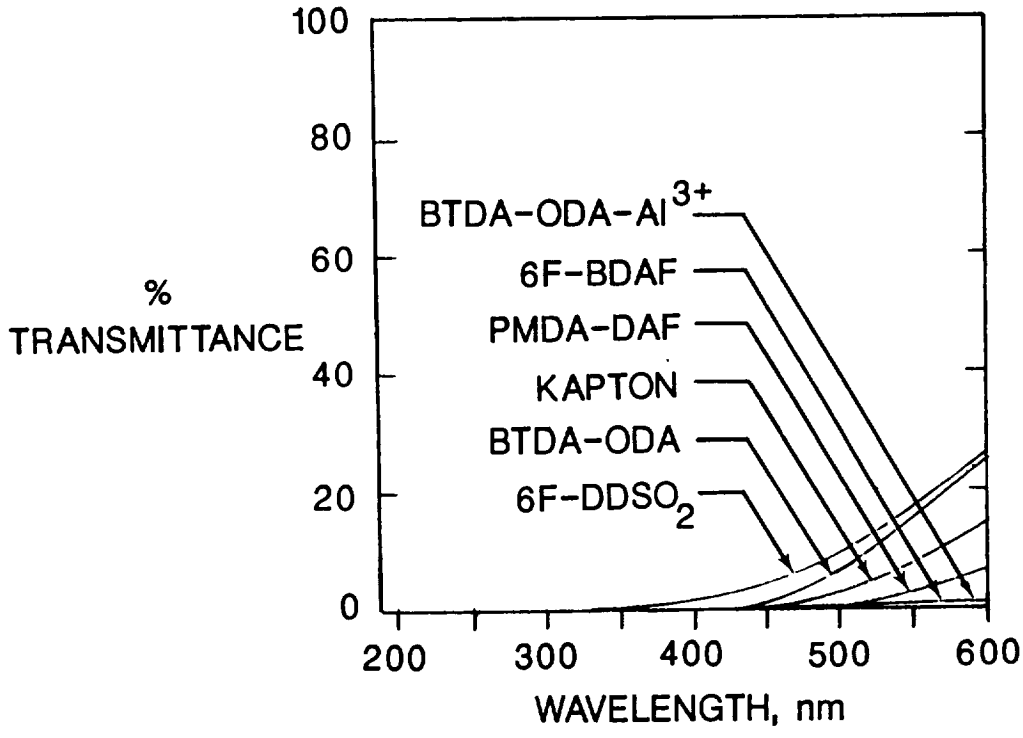

Figure 8. UV-VIS spectra of polyimide films exposed for 10 months on LDEF.

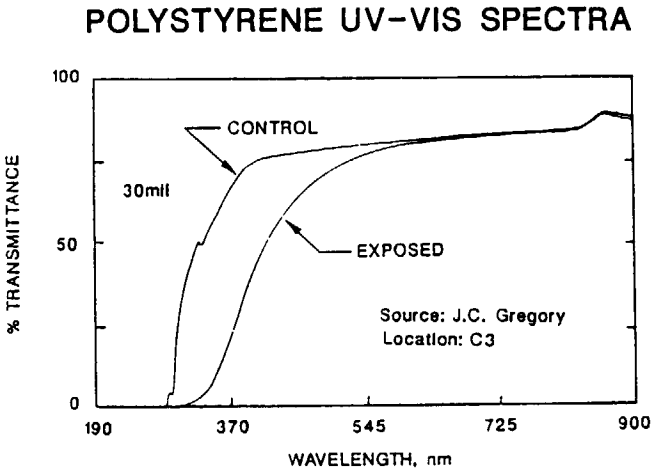

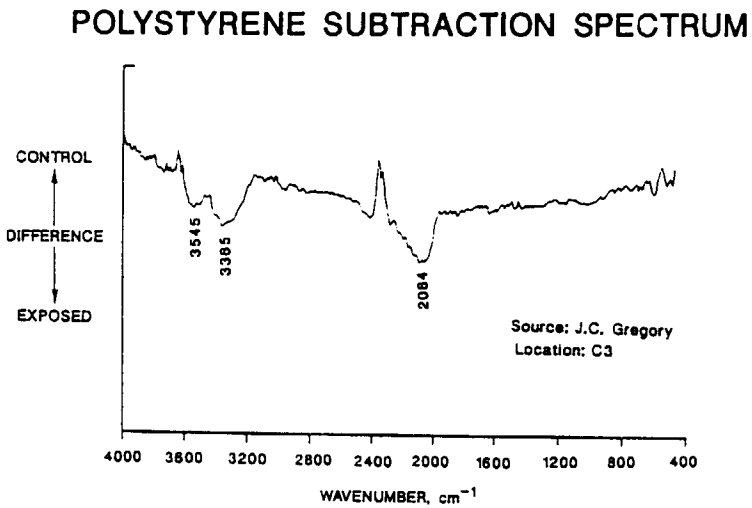

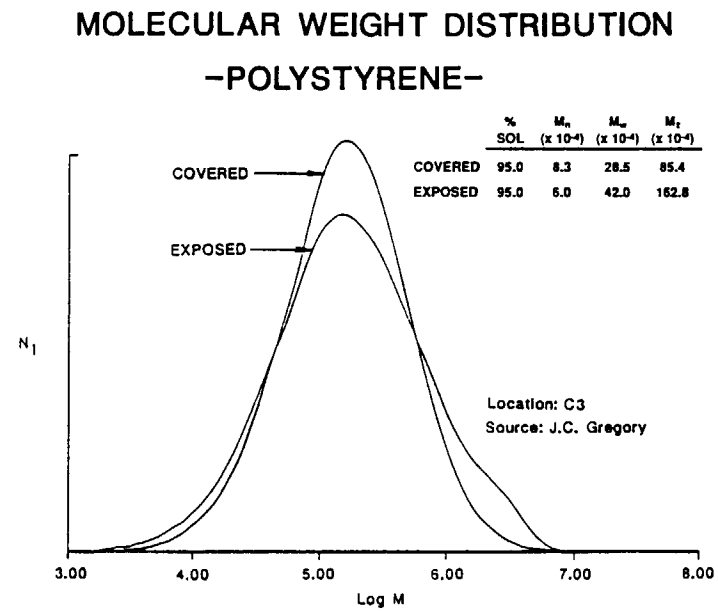

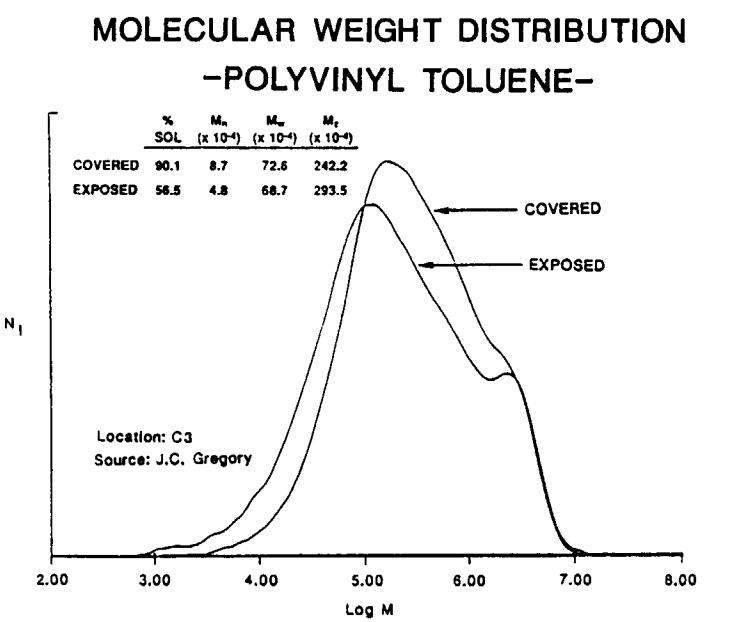

Figure 9. A summary of polystyrene and polyvinyl toluene characterization results; 5.8 years of Row 3 exposure.

N94-31024

ATOMIC OXYGEN INTERACTION AT DEFECT SITES IN PROTECTIVE COATINGS ON POLYMERS FLOWN ON LDEF

Bruce A. Banks, Kim K. de Groh, and Bruce M. Auer
NASA Lewis Research Center
Cleveland, Ohio
Phone: 216/433-2308, Fax: 216/433-6106

Linda Gebauer and Cynthia LaMoreaux
Cleveland State University
Cleveland, Ohio
Phone: 216/433-2308, Fax: 216/433-6106

ABSTRACT

Although the Long Duration Exposure Facility (LDEF) had exposed materials with a fixed orientation relative to the ambient low-Earth-orbital environment, arrival of atomic oxygen is angularly distributed as a result of the atomic oxygen's high temperature Maxwellian velocity distribution and the LDEF's orbital inclination. Thus, atomic oxygen entering defects in protective coatings on polymeric surfaces can cause wider undercut cavities than the size of the defect in the protective coating. Because only a small fraction of atomic oxygen reacts upon first impact with most polymeric materials, secondary reactions with lower energy thermally accommodated atomic oxygen can occur. The secondary reactions of scattered and/or thermally accommodated atomic oxygen also contribute to widening the undercut cavity beneath the protective coating defect. As the undercut cavity enlarges, exposing more polymer, the probability of atomic oxygen reacting with underlying polymeric material increases because of multiple opportunities for reaction. Thus, the effective atomic oxygen erosion yield for atoms entering defects increases above that of the unprotected material. Based on the results of analytical modeling and computational modeling, aluminized Kapton multilayer insulation exposed to atomic oxygen on row 9 lost the entire externally exposed layer of polyimide Kapton, yet based on the results of this investigation, the bottom surface aluminum film must have remained in place, but crazed. Atomic oxygen undercutting at defect sites in protective coatings on graphite epoxy composites indicates that between 40 to 100 percent of the atomic oxygen thermally accommodates upon impact, and that the reaction probability of thermally accommodated atomic oxygen may range from 7.7×10^{-6} to 2.1×10^{-3}, depending upon the degree of thermal accommodation upon each impact.

INTRODUCTION

Polymers anticipated for use on long-duration spacecraft or high atomic oxygen fluence spacecraft, such as Space Station *Freedom* and Earth Observing Systems, will require atomic oxygen protective coatings to assure functional durability of materials throughout the mission duration. Although the rate of atomic oxygen attack for many materials is now reasonably well understood as a result of LDEF, the long-term durability of protected materials is less understood because it is highly dependent upon the reactivity of thermally accommodated atomic oxygen at defect sites in protective coatings. The scattered, thermally accommodated atomic oxygen gradually increases the diameter of the undercut cavities, leading to thermal and/or structural performance degradation of the polymer. The probability of reaction of atomic oxygen with polymers is known to be energy depen-

dent. Thus, it is of great value to understand the degree to which 4.5 eV ram atomic oxygen thermally accommodates upon each impact, as well as the reaction probability of the thermally accommodated atomic oxygen, to be able to develop undercutting growth models that replicate actual in-space performance of polymers with protective coatings. SiO_X (where $1.9 \leq X \leq 2.0$) sputter-deposited protective coatings 1300Å thick on Kapton H (rough surface) typically have 3500 pin window defects/cm^2 (ref. 1). Thus, degradation processes for polymers with atomic oxygen protected coatings are dominated by undercutting oxidation at defect sites, as opposed to degradation or loss of the protective coating itself.

ALUMINIZED KAPTON MULTILAYER INSULATION

Aluminized Kapton multilayer insulation retrieved from the LDEF Cascade Variable-Conductance Heat Pipe Experiment (A0076) located on row 9 was examined to assess effects of atomic oxygen attack. Figure 1 is a photograph of the top surface and edge view of a piece of the retrieved sample. As can be seen from Figure 1, the outermost Kapton layer is missing as a result of oxidation by atomic oxygen. The aluminization layer, which was deposited only on the bottom side of this Kapton layer, as shown schematically in Figure 2, is also missing. Thus, the second layer of Kapton, which was aluminized on both sides, is the surface shown in Figure 1a. Direct atomic oxygen exposure of the underlying layer of aluminized Kapton may have occurred, depending upon the integrity of the aluminization layer on the bottom of the outermost layer, as well as the degree to which it stayed resident on the underlying aluminized Kapton layer. If the aluminized film curled up or drifted away from the second layer of multilayer insulation after atomic oxygen erosion of the 0.0762-mm layer of Kapton, then a known atomic oxygen fluence impingement upon the second layer would result, and measurements of the atomic oxygen undercutting could then be made and compared with theoretical predictions, thus allowing quantification of accommodation and reaction probabilities of thermally accommodated atomic oxygen.

Atomic oxygen undercutting of the second layer of multilayer insulation was observed by taking scanning electron micrographs of defect sites in the top surface of the second layer of multilayer insulation prior to and after the aluminum was removed by means of dilute hydrochloric acid. After deposition of a gold conductive layer, the undercut cavity was then visible by scanning electron microscopy, allowing measurements of defect undercut cavity size and shape. Figure 3 shows scanning electron micrographs of the top surface of the second layer of multilayer insulation before and after removal of the aluminized surface. The shapes of most of the undercut cavities below pin window defects were found to be hemispherical. The fact that the undercut cavities were mostly hemispherical, as opposed to having a high aspect ratio (deep and narrow), is the first indication that the atomic oxygen which entered the defects was arriving isotropically, as opposed to directly from space. This implies that the gossamer aluminization layer from the top multilayer insulation sheet may have prevented direct impact of the underlying multilayer insulation. Some isolated areas did have deep high aspect ratio undercut cavities. These areas were probably at sites where the aluminization had torn, allowing the underlying blanket to be exposed to direct ram.

It is possible to predict the diameter of the undercut cavity for a given defect diameter if one assumes circular defects with hemispherical undercut cavities, and makes appropriate assumptions for the reaction probability of 4.5 eV, as well as thermally accommodated atomic oxygen. One can then compare the predictions with the observations to determine whether or not directed atomic oxygen or scattered atomic oxygen entered the defects. As shown in Figure 4, energetic atomic oxygen which enters the defect cavity must first strike Kapton. Upon hitting the Kapton, it has an initial reaction probability of P_I for reacting with the Kapton. Based on mechanistic assumptions and

in-space atomic oxygen erosion yields, the probability of energetic atomic oxygen reaction with Kapton is thought to be approximately 0.138 (ref. 2). Atomic oxygen which does not react can then leave the Kapton surfaces in a variety of directions, enabling secondary impacts with Kapton or aluminum (where the undercut cavity allows exposure of the bottom side of the aluminized layer), or allowing it to exit out of the defect opening. For purposes of this model, it is assumed that the energetic atomic oxygen thermally accommodates with the Kapton upon first impact, thus reducing the reaction probability for subsequent impacts to a much lower value. Based on computational Monte Carlo modeling investigations of atomic oxygen undercutting presented in reference 3, the reaction probability of thermally accommodated atomic oxygen, P_S, is assumed to be 0.00134. In Figure 4, the undercut cavity surface area of exposed Kapton is given by A_K, the area of the undercut exposed aluminum is given by A_G, the area of the circular defect is given by A_D, and the total surface area of the undercut cavity, A_T, is

$$A_T = A_K + A_G + A_D \ . \tag{1}$$

The effective reaction probability of atomic oxygen entering the defect, and ultimately reacting with Kapton, P_E, is then given by the sum of the reaction probabilities of the initial impact and subsequent impacts with atomic oxygen. The summation of all the terms associated with these reaction probabilities (shown in Fig. 4) is a series with a closed form solution given by:

$$P_E = P_I + \frac{(1-P_I)A_K P_s}{A_D + A_K P_s} \ . \tag{2}$$

One can predict the undercut cavity growth with atomic oxygen fluence by iteratively exposing an atomic oxygen fluence increment, ΔF to the undercut cavity, and computing the volume lost, ΔV, based on the effective reaction probability, P_E, where:

$$\Delta V = E_E A_D \Delta F = \frac{E_o P_E A_D \Delta F}{P_I} \ . \tag{3}$$

E_E is the effective atomic oxygen erosion yield of atomic oxygen entering defect cavities, and E_o is the atomic oxygen erosion yield of unprotected polyimide Kapton (3×10^{-24} cm^3/atom). The volume increase of the undercut cavity can then be used to compute a new undercut volume with its associated total surface area, A_T, and Kapton area, A_K. With these revised values, another fluence increment is then injected, and a new volume increment is oxidized. The results of this iterative process are shown in Figure 5. The iterative development of the undercutting was carried out to a fluence of 6.4×10^{21} atoms/cm^2, which is equal to the row 9 LDEF atomic oxygen fluence of 8.99×10^{21} atoms/cm^2 (ref. 4) minus the amount of atomic oxygen fluence which was predicted to be consumed by the top surface layer of 0.0762 mm Kapton. The predicted results given in Figure 5 can be compared with the LDEF experimental results shown in Figure 6. As can be seen by comparing the predicted results with the experimental results, a large inconsistency exists. For example, for pin window defects of approximately 2.8 microns diameter, the theoretically predicted undercut diameter is approximately 3.6 times larger than the experimentally observed undercut diameter. In addition, the shape of the two curves have opposite second derivatives. Knowledge of these results, as well as the shape of the undercut cavity in the region examined, all consistently lead to the conclusion that oxidation of the top aluminized Kapton sheet resulted in a crazed aluminum thin-film bottom-surface coating which remained in place, thus attenuating the arrival flux of atomic oxygen. This in turn caused a greatly reduced, and much less directed, undercutting to the underlying aluminized Kapton sheet. Thus, the gossamer aluminum film must have remained as a cracked, but in place, film until such time as it was disturbed by retrieval and handling operations. Small aerodynamic loads against the loosely attached film during repressurization and ground handling were a likely cause for

the ultimate removal of this film. Further evidence of this removal process is suggested by the frequency with which small shards of aluminization were found in the clean room in the vicinity of the LDEF after retrieval. These findings that the aluminum film largely remained in place throughout the flight exposure are also consistent with those of reference 5. Thus, based on these conclusions, this particular sample of coated Kapton is not a reliable source of prediction of thermally accommodated atomic oxygen reaction probability.

PROTECTED GRAPHITE EPOXY COMPOSITES

A sample of 934 epoxy composite containing T-300 carbon fibers, with an atomic oxygen protective coating consisting of 400Å of aluminum on 800Å of chromium, was exposed on LDEF row 9 to an atomic oxygen fluence of 8.99×10^{21} atoms/cm^2, as shown in Figure 7. The extremely rough surface morphology of the composite resulted in numerous protective coating defects, which were analyzed by scanning electron microscopy prior to and after removal of the protective coating, as shown in Figure 8. Detailed examination of the profile of undercut crack defect cavities was possible by scanning electron microscopy examination at highly inclined angles at locations where cracks join large pin window undercut defects (Fig. 9).

A Monte Carlo computational model was developed to simulate the erosion processes resulting from atomic oxygen interaction with protected polymers. Although the undercut cavity shown in Figure 9 is graphite epoxy, the Monte Carlo model was developed for polyimide Kapton H, which typically has a higher erosion yield than graphite epoxy. However, the reaction probability of carbon has been reported to be quite similar to that of Kapton (ref. 6). For the Monte Carlo model presented in this paper, Kapton, rather than graphite epoxy, was assumed. The differences in erosion yield, as opposed to reaction probability, would cause the predicted undercut cavities in Kapton to replicate that which would occur for graphite epoxy at a slightly higher fluence. The width-to-depth ratio of the cavities, however, would be largely unaffected for high fluences largely because the reaction probabilities are thought to be similar.

The Monte Carlo computational model allows atomic oxygen to interact with polymers at defect sites in the protective coatings on the polymers. The computational interactions are carried out on the basis of the prescribed mechanistic interaction assumptions listed below:

1. The model is two-dimensional with atomic oxygen trajectories confined to a plane that simulates a crack or scratch defect in the protective coating.

2. Reaction probability with Kapton is proportional to the square root of the cosine of the angle between the surface normal and the arrival direction.

3. Reaction probability with Kapton at normal incidence is equal to:

   a. 0.138 for space (first impact) (ref. 2).
   b. Prescribed, and to be discussed, for space (for second and subsequent impact).

4. Ram energy (approximately 4.5 eV) atomic oxygen has a prescribed probability (to be discussed) of thermally accommodating with the surface impacted if it does not react.

5. Atomic oxygen does not react with protective coatings, nor recombines, and remains atomic after impacting protective coatings.

6. Unreacted atomic oxygen leaves surfaces in a cosine ejection distribution if it is thermally accommodated, and scatters off surfaces approximately specularly if it is nonaccommodated (elastic scattering).

7. Arrival direction of space atomic oxygen is angularly distributed because of the high temperature (assumed to be an average of 1,227 K for the LDEF mission) Maxwellian distribution (ref. 7).

Using the Monte Carlo computational model, one can simulate the growth of the LDEF undercut cavities in graphite epoxy with fluence as shown in Figure 10. Each undercut cavity shown in Figure 10 portrays the predicted growth in the undercut cavity for an additional 10,000 atoms entering the defect as one views defects from left to right in the figure. These profiles are a result of assuming 100 percent of the arriving atoms thermally accommodate upon first impact, and that the thermally accommodated atomic oxygen reaction probability is 0.00134 (ref. 3).

If one computes the effective reaction probability of atomic oxygen entering defect cavities by counting the number of Monte Carlo computational cells removed, and dividing it by the number of atoms entering, then one would expect to find that atoms which enter defect cavities have a greater probability of ultimately reacting, compared to those which impinge upon unprotected materials which, to a far lesser degree, have multiple opportunities for reaction. Figure 11 shows the growth of effective reaction probability as a function of fluence based on Monte Carlo calculations, assuming 100-percent thermal accommodation upon first impact, and thermally accommodated reaction probabilities of 0.00134. As can be seen in Figure 11, even though the initial impact reaction probability is 0.138, the effective reaction probability quickly drops down to approximately 0.12, then gradually rises as the undercut cavity tends to trap more and more thermally accommodated atomic oxygen, which then has further opportunities to react. Although it is believed that the effective reaction probability at zero fluence is 0.138, the reason the effective reaction probability is lower than that for low fluences is probably related to the fact that the surface of the polymer quickly roughens upon atomic oxygen attack, thereby reducing the reaction probability because of its square root dependence upon the cosine of the angle between the surface normal and the arrival direction. This square root of the cosine of the angle of attack dependence has been observed in space for Mylar, Kapton, and FEP Teflon (refs. 6, 8, and 9). If one changes the Monte Carlo modeling assumptions to assume that the thermally accommodated atomic oxygen reaction probability is controlled by an activation energy of 0.38 eV, as proposed in reference 10, then a thermally accommodated reaction probability of 7.7×10^{-6} is predicted for 0.04 eV atoms. This much lower thermally accommodated atomic oxygen reaction probability does not replicate the observed atomic oxygen undercutting shown in figure 9 if 100-percent thermal accommodation is assumed upon each impact. However, as will be discussed later, 40-percent thermal accommodation does produce undercutting profiles which more closely replicate those experimentally observed on LDEF. Figure 12 is a plot of effective reaction probability as a function of fluence, assuming 40 percent of the ram energy atoms thermally accommodate upon each impact, and a reaction probability of 7.7×10^{-6} for thermally accommodated atoms. As can be seen by comparing Figure 12 with Figure 11, lowering the thermally accommodated atomic oxygen reaction probability and increasing the fraction of atoms which energetically scatter causes the effective reaction probability to increase more quickly with fluence. The reason for this is that the scattered energetic atomic oxygen is directed deeper toward the root of surface irregularities, allowing additional opportunity for reaction.

By inspection of a variety of graphite epoxy composite coating cracks, and their associated undercut defect widths, one observes, as expected, that wide cracks are not as effective at trapping atomic oxygen as narrow cracks. As a result, undercut widths are less than proportional to the crack defect widths, as shown in Figure 13. Whether one measured crack undercut geometries or pin window undercut geometries, one would expect this same less-than-proportional dependence of under-

cut size width on defect size. Figure 13 is quite similar in shape to Figure 5, which is predicted on the basis of modeling of undercut cavity trapping of atomic oxygen.

One can use the Monte Carlo computational model to attempt to match the experimentally observed LDEF results as shown photographically in figure 9. To obtain predicted undercut cavities which replicate experimentally observed cavities, one can assume 100 percent of the ram atomic oxygen thermally accommodates upon first impact, and iteratively solve for the reaction probability of thermally accommodated atomic oxygen that produces the best match to the LDEF-observed undercut cavities, or assume a thermally accommodated atomic oxygen reaction probability, and optimize the fraction of energetic ram atoms which thermally accommodates upon each impact. Figure 14 shows the dependence of Monte Carlo model predicted undercut width-to-depth ratio dependence upon thermally accommodated atomic oxygen reaction probability, assuming 100 percent of the ram atomic oxygen thermally accommodates upon impact. The predicted thermally accommodated atomic oxygen reaction probability which best matches the observed LDEF undercut width-to-depth ratio is 0.00211. Figure 15 compares an experimentally observed graphite epoxy composite undercut cavity with a Monte Carlo model predicted undercut cavity, assuming 100 percent of the ram atomic oxygen atoms thermally accommodate upon impact, and assuming a thermally accommodated atomic oxygen reaction probability of 0.00211. As can be seen by comparing the two profiles, although the top surface undercut-width-to-undercut-cavity-depth ratios match, the lower portion of the LDEF undercut cavity is slightly wider than the Monte Carlo predictions.

If one assumes that the thermally accommodated atomic oxygen reaction probability is 7.7×10^{-6}, as previously discussed, then various undercut cavity width-to-depth ratios can be predicted, assuming various probabilities for accommodation of the ram atomic oxygen upon each impact, as shown in Figure 16. The predicted accommodation fraction which matches the experimentally observed LDEF results is approximately 0.4. Figure 17 compares the experimentally observed LDEF graphite epoxy composite results with the Monte Carlo model predicted results, assuming a 40-percent probability of thermal accommodation and a thermally accommodated reaction probability of 7.7×10^{-6}. As can be seen by comparison of Figure 15 and Figure 17, the assumption of a lower thermally accommodated atomic oxygen reaction probability and a lower fraction thermal accommodation, produces a closer match to the experimentally observed LDEF results.

SUMMARY

An analytical model was developed to predict atomic oxygen undercutting at pin window defect sites in aluminized Kapton multilayer insulation flown on LDEF. Comparison of the results of these predictions with experimentally observed results indicates that the aluminized coating on the unexposed surface of the top layer of multilayer insulation remained in place, but crazed after the exposed polyimide Kapton was completely oxidized by atomic oxygen. Although sporadic locations of direct atomic oxygen attack did occur on the second layer of multilayer insulation, much of the remains of the top layer aluminization prevented direct ram atomic oxygen attack of the underlying layers of multilayer insulation. Because of the uncertainty of knowing whether or not direct atomic oxygen attack occurred on the second layer of multilayer insulation, predictions of undercutting based on mechanistic models are not possible. The gossamer remains of the free-standing aluminized film, which had been attached to the outermost Kapton multilayer insulation sheet, was probably blown away during retrieval and handling operations.

Monte Carlo computational model simulation of atomic oxygen undercutting observed on a protected graphite epoxy composite sample retrieved from LDEF indicates a range of thermally accommodated atomic oxygen reaction probabilities based on an assumed fraction of ram atomic

oxygen which thermally accommodates upon each impact. Thermally accommodated atomic oxygen reaction probabilities range from 7.7×10^{-6} to 2.11×10^{-3} for probabilities of thermally accommodating ranging from 0.4 to 1.0. The lowest reaction probability and thermal accommodation fraction produced the closest fit to the experimentally observed LDEF results.

REFERENCES

1. Banks, B.A., Rutledge, S.K., Gebauer, L., and LaMoreaux, C.: "SiO_X Coatings for Atomic Oxygen Protection of Polyimide Kapton in Low Earth Orbit." AIAA paper 92-2151, Proceedings of the Coatings Technology for Aerospace Systems Materials Specialists Conference, Dallas, Texas, April 16–17, 1992.

2. Banks, B.A., Rutledge, S.K., Auer, B.M., and DiFilippo, F.: "Atomic Oxygen Undercutting of Defects on SiO_2 Protected Polyimide Solar Array Blankets." Published in *Materials Degradation in Low Earth Orbit (LEO)*, edited by V. Srinivasan and B.A. Banks, The Minerals, Metals, and Materials Society, pp. 15–33, 1990.

3. Banks, B.A., Auer, B.M., Rutledge, S.K., de Groh, K.K., and Gebauer, L.: "The Use of Plasma Ashers and Monte Carlo Modeling for the Projection of Atomic Oxygen Durability of Protected Polymers in Low Earth Orbit." Paper presented at the 17th Space Simulation Conference, Baltimore, Maryland, November 9–12, 1992.

4. Bourassa, R., personal communication.

5. Smith, C.A., Hasegawa, M.M., and Jones, C.A.: "Space Station WP-2 Application of LDEF MLI Results." LDEF Materials Results for Spacecraft Applications Conference, Huntsville, Alabama, October 27–28, 1992, NASA CP- , 19 .

6. Brinza, D.E.: "Proceedings of the NASA Workshop on Atomic Oxygen Effects." JPL Publication 87-14 (June 1, 1987), Pasadena, California, November 10–11, 1986.

7. Bourassa, R.J., and Gillis, J.R.: "Atomic Oxygen Exposure of LDEF Experiment Trays." NASA CR 189627, May, 1992.

8. Banks, B.A., Dever, J.A., Gebauer, L., and Hill: "Atomic Oxygen Interactions with FEP Teflon and Silicones on LDEF." Proceedings of the 1st LDEF Post-Retrieval Symposium, Kissimmee, Florida, June 2–8, 1991.

9. Levadou, F., and Eesbeek, M.: "Followup on the Effects of Space Environments on UHCRE Thermal Blankets." LDEF Materials Results for Spacecraft Applications Conference, Huntsville, Alabama, October 27–28, 1992, NASA CP- , 19 .

10. Koontz, S., Albyn K., and Leger, L.J.: "Atomic Oxygen Testing with Thermal Atoms Systems: A Critical Evaluation." *Journal of Spacecraft and Rockets*, vol. 28 No. 3, May–June, 1991.

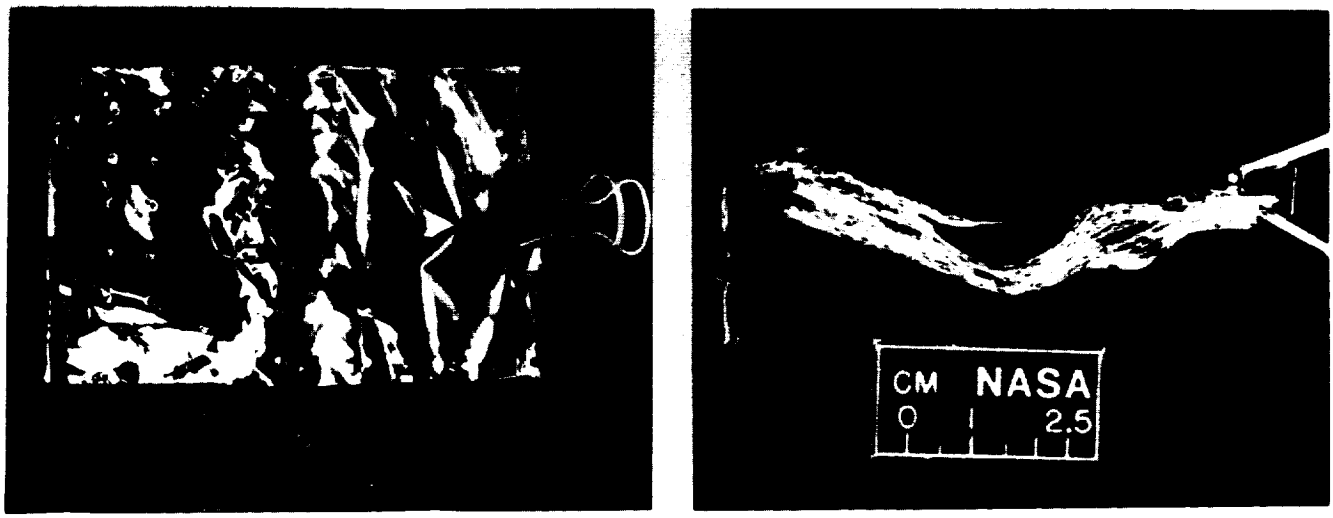

1a. Showing outermost surface as retrieved. 1b. Edge view.

Figure 1. Aluminized Kapton multilayer insulation retrieved from LDEF from row 9.

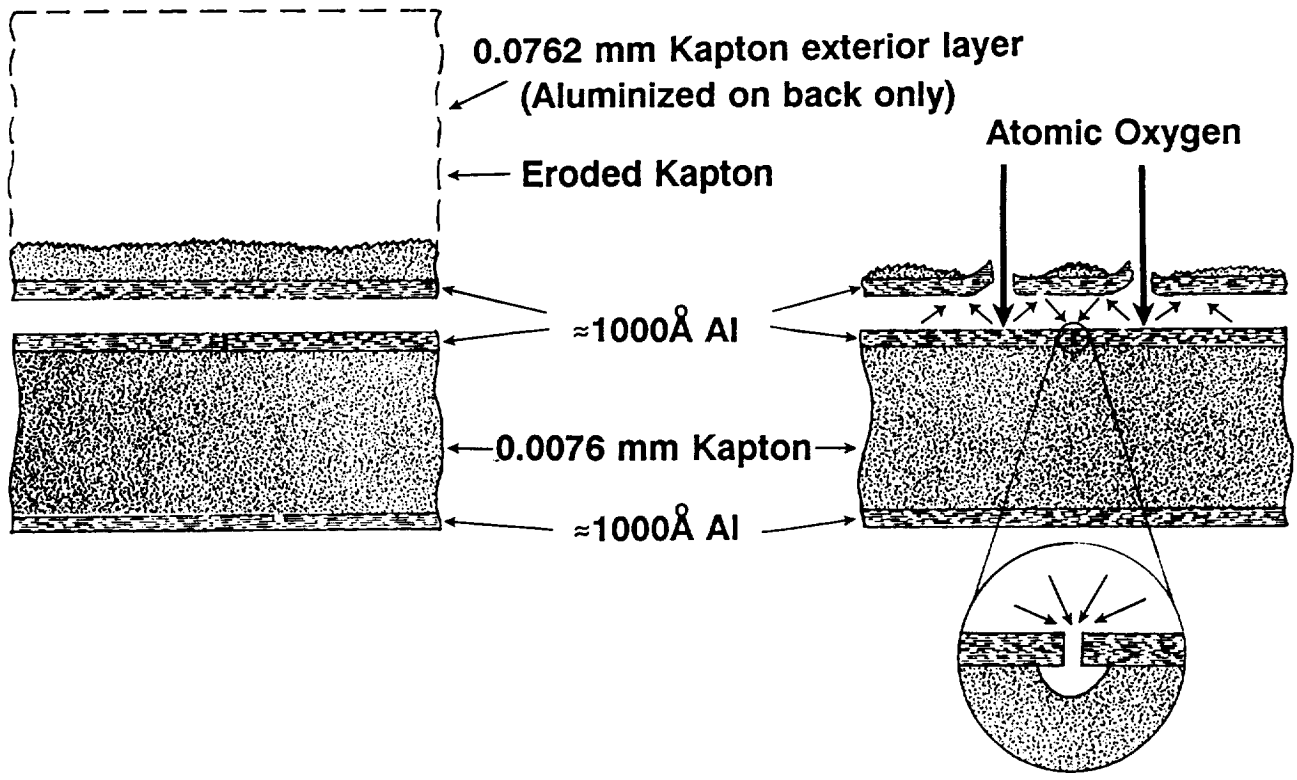

Figure 2. Section view of top two layers of aluminized Kapton multilayer insulation.

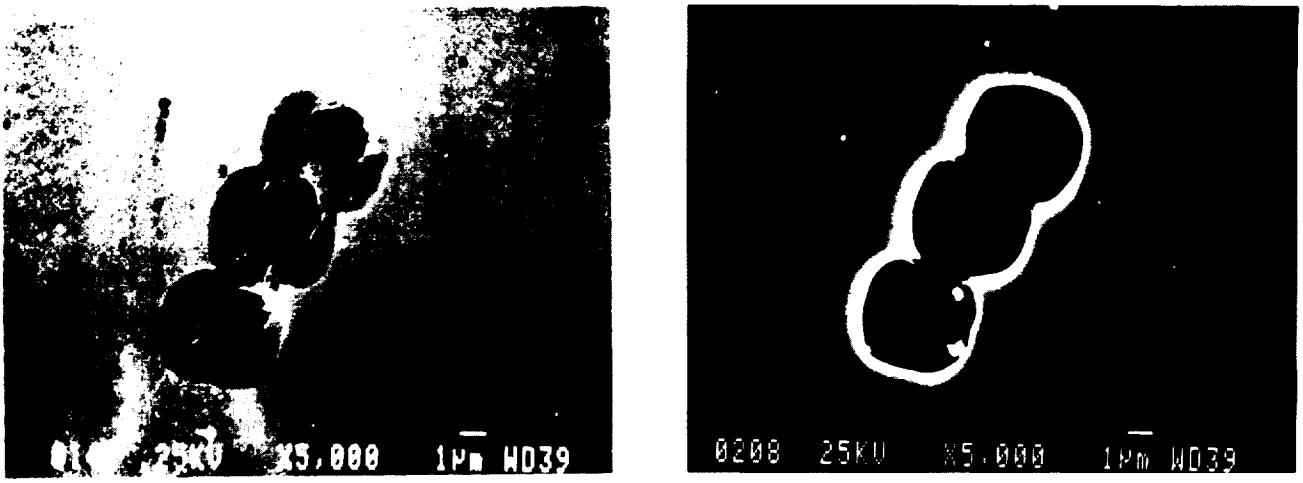

3a. Prior to removal of the aluminization.

3b. After chemical removal of the aluminization.

Figure 3. Top surface of the second layer of aluminized Kapton multilayer insulation retrieved from LDEF.

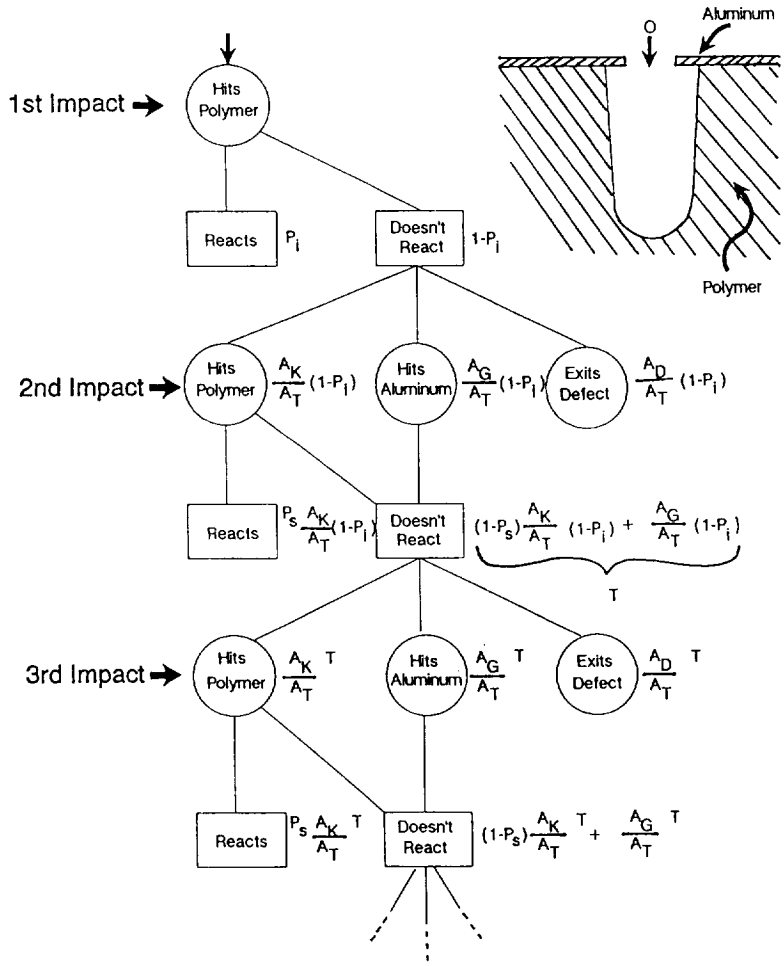

Figure 4. Atomic oxygen interactions in defect cavities, assuming multiple collisions.

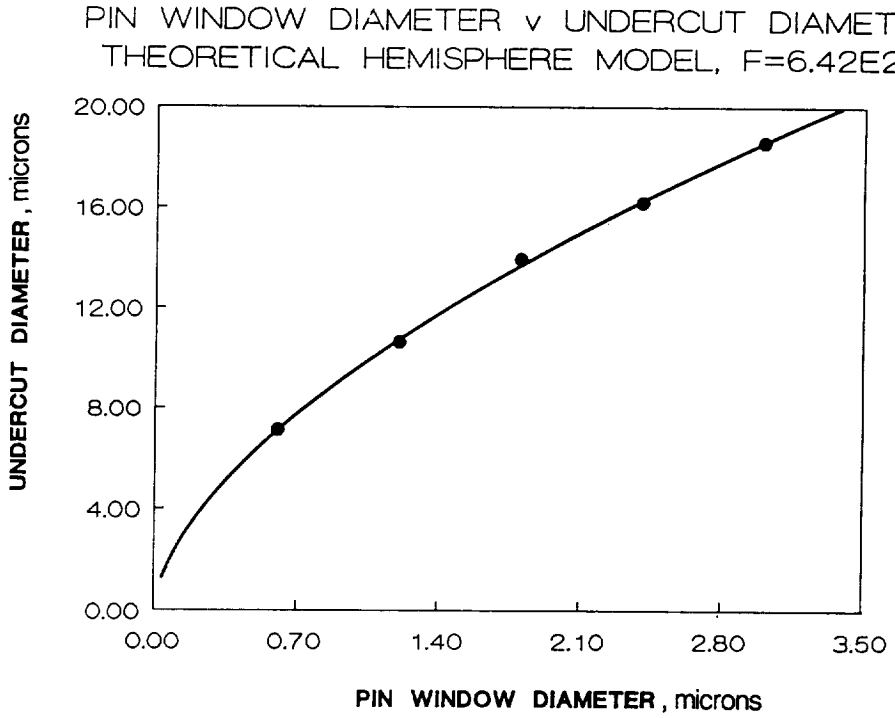

Figure 5. Theoretical prediction of atomic oxygen undercut diameter as a function of pin window diameter for defects in protected Kapton exposed to an atomic oxygen fluence of 6.4×10^{21} atoms/cm^2 assuming an initial impact reaction probability of 0.138, a thermally accommodated reaction probability of 0.00134, and 100-percent thermal accommodation of atomic oxygen upon initial impact.

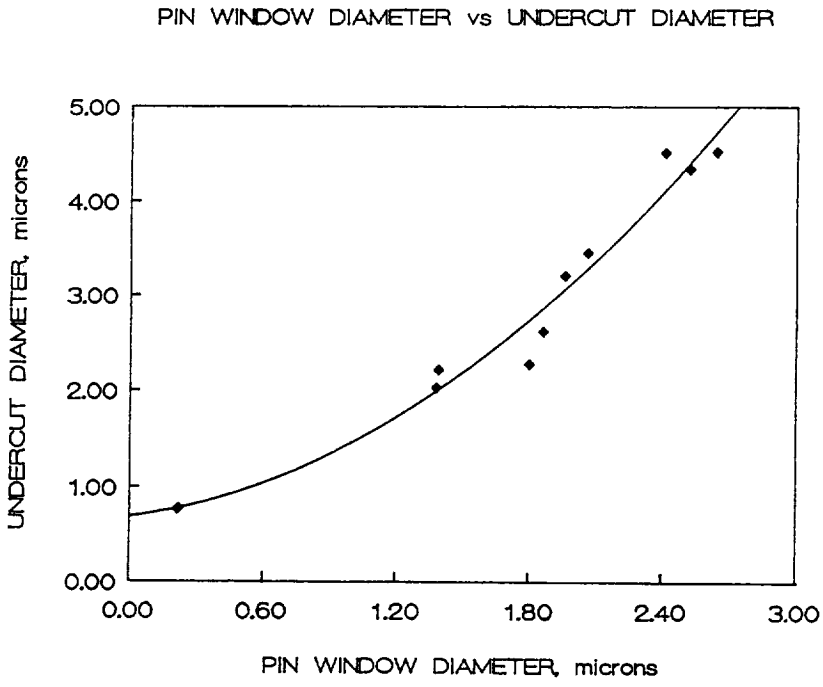

Figure 6. LDEF undercut diameter dependence upon pin window diameter for defects in the aluminization of the second layer of multilayer insulation on row 9.

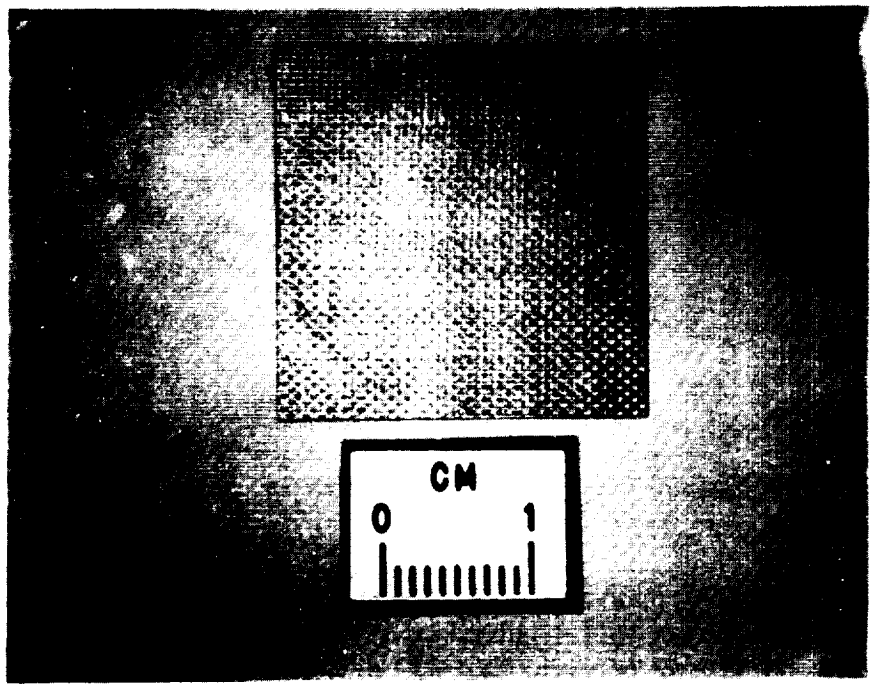

Figure 7. Graphite epoxy composite (934 epoxy with T-300 carbon fibers) coated with 400Å of Al on 800Å of Cr after retrieval from LDEF.

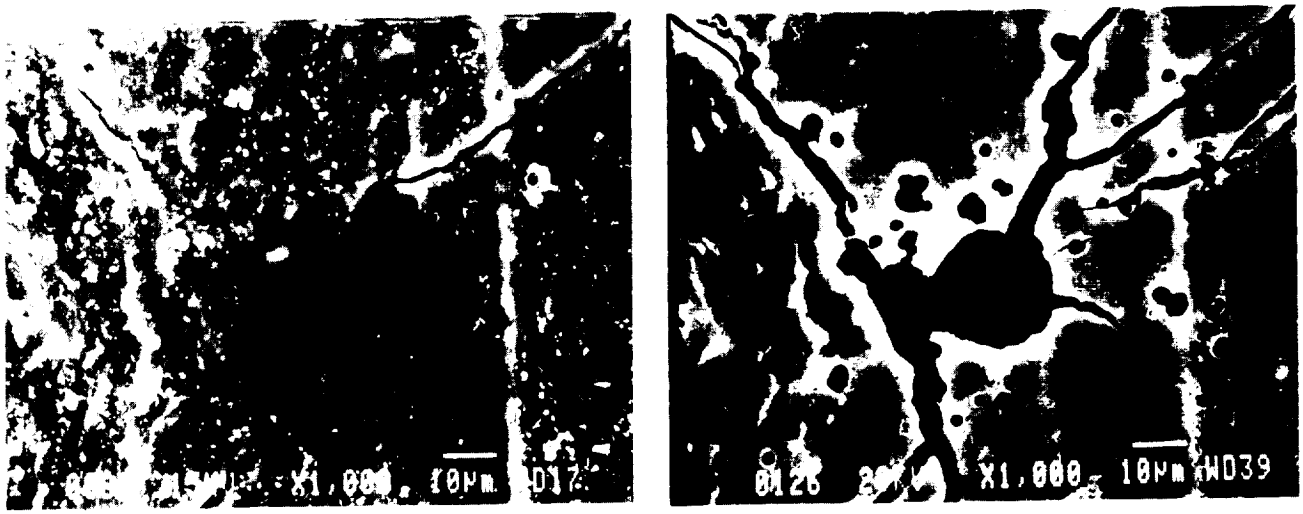

8a. With Al/Cr film.

8b. Al/Cr film removed.

Figure 8. Scanning electron micrographs prior to and after removal of protective coating.

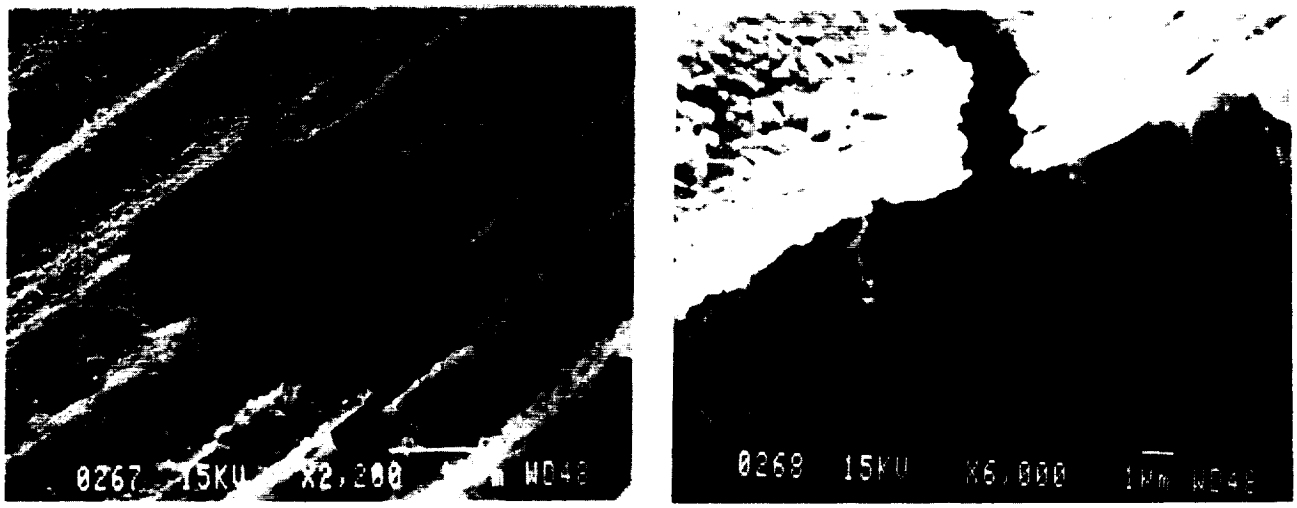

9a. Lower magnification.

9b. Higher magnification.

Figure 9. Scanning electron micrograph of coated graphite epoxy composite showing crack undercut cavity profile imaged through a large pin window undercut defect.

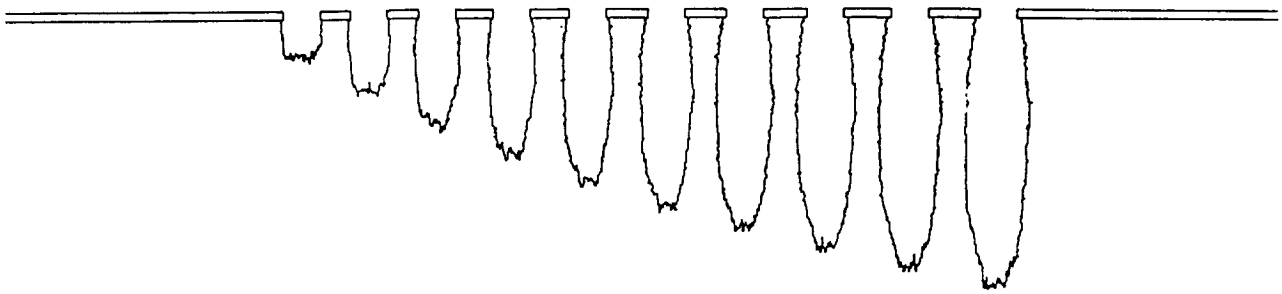

Figure 10. Monte Carlo computational model predicted undercut cavity growth with fluence.

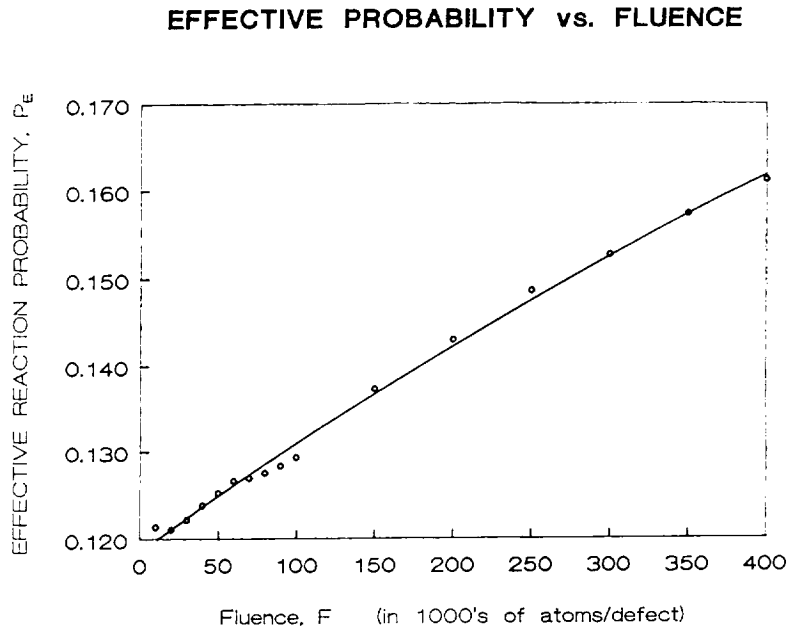

Figure 11. Monte Carlo model predicted effective reaction probability dependence in undercut cavities upon fluence for when 100 percent of the ram atoms thermally accommodate upon each impact, and the probability of reaction of thermally accommodated atoms is 0.0134.

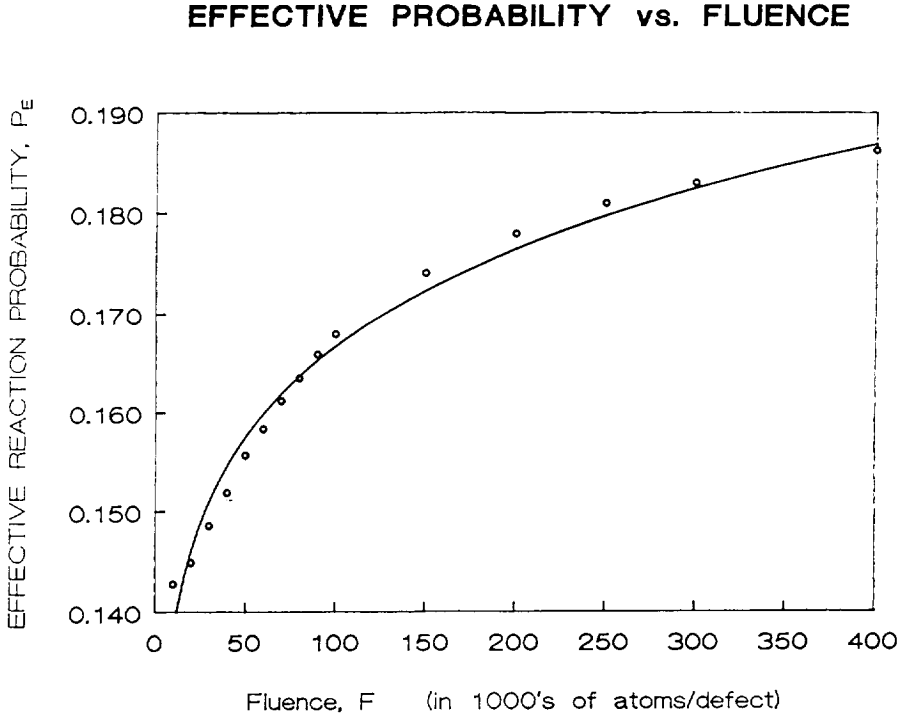

Figure 12. Monte Carlo model predicted effective reaction probability dependence in undercut cavities upon fluence for when 40 percent of the ram atoms thermally accommodate upon each impact, and the probability of reaction of thermally accommodated atoms is 7.7×10^{-6}.

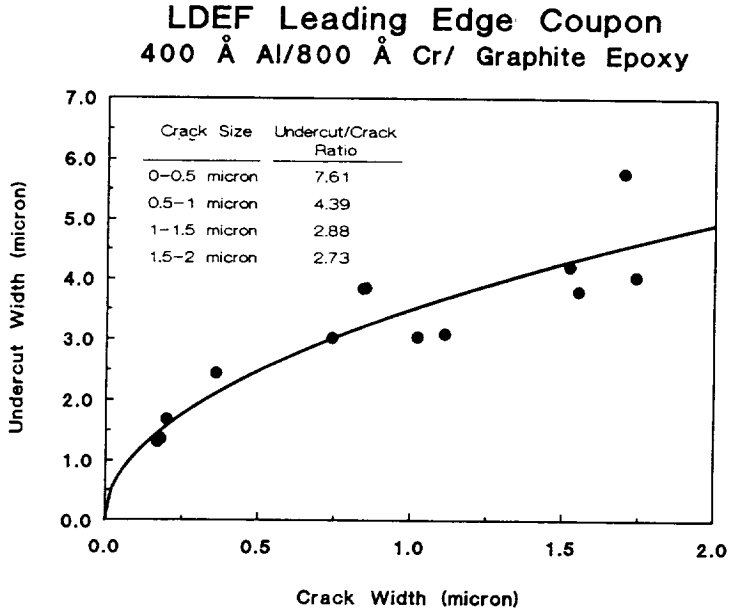

Figure 13. Dependence of undercut cavity width to protective coating crack widths for protected graphite epoxy composite retrieved from LDEF

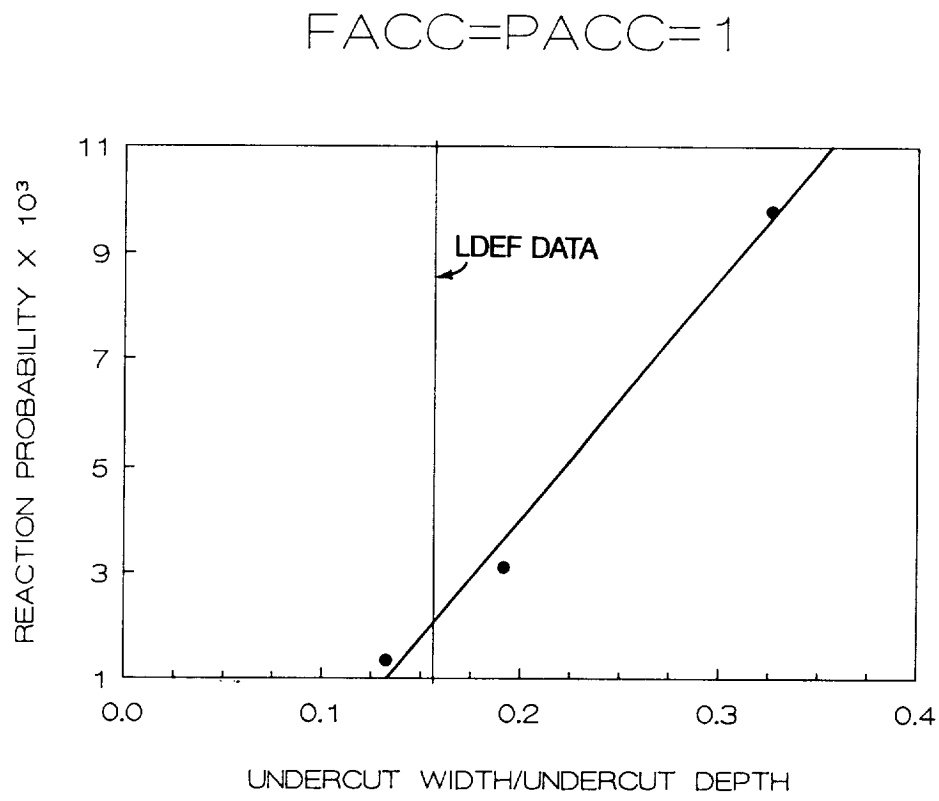

Figure 14. Monte Carlo model predicted undercut cavity width-to-depth ratio dependence upon thermally accommodated atomic oxygen reaction probability assuming 100 percent of ram atomic oxygen atoms thermally accommodate upon impact.

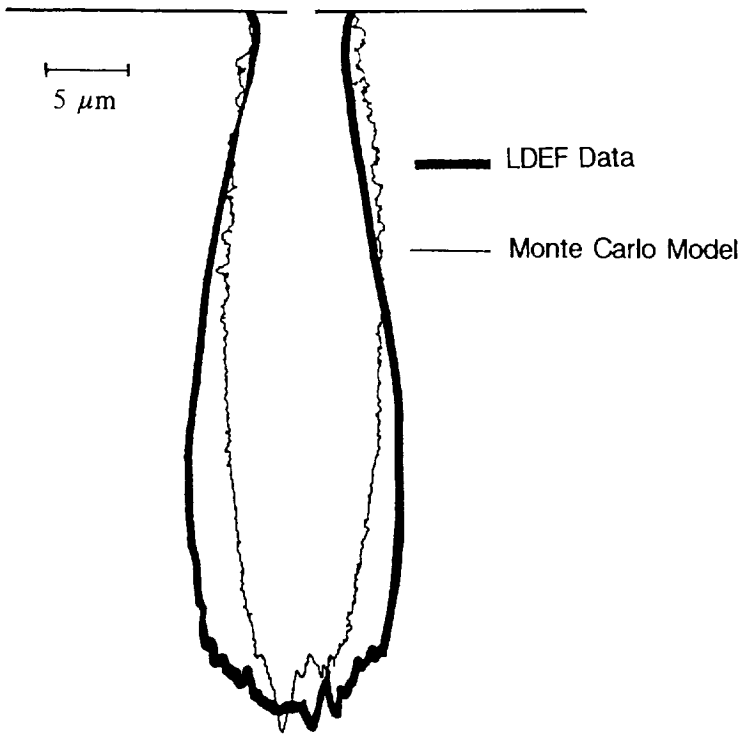

Figure 15. Comparison of an experimentally observed graphite epoxy composite undercut cavity with a Monte Carlo model predicted undercut cavity, assuming 100 percent of the ram atomic oxygen atoms thermally accommodate upon impact, and a thermally accommodated atomic oxygen reaction probability of 0.00211.

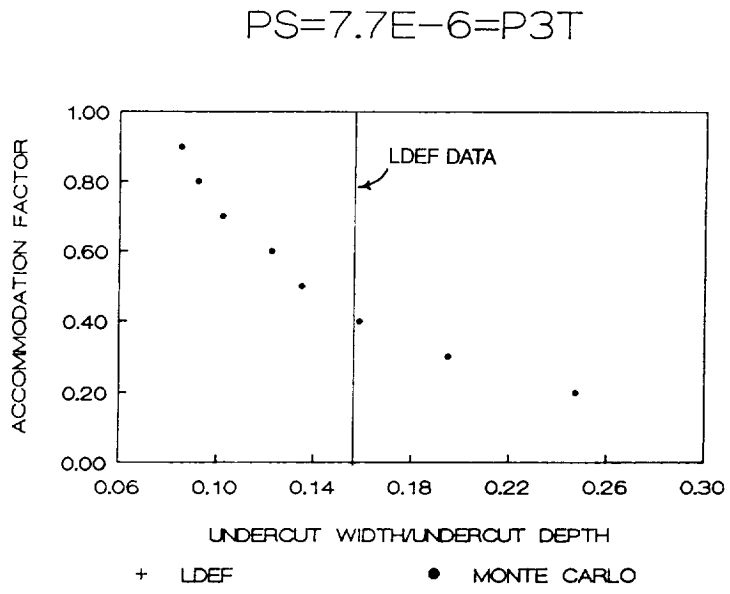

Figure 16. Monte Carlo model predicted undercut cavity width-to-depth ratio dependence upon fraction of ram energy oxygen atoms which thermally accommodate upon impact.

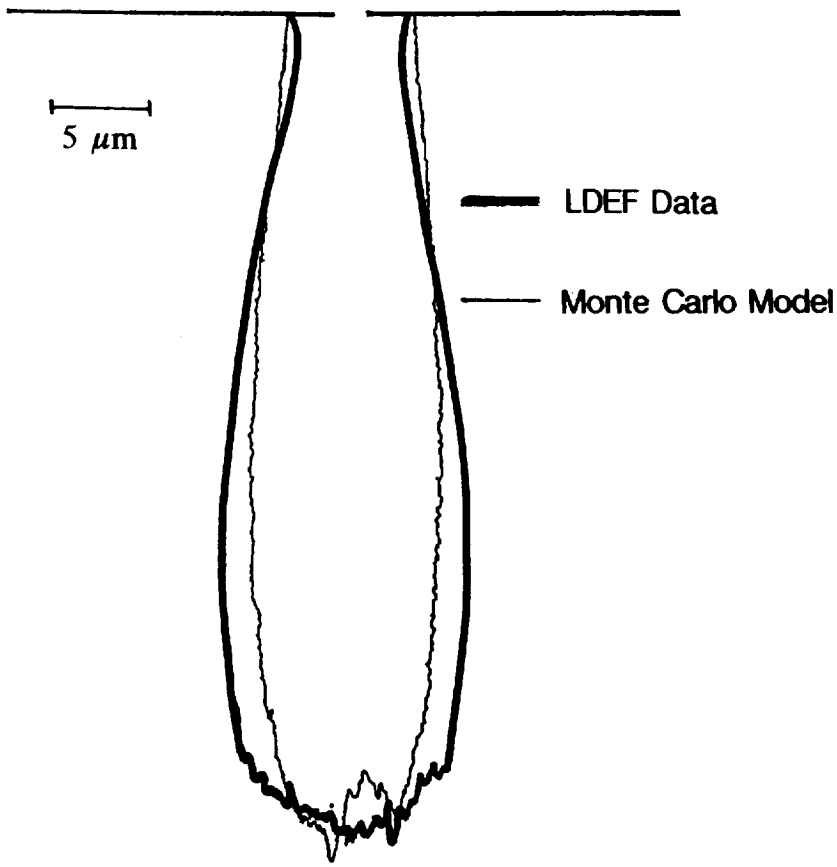

Figure 17. Comparison of an experimentally observed graphite epoxy composite undercut cavity with a Monte Carlo model predicted undercut cavity, assuming 40 percent of the ram atomic oxygen atoms thermally accommodate upon impact, and a thermally accommodated atomic oxygen reaction probability of 7.7×10^{-6}.

FLUORESCENCE OBSERVATIONS OF LDEF EXPOSED MATERIALS AS AN INDICATOR OF INDUCED MATERIAL REACTIONS

Roger C. Linton, Dr. Ann F. Whitaker, and Rachel R. Kamenetzky
NASA George C. Marshall Space Flight Center
Marshall Space Flight Center, AL 35812

INTRODUCTION

Observations and measurements of induced changes in the fluorescent emission of materials exposed to the space environment on the Long Duration Exposure Facility (LDEF) have revealed systematic patterns of material-dependent behavior. These results have been supplemented by inspection of similar materials exposed on previous space shuttle missions and in laboratory testing. The space environmental factors affecting the fluorescence of exposed materials have been found to include (but are not necessarily limited to) solar ultraviolet (UV) radiation, atomic oxygen (AO), thermal vacuum exposure, and synergistic combinations of these factors. Observed changes in material fluorescent behavior include stimulation, quenching, and spectral band shifts of emission. For example, the intrinsic yellow fluorescence of zinc oxide pigmented thermal control coatings undergoes quenching as a result of exposure, while visible coloration is stimulated in the fluorescent emission of several polyurethane coating materials. The changes in fluorescent behavior of these materials are shown to be a revealing indicator of induced material reactions as a result of space environmental exposure.

BACKGROUND

Light emission processes excluding thermal and electrical excitation are generally referred to as luminescence. Photoluminescence is further defined as UV radiation-stimulated light emission from chemical compounds. Fluorescence, as usually defined and as used in this paper, is then photoluminescence distinguished by the lifetime of excited states (usually on the order of 10 nanoseconds). Quenching usually refers to the deactivation of a molecule from an excited electronic state without the emission of a photon. Suppression of emission by absorption of another compound in the excited material (the "inner filter effect"), though not strictly "quenching," has the same effect (ref. 1). In this paper, "quenching" refers to the decreased fluorescent emission of materials as a result of exposure.

Most of the observations and measurements of fluorescence in the materials of interest were made with flight specimens from two LDEF experiments. These two experiments were A0171 (Solar Array Materials LDEF Experiment) and A0034 (Atomic Oxygen Stimulated Outgassing). Experiment A0171 was mounted on row 8 of the LDEF, oriented 38° from the leading edge RAM velocity vector (ref. 2). This passive full-tray experiment included six plates of solar array and solar concentrator component elements and candidate materials, including thermal control coatings, protective coatings, composites, metals, and polymeric materials (Figure 1). Experiment A0171 materials were exposed to an AO fluence of 6.93E21 atoms/cm^2 and approximately 10,000 equivalent Sun hours (esh) of solar radiation. Experiment A0034 included two separate modules of thermal control coatings and collector mirrors, one mounted on the leading edge (row 9) and one mounted on

the trailing edge (row 3). The coatings were housed at the base of aperture-limited compartments in the modules with adjacent witness mirrors to provide an assessment of the role of AO in the outgassing of thermal control coatings (ref. 3). In the compartmentalized design of experiment A0034, coatings that were exposed to the combined space environment under open apertures were duplicated for exposure under sealed ("covered") apertures and apertures sealed with UV-grade optical windows (Figure 2). Thermal control coatings in the modules of experiment A0034 were exposed to an AO fluence of 8.72E21 atoms/cm^2 on the leading edge and 1.32E17 atoms/cm^2 on the trailing edge. As a result of the aperture limited exposure of the coatings on the leading and the trailing edges, the exposure to solar radiation was considerably limited and is estimated to be less than 2,000 esh.

Since the 5.8-year life in low-Earth orbit (LEO) of the LDEF mission exceeded all previous space exposure doses for retrieved material specimens, it was considered relevant to review the fluorescent behavior of similar materials from shorter space missions. For this purpose, stored specimens of materials from AO experiments flown on STS 5, 8, and 17 (41-G) (references 4,5) were reexamined under black light illumination and the spectral fluorescence measured. Materials of the STS-5 AO experiment were exposed to an estimated fluence of 1.0E20 atoms/cm^2, while materials of the other two experiments accumulated fluences of 3.5E20 and 3.0E20 atoms/cm^2, respectively. The exposure to solar UV radiation during these relatively short duration missions (nominal seven days) was inherently limited. The comparison of induced fluorescence behavior in material specimens of these early shuttle flights to LDEF mission results is constrained by the unknown changes induced by years of laboratory environment storage; however, recent results from laboratory testing and more recent flight experiments (STS-46) indicate that the general nature of these results are valid for comparison. Other observations and measurements of some of the materials to be discussed in this paper have been previously published based on materials exposed in LDEF experiments S0069 and AO114 (ref. 6).

Fluorescence in the materials to be discussed is readily visible with conventional black-light illumination. These types of observations are useful indicators of induced changes in emission coloration as a result of exposure, and the observations generally confirm and even supplement the more detailed information obtainable from instrumented spectral fluorescence measurements. Fluorescence observations reported in this paper were obtained using both "long wave" and "short wave" illumination sources. The "long wave" source is a Dart Products B100A "Blak-Ray," providing approximately 7 mW/cm^2 irradiance at 15 cm, at a peak wavelength of 365 nm (320 to 380 nm). This filtered mercury emission source produces bright, rich colors in the NIST yellow and blue fluorescence standards (SRM 1931) stimulated by wavelengths in excess of 340 nm, while producing no visible color in the green standard (excitation wavelength 280 nm) and only a very dim glow in the orange (235 nm excitation). All four of the NIST standards fluoresced brightly under "short wave" excitation, using a Spectrolin B-14F 15 W lamp with 1,100 mW/cm^2 irradiance at 30 cm (peak wavelength 254 nm). For purposes of comparison to the detailed spectral fluorescence data to be discussed, a summary of the visible observations with these black light sources is provided in Table 1.

Measurements of fluorescence in the materials of interest were obtained using an SLM Aminco SPF-500C dual monochromator spectrofluorometer (see Table 2 for specification). Narrow-band filters at the exit slit of the excitation source and excitation wavelength-absorbing glass at the entrance aperture of the emission port were used to exclude extraneous light. For most of the materials examined to date, a narrow-band excitation of 260-nm wavelength was used. The results indicate a (nearly invisible) UV band of fluorescent emission for most of the materials and, for many of these materials, one or more bands of visible emission. These results are summarized in tabular form for most of the materials discussed in this paper in Table 3. It is necessary to state that the "assignment" of a peak wavelength to fluorescent bands of often very broad wavelength width is a

highly speculative endeavor and is only attempted here to provide a measure of comparison for different environmental exposures and materials. The spectral fluorescence curves presented in this paper include the results of "short wave" black light observations for comparison.

RESULTS

Changes in material fluorescence as a result of space environmental exposure were revealed as one or more of the following effects:

1. Quenching of emission

2. Stimulated emission (new or altered color)

3. Emission wavelength shift

4. Enriched emission (same color).

Induced quenching of the UV and visible fluorescent emission bands of S13G-LO paint (Figure 3) from LDEF experiment A0171 is characteristic of all of the investigated zinc-oxide pigmented thermal control coatings (S13G, S13G-LO, Z93, and NS43C). The level of quenching was found to be proportional to the degree of exposure to the space environment. Fluorescent quenching of Z93 (Figure 4) resulted from exposure on the leading edge of the LDEF, with relatively high levels of AO and solar UV radiation, and from exposure on the trailing edge, with a similar level of UV irradiance and orders of magnitude less AO (the small feature of the fluorescence curves for Z93, peaked at 780 nm, is considered to be third-order reflected source light). Exposure of these coatings under sealed UV-grade quartz windows on the LDEF modules resulted in similar quenching, though diminished in magnitude. Further testing and analysis is required to understand the apparent quenching of the Z93 coating exposed under a metal cover ("closed") during flight (Figure 5). Experiment A0034 coatings exposed in this manner experienced the flight thermal vacuum environment in the absence of AO and UV radiation. Quenching of a similar nature has been found for S13G-LO coatings exposed on limited duration space shuttle missions (Figure 6). For these shuttle missions, the level of solar UV irradiation is estimated to have been less than 100 ESH. Low levels (400 esh or less) of laboratory UV irradiation of these type coatings have not resulted in detectable quenching of fluorescence. In other laboratory testing, AO exposure alone resulted in quenching of the UV and visible fluorescent emission of the white conductive zinc-oxide pigmented paint NS43C (Figure 7). This exposure was done in the MSFC Drift-Tube system, providing approximately 1E21 atoms/cm^2 of thermal energy AO at ambient temperature in the absence of UV radiation. The emission peaked at 780 nm in Figure 7 is third-order reflected source light.

Stimulated emission can be clearly seen (Figure 8) in the response to exposure of bulk RTV 511 resin material from A0171, in addition to quenching of the intrinsic UV fluorescence band and alteration of the intrinsic "red" emission. Direct ("open") exposure of Chemglaze A276™ on the leading edge of the LDEF (experiment A0034) resulted in apparent total erosion of the polyurethane binder from the titanium dioxide pigment and effectively total quenching of fluorescence (Figure 9). Adjacent A276™ material exposed to UV radiation under a sealed quartz window was visibly darkened, resulting in a stimulated yellow/orange fluorescent glow under black light. Laboratory testing using near UV sources (mercury-xenon arc lamps) at one "UV Sun" intensity level showed that this stimulated fluorescence results from less than 100 esh irradiance. A final example of laboratory exposed material (Figure 10) is provided summarizing the effects of thermal energy AO, near-UV

irradiation, and material temperature on the fluorescence of a candidate silicone seal material S383. The stimulated emission following these various types of exposure is visible as a yellowish glow under black light illumination. Testing further indicated that exposure to AO alone did not perceptibly change the intrinsic fluorescence of this material. Exposure to UV radiation, whether alone or following AO exposure, was done in vacuum to a level of approximately 1,700 esh. These tests revealed a visible fluorescent glow under black light following only a very few hours of UV irradiation, similar in effect to testing results with the Chemglaze polyurethane coatings; comparison of the fluorescence spectra of control S383 to control Chemglaze Z306™ (Figure 19) indicates similar structure at the short and long wavelength ends of the spectra. From Figure 10, it can be seen that the effect of elevated temperature on materials exposed sequentially to AO and UV radiation was in reducing the intensity of stimulated fluorescence compared to ambient temperature test sequencing. This is presumably a result of enhanced reactivity of the S383 to AO at the elevated temperature. In contrast, elevated temperature exposure to UV radiation alone of the silicone S383 material resulted in enhanced stimulation of fluorescent glow (Figure 10).

A definitive example of an emission wavelength shift is provided in Figure 11 for A0171 PEEK resin material. An emission wavelength shift is considered to be distinguished from stimulated emission by the degree of stimulation of significantly new or altered coloration in the black light illuminated glow.

Enriched emission as a result of space exposure on PMR neat resin (Figure 12) from A0171 is the rarest effect revealed in the examined materials. This effect in the PMR neat resin is accompanied by quenching of emission in the UV bands.

DISCUSSION

Measurements of spectral fluorescence distributions in solid materials are subject to variability resulting from ambient laboratory changes in temperature and humidity. These effects were found most pronounced in the zinc oxide-pigmented thermal control coating, as the differences in the measurements on the same flight sample (S13G-LO) on two different dates show (Figure 12). Significant differences are found in the fluorescence distributions of another S13G-LO flight sample when artificially heated compared to ambient environment measurements (Figure 14). Differences were also found for samples stored in desiccators prior to measurement (Figure 15). Measurements of the fluorescence distributions of materials investigated for this paper were all completed, for each set of samples including controls, in a timely sequence equalizing the laboratory environment following desiccator conditioning. In addition, frequent reference to measurements of the NIST fluorescence standards provided confidence in the wavelengths of identified spectral features and provided a means of normalizing intensity levels.

Two exceptions were found to the general classification of environmentally induced fluorescent behavior based on material commonalty. These exceptions are in specimens of YB-71 (Illinois Institute of Technology Research Institute's zinc orthotitanate) and Lord Chemical's Chemglaze Z306™.

Visible observations under black-light illumination of fluorescent emission from unexposed or exposed YB-71 coatings reveal only varying shades of reddish-purple coloration. Two distinct bands of emission on opposite ends of the visible spectrum are revealed in fluorescence measurements of unexposed YB-71 coatings (Figures 16 and 17). In general agreement with the observations, for LDEF leading edge A0034 coatings of YB-71, the effects of "open" exposure to the combined space

environment are complex (Figure 16); the principal emission band at approximately 420 nm is decreased in intensity with (poorly resolved) evidence of associated stimulated emission bands. The reddish emission (peaked at 710 nm) is relatively unchanged as a result of the exposure. LDEF trailing edge exposure (Figure 17), with four orders of magnitude less AO for "open" samples, also resulted in decreased emission (quenching) of the 420-nm band, although the "new" bands of resolved emission are significantly different. Exposure of YB-71 under a UV-grade quartz window ("UV only") on the trailing edge resulted in a more intense band of spectrally shifted emission than "open" exposure that appears similar in resolved structure. Flight exposure of YB-71 under a metal cover ("vacuum only") also resulted in quenching and a somewhat different resolved emission band pattern.

Exposure-induced changes in fluorescence of Chemglaze Z306™ coatings were found to be somewhat material-batch dependent, although laboratory testing as well as flight results does generally result in stimulated emission under black-light illumination. The effects of "open" exposure on LDEF experiment A0034 (leading edge) are apparently slightly spectrally shifted, enhanced emission intensity of all three of the intrinsic emission bands. Exposure restricted to solar UV radiation resulted in a new single broadband of stimulated emission, in agreement with black light observations. In contrast, exposure on STS-5 and STS-8 resulted in wavelength band dependent variations in quenching and stimulated, spectrally shifted emission (Figures 18 and 19). These data also indicate differently resolved patterns of emission in the unexposed control material. These differences in the control coatings of Z306™ are visibly apparent under black light illumination. Despite these differences in the fluorescence of flight exposed Z306™ coatings, there is a systematic pattern of decreasing emission wavelength correlated with increasing integrated flux (fluence) of AO (Table 4), based on the apparent middle band of emission. These results do not correlate with accumulated solar UV radiation exposure.

Extended exposure of organic materials to the intense sources required for spectrofluorometric investigations can lead to sample surface photodecomposition (ref. 1). This effect was most pronounced with the polyurethane binder coatings exposed to the spectrally dispersed exit beam of the SLM SPF-500C excitation monochromator. The photodecomposition following exposure was readily observed visually under black light illumination as a distinct image of the emission monochromator exit beam. Laboratory procedures optimizing the minimum beam intensity and minimizing the time allotted for measuring exposure eliminated detectable photodecomposition.

Optical measurements of fluorescent materials using conventional integrating spheres for hemispherical reflectance detection are subject to error at UV wavelengths. The photomultiplier detector, usually operating with the highest gain sensitivity at UV wavelengths, cannot distinguish surface-reflected light from excited fluorescent emission. This effect can lead to the variable fluorescent emission in the exposed materials being misleadingly interpreted as variations in diffuse reflectance at UV wavelengths in integrating spheres. This proved particularly significant for thermal control coatings of intrinsically low diffuse reflectance for wavelengths less than 400 nanometers. The effect was verified by measurements of diffuse reflectance of visibly fluorescing coatings in a Gier Dunkel integrating sphere with the photomultiplier detector, at excitation wavelengths, alternately covered and uncovered by a transparent (UV opaque) filter. Though clearly a measurable effect, testing appears to indicate that the effect is minimal on solar absorptance values.

CONCLUSIONS

Materials exposed to the space environment demonstrated changes in light emission characteristics. The primary environmental factors responsible for the detected changes in fluorescence have been attributed to exposure to AO and UV radiation. The fluorescent properties of materials considered highly resistant to conventional optical degradation in the space environment, such as Z93 and YB-71 coatings, were altered in degree and nature as much as the other materials that are highly susceptible to conventional induced optical degradation. These effects on thermal control coatings and a variety of polymeric materials exposed on the LDEF were also found in similar materials exposed on much shorter duration space shuttle missions.

Fluorescence is a revealing indicator of induced material reactions as a result of space environmental exposure. Detected changes in fluorescence were revealed as quenching, stimulated emission, enhanced emission, and spectral shifts in emission. Comparison of effects found in materials exposed on the leading and trailing edges of the LDEF, on shorter duration space shuttle missions, and in laboratory testing indicate that thermal vacuum exposure, AO impingement, and UV radiation, acting individually or in combination, are the causative factors in altered fluorescence. The fluorescent properties of these materials are generally more sensitive to exposure than more conventional characterization techniques, whether revealed by visible observations under black light illumination or detailed spectrofluorometric analysis.

ACKNOWLEDGMENTS

The authors appreciate the helpful discussions with Dr. Charles Neely of Auburn University.

REFERENCES

1. Rendell, D.: "Fluorescence and Phosphorescence Spectroscopy." John Wiley & Sons, New York, NY, 1987.

2. Whitaker, A.F.: "Orbital Atomic Oxygen Effects on Thermal Control and Optical Materials—STS-8 Results." AIAA-85-0416, presented at the AIAA 23rd Aerospace Sciences Meeting, January 14–17, 1985, Reno, NV.

3. Whitaker, A.F., and Young, L.E.: "An Overview of the First Results on the Solar Array Materials Passive LDEF Experiment (SAMPLE), AO171." NASA Conference Publication 3134, Part 3, proceedings of First LDEF Post-Retrieval Symposium, June 2–8, 1991.

4. Linton, R.C., et al.: "LDEF Experiment AOO34: Atomic Oxygen Stimulated Outgassing." NASA Conference Publication 3134, Part 2, proceedings of First LDEF Post-Retrieval Symposium, June 2–8, 1991.

5. Zwiener, J.M., et al.: "Unusual Materials Effects Observed on the Thermal Control Surfaces Experiment (SOO69)," NASA Conference Publication 3134, Part 2, proceedings of First LDEF Post-Retrieval Symposium, June 2–8, 1991.

Table 1. Long wave and short wave black light visual observations.

Sample	Exposure	Color	L.W. UV	S.W. UV	Comments
STS-5 Z306	Control	Black	Dk. Brown	Mustard Brown	
	Exposed		Tan/Green	Yellow/Green	
STS-8 Z306	Control		Chocolate	Pea Green	
	Exposed		Lt. Pea Green	Lt'er Pea Green	
AO171-IV-44 Z306	Control		Chocolate	Pea Green	
	Exposed		Lt. Chocolate/Yellow	Brown	
AOO34 Z306	Control		Dk. Chocolate/Black	Pea Green	
	01-14 Window		Tan/Green	Brown	
	01-44 Open		Tan/Greater Green	Pea Green	
STS-5 S13GLO	Control	White	Bright Yellow	Bright Yellow	
	Exposed		Yellow	Paler Yellow	
AO171-IV-13 S13GLO	Control		Yellow	Bright Yellow	
	Exposed		Burnt Sienna/Brown	Burnt Sienna	Browned in exposed area
AOO34 S13GLO	Control		Yellow	Yellow	
	02-21 Open		Orange/Yellow	Orange/Yellow	
	02-15 Closed		Yellow	Brt. Yellow	
	02-12 Window		Yellow	Yellow	
	01-25 Open		Lt. Purple/Yellow	Lt. Purple/Yellow	
	01-11 Closed		Yellow	Yellow	
	01-12 Window		Yellow	Yellow	

Table 2. SLM Aminco SPF-500C spectrofluorometer specifications.

- Source: High Intensity 250W Xenon Arc Lamp
- Dual Monochromator, 200 to 900 nm
- Excitation Monochromator: 1200 line/mm holographic grating, maximized to 300 nm
- Emission Monochromator: Classically ruled 1200 line/mm grating, blazed at 500 nm
- Focal Length: 250 mm
- Aperture: f/4
- Resolution: 0.1nm
- Bandwidths: 0.1, 0.2, 0.5, 1, 2, 2.5, 4, 5, 7.5, 10, 20 nm
- Fluorescence Channel PMT: Hamamatsu R928P extended red response side window tube
- Reference Channel PMT: Hamamatsu R777 or equivalent side window PMT

Table 3. Selected fluorescence peaks.

Material	Peak (nm) ± (nm)	Peak (nm) ± (nm)	Peak (nm) ± (nm)	Peak (nm) ± (nm)
Z93	388 ± 1		512 ± 1	
S13G	385 ± 2		515 ± 2	
S13GLO - LE	384 ± 2		512 ± 2	
S13GLO - TE	382 ±1		526 ± 3	
NS43C	384 ±2		516 ± 2	
NS43C - AODTS Exposed	384 ± 1		523 ± 2	
A276	364 ± 4	414 ± 1	496 ± 2	
A276 UV Only			560 ± 2	
A276 AO + UV				
Z306 AOO34 Control	333 ± 2	446 ± 5		656 ± 2
Z306 AOO34 UV Only			579 ± 5	
Z306 AOO34 AO + UV	343 ± 2	449 ± 5		653 ± 3
Z306 STS 5 Control	337 ± 2	438 ± 5	538 ± 4	653 ± 3
Z306 STS 5 Exposed	341 ± 2		500 ± 17	
Z306 STS 8 Control	333 ± 2	446 ± 5		656 ± 2
Z306 STS 8 Exposed	336 ± 2	469 ± 5		
Z306 AO171 Control	333 ± 2	446 ± 5		654 ± 3
Z306 AO171 Exposed	339 ± 2	453 ± 5		651 ± 2
Z302 STS 5 Control	338 ±2	414 ± 5		663 ± 3
Z302 STS 5 Exposed	340 ± 2 Shoulder	488 ± 5		
Z302 STS 8 Control	339 ± 1	447 ± 4		662 ± 2
Z302 STS8 Exposed	339 ± 1	459 ± 2		662 ± 2
Z302 AO171 Unexp	337 ± 2	457 ± 2		656 ± 2
Z302 AO171 Exp	340 ± 2	495 ± 10 (Wide)		647 ± 5
Na Saly		419 ± 1		
S383 EOIM-3 Control	338 ± 2			663 ± 2
S383 EOIM-3 Exp.60-38		468 ± 5	588 ± 2	
Viton EOIM-3 Control		470 ± 15		
Viton EOIM-3 Exposed		455 ± 2		
AO171 PEEK Control		466 ± 5		
AO171 PEEK Exposed			512 ± 1	
AO171 PMR Neat Con	396 ± 3		515 ± 2	
AO171 PMR Neat Exp			512 ± 2	
AO171 RTV 511 Con	340 ± 3		526 ± 3	665 ± 3
AO171 RTV511 Exp			548 ± 3	

Table 4. AO exposure and wavelength shifts in exposed Z306™ fluorescence.

Spaceflight/Experiment	Peak λ (nm)*	AO Fluence (atoms/cm^2)
STS 5	516	9.99×10^{19}
STS 8	470	3.5×10^{20}
LDEF AO171, Row 8	452	6.93×10^{21}
LDEF AOO34, Row 9	439	8.72×10^{21}

*Estimated Peak Wavelength - Visible Emission

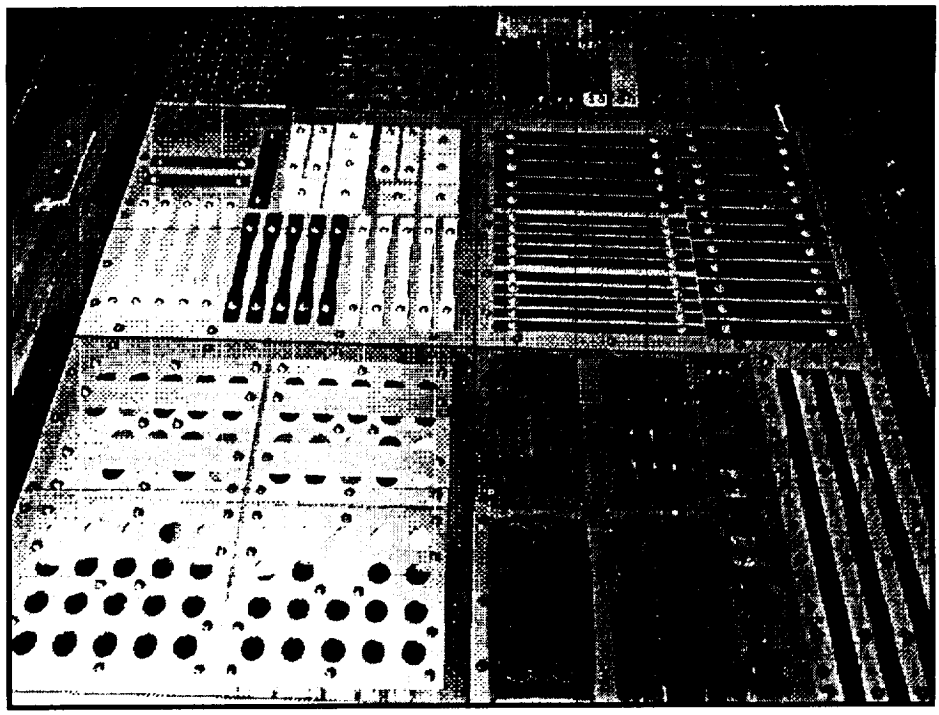

Figure 1. Solar array materials passive LDEF experiment AO171.

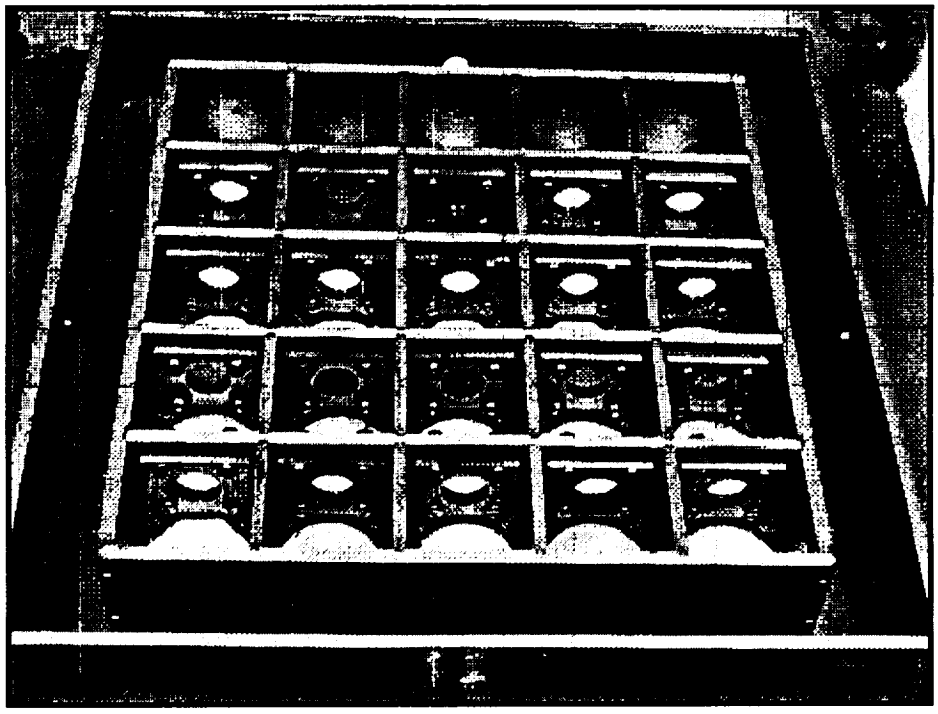

Figure 2. LDEF AO stimulated outgassing experiment AOO34.

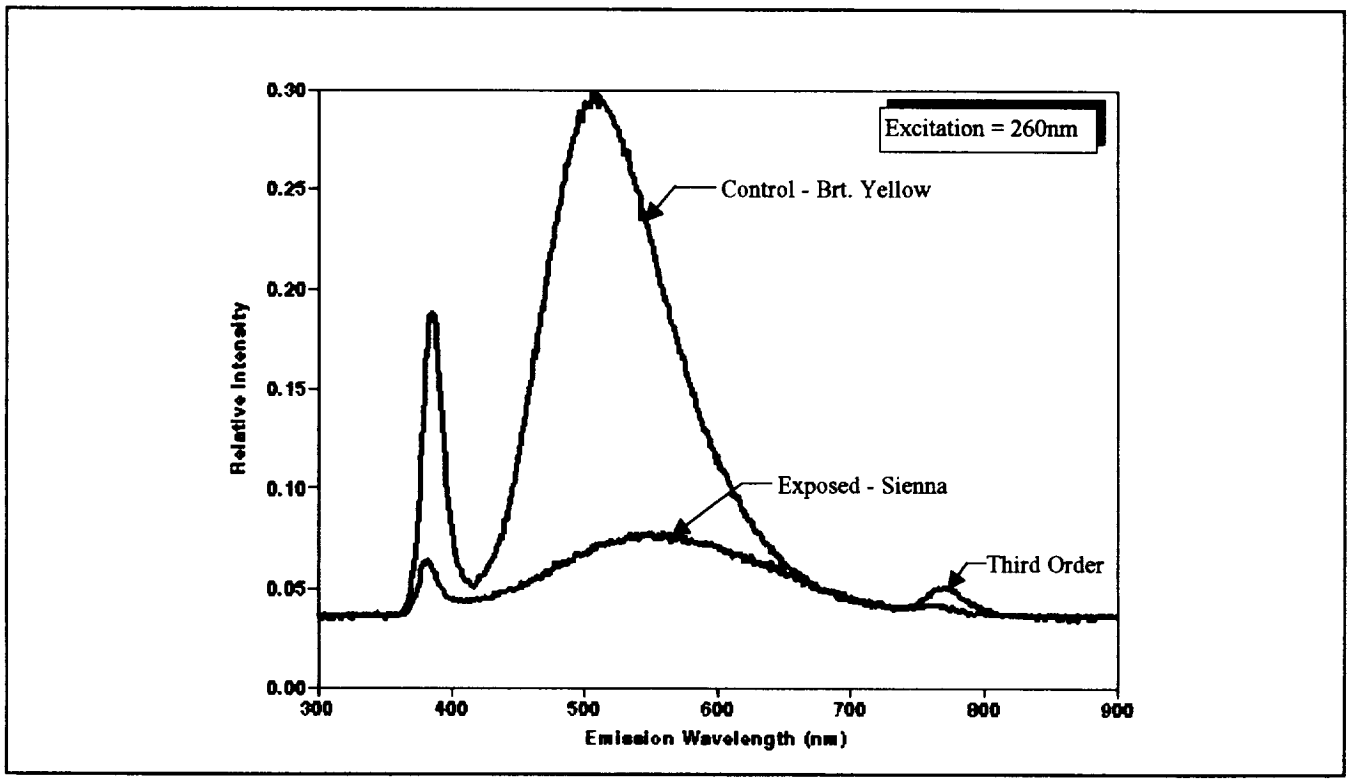

Figure 3. LDEF AO171 S13-GLO paint fluorescence curve.

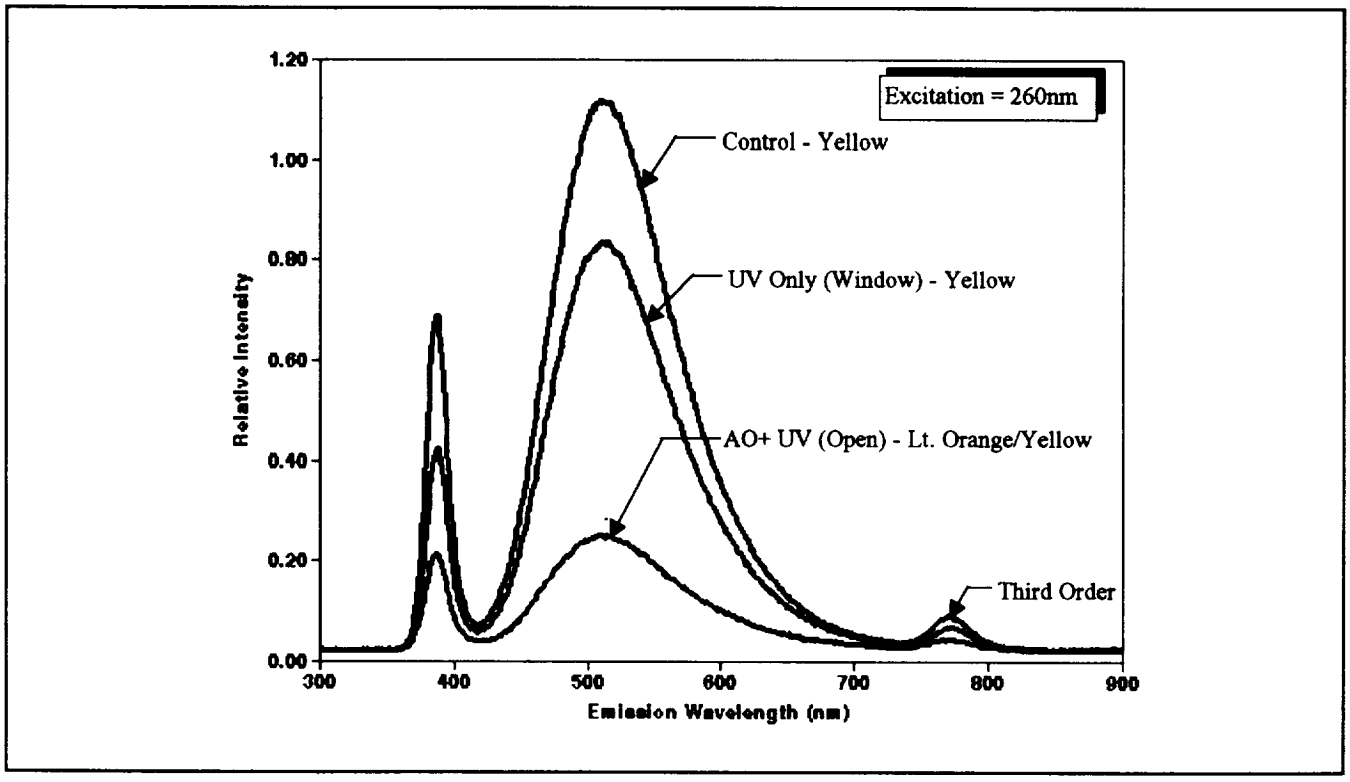

Figure 4. LDEF A0034 Z93 leading edge paints fluorescence curves.

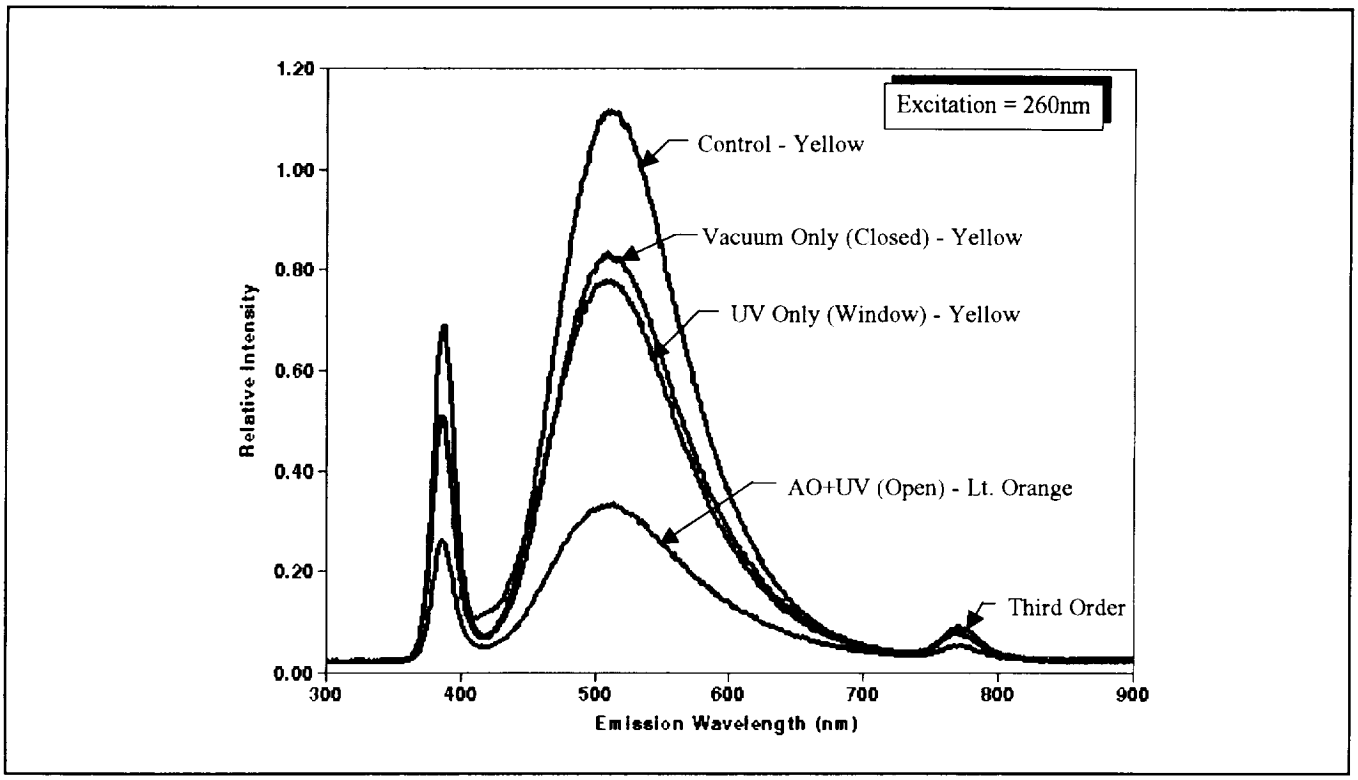

Figure 5. LDEF A0034 Z93 trailing edge paints fluorescence curves.

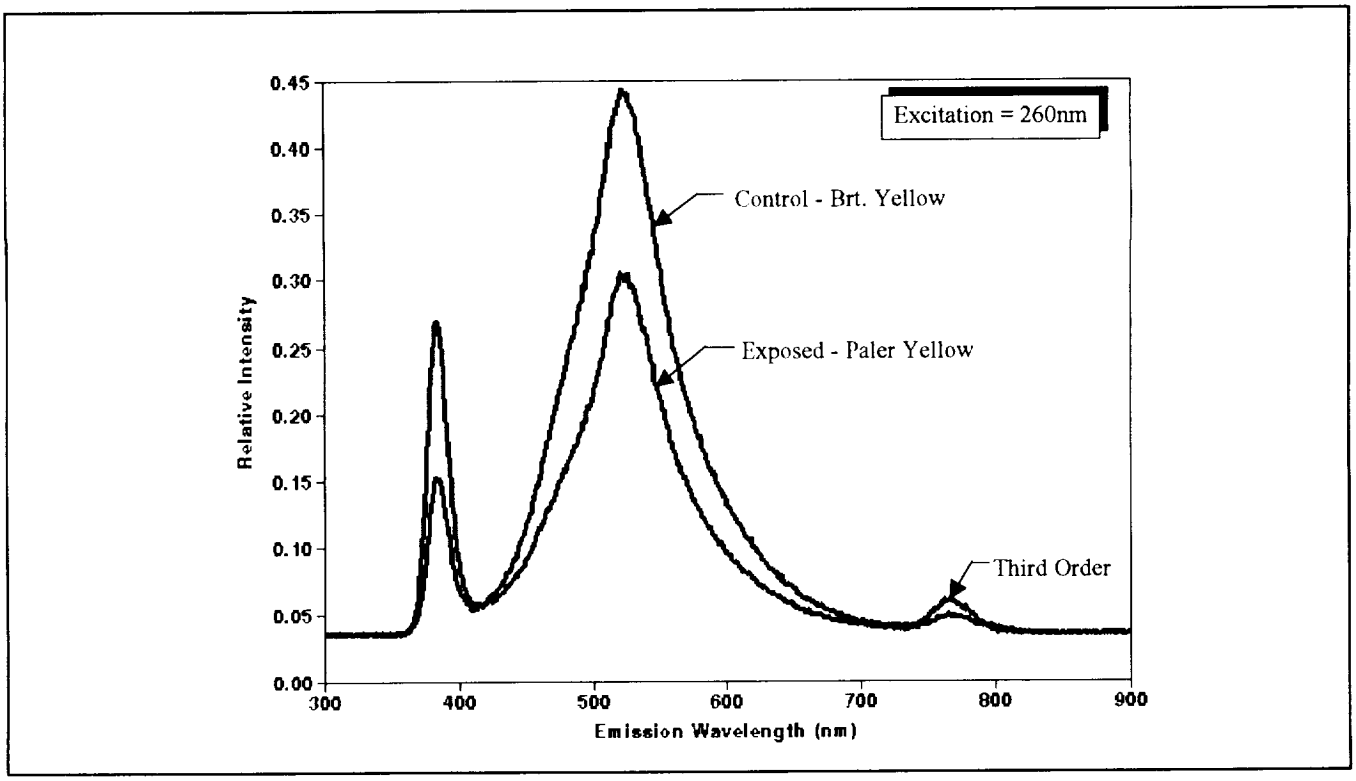

Figure 6. STS-5 S13-GLO paint fluorescence curve.

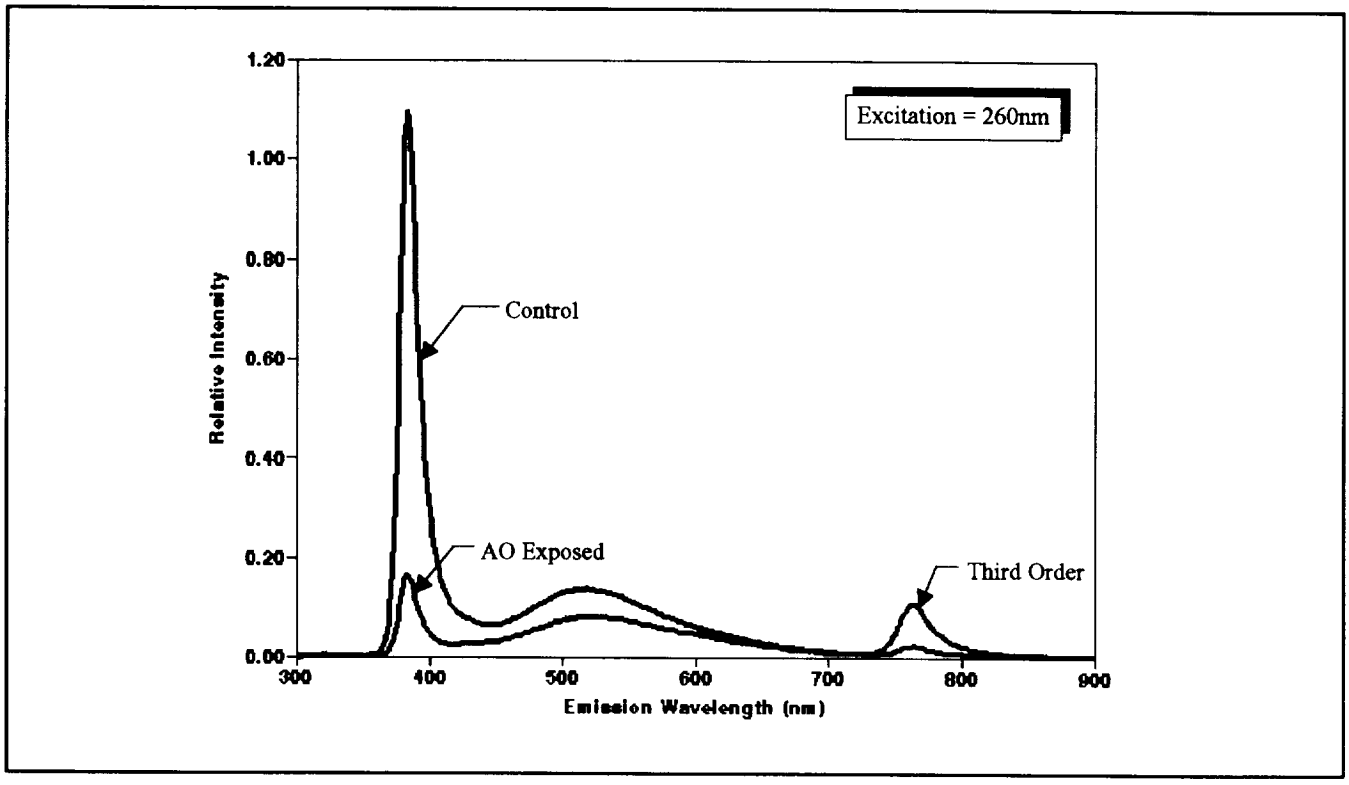

Figure 7. Fluorescence curve for NS43C paint exposed in the MSFC AODTS AO system.

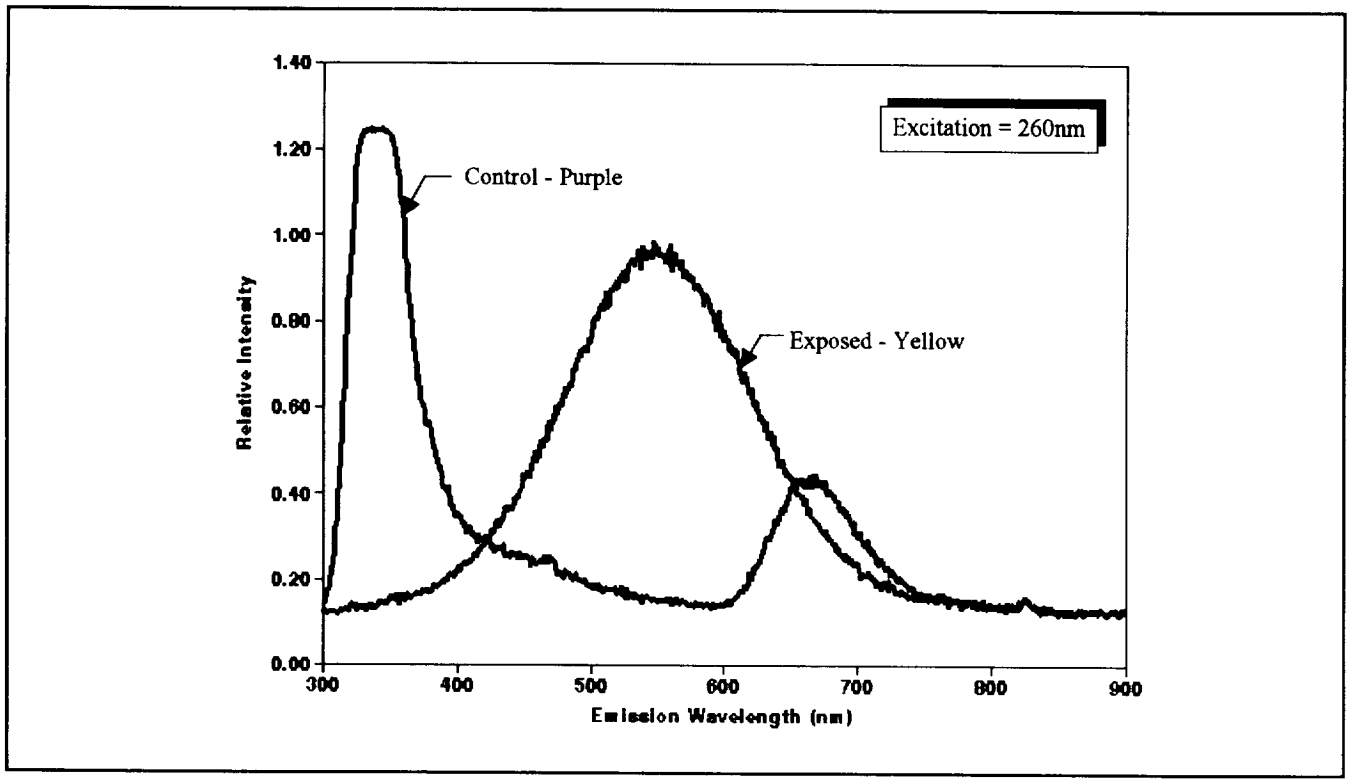

Figure 8. LDEF A0171 RTV 511 fluorescence curve.

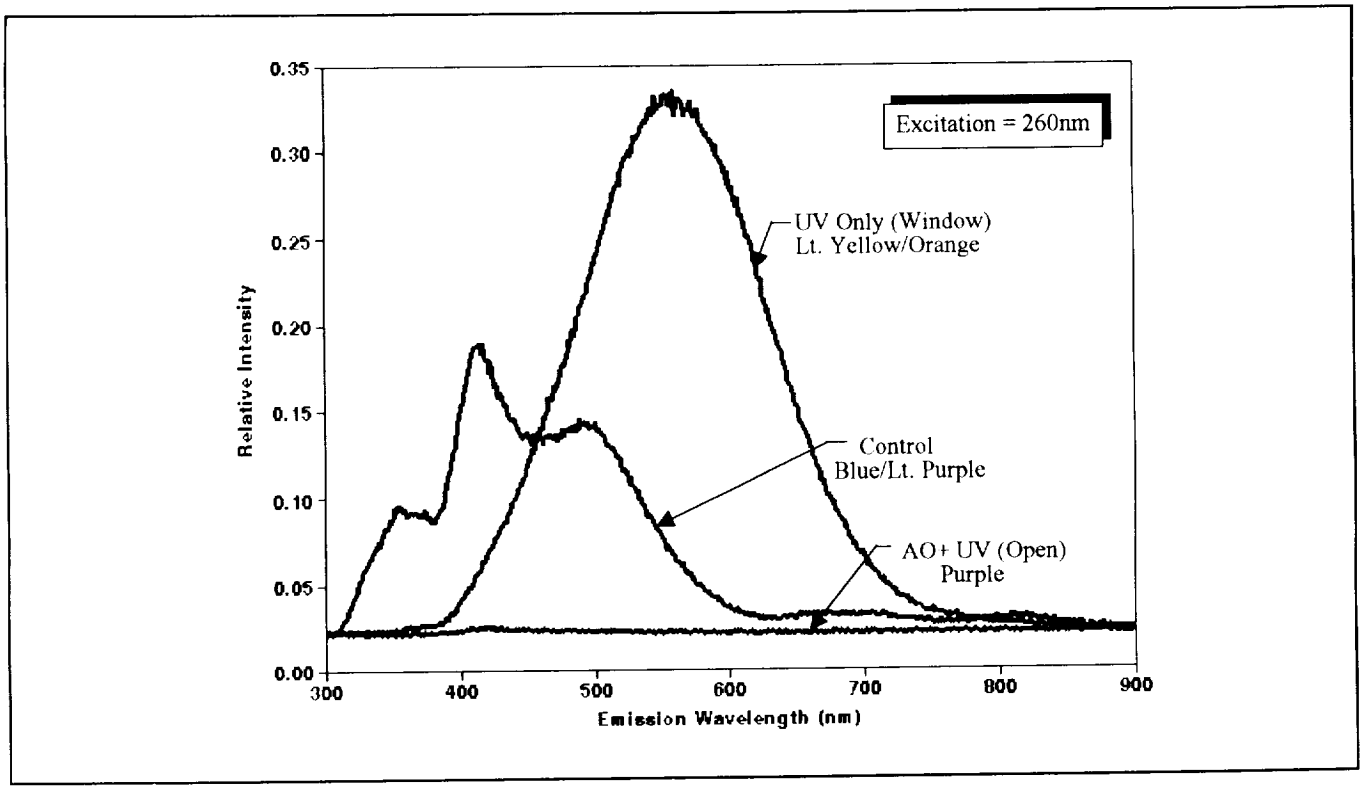

Figure 9. LDEF A0034 Chemglaze A276™ leading edge paint fluorescence curves.

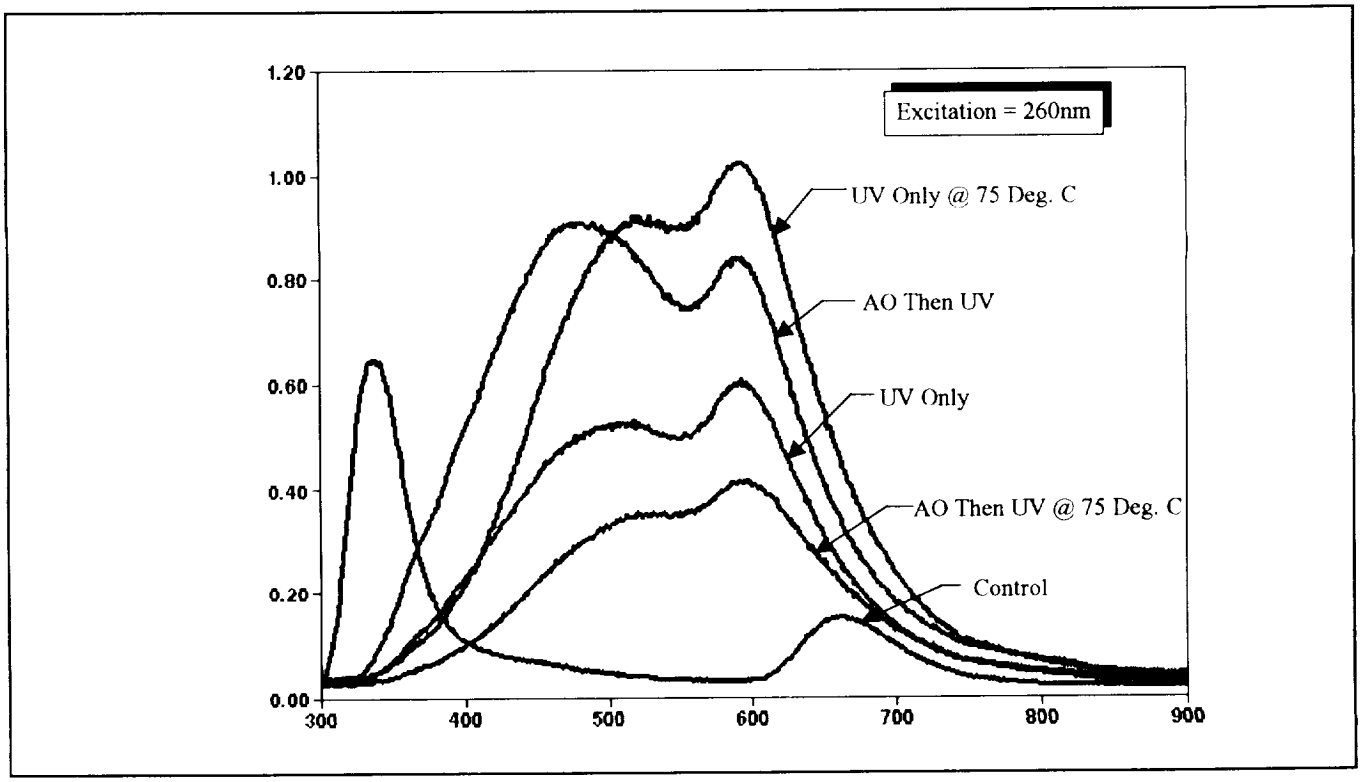

Figure 10. Fluorescence of laboratory AO and UV exposed S383 as a function of temperature.

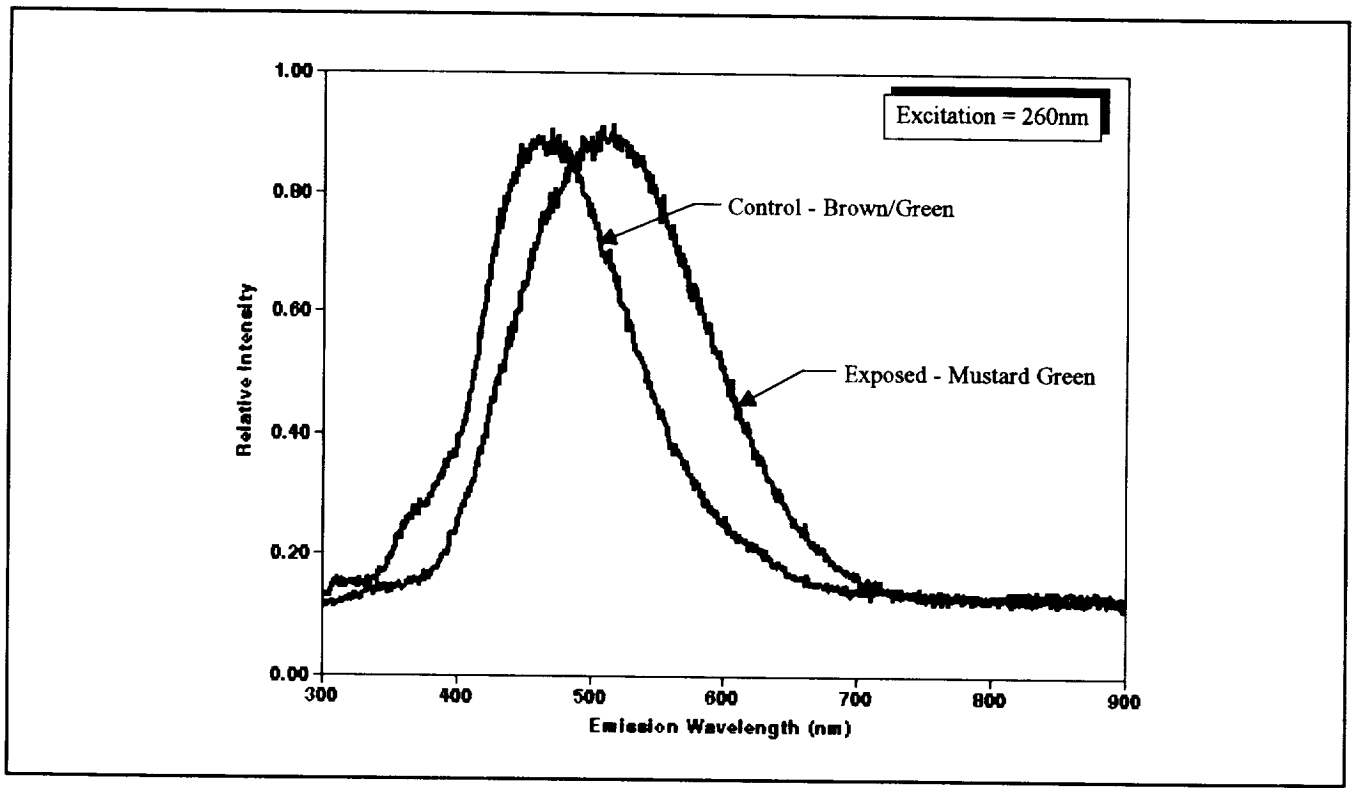

Figure 11. LDEF A0171 PEAK fluorescence curve.

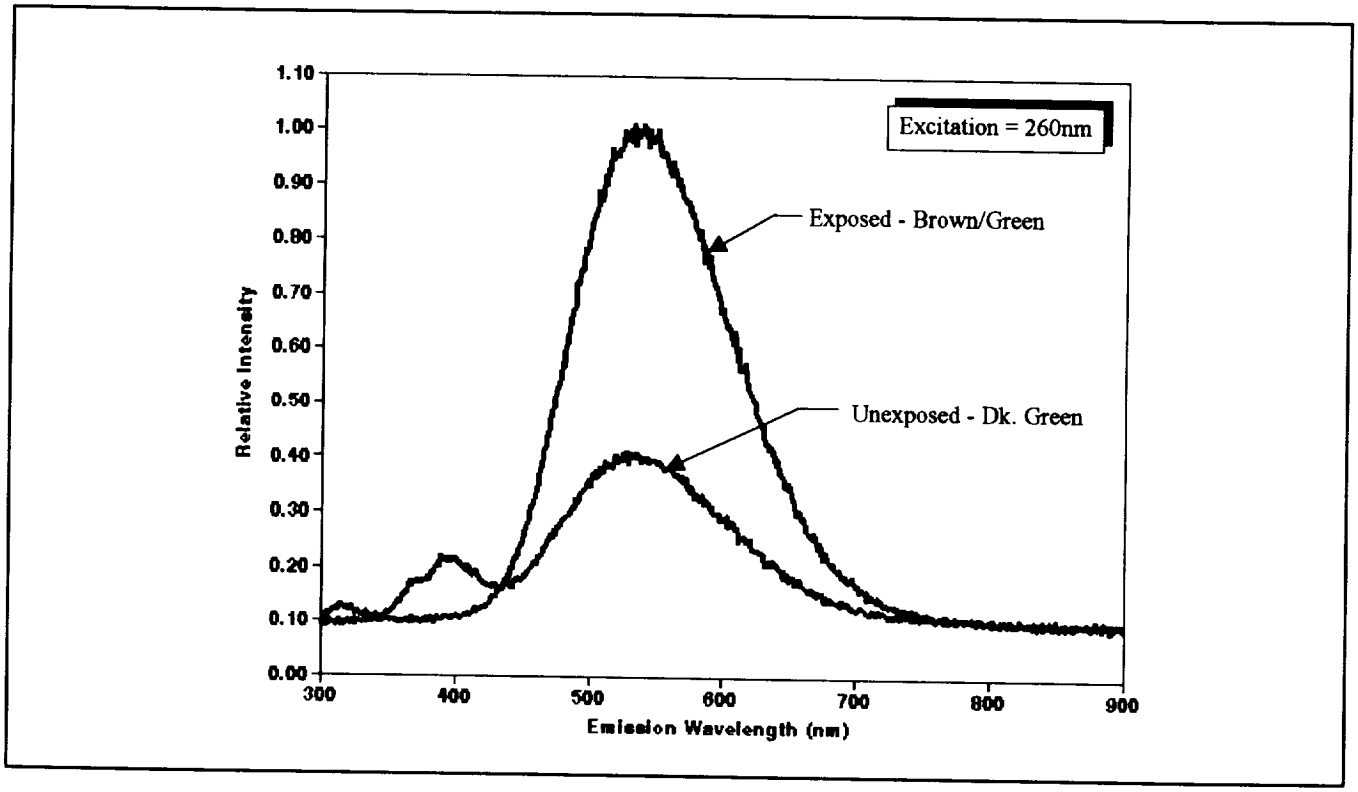

Figure 12. LDEF A0171 PMR neat resin fluorescence curve.

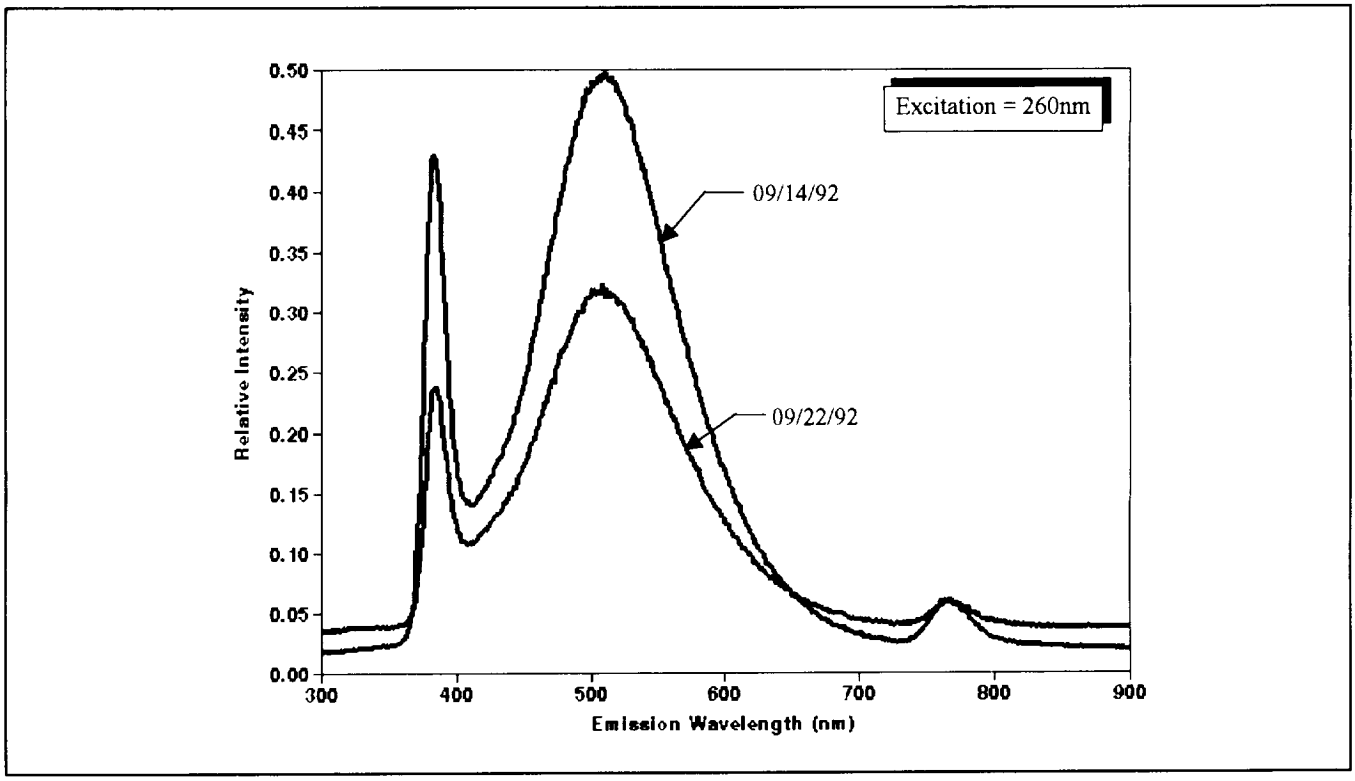

Figure 13. Fluorescence curves for A0034 S13-GLO measured on separate days in ambient laboratory conditions.

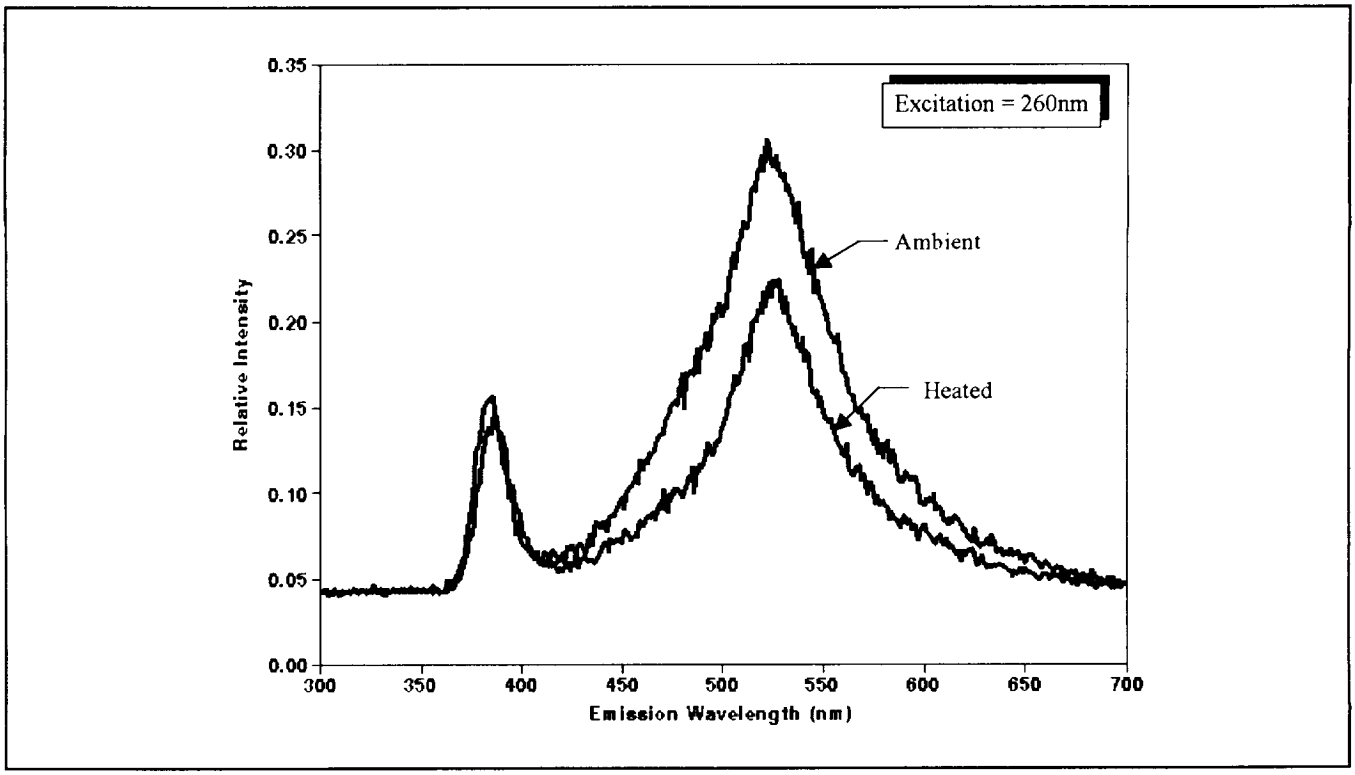

Figure 14. STS-5 exposed S13-GLO fluorescence curves as a function of temperature.

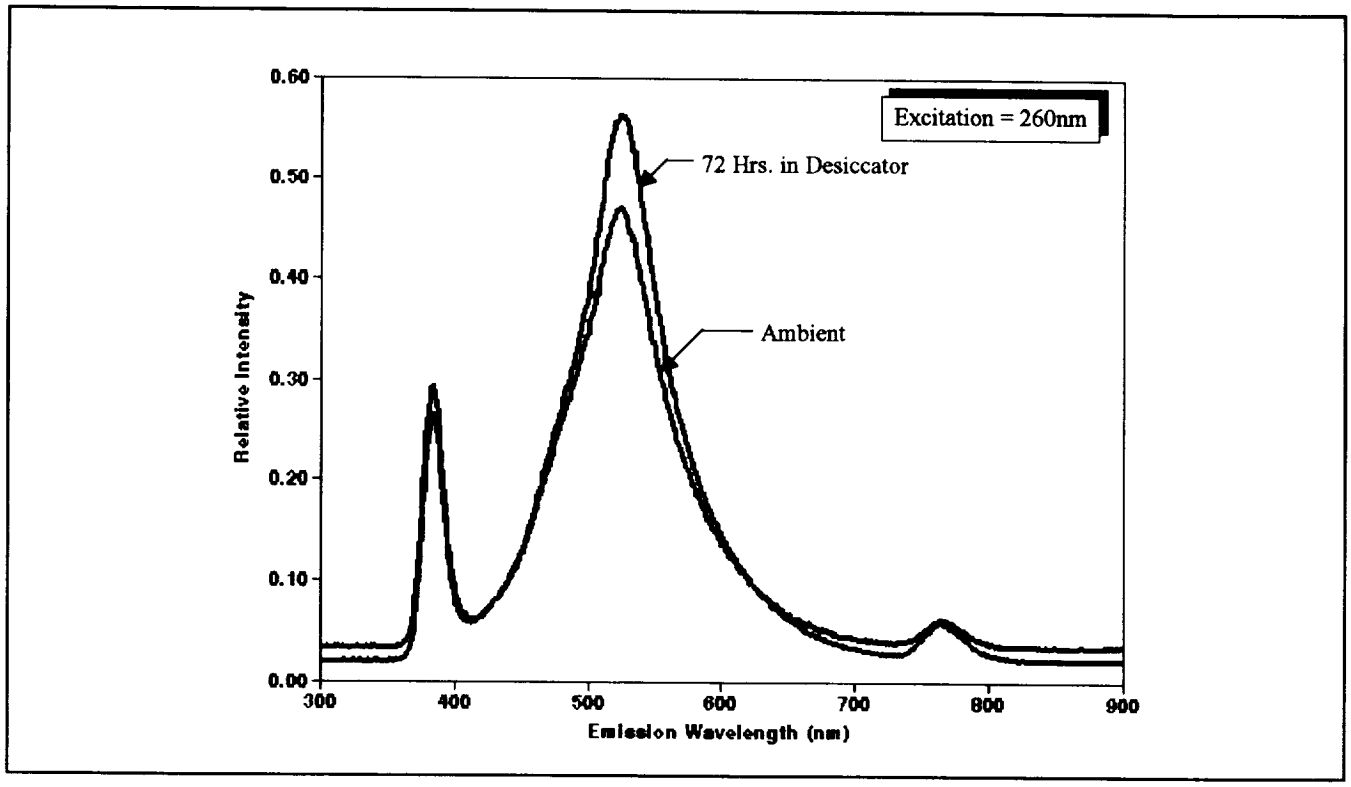

Figure 15. Humidity effects on the fluorescence of A0034 S13-GLO flight sample.

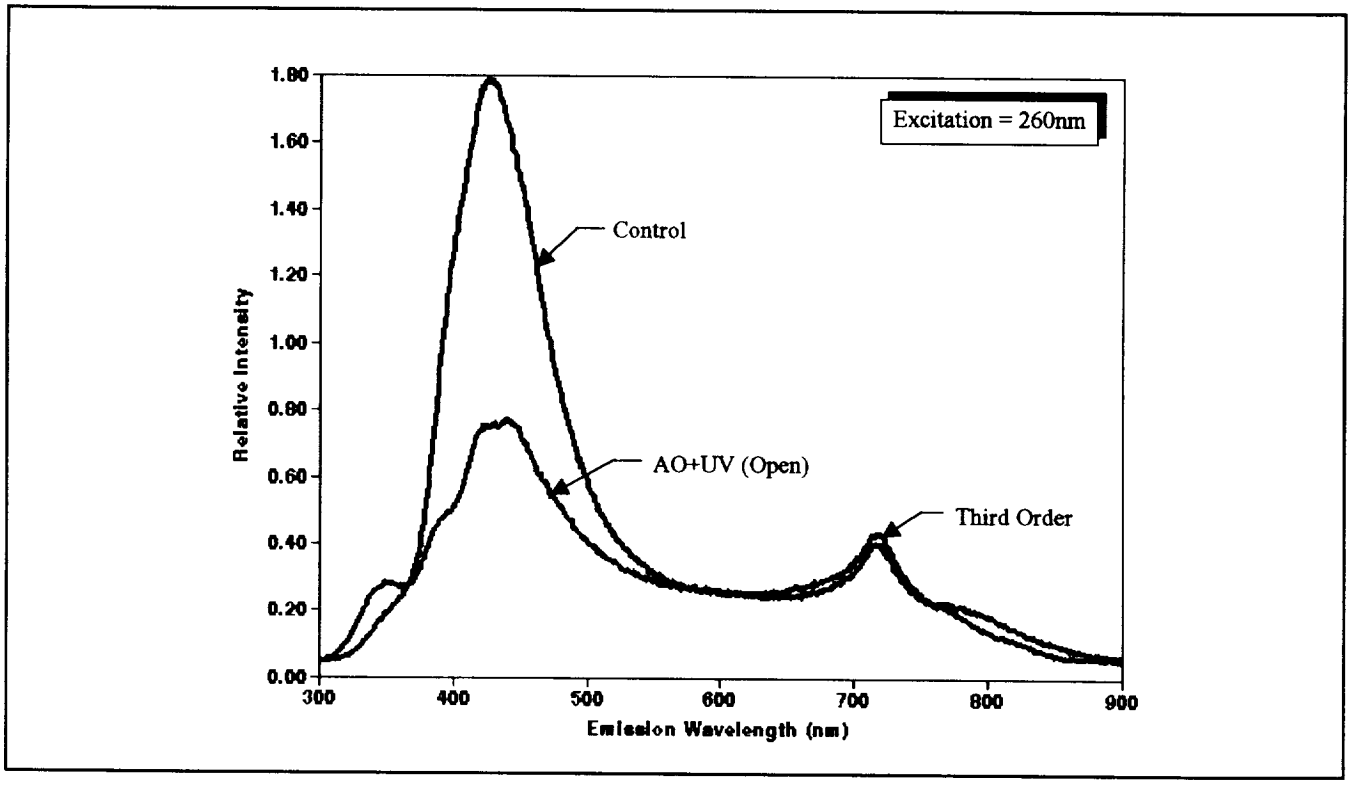

Figure 16. LDEF A0034 YB-71 leading edge paints fluorescence curves.

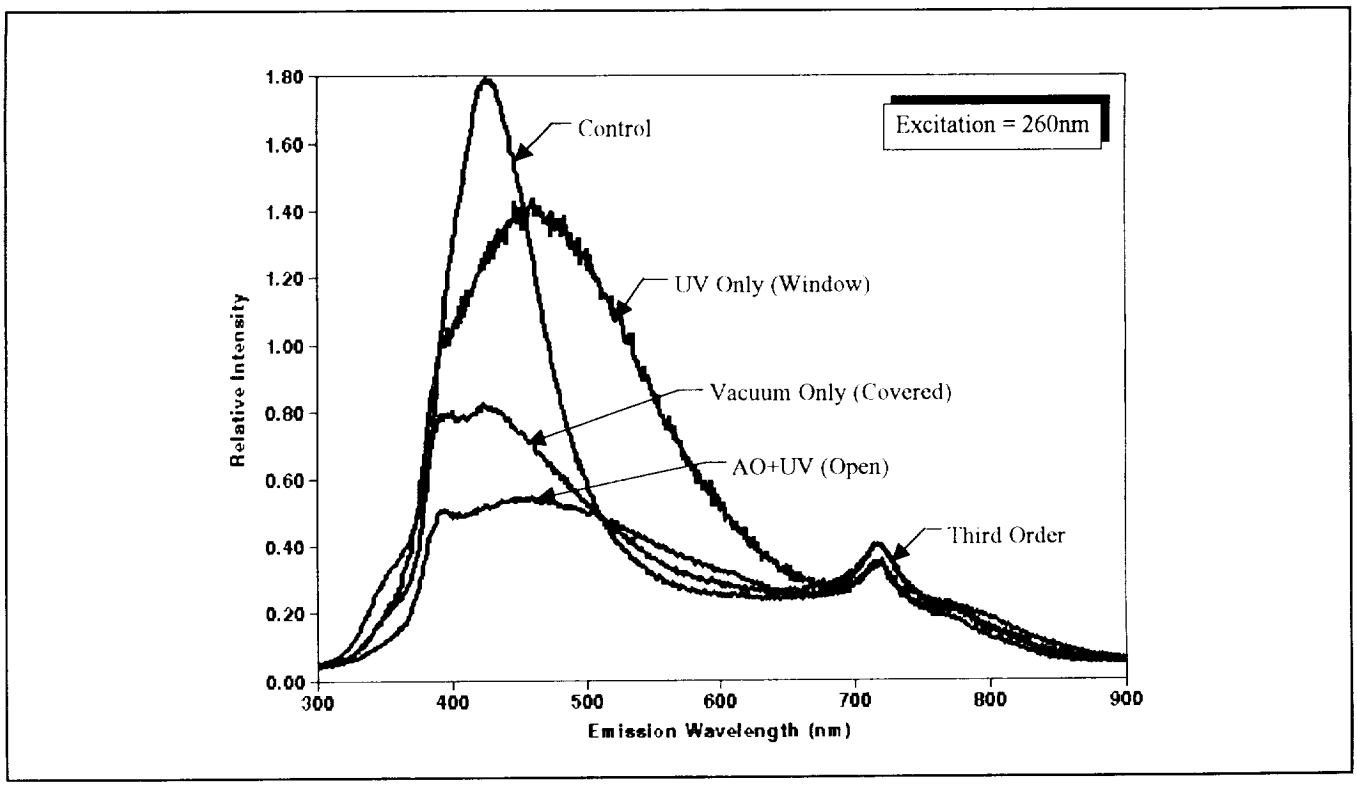

Figure 17. LDEF A0034 YB-71 trailing edge fluorescence curves.

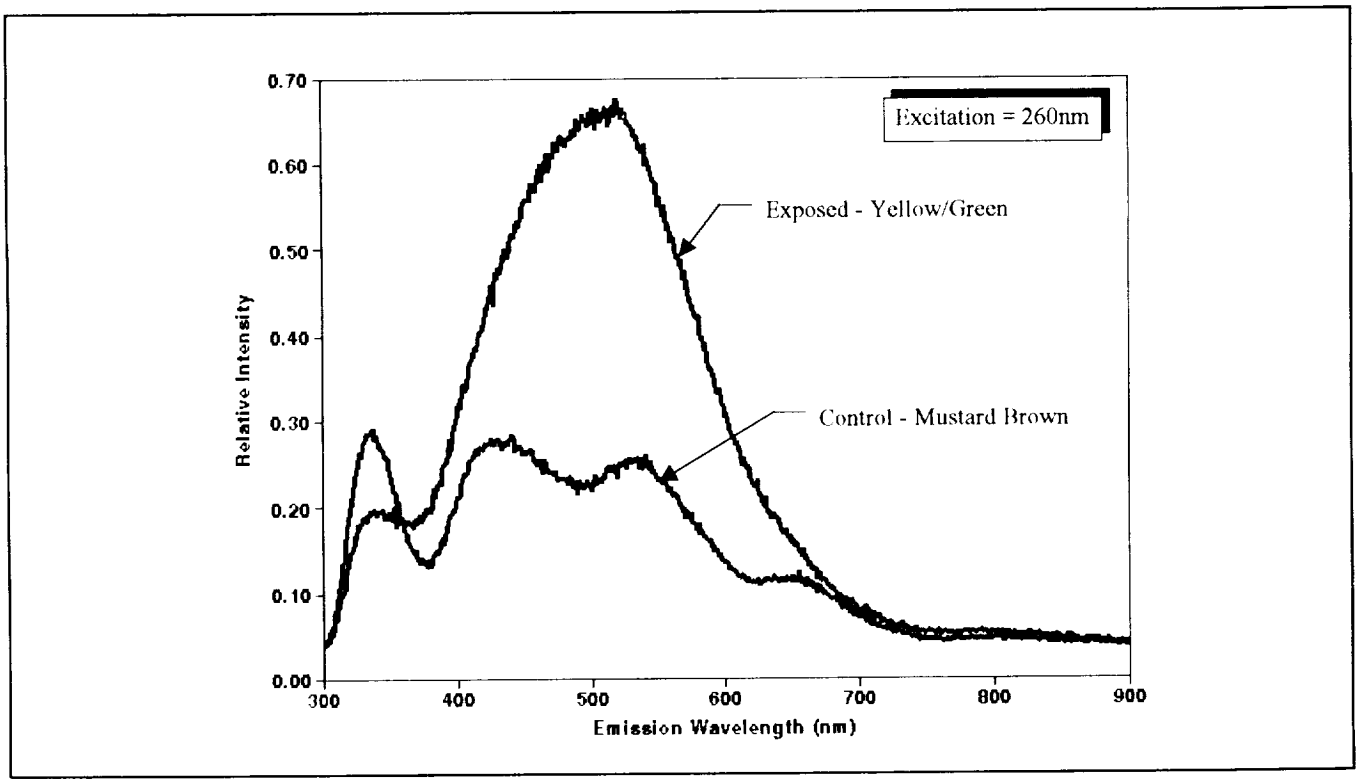

Figure 18. STS-5 Z306™ paints fluorescence curves.

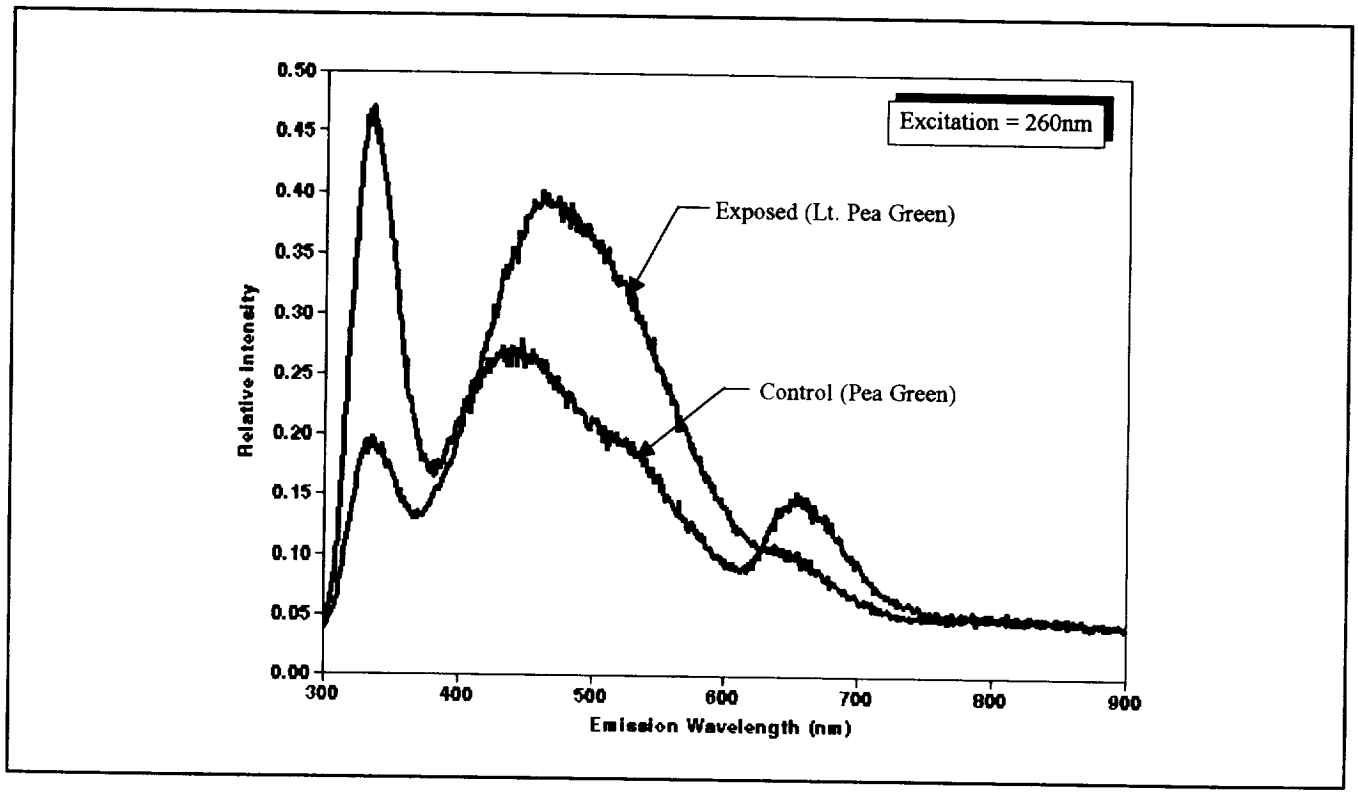

Figure 19. STS-8 Z306™ paints fluorescence curves.

N94-31026

LASER-INDUCED FLUORESCENCE OF SPACE-EXPOSED POLYURETHANE

Ralph H. Hill, Jr.
Instrumentation and Space Research Division
Southwest Research Institute
6220 Culebra Road
San Antonio, TX 78238-5166
Phone: 210/522-3358, Fax: 210/647-4325

SUMMARY

The objective of this work was to utilize laser-induced fluorescence techniques to characterize several samples of space-exposed polyurethane. These samples were flown on the Long Duration Exposure Facility (LDEF), which was in a shuttle-like orbit for nearly 6 years. Because of our present work to develop laser-induced-fluorescence inspection techniques for polymers (U.S. Patent No. 4,802,762), space-exposed samples and controls were lent to us for evaluation. These samples had been attached to the outer surface of LDEF; therefore, they were subjected to thermal cycling, solar ultraviolet radiation, vacuum, and atomic oxygen. It is well documented that atomic oxygen and ultraviolet exposure have detrimental effects on many polymers. This was a unique opportunity to make measurements on material that had been *naturally* degraded by an unusual environment. During our past work, data have come from *artificially* degraded samples and generally have demonstrated a correlation between laser-induced fluorescence and tensile strength or elasticity.

Laser-induced fluorescence techniques using 488-nm excitation (visible) were successfully used to inspect the space-exposed polyurethanes, with enhanced sensitivity over standard blacklight inspection. For example, degradation variations on absorptive (black) polyurethane samples could be observed. (Compared to ultraviolet excitation, visible-wavelength excitation techniques sometime reveal additional features, such as tensile strength degradation.) Anomalies between the control samples from LDEF integration and fresh samples were also observed. Laser-induced fluorescence techniques were also used together with video-imaging technology to reveal artifacts that may not have been detected with standard blacklight inspection. Effects that were slightly visible under standard blacklight inspection were more easily measured using laser-induced fluorescence because of the ease of handling the laser beam with fiber optics and the capability to increase the power density on the sample.

The laser-induced fluorescence technique has good potential for remote, nondestructive inspection of polymers. One future application may be remote sensing of polymer degradation from the space environment such as might occur on the outside of the space station or defense satellites. Another application may be in the laboratory for rapid inspection with enhanced sensitivity as compared to blacklight-inspection methods. Future work is needed to address the correlation between fluorescence intensity and degradation parameters, such as tensile strength or elasticity, for materials used in space applications.

TECHNICAL BACKGROUND

Laser-Induced Luminescence

Laser-induced luminescence (LIL) is emission of light resulting from absorption of laser energy by a substance. Re-radiated light contains a major component at the wavelength of the exciting laser light (reflected light); however, there are also many new wavelengths (luminescence) that are determined primarily by the electronic structure of the substance. Laser-induced luminescence includes both laser-induced fluorescence (LIF), which is fast luminescence occurring on time scales of the order of several nanoseconds, and laser-induced phosphorescence (LIP), which is slower luminescence occurring on time scales as long as several seconds. The luminescence spectrum is not only a function of time, but also a function of the excitation spectrum. Fluorescence and phosphorescence have been studied for a number of years and have been used in numerous ways in the laboratory environment. Laser-induced luminescence is finding widespread use in many new and diverse applications; for example, it is currently being used to measure polymer degradation (refs. 1–4), to detect fingerprints, and to map flowfields in chemical lasers. In recent years, advances in laser technology have increased reliability and portability of lasers and have also generally reduced costs.

In many applications, fluorescence dominates phosphorescence. Fluorescence is characterized by many spectra depending on the excitation wavelength. A fluorescent molecule emits a fluorescence spectrum after it absorbs radiation within its excitation spectrum. The spectral distribution of the fluorescent radiation is a physical and absolute characteristic of a given substance for a given excitation wavelength and is useful for qualitative considerations. Emission intensity of fluorescence at a given wavelength is useful for quantitative analysis with a given instrument after standardization. Quantitative measurements show that there is sometimes a very strong correlation between laser-induced luminescence and some physical characteristic of the material, such as tensile strength or elasticity; many times this is because fluorescence primarily reveals relationships between molecular functional groups, such as conjugation. Because relationships between certain molecular functional groups are altered during degradation, laser-induced luminescence can be used to monitor these processes.

With the monochromaticity and power density available from lasers, molecules can be probed that are not normally thought of as fluorescent. For instance, samples that exhibit ultraviolet absorption can sometimes be induced to fluoresce with laser excitation in the visible region of the spectrum. This effect can be very important from the viewpoint of practical implementation.

When laser-induced fluorescence is measured with a video camera or visually assessed using optical filters instead of a narrow-bandwidth spectrometer, fluorescence signals of several wavelengths are measured simultaneously. Laser-induced fluorescence measured in this fashion is referred to as "integrated fluorescence" because the signal is related to the integral of the fluorescent-light intensity, weighted by the filter-detector response, over the wavelengths to which the system responds. Hence,

$$I(\lambda_e) = \int LIF(\lambda_e,\lambda) D(\lambda) f(\lambda) d\lambda \ , \tag{1}$$

$I(\lambda_e)$ = integrated fluorescence for excitation wavelength λ_e

$LIF(\lambda_e,\lambda)$ = laser-induced fluorescence at wavelength λ when excited with wavelength λ_e

$D(\lambda)$ = detector response at wavelength λ

$f(\lambda)$ = filter response at wavelength λ.

Note that $LIF(\lambda_e,\lambda)$ is also a function of the penetration depths (absorption and scattering parameters) for both the excitation and detection wavelengths, as well as the quantum yield for fluorescence of the material.

Long Duration Exposure Facility

The LDEF was placed into orbit in April 1984 during Space Shuttle *Challenger* mission STS-41C (refs. 5–6). This 4.3-m×9.1-m (14-ft×30-ft), 9,979-kg (11-ton) satellite contained 57 international experiments which were designed to investigate effects of long exposure to the harsh space environment on electronics, optics, biological samples, and various materials that may ultimately be flown in space for long periods of time. In January 1990, LDEF was recovered by Space Shuttle *Columbia* during mission STS-32. LDEF was deployed at 475 km (295 miles) and retrieved at 330 km (205 miles).

Samples

It was reported that under blacklight (ultraviolet) illumination, some of the space-exposed polyurethane-based thermal control paint samples visibly fluoresced (ref. 7). From past experience (refs. 1–4), we know that laser-induced fluorescence can be used to give additional degradation information as compared to either blacklight fluorescence or visible reflectance. Boeing Defense and Space Group (Seattle, WA) lent us three samples of the space-exposed polyurethane so that we could experiment with our laser techniques on the samples. (The differences in fluorescence between ultraviolet and visible excitation form the basis for one our patents in this field (ref. 1); therefore, some differences were expected.)

The three tray-clamp samples from the outside surface of LDEF were designated as DO4-6, HO9-11, and HO7-11. Each sample consists of a white (reflective) and black (absorptive) section, originally painted with ChemGlaze (manufactured by Lord Corp.) A276 reflective moisture-curing aliphatic (straight-chain structured) polyurethane and Z306 absorptive moisture curing aromatic (ring structured) polyurethane. One sample (H07-11) has various levels of degradation due to "shadowing" effects. One of the samples (H09-11) may be contaminated with silicone which outgassed from another part of LDEF (ref. 8). A list of the samples is given in Table 1. The aluminum tray clamps were approximately 12.7 cm (5 in) in height and 5.1 cm (2 in) in width, with the polyurethane samples deposited as round discs on the tray clamps. The white (reflective) inner-disc

diameter was 3.2 cm (1.25 in) and the black (absorptive) outer-disc diameter was 4.4 cm (1.75 in). (Mounting holes were used as positional reference; thus when they were on the left, the 12 o'clock position corresponded to "up".)

LDEF was gravity-gradient stabilized so that one end was always pointed away from the Earth. Furthermore, LDEF did not spin and so the exposed samples had well defined positions and orientations with respect to outer space and the spacecraft motion. Therefore, various samples were exposed to different levels of atomic oxygen fluence, etc.

APPARATUS AND PROCEDURES

Spectral Measurements

The following describes the laboratory apparatus and procedures used to make the experimental laser-induced fluorescence spectral measurements. A schematic diagram of the apparatus is shown in Figure 1.

Excitation Source

A Spectra Physics model 2025-005 argon-ion laser operating at 488 nm was used as the excitation source. For measurements described in this report, the "constant-light output" mode was utilized so that drifts in output power were negligible. Laser plasma-discharge lines were removed from the beam with an Edmund Scientific P/N 03907 interference filter with central passband centered at 488 nm ("F1" in the figure). The beam was directed with front-surface turning mirrors so that it hit the sample at a 180° angle with respect to the detection axis. The beam was unfocussed and had a spot size approximately 2 mm in diameter where it hit the sample. Laser power at the sample was 28.4 mW measured using an Eppley thermopile. Laser power was constant for both the white and black samples so comparisons could be made. In future measurements, higher power or longer integration times will be used on the dark samples to increase the signal-to-noise ratio.

Collection Optics

Light was collected with a simple f/2.25 lens arrangement. Scattered laser light was filtered from the fluorescence using a 3-mm thick piece of Schott OG530 glass ("F2" in the figure). For these measurements, alignment and matching into the spectrometer were not critical because the fluorescence was relatively intense. (Fluorescence could be easily seen with the unaided eye when viewed through a OG530 filter or argon-ion laser safety goggles.)

Spectrometer System

A Jarrell-Ash 0.275-m spectrometer (f/3.8) with a 150 groove/mm grating and a 25-micron wide slit was used to disperse the light. This is the front-end to an EG&G/PAR optical multichannel analyzer (OMA) system. The detector was a model 1455R-700-HQ microchannel-plate (MCP) intensified diode array. The multi-alkali photocathode has a nominal "S1" response (200–900 nm). It was operated with a Peltier cooler (5° C) and the MCP gain set at 70 percent of maximum. Typical

OMSsettings were: 30 ms/scan and 100 scans (accumulated). Spectra were digitally stored on 5.25-inch floppy disks for subsequent analysis. Typical spectra show a rapid fall-off of the response at approximately 750 nm and longer wavelengths which was an instrumental artifact caused by physical blockage of the diode array in the present mounting configuration. (Note that the fall-off of response below 530 nm is due to the Schott glass OG530 blocking filter.) Wavelength calibrations were routinely made against a low-pressure mercury discharge.

Imagery

The video set-up is depicted in Figure 2; details are as follows.

Excitation Source

The argon-ion laser described above was also used as the source for the imagery experiments. In this case, the 488-nm light was directed at the samples through a multimode, multistranded fiber-optic bundle ("FO" in the figure). This bundle served the purpose of scrambling the coherence of the beam so that interference fringes would not be superimposed on the images. The beam intensity at the sample surface was approximately 11 mW/cm^2.

Collection Optics and Processor

A Sony model XC-57/HV solid-state monochrome camera was used to image the sample ("C" in the figure). This camera had a macro-zoom lens (Computar LMZ45C5, "L" in the figure), internal infrared-cut filter, and an external 3-mm thick Schott OG530 glass laser-blocking filter ("F" in the figure). The image was captured with an Imaging Technology, Inc., model VP1100 overlay frame grabber installed in a Compaq DeskPro 486/33M personal computer, running Optimas 3.01 (written by Bioscan, Inc.) image-analysis software. Parameters were set so that the system response was linear over the range of interest. Images were analyzed, but <u>not</u> enhanced using the software.

Ultraviolet Inspection

Because blacklight ultraviolet inspection has been used extensively in the past, we also inspected these samples under blacklight. The source that was used was a Spectroline model MB-100 High Intensity Blacklight Lamp (365 nm); this is an industrial grade inspection unit (115 VAC at 3.3 amps). Under this excitation, the 3 o'clock portion of H07-11 showed up as brighter than the rest; H07-11 and D04-06 appeared about the same, but not too fluorescent.

Additionally, a helium-cadmium laser (Omnichrome model 56-XL) which produces approximately 15 mW over a 2-mm spot diameter at 325 nm was used to visually inspect the samples. In this mode, the silicon contamination on the aluminum part of the H09-11 tray clamp was apparent in the area near the middle mounting hole.

DATA AND RESULTS

Specific Experiments

Selected measurements will be discussed in the following. Care must be exercised in comparing spectra between different experiments as the detailed experimental parameters may have been slightly different. If curves are on the same graph, however, they were taken under identical circumstances and can therefore be compared. Additional data is given elsewhere (ref. 9).

Comparative Data on Same Sample

Typical laser-induced fluorescence spectra are shown in Figure 3. In this figure, spectra from the reflective (white) portion of sample H07-11 is shown from three different locations, i.e. 1 mm into the 3 o'clock position (upper curve), center, and 1 mm into the 9 o'clock position (lower curve). Under visible room light examination, this sample shows degradation, with the 9 o'clock area darkened. Figure 4 shows laser-induced fluorescence spectra from the same tray clamp, but on the absorptive (black) portion. Large differences can be easily seen between the two spectra, the upper curve from the 3 o'clock position and the lower curve from the 9 o'clock position. The differences could be detected under standard blacklight-inspection for the white portions, but not for the black portions. Laser-induced fluorescence differences can also be detected on the other samples, but are much smaller, typically less than 15 percent or less.

Comparison Between Samples

Figure 5 shows the laser-induced fluorescence spectra from the center of the three samples; with the most fluorescence from H07-11, decreasing with D04-06, and H09-11 respectively.

Comparison Between Control Samples from LDEF Integration and Fresh Samples

Significant differences were found when comparing the control samples from LDEF integration and sample D04-06. Two significant differences are present for both the reflective and absorptive polyurethane. (1) The control samples fluoresce more than the space-exposed samples in the 550-nm wavelength region. (2) There is more fluorescence in the red wavelength region (650 nm and longer) for the space-exposed samples. This unexpected result led us to investigate the control samples in greater detail. Differences between the spectra from the control samples and fresh samples, which were obtained in early 1992 from Lord Corporation, were also found. For both the reflective and absorptive polyurethanes, the fresh paint fluoresces significantly less than the LDEF-integration control samples. This could be because the details of the formulation have been changed since the control samples were made (ca. 1983), or the control samples have actually aged during storage or degraded in some way. These control samples did not go into space, so they are not contaminated with silicon, or other space debris.

Video and Digital Image Analysis

Figure 6 shows the laser-induced fluorescence digital photograph of sample H07-11. The top part of the picture corresponds to the 9 o'clock position on the sample. The brightness (offset) has been adjusted so that the fluorescence from the absorptive portion does not show up in this

presentation. Figure 7 is a graph of the luminance value along a vertical line from the 9 o'clock position (on the sample) to the 3 o'clock position (on the sample) taken from the digital information contained in Figure 6. Note that the fluorescence spectra shows much structure and a possible microcracking effect.

Microscopy

The saturated (overexposed) portion of Figure 6 was examined further. Under 40× macroscopic examination, it appears as a small impact crater with observable polyurethane displacement. Because of its intense fluorescence, it was possible to examine it under a standard fluorescence microscope (Polyvar MET, 40×). It appears to be some sort of fibrous material. Because of the apparent impact crater, it is believed that this contamination is space debris of some kind. (Destructive examination to determine the exact nature of this material was beyond the scope of this investigation.)

Summary

- Laser-induced fluorescence techniques were used to inspect the space-exposed polyurethanes, with enhanced sensitivity over standard blacklight inspection.
- Degradation of absorptive (black) polyurethanes was also observed using laser-induced fluorescence techniques.
- Fresh samples (1992) of the A276 and Z306 polyurethane (manufactured by Lord Corp.) do not fluoresce nearly as much as the LDEF-integration control samples.
- Increases or decreases in the 488-nm excited laser-induced fluorescence of the polyurethane with degradation depends upon the wavelength region of the fluorescence.
- Laser-induced fluorescence techniques, when using 488-nm excitation, may not be affected by some contaminants, because they are basically transparent at that excitation wavelength.
- Laser-induced fluorescence techniques can be used with video imaging technology to reveal artifacts that may not be revealed with standard blacklight inspection, such as the subtle differences between samples H09-11 and D04-06. The capability for real-time assessment of the validity of the data is a very valuable advantage. (Overexposures or underexposures can be immediately noticed and compensated for.)
- Effects that were slightly visible under standard blacklight inspection are more easily extracted using laser-induced fluorescence because of the ease of handling the laser beam with fiber optics and capability to increase the power density on the sample.

DISCUSSION

Space degradation of polymer materials is a very complex process. The A276 white polyurethane paint darkened during ultraviolet exposure (ref. 7); however, for some samples the atomic oxygen fluence was sufficient to "scrub" (oxidize and remove) the damaged resin from the surface. In some cases this left behind a fragile agglomeration of pigment particles that displayed optical properties similar to those of the original material. Presently, all the processes are not completely understood, although it is clear that polymers and organic binders involved are attacked (refs. 10–11).

Laser-induced fluorescence can be used to monitor and/or study some of these processes. More work is needed to correlate fluorescence with the degree of degradation of the tensile strength, for instance, for these particular materials. The technique has good potential for remote, nondestructive inspection of polymers. One future application may be remote sensing of polymer degradation from the space environment such as may occur on the outside of the space station or defense satellites. Another application may be in the laboratory for rapid inspection with enhanced sensitivity as compared to blacklight-inspection methods.

ACKNOWLEDGMENTS

This work was supported by the Southwest Research Institute (SwRI) Advisory Committee for Research under SwRI Project 15-9682.

REFERENCES

1. Hill, Ralph H., Jr.: "Optical Inspection of Polymer-Based Materials," U.S. Patent No. 4,802,762, February 7, 1989.

2. Hill, R.H., Jr.: "Laser-Induced Fluorescence Inspection of Polyurethane and Related Materials," Final Report/Phase 1, SwRI Project No. 17-7958-828, November 15, 1988.

3. Hill, R.H., Jr., and Feuer, H.O., Jr.: "Laser-Induced Fluorescence Inspection of Polyurethane," *Proceedings of the 17th Symposium on Nondestructive Evaluation*, San Antonio, TX, April 17–20, 1989.

4. Hill, R.H., Jr.: "Laser-Induced-Fluorescence Analytical Technologies-Phase II," Interim Report BFLRF No. 276; ADA 248486, Contract DAAK70-87-C-0043, September 1991.

5. Photos of LDEF Retrieval Reveal Condition of Experimental Panels, *Aviation Week and Space Technology*, January 29, 1990, pp. 64-65.

6. Canby, Thomas Y.; and Schneeberger, Jon: "Satellite Rescue," *National Geographic*, vol. 180, no. 5, November 1991, pp. 106–130.

7. Golden, J.L.: "Thermal Control Materials," *LDEF Spaceflight Environmental Effects Newsletter*, vol. II, No. 3, June 15, 1991, pp. 17–18.

8. Golden, John: Boeing Defense and Space Group, private communication, October 31, 1991.

9. Hill, Ralph H., Jr.: "Laser-Induced Fluorescence of Space Exposed Polyurethane," Final Report SwRI Project 15-9682, April 6, 1992. (Available upon request from the author.)

10. Bohnhoff-Hlavacek, G.; et al.: *LDEF Spaceflight Environmental Effects Newsletter*, vol. II, No. 8, January 15, 1992. (Summary of the LDEF Materials Workshop 1991.)

11. Hamid, S.H., Amin, M.B., and Maadhah, A.G., eds.: *Handbook of Polymer Degradation.* Marcel Dekker, Inc., 1992.

Table 1. Samples (LDEF samples, material data, and preliminary fluence and exposure data supplied by Boeing Defense and Space Group, Seattle, WA. Fresh samples and data sheets were supplied by Lord Corp., Saegertown, PA).

Sample Designation	Comments	Absorbance/Emittance (for white samples)	Atomic Oxygen Fluence (atoms/cm^2)	Ultraviolet Exposure (ESH Units)
H07-11	Space end (visible degradation; in room light, visibly darker toward the 9 o'clock position)	0.61	4.27×10^{20} (at incident angle of 91°)	14,500
H09-11	Space end (near silicone coated reflector, slightly contaminated)	0.70	4.27×10^{20} (at incident angle of 91°)	14,500
D04-06	Side tray	0.64	2.56×10^{8} (at incident angle of 143°)	9,400
Control	Left over from LDEF integration	N/A	N/A	N/A
Fresh Samples	Jan. 1992.	0.23/0.90 = 0.26 (from data sheet)	N/A	N/A

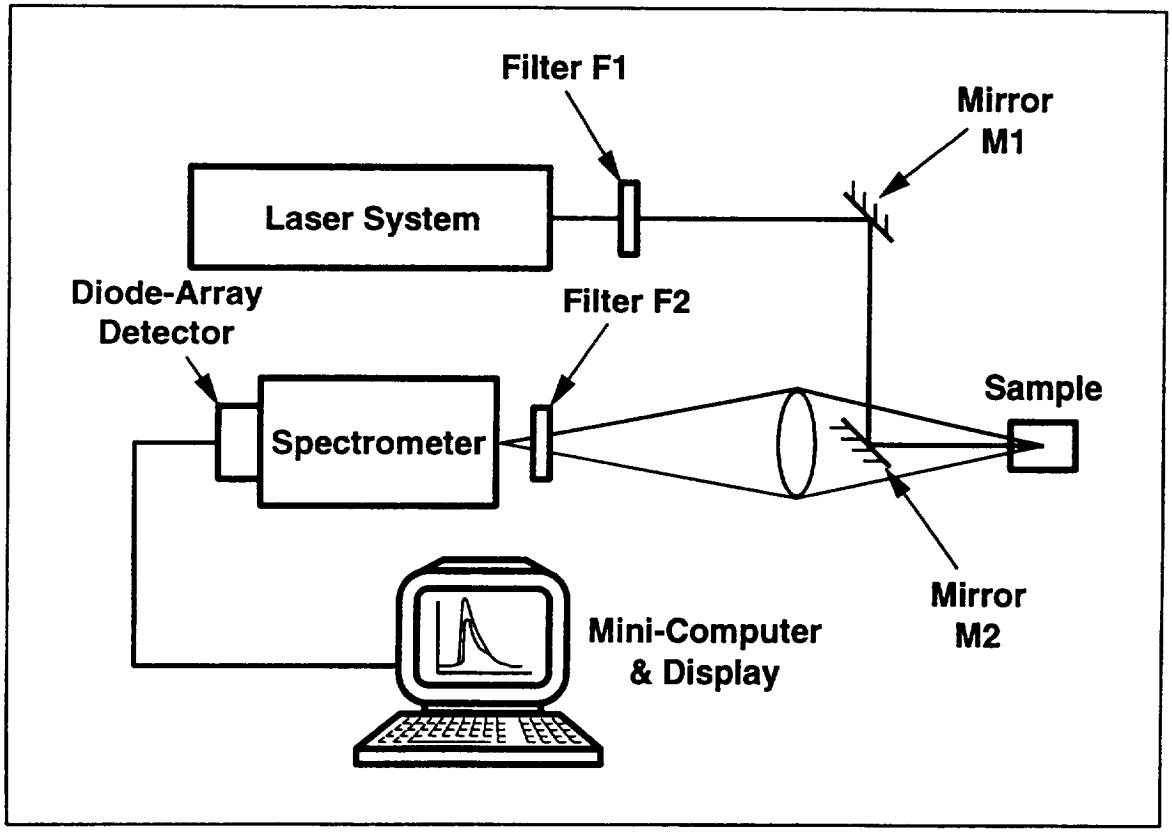

Figure 1. Experimental apparatus for spectral measurements.

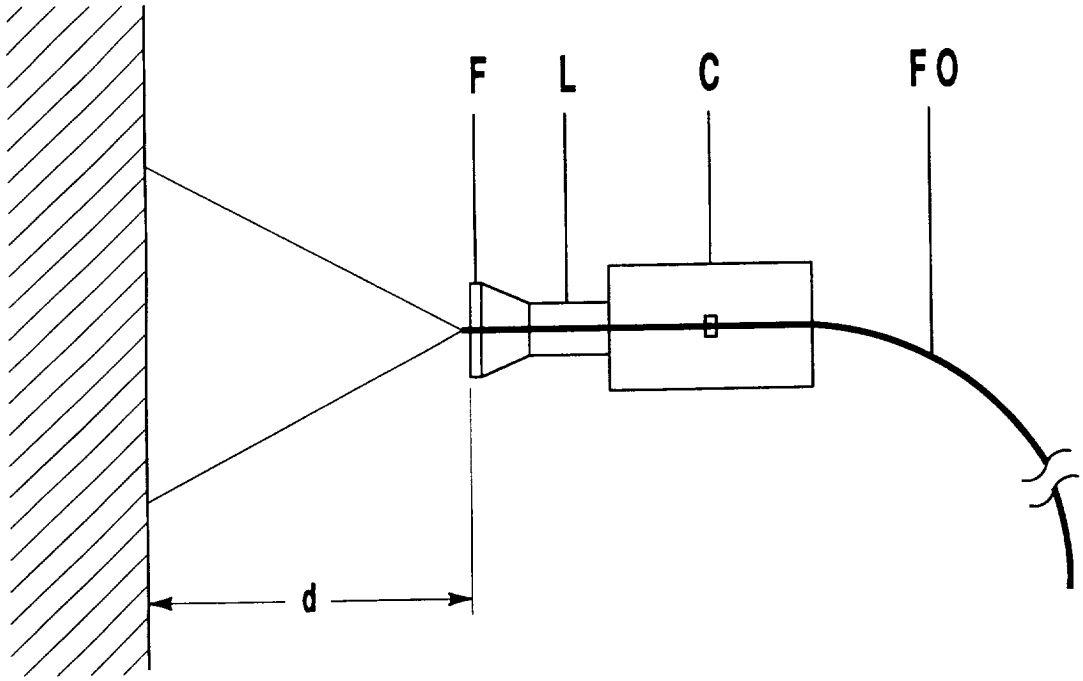

Figure 2. Experimental apparatus for video imaging. ("F" is the laser-blocking filter, "L" is the macro-zoom lens, "C" is the camera, "FO" is the fiber-optics bundle, and "d" is the standoff distance to the sample.)

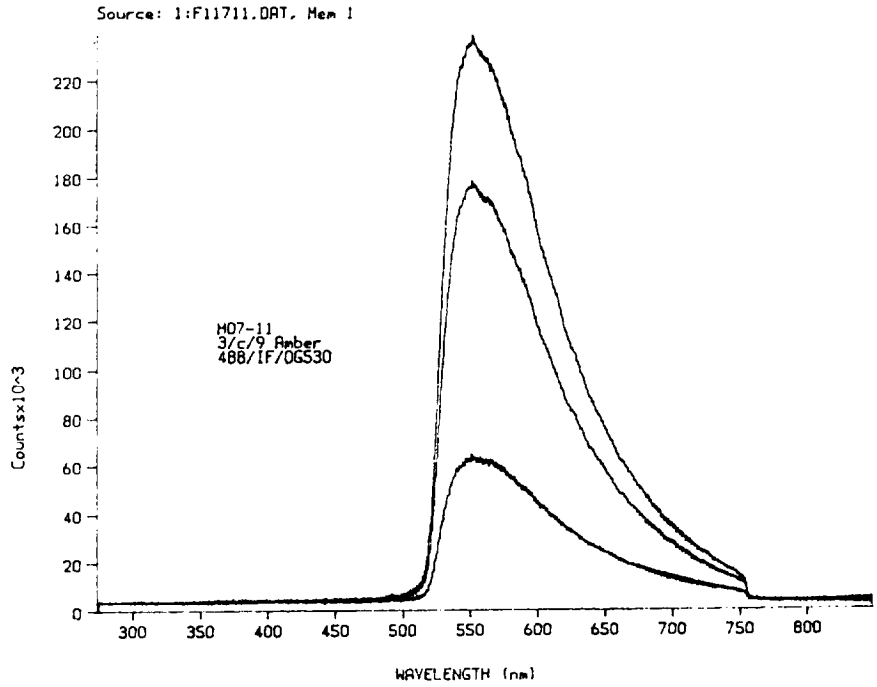

Figure 3. Laser-induced fluorescence spectra from the center reflective portion of H07-11. (Upper curve is from the 3 o'clock position, middle curve is from the central position, lower curve is from the 9 o'clock position.)

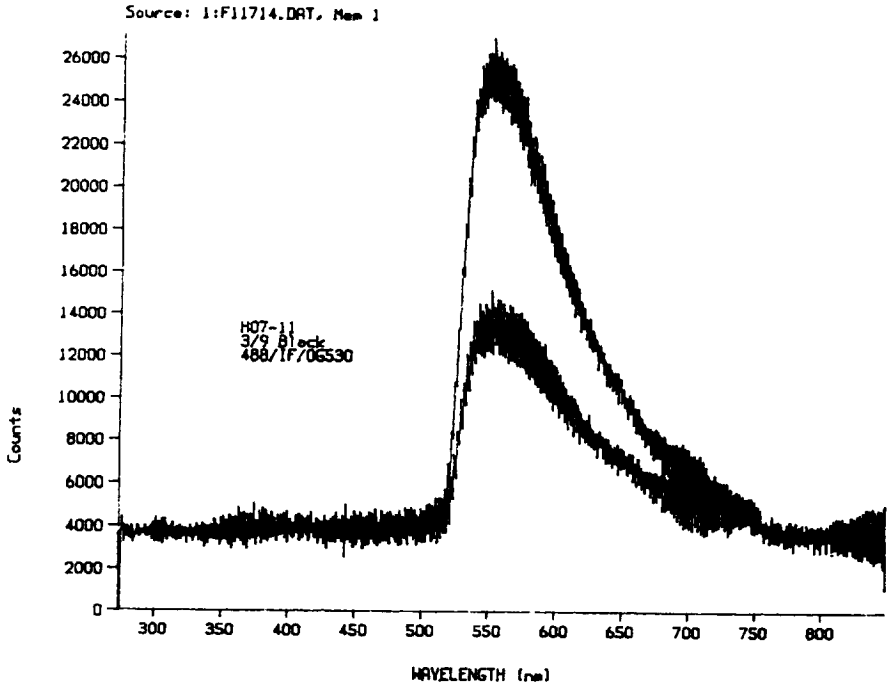

Figure 4. Laser-induced fluorescence spectra from the absorptive portion of H07-11. (Upper curve is from the 3 o'clock position, lower curve is from the 9 o'clock position.)

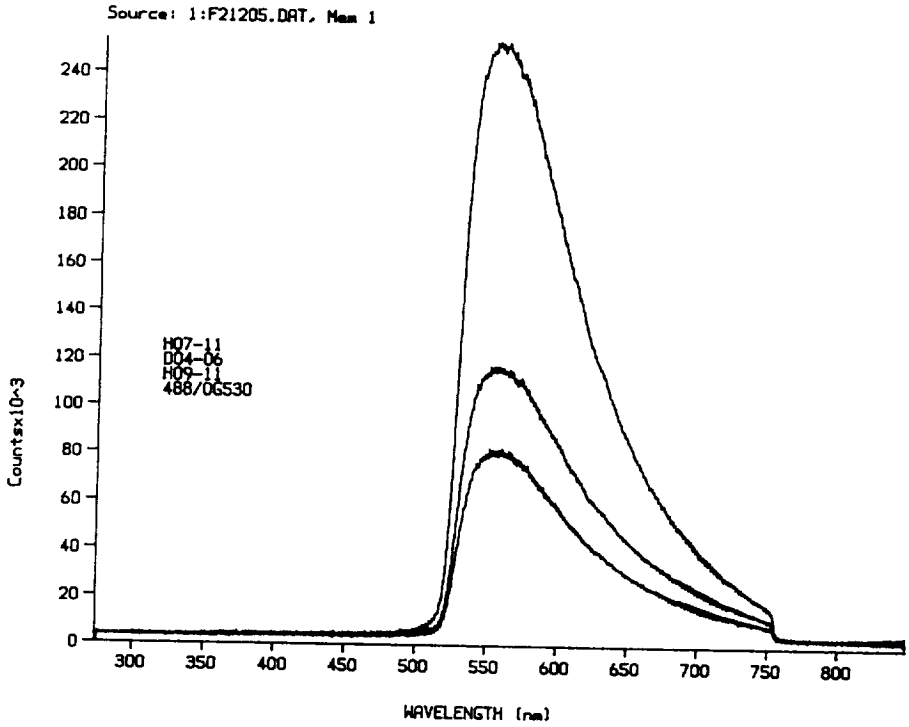

Figure 5. Laser-induced fluorescence spectra from the central reflective portion of three samples. (Upper curve is from H07-11, middle curve is from D04-06, lower curve is from H09-11.)

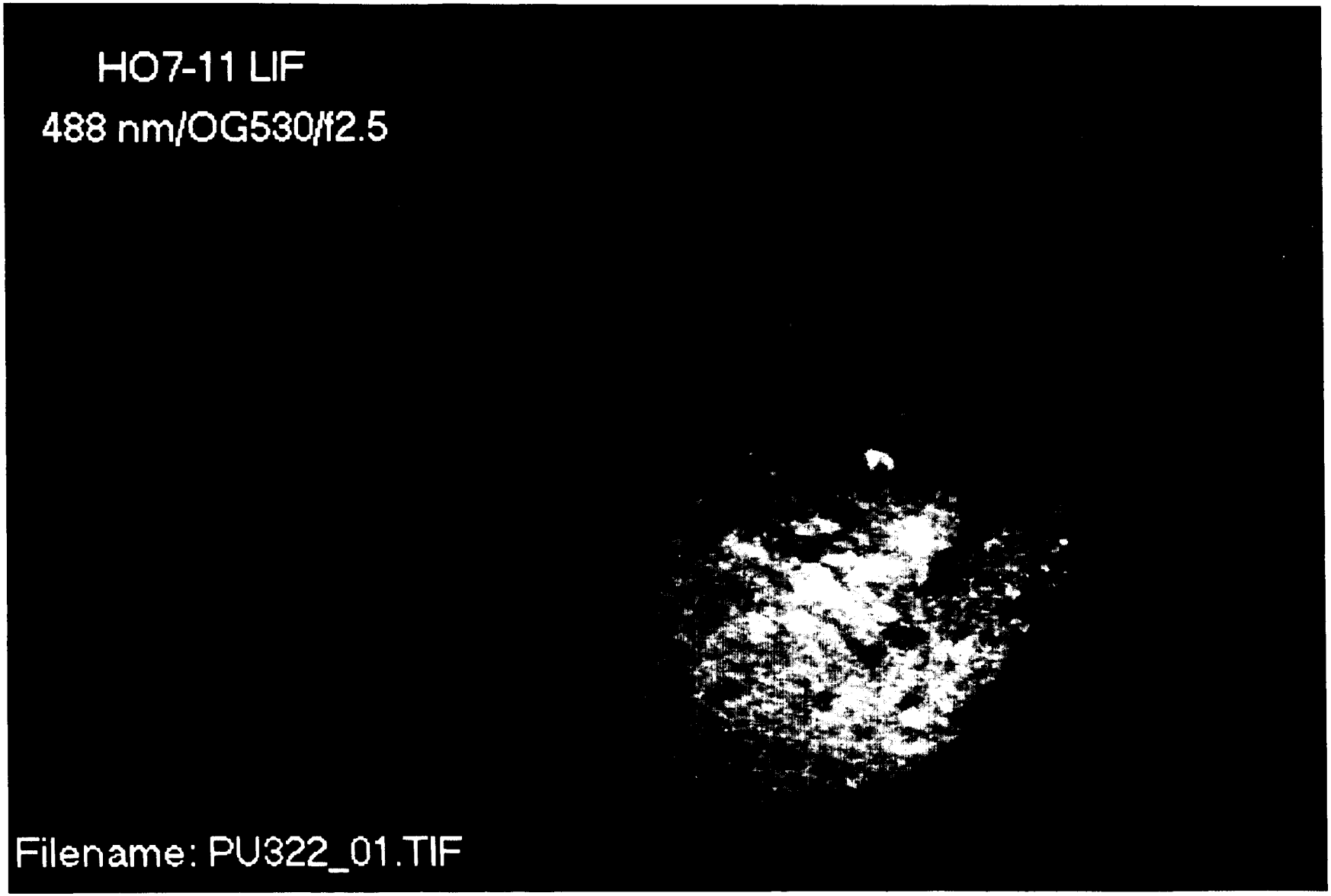

Figure 6. Video image of integrated laser-induced fluorescence from sample H07-11. (Top of the picture corresponds to the 9 o'clock position on the sample. Note the saturated area on the image is possibly embedded fibrous debris.)

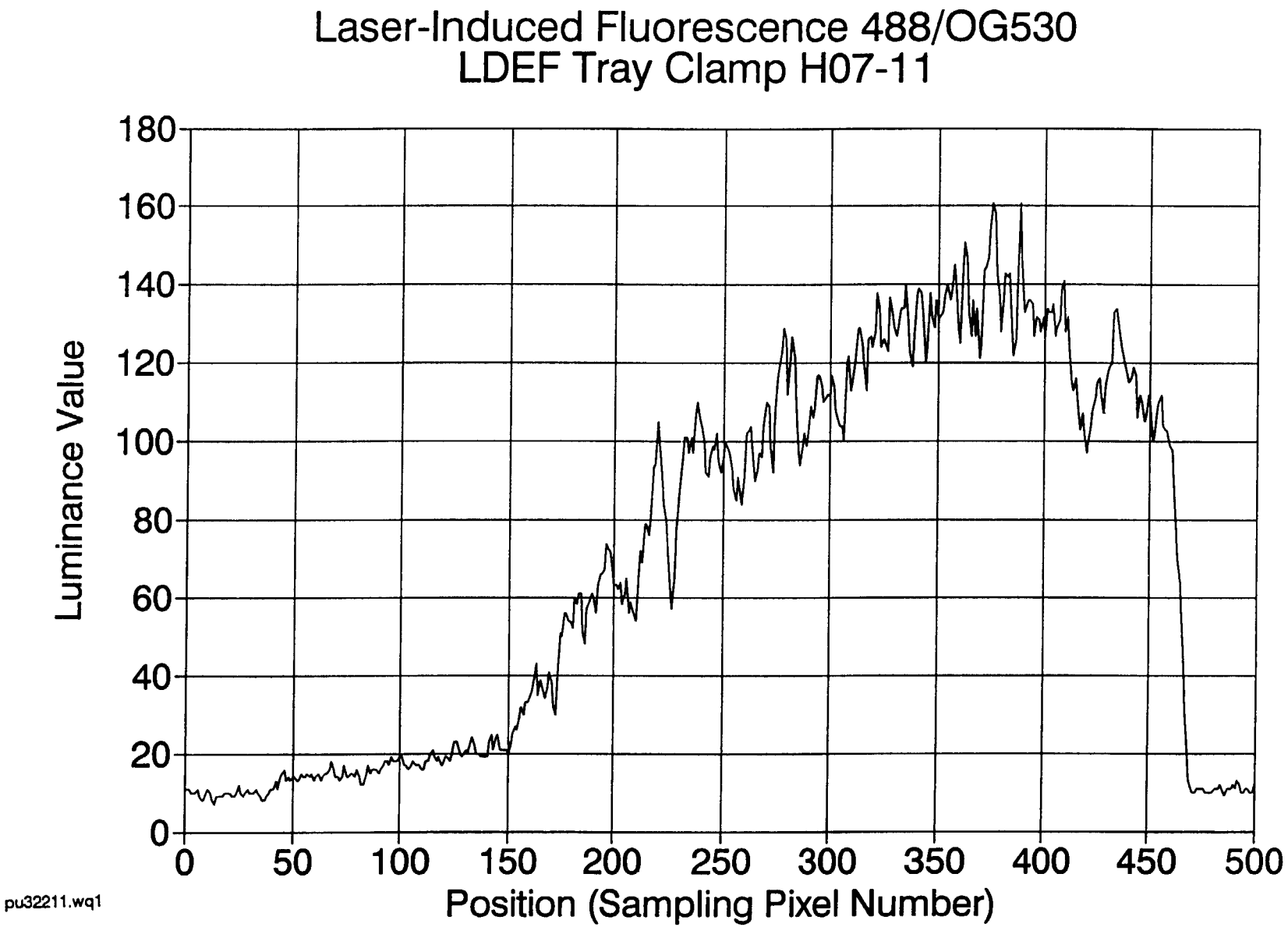

Figure 7. Integrated laser-induced fluorescence line scan from the image in Figure 6. (Along a line from the 9 o'clock position on the sample to the 3 o'clock position, i.e., vertical scan on Figure 6.)

ON THE LINEARITY OF FAST ATOMIC OXYGEN EFFECTS

J.C. Gregory
The University of Alabama in Huntsville
Surface Science Laboratories
Department of Chemistry
Huntsville, AL 35899
Tel: (205) 895–6028, Fax: (205) 895–6061

INTRODUCTION

The effect of bombardment of 8 km per second atomic oxygen (AO) experienced by exposed surfaces of satellites in low Earth orbit must be considered in the selection of materials to be used in instruments and functional systems on these satellites. The degree of importance of the effects varies widely depending on the material, the application, and the exposure (fluence of atoms) to which it is to be subjected. Some highly erodible thin polymer film materials might be considered unacceptable on a long-lived space station, but may be perfectly serviceable on a normal shuttle flight. In order to determine the acceptability of a material for a particular environment, a designer must know the relationship between the magnitude of the effect (for example, mass-loss) and the magnitude of the fluence. To determine this relationship, we need data over a useful range of fluence.

Until the return of the Long Duration Exposure Facility (LDEF), the bulk of the data on materials effects was obtained from a few shuttle flights, and the bulk of that data from the flight of experiment Evaluation of Oxygen Interaction With Materials (EOIM-2) on STS-8 in 1983. EOIM-2 obtained a fluence of 3.5×10^{20} atoms cm^{-2}, while the LDEF fluence approached 10^{22} atoms cm^{-2}, or about 30 times greater. Although other flight exposures had been obtained with lower fluences, considerable uncertainty was attached to these results because of the possibility of large relative systematic errors and of other factors such as sweeping angle of attack.

In the future, it is hoped that simulation facilities in the laboratory will allow testing of materials without the necessity of flying them in space. In addition, if the relationship of effect with oxygen fluence is well determined, it should not be necessary to expose a material for an entire mission fluence. In this paper, we shall avoid a comparison of flight data with results from simulators, though that comparison is important for the materials community. The present discussion will be limited to flight data only.

We may divide materials into two broad classes in their reaction with fast AO, according to the nature of their oxide products.

- *Materials with gaseous oxide products.*
  These include carbons of various kinds, and most of the commercially available useful organic polymers (including polyimides, polyesters, polycarbonates, and many others). The class does not include silicon-containing materials such as polysiloxanes. The metal osmium is included, since it appears to readily form the labile oxide O_5O_4 (ref. 1).

If the rate of product-oxide evaporation is rapid compared to the rate of oxygen adsorption, the presumed relationship between erosion and fluence is linear. While such a statement may seem obvious, it should be remembered that from some earlier data such a relation was often far from obvious and "incubation periods" were discussed. To the present day, only preliminary work has been done to investigate the mechanisms of reactions in the hyperthermal regime.

- *Materials with refractory oxide products, or with oxides strongly bound to the substrate surface.*
  Most metals fall into this category; Cu, Ni, Al, Cr, Nb, Ir. (ref. 1). Silver is a member of this class, though a special case since it oxidizes to depths of several microns at ambient temperature. The class also includes nonmetals such as Si and Ge, and compounds such as SiC, Si_3N_4 , and GaAs. In the case of oxidation of materials of this class, the presence of an oxide layer tends to reduce the rate of reaction, so that a rate law is obtained which follows a parabolic or similar function (ref. 2). We shall address this second class elsewhere and limit this present discussion to the evidence for linearity in the first class.

If we examine the data for evidence to support the linearity hypothesis, we must be aware of systematic differences in the data which may affect the conclusions drawn. Such systematic effects may depend on the measurement method, specific material properties, and even mission- or flight-related parameters.

Some experimental factors affecting data comparison include:

- The presence of contaminant films can affect the rate of reaction of oxygen with the substrate. This is particularly true for silicones which form, under the proper conditions, a continuous layer of SiO_2 on the surface. This can occur with thicknesses of only 30 to 50 Å, effectively preventing further reaction with the surface. Such contamination may be produced by poor handling procedures prior to flight, or may occur on orbit.

- Some erodible materials may contain particulates, which, if relatively unreactive, may remain on the eroded surface and reduce reaction efficiency as the erosion proceeds.

- Some materials such as the fully halogenated hydrocarbons may show increased reactivity to oxygen after they have received UV irradiation.

- Erosion rate data may vary systematically depending on the measurement technique. We note the dispersion of values, for example, of the mass-loss rate of Kapton®, obtained by different laboratories after the STS-8 flight. This dispersion has greatly decreased during the period up to the present time. There has also been a convergence of values obtained by stylus-profilometry with those obtained by weighing.

- Reaction rates often show a temperature dependence (ref. 3), and data from different experiments may have been obtained at different temperatures.

- Fluences calculated from orbital parameters and the Man Systems Integration Standard (MSIS) model have varied somewhat depending on some variations of the manner of computation.

COMPARISON OF THE DATA

Though there was a large number of erodible materials exposed on STS-8 (EOIM-2) (1983), and an even larger variety on EOIM-3 in 1992, very few of those polymers were also flown on LDEF. In addition, even if the polymers were present, they may not have been in a condition or form suitable to provide useful erosion data. For example, although much Kapton® was flown on LDEF, in all cases except that of the University of Alabama in Huntsville (UAH) experiment, the thickness was insufficient to withstand total erosion. It should be remembered that not only was the actual LDEF exposure some 5 to 10 times greater than expected, but also that LDEF experiments were delivered and stored before the flight of STS-8 in 1983, even though LDEF was not launched until 1984. Thus, there was no opportunity to apply lessons learned from the earlier flight.

The measurements of erodible polymers obtained from experiment A0114 are shown in Table 1. Calculated reactivities are based on a mission fluence of 9.0×10^{21} atoms cm^{-2}. The measurements were obtained using a Taylor-Hobson Talysurf stylus profilometer, and a sample scan from two separate samples of polystyrene exposed on the LDEF is shown in Figure 1. The actual erosion depth is measured by constructing a line through the peaks and valleys as shown in the figure. Large peaks, or mesa-like regions, are ignored as evidence of erosion-protection caused by contaminants of some kind. It is seen from the example shown that even for extremely rough etched surfaces, and even in the case of total erosions of one-half millimeter, the agreement between different samples of the same material is good. This is also true for multiple scans of different areas of a sample.

Table 1. Erosion depths and rates for polymers measured on LDEF. Experiment A0114 (UAH). All data from samples on Row 9 (leading edge - 8°).

Polymer	Erosion Depth† (μm)	Reaction Rate * 10^{-24} (cm^3 $atom^{-1}$)
Kapton®	260±5	2.89±0.06
Nylon	253±19	2.8±0.2
Polystyrene	375±15	4.17±0.17
PVT	396±27	4.4±0.3
PMMA	566±28	6.3±0.3
Polyethylene	357±21	3.97±0.23
PTFE	33.5±5	0.37±0.06

* Assuming an LDEF fluence for row 9 of 9.0×10^{21} atoms cm^{-2}.

† Errors quoted in parenthesis (except for Kapton®) are simply the RMS roughness of the exposed area. This is usually much rougher than the unexposed.

Some general observations may be made on the results in Table 1. With the exception of polytetrafluoroethylene (PTFE), all the reactivities are the same within a factor of 2 for polymers of widely different chemical nature. Reaction rates may be controlled by an adsorption process involving a precursor step which is largely independent of the nature of the surface. The reaction rates of polystyrene and polyvinyltoluene are very similar, as are their structures (they differ only in that

PVT has a $-CH_3$ group attached to the benzene ring of polystyrene). However, the rate for polyethylene is about the same, even though no benzene ring is present at all. While aromatic structures often confer stability against environmental degradation such as autoxidation or thermal oxidation in normal air, this is not noticeably true in the case of oxidation by fast AO. This is good evidence that surface oxidation is proceeding by different mechanisms in the two cases. The reactivity of PTFE, lower by a factor of 10 than the other polymers listed, is attributed to the failure of the hydrogen-abstraction mechanism for oxidation of this fully fluorinated molecule.

Table 2 compares reactivities of erodible materials which were both flown on STS-8 and on LDEF. Nylon and polyvinyltoluene were not flown on STS-8. Some carbon results are shown here, but do not include the glassy or vitreous isotropic carbons, which were not included on LDEF.

Table 2. Comparison of erosion yields from LDEF experiment A0114 with previous data from STS-8 and STS-41g.

Material	Erosion Yields†; $cm^3 \times 10^{-24}$ (oxygen atom)$^{-1}$	
	LDEF Value (this work)	Prior Value
Kapton®	2.89±0.06	3.00**
PTFE (or FEP)	0.37±0.06	0.1–0.5
polyethylene	3.97±0.23	3.32–3.74
PMMA	6.3 ±0.3	4.91*
polystyrene	4.17±0.17	1.7
Carbon; (HOPG)	1.04	0.6*
Carbon; pyrolytic polycrystalline	0.61	0.58

*Indicates UAH measurement on STS-8. Other values are from tabulations of others' data by JSC and LeRC.
**Error not quoted, may be 10 to 20 percent.
†Erosion yields for LDEF are based on a preliminary fluence of 9.0×10^{21} atoms cm^{-2}.

The comparison in data in the case of Kapton® is particularly noteworthy because of the large number of reactivity measurements that have been reported from STS-8 and elsewhere (though not by our group). The details of the UAH LDEF Kapton® measurement are reported elsewhere (ref. 4). This value $(2.89 \pm 0.06) \times 10^{-24}$ cm^3 $atom^{-1}$ is within 3 percent of the normally quoted value of 3.0 based on many measurements. The reactivity of Kapton® is usually quoted without errors, but these might reasonably be about ±10 percent. It is interesting to note that the silicone contamination known to be present on LDEF (and indeed on all shuttle-borne vehicles) does not seem to affect the linearity of the erosion. Perhaps the silicones aggregate upon adsorption or oxidation, or perhaps adsorption is low on these materials. It is, however, well known that if a continuous film of SiO_2 is actually formed, such a film is very effective in preventing oxidation by fast AO.

The fluorinated polymer flown on A0114 was a commercial grade bulk PTFE. The measured rate of $(0.37 \pm 0.06) \times 10^{-24}$ cm^3 $atom^{-1}$ is within the range of reported prior values for PTFE and FEP at lower fluences.

Our value for polyethylene from LDEF is a little higher than the range of values reported by others from STS-8. (We did not include polyethylene on our STS-8 experiment). However, the values are still within experimental errors. Our value for PMMA of $(6.3\pm0.3)\times10^{-24}$ cm^3 $atom^{-1}$ is higher than our own STS-8 value (4.91) and considerably higher than the tabulated values of others. In the case of polystyrene (which we did not fly on STS-8), the difference is even greater from the reported values of others. These other values were obtained by weighing, a technique which underestimates the erosion rate if nonerodible contamination is present.

SUMMARY AND CONCLUSIONS

In general, agreement is good between erosion rates or reactivities obtained from the LDEF experiment AO114 and prior flight data obtained at much lower mission fluences. Agreement is particularly satisfactory in the case of Kapton®, for which the prior data base is large and which is often used as a reference material for comparing erosion rates obtained in terrestrial simulators. Within experimental errors, LDEF and STS-8 reactivities are also in good agreement for PTFE, polyethylene, PMMA (Lucite) (our values), and pyrolytic polycrystalline graphite. Our LDEF value for PMMA and polystyrene is about twice that of earlier data at lower fluences obtained by weighing. The value for HOPG or "single-crystal" graphite obtained from LDEF appears high, but we note that there was only one small sample of this material available.

Polymers consisting only of C, H, O, and N show reactivities which are both independent of fluence and remarkably similar to each other despite great differences in chemical structure. Low reactivities are exhibited by polymers (e.g., graphite, PTFE) for which the H-abstraction process by fast oxygen is not possible.

On the other hand, reactivities higher than average are shown by materials like PMMA, which is known to depolymerize, or "unzip" readily upon heating, and by CR-39 (ref. 1) which has a high oxygen content to begin with.

Erosion measurements by stylus profilometry of these highly erodible materials does not appear to be affected by surface silicone contamination occurring during shuttle flights.

REFERENCES

1. Peters, P.N., Gregory, J.C., and Swann, J.: "Effects of 5 eV Atomic Oxygen Exposure on Space Optics." Applied Optics, vol. 25, 1986, p. 1290.

2. de Rooij, A.: "The Oxidation of Silver by Atomic Oxygen." ESA Journal, vol. 13, 1989, p. 363.

3. Gregory, J.C., and Peters, P.N.: "Reaction of 5eV Oxygen Atoms with Polymeric and Carbon Surfaces in Earth Orbit." American Chemical Society, Polymer Preprints, vol. 28, No. 2, 1987, p. 459.

4. Gregory, J.C., Leger, L.J., Koontz, S.C., and Visentine, J.: "Effects of Long Term Exposure of Polymide Films to the Space Environment," in preparation.

a) Sample C9H-12 Polystyrene.

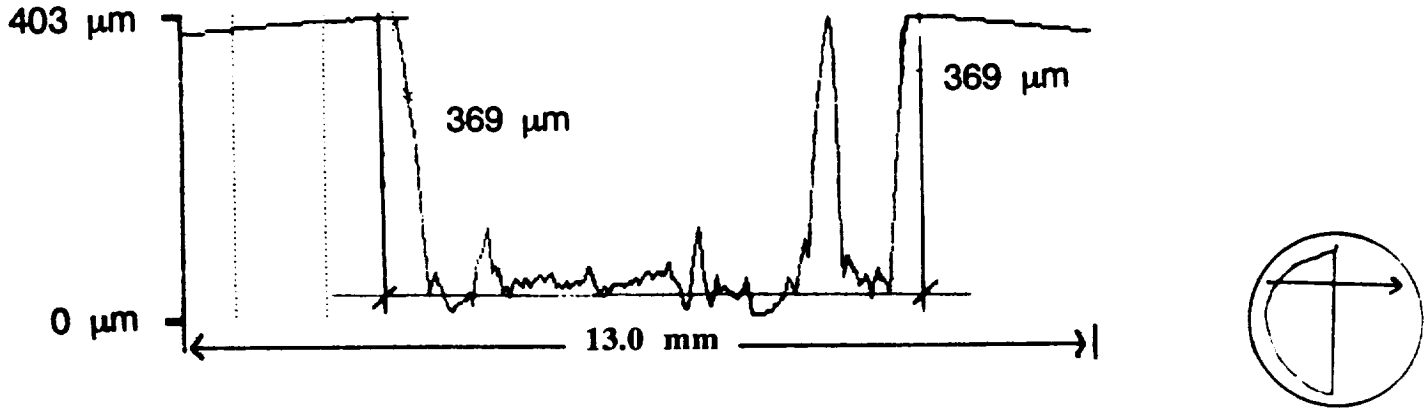

b) Sample C9-47 Polystyrene.

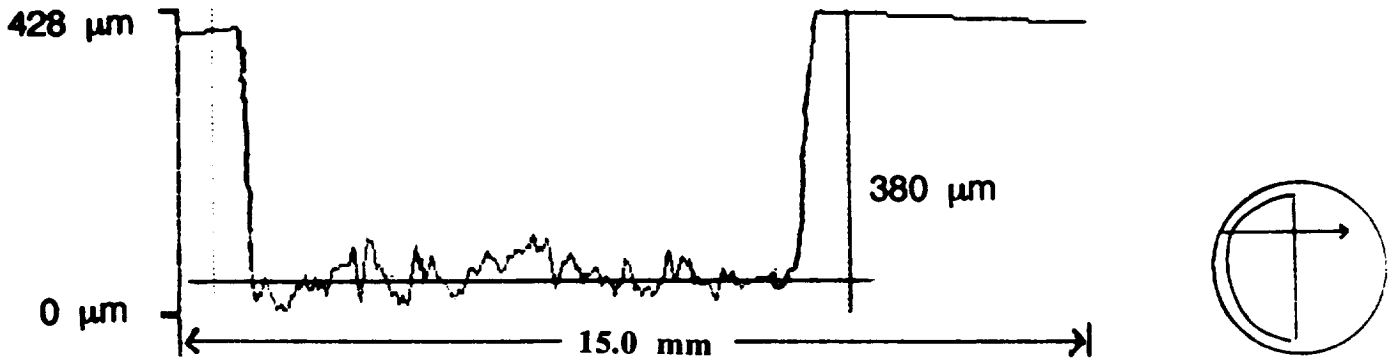

Figure 1. Taylor-Hobson Talysurf profilometry scans of two polystyrene solid samples exposed on the C0 leading surface of LDEF (experiment AO114).

The diagram to the right of each scan shows the physical location of the trace across the 1-in samples. The inverted D-shaped portion of the sample was that exposed to fast oxygen atoms, while the surrounding portion was protected with a mask. Each horizontal scan is about 1/2 inch in length. The different vertical scale should be noted. In spite of considerable roughness induced after prolonged etching, repeated scans in different portions of these samples yield an etch value reproducible to about 5 percent.

ENVIRONMENTAL EFFECTS ON OPTICAL ELEMENTS AND MATERIALS

IMPACT OF LDEF PHOTOVOLTAIC EXPERIMENT FINDINGS UPON SPACECRAFT SOLAR ARRAY DESIGN AND DEVELOPMENT REQUIREMENTS

Leighton E. Young
NASA Marshall Space Flight Center
Marshall Space Flight Center, AL 35812
Phone: 205/544-0707, Fax: 205/544-5847

SUMMARY

Photovoltaic cells (solar cells) and other solar array materials were flown in a variety of locations on the Long Duration Exposure Facility (LDEF). With respect to the predicted leading edge, solar array experiments were located at 0° (row 9), 30° (row 8), and 180° (row 3). Postflight estimates of location of the experiments with respect to the velocity vector add 8.1° to these values. Experiments were also located on the Earth end of the LDEF longitudinal axis. Types and magnitudes of detrimental effects differ between the locations with some commonality. Postflight evaluation of the solar array experiments reveal that some components/materials are very resistant to the environment to which they were exposed while others need protection, modification, or replacement. Interaction of materials with atomic oxygen (AO), as an area of major importance, was dramatically demonstrated by LDEF results. Information gained from the LDEF flight allows array developers to set new requirements for on-going and future technology and flight component development.

INTRODUCTION

Emphasis in this paper is placed on the experiments for which the author was directly responsible. However, where appropriate, references to other LDEF experimenters' results will be made. In particular, the Marshall Space Flight Center (MSFC) portion of the Solar Array Materials Passive LDEF Experiment (SAMPLE-A0171) and the MSFC portion of the Advanced Photovoltaic Experiment (APEX-S0014) will be discussed. SAMPLE was located 30° off the LDEF leading edge. APEX was located on the leading edge.

The longer than planned (5.8 years versus 1 year) LDEF flight provided an environment that caused considerable change to most experiments. That environment, derived from references 1 and 2, is summarized in Table I. Figure 1 is a preflight picture of SAMPLE. Figure 2 is a picture of SAMPLE taken by a shuttle crew member at the time of retrieval. Considerable damage and contamination can be seen in Figure 2. The MSFC solar cell experiments can be seen in Figure 1 as 4 modules and 5 single cells on one of the SAMPLE plates. The descriptions of these experiments are given in Figure 3. A top-to-bottom assembly sketch of the MSFC SAMPLE solar cell test articles is given in Figure 4. Table II describes the cells and coverslides that are used on MSFC SAMPLE and APEX experiments. All of these experiments were built for MSFC by the Lockheed Missiles and Space Company (LMSC).

Two single-cell concentrator assemblies were also tested on APEX for MSFC. These assemblies, identified as Concentrators 1 and 2, utilized a cell/coverslide stack mounted between 2 planar reflectors at 60° to the cell plane. This arrangement provides an ideal concentration ratio of two (2/1). The reflector

material was 1,200 Å of aluminum deposited on 1.0-mil Kapton and 1.0-mil Mylar film for Concentrators 1 and 2, respectively. The cell and coverslide are described under the APEX column in Table II. The objective of these experiments was to determine how well the materials selected as reflectors would perform in the actual outer space solar spectrum, i.e., what is the effective concentration ratio for solar arrays which use this configuration and these materials in space?

VISUAL OBSERVATIONS

Atomic Oxygen Interaction Effects

At first observation, the most striking changes to materials resulted from interactions with AO. Erosion of polymeric (Kapton) substrates on the SAMPLE experiments resulted in loss of two out of the four MSFC multicell test articles (modules) to space (see Fig. 2). Module 2 (Fig. 3) was missing upon shuttle rendezvous with LDEF. Module 3 drifted away upon grapple with the shuttle arm. Module 5 (Fig. 5) had lost structural attachment at three out of four points and was recovered from the floor of the shuttle cargo bay when LDEF was removed at Kennedy Space Center. The MSFC single-cell test articles (Cell 6 through Cell 9) in Figure 3 also showed considerable erosion to their Kapton substrates. Some parts of these substrates showed less erosion than others, apparently as a result of shading from the AO flux offered by adjacent test articles.

Exposed silver metalization showed differing effects of AO interactions depending upon application. SAMPLE cell "Cell 6," which was flown without a coverslide, leaving its silver gridlines exposed to the AO flux, exhibited oxidation of grid lines but no noticeable erosion. Removal of the oxide layer revealed that it composed only about 10 percent of the gridline thickness. Some cells on Module 5 exhibited considerable erosion (Fig. 6) of the silver metalization that wraps the front side electrical connections of the solar cell to the cell rear surface. This erosion manifests itself in severe electrical performance degradation, to be discussed later in this paper. APEX cells B32 to B35, which had polymeric cover materials, showed differing oxidation effects. Cells B32 and B33, which employed a 1-mil silicone (Dow-Corning 93-500) protective cover had gridlines that were still bright even in areas where the cover layer had been peeled from the cell. Cells B34 and B35, which had cast fluorinated ethylene propylene (FEP-LMSC Spraylon) covers showed apparent oxidation of the gridlines with no observable cover peeling. Considerable cracking of the Spraylon covers was observed under 32× magnification. Differences in the level and type of AO interactions with silver in applications which are similar must be attributed to synergistic effects.

Postflight visual inspections of the MSFC concentrator modules revealed discoloration in S-glass epoxy solar cell substrates, wire insulation, and wire staking adhesives. The most striking damage occurred in the aluminized reflector film as a result of AO attack upon the polyimide substrates. One reflector side was missing on Concentrator 1 which employed the aluminized 1-mil Kapton as the reflector material. The other side had become loose at three out of four attachment points and was severely distorted and torn. Concentrator 2 with the aluminized 1-mil Mylar was in about the same condition with two of four attachment points detached on each reflector and the reflector material also distorted and torn. The aluminum layer for both concentrators still appeared bright and shiny. The scenario for these failures is not readily apparent since the aluminum side of the reflectors faces outward into the velocity direction. It appears that AO could interact with the polymers only by AO bouncing off adjacent structures and/or penetration through pin holes in the aluminum reflective layer. Study of electrical

performance data taken by the APEX recorder indicates that reflector material failure probably occurred after APEX quit taking reliable data (328 days).

Micrometeorite/Space Debris Effects

Micrometeorite/space debris craters were observable on MSFC SAMPLE solar cells, under 25× magnification, ranging from very small up to approximately 100 microns (three each). Density of impacts was calculated to be 0.135 per square centimeter (cm). Data reported by Paula Stella in reference 4 were consistent at 0.148 impacts per square cm. One of the largest impacts to the MSFC SAMPLE experiments caused a crack diagonally across one of the two 0.002-in microsheet coverslides on Module 4. The other two large craters were caused by impacts to the rear side of Module 5. The particles penetrated the Kapton substrate causing craters in two cells (PC1L and PC2R) that left their signature at the front surface of the cells (cell/coverslide interface). Figure 7 is a picture taken at 100× by an optical camera of the front surface of cell PC1L. A crater made by impact of a particle on the rear surface of cell PC2R on Module 5 is shown in Figure 8. The impacting particle had to first penetrate the Kapton that composes the cell substrate before impacting the cell. The crater in PC1L appeared very similar, causing about the same level of visual damage. Looking at Figure 7, it is obvious that impact energy causing the crater also caused cleavage along crystal planes in the vicinity of the impact. This type of damage has to result in some level of electrical performance degradation which will be discussed later in the report.

Cell to Interconnect Bonding

Solar cell to solar cell interconnect bonds on the MSFC SAMPLE test articles were made by parallel-gap welding of the rolled annealed copper interconnects to the silver metalization on the rear surface of the cells. All cells had wrap-around contacts so that both bonds could be made on the same side of the cells (Fig. 4). With the interconnects an integral part of the cell substrate, this approach simplifies manufacturing processes. The bonds were subjected to approximately 32,000 thermal cycles within the range –85 °C to +80 °C. There were no failed bonds found on any of the test articles. Pull tests to separate the cell from the interconnect resulted in yield in the copper interconnect or divoting in the solar cell. Previous ground testing of the same technology for over 50,000 thermal cycles in a thermal vacuum chamber at the MSFC provided the same results.

Solar Cell Coverslides

Conventional (glass) coverslides as described in Figure 3 and Table II were flown as part of the solar cell assemblies on the MSFC SAMPLE experiments. The APEX contained MSFC provided cells with conventional and polymer covers as described in Table II. Comparing the postflight electrical performance of the MSFC SAMPLE cells Cell 6 through 10 (C6 through C10 in Figure 9), it can be observed that conventional covers provided considerable protection against the space environment. The extra degradation experienced by Cell 6 (no coverslide) can be attributed largely to the proton/electron radiation environment. Postflight visual (no magnification) comparison of Cell 6 antireflective coating with the antireflective coating of Cell PC1L with its coverslide removed did not reveal any differences.

Reference 3 reports contamination on solar cell coverglasses flown on LDEF leading and trailing edges with the higher degree of contamination being found on the trailing edge. Evaluation of MSFC

test articles flown on SAMPLE and APEX confirm that contamination layers exist but electrical performance degradation from contamination was not discernible in MSFC illumination testing of coverglass/solar cell assemblies. Reference 3 also reports changes in coverglass magnesium fluoride antireflective coatings. Early tests and evaluations at MSFC confirm changes but work remains to be performed before the changes can be properly characterized. Results of MSFC coverglass evaluations will be reported in a later report.

ELECTRICAL PERFORMANCE

MSFC SAMPLE Photovoltaic Test Articles

Figure 3 describes the layout and characteristics of the MSFC SAMPLE test articles. Module 5, the only SAMPLE 12 cell module not lost to space, was first illumination tested as a module showing approximately 32-percent degradation in its maximum power capability from the preflight value. It was then dissected into individual cells (PC1L, PC2L, ..., PC4R in Fig. 9), and performance curves of the individual cells were taken under a flash solar simulator. Degradation in the maximum power point power (PMP) of the individual cells ranged from 4.6 to 80 percent (Fig. 9). Although not visually discernible, it was originally thought that the high electrical performance degradation in Module 5 must have resulted from its fall to the shuttle cargo bay since test articles that stayed in place exhibited much lower degradation. Current/voltage (I/V) curves indicated a dramatic increase in series resistance of the poorly performing cells. Figure 10 shows I/V curves for the three highly degraded and the least degraded cells from Module 5. There were also slight indications of decreased cell shunt resistance in some Module 5 cells. Low power optical inspections did not reveal any clues as to the cause of the increased series resistance. However, the Kapton module substrate had been eroded to the extent that holes/cracks were made that would allow AO flux to impinge upon the silver back-surface metalization and wraparound contacts. It was postulated that interaction of the AO with the wraparounds could cause erosion which would result in increased series resistance. Coverslides were removed on four of the most degraded cells, and scanning electron microscope images were made on the wraparounds to confirm this postulate. These images showed a high percentage loss of material in the wraparound metalization (Fig. 6). Electrical resistance measurements were taken across the wraparound and found to be high. Cell PC2C (PMP degraded 80 percent) resistance measured 2.78 ohms. A resistance test on the wraparound of the same type cell that had not flown showed 0.007 ohms. Bridging of the wraparounds with a small wire soldered on the front and rear surfaces restored good performance on the cells that were evaluated in this manner (see Fig. 11). Another observation of data from these tests is that degradation is proportional to the series resistance increase, further indicating that it is the major contributor to the degradation in the highly degraded cells. Modern cells with all contacts on the rear surface of the cells would not have this problem because the wraparound would be replaced by a wrap-through or be protected with a coating. A comparison of electrical performance of cells with impact craters (PC1L and PC2R) with that of cells without craters (Cell 7 to Cell 10) in Fig. 9, indicates that the crater damage could cause 2- to 4-percent degradation in PMP. However, since these cells have not been evaluated in terms of other performance degradation mechanisms, these values can only be taken qualitatively, i.e., craters up to 100 micron in diameter cause relatively small performance degradation. Electrical performance degradation caused by small craters on the cell coverslide was not discernible in measurement.

Cells 6 through 10 were flown on SAMPLE to determine the space environmental effects upon different types of coverglasses and the resulting changes in electrical performance of the cell/coverglass stack. Changes in the coverglass light transmission qualities from space environmental

exposure between Cells 7 through 10 were not discernible from electrical performance measurements. The 20.7-percent degradation in PMP experienced by Cell 6 (no cover) can be attributed mostly to charged particle radiation damage which was equivalent to approximately 5E14 1.0 MeV (million electron volts) electrons per square centimeter.

MSFC APEX Photovoltaic Test Articles

Comparison of pre- and postflight test data taken on the MSFC APEX experiments revealed that the preflight data taken on contract to the Lewis Research Center (LeRC) was obviously in error. The average difference between MSFC and LeRC postflight data was slightly less than 1 percent. For cells with conventional coverslides that provide a high degree of cell protection against the charged particle environment, pre- and postflight open circuit voltage (VOC) data agreed within 1 percent. However, for these cells, preflight short circuit current (ISC) values ranged from 5 to 9 percent below postflight values, indicating that preflight values were in error since any change outside experimental error should be performance degradation. In addition, preflight fill factor [(ISC x VOC)/PMP] values were less than postflight values, which indicates an undesirable series resistance in electrical current instrumentation used in preflight testing. Comparison of the preflight I/V curves for the APEX cells with the preflight curves of SAMPLE cells reveals that the APEX cells were the poorer performer, having lower ISC and VOC.

Figure 12 shows the pre- and postflight maximum power point (PMP) data taken for the MSFC solar cells flown on APEX. The postflight data shown in Figure 12 are the average of the MSFC and LeRC data. Three observations are readily made from this figure: (1) relative performance between cells was the same for pre- and postflight data; (2) except for B35, unadjusted preflight measurements of PMP were lower than postflight of all the cells; and (3) cell assemblies with polymer covers (B32 to B35) degraded more than assemblies with conventional covers. In order to obtain degradation data for the cells with polymer covers, it was assumed that performance of cells with conventional covers (B36 to B57) did not measurably degrade. Using this assumption, postflight data could be used as preflight data for these cells, allowing correction factors to be developed for the actual preflight data. This is a reasonable assumption to use since the configuration of APEX had the cells recessed in aluminum structure, providing protection over most of the 4 pi solid angle against charged particle radiation, micrometeorite space debris impact, and ultraviolet radiation. Preliminary analyses of APEX flight data provided by LeRC reinforces this assumption about B36 to B57 by giving flight data over the first 328 days of LDEF flight that agrees closely with MSFC and LeRC postflight data. Using this approach, correction factors were developed and applied to cells B32 to B35 preflight data to determine their electrical performance degradation. The following observations were made for the polymer-covered cells: (1) cells B32 and B33, which used Dow Corning 93-500 adhesive as protective covers, underwent mostly current degradation. Adhesive darkening is the most probable major contributor. (2) Cells B34 and B35, which had LMSC FEP Spraylon protective layers, degraded in VOC and fill-factor; an indication of decreased shunt resistance. The cause of this degradation was not determined. In reference 4, data are also reported on solar cells with polymer covers that were flown on LDEF as part of the JPL SAMPLE experiment. Degradation (ISC) reported therein was substantially higher than that observed for the MSFC cells on APEX. Reference 4 reports ISC degradation values for cells with silicone and FEP Teflon covers averaging 13 and 22 percent, respectively. These higher values can be justified to an undetermined extent by the fact that SAMPLE cells were not recessed in structure as were APEX cells, thereby allowing them to be exposed to a harsher ultraviolet and charged-particle radiation environment. The SAMPLE environment would more closely represent the flight solar array environment supporting the

higher degradation values for polymer covers. In either case, polymer covers for typical space solar array applications are not presently adequate, requiring further development and demonstration.

Electrical performance evaluations of the concentrator assemblies flown on APEX for MSFC are in the preliminary stage. Scatter in flight data and lack of preflight data has made determination of the effective concentration ratio difficult. In order to obtain preliminary values, the concentrator cells were illumination tested in the laboratory after the flight without the reflector assemblies. The short circuit currents (ISC) from these tests were then divided into the ISC from flight data. Results gave a concentration ratio of 1.57 for Concentrator 1 and 1.86 for Concentrator 2. This large difference was not expected and is still in question. However, the results obtained from flight supports the viability of the use of low-concentration solar arrays in space.

CONCLUSIONS

The LDEF flight dramatically demonstrated what can happen to a spacecraft solar array when it is improperly designed for the space environment. Atomic oxygen was especially degrading to solar cell experiments on the SAMPLE and APEX because they were exposed to several times the AO fluence to which they were designed. AO was the most degrading environment to the solar cell experiments, taking its toll on solar cell contact metalization, cover glass coatings, and Kapton substrates. Many of the processes used in the development of these experiments worked very well. Solar cells performed to expectations where they were adequately protected against the environment. Adhesives used to attach glass protective covers to the cells and the cells to the substrates worked very well. There were no failures in the copper interconnects and the parallel-gap welds that bond the interconnect to the cell metalization. Glass cell covers experienced damage to their anti-reflective coating but provided good protection against micrometeorite/space debris and charged particle radiation. However, if polymer-type covers which may be attractive from the cost standpoint, are to replace conventional covers, they must undergo further development.

Evaluation of LDEF solar cell experiment results facilitates the following recommendations for ongoing and future solar array development:

1. Protect solar array components against the AO environment. Where possible, select materials that do not interact strongly with AO. If AO resistant materials are not available, use protective coatings. Replacement of solar cell silver metalization, which has been used extensively in conventional space solar arrays, with copper metalization, should receive attention. This approach not only introduces a less AO interactive material, but could contribute to lower array costs since copper is substantially less expensive than silver.

2. Provide appropriate protection against micrometeorites and space debris. Although LDEF solar cells did not degrade appreciably from micrometeorite/space debris impact, the potential for performance degradation from debris impact damage requires that protection to the front and rear cell surfaces be provided. On the SAMPLE experiment, the protective glass covers provided sufficient protection to the cell front surface, but the thin Kapton substrate on SAMPLE Module 5 allowed the larger particles to penetrate the substrate and cause crater damage to the cells back surface. The trend to reduce the weight of solar arrays by reduction of structure should not neglect protection against this environment.

3. Continue to develop higher performance solar array component and systems technology. The space station requires a high power, light weight, long life solar array. Other spacecraft, while not requiring such high power, require solar arrays that are light weight and have long life. Gallium arsenide (GaAs) cells are being made and used with efficiencies greater than 18 percent. They have lower power performance degradation with temperature and degrade less under charged particle irradiation than conventional silicon solar cells. Although GaAs cells presently cost more per watt as delivered from the manufacturer, their characteristics make GaAs arrays more competitive with silicon arrays when cost per watt-hour for long life missions are taken into consideration. Knowledge gained from LDEF with respect to materials utilization can be used to support development of long life, high performance planar and concentrator arrays. Low to medium concentration concentrator arrays are more viable than in the past when considered in terms of GaAs and silicon solar cell technology now available. Concentrator arrays potentially offer lower costs since the concept trades off use of high cost solar cells against more complex design but lower cost concentrator assembly materials (i.e., reflector materials). For these reasons, future solar array component and systems technology development should address concentrator arrays along with planar arrays.

4. Based on the knowledge gained from LDEF about solar arrays in the space environment, improved solar arrays will be developed. Should reflight of an LDEF occur, it undoubtedly should again contain solar array experiments to space prove the new developments. Solar array developers should support reflight of an LDEF.

ACKNOWLEDGMENTS

Sincere appreciation is extended to the following scientists and engineers who contributed substantially toward the development of this report; and also to my supervisors William E. Taylor and Gerald F. Flanagan who extended to me the opportunity and encouragement to perform this intriguing work.

Dr. Ann F. Whitaker (MSFC) – SAMPLE Experiment Co-investigator

Douglas J. Willowby and Douglas W. Alexander (MSFC) – LDEF Solar Cell Performance Evaluations

David P. Nicholas, Dion D. Jones, James E. Coston Jr., Dr. Ilmars Dalins (MSFC) – Microscopic Evaluations of Experiment Components.

Miriam M. Finckenor and Joseph K. Norwood (MSFC) – Materials Surface Evaluations

David Brinker (NASA Lewis Research Center) – APEX Flight Data

REFERENCES

1. Watts, J.W., Parnell, T.A., Derrickson, J.H., Armstrong, T.W., and Benton, E.V.: "Prediction of LDEF Ionizing Radiation Environment." LDEF 69 Months in Space, Part 1, First Post-Retrieval Symposium, NASA CP-3134, February 1992, pages 220–221.

2. Bourassa, R.J., Gillis, J.R., and Rousslang, K.W.: "Atomic Oxygen and Ultraviolet Radiation Mission Total Exposures for LDEF Requirements." LDEF 69 Months in Space, Part 2, First Post-Retrieval Symposium, NASA CP-3134, February 1992, pages 653 and 660.

3. Trumble, T.M.: "Experiment M0003-4 Advanced Solar Cell and Coverglass and Analysis, An Overview." LDEF 69 Months in Space, Part 3, First Post-Retrieval Symposium, NASA CP-3134, February 1992, page 1255.

4. Stella, P.M.: "LEO Effects on Conventional and Unconventional Solar Cell Cover Materials." IEEE Photovoltaics Specialists Conference, October 1991.

Table 1. LDEF environmental factors.

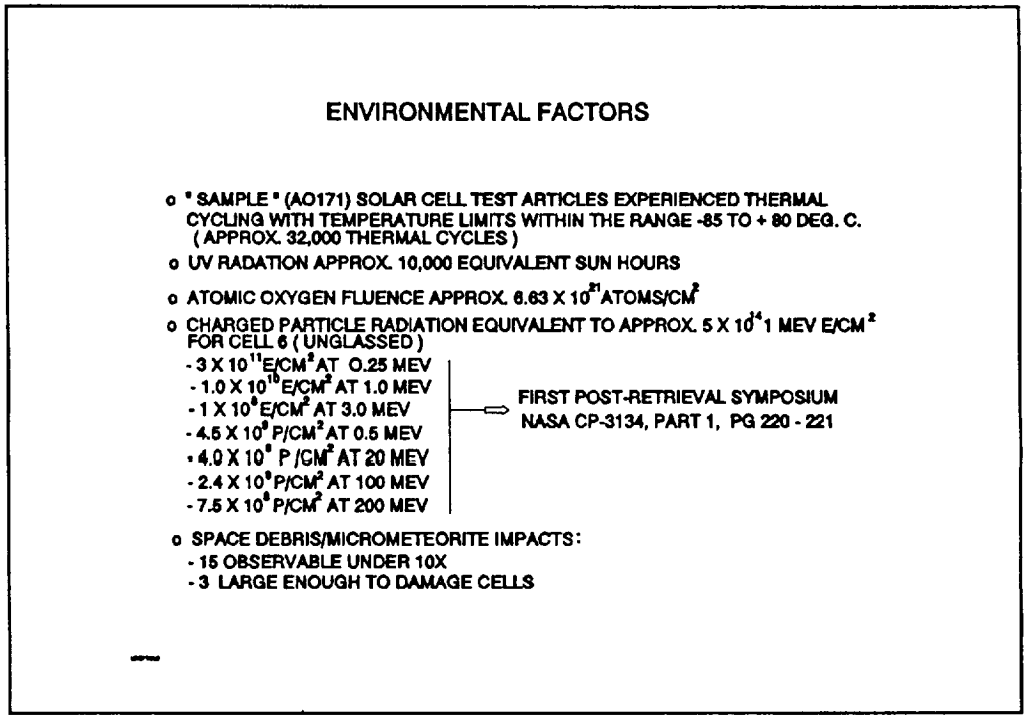

Table 2. Solar cell and coverslide characteristics of MSFC SAMPLE and APEX experiments.

SOLAR CELL CHARACTERISTICS	SAMPLE	APEX
o MANUFACTORER	ASEC	SAME
o TYPE	N ON P, 2 OHM-CM	SAME
o JUNCTION DEPTH	APPROX 0.3 MICRON	SAME
o SURFACE FINISH	UNREPORTED	CHEM ETCHED
o CONTACTS	CVD DIELECTRIC, SIDE WRAP-AROUND	CVD DIELECTRIC, END WRAP-AROUND
o METALIZATION	Ti-Pd-Ag	Cr-Pd-Ag
o CONTACT THICKNESS	4 To 8 MICRON	SAME
o AR COATING	DUAL AR	TANTALUM PENTOXIDE
o BACK SURFACE REFLECTOR	ALUMINUM	NONE
COVERSLIDE TYPES	**SAMPLE**	**APEX**
o NONE	CELL 6	
o DOW CORNING 93-5000		B32, B33
o FEP TEFLON (LMSC SPRAYLON)		B34,B35
o OCLI, 6 MIL, MICROSHEET, ARC & UVF	MODULE 5, CELL 8	
o OCLI, 6 MIL, MICROSHEET, ARC	CELL 7	
o OCLI, 6 MIL, FUSED SILICA (FS), FROSTED, ARC & UVF	CELL 9	
o OCLI, 6MIL, FS, ARC & UVF	CELL 10	B38, B41, CONC'S 1 & 2
o PILKINGTON P. E., 2 MIL, MICROSHEET,	MODULE 4	
o PILKINGTON, 5.5 MIL, CERIA STABILIZED MICROSHEET, ARC		B36, B37

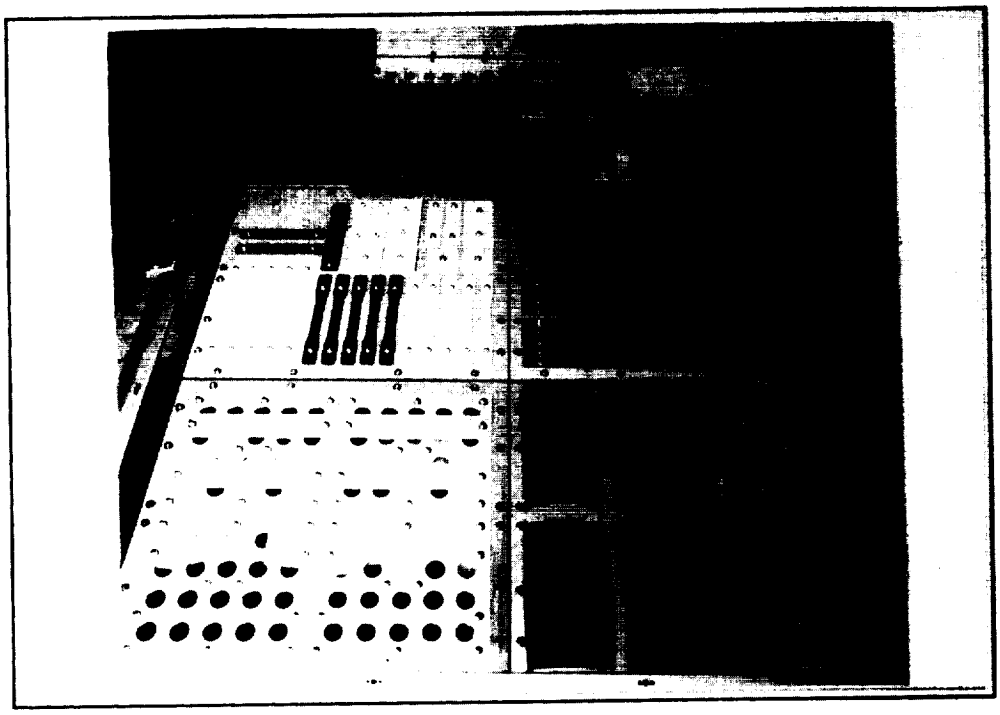

Figure 1. Picture of SAMPLE in laboratory before installation on LDEF.

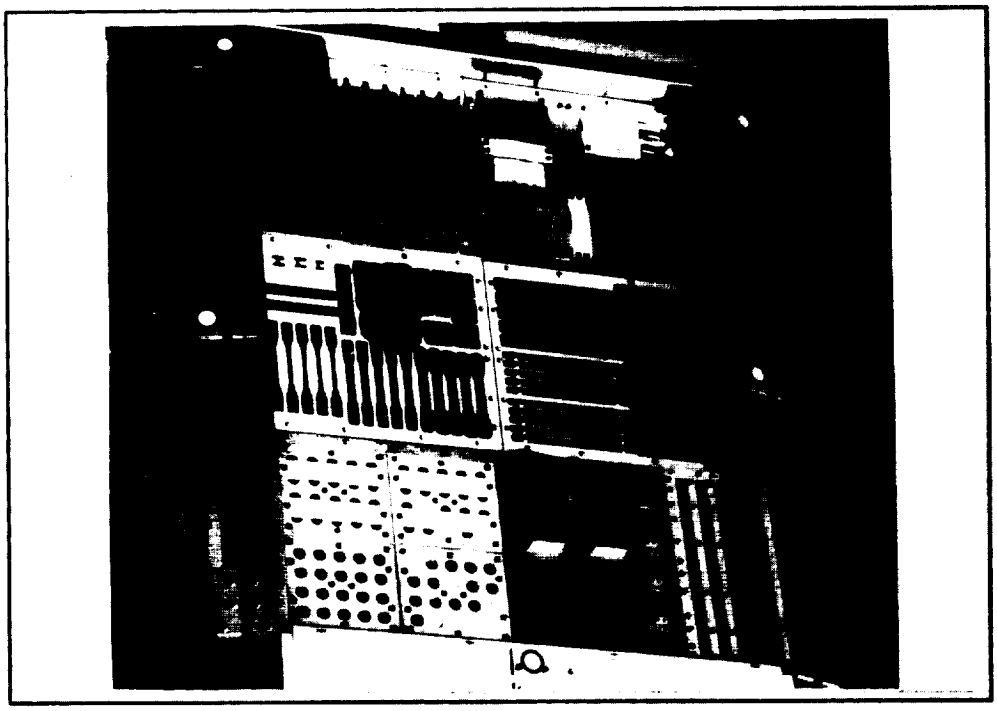

Figure 2. Picture of SAMPLE upon shuttle rendezvous.

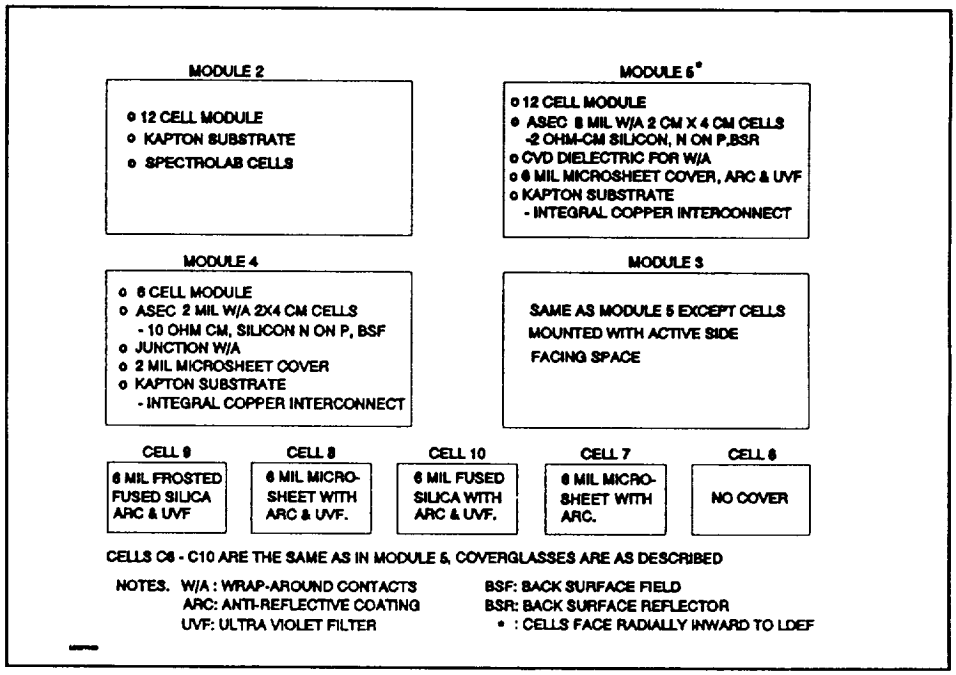

Figure 3. Description of MSFC SAMPLE solar cell test assemblies.

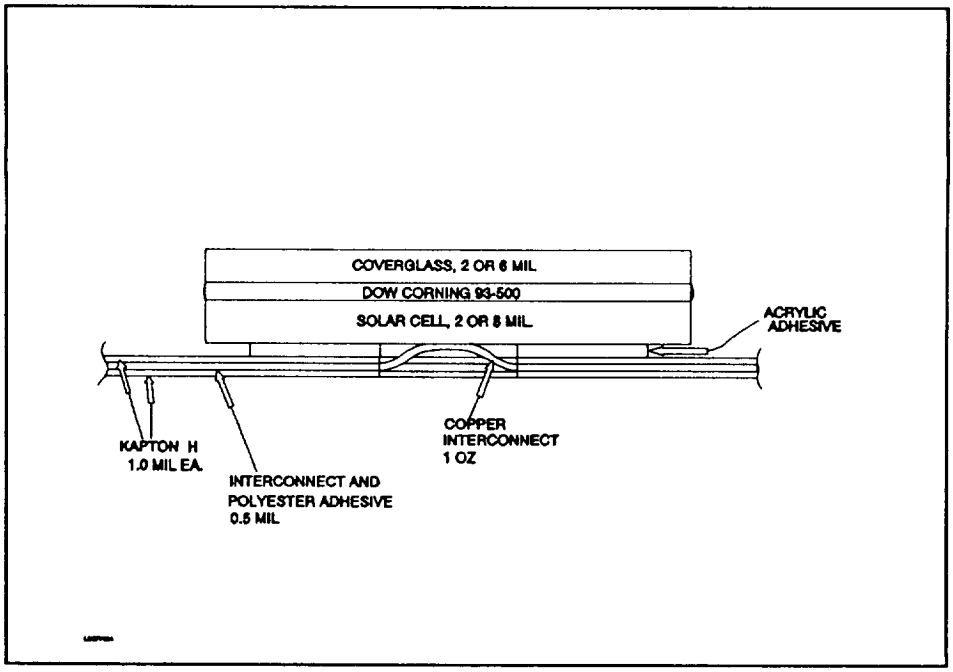

Figure 4. Cross-sectional sketch of MSFC SAMPLE solar cell test assemblies.

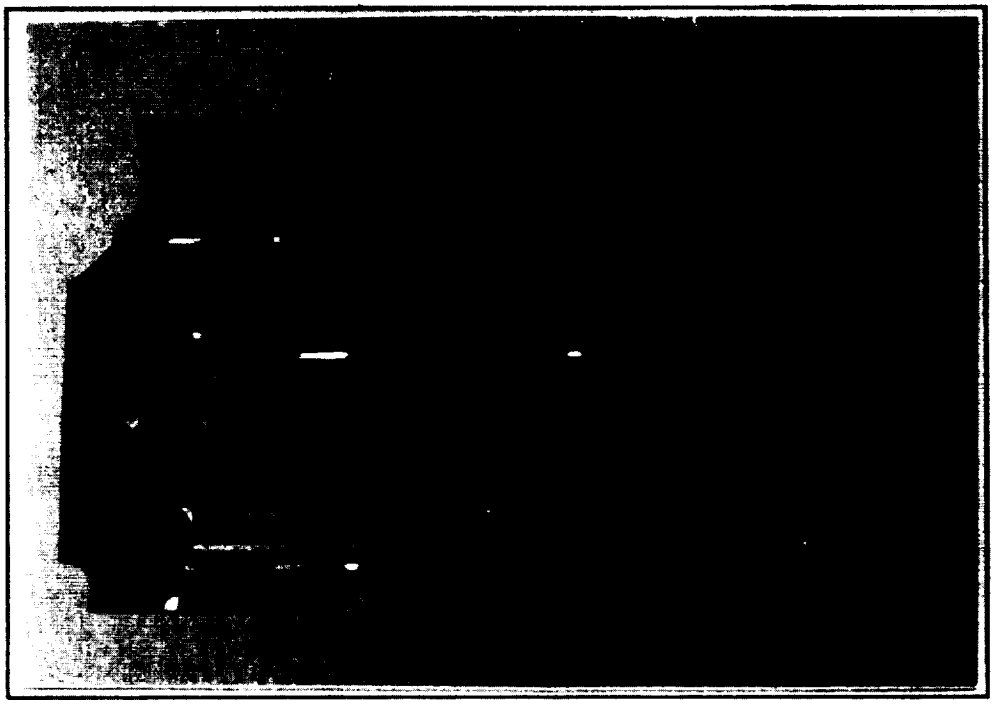

Figure 5. Postflight picture of SAMPLE Module 5 showing AO erosion of Kapton H substrate.

Figure 6. Scanning electron microscope image of SAMPLE solar cell wraparound contact erosion from AO.

Figure 7. Front surface damage to SAMPLE solar cell PC1L from micrometeorite/space debris impact to rear surface.

Figure 8. Scanning electron microscope image of micrometeorite/space debris crater on the rear surface of SAMPLE solar cell PC2R.

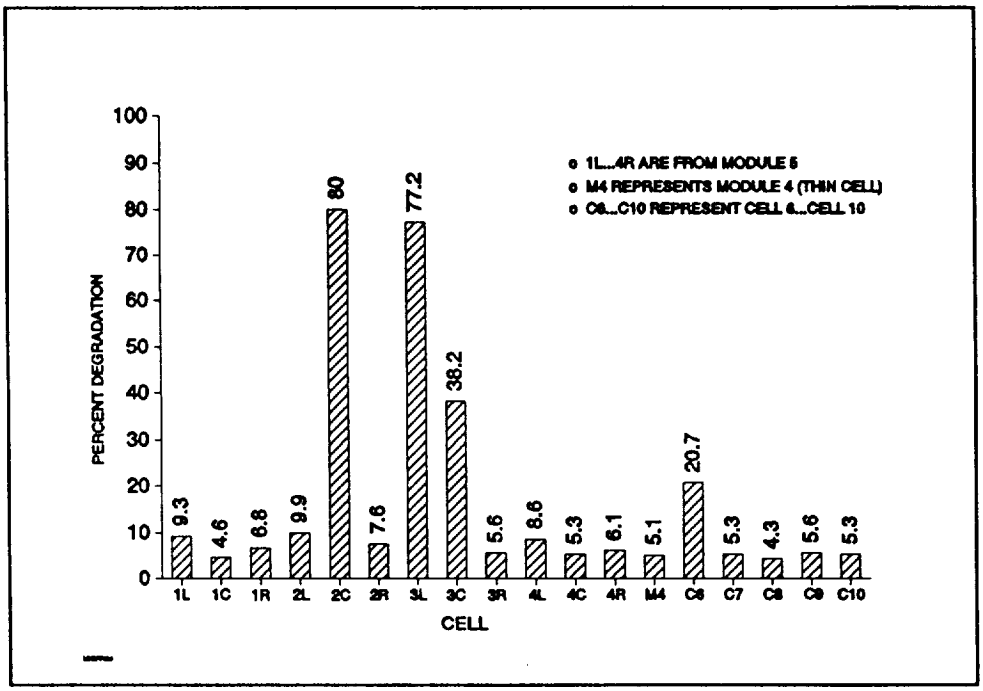

Figure 9. MSFC SAMPLE solar cell maximum power point degradation.

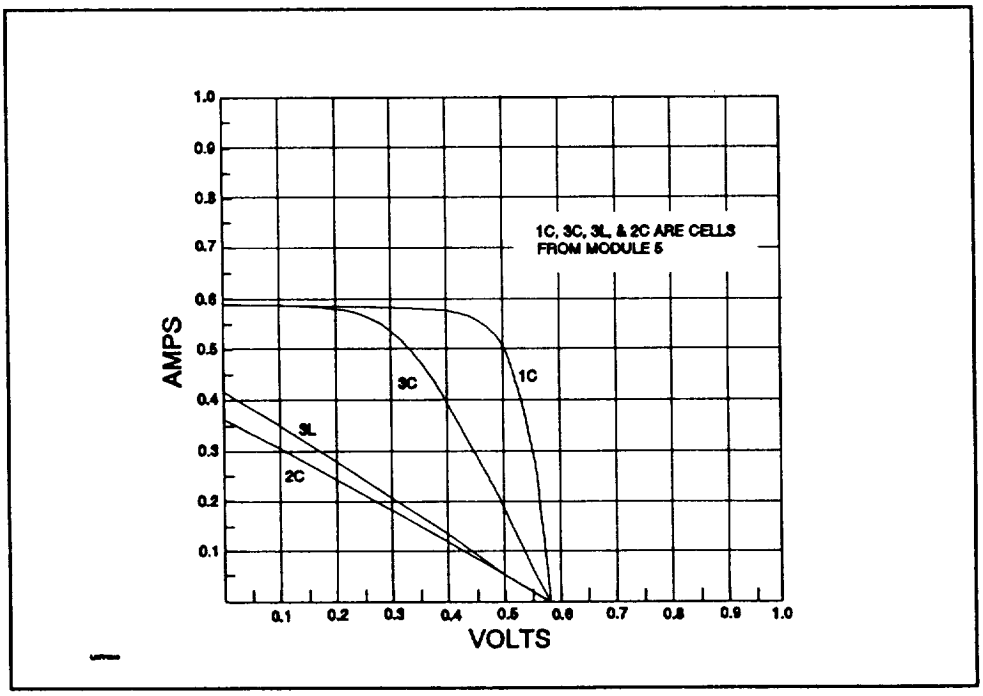

Figure 10. Range of SAMPLE solar cell Module 5 individual cell electrical performance.

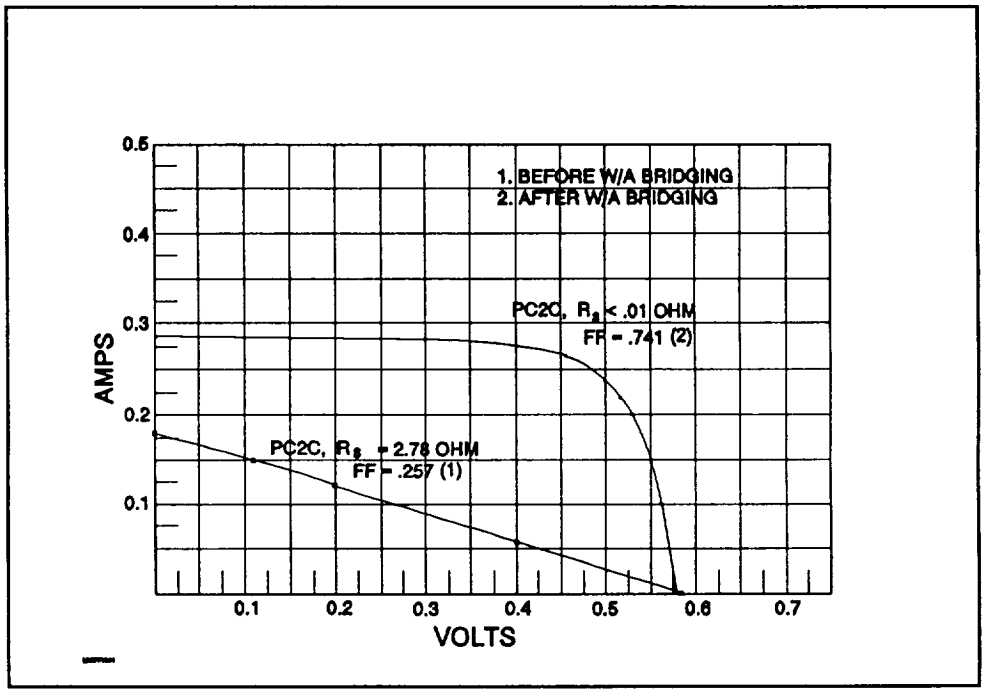

Figure 11. SAMPLE solar cell PC2C series resistance assessment.

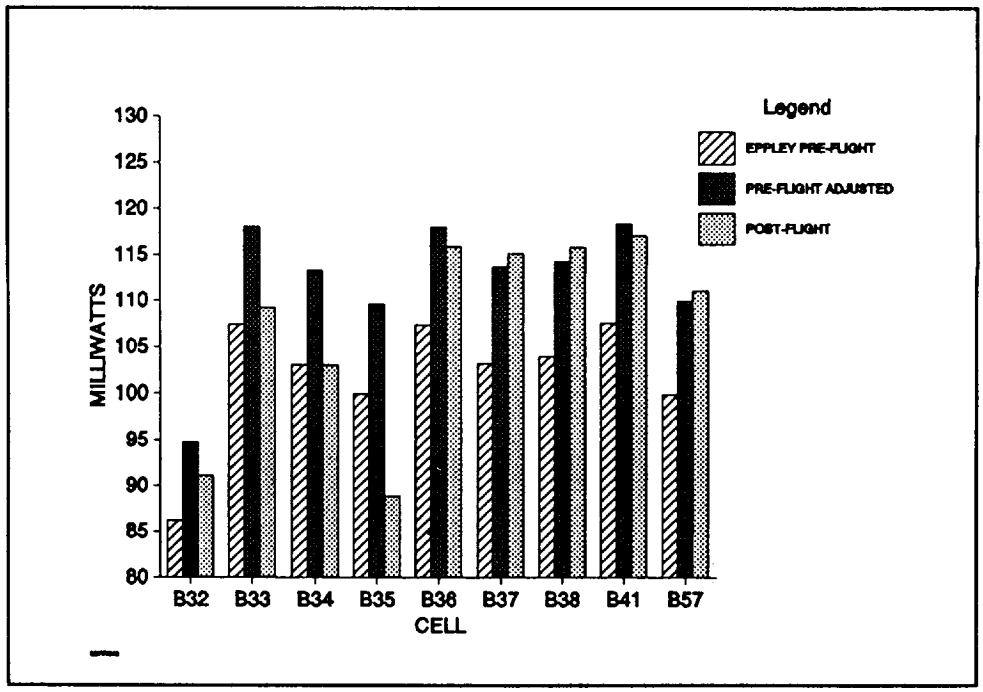

Figure 12. Pre- versus postflight maximum power point performance of APEX MSFC solar cell assemblies.

N94-31029

DEGRADATION OF OPTICAL COMPONENTS IN SPACE

M. D. Blue
Georgia Tech Research Institute
Atlanta, Georgia 30332
Phone: (404) 894-3646 Fax: (404) 894-3628

ABSTRACT

This report concerns two types of optical components: multilayer filters and mirrors, and self-scanned imaging arrays using charge coupled device (CCD) readouts. For the filters and mirrors, contamination produces a strong reduction in transmittance in the ultraviolet spectral region, but has little or no effect in the visible and infrared spectral regions. Soft substrates containing halides are unsatisfactory as windows or substrates. Materials choice for dielectric layers should also reflect such considerations. Best performance is also found for the harder materials. Compaction of the layers and interlayer diffusion causes a blue shift in center wavelength and loss of throughput. For sensors using CCD's, shifts in gate voltage and reductions in transfer efficiency occur. Such effects in CCD's are in accord with expectations of the effects of the radiation dose on the device. Except for optical fiber, degradation of CCD's represents the only ionizing-radiation induced effect on the Long Duration Exposure Facility (LDEF) optical systems components that has been observed.

INTRODUCTION

Several reports covering various aspects of our postrecovery measurements of the set of optical components on the tray prepared by GTRI have already been published (refs. 1–3). Here we wish to provide additional information on two subjects: multilayer filters and mirrors, and self-scanned imaging arrays using CCD readouts.

A review of the reports of other LDEF investigators concerning performance of optical filters and mirrors indicates some common degradation effects in these components. In the first part of this report, we discuss and summarize some of these effects, and attempt to provide some general guidelines. In the following section, we present the results of measurements of the performance of silicon devices forming part of the signal conditioning circuitry for a Pd_2-Si imaging array with a CCD serial readout register. Here, the results are in agreement with a radiation-induced degradation mechanism.

OPTICAL FILTERS AND MIRRORS

Contamination

All trays were coated with a contamination layer (silicates and hydrocarbon compounds) of a thickness which varied with tray location and substrate characteristics. The amount of contamination varied from a few monolayers (ref. 4) to as much as 2 gm/ft^2 from an LDEF end plate scraping (ref. 5). The optical effects of the contamination layer are of interest. Figures 1 to 3, taken from other

LDEF reports, show transmittance in the visible and ultraviolet spectral regions for a Mg-F_2 window (ref. 6), quartz windows (ref. 7), and ultra-low-expansion glass (ref. 8). These figures illustrate the general result that attenuation of radiation is very strong in the ultraviolet region, but drops to much lower values in the visible and infrared regions. Our measurements in the visible region indicated no measurable change in transmittance after cleaning the contamination layer from optical filters (ref. 2). A similar result was reported for the Reading University experiment (ref. 9).

The transmittance of window materials with a contamination layer is similar to the transmittance of substrate materials after irradiation. As an example, Figure 4 shows spectral transmittance of fused quartz after irradiation by neutrons at a temperature of 500 °C (ref. 10).

While the ram-facing surfaces of the LDEF were scrubbed by atomic oxygen affecting material such as metal mirrors, no effects on other optical components caused by atomic oxygen have appeared in NASA reports at this time. Nonetheless, the potential for degradation by atomic oxygen erosion appears to be present.

Materials

The University of Reading experiment contained a group of uncoated substrate materials (ref. 9). The materials were distributed among two locations; near the leading edge and on the Earth-facing end. Comparison of average prelaunch and postrecovery transmittance for these samples indicated no major changes within the accuracy of the spectrometer except for the soft materials KRS-5 and KRS-6 (Tl-Br-I and Tl-Cl-Br respectively). For these soft materials, postrecovery transmittance was irregularly lower.

KRS-5 windows were used on several pyroelectric detectors used in a NASA Langely Research Center LDEF experiment (ref. 11). Postrecovery examination showed nonuniform cloudy (white) or slightly metallic-appearing regions on the front surface of the windows. Transmittance losses ranged from 17 to 50 percent with the larger losses corresponding to regions with greater physical damage. The KRS-5 window on a control detector was unchanged. Surface analysis indicated the presence of silicon (in the form of silicates) on the space-exposed windows with higher concentrations on the regions of least damage, lower concentrations in the regions of highest damage. The conclusion, supported by measurements of the Th:Br ratio at the surface, was that the presence of silicates inhibited the general loss of bromine from the surface.

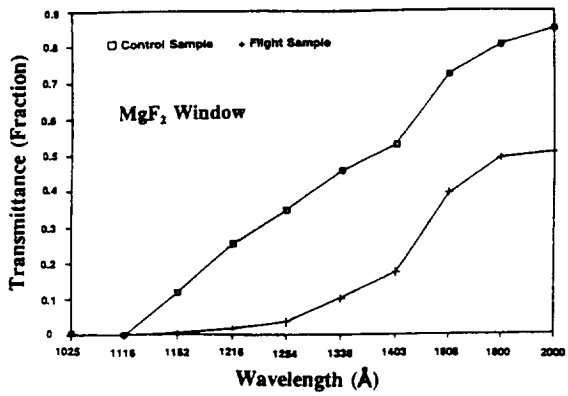

Figure 1. Spectral transmission of a Mg-F_2 window with contamination at the front surface (ref. 5).

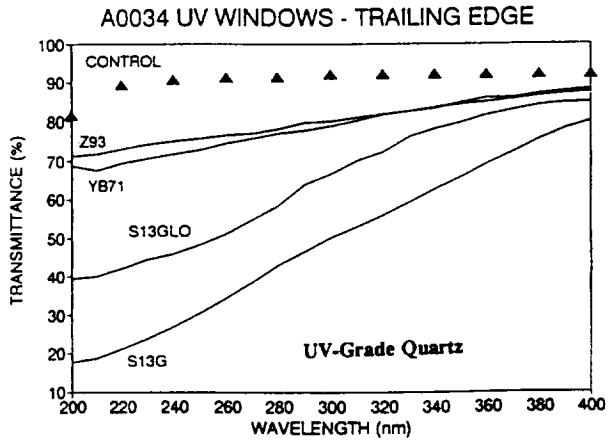

Figure 2. Spectral transmittance of ultraviolet-grade quartz windows from the trailing edge of the LDEF. Contamination produced even greater reductions in transmittance for the leading-edge windows (ref. 6).

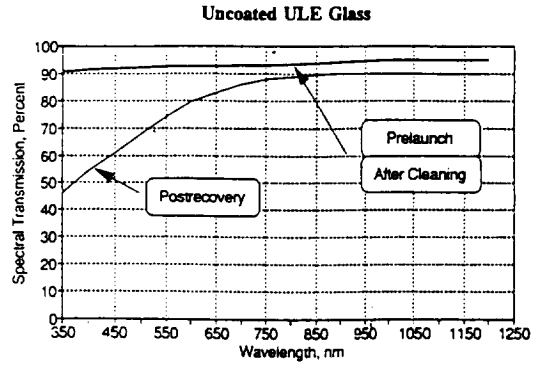

Figure 3. Spectral transmittance for an uncoated ULE-glass sample (ref. 7).

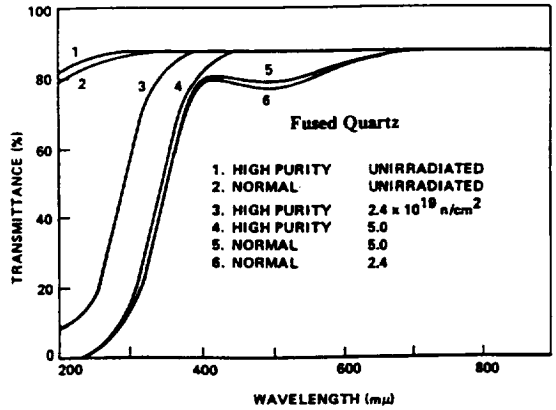

Figure 4. Spectral transmittance of fused quartz irradiated by neutrons at a temperature of 500 °C (ref. 9).

Component Degradation

Several LDEF experiments contained multilayer dielectric filters and mirrors. The common degradation effects included the following:

Small shift of center wavelength toward the blue,
Reduction in peak transmittance,
Disruption in design tolerances,
Soft substrate material degradation.

Figures 5 to 7 show prelaunch and postrecovery transmittance of narrow-band filters from the GTRI (ref. 2), Reading University (ref. 9), and FRECOPA (ref. 12) experiments respectively. In all cases, a small shift of the peak transmittance wavelength in the range of a few nanometers was a typical result for these filters. Even the control filters showed a shift in many cases. The effect is in agreement with the effect of a slight compaction of the deposited layers with time (aging effect). On-orbit temperature cycling may aid in attaining equilibrium more rapidly but the effect should, and does, take place in the control filters as well. For the GTRI filter, Figure 5, the shift in peak transmittance corresponds to a reduction of 1/55 Å in the thickness of a layer. The effect will only be significant for the very narrow-band filters.

Reduction in peak transmittance was a typical result for filters on LDEF. Reductions of about 5 to 10 percent were typical. Degradation of Mg-F_2 was suggested as a possible source of deterioration for the filters in the FRECOPA experiment (ref. 12). A study by Fogdall et al. (ref. 13) was performed to simulate expected degradation effects of ultraviolet and charged particle radiation on multilayer dielectric mirrors at the Boeing Radiation Effects Laboratory. As pointed out by Donovan et al. (ref. 14), the results indicated that anticipated stability of the optical properties varies greatly among different material combinations. Degradation of Zn-S/Th-F_4 mirrors in the Boeing work was suspected as being the result of the reaction of Zn-S with water impurities in the coating. Materials such as Si-O_2, Al_2-O_3, and Si performed well.

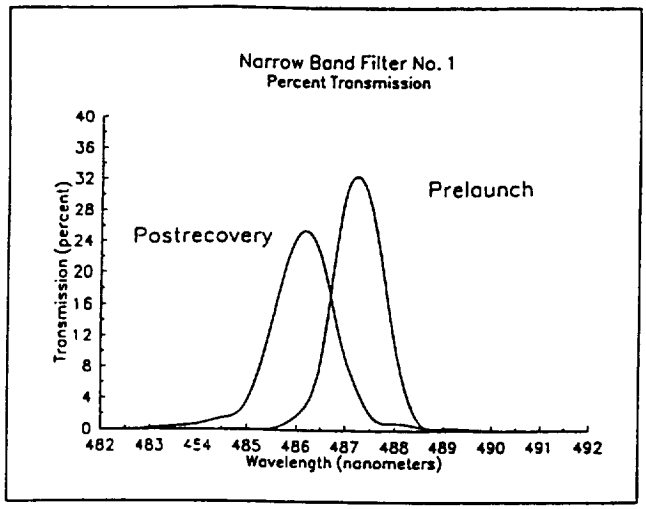

Figure 5. Prelaunch and postrecovery spectral transmittance of a narrow-band filter from the GTRI tray. (ref. 2).

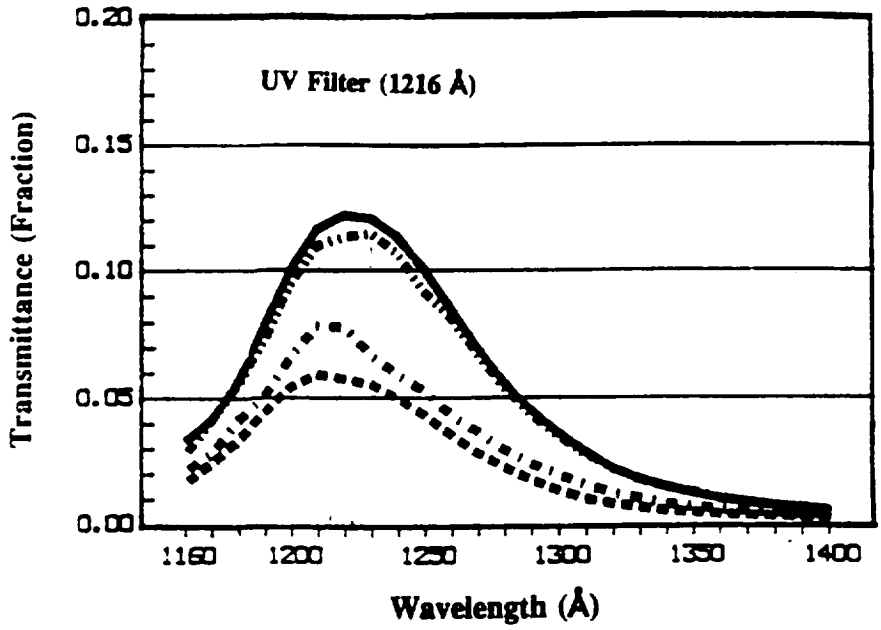

Figure 6. Spectral transmittance of a narrow-band ultraviolet filters before and after Earth orbit. The outer pair of curves refer to a filter exposed directly to space, the inner pair of curves refer to a filter mounted to look inward (ref. 11).

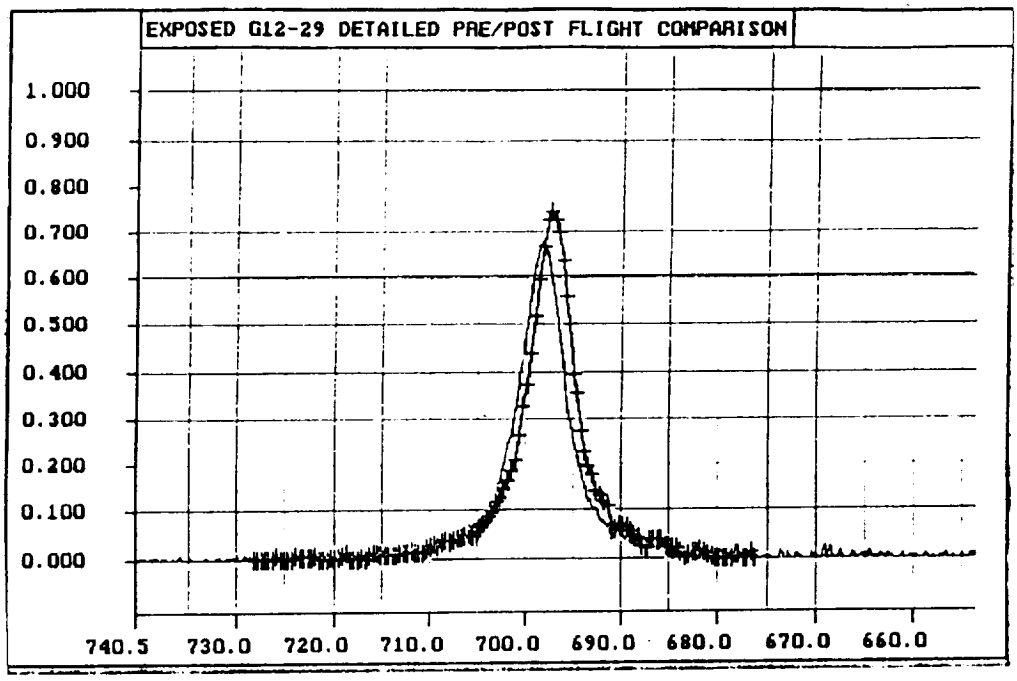

Figure 7. Prelaunch and postrecovery for one of the narrow-band optical filters from the Reading University set (ref. 9).

The GTRI narrow-band filters (i.e., Fig. 5) tended to have a somewhat larger reduction in transmittance than the typical result. These filters were constructed with a cover glass cemented over the dielectric stack for protection. We believe that deterioration of the cement used to attach the cover glass gives rise to additional loss in transmittance.

Again, substrate choice is important. Quartz and ULE glass performed well. Reading University filters using KRS-5 and KRS-6 substrates had much lower transmittance in the infrared region and showed substantial physical degradation such as "delamination of the coatings and/or substrate materials."

CCD PERFORMANCE

Discussion

In the early 1980's, silicon Schottky-barrier detector arrays represented a promising new technology for imaging arrays operating in the near- and mid-infrared spectral region. The potential for this technology is now being largely fulfilled. While normal operating temperatures for these arrays is 77K or lower, degradation effects at ambient temperatures are also of interest, and the devices were not cooled in this experiment. Two different chips were used. The first was an integrated circuit containing process test devices. The second chip contained the Pd_2-Si Schottky-barrier 32 by 64-pixel IRCCD imaging array. The arrays were produced and characterized by the RCA Advanced Technology Laboratories which was later disbanded following the purchase of RCA by GE. The postrecovery characterization of the arrays was carried out by the David Sarnoff Research Center, and their data are discussed in the section. The sample from the LDEF tray and a control sample (prepared from the same wafer as the spaceborne sample) were compared for shift of threshold bias voltage, dark current, and transfer inefficiency.

Ionizing radiation produces three different types of permanent degradation on CCD arrays. First, radiation effects can increase the thermal generation rate of minority carriers which increases the dark current and shortens the storage time of the device. Second, because of a tendency for some charge to be left behind in each transfer step from gate to gate, there is an inherent charge transfer loss in CCD's. This transfer loss or transfer inefficiency is enhanced by radiation and works to degrade image resolution. Finally, irradiation of a CCD causes a shift in the range of bias voltages in the propagation and transfer gates over which satisfactory operation can be obtained.

The major radiation damage mechanism in these devices is the production of positive charge which can be trapped in the Si-O_2 insulator or at the semiconductor-insulator interface. The amount of energy required to create a hole-electron pair in Si-O_2 is 18 ev/pair. Thus, the total effective radiation dose must be adjusted to reflect the lack of pair production by lower energy radiation. However, because of the high energy of the electrons and protons incident on the LDEF, this correction is negligible. For 18 ev/pair, one calculates that 7.6×10^{12} pairs/cm^3 are created per rad (Si) dose (ref. 15).

The devices were mounted on the tray so as to allow backside illumination. Ionizing radiation reached the arrays by passing through the holes in the sunscreen as well as by penetrating the solid aluminum portions of the screen. The total dose for these devices was calculated to be 68 krads (Si)/cm^2. As a result, the maximum possible density of hole-electron pairs created during space exposure would be 5.2×10^{17} pairs/cm^3. Of these, 95 percent would recombine quickly, and most of the defects produced by the remaining 5 percent would be expected to be removed by annealing. A

reasonable estimate is that 1 percent of the total radiation flux results in trapped charge. Thus, 5×10^{15} traps/cm^3 would be expected in the silicon dioxide gate insulators which could shift the bias potentials and provide traps to reduce the CCD transfer efficiency.

This estimated dose is about two orders of magnitude greater than the planned dose because of the extended time in orbit and a higher radiation flux than originally expected. A realistic space-borne sensor using an array of this type would mount the sensor in a cryogenic dewar at the focal plane of a telescope, and the assembly would likely be contained within additional structure providing additional radiation protection. Therefore, the results reported here represent manifestly worst case conditions.

Pt_2-Si CCD Transfer Efficiency

Figures 8 and 9 show the construction and operation of the input and output stage of the serial output C-register of the array. The C-register was operated in a two-phase clocking mode with a data rate near 2×10^5 to determine the effects of the space environment on transfer efficiency and operating voltages. The two-phase mode provides better transfer efficiency than the usual four-phase mode. A dc charge component could be added to the input charge at the input end of the C-register (fat zero injection) as a means of improving charge transfer efficiency by filling fast trap states. Bias voltages were adjusted for maximum transfer efficiency. Each charge packet received 128 transfers (64 stages by 2 transfers/stage).

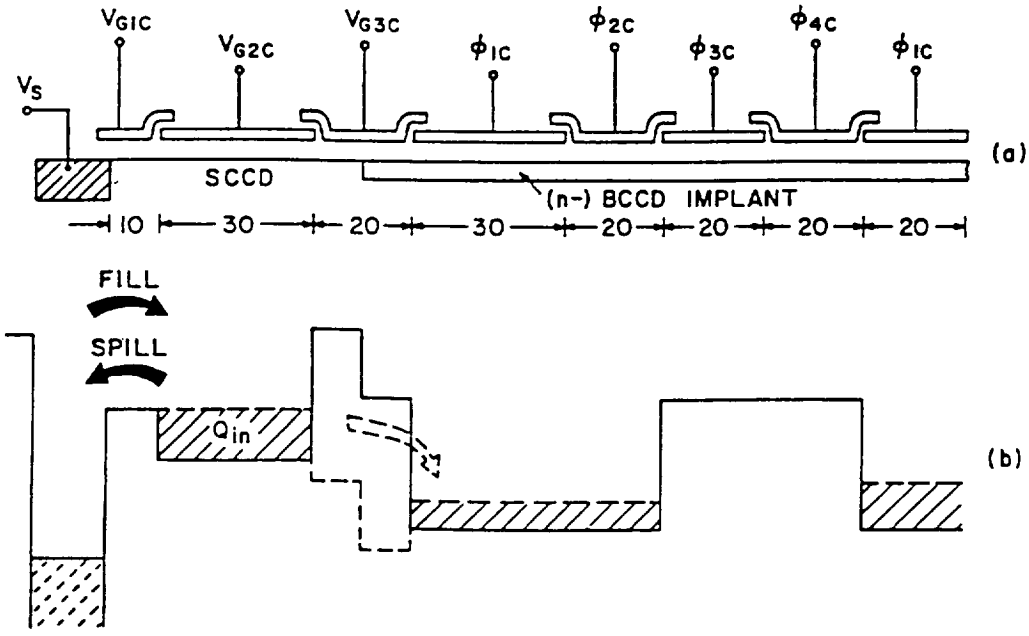

Figure 8. Schematic showing the construction (a) and operation (b) of the input stage of the serial-output C-register of the imaging array.

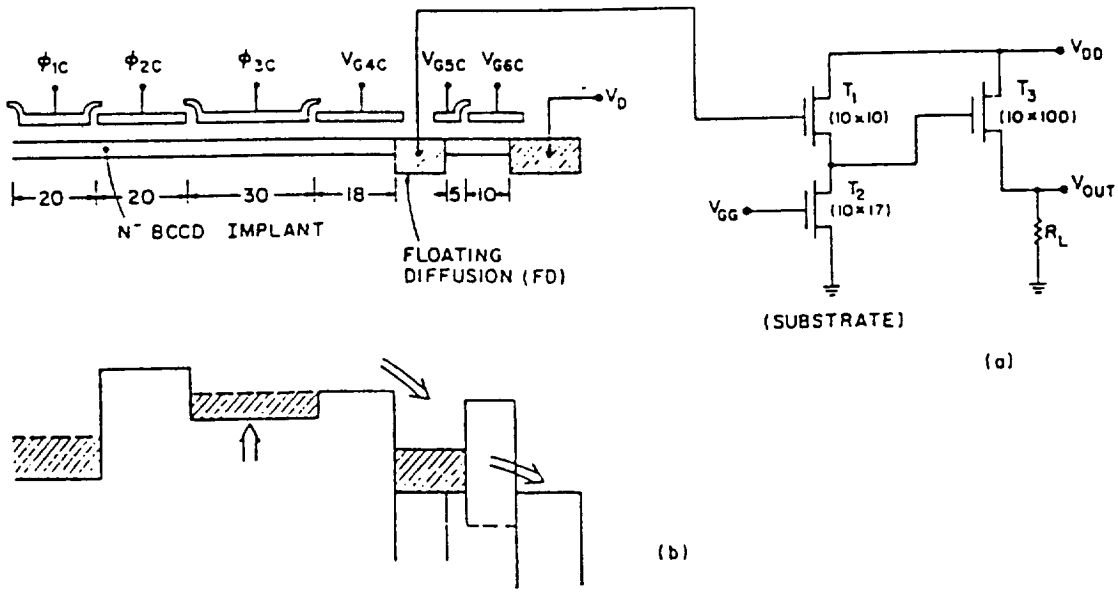

Figure 9. Schematic showing the construction (a) and operation (b) of the output stage of the serial-output C-register of the imaging array.

The spaceborne array required a more positive bias (2.5 V and 4.8 V) than the control array. The cause of these shifts is not understood, and the direction of the shifts is opposite to the expected direction. Also, the magnitude of the shifts is greater than the threshold shifts measured in the test transistors included on the die. Transfer efficiencies exceeding 0.999 (or an inefficiency of 10^{-3}) will provide acceptable resolution. The control sample showed a transfer inefficiency of 10^{-4} at room temperature, and 2×10^{-3} at 80 K.

For the spaceborne sample, the transfer inefficiency at room temperature was 5×10^{-3}, and at 80 K the inefficiency had degraded to 10^{-2}, indicating very poor operation. Injection of additional charge to fill the traps in the C-registers improves operation. With a charge injection equivalent to 2×10^{6} electrons per pixel, the transfer efficiency at 80 K improved to 0.998, equivalent to an inefficiency of 2×10^{-3}.

The density of ionizing-radiation-induced trap density can be estimated from the area of the CCD electrode (80-μm by 30-μm), the electrode thickness (1,200-Å), and the calculated density of charge created by the ionizing radiation (5×10^{15} cm^{-3}). The product of these factors gives an estimated 1.5×10^{6} traps per cm^3. This number is to be compared with the 2×10^{6} electrons per pixel used as a fat zero charge injection to increase transfer efficiency. The agreement tends to support the conclusion that the loss of transfer efficiency is the result of the rather excessive radiation dose received by the array while in orbit.

Dark Current Increase

Dark current in the control and spaceborne samples was significant, equivalent to 1.3×10^{6} and 2.5×10^{6} electrons per pixel respectively at room temperature. At 80 K, dark current drops by a factor of 5. The dark current in the control sample was very probably caused by defects in an adjacent register causing a current leak into the C-register. The additional dark current in the spaceborne sample is believed to result from degradation caused by the ionizing radiation dose.

Threshold Potential Shifts

Threshold measurements for separate FET transistors on the chip provide an indication of process variations and the effects of space exposure. The measured values for threshold voltages for control and spaceborne devices are listed in Table 1. The threshold differences between control and spaceborne samples for the buried and surface channel devices were less than 0.5 V, which would have a minimal effect on device operation. While some of this shift may be caused by radiation induced charging of the gate oxide, shifts of about half or less of this value would be expected from normal die-to-die process variations within a wafer. The test structures also allowed the potential difference between the buried channel potential minimum and the substrate to be measured. For the space-borne sample, the zero-bias values are very close to one of the reference samples, although this value also varies by a volt between the reference samples.

The drain diffusion of the output transistor of the spaceborne array had a reverse-bias leakage current of about 10 μA. While leakage current of this magnitude would have little effect on the amplifier operating point and transfer characteristics because the normal operating current is about 1 mA, additional noise from this source could be important. There was no leakage current in other diffusion regions such as the C-register drain and test structures. Since the leakage current in this transistor is the exception, it may be caused by a defect and not related to the radiation dose.

Table 1. FET threshold voltages.

Device Location	Control Sample Voltage	Spaceborne Sample Voltage
Surface Channel	–0.119 V	–0.214 V
Polysilicon 1 Buried Channel	–8.33 V	–7.92 V
Polysilicon 2 Buried Channel	–7.55 V	–7.11 V

In summary, several differences between control and spaceborne samples were observed. FET transistor threshold voltages exceeded normal process variations by a small amount; there was junction leakage in at least one case. The optimal CCD operating voltages changed in the spaceborne sample, and CCD transfer efficiency degraded.

The changes in operating voltage are of a magnitude that can be accommodated by the drive electronics. As the parameters of the imaging system change, periodic calibration would allow for gradual changes in drive parameters.

The degradation in CCD transfer efficiency is the most serious issue to be addressed. A very large fat zero injection was necessary to provide minimal transfer inefficiency in the spaceborne device. The magnitude of the fat zero used in these measurements is in agreement with the estimated trap density and the resulting charge density arising from the received radiation dose.

The construction of these chips represents technology over 10 years old. Since these arrays were produced in the early 1980's, alternative insulating systems have been developed which provide greater radiation hardness. Newer devices also have shorter gate lengths and better transfer efficiency, which suggests better performance in a radiation environment. Also, because of the known sensitivity of CCD registers to radiation, radiation protection must be provided sufficient to hold the total dose to an acceptable level. Because of the protection provided by the metal cryogenic dewar and mounting structure, this requirement should pose no significant problem to the system designer.

REFERENCES

1. Blue, M.D., and Perkowitz, S.: "Space-Exposure Effects on Optical-Baffle Coatings at Far-Infrared Wavelengths." Appl. Optics, vol. 31, No. 21, July 20, 1992, pp. 4305–4309.

2. Blue, M.D., and Roberts, D.W.: "Effects of Space Exposure on Optical Filters." Appl. Optics, vol. 31, No. 25, September 1, 1992, pp. 5299–5303.

3. Blue, M.D.: "Effects of Space Exposure on Electro-Optic Components." Ga. J. Sci., vol. 49, No. 3, 1991, pp. 107–116.

4. Preuss, Ludwig: "Evaluation of LDEF Experiment S 1002." Final Report, LDEF-69 Months in Space, NASA Conf. Pub. 3134, 1992, pp. 1405–1417.

5. Harvey, Gale A.: NASA Langley Research Center, Hampton, VA, personal communication, March 1991.

6. Harvey, Gale A.: "Effects of Long-Duration Exposure on Optical System Components." LDEF-69 Months in Space, NASA Conf. Pub. 3134, 1991, pp. 1327–1328.

7. Linton, R.C., Kamenetzky, R.R., Reynolds, J.M., and Burris, C.L.: "Atomic Oxyten Simulated Outgassing." LDEF-69 Months in Space, NASA Conf. Pub. 3134, 1991, pp. 763–767.

8. Havey, Keith, Mustico, Arthur, and Vallimont, John: "Effects of Long Term Space Exposure on Optical Substrates and Coatings." Presented at the Second LDEF Post-Retrieval Symposium, Sponsored by the National Aeronautics and Space Administration, June 1–5, 1991.

9. Seeley, J.S., Hunnemen, R., and Harkens, G.J.: "Exposure to Space Radiation of High-Performance Infrared Multilayer Filters and Materials Technology Experiment (A0056)." Final Report, Reading University, 1991.

10. Suzuki, H., Iseki, T., and Yamamoto, A.: "Effect of Reactor Irradiation on the Physical Properties of Fused Quartz." Bull. Toky. Inst. of Tech., No. 121, 1974, pp. 83–88.

11. Robertson, James B.: "Effects of Space Exposure on Pyroelectric Infrared Detectors." LDEF Materials Workshop '91, NASA Conf. Pub. 3162, 1992, pp. 501–506.

12. Charlier, Jean: "Vacuum Deposited Optical Coatings Experiment." LDEF-69 Months in Space, NASA Conf. Pub. 3134, 1991, pp. 1343–1360.

13. Fogdall, L.B.: "Natural and Induced Space Radiation Effects on Optical Coatings and Materials, Final Report." Contracts N00123-78-C-0989 and N60530-79-C-0263. Naval Weapons Center, Boeing Radiation Effects Laboratory, April 1981.

14. Donovan, T.M., Bennett, J.M., Dalbey, R.Z., Burge, D.K., and Gyetvay, S.: "Space Environmental Effects on Coated Optics." LDEF-69 Months in Space, NASA Conf. Pub. 3134, 1992, pp. 1361–1375.

15. Duffey, J.R., Powell, W.W., Song, S.H., Manpearl, D.G., and Kalma, A.H.: "Gamma Radiation Tests of Bulk and IBC Si: As Mosaic Detector Arrays." Proc. IRIS Detector, vol. II, 1986, pp. 147–162.

N94-31030

PHYSICAL PROPERTIES OF GLASSES EXPOSED TO EARTH-FACING AND TRAILING-SIDE ENVIRONMENTS ON LDEF

David E. Wiedlocher, Donald L. Kinser, Robert A. Weller,
Robert A. Weeks, and Marcus H. Mendenhall
Vanderbilt University
Nashville, TN 37235

ABSTRACT

The exposure of 108 glass samples and 12 glass-ceramic samples to Earth-orbit environments permitted measurements which establish the effects of each environment. Examination of five glass types and one glass ceramic located on both the Earth-facing side and the trailing edge revealed no reduction in strength within experimental limits. Strength measurements subjected less than 5 percent of the sample surface area to stresses above 90 percent of the glass's failure strength. Seven micrometeorite or space debris impacts occurred on trailing edge samples. One of those impacts occurred in a location which was subjected to 50 percent of the applied stress at failure. Micrometeorite or space debris impacts were not observed on Earth-facing samples. The physical shape and structure of the impact sites were carefully examined using stereographic scanning electron microscopy. These impacts induce a stress concentration at the damaged region which influences mechanical strength. The flaw size produced by such damage was examined to determine the magnitude of strength degradation in micrometeorite or space-debris impacted glasses. Scanning electron microscopy revealed topographical details of impact sites which included central melt zones and glass fiber production. The overall crater structure is similar to much larger impacts of large meteorite on the Moon in that the melt crater is surrounded by shocked regions of material which fracture zones and spall areas. Residual stresses arising from shock compression and cooling of the fused zone cannot currently be included in fracture mechanics analyses based on simple flaw size examination.

Optical degradation of samples located in Earth-facing or trailing-edge environments was limited to transmission loss due to surface contamination. Contamination was observed primarily on samples which were transparent in the ultraviolet (UV). Contamination was found to be primarily carbon, and it was concluded that the origin of the film was photolysis of the optically absorbing paint* on internal surfaces of the experiment trays. Optical properties of samples were measured by dual-beam spectrophotometric techniques from 200 nM to 2,500 nM. No optical degradation was observed within the limits of the instrumentation.

Electron paramagnetic resonance (EPR) examination at 35 GHz of commercial optical grade fused silica glass exposed on the Long Duration Exposure Facility (LDEF) revealed no detectable change in paramagnetic states arising from exposure to the space environment except that attributable to Mn^{2+}. The spectra of the exposed glass displays a three-fold decrease of intensity for the Mn^{2+} lines which we attribute to solarization.

*Chem Glaze type Z-306 black pigmented paint.

INTRODUCTION

The LDEF, host to 120 glass and glass-ceramic samples which are the subject of this report, was placed in Earth orbit April 7, 1984, and retrieved 5.8 years later. Samples were exposed to both radiation and space debris in the Earth-orbit environment. Radiation incident on the trailing edge of LDEF originated primarily from the Sun. Earth-facing samples were shielded from this radiation by the LDEF module; however, albedo radiation was present as indicated by the discoloration of the TiO_2 pigmented paint on the Earth-facing tray.

Concern about radiation damage to components used in space arises, in part, because of studies by Jaffe and Rittenhouse (ref. 1), who found ionizing radiation levels in Earth orbit to be of energy and intensity likely to produce damage in glasses. Though the highest radiation flux is in the upper Van Allen belts, the extent of radiation damage to glass in a lower orbit was uncertain. Malitson (ref. 2) attempted to simulate the space environment by irradiating glasses with 10^6 rad of ^{60}Co gamma rays and 10^{15} 2 MeV electrons. He concluded that optical centers were produced in the simulated environment and observed color center bleaching within days after removal from the radiation environment. Some investigators (ref. 3) have found the influence of gamma radiation on mechanical properties of borosilicate glasses to be negligible, while others have observed changes in both optical and mechanical properties in glasses exposed to gamma radiation (refs. 4–6) and higher energy particles (ref. 7). The solarization of glass was documented by Faraday (ref. 8) more than a century ago. Optical absorption in the glasses Faraday examined was produced by a change in the valence state of an impurity transition metal such as $Mn^2 \rightarrow Mn^{3+}$. UV radiation is sufficiently energetic to cause the transition in glasses containing this ion.

Radiation-induced defects may result from ionization or knock-on damage by electrons or neutrons which can produce electronic and structural defects in silicate glasses. Electronic states of atoms associated with impurity ions, vacancies, or intersticials are susceptible to ionizing radiation-induced modification. Defects such as ion vacancies are inherent in glass systems just as they are in crystals (ref. 9); thus, electronic states associated with intrinsic defects may be modified by ionizing radiation. EPR measurements (ref. 10) provide sensitive analyses of these electronic states and to changes introduced by ionizing radiation.

Earth orbit environments include meteorites and man-made debris, particles of paint, rocket fuel residue, fragments of space vehicles and other debris arising from activities in orbit. Elemental aluminum and Al_2O_3 are among the particles found (ref. 11) to be responsible for impacts on the trailing-side of LDEF. These particles are thought to exist in highly elliptical orbits which provide a conduit for debris that may impact on the rear of equatorial orbit vehicles. The 6° difference between the Earth-facing plane and ram direction exposed samples on the Earth-facing side to low angle incidence of particles at 8 km/s. The trailing side of LDEF was oriented such that velocity due to orbital motion was –8 km/s.

EXPERIMENTAL PROCEDURE

The compositions of glasses used in these experiments are described in Table 1. Mechanical test samples were abraded with a 120 SiC grit before deployment on LDEF. After recovery of LDEF, mechanical test samples were loaded to failure using a symmetric flexure procedure as described by Wiedlocher et al. (ref. 12). Micrometeorite or space debris impact sites were gold coated and examined in a Hitachi X-650 scanning electron microscope (SEM) with an ultimate resolution of 5.0 nm. Stereomicrographs of each crater were taken at several magnifications and examined in stereo.

Energy dispersive x-ray analysis was performed for each impact using the Hitachi SEM and a Princeton-Gamma-Tech HX-650 analyzer between 0.8 and 20 keV. Each crater was scanned in several locations including any trapped fragments. Results of these analyses were compared with those of the same sample away from the impact site.

Optical measurements of control and exposed samples were conducted using a dual beam optical spectrophotometer over the wavelength range from 200 to 2,500 nm. Visual inspection immediately after retrieval from orbit revealed no perceptible coloration of any samples except the commercial fused silica which was slightly darker than the corresponding control sample.

Table 1. Nominal compositions of glasses in LDEF experiment.

Type	Comment	SiO_2	Na_2O	CaO	B_2O_3	Al_2O_3	Other
Fused Silica	Fused Natural Quartz	100	-	-	-	-	-
BK-7*	Optical Crown	70	5.5	2.5	7.5	-	$15K_2O$
Pyrex*	Corning 7740	81	4	-	13	2	-
Vycor*	Corning 7913	96.5	-	-		0.5	
Soda-lime	ASG Low Fe	71	12	3	-	1	<0.05Fe
Zerodur*	Schott Low α	57	0.7	2.0	-	2.5	$3TiO_2$

Surfaces of the commercial purity fused silica were examined using time-of-flight medium energy backscattering spectrometry (MEBS) (ref. 13). The analysis employed 275 keV He^+ ions scattered at a laboratory angle of 150°. For presentation, the resulting time-of-flight spectra were mathematically rendered as energy spectra after subtraction of a time-independent background. Two additional multilayered thin film samples, also flown aboard LDEF (ref. 14), were analyzed for comparison. These were a SiO_2 film on a Ni with an Ag overlayer, and a SiO_2 film on a Ni substrate with an Al overlayer. Aboard the spacecraft, both of these samples were positioned on the leading edge.

EPR measurements were conducted employing an IBM/Brucker instrument operating at 9 and 35 GHz with samples at 21 C. Samples for measurement were cut from the surface exposed to the space environment and from the unexposed interior of the original 3 to 5 mm thick samples.

RESULTS

Seven impacts sites were detected with optical microscopy in the 120 samples aboard LDEF. All impacts were observed in the tray located in row 2 (ref. 15) on the trailing side of LDEF. Four impacts occurred in glass samples while the three remaining impacts were observed in the glass-ceramic samples. Scanning electron microscopy revealed that six of the seven craters contained a

*Pyrex and Vycor are manufactured by Corning Glass Inc., while BK-7 glass and Zerodur are manufactured by Schott Glass Company, Inc. The names are used only for purposes of identification, and no product endorsement is intended.

central melt zone surrounded by a halo of fragmented material. Numerous radial cracks extended from the point of impact to a radius as given in Table 2. The annular region of fragmentation adjacent to the melt zone is typified by the micrograph of the Zerodur sample shown in Figure 1. Damage on the sample surface away from the fragmented area is not due to the micrometeorite or space debris impact, but is the result of the SiC surface abrasion performed on the glass during sample preparation prior to deployment.

Table 2. Crater dimensional details.

Sample	Central melt pit diameter (μm)	Crater diameter (μm)	Spall surface diameter (μm)
BK-7	40	100	200
Fused SiO_2	50	120	250
Soda-lime-silica	80	175	475
Pyrex 7740	85	200	400
Vycor 7913	No impact	No impact	No impact
Zerodur I	No melt	100	275
Zerodur II	75	200	400

Bubbles trapped in the melt region of the BK-7 visible in Figure 2 indicate temperatures and pressures at impact reached those necessary for vaporization of the micrometeorite and glass. Vaporization was evident in the BK-7 and soda-lime-silica glasses, both of which contain volatile components. No element absent in the glass matrix was detected using energy dispersive x-ray analysis. Figure 3 is a micrograph of the impact in fused silica. Numerous fibers extending from the rim of the central melt crater were produced during jetting of the molten glass. Fibers as long as 100 μm were observed projecting from the fused zone. Similar features were also observed at impact sites in the Pyrex glass as shown in Figure 4. Three impacts occurred in the glass ceramic samples, one of which, shown in Figure 5, showed no sign of melting. However, radial damage associated with this impact is similar to those displaying melting. Fragmentation in this sample was observed to dimensions of 5 μm.

No effect attributed to atomic oxygen in the LDEF orbit was observed; though, the flux of atomic oxygen on the Earth-facing side was estimated by others to be 10^{21} atoms/cm^2/yr (ref. 16). Optical transmission measurements of all samples, except the commercial purity SiO_2 glass, revealed no detectable change in optical transmission. Measurements on the SiO_2 glass, shown in Figure 6, revealed changes in optical transmission between 600 and 200 nm. The transmission at 200 nm was reduced from 85 to 45 percent in fused silica samples which were positioned on the trailing edge of LDEF. The absorption of an SiO_2 sample, coated with a thin carbon film in a carbon evaporation source, is included in Figure 6. This sample displays degraded optical transmission in the UV which is similar, but not identical, to that observed on LDEF.

Medium energy backscattering results in Figures 7 and 8 show spectra which were obtained from the exposed and unexposed surfaces of the SiO_2 samples. Note the displacement of the surface Si edge on spectra obtained from the unexposed surfaces and the presence of significant peaks

attributable to surface carbon. The Si edge shift in these spectra is caused by the presence of a contaminant overlayer which may be inferred to arise from two surface carbon layers of condensed hydrocarbon fragments. Figure 9 is a composite spectra from an uncontaminated SiO_2 surface, the surfaces of leading edge and trailing edge SiO_2 samples, and the SiO_2 sample supporting an evaporated carbon film. Note the progressive shifts in the position of the silicon edges. Figure 10 shows an expanded view of the contaminated surface of the leading-edge sample. Note the presence of a peak near 215 keV. This indicates the presence of about 10^{15} cm^{-2} of a trace contaminant with a mass near 64 u either at the surface or, possibly, distributed throughout the hydrocarbon film.

The EPR spectra of silica samples from virgin glass, solar-exposed surface, and Earth-exposed surface show no detectable change of 9 GHz EPR spectra with samples at room temperature. The 35-GHz spectra, shown in Figure 11, from the solar exposed surface of a commercial optical quality fused silica disk shows a fine structure which was diminished in intensity over that of the control samples stored on Earth. This structure is the characteristic structure of Mn^{2+} which decreased in intensity by a factor of approximately 3 with the LDEF exposure. This change appears to be a consequence of solarization of manganese present in the virgin glass.

DISCUSSION

Impact damage is certainly important when considering damage to spacecraft windows. Impacts in orbiters including the Gemini spacecraft (ref. 17) have prompted the study of impact damage in the space environment. Simulated impacts (ref. 18) in orbiter windows suggest possible catastrophic failure could occur in the space environment. Early interest in the formation of lunar craters and incorrect measurements of particles in space (ref. 19) produced estimations that space travel may be too hazardous to venture. Lunar fines collected during the Apollo 11 mission revealed micrometeorite impacts in glass spheres (ref. 20). These spheres were formed in the ejecta of melted lunar soil during impact of larger meteorites. The impacts exhibited central melt zone and spall region characteristic features observed on several of the LDEF glasses. The melt zones imply that velocities of the micrometeorites or space debris exceeded the hydrodynamic range of impact. Laboratory impact studies (ref. 21) suggest that the lowest velocity necessary to produce melting is about 10 km/s; however, melting in glass due to impact has been reported (ref. 22) at velocities as low as 6 km/s. Melting in the later case was observed in ejecta fragments and did not occur in all impacts, while at higher velocities melting was clearly visible in the center of impact. According to these observations, we conclude that the six impacts in glasses on the trailing-edge, which exhibit melting, were produced by micrometeorites or space debris with velocities on the order of 10 km/s or greater. This is in agreement with studies (ref. 23) of impact velocities on LDEF, which estimate mean velocities on row 2 to be about 13 km/s. Figure 12 illustrates the velocity of ejecta associated with impact. According to the model after Melosh (ref. 21) a particle impacting at a velocity of 13 km/s produces ejecta near the central pit with velocities up to 5 km/s. Presuming the fibers formed in the fused silica were produced by the highest velocity ejecta, the time to form fibers 100 μm in length was about 2×10^{-8} s.

Samples in this experiment displaying bubble evolution include the glasses with the most volatile components. Glasses such as the fused silica or Pyrex, which did not show evidence of boiling include relatively low boiling components. Vaporization in these samples may be due to their composition or may be due to a higher energy impact. Vaporization generally occurs at velocities of order 15 km/s (ref. 24). Since estimations of impact velocities are of this magnitude, the pressures/temperatures and the volatility of the glasses may have contributed to the reboil phenomena.

Strength measurements are summarized in Wiedlocher et al. (ref. 12). The symmetric flexure test employed in that work imposed stresses on the surface of the circular sample as illustrated in Figure 13. The highest stress levels occur in the geometric center of the sample. The impact nearest the geometric center occurred at a position where the stress was less than 50 percent of failure stress; thus, we argue that the effect of micrometeorite or space debris impacts experienced in this work reduced the glass strength by less than 50 percent.

Stress concentration due to a flaw has square root dependence on flaw size. Application of the fracture toughness equation (ref. 25) permits calculation of strength from flaw size and fracture toughness values:

$$K_{IC} = 1.12\sigma\sqrt{\pi a} \ ,$$

where 1.12 is the free surface correction factor, a is the flaw size, and σ is the failure strength. K_{IC} for Zerodur (ref. 26) is 0.9 $MPam^{1/2}$. Using this equation and the average strength from Wiedlocher et al. (ref. 12), the calculated flaw size at the fracture initiation point is approximately 10 μm. Calculations of this type generally assume a half penny crack shape, which sets the crack depth equal to the crack tip radius. This approach estimates that a crack with a radius of 100 μm would initiate failure at 35 percent of the sample strength. Based on these arguments, failure of the Zerodur sample should have initiated at the impact site with an applied load of less than 100 MPa. This suggests the damage below the impact site penetrates no greater than one-fourth of the surface crack radius. This damage depth conclusion is in agreement with geological cratering observations which have determined depth to diameter ratios of meteorite impacts on the Earth to be about one-third to one-fourth.

Literature on cratering often discusses crater diameters determined by the distance between the uplift in the crater rim. Generally, the uplift is characteristic of plastically deformed metals or deformed soils. Impacts in glasses show no distinct crater rim uplift, but contain a central fragmented zone surrounding a melt pit, and a damage field comprised of radial cracks extending from the impact site. Crater dimensions reported in this work on glasses are potentially misinterpreted if they are compared with uplift zone diameters in materials which display uplift. Cratering mechanics (ref. 21) suggest typical projectile diameters are about one-third the crater diameter. Assuming the crater diameter in the glasses to be the central melt pit diameter, the micrometeorites or space debris dimensions are about 15 to 30 μm for most impacts observed.

The crater shape depends on the shape of the projectile and is relatively independent of angle for impact angles greater than 10° (ref. 21). Most impacts observed here displayed a circular central pit with the exception of the impact in the Pyrex sample. Close examination of the Pyrex crater reveals that the glass ejecta and debris field are unsymmetric. Strands of glass are clearly unidirectional along the same line as the elongation of the central melt pit. Since the glass strands are produced in the early stages of impact, fibers would form in the ejecta before excavation of the crater was complete. This accounts for the fibers being directional while the fragmentation surrounding the central pit appears uniform. This is also substantiated by the extrapolation of radial cracks which lead to an origin off center of the excavation in the same direction as the splash. We thus argue that the impact was due to a projectile with a large component of velocity in the direction of the debris field.

The optical absorption present in the UV region for the exposed silica glasses could, in principle, arise from radiation damage (ref. 27) from the presence of contaminants on the sample surface or from a combination of the two. The UV solar fluence, for the trailing edge determined by other investigators (ref. 28), was approximately five times that of the leading edge. Optical absorption at 200 nm for the trailing-edge sample is significantly larger than that for the sample positioned on the

leading edge. MEBS results indicate that the external surfaces of the exposed samples have no detectable contamination; however, the internal surface of the trailing-edge sample was covered with approximately 30 nm of carbon-containing material. The thickness of contamination on the leading-edge sample is approximately 25 percent of that observed on the trailing-edge sample which received direct solar radiation. Thus, the thickness of carbon on the interior surface is approximately proportional to the UV exposure received by the samples.

Indirect evidence that the carbon is in the form of hydrocarbon fragments comes from Figures 6 and 9. The optical absorption profile of the carbon coated SiO_2 glass shown in Figure 6 is similar to, but not the same as, that of the two samples exposed on LDEF. The absorption of the carbon-coated sample is larger than that of the exposed samples, and the general form of the absorption curve is clearly different. Referring to Figure 9, we observe that the offsets of the various silicon edges from the SiO_2 surface edge are measures of the thicknesses of the carbonaceous layers. It is significant that the evaporated carbon layer is only about 50-percent thicker than the contaminant layer on the trailing-edge sample. By contrast, the transmission data of Figure 6 show a transmission ratio of approximately 2.2. This difference is the result of the chemical state of the films and is evidence that the contamination encountered in space is not graphite, but a more complex carbon-based material.

The only known source of carbon in the interior of the sample tray was the organic binder of the absorbing paint on the inside of the tray. The paint, Chem Glaze Z-306, was not visibly degraded during the experiment, although sections of the interior covered by attached fixtures were distinguishably darker than the uncovered material. We hypothesize that the UV component of the radiation, which penetrated the SiO_2 samples, photolytically decomposed organic molecules in the residual gas which evolved from this paint, and the decomposition products were deposited on the interior surfaces of the samples. Alternatively, the decomposition could have occurred during the time that organic molecules were resident on the surface of the sample. Optical properties of other glasses were not measurably degraded because they are opaque in the UV spectral region, preventing UV radiation from penetrating to the interior of the sample tray.

The presence of photochemically produced surface contamination on spacecraft has been previously suspected by Heath and Heaney (ref. 29) and laboratory simulations have verified that UV light can produce such layers by cracking diffusion pump oil (ref. 30). Heath and Heaney speculated that the observed degradation of UV systems on the Nimbus spacecraft could be attributed to the deposition of micron-size droplets from spacecraft outgassing and the consequent formation of nonvolatile thin films by the action of solar UV radiation. The laboratory results reported by Heaney et al. (ref. 30), together with prior experience in the development of carbonaceous layers on surfaces under ion bombardment (refs. 31 and 32), suggest that it is not necessary to condense large amounts of material prior to photolysis. It is likely that the normal residence time of molecules on surfaces provides ample opportunity for UV light to crack volatile molecules into nonvolatile fragments. Such a process would be expected to lead to a uniform layer of contamination as was observed on LDEF samples. This process could also be responsible for deposition of heavy species such as the one shown in Figure 10; however, examination of the constituents on the sample tray and of Chem Glaze Z-360 does not provide a candidate source for this contamination. As a result, we are unable to speculate about its origin.

It is interesting to note that the presence of layers such as those found on these sample trays may have a beneficial effect. In a recent study of 270-keV alpha particle irradiation on MgF_2 optical coatings on atomically clean surfaces in ultrahigh vacuum, Mendenhall and Weller (ref. 33) found selective removal of fluorine at a rate of approximately two flourine atoms per incident alpha particle. This phenomena led to the rapid metallization of the film and to the loss of its usefulness as an

optical coating. This unusual surface effect was presumably caused by a combination of highly mobile flourine in the MgF_2 film and an efficient mechanism for removing the flourine from the surface. The presence of even a thin contamination layer of the kind observed on the LDEF samples would almost certainly have suppressed this sputtering; thus, contaminations of the kind observed here may actually inhibit some radiation damage mechanisms.

The electron spin resonance spectrum of Mn^{2+} detected in unexposed virgin samples decreased in intensity by a factor of approximately three after exposure. This is consistent with observations by many previous authors during Earth-based (ref. 34) exposure to solar radiation.

CONCLUSIONS

Six of the seven impacts on glass and glass-ceramic samples exposed to the trailing-edge of LDEF produced melting or vaporization in craters which are similar to those produced by laboratory impacts at velocities above 10 km/s. No impacts were observed on samples located on the Earth-facing side of LDEF.

The impact observed on the Pyrex sample may have occurred at an oblique angle.

The depth of the damage field associated with the seven impact events is approximately one-fifth the crater diameter. Based on this flaw size, the mechanical strength of the glass and glass-ceramic samples after impact is approximately one-half the original strength.

Optical samples of all glass types suffered no measurable radiation damage from the space environment and this was confirmed by EPR.

Glass fibers produced in the ejecta of the fused silica impact were observed to have lengths up to 100 μm. Formation of these fibers occurred in about 2×10^{-8} s.

Medium energy backscattering spectrometry has established that the optical property degradation of glass samples exposed to the Earth orbit environment aboard LDEF is a consequence of deposition of layers of carbon-containing contamination on the interior surfaces of the fused silica samples. The contamination is presumed to be composed of photolytically cracked hydrocarbons which evolved from the paint on the interior of the mounting tray and formed a tenuous residual atmosphere within the region directly below the sample. No contamination was found on the exterior surface of the samples. The origin of additional thin film contamination by a species with atomic mass near 64 u has not been identified.

No mechanical property changes have been detected which are attributable to the direct action of gamma or UV radiation on the glass samples. Potentially important degradation of UV transmission has been observed, but this is a consequence of radiation induced dissociation of contamination.

ACKNOWLEDGMENTS

We wish to acknowledge financial support of NASA under grants NAS-8-32695 and NAG-8-156 and contract L-17761D.

REFERENCES

1. Jaffe, L.D., and Rittenhouse, J.B., Am. Rocket Soc., vol. 32, 1962, p. 320, cited from Becker, R.A., "Optical Material Problems of Interplanetary Space," Applied Physics, vol. 6, No. 5, 1962, p. 958.

2. Malitson, I.H., Dodge, M.J., and Gonshery, M.E., Proceedings of the Annual Conference of Photographic Science and Engineering, San Francisco, CA, Society of Photographic Scientists and Engineers, Washington, DC, 1966, p. 75.

3. Zdaniewski, W.A., Easler, T.E., and Bradt, R.C.: "Radiation Effects on the Strength of a Borosilicate Glass." J. Am. Ceram. Soc., vol. 66, No. 5, 1983, pp. 311–313.

4. Swift, H.R.: "Effect of Gamma Radiation on the Strength of Plate Glass of Varying Arsenic Content." Communications of the American Ceramic Society, C-145, October 1981.

5. Ananaba, T.O., and Kinser, D.L.: "Gamma Radiation Induced Effects on the Dynamic Fatigue Measurements of Glass Discs." J. Matl. Sci. Let., vol. 4, 1985, pp. 580–584.

6. Shelby, J.E.: "Effect of Radiation on the Physical Properties of Borosilicate Glasses." J. Appl. Phys., vol. 51, No. 5, 1980, pp. 2561–2565.

7. Higby, P.L., Frieble, E.J., Shaw, C.M., Rajaram, M., Graham, E.K., Kinser, D.L., and Wolff, E.G.: "Radiation Effects on the Physical Properties of Low-Expansion-Coefficient Glasses and Ceramics." J. Am. Ceram. Soc., vol. 71, No. 9, 1988, pp. 796–802.

8. Faraday, M.: "Sur la Coloration Produite par la Luminiere, Dans Une Espece Particuliere de Carreaux de Vitres." Ann. Chem. Phys., vol. 25, 1824, pp. 99.

9. Sun, K., and Kreidl, N.J.: "Coloration of Glass by Radiation." The Glass Industry, vol. 33, No. 10, 1952, p. 511.

10. Weeks, R.A.: "The Uses of Electron and Nuclear Magnetic Resonance and Nuclear Resonance Fluorescence in Studies of Glass." Introduction to Glass Science, edited by L.D. Pye et al., Plenum Press, NY, 1972, p. 182.

11. Horz, F.: "Compositional Analysis and Classification of Projectile Residues in LDEF Impact Craters." NASA TM 104750, June 1992.

12. Wiedlocher, D.E., et al.: "Low-Earth-Orbit Effects on Strength of Glasses." J. Am. Ceram. Soc., vol. 75, 1992, pp. 2893–2895.

13. Medenhall, M.H., and Weller, R.A.: "High Resolution Medium Energy Backscattering Spectrometry." Nucl. Inst. and Methods B59/60, 1991, p. 120.

14. Whitaker, A.F., and Young, L.E.: "An Overview of the First Results on the Solar Array Materials Passive LDEF Experiment A0171." LDEF—69 Months in Space, NASA CF 3134, Part 3, pp. 1241–1254.

15. Anon: "LDEF Space Flight Environmental Effects Newsletter II," No. 3, 1991, p. 7.

16. LDEF Space Flight Environmental Effects Newsletter, Summary Issue, vol. II, No. 3, Code 720, NASA, GSFC, Greenbelt, MD, June 15, 1991.

17. Singletary, J.B., and Rittenhouse, J.B.: "Spacecraft Materials Experience." Space Materials Handbook, third edition, NASA SP-3051, 1969.

18. Gehring, J.W. Jr.: "Engineering Considerations in Hyper-Velocity Impact." High-Velocity Impact Phenomena, chapter IX, edited by R. Kinslow, Academic Press, NY, 1970.

19. Chappel, A.: "As Space Debris Multiplies, It's Either Sweep Up, Dodge, or Be Swept Away." Engineering Times, vol. 12, August 1990, p. 8.

20. Frondel, C., Klein, C., Ito, J., and Drake, J.C.: "Mineralogical and Chemical Studies of Apollo 11 Lunar Fines and Selected Rocks." Proceedings of the Apollo 11 Lunar Science Conference, vol. 1, Pergamon Press, NY, 1970, pp. 445–474.

21. Melosh, H.J.: "Impact Cratering: A Geological Process." Oxford 21.Monographs on Geology and Geophysics, No. 11, Oxford University Press, NY, 1989.

22. Gault, D.E., cited by H.J. Melosh in "Impact Cratering: A Geological Process," Oxford Monographs on geology and geophysics, Oxford University Press, NY, 1989.

23. Zook, H.A.: "Meteoroid Directionality on LDEF and Asteroidal Versus Cometary Sources." Lunar Planet. Sci., XXII, 1991, pp. 1577–1578.

24. A. Strauss, Vanderbilt University, private communication, 1992.

25. Freiman, S.W.: "Fracture Mechanics of Glass." Glass: Science and Technology, vol. 5, Elasticity and Strength in Glasses, edited by D.R. Uhlmann and N.J. Kreidl, Academic Press, NY, 1980.

26. Viens, M.J.: "Fracture Toughness and Crack Growth of Zerodur." NASA TM 4185, NASA Scientific and Technical Information Division, 1990.

27. Weeks, R.A., and Sonder, E.: "The Relation Between Magnetic Susceptibility, Electron Spin Resonance and the Optical Absorption of the E1 Center in Fused Silica." Paramagnetic Resonance, vol. 2, Academic Press, NY, 1963, pp. 869–879.

28. Parnell, T.A.: "Ionizing Radiation—LDEF." NASA Conference Publication 10046, edited by B.A. Stein and P.R. Young, NASA, Washington, DC, 1990, pp. 63–94.

29. Heath, D.F., and Heaney, J.B.: "Space Optics." Edited by B.J. Thompson and R.R. Shannon, National Academy of Sciences, Washington, DC, 1990, pp. 340–355.

30. Heaney, J.B., Herzig, H., and Osantowski, J.F.: "Auger Spectroscopic Examination of MgF_2-Coated Al Mirrors Before and After UV Radiation." Applied Optics, vol. 10, 1971, pp. 545–551.

31. Gillette, R.B., and Kenyon, B.A.: "Proton-Induced Contaminant Film Effects on Ultraviolet Reflecting Mirrors." Applied Optics, vol. 19, 1971, pp. 545-551.

32. Tollestrup, A.V., Fowler, W.A., and Lauritsen, C.C.: "Energy Release in Beryllium and Lithium Reactions With Protons." Phys. Rev., vol. 76, 1949, pp. 428–430.

33. Mendenhall, M.H., and Weller, R.A.: "Destruction of a MgF_2 Optical Coating by 250 keV α Particle Irradiation." Appl. Phys. Lett., vol. 57, 1990, pp. 1712–1714.

34. Fanderlik, I.: "Optical Properties of Glass 5." Glass Science and Technology, Elsevier, Amsterdam, 1983, p. 264.

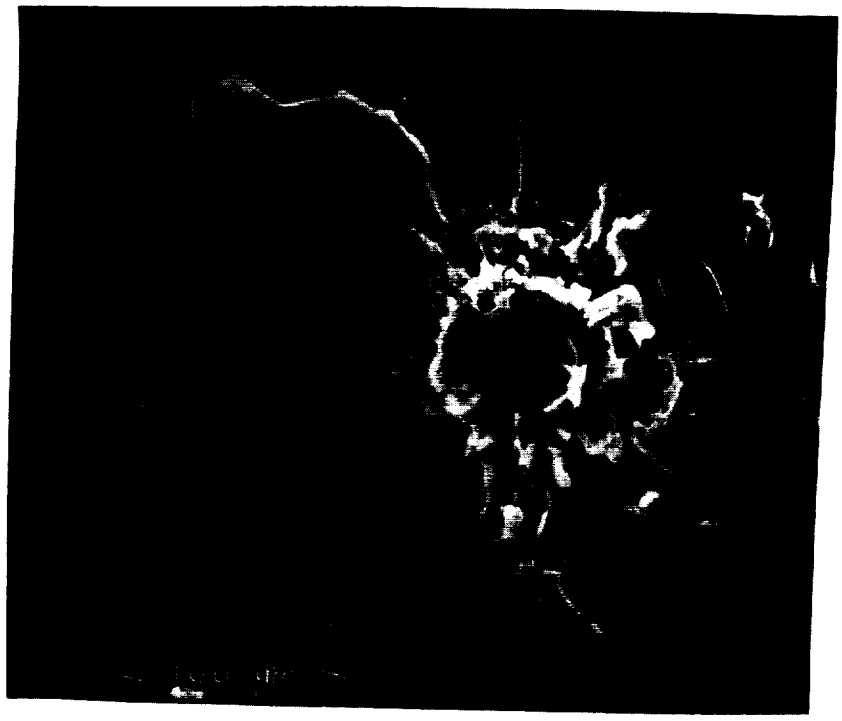

Figure 1. SEM of impact site in Zerodur.

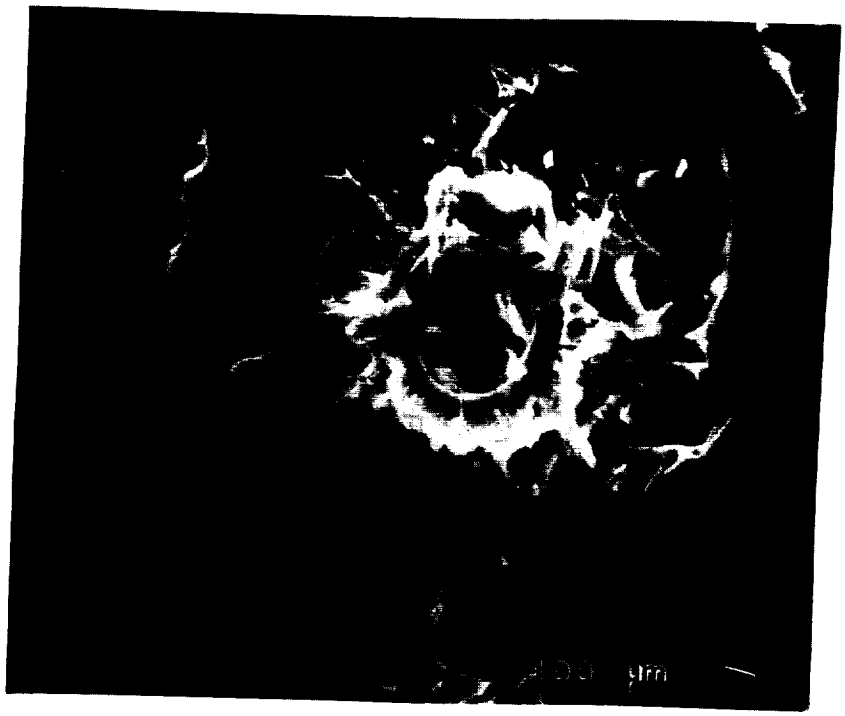

Figure 2. SEM of impact site in BK-7 glass.

Fig. 3. SEM of impact site in commercial optical quality fused SiO_2.

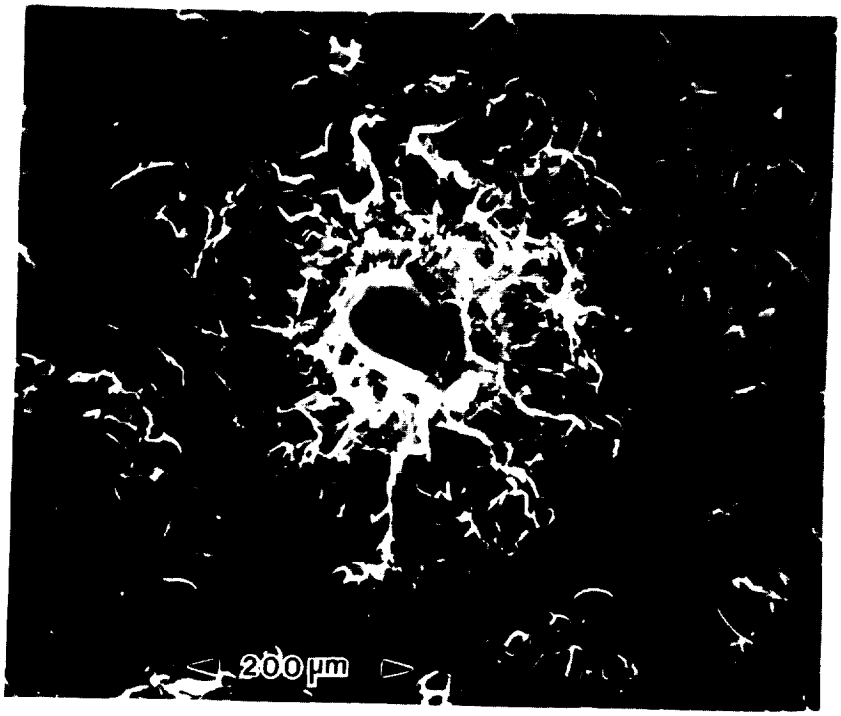

Figure 4. SEM of impact in Pyrex glass sample.

Figure 5. SEM of impact site in Zerodur displaying no melt zone.

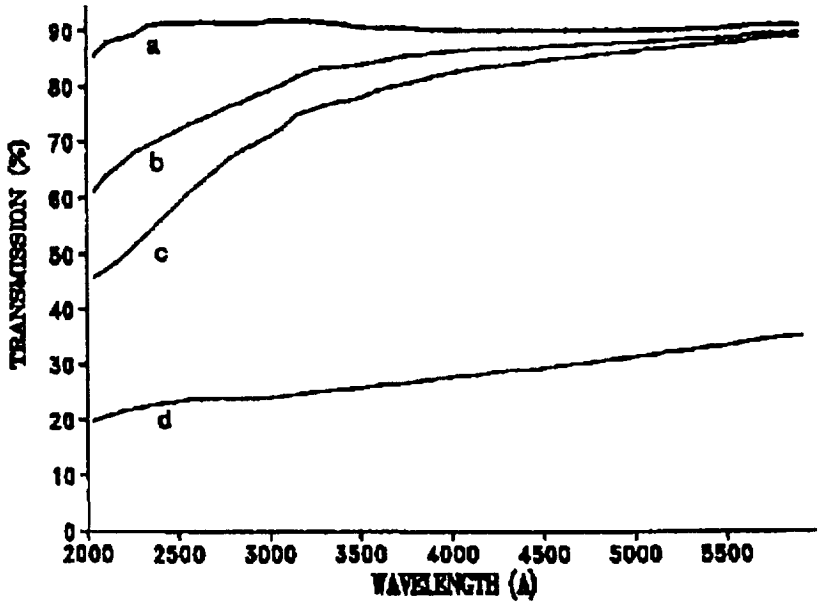

Figure 6. Optical transmission as a function of wavelength for SiO_2 samples (a, control; b, Earth facing; c, trailing edge; and d, sputtered carbon).

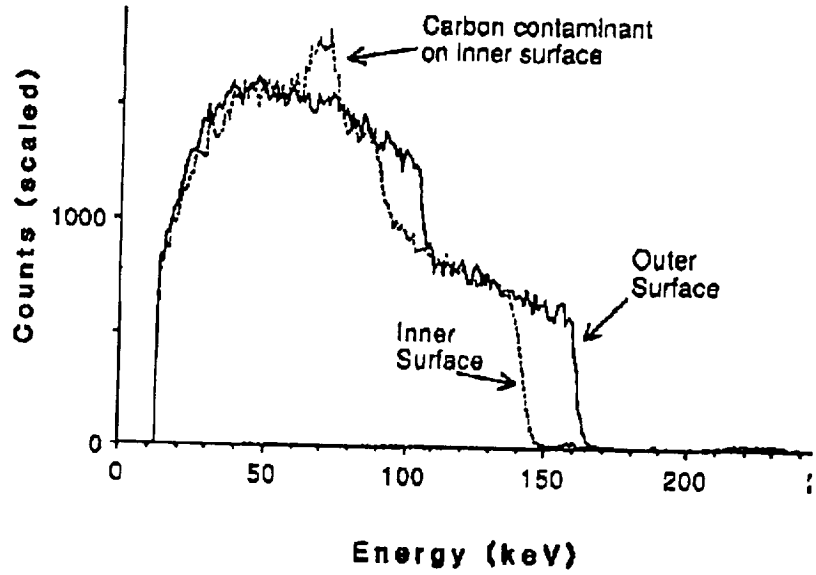

Figure 7. Counts as a function of energy for trailing edge exposure SiO_2.

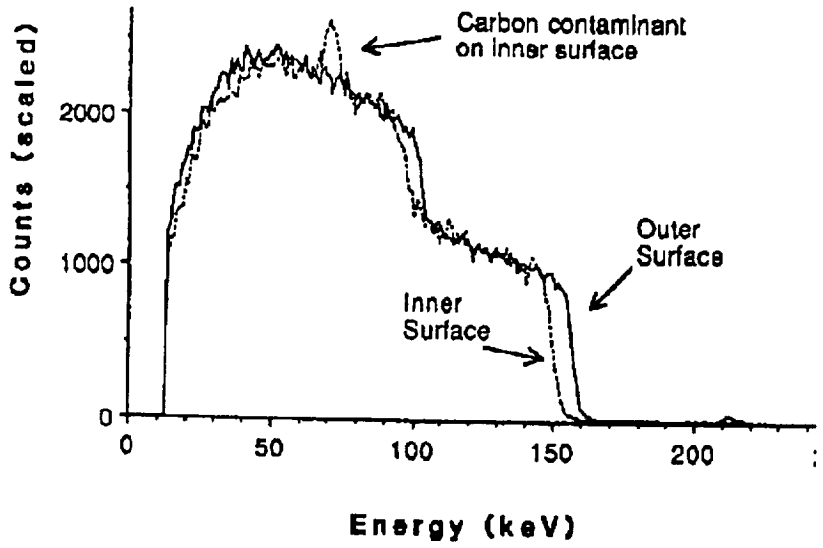

Figure 8. Counts as a function of energy for SiO_2 sample exposed on Earth-facing position.

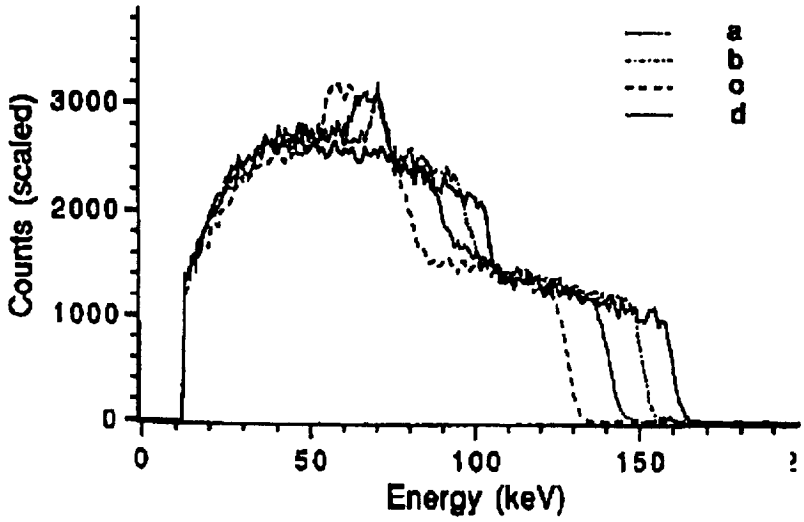

Figure 9. Counts as a function of energy for all SiO_2 samples (a, trailing edge, b, Earth facing; c, carbon coated, and d, control).

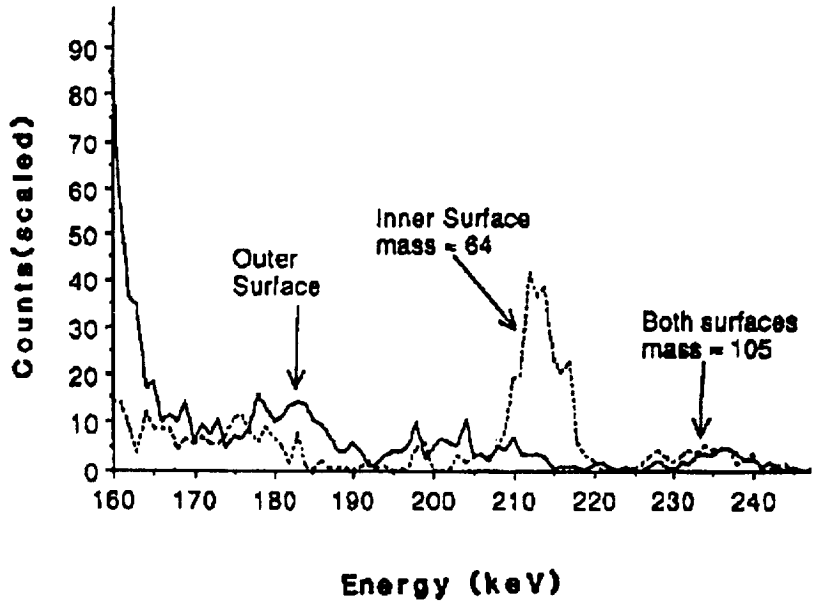

Figure 10. Counts as a function of energy for Earth-facing exposure SiO_2 with peak of 64 u evident.

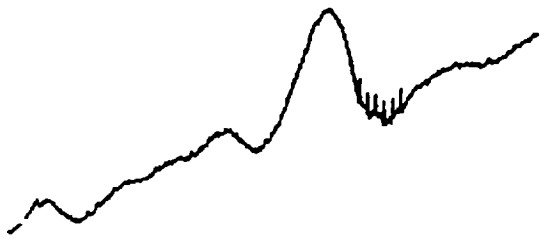

Figure 11. 35-GHz EPR spectra of SiO_2 rear or solar-facing exposure.

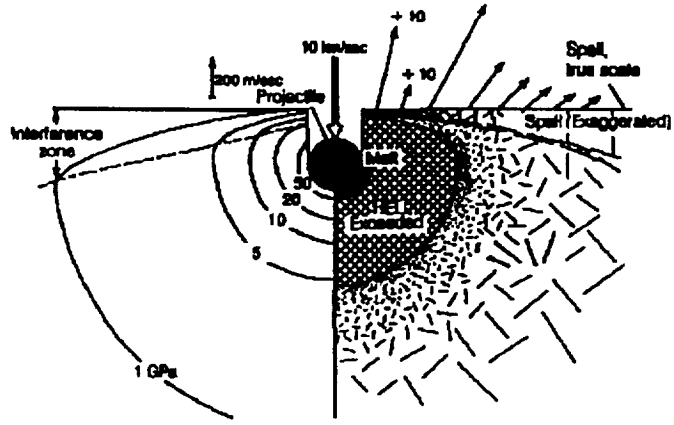

Figure 12. Schematic of impact location and ejecta geometry after Melosh.

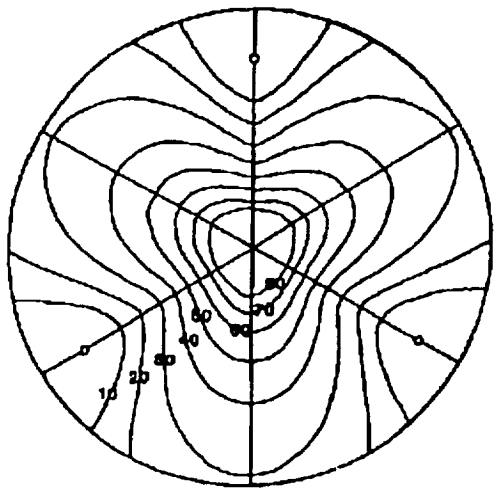

Figure 13. Contours of equal stress for three point support centrally loaded disk.

N94- 31031

MORPHOLOGY CORRELATION OF CRATERS FORMED BY HYPERVELOCITY IMPACTS

Gary D. Crawford
Mechanical Engineering Department
Auburn University, AL 36849
Phone: 205/844–4822

M. Frank Rose
Space Power Institute
Auburn University, AL 36849
Phone: 205/844–5894

Ralph H. Zee
Mechanical Engineering Department
Auburn University, AL 36849
Phone: 205/844-4822

SUMMARY

Dust-sized olivine particles were fired at a copper plate using the Space Power Institute hypervelocity facility, simulating micrometeoroid damage from natural debris to spacecraft in low-Earth orbit (LEO). Techniques were developed for measuring crater volume, particle volume, and particle velocity, with the particle velocities ranging from 5.6 to 8.7 km/s. A roughly linear correlation was found between crater volume and particle energy which suggested that micrometeoroids follow standard hypervelocity relationships. The residual debris analysis showed that for olivine impacts of up to 8.7 km/s, particle residue is found in the crater. By using the Space Power Institute hypervelocity facility, micrometeoroid damage to satellites can be accurately modeled.

INTRODUCTION

The Long Duration Exposure Facility (LDEF) was in LEO for 5 years and 9 months. It was designed to study the space environment and to investigate the effects of this environment on space operations. Upon retrieval of LDEF, NASA personnel of the Meteoroid and Debris Special Investigation Group (M&D SIG) identified a total of approximately 34,000 features caused by micrometeoroid impacts (ref. 1). These results offer staunch proof for the need to successfully model the effects of micrometeoroid impacts on future space missions. While it is unlikely that micrometeoroids could cause catastrophic structural damage to a spacecraft, they can cause extensive damage to windows, solar cells, protective coatings, and other more delicate components.

Micrometeoroids are dust-sized particles in space, and they can be divided into two groups: interplanetary and orbital. As their names imply, the orbital micrometeoroids are in orbit around the Earth, and the interplanetary micrometeoroids come from space. The most important difference between

them is their average collision velocities. For two objects in LEO, their average collision velocity is around 10 km/s. An interplanetary micrometeoroid will impact with an object in LEO at a velocity of 15 to 20 km/s (ref. 2). In order to properly model LEO impacts, a velocity range from 5 to 20 km/s must be examined. The term "hypervelocity" is used to describe objects traveling at these speeds.

The chemical composition of micrometeoroids varies depending on their origin, which is either natural or man-made. Natural micrometeoroids are composed of metallic mixtures of elements such as iron, magnesium, silicon, aluminum, calcium, and/or sulfur (ref. 3). The relative amounts of each element vary. The man-made micrometeoroids, as their name implies, are a result of debris placed in space by man. Their chemical composition varies widely. For example, a window on one of the space shuttles had to be replaced due to an impact by what was thought to be a paint chip (ref. 4).

Therefore, in order to simulate hypervelocity impacts of micrometeoroids, care must be taken in choosing proper particle velocities and composition.

OBJECTIVE

There are three main objectives to this research: (1) verify the ability of the Auburn University Space Power Institute hypervelocity impact facility to simulate micrometeoroid collision phenomena; (2) develop a procedure for analyzing hypervelocity impact experiments at the Space Power Institute; and (3) examine the correlation between various crater and impacting particle parameters for micrometeoroid impacts. The facility is already being used to simulate micrometeoroid impacts, and this research is designed to help improve the techniques for material analysis. This kind of information can be used to duplicate micrometeoroid phenomena on LDEF, or test how well future materials can survive the orbital environment.

Hypervelocity Simulation

The Space Power Institute at Auburn University has a unique hypervelocity simulation system. The hypervelocity impact facility (HIF) accelerates microgram size particles to speeds in excess of 5 km/s. Velocities of 8 to 10 km/s are reached on a regular basis, and velocities of around 15 km/s have been attained. The HIF accelerates the particles using a mixture of electromagnetic acceleration, thermal expansion, and plasma drag. The firing environment is fully enclosed, and a vacuum is held which is comparable to that of space.

In general, hypervelocity impacts follow the relationship of equation

$$V = K*E \tag{1}$$

where V is the volume of the crater, E is the kinetic energy of the particle, and K is a proportionality constant (ref. 5). In order to verify this relationship, the mass and velocity of the incoming particle must be known, along with the volume of the resulting crater.

The velocity of the impacting particle that causes each crater is found using streak photography methods (Figure 1). The streak camera looks across the surface of the target plate, so each impact is registered as a bright flash on the camera film. The camera is also set up to view the target plate from two directions which are 90° from each other, thus providing an X-axis and a Y-axis view of the impact.

The resulting streak photograph is shown at the bottom half of Figure 1. The photograph tells the time at which a particular impact occurred, and because each impact is viewed from two directions, the location of the impact on the plate can be found. By knowing the time of impact for a particular crater, and by knowing the distance of the flight tube, the velocity of the impacting particle is calculated (ref. 6).

A thin Mylar™ film of about 1 micron is placed an inch above the target plate. The particles must pass through this Mylar™ before impacting. Although some of the particles break up upon hitting the Mylar™, most are of sufficient size (50 to 100 microns in diameter, or more) to remain intact. Immediately after a launch, the target plate (with its Mylar™ still in position above the plate) is taken to a specially designed optical inspection device. Here, the cross-sectional area of the impacting particle is measured, and this is compared to earlier particle size measurements.

Experimental Procedure

The procedure developed for this research can be divided into five main steps:

1. Choose the target and particle materials

2. Conduct the hypervelocity simulation, gathering velocity and size information

3. Use the energy-dispersive spectrometer (EDS) of the scanning electron microscope (SEM) to check for particle residue

4. Use the confocal scanning laser microscope (CSLM) and the planar morphometry digitizer (PMD) to measure crater volume

5. Correlate the above information to describe the hypervelocity impact phenomena.

A cold-rolled annealed copper plate was used for a target plate. Copper was chosen for reasons of chemical analysis. The EDS of the SEM tells the presence and relative amounts of elements on a material's surface, but it does not tell the chemical structure. When the HIF launches the particles, a certain amount of debris is carried down the launch tube along with the particles. This debris is composed of several different elements, but copper is not one of them. The residual debris from an impacting particle is much easier to distinguish against the copper material background. Another reason for using copper was because it is a conductor of electricity and this gives better imagery on the SEM.

Olivine was chosen as the particle material. This substance is a metallic mixture of mainly magnesium, silicon, and iron. Olivine was used because several of the craters on LDEF had olivine residue in them (ref. 7), and the magnesium in the olivine distinguishes it from other hypervelocity debris produced by the HIF launching process. The particles were spheroidized by a private contractor prior to firing, so they would have a relative uniform shape. Figures 2 and 3 show the olivine spheres. The spheres were between 40 and 70 micrometers in diameter, and a preliminary EDS analysis of the olivine was made before firing. Note the different particle morphologies shown in Figure 3. Even though the particles looked different, they had the same elemental compositions. The different particle textures may have caused some of the different crater morphologies.

A CSLM and a PMD were used to measure the volume of the craters. The CSLM is unique in that it has a small depth of field, and areas which are not in focus are not visible (ref. 8). The result is photographs which show "slices" of a crater (Figure 4). These "slices" are cross sections of a crater at

various elevations above the bottom of the crater. The area of the cross sections was found using the PMD. By taking slices at various heights above the crater bottom, a direct calculation of the crater volume was made. Between 12 and 15 slices were taken of each crater, up to the original material surface (this was done on all the craters for uniformity). The CSLM also produces a profile of the crater, as shown in Figure 5. This side view was used to check the crater depth and diameter.

One of the problems with the CSLM was the reflectivity of the material surface, and this is the reason for much of the "fuzziness" in the pictures. This was partially compensated for by coating the copper surface with carbon, which had the added effect of making the craters easier to photograph on the SEM. The coating seemed to be less effective on the smaller crater, but accurate measurements were still made by making comparisons with some of the clearer CSLM photos.

Data Analysis

Table 1 shows the characteristics of the craters that were analyzed, and Table 2 shows relevant information about the particles that caused the craters. The tables list the data from highest to lowest particle velocities.

The crater diameter to crater depth relationship shown in Table 1 is between 2 and 2.6, which is typical for hypervelocity impacts into a copper plate (ref. 9). The crater volume calculations are of particular interest. The measured crater volume values were obtained from the CSLM measurements, and the calculated values came from using the equation for the volume of a sphere. Some of the calculations are almost equal to the measurements, while others differ by a factor of 2. On average, the calculated volume was around 28 percent larger than the measured volume.

The particle mass, given in Table 2, was calculated by multiplying the density of the olivine by the volume of the particle. As shown in Figures 2 and 3, the olivine was approximately spherical. The radius of a given particle was found from the area of the hole in the Mylar™ (which was roughly spherical), and the volume was calculated using the equation for a sphere. The particle energy is simply the kinetic energy of the particle.

From the tables, a plot of crater volume versus particle energy was made. This is Figure 6, and the plot shows the linear relationship described earlier in this report. Thus, the characteristic hypervelocity relationships were attained by the HIF.

There are several areas for error in the data collection, and these areas were probably what caused the scattering of the data. The olivine particles were assumed to have uniform density, but the spheroidization process may have varied their densities some. The Mylar™ film is susceptible to a certain amount of shrinking and expanding due to the environmental temperatures. Ejecta from the craters causes holes in the Mylar™, and some of these holes may have been mistaken as being caused by particles. As many as 40 to 100 particles may impact on a 12-cm^2 target plate in one simulation, which makes the streak record difficult to read. Several craters were not used in the analysis because the streak data did not match. (This problem has now been solved by decreasing the number of particles striking the target.)

Photographic Analysis

Figures 7 through 10 show two of the craters. Figures 7 and 8 were formed by the particle moving 8.7 km/s, and Figures 9 and 10 were formed by the particle moving 8.1 km/s. Even though these are two of the faster impacts, their shape and characteristics were endemic to all the craters.

Figure 7 is an overhead view of the crater. Note the distinctive lip all around the crater, and the number of nearby smaller craters. The smaller craters were probably caused by particle breakup as it went through the Mylar™. The inside of the crater is coated with olivine particle residue, which is very similar to many of the craters analyzed on LDEF (ref. 10). The residue is thick on the side of the crater, and appears thinner in the bottom of the crater. This is shown better in Figure 8. On the right edge of the photo some porosity is visible, and the light gray area is the exposed copper surface at the bottom of the crater. The surrounding dark gray region is olivine residue from the impacting particle.

The crater in Figure 9 is also an olivine crater, and had a practically identical EDS analysis. Yet there is a very different morphology. Olivine residue was found throughout the interior of the crater, although there appears to be less residue on the crater lips than was on the previous crater. Figure 10 shows the morphology in the crater base. It had the same material composition as the previous crater, but a very different texture. There appears to be no thinning of residue in the bottom of the crater. Most of the residue appears to have melted (i.e., it has a smooth surface), but some of the residue shows a racked, granular structure associated with a brittle fracture (ref. 11).

One of the most important features of both craters is the lack of gun debris in the craters. In those craters that are thought to have been caused by gun debris, particle residue was found along the lips of the crater. This residue was composed of as many as 10 different elements from various parts of the gun. There was no such residue around or in the olivine craters, thus showing there was no mixing of olivine and gun debris.

CONCLUSIONS

The Space Power Institute HIF accurately models space micrometeoroid phenomena. For olivine-like substances, a certain number of particles will arrive at the target intact. There will be some gun debris and some particle disfigurement, but accurate impact simulations can be made.

By reproducing known hypervelocity relationships, it has been shown that the methods for finding the various particle and crater parameters are reasonably accurate. The HIF can be used to test materials' parameters, so engineers can characterize the best materials to survive the micrometeoroid environment.

Olivine impacts into a copper plate leave particle residue in the crater for velocities of up to at least 9 km/s. The analysis so far suggests that there is a velocity at which no olivine would be left in the crater, and this research is currently being continued at the HIF. Once this upper limit has been established, comparisons can be made with craters on retrieved satellites to provide an additional method for measuring micrometeoroid impact velocities encountered in space.

ACKNOWLEDGMENTS

This research was partially supported by NASA Marshall Space Flight Center and NASA Langley Research Center. Mr. Steve Best of the Space Power Institute at Auburn University is head engineer of the Hypervelocity Impact Facility, and was exceptionally helpful. Dr. Wartan A. Jemian gave advice for using the planar morphometry digitizer, and Dr. Roy Wilcox aided in the scanning electron microscopy evaluations of the materials. Dr. David Hill of the Space Power Institute lent his

expertise of hypervelocity phenomena. The confocal scanning laser microscope that was used for this work is located at the Center for Ultrastructural Studies at the University of Georgia at Athens, and is under the care of Dr. Mark Farmer. Dr. Farmer provided the instruction for its use.

REFERENCES

1. See, T., Allbrooks, M., Atkinson, D., Simon, C., and Zolensky, M.: "Meteoroid and Debris Impact Features Documented on the Long Duration Exposure Facility: A Preliminary Report." NASA JSC No. 24608, August 1990, pp. 59.

2. Kessler, D.J.: "Current Orbital Debris Environment." In *Orbital Debris From Upper-Stage Breakup*, J.P. Loftus, Jr., editor, Progress in Astronautics and Aeronautics, vol. 121, AIAA 89-36977, 1989, pp. 3–5.

3. Horz, F., Bernhard, R.P., Warren, J., See, T.H., Brownlee, D.E., Laurance, M.R., Messenger, S., and Peterson, R.B.: "Preliminary Analysis of LDEF Instrument A0187–1, Chemistry of Micrometeoroids Experiment." In *LDEF—69 Months in Space*, A.S. Levine, editor, NASA CP-3134, June 2–8, 1991, pp. 487–498.

4. Kessler, D.J.: "Current Orbital Debris Environment." In *Orbital Debris From Upper-Stage Breakup*, J.P. Loftus, Jr., editor, Progress in Astronautics and Aeronautics, vol. 121, AIAA 89–36977, 1989, p. 9.

5. Zukas, J.A., Nicholas, T., Swift, H.F., Greszczuk, L.G., and Curran, D.R.: "Impact Dynamics." John Wiley and Sons, Inc., 1982, pp. 216–218.

6. Rose, M.F., and Best, S.: "HYPER: Auburn University's Hypervelocity Impact Facility." Space Power Institute, Auburn University, 1992.

7. Horz, F., and Bernhard, R.P.: "Compositional Analysis and Classification of Projectile Residues in LDEF Impact Craters." NASA TM-104750, June 1992.

8. Kino, G.S., and Corle, T.R.: "Confocal Scanning Optical Microscopy." Physics Today, vol. 42, September 1989, pp. 55–61.

9. Herrman, W., and Wilbeck, J.S.: "Review of Hypervelocity Impact Theories." Int. J. Impact Engng., vol. 5, 1987, pp. 307–310.

10. Horz, F., and Bernhard, R.P.: "Compositional Analysis and Classification of Projectile Residues in LDEF Impact Craters." NASA TM-104750, June 1992.

11. Askeland, D.R.: "The Science and Engineering of Materials." PWS Publishers, Wadsworth, Inc., 1984, pp. 711–725.

Table 1. Crater data.

Particle Velocity (km/s)	Crater Diameter (μm)	Crater Depth (μm)	Crater Diameter/ Depth	Measured Crater Volume (1,000 μm^3)	Calculated Crater Volume (1,000 μm^3)	Percent Difference From Measured Volume
8.7	203	100	2	1,089	2,094	92
8.3	185	88	2.1	1,297	1,539	19
8.1	100	51	2	151	261	73
7.8	250	111	2.3	3,175	3,441	8
7.3	196	77	2.6	1,061	1,403	32
6.6	165	70	2.4	713	928	30
6.1	183	73	2.5	965	1,165	21
6	151	61	2.5	567	665	17
5.8	132	59	2.2	468	511	9
5.7	145	63	2.3	643	651	1
5.7	136	57	2.4	563	511	9
5.6	220	90	2.4	1,931	2,094	8
5.6	200	95	2.1	1,250	1,941	55

Table 2. Particle data.

Particle Velocity (km/s)	Particle Diameter (μm)	Particle Mass (μgram)	Particle Energy (joules)	Particle Energy per Unit Mass (j/μgram)
8.7	53	0.25	9.4	37.6
8.3	45	0.15	5.2	34.7
8.1	36	0.08	2.5	31.3
7.8	77	0.78	23.6	30.3
7.3	64	0.44	11.7	26.6
6.6	54	0.27	5.9	21.9
6.1	42	0.12	2.3	19.2
6	60	0.36	6.5	18.1
5.8	45	0.15	2.5	16.7
5.7	33	0.06	1	16.7
5.7	29	0.04	0.6	15.0
5.6	67	0.51	8	15.7
5.6	71	0.6	9.4	15.7

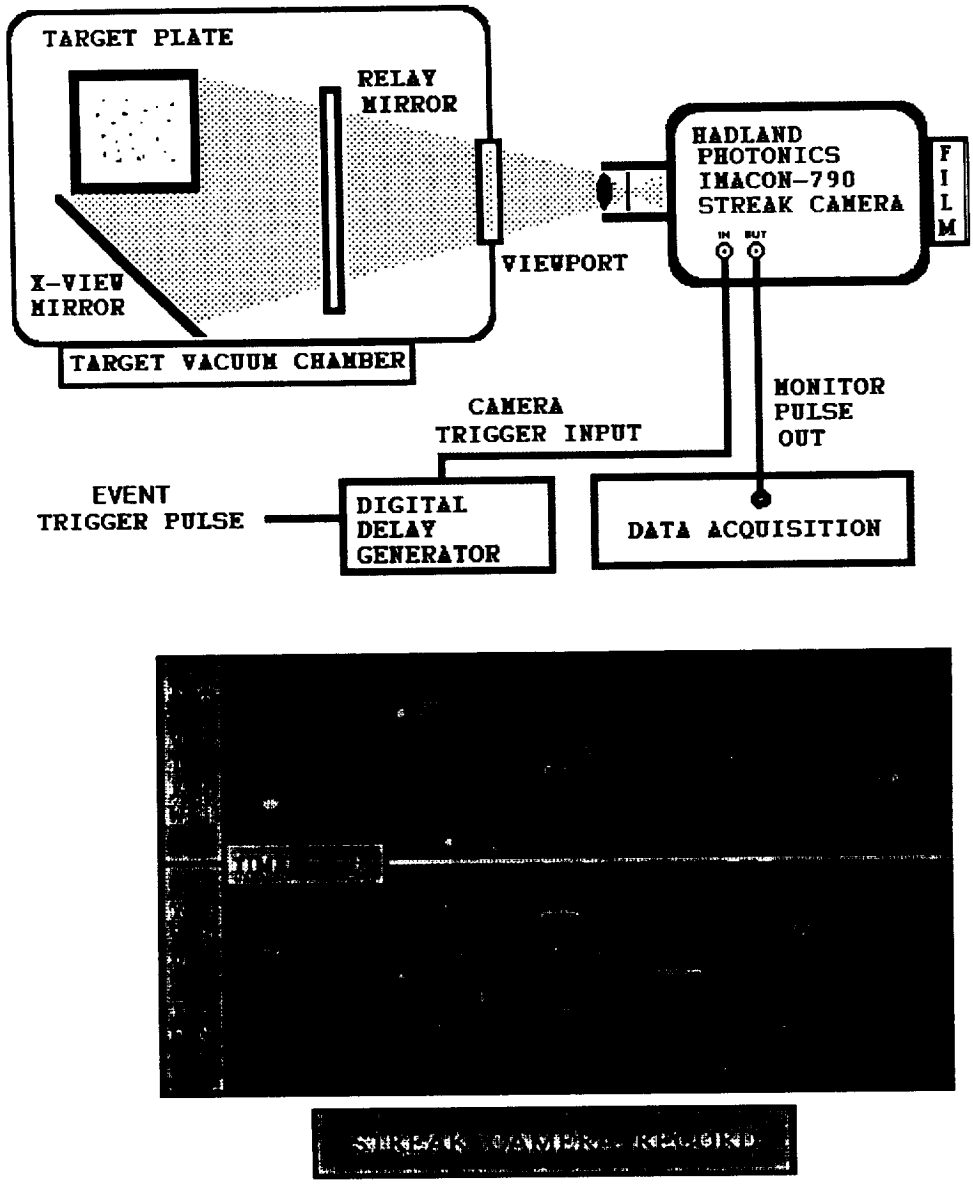

Figure 1. Streak photography diagram.

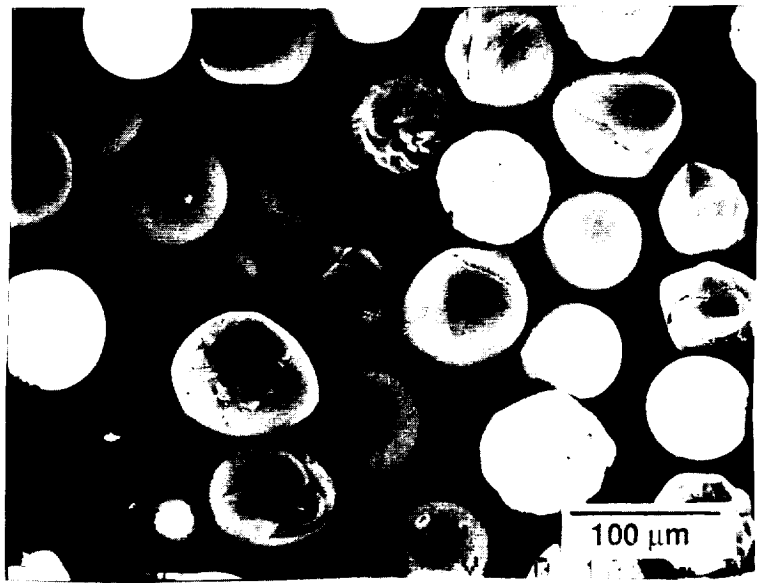

Figure 2. Spheroidized olivine particles that were used in this experiment. Their diameters ranged from 40 to 100 micrometers (× 200).

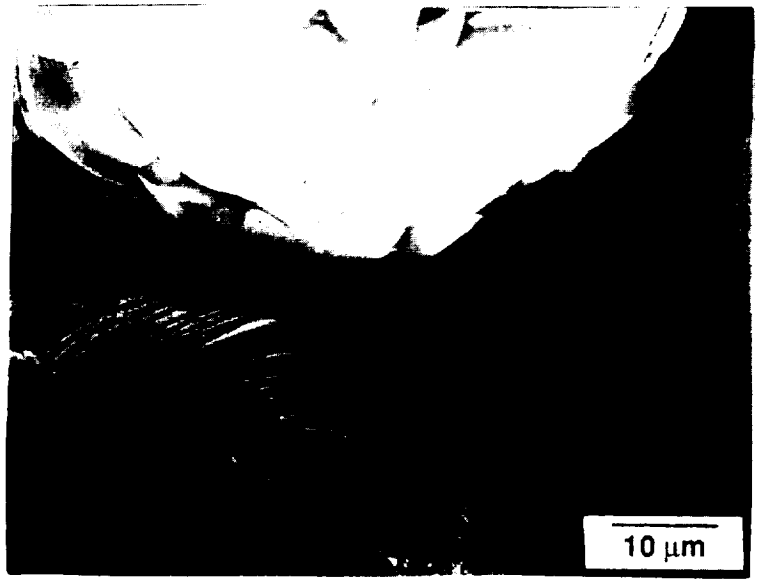

Figure 3. Closeup view of the olivine particles showing the different morphologies (× 1,500).

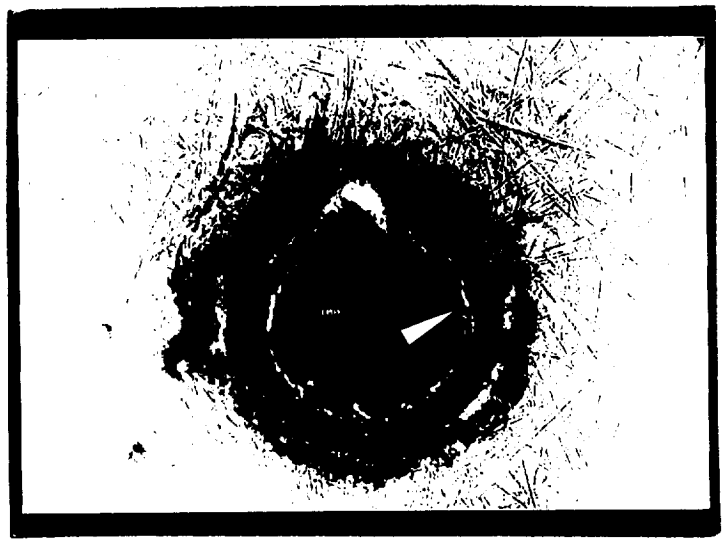

Figure 4. CSLM overhead cross section of a crater formed by a 5.6-km/s particle. The elevation of the cross section above the crater bottom is 100 micrometers, and the white arrow shows the outline of the crater. Note how the irregular shape of the crater is shown.

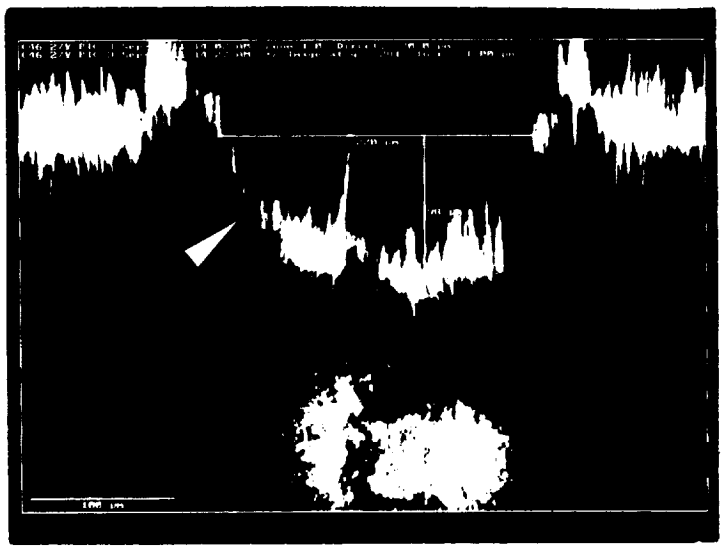

Figure 5. CSLM side cross section of the same crater shown in Figure 4. The white arrow points to the crater surface. Note that the crater depth is measured from the original material surface.

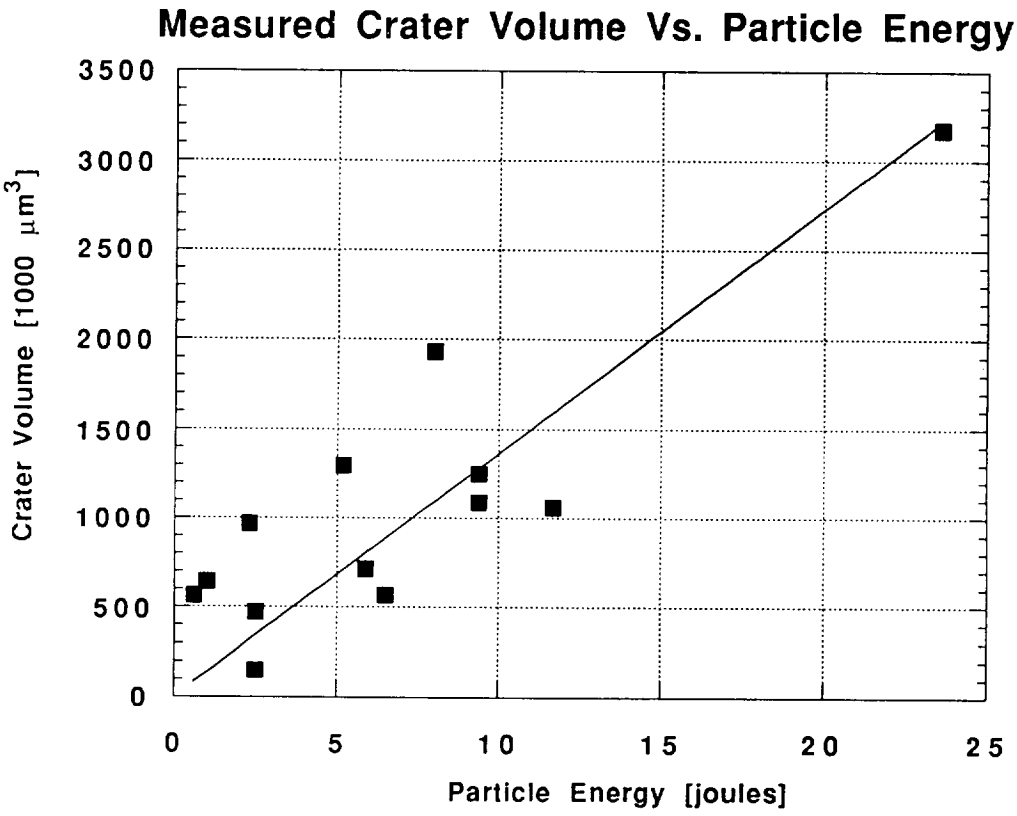

Figure 6. Measured crater volume versus particle kinetic energy. Note the linear correlation, as described in equation (1).

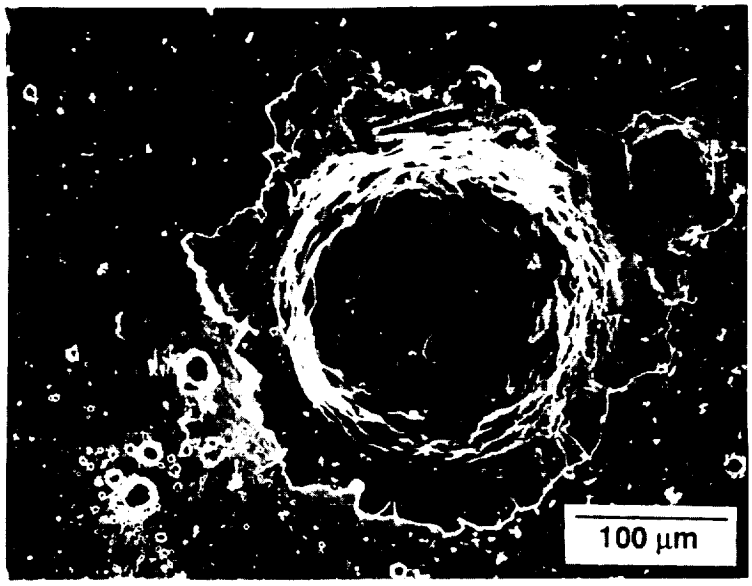

Figure 7. Crater formed by an olivine particle moving 8.7 km/s. Note smaller craters formed by minor particle breakup (× 200).

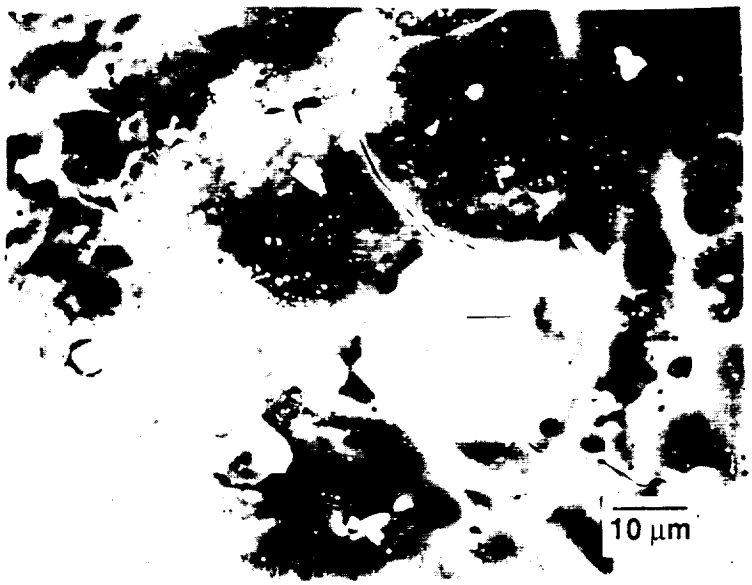

Figure 8. Interior of crater shown in Figure 7. The light colored area to the right of center is the exposed target surface. Note the porosity on the right (× 1,000).

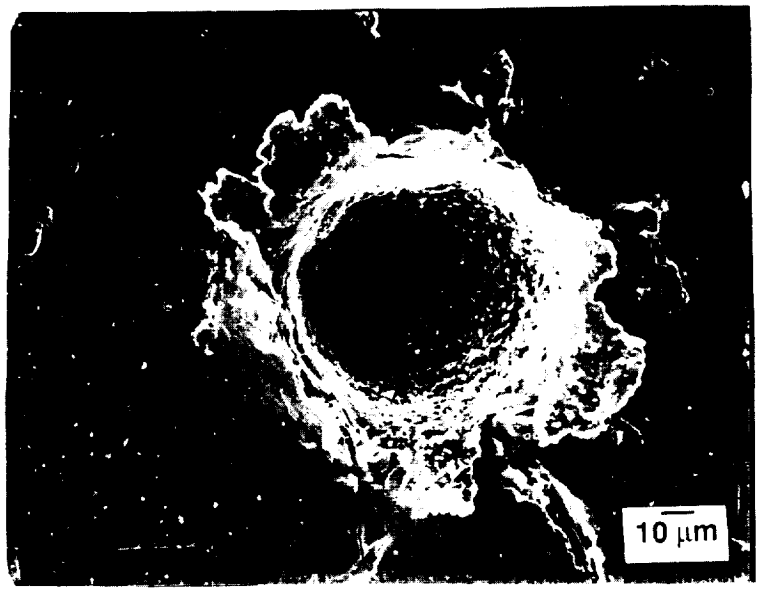

Figure 9. Crater formed by an olivine particle moving 8.1 km/s. The residue has the same EDS scan as the crater in Figure 7 (× 400).

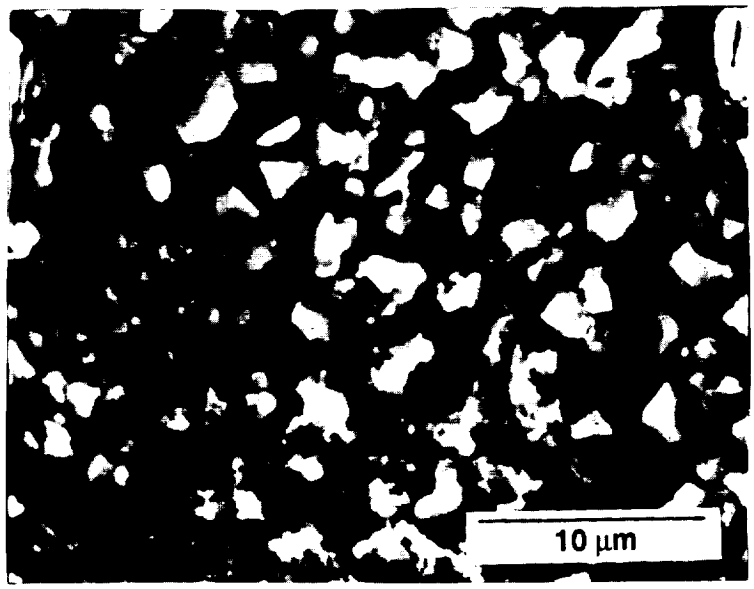

Figure 10. Interior of the crater shown in Figure 9. Compare to the morphology of Figure 8. Note the melted material underneath the jagged grains (× 3,000).

N94-31032

MICROMETEOROID/SPACE DEBRIS EFFECTS ON MATERIALS

James M. Zwiener
Miria M. Finckenor
NASA, George C. Marshall Space Flight Center
Marshall Space Flight Center, Al 35812
Phone: 205/544-2528; Fax: 205/544-5103

SUMMARY

The Long Duration Exposure Facility (LDEF) micrometeoroid/space debris impact data has been reduced in terms that are convenient for evaluating the overall quantitative effect on material properties. Impact crater flux has been evaluated as a function of angle from velocity vector and as a function of crater size. This data is combined with spall data from flight and ground testing to calculate effective solar absorptance and emittance values versus time. Results indicate that the surface damage from micrometeoroid/space debris does not significantly affect the overall surface optical thermal physical properties. Of course the local damage around impact craters radically alter optical properties. Damage to composites and solar cells on an overall basis was minimal.

INTRODUCTION

The purpose of this report is to provide useful information to the spacecraft designers and managers about meteoroid/space debris impacts and their effects on materials, as was learned from the LDEF. Various materials on LDEF were impacted, including thermal control coatings, thin films, solar cells, and composites. Results of impact damage to these materials and their effects are examined in this report.

LDEF was exposed to a meteoroid/space debris environment consisting of numerous natural and man-made particles which impact orbiting spacecraft with closing velocities ranging in the tens of kilometers per second. Those larger than 1 cm in diameter can cause major damage to a spacecraft, but have a low probability of impact. The LDEF satellite was impacted by particles smaller than ~1-mm diameter. Emphasis in this report is only on these high probability small impacts which caused significant surface damage.

Orientation of the LDEF during its 5.75 years flight is shown in Figure 1. During the 5.75 year mission, the LDEF experienced a maximum of approximately 140 significant impact craters/ m^2/year. These impacts have been quantified in terms of size distribution and flux. Impact data were evaluated for impact craters having diameters from 0.1 mm to less than 3 mm. Approximately 10 times more impact craters occurred on the leading edge (RAM) of LDEF compared to the trailing edge. The largest impact was 5.25 mm in diameter. Simple empirical relationships were derived to conveniently model the impact flux in terms of crater diameters and crater size distributions.

Although the LDEF data appear extensive, they are in fact limited in terms of specific damage such as spall to crater ratios for specific paints. For this reason, the LDEF flight data have been supplemented with ground tests at hypervelocities.

Cataloging of all meteoroid and space debris impacts on the satellite surface was performed by the LDEF Meteoroid/Debris Special Investigation Group (M&DSIG). This extensive cataloging was performed during de-integration of the satellite trays at the Spacecraft Assembly and Encapsulation Facility No. 2 (SAEF-2) at Kennedy Space Center. All exposed surfaces of the LDEF, including the experimental trays and all of the exterior satellite surfaces, were optically scanned for impact features.

All impacts, greater than 0.1 mm in diameter as seen with a 10× magnifier, were cataloged. Selected images were recorded by digitizing the video image from a stereo microscope system and storing on a WORM (write once, read many) compact laser disk. The criteria for image storage by digitization was 0.5-mm diameter or larger crater when measured along the major axis, 0.3 mm or larger penetration, and unusual impacts. Preliminary results from this satellite survey are published in reference 1, which is the data source for all the impact crater flux and size evaluations reported in this paper.

At KSC, 34,336 impacts were found, and approximately 4,000 of these impact images were stored on laser disk. The total number of impact features has increased with the discovery of numerous smaller impacts and the analysis of the approximately one-fourth of the experiment trays designed for meteoroid/debris investigation. However, these impacts will not be included in the survey since many of the smaller impacts have no significant damage to material surfaces which could affect the design of spacecraft and selection of spacecraft materials. In addition, results of this report demonstrate that even a factor of two in flux would not significantly affect the overall surface properties, except at the very localized damage sites.

Impact Crater Flux Calculation

In order to calculate the overall surface damage effects from impacts to large surface areas, the flux must be known, ideally, in terms of crater diameters versus the angle from the velocity vector. D. Humes (ref. 2) has shown the significant dependence of meteoroid/orbital debris flux versus angle from velocity vector as derived from model calculations and from the LDEF experiment S0001 data.

Since impact data for LDEF were not reduced in the form required for the calculations, the raw counts of crater impacts were summarized utilizing the data in reference 1. All impact craters above 0.3 mm were summed for each row. This analysis is intended to obtain reasonable (conservative) crater fluxes on surfaces as a function of their surface normal to the velocity vector.

Figure 2 defines the angle "Beta" as the angle from the velocity vector (or RAM) to the normal to each row. Note that Beta increases with increasing row number in a positive value up to 180°. Negative values mean the direction is as shown in Figure 2, with decreasing row number up to a −180°. As an example, row 9 is a minus 8° (ref. 3).

A summary of the crater impact data is provided in Table 1. The "count" column lists the total number of craters (diameter ≥ 0.1 mm) reported for each type of surface in each row. "Area" column lists the area (square meters) used to calculate flux values. "Flux" column provides the reduced counts of impact craters per square meter per year, for each type of surface.

Directional dependence of meteoroid/debris impacts, as a function of the angle from the velocity vector, can be seen from the count and flux data. Apparent flux variations occurred within the same row for different materials. Flux values derived from impacts on experiment surfaces are normally lower than those from the structure or thermal panels. Each experiment was composed of a variety of different materials. Impacts on some surfaces exhibited excellent contrast, making identification for counting fairly easy, while other materials, such as composites, exhibited very poor contrast, making it much more difficult to identify impacts. The LDEF structure and thermal panels have smaller exposed areas than the experiment surfaces, but each consists of the same type material and coating, resulting in a more reliable and consistent count. Attempting to count impacts on such a variety of materials on 24-hour shifts on a tight schedule could account for the variations in flux values listed in Table 1.

All of the flux data listed in Table 1 are plotted graphically in Figure 3. Notice that the flux data for the structure surfaces are skewed from velocity vector zero degree reference. This skewing resulted from assuming the longerons pointed in the same direction as the rows, and combining their count data with that for the intercostals (which do face in the same direction as each row). The offset in angle is 15° which would restore part of the symmetry. It was found that a simple function, defined as the "baseline," encompasses all of these curves as a worst case value.

A simple relationship for the total number of impacts is approximated by equation (1) which is also plotted in Figure 3.

$$\text{Flux } f(\text{Beta}) = a + b \cos^2(\text{Beta}/2) \tag{1}$$

where:

$a = 15$

$b = 125$

Beta = degrees from velocity vector or RAM direction.

Impact Crater Size Distribution

A relationship between total number of impacts per crater diameter is required in order to determine the total damage area based on the impact flux. This relationship was determined by summing all of the impacts on LDEF for each crater diameter. Table 2 lists impacts summed on each row for diameters between 0.1 mm up to 2.5 mm. This count includes impacts on experiments, trays, clamps, structures, and thermal panels. The total count for each diameter was summed for all rows and plotted in Figure 4. This size distribution can be approximated by the following relationship given by equation (2) plotted in Figure 2.

$$\text{Ln}(d) = C1 + (C2 * N) \tag{2}$$

where:

N = number of impacts craters

Ln = natural logarithm

d = diameter of crater in mm.

$C1 = +8.693612$

$C2 = -3.532209$.

This approximation permits an estimation of the actual number of impacts below 0.5 mm where incomplete counting occurred. A summation was made using this relation for all diameters between 0.1 and 3.0 mm. The total sum was used to normalize the size distribution data into a fractional distribution.

Coating Spall Effects

Other information required in order to calculate the overall optical effects of multiple impact craters is the ratio of crater diameter to coating spall diameter. Dependent upon the bond strength and type of coating different, amounts of coating will be removed during impact. Figure 5 schematically defines crater diameter versus spall diameter. The shock waves from the impact can cause coatings to spall, as shown in Figure 5. An example of this spall effect is shown in Figure 6, comparing impact spall on an LDEF flight sample (ref. 4) YB71 ceramic type paint to spall from a similar Z93 white ceramic paint from a ground simulation impact tests at hypervelocity.

As was previously mentioned, impact crater spall data were very limited, even on LDEF samples after almost 6 years in orbit. Most experiment flight samples were about 1 inch in diameter. A flux rate of 140 impact craters per year results in only 0.07 impacts per year on a 1-inch disk. This explains why very few impacts occurred on specific types of experiment sample coatings, which had preflight characterization and normally ground control samples. Of course large areas of LDEF consisted of conversion coatings and silver Teflon™ (Ag/FEP), which provides a large data base for determining spall or effective damage area.

To obtain better spall data for the paint coatings, including Z93 (white ceramic binder type paint) and S13GLO (white silicone binder type paint), a series of hypervelocity impacts were performed by Auburn University (AU) by Dr. F. Rose under contract to MSFC (ref. 5). The hypervelocity impact (ref. 6) system at AU is a plasma drag type accelerator shown schematically in Figure 7. This HVI system is capable of providing a particle impact velocity distribution somewhat similar to Kessler's model (ref. 7), as shown in Figure 8. Another example of impact spall is shown in Figure 9 for S13GLO coatings. This ground simulation sample compares favorably to an impact on LDEF experiment M0003 (ref. 8). Spall to crater diameter ratio is greater for the LDEF exposed sample material.

Impacts on Ag/FEP bonded to aluminum with acrylic adhesive (ref. 9) is shown in Figure 10. An Ag/FEP layer has been lifted up and blown back from the impact site. The adhesive layer was debonded from the aluminum substrate, leaving the bare aluminum exposed. This was one of the larger impacts on experiment S0069.

In comparison, impacts on conversion coatings such as chromic acid anodize (CAA) did not produce any apparent spall. An example is the CAA sample from LDEF experiment S0069. Figure 11 is an enlargement of the impact on the thermal guard ring of the calorimeter flight sample. Even for a very thick conversion type coating, as shown in Figure 11, no measurable spall occurred.

Results for spall to crater ratios, from flight and ground tests, are summarized in Table 3.

EFFECT ON THE THERMAL RADIATIVE PROPERTIES OF COATINGS

Calculative Approach

Since the flux levels as a function of Beta angle, crater size distribution, and spall/crater ratio are known, the change in effective (average) thermal radiative properties can be calculated with respect to time using equation (3).

$$A_s(\text{Beta}) = A_o - [D_{a,e} * F_a * T_{yr}] \quad (3)$$

where:

A_s (Beta, time) = effective or average value of solar absorptance or emittance at each Beta angle

A_o = solar absorptance or emittance of original coating

$D_{a,e}$ = difference between coating and substrate absorptance or emittance

F_a = fraction of damaged surface area per year

T_{yr} = number of years exposed.

The fraction of damaged surface area (F_a) is derived by summing for each angle "Beta" the product of flux, size distribution, and spall area, for crater diameters from 0.1 to 3.0 mm. For convenience a selection of values for "F_a" are provided in Table 4. These values for F_a can be used with equation (3) to predict long-term optical property changes from impact craters. Remember that the values provided in Table 4 are actually the total area in square millimeters of substrate exposed from the impact per square meter (refer to Figure 5) and subsequently includes a multiplication factor of 10^{-6} (as indicated in Table 4). Values in Table 4 are listed for spall to crater diameter ratios ranging from 1 to 15, and for selected Beta angles in the range from 0° through 180°.

Results of Calculations

White Paints (Z93 and S13GLO)

Figures 12 and 13 show the results of impacts on Z93 white coating for three different Beta angles of 0°, 90°, and 180°, for up to 30 years in orbit. Both solar absorptance and thermal emittance decrease slightly with time. The larger spall/crater diameter ratio for Z93 and other ceramic binder paints does not significantly affect the solar absorptance or thermal emittance values. When the coating and substrate thermal radiative properties are significantly different, then the effect of impacts is greater. This effect is shown in Figures 12 and 13, by comparing the larger change in emittance than in absorptance. Bare aluminum substrate has a very low emittance ~4 percent, compared to the Z93 value of ~92 percent. In comparison aluminum absorptance is ~4 percent (low value) and Z93 ~14 percent. Actually, the exposed aluminum absorptance in the spalled area is probably closer to the Z93, which means the changes shown on Figure 12 are even less.

Effects on S13GLO are even less than on the Z93, see Figures 14 and 15, since the spall to crater ratio is much less. The overall effect on S13GLO would be difficult to measure. For these

coatings, the atomic oxygen, ultraviolet radiation, and contamination will have a greater long-term effect than meteoroid/debris impacts (ref. 4).

Conversion Coatings such as CAA

Chromic acid anodized aluminum exhibited no spall on either flight or ground test samples, resulting in changes much less than 0.1 percent in even 100 years for effective absorptance and emittance. Of course, this assumes the orbital debris environment does not change significantly from what LDEF experienced.

Silver Teflon™ Blankets

Changes to the thermal radiative properties of silver Teflon™ (Ag/FEP) blankets utilized the damaged area measured by Nerren (ref. 10). Photograph of a Ag/FEP blanket flown on LDEF as shown in Figure 16, was analyzed for percent of area darkened from impacts. This analysis was performed by Nerren and Sullivan (ref. 9). The photograph image of the silver Teflon™ blanket flown on LDEF experiment No. A0178 on row 10E was scanned to determine the damage area. The Ag/FEP blanket analyzed was positioned +22° from the velocity vector (Fig. 2). A total of 322 penetrations were counted and their associated darkened area measured. The darkened area includes the impact penetration hole area and the discolored area surrounding the impacts, resulting in a 1.44-percent damaged surface area. The darkened area has a higher solar absorptance than the original Ag/FEP, which increases the overall effective solar absorptance. The overall effect to thermal radiative properties is plotted in Figures 17 and 18 utilizing equation (3).

IMPACT EFFECT ON SOLAR CELLS

Electrical properties of solar cells appear to be minimally affected by meteoroid/debris impacts as reported by Young and Trumble (ref. 11). Cracking of the cover glass and even penetrations only have a local effect. Certainly a high level of damage by impacts would cause significant loss in solar cell array outputs. At this time, the damage effect threshold is being determined by impact testing on arrays at Auburn University utilizing their hypervelocity facility and at MSFC (ref. 12) utilizing a light gas gun for impact tests with particles up to 0.5 in (12 mm).

IMPACT EFFECTS ON COMPOSITE MATERIALS

Composite specimens flown on LDEF were carefully examined for impacts before tensile testing. The graphite/epoxy samples did experience several small impacts, but these craters did not serve as crack propagation sites nor had any discernible affect on the tensile test. Erosion of the graphite/epoxy induced variability to the tensile strength measurements which was greater than the effect of meteoroid/debris impacts.

Several small impacts were also found on fiberglass/epoxy samples covered with aluminized thermal control tape. No debonding of the tape was observed. Peel tests of the thermal control tape were not perceptibly affected by the impacts.

CONCLUSION

Overall average effects of meteoroid/space debris (M/OD) impacts on most spacecraft surfaces are not significant even for extended periods. This is true only for non-penetrating small high probability impacts causing craters in the 0.1 to 3 mm range. Even at this minimal average effect, up 140 impacts/year/square meter can be expected and must be planned for and considered in spacecraft designs requiring long periods of exposure in the low earth orbital environment.

For very stable materials where a few percent change in overall properties is critical, then the impact and spalling can be important. Example, is if the overall average emittance of a radiator must be stable for 30 years (change <2 percent), then the effects of the M/OD must be included in life predictions.

Localized damage, if it occurs in the wrong place can cause severe degradation. Although the overall effect of impacts on solar cells is small, impacts that sever connections will cause loss of those cells. These types of events are rare, but they will occur, and redundancy by physical separation can all but eliminate local damage failures.

Optical surfaces such as lenses and mirrors were not discussed, but the flux values can be used to assess the magnitude of impacts these surfaces will experience with time. By always exposing optical systems in the trailing direction the flux can be reduced by a factor of 10. The type of impacts evaluated in this report will normally not cause penetration of optical surfaces, but they will create scatter sites for light.

REFERENCES

1. See, T., and Allbrooks, M.; et al.: "Meteoroid and Debris Impact Features Documented on the Long Duration Exposure Facility." NASA JSC Publication No. 84, JSC No. 24608, August 1990.

2. Humes, D.H.: "Large Craters on the Meteoroid and Space Debris Impact Experiment." NASA CP-3134, part 1, 1992, p. 399.

3. Banks, A., and Gebauer, L: "LDEF Yaw and Pitch Angle Estimates." NASA CP-3162, part 1, November 1991, p. 71.

4. Wilkes, D., and Zwiener, J., et al.: "Initial Materials Evaluation of the Thermal Control Surfaces Experiment (S0069)." NASA CP-3134, part 2, June 1991, p. 899.

5. Rose, F.: "Hypervelocity Impact and Scaling above 10 Km/sec." Contract NAS8- 39131, DO No. 1, through November 1992.

6. Rose, F., et al.: "Hypervelocity Impact Facility for Simulating Materials Exposure to Impact by Space Debris." Second LDEF Post-Retrieval Symposium, NASA Conference Publication (to be published in '93), June 1–5, 1992.

7. Kessler, D., et al.: "Orbital Debris Environment for Spacecraft Designed to Operate in Low Earth Orbit." NASA Technical Memorandum TM-100471, April 1989.

8. Photograph of impact provided by Dr. W.K. Stuckey, The Aerospace Corporation, L. A. Calif,. September 1991.

9. Zwiener, J., and Wilkes, J., et al.: "Unusual Materials Effects Observed on the Thermal Control Surfaces Experiment (S0069)." NASA CP-3134, part 2, June 1991, p. 919.

10. Nerren, B., and Sullivan-Holt, R.: Unpublished data, George C. Marshall Space Flight Center, Huntsville, AL, April 1990.

11. Young, L., and Trumble, T.: "Impact of LDEF Photovoltaic Experiments Findings Upon Future Spacecraft Solar Cell Assembly Design and Development Requirements." (In this proceedings.)

12. Taylor, R.: "A Space Debris Simulation Facility for Spacecraft Materials Evaluation." SAMPE Quarterly, vol. 18, No. 2, January 1987.

Table 1. Crater impact data.

ROW NO.	EXPERIMENTS & TRAYS			LDEF STRUCTURE			THERMAL PANELS			
	COUNT	AREA (m2)	FLUX	COUNT	AREA (m2)	FLUX	COUNT	AREA (m2)	FLUX	ANGLE BETA
1	622	6.58	16.43	112	1.22	15.95	46	0.316	25.33	+ 112°
2	126	6.58	3.33	68	1.22	9.68	36	0.316	19.83	+ 142°
3	399	6.58	10.54	74	1.22	10.54	10	0.316	5.49	+ 172°
4	311	6.58	8.22	96	1.22	13.67	15	0.316	8.26	- 158°
5	846	6.58	22.36	184	1.22	26.20	29	0.316	15.97	- 128°
6	915	6.58	24.15	442	1.22	62.94	12	0.316	6.60	- 98°
7	2108	6.58	55.71	572	1.22	81.46	170	0.316	93.62	- 68°
8	3289	6.58	86.92	939	1.22	133.72	175	0.316	96.37	- 38°
9	3077	6.58	81.40	924	1.22	131.59	246	0.316	117.53	- 8°
10	3118	6.58	82.40	652	1.22	92.85	204	0.316	112.34	+ 22°
11	2435	6.58	64.35	493	1.22	70.21	168	0.316	92.52	+ 52°
12	1620	6.58	42.81	321	1.22	45.71	132	0.316	72.56	+ 82°
SPACE END	112	5.966	3.26	79	--	--	165	4.65	6.16	~ 90°
EARTH END	1095	5.966	31.92	649	--	--	1200	4.65	44.82	~ 90°

FILE:93/LDEF93/TABLE01

Table 2. Impact crater size distribution.

TOTAL NUMBER OF IMPACT CRATERS PER ROW AND PER DIAMETER																							
DIAM(mm) / ROW #	≤0.1	0.5	0.6	0.7	0.8	0.9	1.0	1.1	1.2	1.3	1.4	1.5	1.6	1.7	1.8	1.9	2.0	2.1	2.2	2.3	2.4	≥2.5
1	10	32	34	25	25	13	15	5	0	1	2	0	0	0	0	0	0	1	0	1	0	0
2	25	25	7	10	12		3	2	1	1	1	0	0	0	1	0	0	0	0	0	0	0
3	22	9	13	9	10	4	3	2	2	1	0	2	1	0	2	1	1	0	0	0	0	1
4	29	20	11	5	7	2	2	6	2	0	0	1	0	0	0	0	0	0	0	0	0	0
5	29	29	21	13	15	5	4	4	2	0	1	3	1	1	0	0	0	0	0	0	0	0
6	68	45	43	33	19	16	15	5	2	4	2	3	2	0	0	0	0	0	0	0	0	0
7	65	106	72	61	32	18	15	11	3	0	2	4	2	1	0	2	0	0	2	1	0	1
8	85	132	97	75	42	29	22	9	13	13	5	6	1	1	0	1	0	0	0	1	0	4
9	100	125	95	75	51	24	22	17	15	9	10	0	6	1	5	0	0	1	0	1	0	7
10	124	149	107	79	51	24	30	20	15	11	4	7	5	1	5	2	7	4	1	2	0	6
11	66	106	83	109	55	22	22	9	12	7	3	3	6	2	2	0	0	1	0	1	1	5
12	65	51	46	54	33	11	18	4	9	1	2	4	2	2	1	0	0	0	2	0	0	3
TOTALS:	688	829	629	548	352	178	171	104	76	56	32	41	26	9	16	6	8	6	5	7	1	27

FILE:93/LDEF93/TABLE01a

Table 3. "CN" spall diameter to crater diameter ratio.

	RATIO OF SPALL TO CRATER DIAMETER	
COATING MATERIAL	LDEF FLIGHT SAMPLES	GROUND TEST SAMPLES
S13GLO	3	1.5 to 3.0
YB71	4 to 8	5 to 8
Z93	na	5.5 to 8
Ag/FEP	2 to 6	na
CAA	1	1

FILE:\S\LDEF\S\TABLE\S\3

Table 4. "F_a" fraction of damaged surface per year.

	VALUES FOR Fa X 10^{-6}							
Beta / D_s/D_c	0°	10°	30°	60°	90°	120°	150°	180°
1	21.07	20.93	19.81	16.37	11.66	6.96	3.52	2.26
2	84.28	83.71	79.24	65.47	46.65	27.84	14.07	9.03
3	189.63	188.34	178.29	147.30	104.97	62.65	31.66	20.32
4	337.12	334.83	316.96	261.87	186.62	111.37	56.28	36.12
5	526.75	523.18	495.24	409.17	291.59	174.01	87.94	56.44
6	758.52	753.37	713.15	589.21	419.89	250.58	126.64	81.27
7	1032.43	1025.43	970.68	801.97	571.52	341.07	172.37	110.62
8	1348.47	1339.33	1267.82	1047.48	746.48	445.48	225.13	144.48
9	1706.66	1695.09	1604.59	1325.71	944.76	563.81	284.93	182.86
10	2106.99	2092.70	1980.97	1636.68	1166.37	696.06	351.77	225.75
11	2549.46	2532.17	2396.98	1980.39	1411.31	842.23	425.64	273.16
12	3034.07	3013.49	2852.60	2356.82	1679.57	1002.33	506.55	325.08
13	3560.82	3536.66	3347.84	2765.99	1971.17	1176.34	594.49	381.52
14	4129.70	4101.69	3882.71	3207.89	2286.09	1364.28	689.47	442.47
15	4740.73	4708.58	4457.19	3682.53	2624.34	1566.13	791.48	507.74

FILE:\S\LDEF\S\TABLE\S\4A

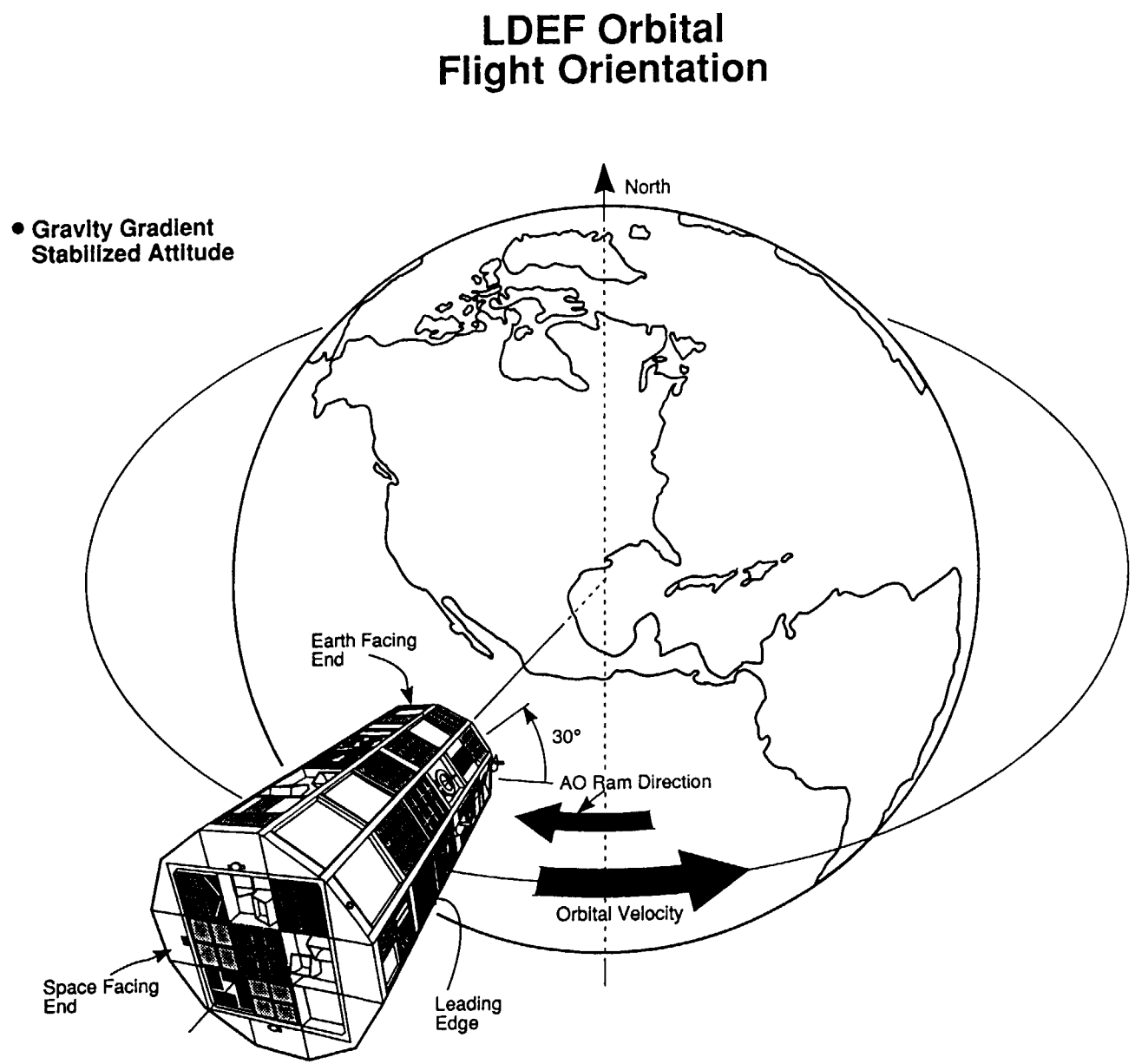

Figure 1. Schematic of LDEF in orbit.

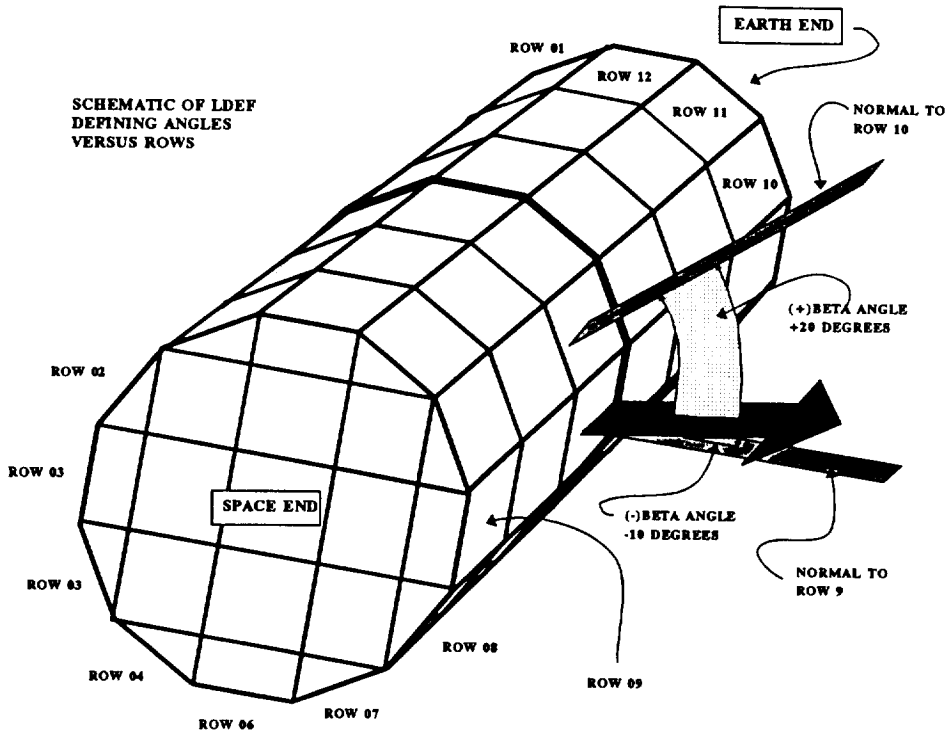

Figure 2. Definition of angle Beta.

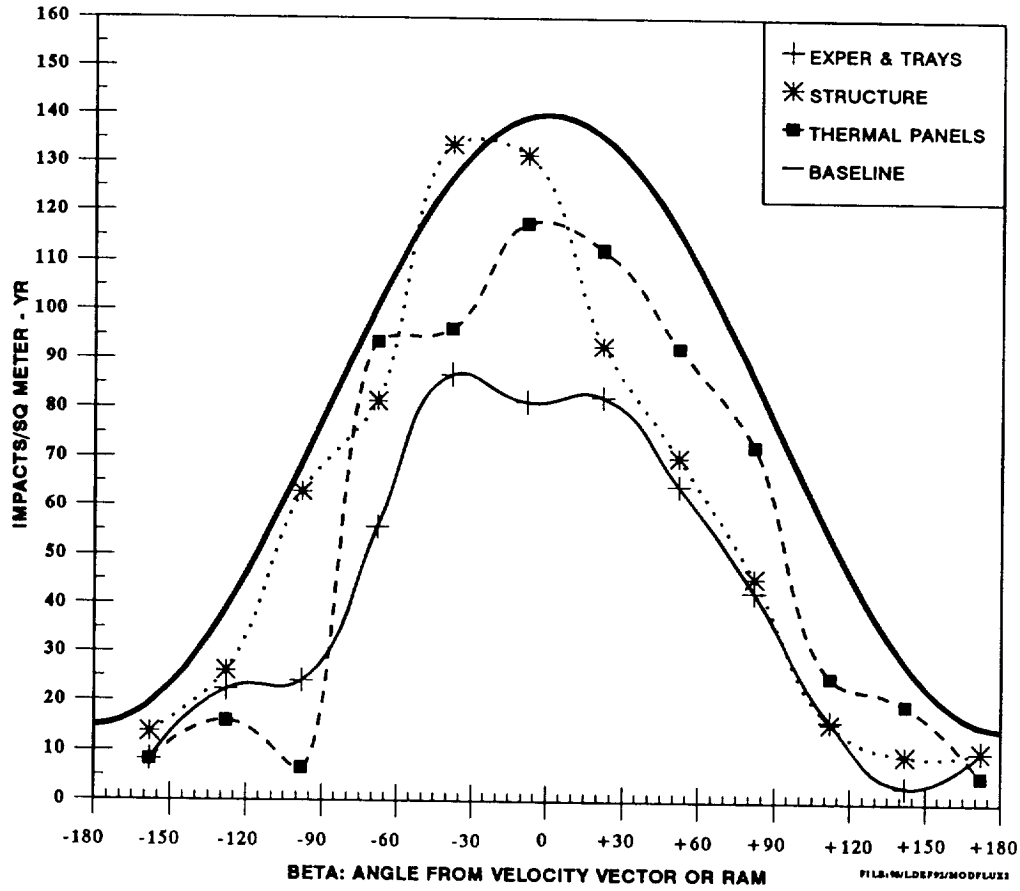

Figure 3. Directional dependence of meteoroid/space debris impact craters.

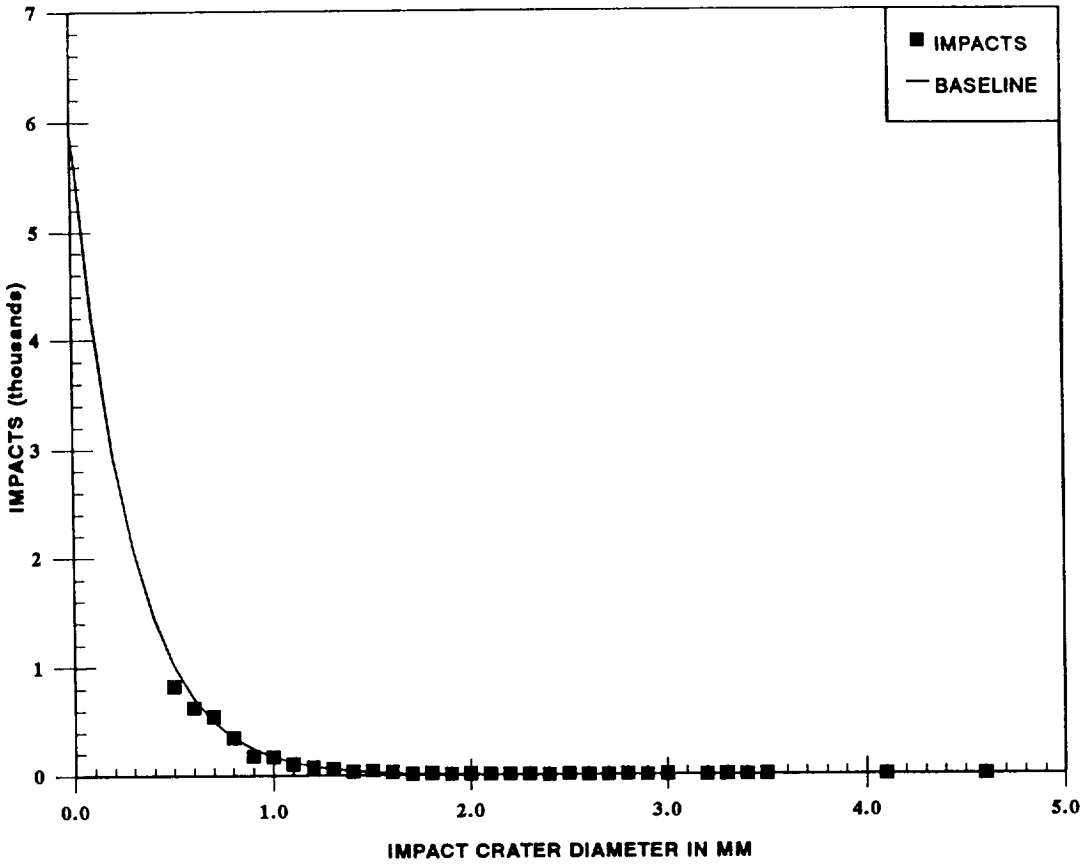

Figure 4. Size dependence of impact craters.

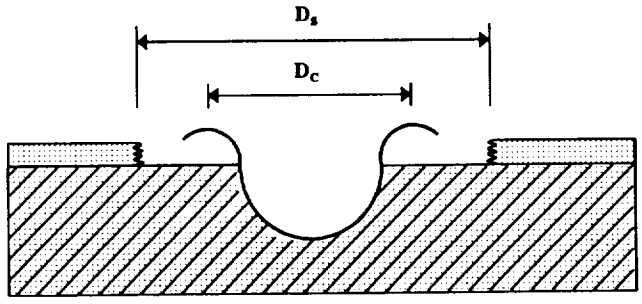

Figure 5. Definition of spall diameter and crater diameter.

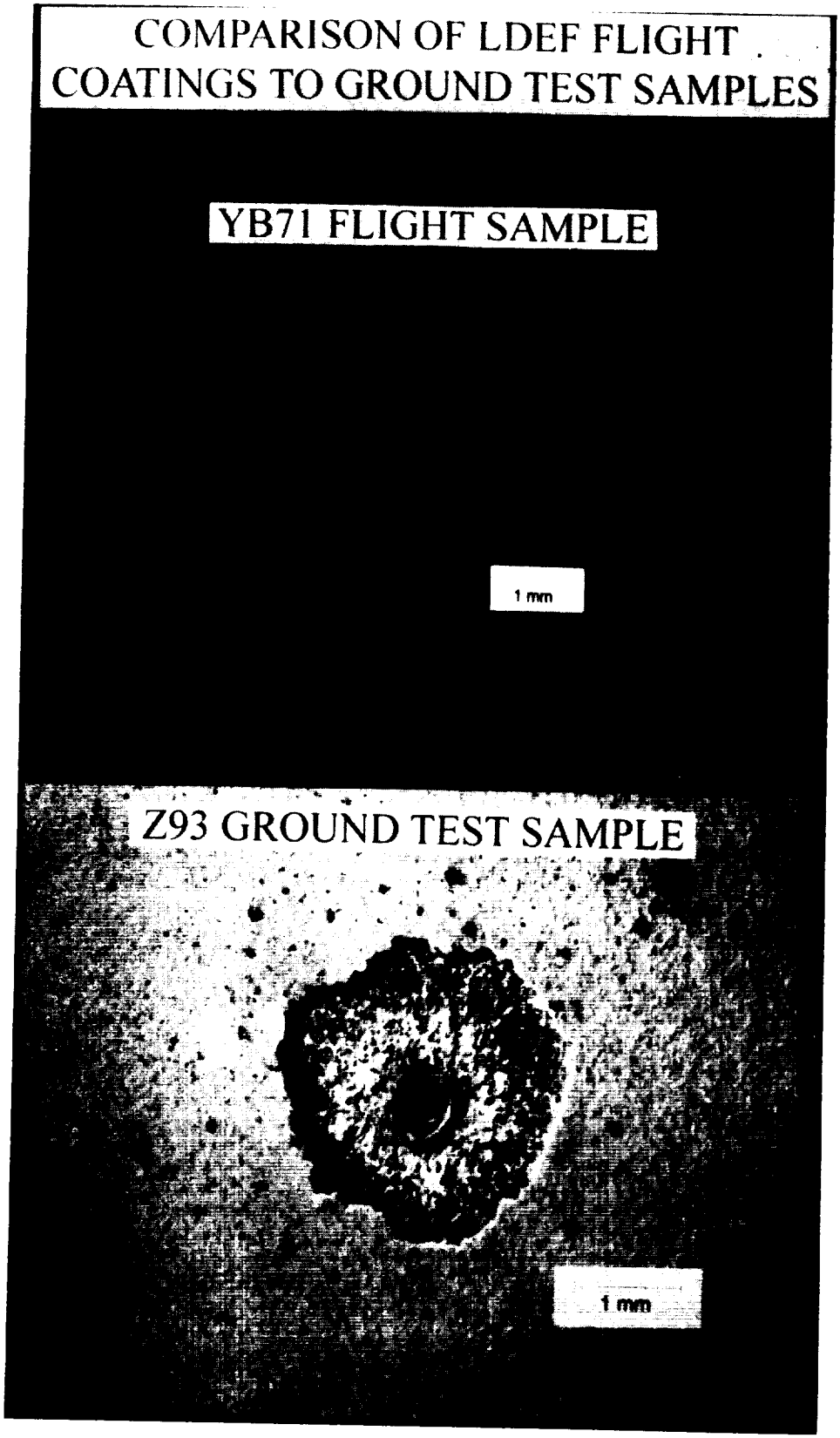

Figure 6. Impact spall damage to white paints Z93 and YB71 having ceramic type binders.

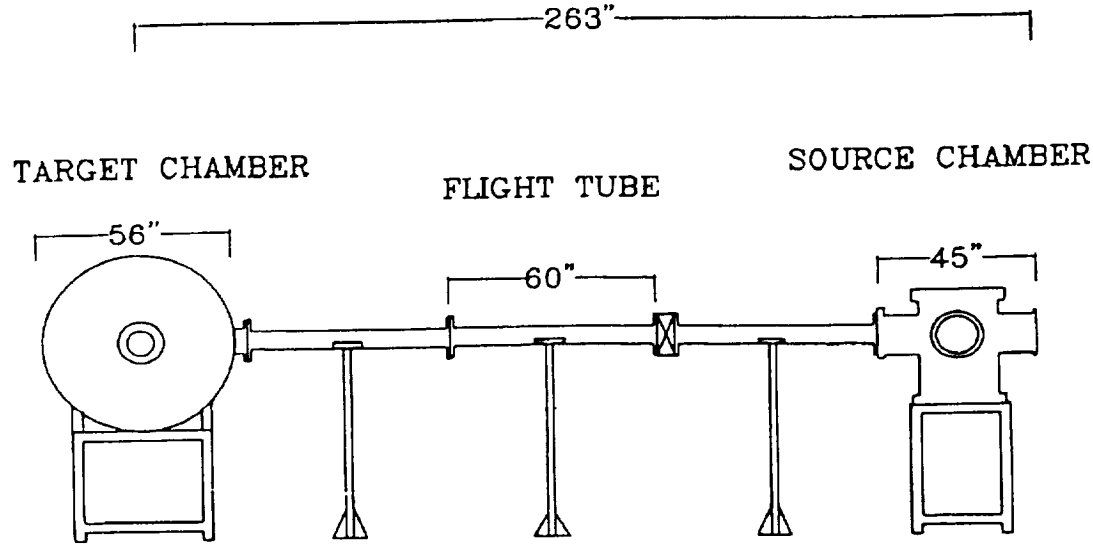

Figure 7. Schematic of AU's hypervelocity accelerator (ref. 6).

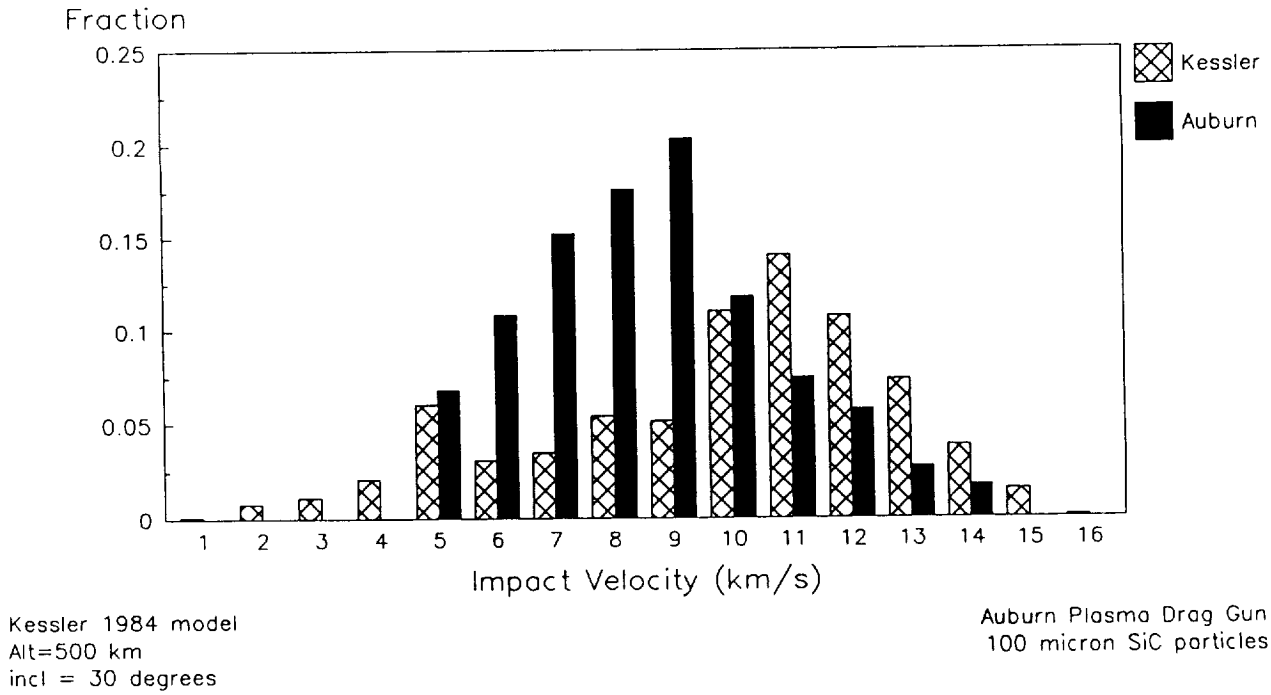

Figure 8. Particle impact velocity comparison between ground testing and flight.

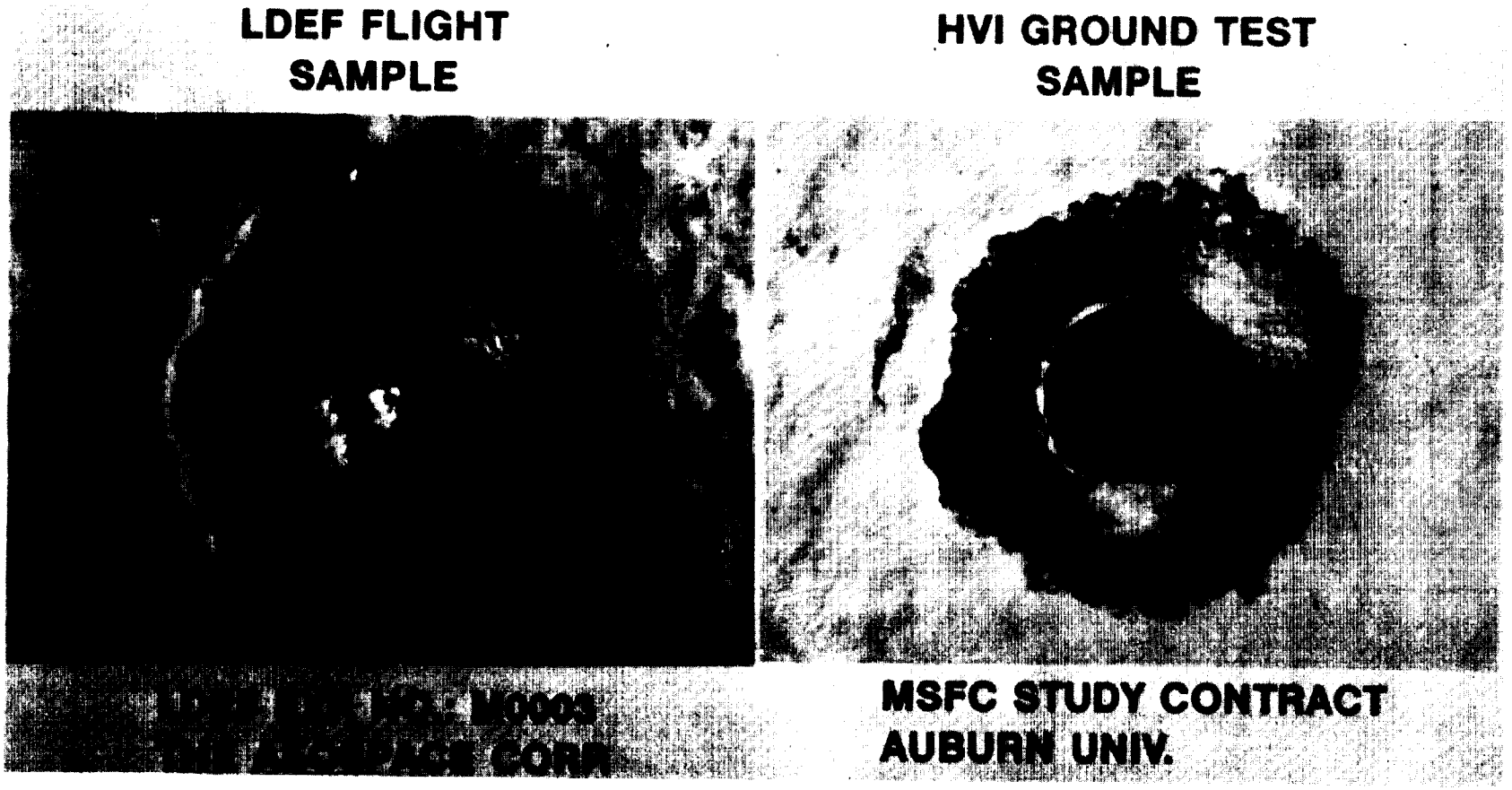

Figure 9. Impact spall damage to S13GLO white paint having a silicone type binder.

Figure 10. Impact spall damage to silver Teflon™ on LDEF experiment S0069 (ref. 9).

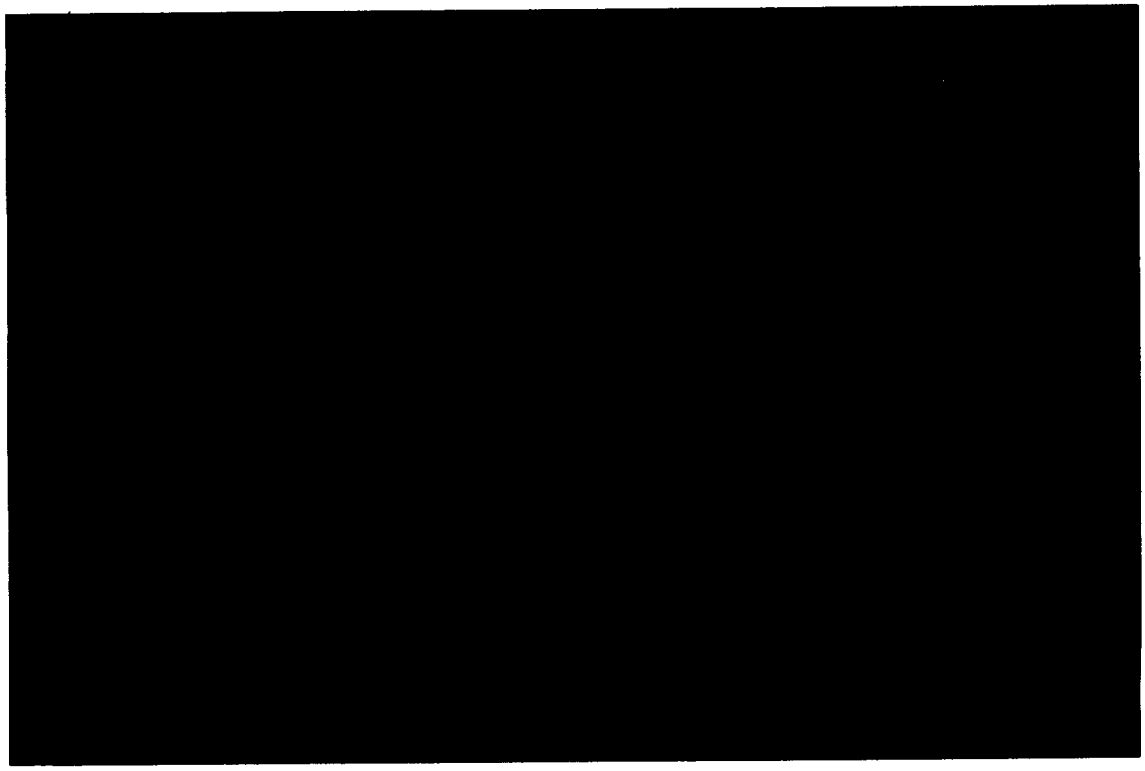

Figure 11. Impact damage to chromic anodized coating on LDEF experiment S0069 (ref. 9).

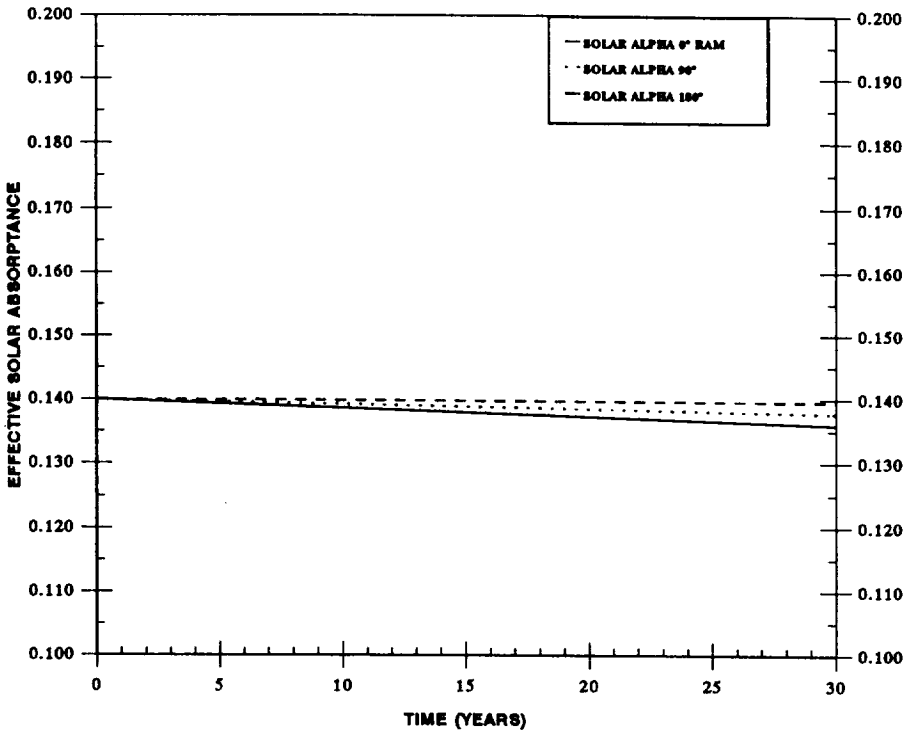

Figure 12. Z93 M/OD effect on solar absorptance versus time.

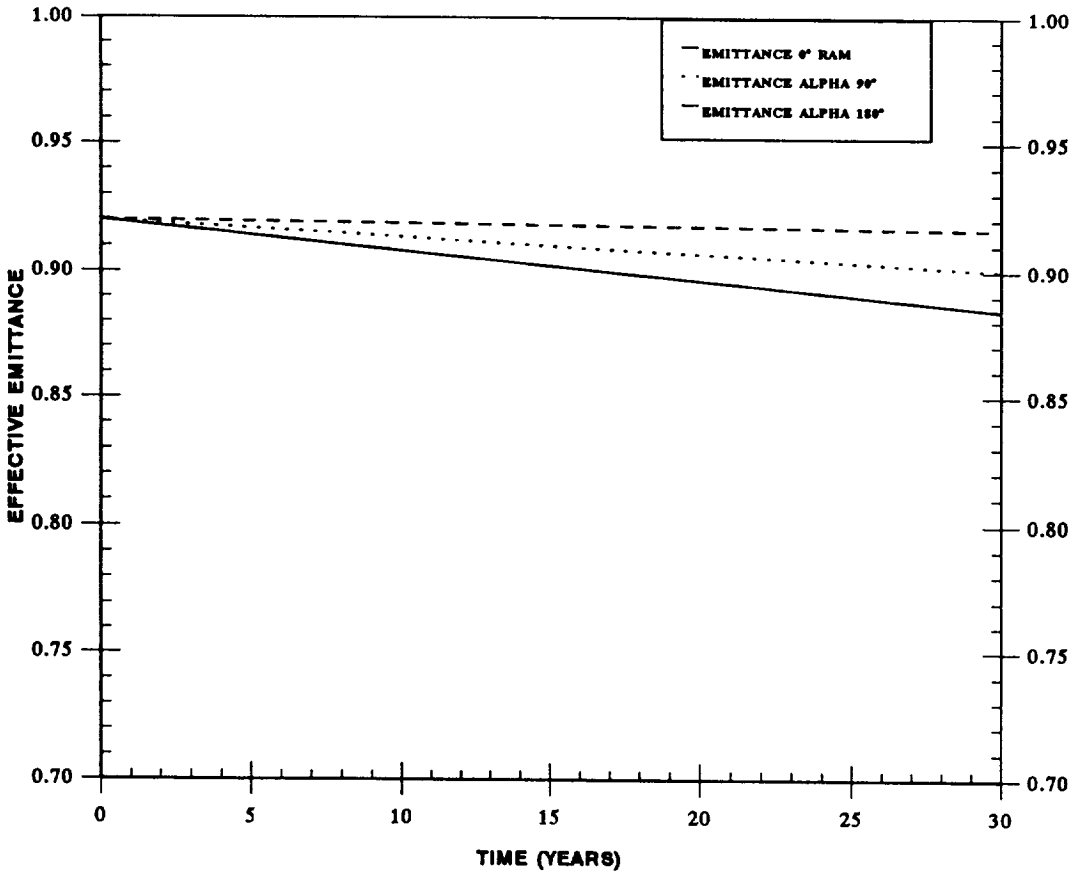

Figure 13. Z93 M/OD effect on emittance versus time.

C-4.

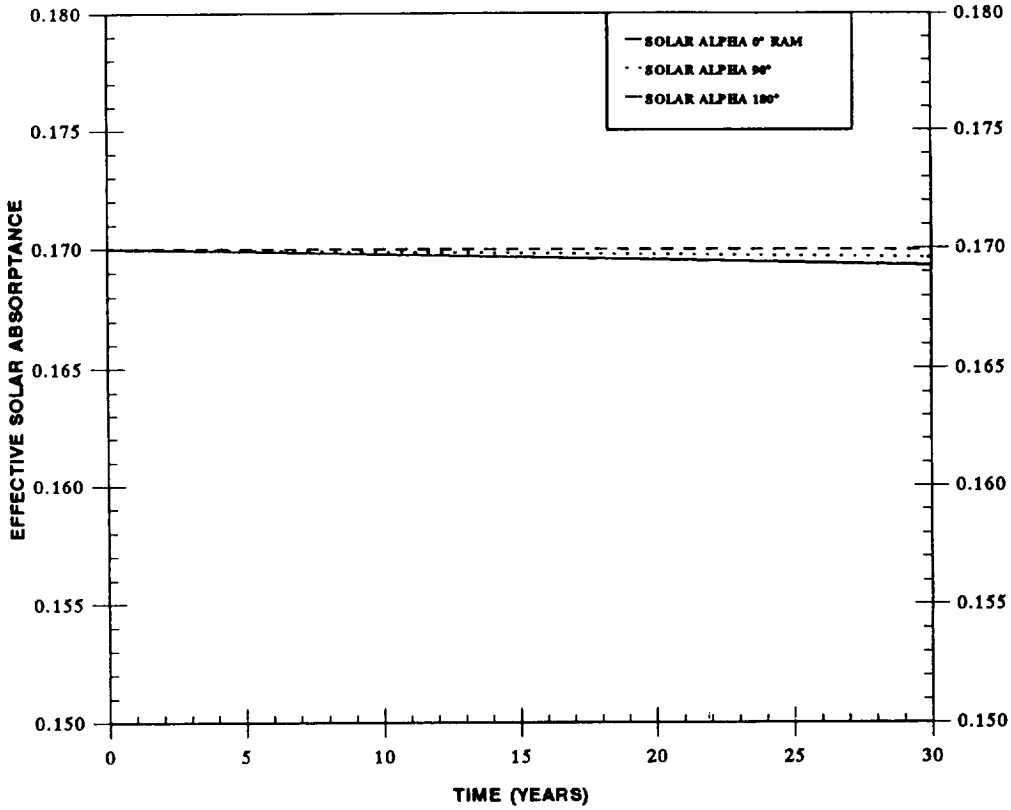

Figure 14. S13G/LO M/OD effect on solar absorptance versus time.

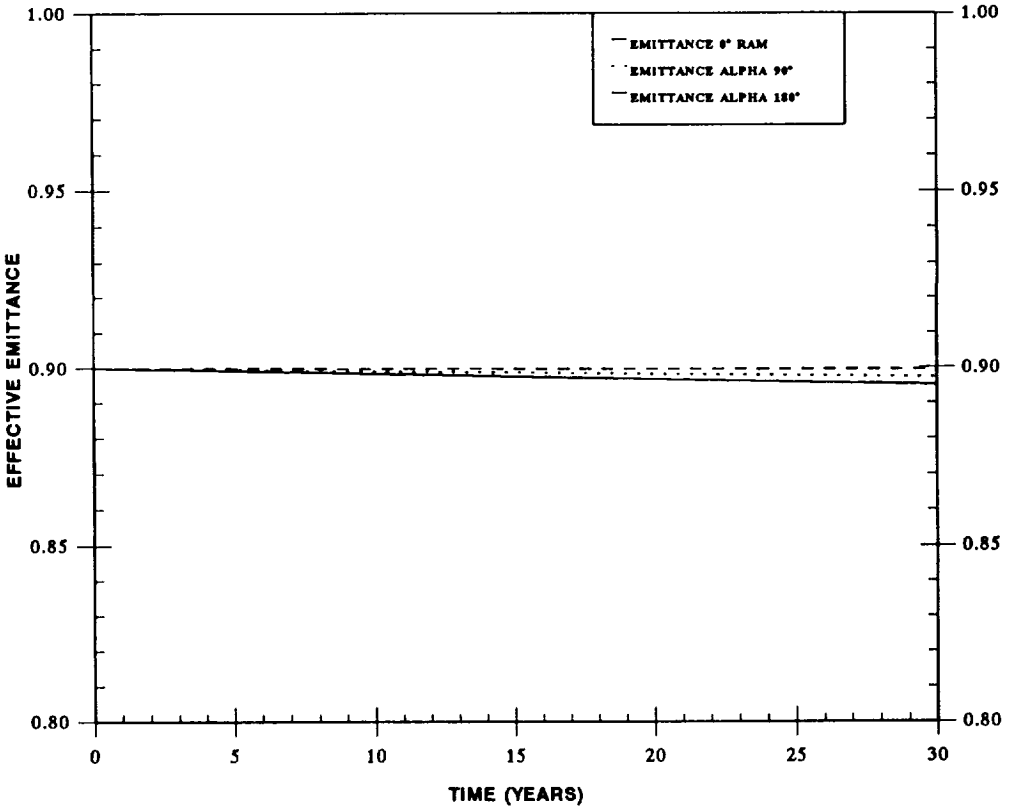

Figure 15. S13G/LO M/OD effect on emittance versus time.

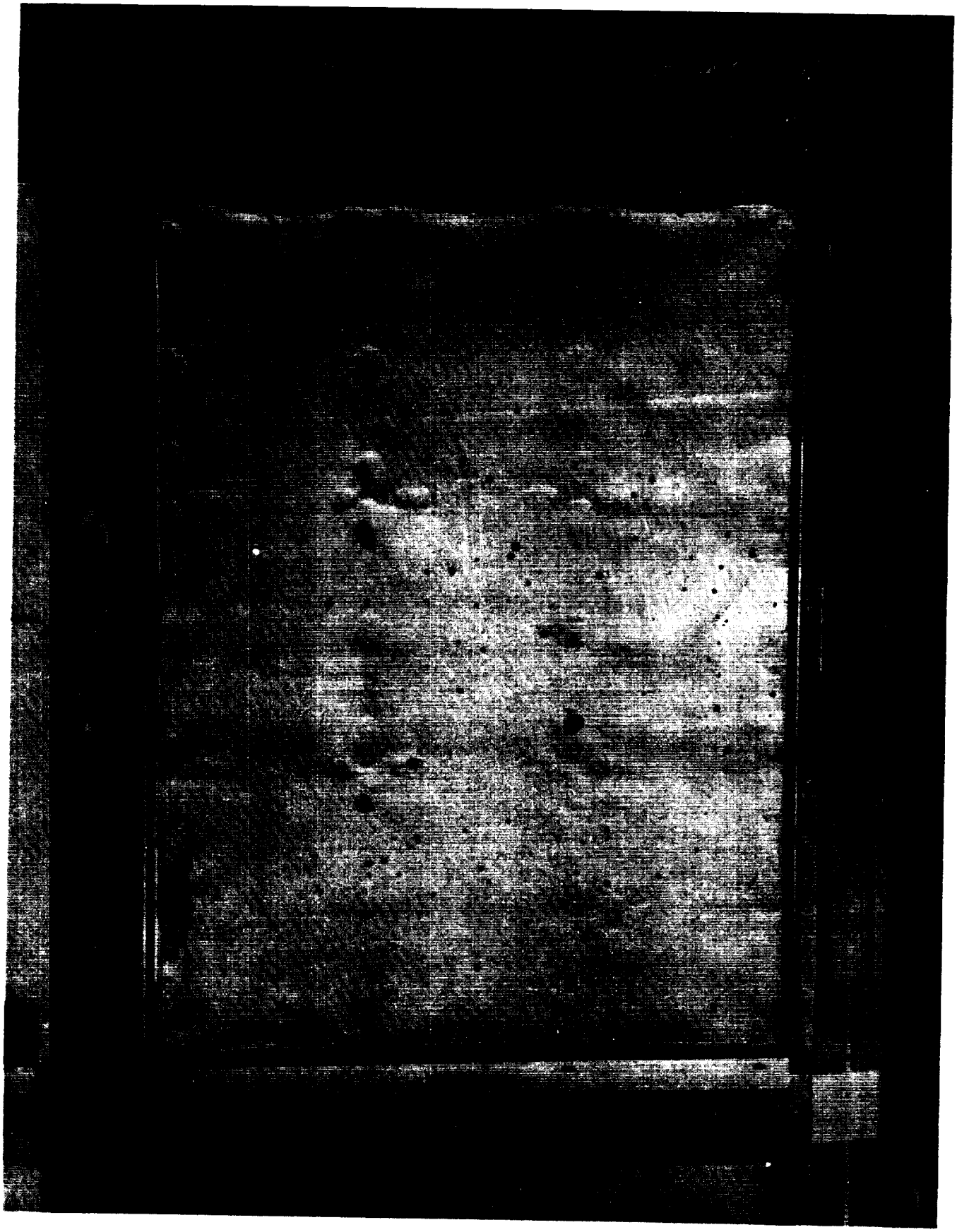

Figure 16. Silver Teflon™ blanket flown on LDEF experiment A0178 row 10E.

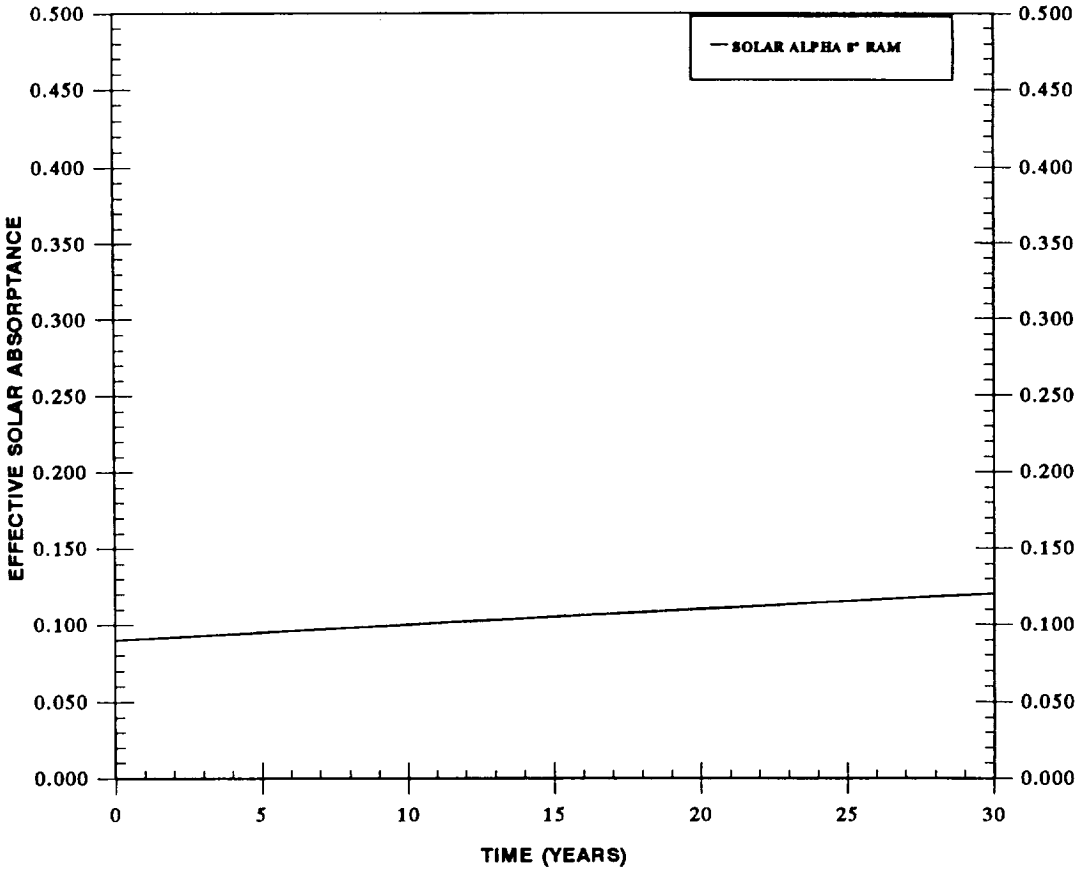

Figure 17. Ag/FEP M/OD effect on solar absorptance versus time.

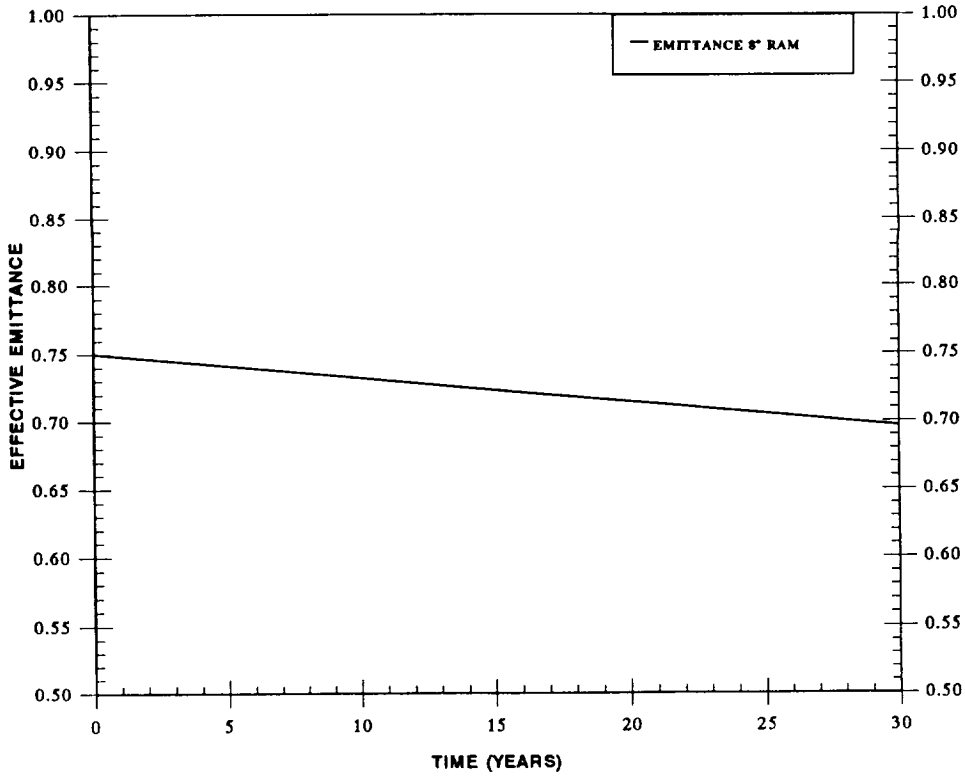

Figure 18. Ag/FEP M/OD effect on emittance versus time.

(a) COMPOSITES AND STRUCTURAL MATERIALS; (b) DATA BASES

N94-31033

THERMAL-VACUUM RESPONSE OF POLYMER MATRIX COMPOSITES IN SPACE

R.C. Tennyson and R. Matthews
University of Toronto Institute for Aerospace Studies
North York, Ontario, Canada, M3H 5T6
Phone: 416/667-7710, Fax: 416/667-7799

SUMMARY

This report describes a thermal-vacuum outgassing model and test protocol for predicting outgassing times and dimensional changes for polymer matrix composites. Experimental results derived from "control" samples are used to provide the basis for analytical predictions to compare with the outgassing response of Long Duration Exposure Facility (LDEF) flight samples. Coefficient of thermal expansion (CTE) data are also presented. In addition, an example is given illustrating the dimensional change of a "zero" CTE laminate due to moisture outgassing.

THERMAL-VACUUM OUTGASSING AND DIMENSIONAL CHANGES OF LDEF POLYMER MATRIX COMPOSITES (AO180)

The University of Toronto Institute for Aerospace Studies (UTIAS) experiment consisted of a variety of graphite, aramid, and boron fiber reinforced epoxy matrix composites located at station D-12 on LDEF (i.e., ~82° relative to velocity vector). Selected samples were instrumented with strain and temperature gauges that were sampled every 16 hours over the first 370 days in orbit. Data were stored on a magnetic tape cassette using a space-qualified data acquisition system designed and constructed at UTIAS. Details on this aspect of our experiment can be obtained from reference 1. It was found that the strain/thermal gauge measuring system worked flawlessly, as evidenced by the measured response of a stainless steel calibration specimen which remained unchanged throughout the 5.75 years in orbit. Typical time/temperature and strain/temperature data for one material (graphite/epoxy, 5208/T300) are shown in Figures 1 and 2, respectively. This data can be replotted as strain versus temperature as given in Figure 3 for the 90° laminate. It can be seen that a "total" dimensional strain change of ~1,600×10^{-6} occurred after about 80 days in orbit. It should be noted that no microcracks were observed in this laminate, and full recovery of the dimensional change resulted once the sample was returned to Earth and exposed to the ambient environment.

From these data, it is possible to estimate the CTE from the final slope once all outgassing is essentially finished. Using this CTE value, one can correct for the temperature variations on-orbit, giving the strain change of the sample, over time, independent of temperature. The formula used to do this is:

$$\Delta_t = \varepsilon_t - (T_t - T_{\mathrm{Ref}}) \cdot \alpha \ , \qquad (1)$$

where Δ_t = strain change at time t, ε_t = measured strain at time t, T_t = temperature at time t, T_{Ref} = reference temperature = 75 °F, and α = CTE of material.

Δ_t was then plotted against time and an adjustment factor (Δ adj) was added to every point. This had the effect of shifting the graph so that the final strain was zero, allowing the total strain change to be read easily. Figure 4 shows the adjusted Δ_t versus time curve for a 90° graphite/epoxy laminate (5208/T300). From this graph it is evident that outgassing was completed in about 80 to 100 days. It is clear that outgassing was very rapid over the first 25 days, then slowed due to the low temperatures encountered (Fig. 1). Outgassing then increased after 50 days as the sample temperature increased, and eventually no further measured dimensional change occurred after about 80 to 100 days exposure. Similar behavior was exhibited by the other composite materials (ref. 1). It is interesting to note that in the fiber direction (i.e., a 0° laminate), very small Δ_t changes were observed, as illustrated in Figure 5 for another graphite/epoxy material (SP288/T300). In general, the outgassing time required to reach an equilibrium state in space depends on such factors as the initial moisture concentration, the volatile content, laminate thickness, ambient temperature, and constituent material diffusion properties.

MOISTURE DESORPTION AND DIMENSIONAL CHANGES

As with many other published analyses, the moisture desorption M can be estimated using Fick's law from the equation (see, for example, ref. 2),

$$M(t)_{T=\text{const}} \cong M_O \exp\left[-7.3\left(\frac{Dt}{h^2}\right)^{0.75}\right] \tag{2}$$

where M_O = initial moisture content, D = diffusion coefficient, and h = thickness. For constant temperature, Shen and Springer (ref. 3) have shown that the diffusion coefficient (D) can be calculated knowing the moisture content at different times from the relation,

$$D_{T=\text{const}} = \frac{\pi h^2}{16 M_o^2}\left[\frac{M_2 - M_1}{\sqrt{t_2} - \sqrt{t_1}}\right]^2 , \tag{3}$$

where M_1, M_2 = moisture contents at times t_1 and t_2, respectively.

Rather than measure moisture content during a test, one can employ strain data (ε). Noting that

$$\varepsilon = M\beta \tag{4}$$

where β = coefficient of moisture expansion (CME), then equations (2) and (3) can be rewritten as,

$$\varepsilon(t)_{T=\text{const}} = \varepsilon_O \exp\left[-7.3\left(\frac{Dt}{h^2}\right)^{0.75}\right] \tag{5}$$

and

$$D(t)_{T=\text{const}} = \frac{\pi h^2}{16 \varepsilon_o^2}\left[\frac{\varepsilon_2 - \varepsilon_1}{\sqrt{t_2} - \sqrt{t_1}}\right]^2 . \tag{6}$$

To develop a model for predicting outgassing of materials in space, it is necessary to take temperature into account. However, Fick's law as previously described applies to constant temperature, constant humidity environments. In space, the humidity level (i.e., vacuum) is constant.

Furthermore it is possible to determine a diffusion coefficient as a function of temperature ($D(t)$) by performing outgassing tests at different temperatures (T_a and T_b) assuming an Arrhenius relation between D and T. This yields the equation,

$$D(T) = \exp\left[\frac{\ln(D_b) - \ln(D_a)}{1 - \frac{T_a}{T_b}} + \ln(D_a)\right] \cdot \exp\left[\frac{\left(\ln(D_b) - \ln(D_a)\right)}{\left(\frac{1}{T_a} - \frac{1}{T_b}\right) \cdot T}\right] . \tag{7}$$

This equation can be used to calculate the diffusion coefficient at any temperature, T, as long as the diffusion coefficients D_a and D_b at temperatures T_a and T_b are known. All of the above temperatures must be absolute (K).

Hence, knowing $D(T)$, the strain associated with outgassing $\varepsilon(T, t)$ can be calculated from equation (5).

LAMINATE ANALYSIS

Consider an N-ply laminate characterized by a set of lamina properties defined by

$$\phi_\ell = \begin{bmatrix} \phi_1 \\ \phi_2 \\ 0 \end{bmatrix} , \tag{8}$$

where ϕ_1, ϕ_2 correspond to the fiber (1) and transverse (2) properties, respectively. Examples of ϕ_m include both CTE and CME coefficients, i.e.,

$$\phi_\ell = \alpha_\ell = \begin{bmatrix} \alpha_1 \\ \alpha_2 \\ 0 \end{bmatrix} \quad \text{and} \quad \phi_\ell = \beta_\ell = \begin{bmatrix} \beta_1 \\ \beta_2 \\ 0 \end{bmatrix} , \tag{9}$$

where $\alpha = \varepsilon/\Delta T$ and $\beta = \varepsilon/\Delta M$. For an actual N-ply laminate consisting of a set of plies $k = 1$ to N having arbitrary orientations θ_k and stacking sequence, the structural properties defined by ϕ_S can be calculated from the following matrix equation (see ref. 4 for example):

$$\begin{bmatrix} \phi_S \\ \kappa_T \end{bmatrix} = \begin{bmatrix} A & B \\ B & D \end{bmatrix}^{-1} \begin{bmatrix} J \\ H \end{bmatrix} \begin{bmatrix} \phi_1 \\ \phi_2 \\ 0 \end{bmatrix} , \tag{10}$$

where

$$\phi_S = \begin{bmatrix} \phi_x \\ \phi_y \\ \phi_{xy} \end{bmatrix} , \qquad \kappa_T = \begin{bmatrix} \kappa_x \\ \kappa_y \\ \kappa_{xy} \end{bmatrix} = \text{laminate curvatures} ,$$

$$\left|\begin{matrix} A & B \\ B & D \end{matrix}\right|^{-1} = \text{inverse of the standard laminate stiffness matrix (see ref. 4)},$$

$$[J] = \sum_{k=1}^{N} T_k^{-1} \cdot Q_k(h_k - h_{k-1}) \quad \text{and} \quad [H] = \sum_{k=1}^{N} \frac{1}{2} \cdot T_k^{-1} \cdot Q_k(h_k^2 - h_{k-1}^2),$$

$$[T] = \left|\begin{matrix} m^2 & n^2 & 2mn \\ n^2 & m^2 & -2mn \\ -mn & mn & m^2-n^2 \end{matrix}\right| = \text{transformation matrix},$$

Q_k = reduced lamina stiffness matrix for kth ply (see ref. 4)

$m = \cos\theta$, $n = \sin\theta$, θ = ply angle, h_k = thickness of kth ply.

APPLICATION OF OUTGASSING DIMENSIONAL CHANGE ANALYSIS TO LDEF SAMPLES

Prior to analyzing the LDEF data in detail, two issues regarding material response and the measuring systems warrant some discussion. The LDEF flight samples were monitored using bonded surface strain gauges whereas the laboratory tests were conducted using laser interferometry. A comparison of both system responses is shown in Figure 6 where it is evident that excellent correlation exists based on the test of a flight sample in the vacuum chamber. The question of whether Fick's law is a good model for the graphite/epoxy composite material is addressed in Figure 7. Using a control sample that was vacuum dried and saturated to 0.49-percent moisture content, then allowed to outgas at T = 22 °C, provided the $\varepsilon(t)$ curve shown. Employing the previous analysis to estimate the diffusion coefficient D, Fick's law prediction was compared to the measured long term response. Excellent agreement was obtained. Thus one can proceed with confidence in the analytical model and test procedures.

EXPERIMENTAL INPUT

The following test protocol was established utilizing LDEF "control" and "flight" samples. It should be noted that all "control" specimens were made at the same time from the same material batch as the flight articles, and stored at "ambient" laboratory conditions.

1. Samples were subjected to vacuum outgassing at elevated temperature to obtain their "dry weight" values.

2. For given temperature (T) and percent RH, moisture uptake (percent) was recorded for a given material from its "dry" state as a function of time (t) to saturation. Figure 8 shows moisture absorption data for LDEF flight and control specimens (see Table 1).

3. Sample strain (ε) was measured as a function of time (t) in vacuum for two temperatures (T_a and T_b). Both experiments employed samples having the same M_o.

Figures 9 to 12 present initial outgassing data for flight (2T13) and control (5T5) samples at temperatures of 22 °C and 55 °C. The strain response was measured in situ using laser interferometry.

ANALYTICAL PROCEDURE

1. Using the $\varepsilon(T, t)$ curves, the initial slope can be calculated from equation (7) to obtain $D_a(T_a)$ and $D_b(T_b)$.

2. Determine $D(T)$ from equation (7) based on $D_a(T_a)$, $D_b(T_b)$, T_a and T_b. Table 1 summarizes the values obtained for $D(T)$ for both "flight" and "control" samples of graphite/epoxy $[90°]_4$ laminates (5208/T300).

3. Using the LDEF temperature/time profile obtained in-orbit (Fig. 1), calculate the dynamic strain change $\varepsilon(t)$ for given time steps (Δt), using the above $D(T)$ equation evaluated at the appropriate temperature. The $\varepsilon(t)$ function is given by (equation (5)),

$$\varepsilon_t = \varepsilon_{t-1} - \varepsilon_{t-1}\left(1 - \exp\left[-7.3\left(\frac{D(T_t)\cdot \Delta t}{h^2}\right)^{0.75}\right]\right), \qquad (11)$$

where T_t = average temperature over Δt, assuming ε_o is known at $t = 0$ from the outgassing test. By using this equation at every time step over the temperature history, it is possible to calculate the strain change of the sample due to outgassing, taking into account temperature effects.

From the outgassing response shown in Figure 4, it is evident that the moisture diffusion process essentially ceases when the temperature drops to freezing or below (i.e., $D \approx 0$ when $T \leq$ 32 °F). This constraint can then be included in the $\varepsilon(t)$ prediction.

COMPARISON WITH LDEF DATA

Based on the data in Table 1, values of $D_a \cong 0.00013$ (mm^2/h) and $D_b \simeq 0.00078$ (mm^2/h) were selected, corresponding to temperatures of 22 °C and 50 °C, respectively. Using these results in equation (7) together with the temperature/time profile shown in Figure 1, the predicted dimensional change for the graphite/epoxy 90° laminate (5208/T300) is plotted in Figure 13 with the measured LDEF response as a function of time in orbit. Curve 1 represents the case when no correction is applied for T ≤ 273 K. One can see the effect of assuming "zero" outgassing of water moisture exhibited by curve 2. Although the initial response prediction agrees well with flight data, it is clear that the predicted times to complete outgassing differ significantly from the flight measurements.

Theoretical predictions were then made for various values of the diffusion coefficients and the dimensional changes plotted in Figure 14. One can see in Figure 15 that for a diffusion coefficient of $D^* \simeq 0.134\ D_m$ (where D_m = measured value in the vacuum chamber), excellent agreement with the flight data is obtained. Clearly the theoretical model is quite capable of predicting the outgassing dimensional changes once the appropriate diffusion coefficient is known, even over the complete thermal cycling environment.

Why is there such a difference in the diffusion coefficients measured in "space" and in the vacuum chamber? The tests reported show good correlation between "control" and "flight" samples. Moisture saturation and uniform distribution through the laminate was achieved. In addition, both measuring systems correlate very well. The only explanation we have to offer is the possible effect of surface contamination of the LDEF flight samples in the early stages of deployment. Over time, this contamination was removed from the samples due to atomic oxygen. Hence, when the flight samples were tested in the vacuum chamber, no contamination effects were observed. Thus one can account for the apparent increase in outgassing time observed in orbit.

COEFFICIENT OF THERMAL EXPANSION

As discussed earlier, after outgassing is essentially completed, one finds the thermal-strain response asymptotes, as can be seen in Figure 3 for the $[90°]_4$ graphite/epoxy material (5208/T300). This behavior was typical of all our LDEF samples (see ref. 1 for example). Table 2 summarizes the slope values of these curves (i.e., the CTE) for a variety of materials studied. The "ambient" values represent pre-flight measurements which compare in most instances reasonably well with the final asymptotic slopes obtained from the actual flight data. Some postflight CTE results are also presented based on laser interferometer measurements after complete outgassing had occurred.

APPLICATION TO DESIGN

To demonstrate how this diffusion data and analysis can be used in the design of low distortion laminates, consider the case of a $(\pm\theta)_s$ structure. The question being addressed is how much axial distortion can occur in a zero CTE laminate?

Figure 16 presents the variation in the α_x and α_y CTE values for a $(\pm\theta)_s$ laminate fabricated from 5208/T300 material. The curves shown were determined using equation (10). The case of $\alpha_x = 0$ occurs when $\theta \cong \pm 46°$. Using diffusion data to calculate the CME values of β_x and β_y from equation (10), one can obtain from Figure 17 a $\beta_x \simeq 200\times10^{-6}/\%\ M$ at $\theta = 46°$.

Assuming a 1-percent moisture uptake prior to launch yields an axial displacement of $\Delta L = 200\times10^{-6}L$ where L = length of structure. Thus for a 10-m long structure, the axial contraction would be 2.0 mm for a zero CTE laminate.

CONCLUSIONS

1. Outgassing produces dimensional changes of polymer matrix composites which asymptote to a constant value once the outgassing process has essentially ceased.

2. A test protocol and analytical model have been formulated that can accurately predict the dimensional changes associated with outgassing as a function of temperature and time in vacuum.

3. Outgassing of the LDEF polymer matrix composites took much longer to asymptote in orbit than in a thermal-vacuum chamber. It is postulated that outgassing caused surface

contamination of the LDEF samples, thus inhibiting the diffusion process. The surface contaminants were then removed over time by the incident atomic oxygen which proceeded to erode the composite material as well.

4. The analytical model was capable of reproducing the LDEF flight sample response extremely well once a modified diffusion coefficient was used.

5. In general, the asymptotic thermal strain response of the flight samples yielded CTE values close to their original ambient measurements.

ACKNOWLEDGMENTS

This research was sponsored by the Canadian Space Agency (CSA) under contract 025SR.9F009-1-1435, and two Ontario Centres of Excellence: the Institute for Space and Terrestrial Science and the Ontario Centre for Materials Research. Special thanks are extended to Dr. D.G. Zimcik of the CSA for his continued support of our work.

REFERENCES

1. Tennyson, R.C.: "Composite Materials in Space—Results from the LDEF Satellite." J. Canadian Aeronautics and Space Institute, vol. 37, No. 3, September 1991.

2. Crank, J., and Park, G.S.: "Diffusion in Polymers." Academic Press, London, 1968.

3. Shen, Chi-Hung., and Springer, George S.: "Moisture Absorption and Desorption of Composite Materials." J. Composite Materials, vol. 10, January 1976.

4. Halpin, J.C.: "Primer on Composite Materials: Analysis." Technomic Publishing Company, 1984.

Table 1. Comparison of flight and control sample diffusion coefficients for $[90]_4$ graphite/epoxy laminates (5208/T300) as measured in vacuum chamber.

Sample No.	Status	Temp [°C]	M_i [%]	$\Delta\varepsilon$ [$\mu\varepsilon$]	CME [$\mu\varepsilon$/percent]	D [mm^2/h]
5T5	Control	22	0.490	-1,200	2,449	0.00010
5T5	Control	50	0.550	-1,939	3,525	0.00047
2T13	Flight	22	0.505	-1,212	2,400	0.00013
2T13	Flight	22	0.510	-1,224	2,400	0.00008
2T13	Flight	50	0.632	-1,517	2,400	0.00078
3T6	Flight	22	0.500	-1,200	2,400	0.00014
3T6	Flight	22	0.510	-1,219	2,400	0.00009

Table 2. Comparison of CTE data from LDEF experiment AO180.

Sample	Material	Laminate Type	Ambient CTE [10^{-6}/C]	Space CTE [10^{-6}/C]	Postflight* CTE [10^{-6}/C]
Control	T300/5208	$(90)_4$	—	—	24.5
Flight	T300/5208	$(90)_4$	—	—	24.7
Flight	T300/5208	$(90)_4$	28.1	28.9	—
Control	T300/5208	$(\pm45)_s$	—	—	1.93
Flight	T300/5208	$(\pm45)_s$	—	—	-6.53
Flight	T300/934	$(90)_4$	26.5	27.3	—
Flight	T300/SP-288	$(90)_4$	26.3	26.8	—
Flight	SP-290	$(\pm30)_s$	2.8	2.21	—
	Boron/Epoxy	$(\pm60)_s$	21.1	20.9	—
Flight	SP-328	$(90)_4$	61.0	59.2	—
	Kevlar/Epoxy	$(0)_4$	0.18	0.83	—
Control	SP-328	$(\pm45)_s$	—	—	-0.04
Flight	SP-328	$(\pm45)_s$	—	—	2.52

*Measured after complete vacuum outgassing

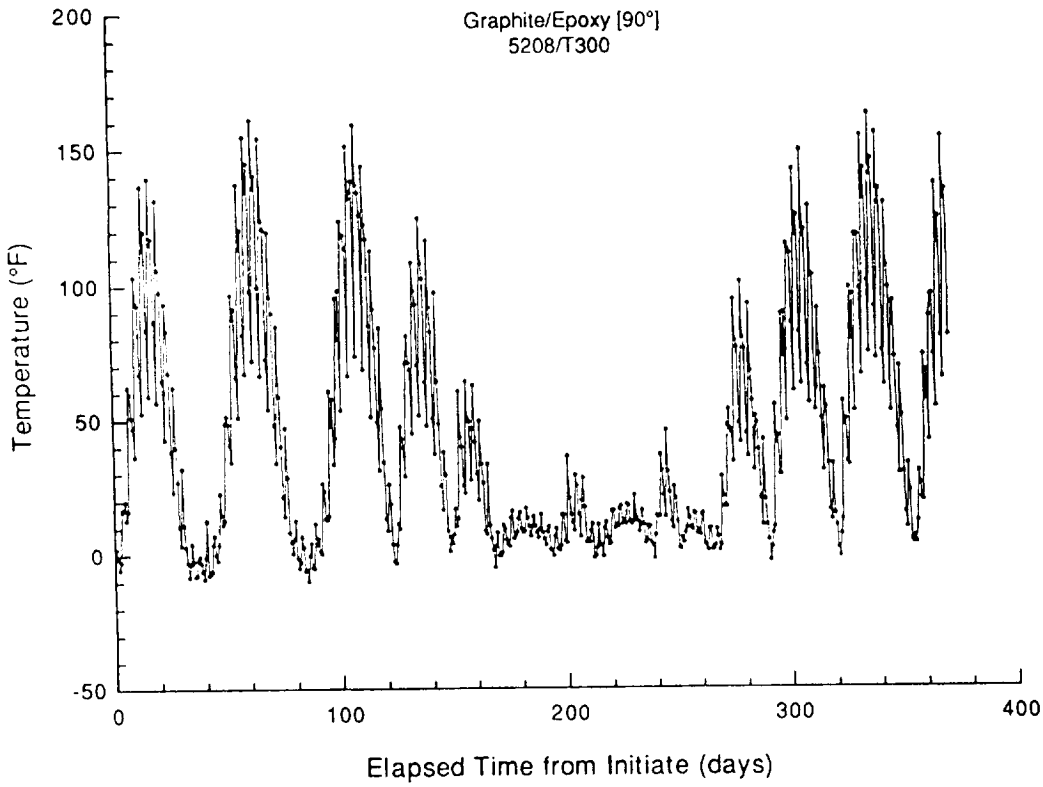

Figure 1. Thermal history of LDEF specimen (3T6).

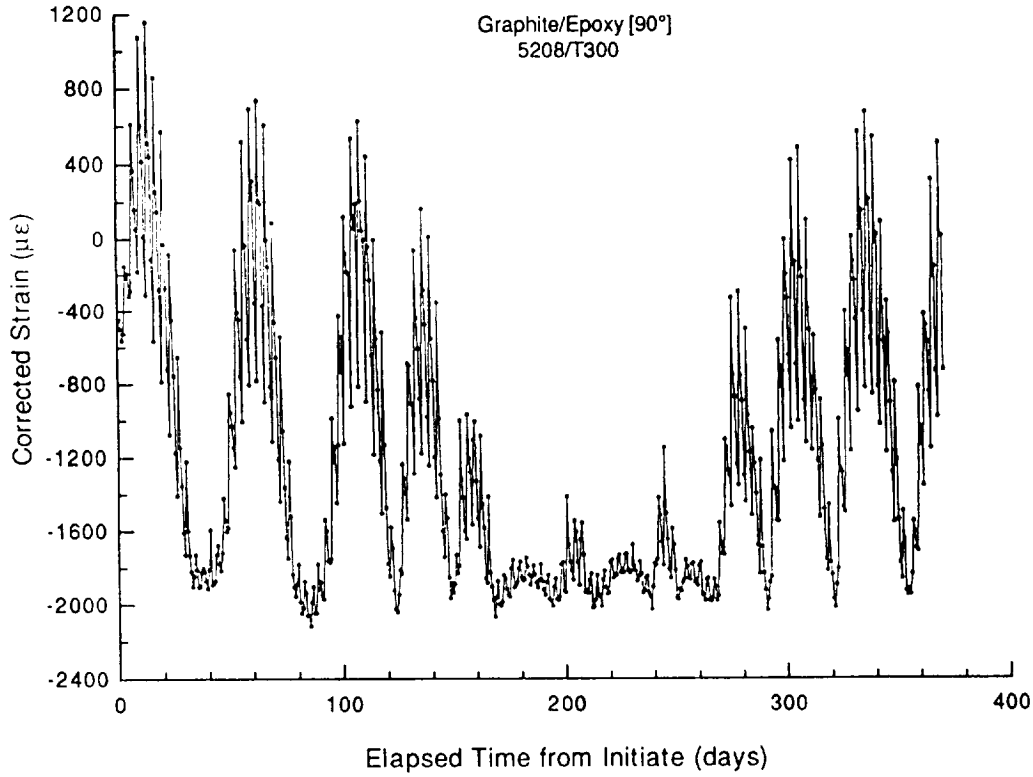

Figure 2. Strain-time history for LDEF specimen (3T6).

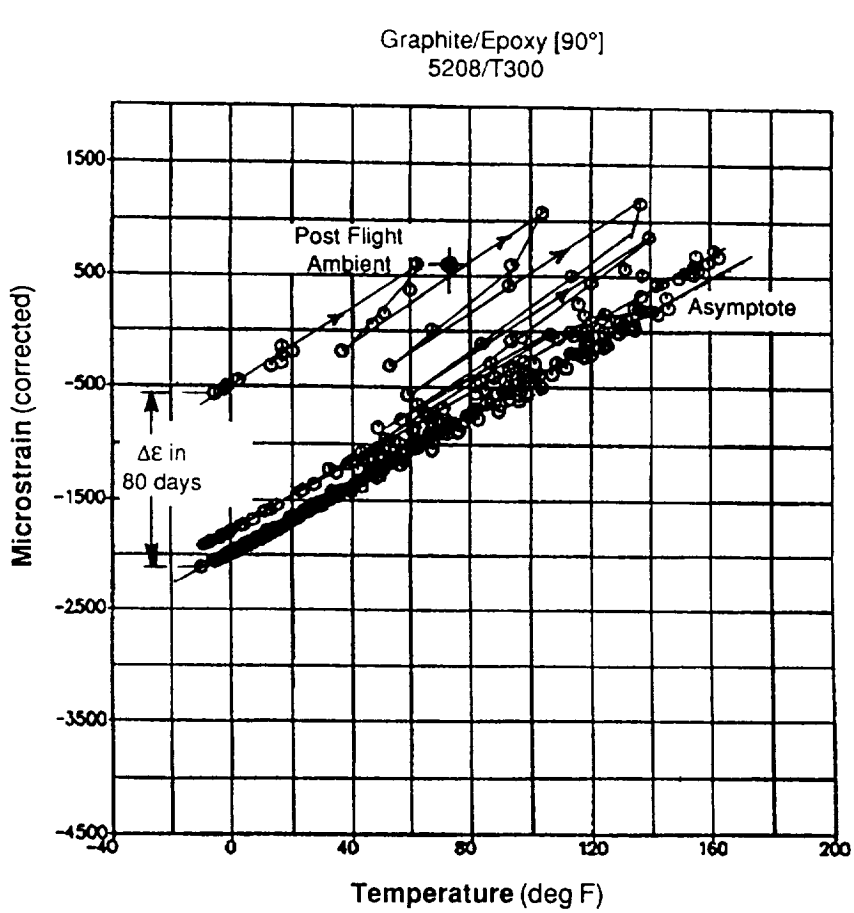

Figure 3. Thermal/strain response of LDEF specimen (3T6).

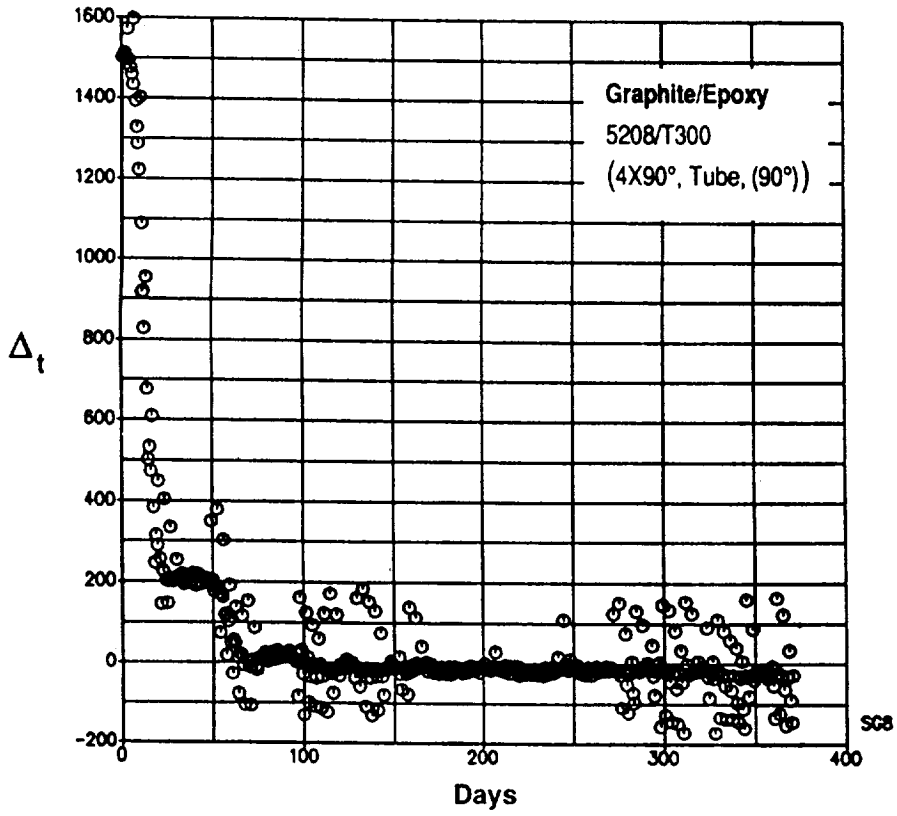

Figure 4. Plot of Δ_t strain versus time in orbit for LDEF specimen (3T6).

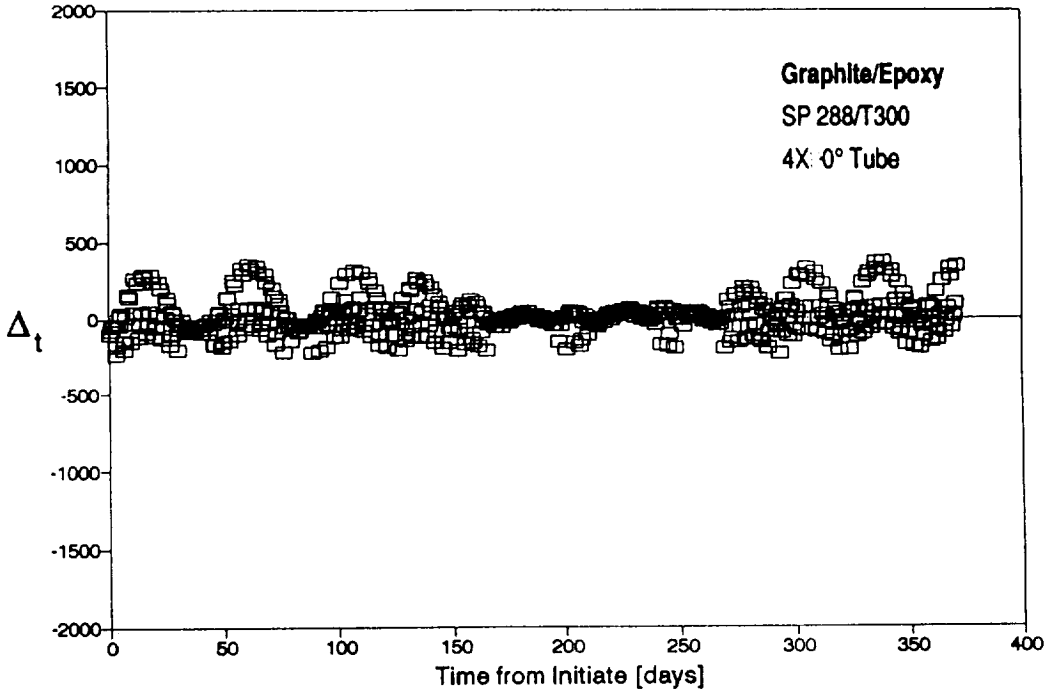

Figure 5. Plot of Δ_t strain versus time in orbit for LDEF specimen.

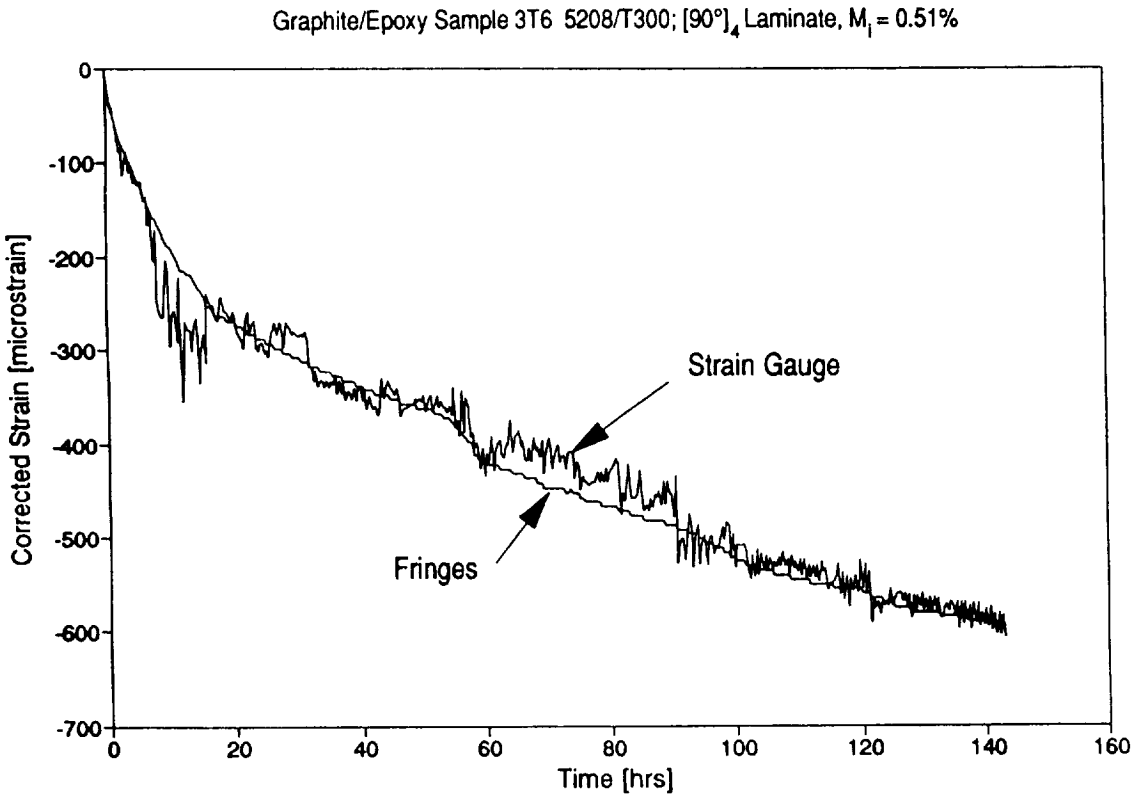

Figure 6. Comparison of outgassing response measured by strain gauge and laser interferometry.

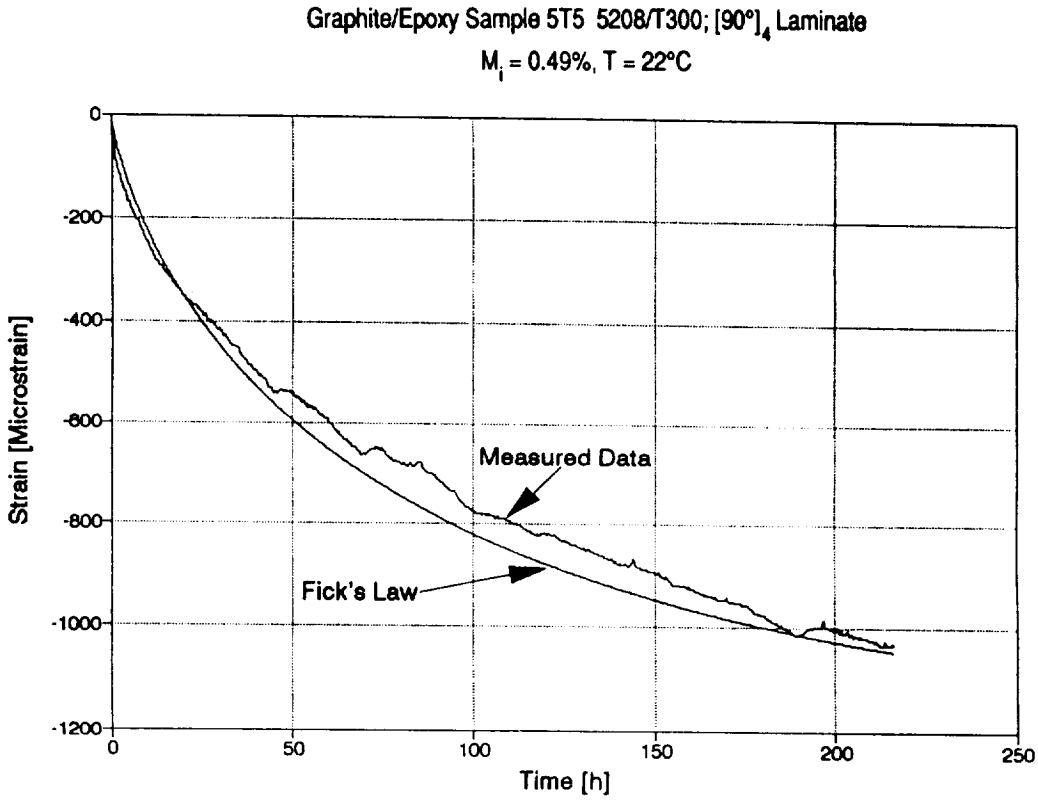

Figure 7. Comparison of outgassing response with Fick's law prediction.

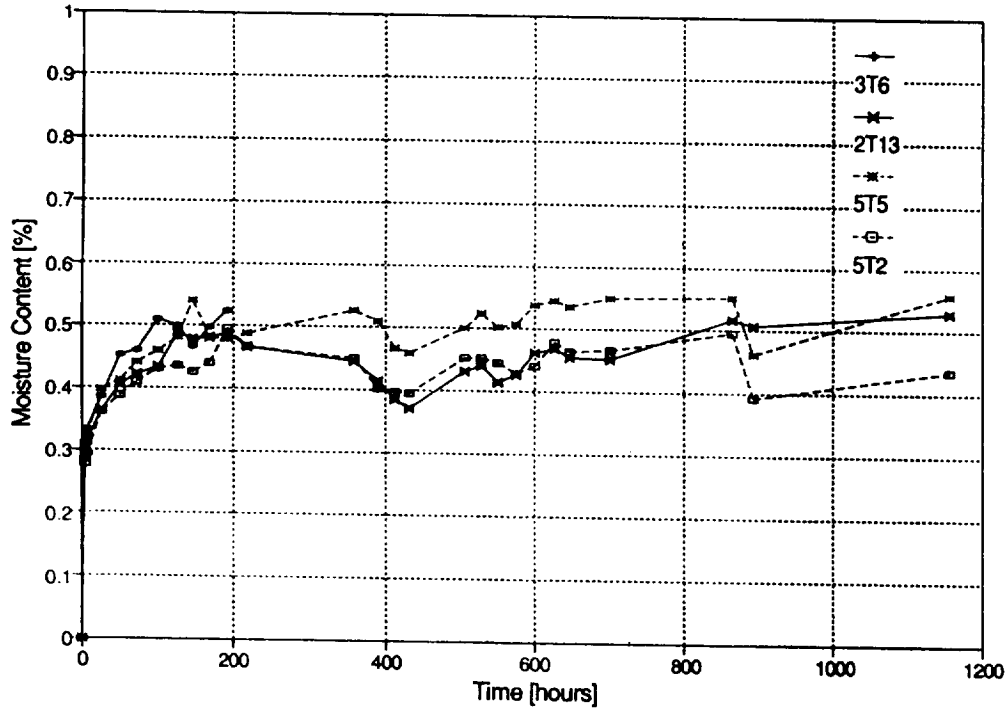

Figure 8. Moisture absorption response of LDEF samples at 50 °C and 75-percent RH.

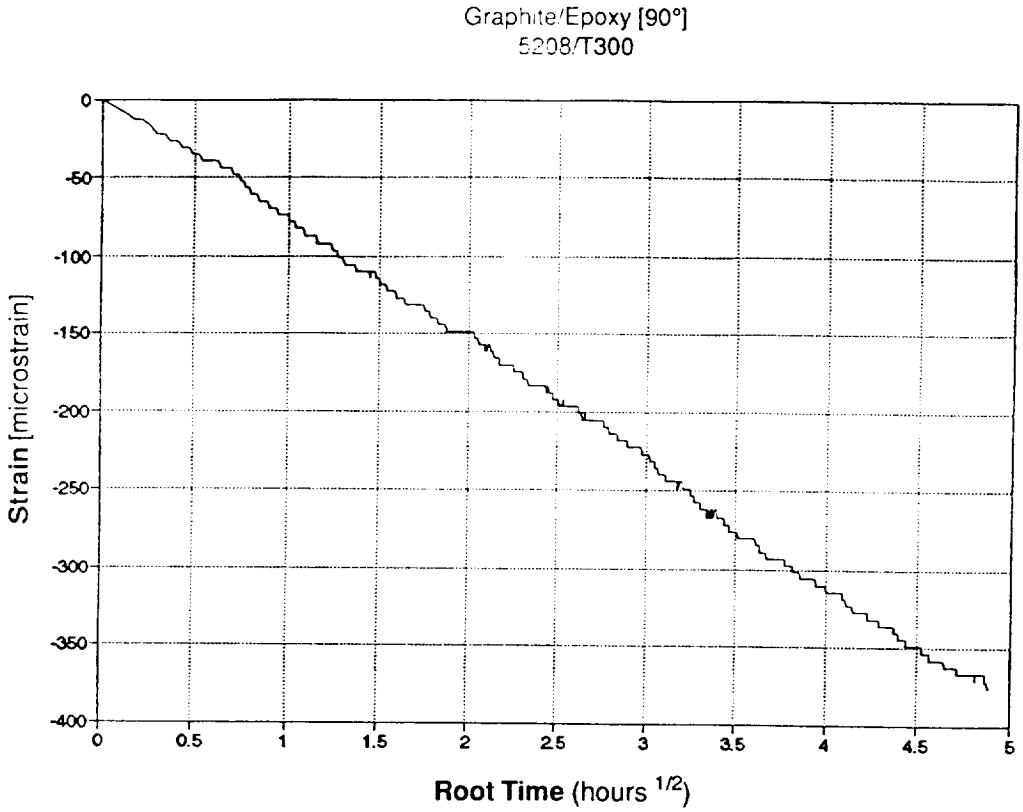

Figure 9. Outgassing test on control specimen (5T5) at 22 °C.

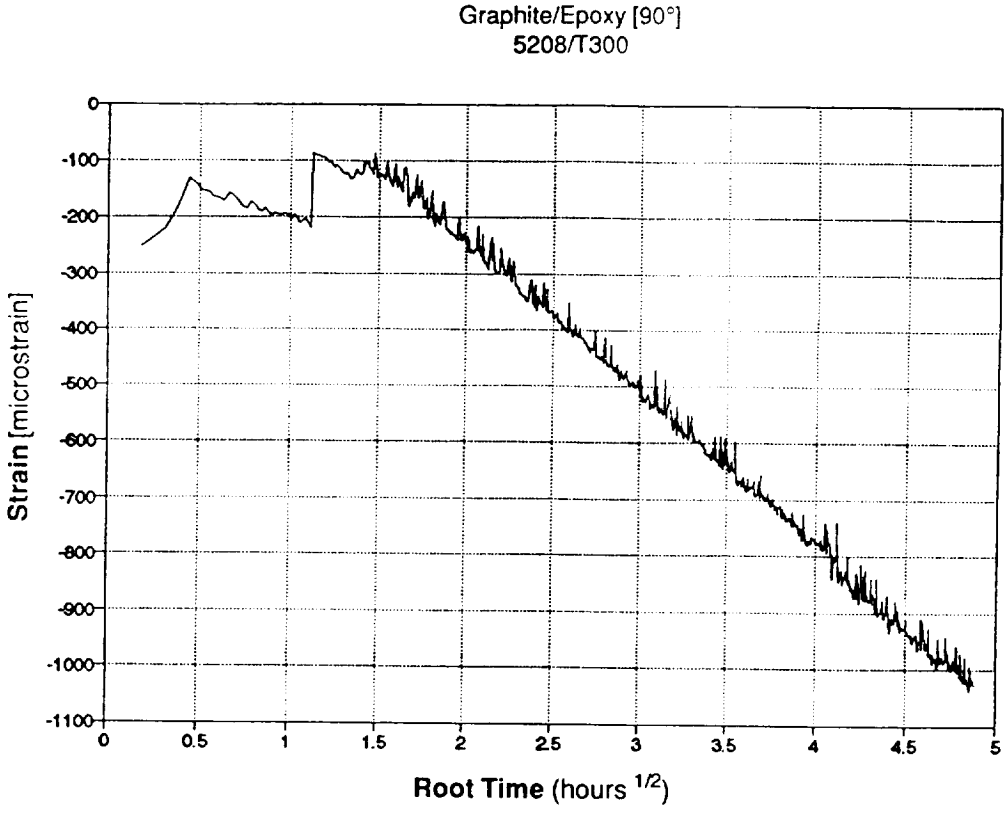

Figure 10. Outgassing test on control specimen (5T5) at 55 °C.

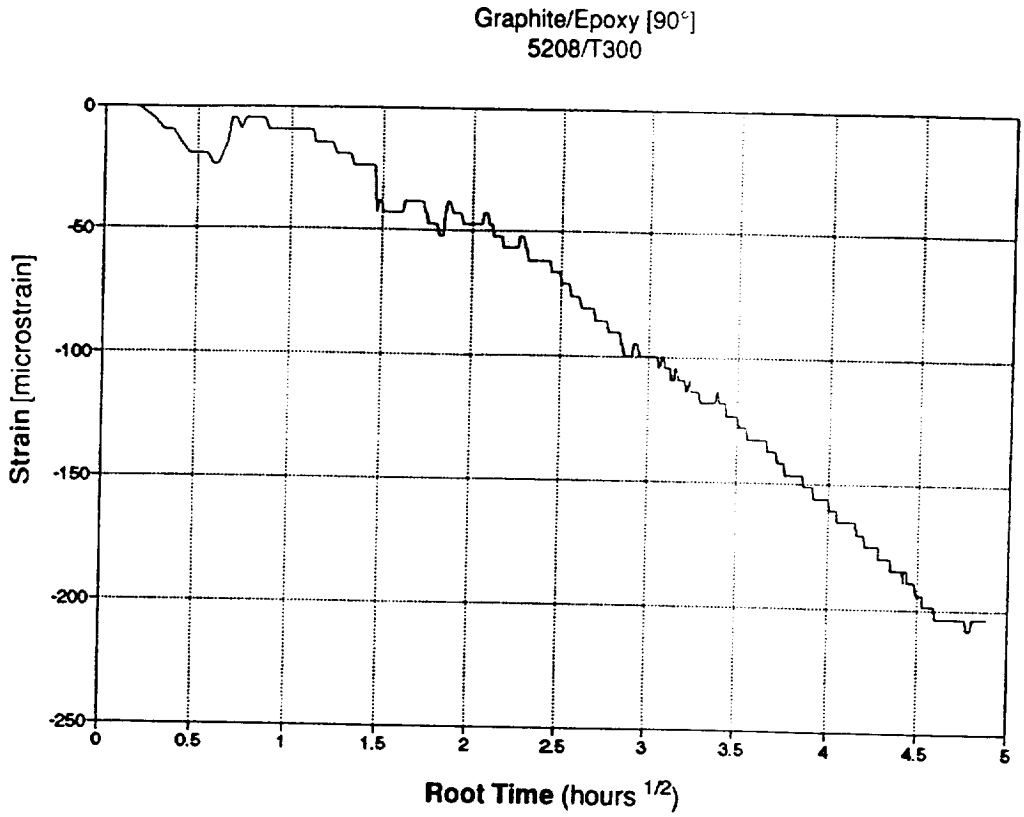

Figure 11. Outgassing test on LDEF flight specimen (2T13) at 22 °C.

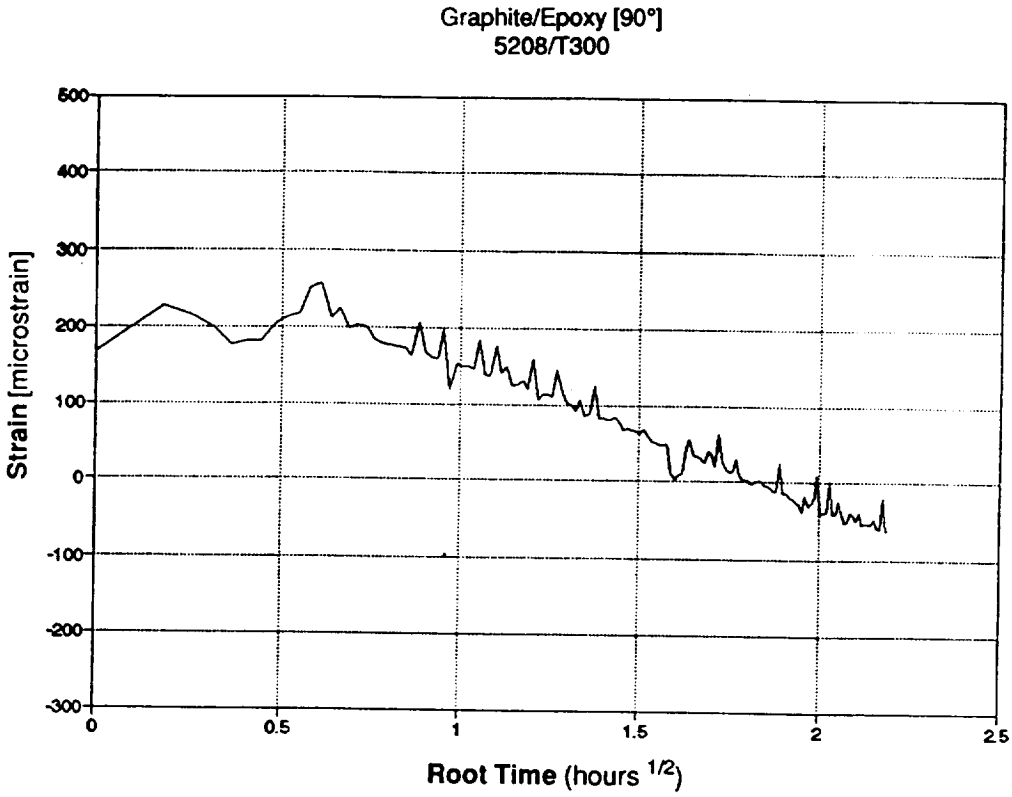

Figure 12. Outgassing test on LDEF flight specimen (2T13) at 50 °C.

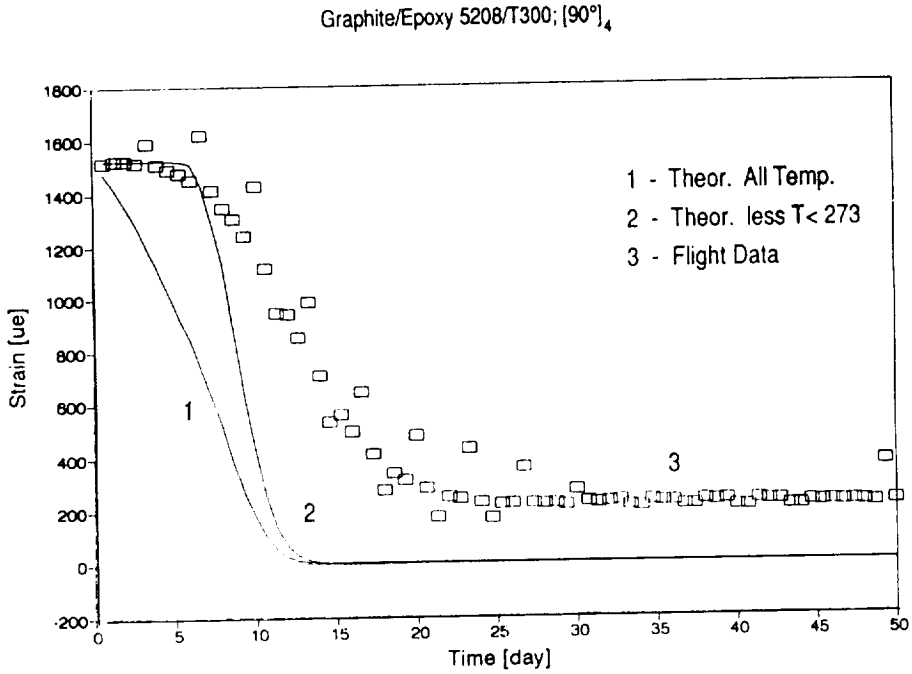

Figure 13. Comparison of predicted outgassing response with LDEF flight sample.

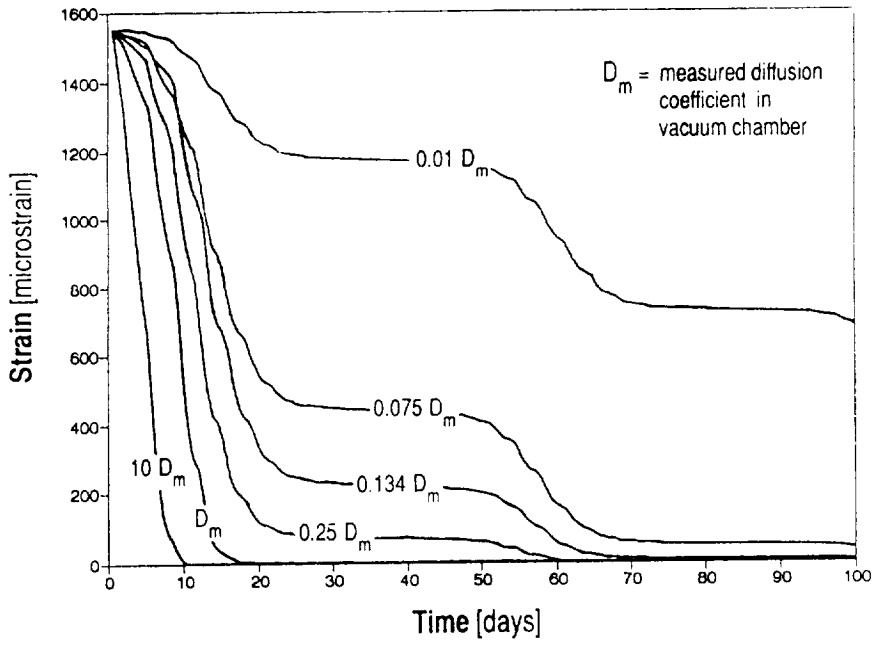

Figure 14. LDEF outgassing predictions for T300/5208 $(90)_4$ laminate.

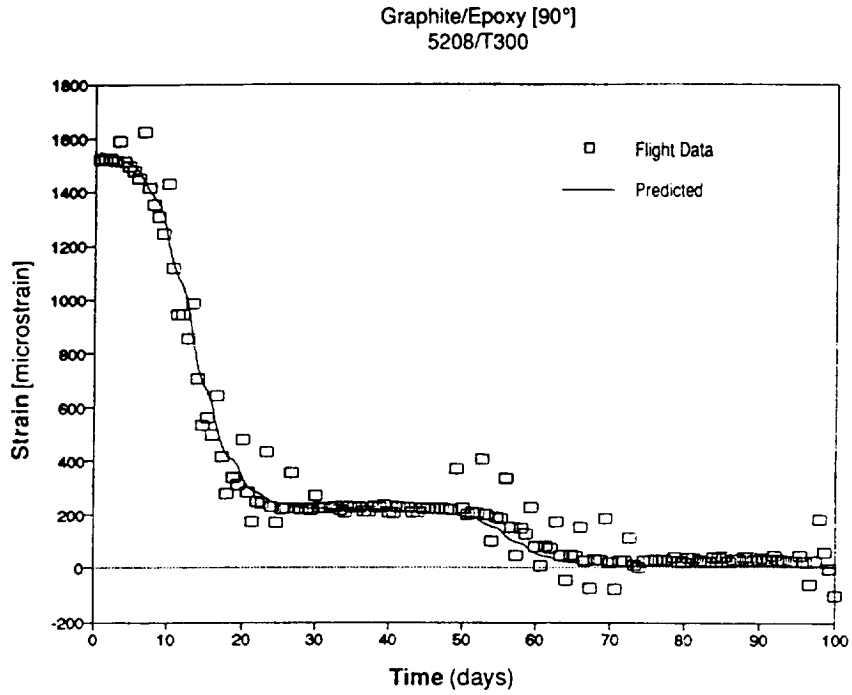

Figure 15. Comparison of corrected prediction of strain/time response in space with LDEF flight specimen ($D^* = 0.134D$).

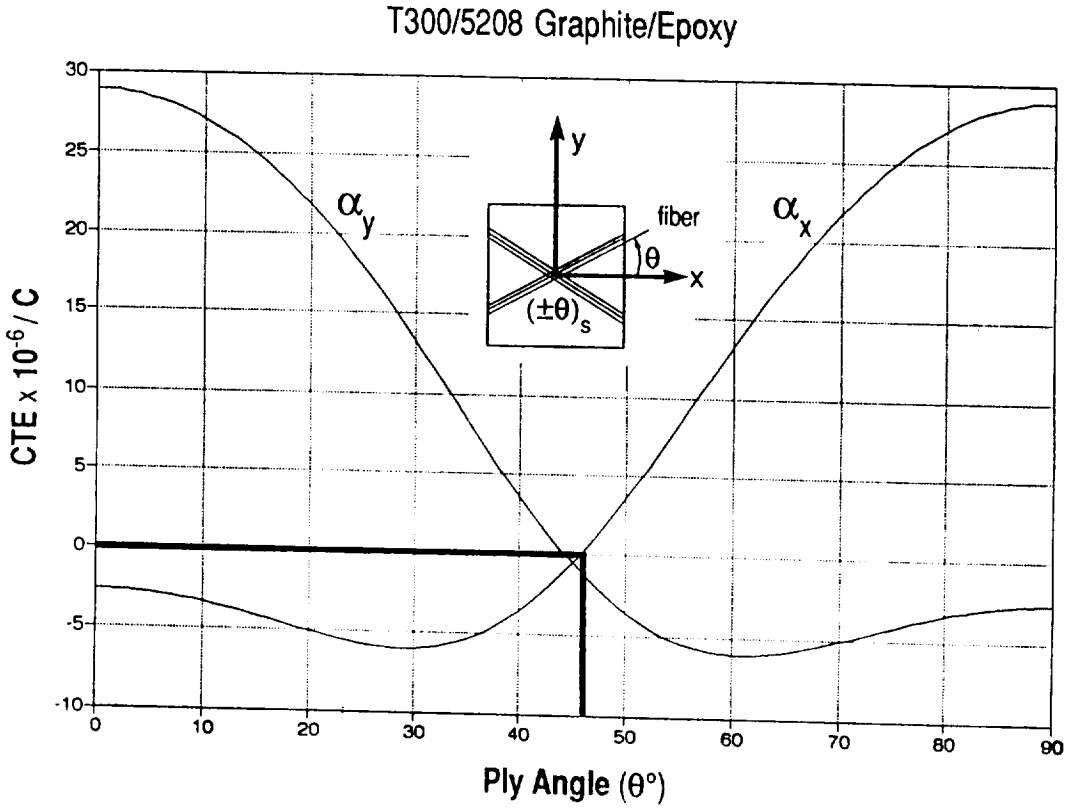

Figure 16. CTE for angle-ply laminates.

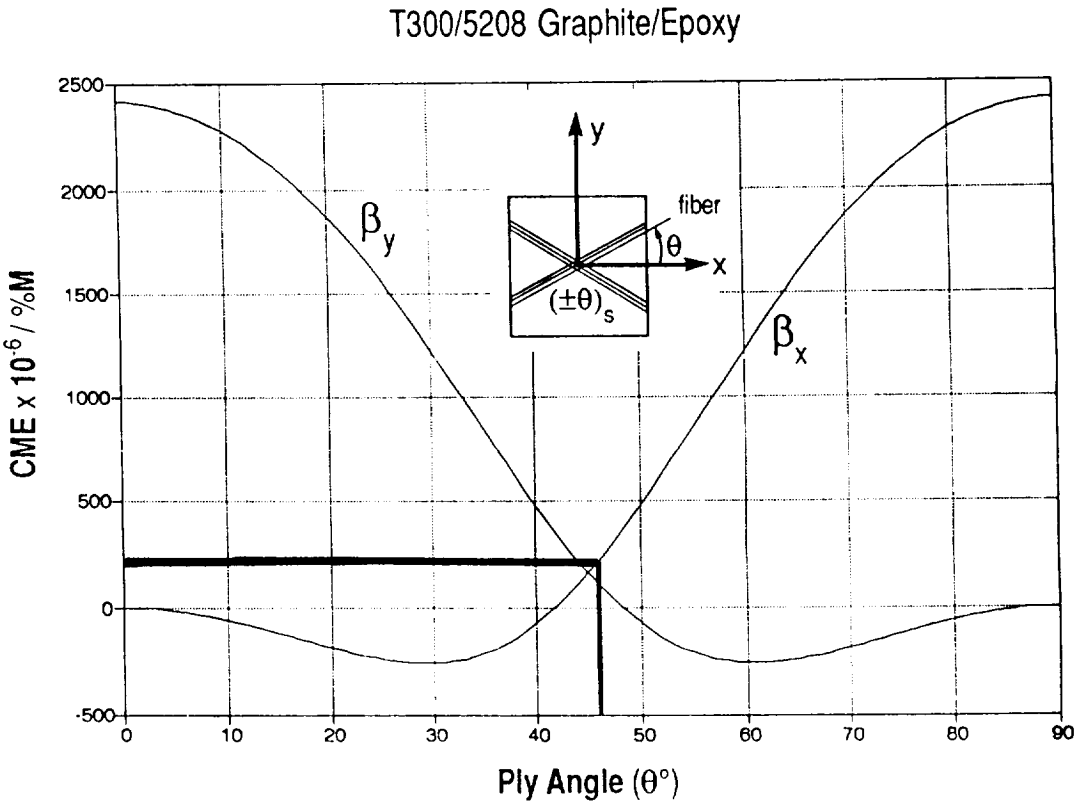

Figure 17. CME for angle-ply laminates.

THE IMPACT OF LDEF RESULTS ON THE SPACE APPLICATION OF METAL MATRIX COMPOSITES*

Gary L. Steckel
The Aerospace Corporation
El Segundo, CA 90245
Phone: 310/336-7116, Fax: 310/336-7055

Tuyen D. Le
The Aerospace Corporation
Phone: 310/336-7864, Fax: 310/336-7055

SUMMARY

Over 200 graphite/aluminum and graphite/magnesium composites were flown on the leading and trailing edges of LDEF on the Advanced Composites Experiment. The performance of these composites was evaluated by performing scanning electron microscopy and x-ray photoelectron spectroscopy of exposed surfaces, optical microscopy of cross sections, and on-orbit and postflight thermal expansion measurements. Graphite/aluminum and graphite/magnesium were found to be superior to graphite/polymer matrix composites in that they are inherently resistant to atomic oxygen and are less susceptible to thermal cycling induced microcracking. The surface foils on graphite/aluminum and graphite/magnesium protect the graphite fibers from atomic oxygen and from impact damage from small micrometeoroid or space debris particles. However, the surface foils were found to be susceptible to thermal fatigue cracking arising from contamination embrittlement, surface oxidation, or stress risers. Thus, the experiment reinforced requirements for carefully protecting these composites from prelaunch oxidation or corrosion, avoiding spacecraft contamination, and designing composite structures to minimize stress concentrations. On-orbit strain measurements demonstrated the importance of through-thickness thermal conductivity in composites to minimize thermal distortions arising from thermal gradients. Because of the high thermal conductivity of aluminum, thermal distortions were greatly reduced in the LDEF thermal environment for graphite/aluminum as compared to graphite/magnesium and graphite/polymer composites. The thermal expansion behavior of graphite/aluminum and graphite/magnesium was stabilized by on-orbit thermal cycling in the same manner as observed in laboratory tests.

EXPERIMENT DESCRIPTION

Nearly 500 samples of metal matrix, glass matrix, and polymer matrix composites were flown on LDEF Experiment M0003-10, "The Advanced Composites Experiment," a subexperiment of LDEF Experiment M0003, "Space Environmental Effects on Spacecraft Materials." The subexperiment is a joint effort between government and industry with Air Force Wright Laboratory, Flight

*Funding for this effort was processed through Air Force Space Systems Division Contract F04701-88-C-0089 under an interagency agreement with Air Force Wright Laboratory.

Dynamics Laboratory, and The Aerospace Corporation, Mechanics and Materials Technology Center, serving as experimenters. Each organization that participated in the experiment supplied a set of samples which were integrated into the overall experiment by The Aerospace Corporation. Following postflight deintegration, the samples were returned to the suppliers for analysis. In this paper, the most significant results for the metal matrix composites will be summarized. The metal matrix composites included primarily graphite fiber-reinforced aluminum and magnesium and were supplied and evaluated by The Aerospace Corporation.

The polymer matrix composites in the experiment included graphite/epoxy, graphite/polysulfone, and graphite/polyimide composites with and/or without various thermal control or protective coatings. These composites were supplied by General Dynamics Space Systems Division, Lockheed Missiles and Space Company, Boeing Aerospace & Electronics, and McDonnell Douglas Space Systems Company. The results for the polymer matrix composites in the experiment were presented at the 1991 LDEF Materials Workshop (ref. 1). The results were consistent with the findings of other experiments for polymer matrix composites that are included in this publication (refs. 2,3). The glass matrix composites were also reinforced with graphite fibers and were provided by United Technologies Research Center. They were uncoated and had either GY70 or Celion 6000 graphite fibers in a borosilicate glass matrix. Tredway and Prewo (ref. 4) evaluated the effects of the space exposure on graphite/glass composites from visual observations, optical microscopy, scanning and transmission electron microscopy, and diffuse reflectance, thermal expansion, and mechanical property measurements. They found that graphite/glass composites were essentially unaffected by the extended space exposure on LDEF. Since the impact of the LDEF results on the space application of the polymer and glass matrix composites was discussed in references 2 to 4, the results for these composites were omitted from this paper.

The experiment occupied approximately one-sixth of a 6-in deep peripheral tray on both the leading and trailing edges of LDEF. The trays were located on LDEF Bay D, Row 4 on the trailing edge and Bay D, Row 8 on the leading edge. The samples were mounted on both sides of cassettes with one side (Deck A) exposed to the space environment and the other side (Deck B) facing inward. The environments for the samples mounted on the leading and trailing A decks were similar except those on the leading edge were also exposed to relatively high fluxes of atmospheric constituents, primarily atomic oxygen. Although the samples on the B decks were not exposed to the radiation environment, the experiment design was such that they experienced thermal excursions similar to those of the exposure samples. The sample cassettes were decoupled from LDEF in order to maximize the thermal excursions. For most materials, at least one sample was located on each deck and additional samples were maintained in a laboratory environment. Although this was essentially a passive experiment, one or more samples of most classes of metal and polymer matrix composites were instrumented with thermistors and strain gauges to monitor the thermal excursions on the leading and trailing edges and the resulting dimensional changes.

COMPOSITE MATERIALS

Most of the composite samples were 3.5 by 0.5 in (8.9 by 1.3 cm) strips. There were also a limited number of 1-in (2.5-cm) diameter mirror samples, a few 2.4- by 0.5-in (6.1- by 1.3-cm) strips and several continuous fiber-reinforced wires. Most of the wires were approximately 0.025 in (0.064 cm) in diameter. The metal matrix composites are listed in Table 1. The graphite/aluminum (Gr/Al) strip and mirror samples included three different graphite fibers and two different alloy

matrices. These composites also had four different lay-ups. The graphite/magnesium (Gr/Mg) strips and mirrors included P100/EZ33A/AZ31B and P100/AZ91C/AZ61A composites. The samples for LDEF were prepared during the early stages of the development of graphite/magnesium. At that time, P100/EZ33A/AZ31B was considered a leading candidate system for space applications. However, it was subsequently discovered that poor strength properties were inherent in this system and it was replaced by the P100/AZ91C/AZ61A system. Therefore, several P100/AZ91C/AZ61A samples were added to the test matrix shortly before the experiment trays were delivered to NASA. These samples are of great interest as they are representative of the current state-of-the-art for graphite/magnesium. The silicon carbide/aluminum composites included both discontinuous whisker-reinforced and continuous fiber-reinforced strips. The metal matrix wires included five fiber-matrix combinations for graphite/aluminum, three fiber-matrix combinations for graphite/magnesium, and Nicalon SiC fiber-reinforced 6061 aluminum. Most of the wires were prepared by infiltrating a single row of fibers with the molten matrix alloy, but in some cases, several rows were infiltrated to form a larger diameter wire.

The detailed results for the Gr/Al and Gr/Mg composites were presented in earlier papers (refs. 5–7). Therefore only the most significant results relative to the space application of these composites will be reviewed. The results of surface observations, microscopy of cross sections, the on-orbit temperature and strain measurements, and postflight thermal expansion measurements on Gr/Al and Gr/Mg are included. Evaluation of the silicon carbide/aluminum samples is still in progress and no results will be presented for these composites.

VISUAL AND MICROSCOPIC OBSERVATIONS FOR GR/AL AND GR/MG

A postflight photograph of the exposed side of the leading edge cassette is shown in Figure 1. The mirror samples were mounted in the upper right corner of the cassette with the metal matrix wires located immediately to the left of the mirrors and the 3.5-in by 0.5-in strips filling the remainder of the cassette. It was noted that all of the composites survived in excellent physical condition. Surface roughening due to atomic oxygen erosion for uncoated organic matrix composites mounted on the exposed leading edge was the only significant visible damage. However, the erosion depth appeared to be shallow relative to the overall thickness of the affected composites. Contamination was evident on both the leading and trailing edges. For example, a large contaminated area is apparent on seven samples in the upper left corner of the photograph in Figure 1. It will be shown below that contaminants may have induced surface cracks in some of the Gr/Al composites.

A micrometeoroid/debris crater on a Gr/Al composite is shown in Figure 2. This crater is typical of those observed on both Gr/Al and Gr/Mg. Since Gr/Al has an aluminum alloy surface foil, the crater has the same appearance as for monolithic aluminum. A cross section of this crater shows that it extended completely through the 0.004 in (0.010 cm) 2024 aluminum surface foil, but did not extend into the underlying graphite fiber-reinforced interior. This may imply that penetration through the foil is much easier than through the fiber-reinforced region of the composite, but may also be the characteristic depth of penetration into aluminum for this particular size of impact particle. Most of the craters observed on Gr/Al and Gr/Mg composites were approximately the same size. Thus, the effects of particle size on the penetration depth could not be determined. Perhaps the most significant observation in Figure 2 is the presence of a delamination of the surface foil over an area approximately three times the crater diameter. It is not known whether the delamination occurred due to the impact energy or formed later due to thermal fatigue. Surface foil delaminations affect important

through-thickness properties, such as the thermal conductivity. In addition, most of the transverse strength of Gr/Al and Gr/Mg is provided by the surface foil. Large foil delaminations could therefore have serious consequences on the performance of these composites. Thus, if the delaminations propagate due to thermal fatigue, they could reach much larger sizes during extended missions and have adverse effects. Additional studies are needed to determine whether the delaminations form due to the impact or if they develop and/or propagate during subsequent thermal cycling.

Etching of cross sections of Gr/Al and Gr/Mg flight samples produced matrix darkening in the fiber-reinforced regions as shown in Figure 2. The dark etching is an indication of plastic deformation of the matrix. This is not surprising since the coefficient of thermal expansion mismatch between the graphite fibers and matrix induces high stresses in the matrix during thermal cycling. Nevertheless, there was no evidence of matrix microcracking in any Gr/Al or Gr/Mg composites. Since the samples were subjected to over 33,000 thermal cycles, this indicates that these composites have excellent resistance to thermal fatigue for the LDEF thermal environment. Extensive thermal fatigue cracking was observed, however, on the surface foils of selected GY70/201/2024 Gr/Al samples (Fig. 3). This was surprising since the thermal stresses should be lower within the surface foils than within the fiber-reinforced regions of the composites. However, further inspection revealed that the cracks were always associated with a surface contaminant that was clearly visible on several trailing edge samples that had been mounted adjacent to one another. X-ray Photoelectron Spectroscopy (XPS)† showed the presence of silicon and oxygen, probably from on-orbit silicone contamination. The cracks probably initiated in a brittle oxide or aluminum silicate layer on the sample surface. Once the cracks were initiated, they propagated into the bulk of the foil. In some cases (Fig. 3), the cracks propagated completely through the surface foil. However, there was no evidence of the cracks extending into the underlying Gr/Al region or along the interface between this region and the foil.

Less severe, isolated fatigue cracks were also observed on a few GY70/201/2024 Gr/Al composites. These cracks were always associated with surface defects such as surface foil blemishes, micrometeoroid craters or engraved sample identification numbers (Fig. 4). Apparently, these defects acted as stress concentrators and initiated thermal fatigue cracks. All of the Gr/Al composites that had surface foil cracks, due to either contamination or stress risers, had 2024 surface foils. No composites having 6061 surface foils showed any evidence of foil cracking. The composites having 6061 surface foils were heat treated to a T6 condition, whereas those having 2024 foils were in the as-fabricated condition. Thus, the 6061 foils probably had a higher yield strength, which would also tend to increase the fatigue life of the 6061 foils relative to the 2024 foils (ref. 8). These observations are consistent with postflight microhardness measurements, which verified that the 6061 foils were significantly harder than the 2024 foils.

Surface foil cracks were also observed on several Gr/Mg composites. In this case, all of the cracked samples had a very rough, mottled surface appearance (Fig. 5), which XPS indicated was due to extensive surface oxidation. Several observations concerning the oxidation and foil cracking were made from an evaluation of all of the P100/AZ91C/AZ61A Gr/Mg composites. These included samples from two panels, one having a single-ply, unidirectional lay-up and a second panel having four plies in a $(\pm 10°)_S$ lay-up. The unidirectional panel had been stored in a laboratory for 2 years before we decided to use it for LDEF. The surface of the panel was heavily oxidized and required abrading to prepare samples having clean surfaces. The resulting rough surface was, however, susceptible to additional oxidation, which was observed for all samples from this panel that were

†C.S. Hemminger was responsible for the x-ray photoelectron spectroscopy and its interpretation.

mounted on the A decks for both the leading and trailing edges. All of these samples also had extensive surface foil cracking. Samples mounted on the interior B decks showed much less oxidation and no foil cracking. Since the degree of oxidation was the same on the leading and trailing edges, we believe that these observations are indicative of prelaunch oxidation. The four-ply panel was prepared for LDEF shortly before the experiment trays were delivered to NASA. This panel had very smooth surfaces that were not as prone to oxidation. As a result, the flight samples showed only light oxidation and no surface foil cracking. Thus, it was concluded that the surface foil cracking on Gr/Mg was due to the formation of a brittle oxide layer that formed prior to launch, but can be eliminated by the application of suitable prelaunch handling and surface preparation procedures.

THERMAL EXPANSION BEHAVIOR OF GR/AL AND GR/MG

The effects of the long-term space exposure on the thermal expansion behavior of Gr/Al and Gr/Mg were evaluated by: (1) analyzing the flight data that was recorded on-orbit to determine the influence of orbital time and orbital heating and cooling conditions, and by (2) postflight laboratory measurements of LDEF samples and laboratory control samples. In this analysis, temperature change versus time, dimensional change versus temperature, coefficient of thermal expansion (CTE), and thermal hysteresis were considered in evaluating the dimensional stability.

Eleven Gr/Al and five Gr/Mg samples were instrumented with thermistors and/or strain gauges to monitor the thermal cycling and associated thermal strains during orbiting. The strain gauges and thermistors were mounted on the back surface of both leading and trailing edge exposure samples. None of the flight control samples were instrumented. The sensors were placed on the back surface to avoid any possible damage caused by atomic oxygen erosion, UV radiation, or micrometeoroid bombardment. The disadvantages of this approach were that any temperature gradients through the thickness of the radiantly heated and cooled samples were undetected, as were any bending deformations associated with temperature gradients. It will be shown that for some materials this had a dominant influence on the data. The strain gauges were mounted to measure the change in dimension along the length of the strips. The data acquisition system was set up to record temperatures and strains during the duration of an orbit once every 107 hours (approximately 78 orbits). Data were collected approximately every three minutes during the selected orbits. The first set of data was collected approximately 44 hours after LDEF was placed into orbit. The data were recorded on magnetic tape until the tape was fully loaded, approximately fourteen months into the flight. No data were recorded during the unplanned final 4.5 years of the flight.

The absolute values of linear thermal expansion in graphite fiber-reinforced composite materials are extremely small, particularly in the direction parallel to the fibers. This requires the use of a high resolution apparatus such as a laser interferometer to make accurate thermal expansion measurements. In this study, a Michelson laser interferometer was utilized for the postflight laboratory measurements. In all cases, thermal cycling was carried out by first heating the sample to the maximum temperature, followed by cooling to the lowest temperature, and then heating back to room temperature. The heating and cooling rates were limited to approximately 1 °C/min (2 °F/min) to ensure thermal equilibrium throughout the sample. For the purpose of comparison with the flight data, the samples were thermal cycled over the same range of temperature that was derived from the flight data analysis.

Plots of the maximum and minimum temperatures for each orbit for which data were taken are shown in Figure 6 for a P100/EZ33A/AZ31B Gr/Mg composite. Large fluctuations in the thermal cycling occurred due to seasonal variations and orbital mechanics. For the flight data analyses, it was desirable to select typical thermal expansion curves for orbits at the beginning, middle, and the end of the recording time. In addition, equivalent temperature ranges for the selected orbits were preferred in order to facilitate comparisons. Therefore, the orbital times indicated by vertical lines on the Figure at approximately 40, 5,000, and 10,000 hours (2, 208, 416 days) after LDEF was placed into orbit were selected for the data analyses. The temperature range for these orbits was approximately –20 to 70 °C (–5 to160 °F), but varied somewhat between the leading and trailing edges and between Gr/Al and Gr/Mg. In general, higher temperatures for these orbits were measured for Gr/Mg versus Gr/Al and for the trailing versus the leading edge.

A listing of all the Gr/Al and Gr/Mg composite systems for which flight data were obtained and analyzed is given in Table 2. The composites for which postflight laboratory measurements were made are also indicated. Note that no flight data were obtained for the P100/201/2024 Gr/Al or P100/AZ91C/AZ61A Gr/Mg composites because of their late addition to the experiment. The results for each of these composites were discussed previously (ref. 7). Only the data for the GY70/201/2024 Gr/Al composites and P100/EZ33A/AZ31B and P100/AZ91C/AZ61A $(\pm 10°)_S$ Gr/Mg composites will be reviewed in this paper.

Figure 7 shows a typical thermal cycle for one orbit and the corresponding dimensional changes plotted as a function of time for a Gr/Al composite on the trailing edge. The temperature plot shows that the initial heating and cooling rates as LDEF came out of or went into the Earth's shadow, respectively, were very rapid, around 7 °F/min. The rates were even higher, around 15 °F/min, on the leading edge. It is reasonable to assume that the heating and cooling rates were even higher on the front surface of the sample, so that a temperature gradient through the sample causing bending deformations would not be surprising. Since Gr/Al has a positive CTE, these bending deformations would tend to reduce the thermal strains measured by a back surface strain gauge. However, the slope changes for the strain in Figure 7 were consistent with those for the temperature. Thus, the through-thickness thermal conductivity of Gr/Al was apparently sufficient to prevent significant thermal distortions for these heating and cooling rates.

In Figure 8, the on-orbit thermal expansion curves are shown for GY70/201/2024 composites mounted on the leading and trailing edges of LDEF. The curves are shown for the three selected orbits (40, 5,000, and 10,000 hours). The thermal expansion behavior was fairly linear with only a small degree of hysteresis. In addition, the thermal expansion was very stable in that it showed no significant change with orbital time. The postflight laboratory data for the same leading and trailing edge GY70/201/2024 samples are shown in Figure 9. The laboratory curves were more linear, suggesting that the flight data may have been somewhat influenced by the rapid on-orbit heating and cooling rates. The trailing edge sample showed a small degree of hysteresis as compared to the leading edge sample in both the flight data and laboratory measurements. This observation is probably due to differences between the two samples, such as slightly different fiber contents, rather than any differences between the leading and trailing edge exposures. Figure 10 compares the thermal expansion curve of a laboratory control sample with the leading edge sample. The thermal expansion behavior of the laboratory control sample was similar to the flight samples except for a small, but readily noticeable, hysteresis loop over the entire temperature range. The reduced hysteresis in the flight samples is probably indicative of strain hardening of the matrix further stabilizing the composites after a few thermal cycles. However, the small degree of hysteresis indicated that even the uncycled, laboratory control samples were quite stable. The P55/6061/6061 composites showed

basically the same behavior, except no hysteresis was observed for the flight or laboratory control samples. The average postflight CTEs measured in the laboratory for the GY70/201/2024, P55/6061/6061, and four-ply P100/201/2024 Gr/Al composite systems are given in Table 3. The CTE was not affected by the extended space exposure for any of the Gr/Al composites. Note that the CTE was much lower for the P100/201/2024 composites because of the more negative CTE of the P100 fiber compared to the P55 and GY70 fibers and the $(\pm 20°)_S$ lay-up. The results indicate that the extended space exposure on LDEF had little effect on the thermal expansion of Gr/Al. Thermal cycling in orbit further stabilized the Gr/Al composites, eliminating thermal hysteresis after less than 40 cycles. Although the rapid temperature changes encountered on LDEF may have had a small effect on the strain measurements, temperature gradients were not sufficient to induce significant bending.

Plots of the temperature and strain gauge response versus time for a Gr/Mg composite are shown in Figure 11. Anomalous behavior was observed for the Gr/Mg composites when the heating or cooling rates were very rapid. This particular Gr/Mg composite had a positive CTE, but when the heating rate became very rapid, the sample appeared to contract instead of expanding. Furthermore, with rapid cooling, the strain increased rather than decreasing. When the heating and cooling rates were relatively slow, the measured strains increased or decreased as anticipated. This behavior is consistent with the development of bending deformations in the strips during the rapid heating and cooling. The thermal conductivity of Gr/Al composites is significantly greater than for Gr/Mg due to the much higher Al matrix conductivity. For example, the conductivities at 70 °F for 6061-T6 Al and AZ91C Mg are 97 and 58 Btu/ft-hr-°F, respectively (ref. 8). The through-thickness conductivities of P100/6061/6061 Gr/Al and P100/AZ91C/AZ61A Gr/Mg composites having fiber contents of approximately 40 vol. percent are around 40 and 20 Btu/ft-h-°F at 70 °F, respectively (ref. 9). In addition, higher heating and cooling rates were measured on the leading and trailing edges for Gr/Mg (20 and 10 °F/min, respectively) than for Gr/Al (15 and 7 °F/min). This would also tend to increase bending deformations in Gr/Mg relative to Gr/Al.

Figure 12 shows the measured strain versus temperature for single-ply P100/EZ33A/AZ31B composites mounted on the leading and trailing edges of LDEF. The postflight thermal expansion curves for these same samples are plotted in Figure 13 along with the curve for a laboratory control sample. Comparing Figures 12 and 13 clearly shows that the flight data were severely altered by the high heating and cooling rates. The interpretation of these data can only be accomplished by performing analyses to calculate the front surface temperatures and bending deformations. Similar problems were encountered for the polymer matrix composites. The thermal conductivity is even lower for these composites. In addition, the polymer matrix composites were thicker and had higher solar absorptance and emittance properties than Gr/Al and Gr/Mg. All of these factors would tend to increase the the through-thickness temperature gradients and the bending deformations in the polymer matrix composites.

The thermal expansion of the laboratory control P100/EZ33A/AZ31B composite in Figure 13 was extremely unstable. The behavior was nonlinear with a large residual thermal strain at room temperature of nearly 300 microstrain. The large residual strain of the material is attributed to yielding of the low-strength matrix alloy. The composite behavior near the cold end of the cycle was dominated by the expansion of the fibers causing yielding in the matrix. This led to an increase in dimension and consequently an open loop with large permanent offset at room temperature. A comparison of the laboratory control sample with the postflight samples showed that the amount of hysteresis decreased remarkably following the on-orbit thermal cycling. The implication is that extensive thermal cycling had a large effect in stabilizing the behavior of the P100/EZ33A/AZ31B

Gr/Mg composites. However, even after over 30,000 thermal cycles on LDEF, the thermal hysteresis could not be cycled out as it was for Gr/Al composites. As discussed above, P100/EZ33A/AZ31B composites have inherently low strength properties due to chemical reactions between the rare Earth elements in the EZ33A matrix alloy and the P100 fibers. These reactions may also affect the matrix and limit its work hardening so that hysteresis in the thermal expansion curves could not be eliminated. It should be noted however that the total dimensional change and average CTE for the Gr/Mg composites were smaller than those for the Gr/Al composites. This is due to the low elastic modulus of the magnesium matrix alloy (6.5 Msi) and the higher modulus and more negative CTE of the P100 fiber as compared to the P55 and GY70 fibers.

Post-flight thermal expansion curves for leading edge and laboratory control samples of the 4-ply, $(\pm 10°)_S$ P100/AZ91C/AZ61A composites are shown in Figure 14. These measurements were made at Composite Optics, Incorporated, over a much broader temperature range than the samples were exposed to on LDEF. The laboratory control and postflight samples had nearly identical curves. Both samples had a hysteresis of around 75 microstrain, but the CTE's were extremely small, around 0.07×10^{-6}/°F. The similarities between the two samples indicated that the thermal expansion was originally quite stable and that extensive thermal cycling over the LDEF temperature range did not have much effect on the thermal expansion over the ±250 °F range. However, making measurements over a broader temperature range than the on-orbit temperatures undoubtedly diminished the stabilizing effects of the thermal cycling. A second set of laboratory control and flight samples need to be evaluated over the LDEF temperature range. This will give a better indication of the stabilizing effect of the LDEF thermal cycling for these low-CTE composites.

CONCLUSIONS

(1) All of the composites flown on LDEF in the Advanced Composites Experiment survived the extended space exposure in excellent physical condition. The only significant visible damage was surface erosion on uncoated polymer matrix composites from atomic oxygen on the leading edge of LDEF. Gr/Al, Gr/Mg, silicon carbide/Al, and graphite/glass composites were not susceptible to atomic oxygen attack.

(2) The largest micrometeoroid or debris craters observed on Gr/Al and Gr/Mg were approximately 0.006 in (150 micrometers) in diameter. Minimal damage was caused to these composites, in part because the aluminum or magnesium surface foils protected the graphite fibers for these small impact particles. However, even small particle impacts can cause localized delamination of the surface foil which may propagate due to subsequent thermal cycling. This could degrade through-thickness properties such as thermal conductivity or transverse properties.

(3) No evidence of any internal microcracking was observed for Gr/Al or Gr/Mg for any of the fiber/matrix combinations or lay-ups flown on LDEF.

(4) Several GY70/201/2024 Gr/Al composites had thermal fatigue cracks within the 2,024 surface foils. These crack appeared to initiate at the outer foil surface. In some instances the cracks extended through the foil, but no cases were observed in which the cracks propagated into the fiber reinforced region of the composite or caused foil delaminations. These cracks were attributed to surface contamination or stress risers such as engraved sample numbers or micrometeoroid craters. No cracks were observed for Gr/Al composites having 6061 Al surface

foils. The presence of these cracks accentuates the need to be very careful in the surface preparation and design of composite structures to minimize stress concentrators and the need to avoid contamination on all spacecraft surfaces.

(5) Fatigue cracking due to prelaunch oxidation was observed on numerous P100/EZ33A/AZ31B and P100/AZ91C/AZ61A Gr/Mg composites. It was shown that this can be prevented by the application of suitable prelaunch handling and surface preparation procedures.

(6) Gr/Al composites showed a stable, linear thermal expansion behavior with near-zero thermal hysteresis over the LDEF temperature range. In contrast, Gr/Mg composites, even after extensive cycling during orbiting, showed nonlinear, unstable behavior with significant hysteresis. However, the hysteresis for Gr/Mg was significantly reduced as compared to the as-fabricated samples. The thermal expansion data for Gr/Mg composites indicated that near-zero CTE over the LDEF temperature range can be obtained and maintained on-orbit. These results are consistent with and validate ground-based thermal cycling test results on Gr/Al and Gr/Mg composites.

(7) The flight data revealed that in the space environment, the temperature distribution in a structure is often time varying or nonuniform due to radiant heating. For a satellite like LDEF in a low Earth orbit with alternating eclipse and sun exposure, the data showed that the materials experienced thermal cycling over varying temperature extremes with different heating and cooling rates depending on the location of samples on the satellite. During a single orbit, the heating and cooling rates could vary from less than 1 °F/min to 20 °F/min when LDEF was going in or out of the Earth's shadow. The maximum heating and cooling rates on the leading edges were nearly twice those on the trailing edge. Bending deformations due to temperature gradients through the thickness of the Gr/Mg and polymer matrix composites were implied from the strain gauge data and attributed to the low thermal conductivity of these composites as compared to Gr/Al. The flight data implies that structures in space are always subjected to nonuniform temperature distributions and thermal conductivity of a material is an important factor in establishing a uniform temperature distribution. Therefore in addition to CTE and thermal hysteresis, thermal conductivity is an important consideration when selecting materials for dimensionally stable space structures.

REFERENCES

1. Steckel, G.L., Cookson, T., and Blair, C.: "Polymer Matrix Composites on LDEF Experiments M0003-9 & 10." *Proceedings of LDEF Materials Workshop '91*, NASA CP-3162, pp. 512–542.

2. Tennyson, R.: "Space Environmental Effects on Composite Structures." *LDEF Materials Results For Spacecraft Applications Conference*, NASA CP- , 1992.

3. George, P.: "Low Earth Orbit Effects on Organic Composite Materials Flown on LDEF." *LDEF Materials Results For Spacecraft Applications Conference*, NASA CP- , 1992.

4. Tredway, W.K. and Prewo, K.M.: "Analysis of the Effect of Space Environmental Exposure on Carbon Fiber Reinforced Glass." United Technologies Research Center Report R91-112542-4, 1991.

5. Steckel, G.L. and Le, T.D.:: "Composites Survive Space Exposure." *Advanced Materials and Processes*, vol. 139, No. 8, 1991, pp. 35–38.

6. Steckel, G.L. and Le, T.D.: "M0003-10: LDEF Advanced Composites Experiment." First LDEF Post-Retrieval Symposium, NASA CP-3134, 1991, pp. 1041–1053.

7. Le, T.D. and Steckel, G.L.: "Thermal Expansion Behavior of LDEF Metal Matrix Composites." Second LDEF Post-Retrieval Symposium, NASA CP-3194, 1992, pp. 67.

8. *Metals Handbook Ninth Edition, Volume 2, Properties and Selection: Nonferrous Alloys and Pure Metals*. American Society For Metals, 1979.

9. Taylor, R.E. and Groot, H.: *Thermophysical Properties of Graphite Aluminum and Graphite Magnesium*, Thermophysical Properties Research Laboratory Report TPRL 330, Purdue University, West Lafayette, IN, 1984.

Table 1. List of metal matrix composites.

MATERIAL DESCRIPTION FIBER/MATRIX/SURFACE FOIL	LAY UP	NUMBER OF SAMPLES LEADING A	LEADING B	TRAILING A	TRAILING B	CONTROL
GRAPHITE/ALUMINUM						
GY70/201/2024 STRIPS	0, 90, OR $(0/\pm60)_S$	15	14	13	18	20
P55/6061/6061 STRIPS	0 OR 90	8	10	8	8	12
P100/201/2024 STRIPS	$(\pm20)_S$	2	2	2	2	2
P100/6061 WIRES	0	4	1	4	1	2
P55/6061 WIRES	0 OR $(0)_5$	8	3	8	3	6
GY70/201 WIRES	$(0)_8$	2	1	2	1	2
T300/6061 WIRES	0	2	1	2	1	2
GRAPHITE/MAGNESIUM						
P100/EZ33A/AZ31B STRIPS	0, 90, OR $(0/\pm60)_S$	9	11	7	8	33
P100/AZ91C/AZ61A STRIPS	0, 90 OR $(\pm10)_S$	6	4	6	6	3
P100/AZ31B WIRES	0	3	1	3	1	2
P100/AZ61A WIRES	0	4	1	4	1	2
P55/AZ91C WIRES	$(0)_5$	3	1	3	1	4
SILICON CARBIDE/ALUMINUM						
SiC_w/2124 STRIPS	DISCONTINUOUS	1	1	1	1	5
SiC_w/6061 STRIPS	DISCONTINUOUS	1	1	1	1	5
SCS2$_f$/Al STRIPS	$(0)_8$	2	2	2	2	6
NICALON SiC$_f$/6061 WIRES	0	18	5	18	5	5

The discontinuous SiC/Al was supplied by AFWL/Flight Dynamics Laboratory. All other metal matrix composites were supplied by The Aerospace Corporation.

Table 2. Gr/Al and Gr/Mg composites for on-orbit and laboratory thermal expansion measurements.

AEROSPACE MATERIAL NO.	MATERIAL DESCRIPTION FIBER/MATRIX/SURFACE FOIL	FLIGHT DATA	POST-FLIGHT LABORATORY DATA
AL3 - AL6	GY70/201/2024 (1 PLY, 0°)	LE & TE	LE, TE, & LC
AL7	GY70/201/2024 $(0,\pm60°)_S$	LE & TE	
AL12 & AL14	P55/6061/6061 (1 PLY, 0°)	LE & TE	LE, TE, & LC
AL15	P55/6061/6061 (1 PLY, 90°)	LE & TE	
AL33	P100/201/2024 $(\pm20°)_S$		LE & LC
MG3-MG6	P100/EZ33A/AZ31B (1 PLY, 0°)	LE & TE	LE, TE, & LC
MG9	P100/AZ91C/AZ61A (1 PLY, 0°)		LE & LC
MG10	P100/AZ91C/AZ61A $(\pm10°)_S$		LE & LC

LC = LABORATORY CONTROL, LE = LEADING EDGE, TE = TRAILING EDGE

Table 3. Postflight CTE data for Gr/Al composites.

MATERIAL DESCRIPTION FIBER/MATRIX/SURFACE FOIL	COEFFICIENT OF THERMAL EXPANSION, 10^{-6}/°F		
	LABORATORY CONTROL	LEADING EDGE	TRAILING EDGE
GY70/201/2024 (1 PLY, 0°)	3.5	3.2	3.8
P55/6061/6061 (1 PLY, 0°)	3.0	3.3	3.5
P100/201/2024 $(\pm 20°)_S$	1.2	1.1	

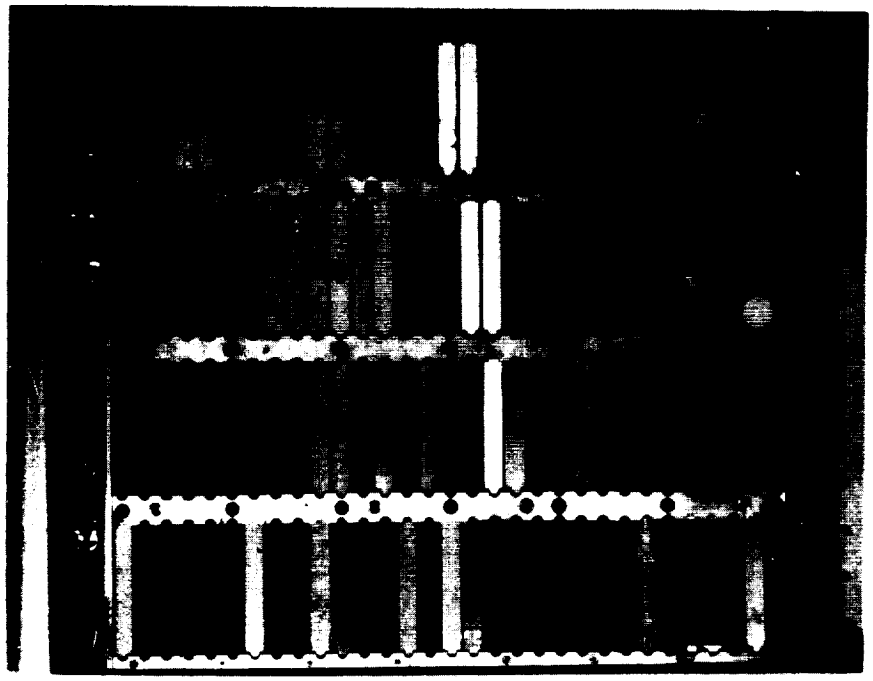

Figure 1. Postflight photograph of exposed side of leading edge cassette.

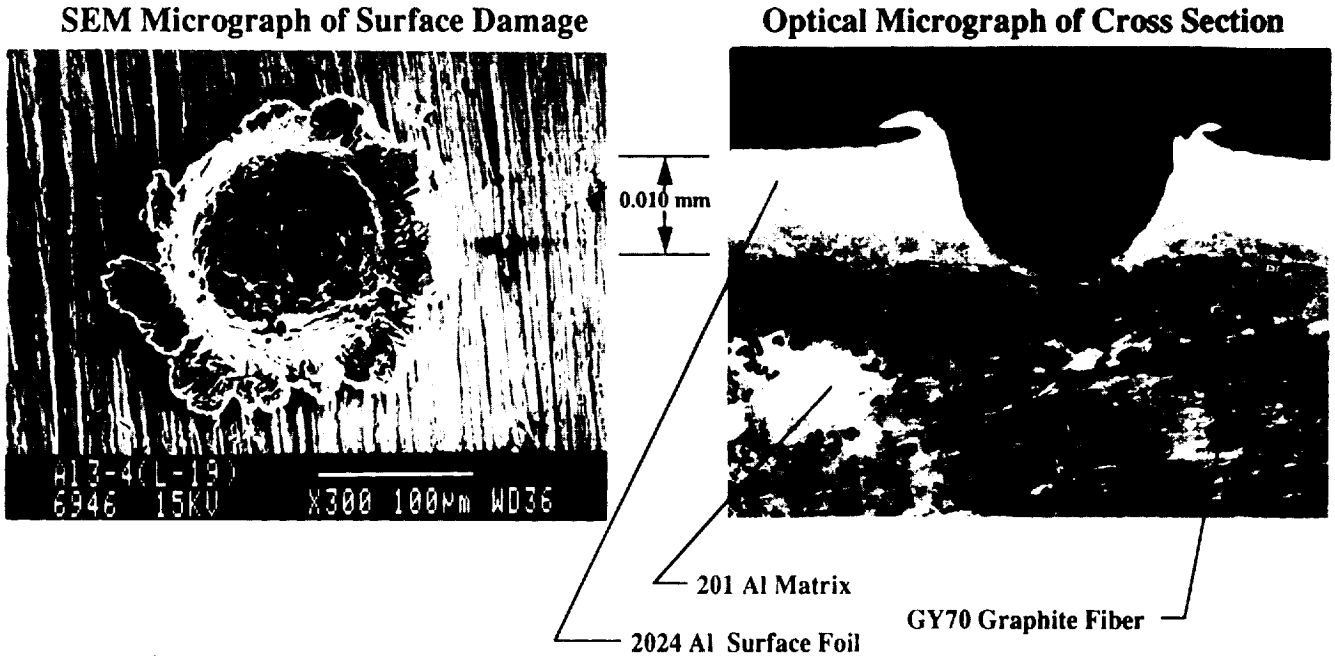

Figure 2. Micrometeoroid/debris damage to a GY70/201/2024 graphite/aluminum composite.

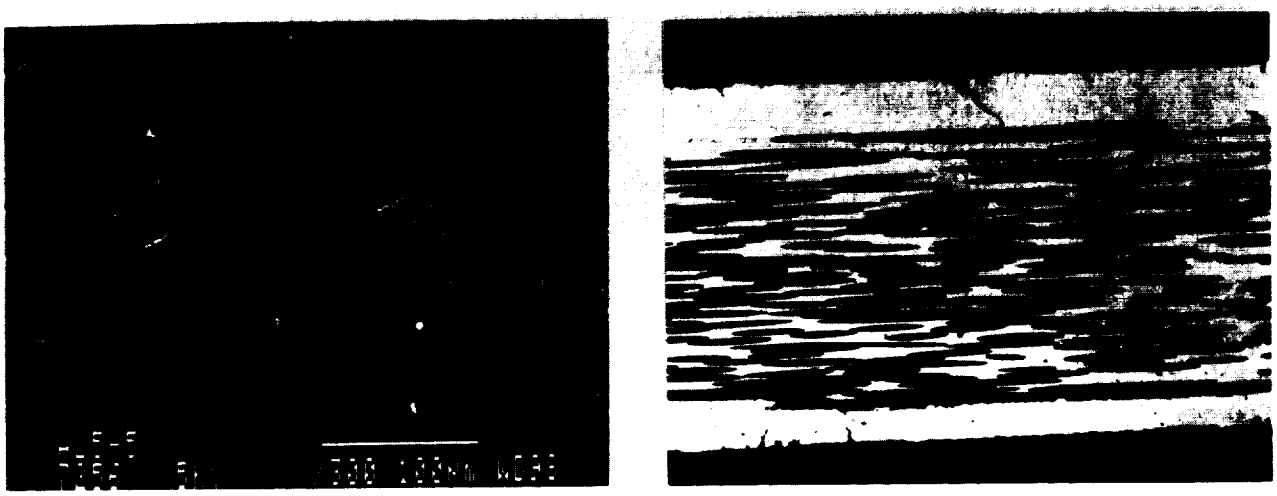

SEM Micrograph of Cracks in Surface Foil **Optical Micrograph of Cross Section**

Figure 3. Surface foil cracking of a GY70/201/2024 graphite/aluminum composite resulting from thermal fatigue of a brittle contaminated surface.

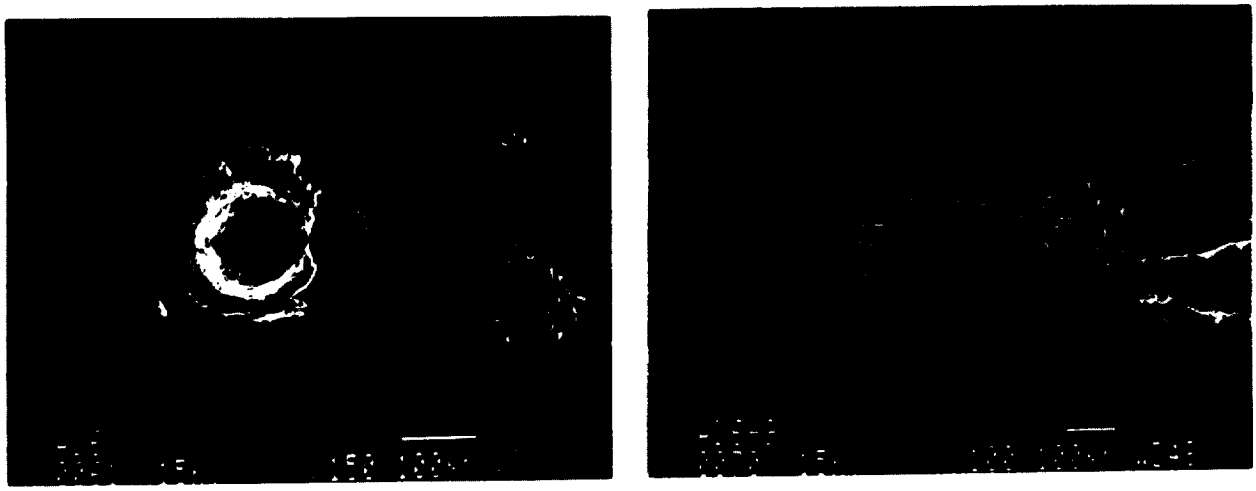

Figure 4. Isolated fatigue cracks that initiated at micrometeoroid craters and sample number engravings on the surface of GY70/201/2024 graphite/aluminum composites.

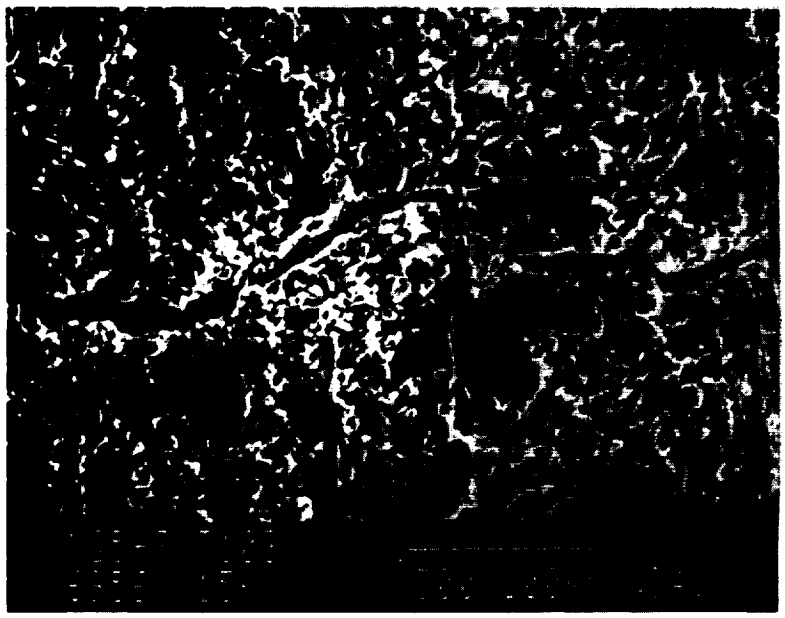

Figure 5. Scanning electron micrograph of a P100/EZ33A/AZ31B graphite/magnesium composite showing a fatigue crack that formed within a brittle oxide layer.

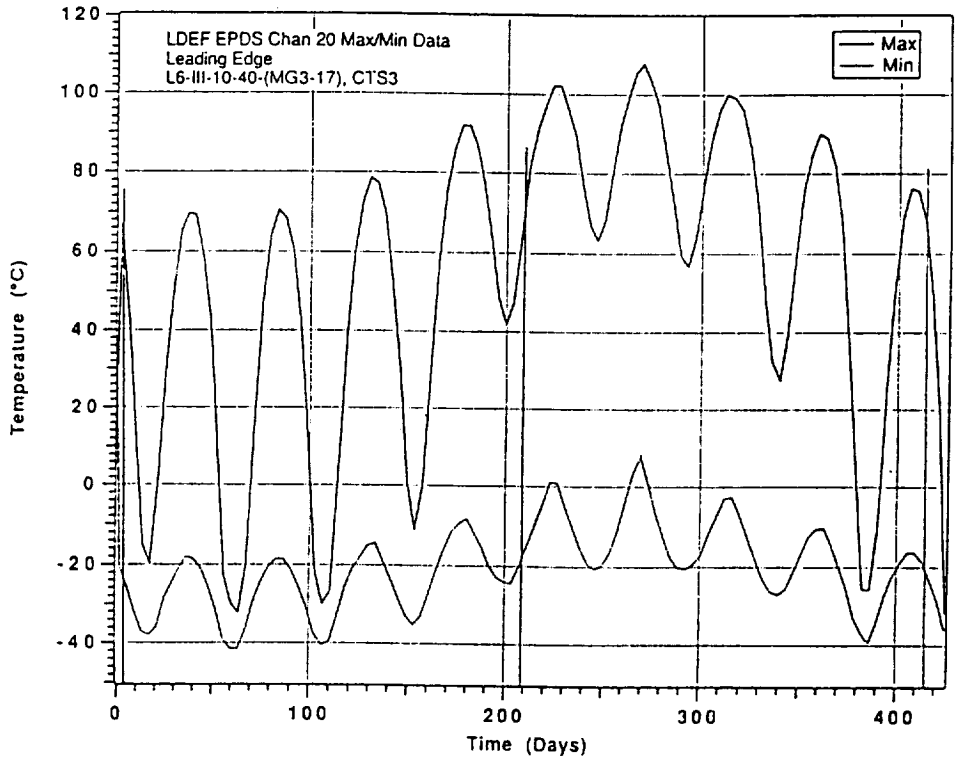

Figure 6. Maximum and minimum temperature recorded for each orbit for a P100/EZ33A/AZ31B Gr/Mg composite mounted on the leading edge of LDEF. Vertical lines indicate orbits selected for strain data analyses.

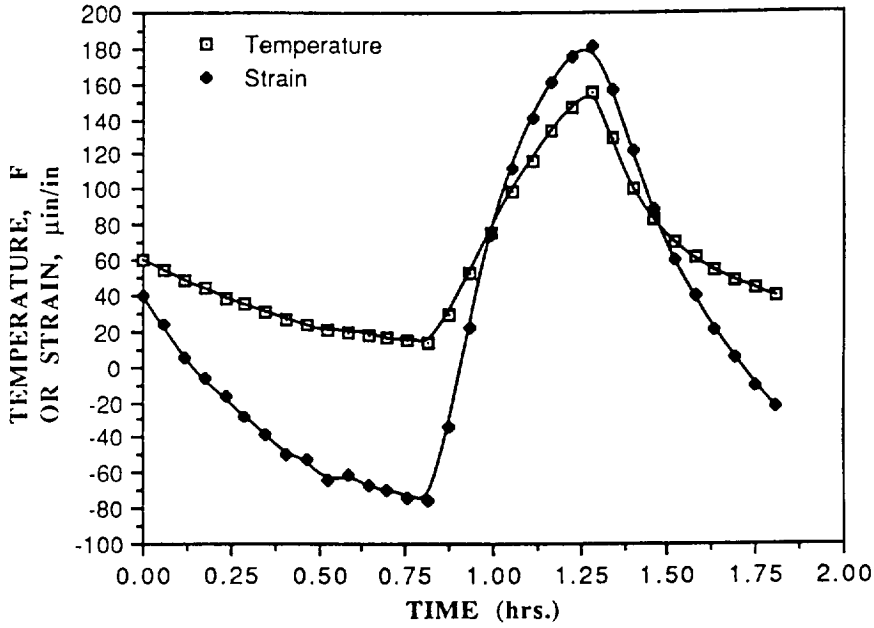

Figure 7. Flight data showing changes in temperature and strain as functions of time during one orbit for a P55/6061/6061 Gr/Al composite on the trailing edge.

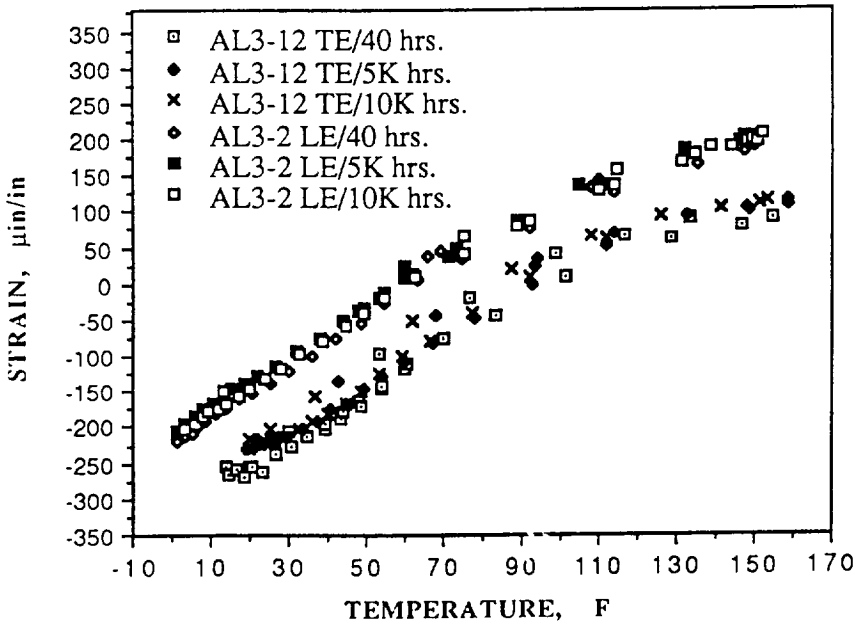

Figure 8. Flight data showing the change in strain as a function of temperature for GY70/201/ 2024 Gr/Al composites for three different orbits on the leading and trailing edges.

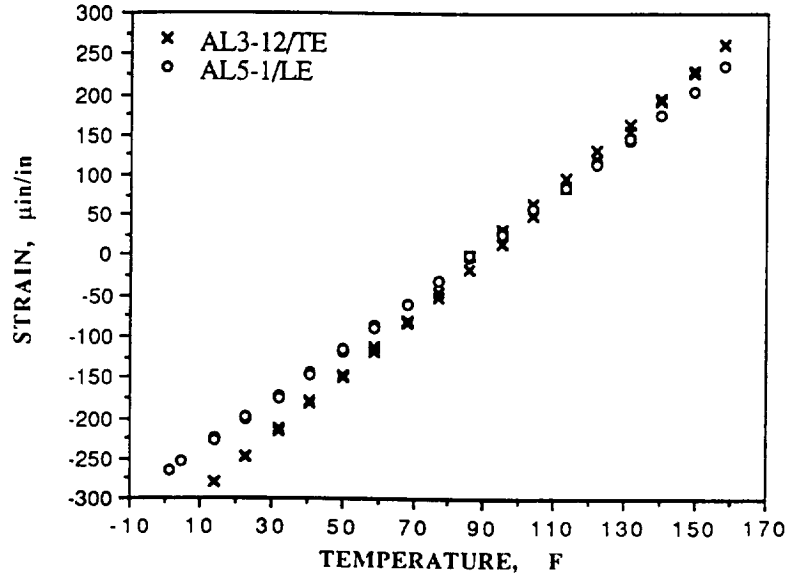

Figure 9. Postflight laser interferometer thermal expansion curves for leading and trailing edge GY70/201/2024 Gr/Al composites.

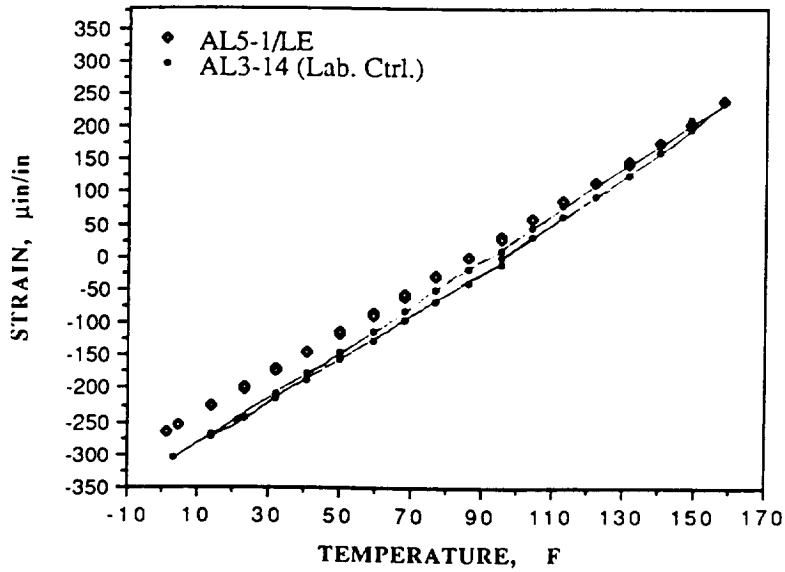

Figure 10. Postflight laser interferometer thermal expansion curves for leading edge and laboratory control GY70/201/2024 Gr/Al composites.

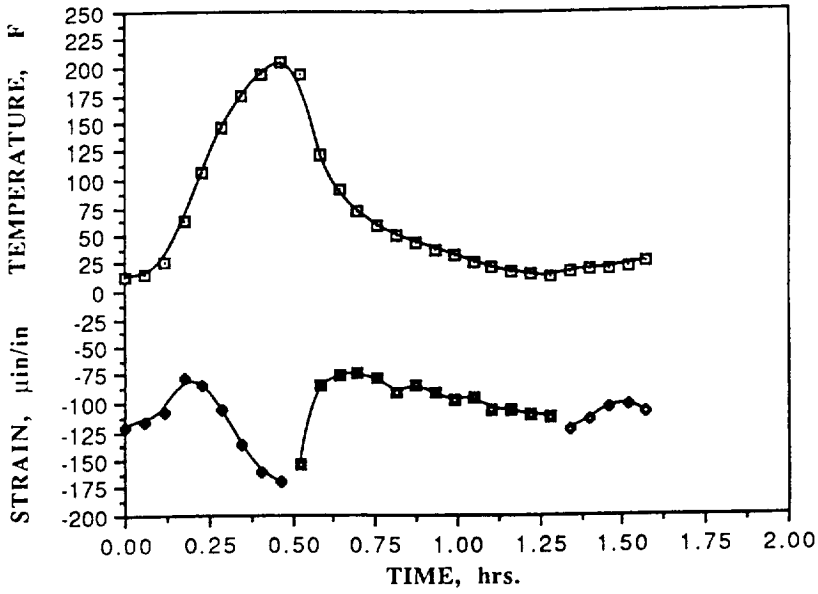

Figure 11. Flight data showing changes in temperature and strain as functions of time during one orbit for a P100/EZ33A/AZ31B Gr/Mg composite on trailing edge.

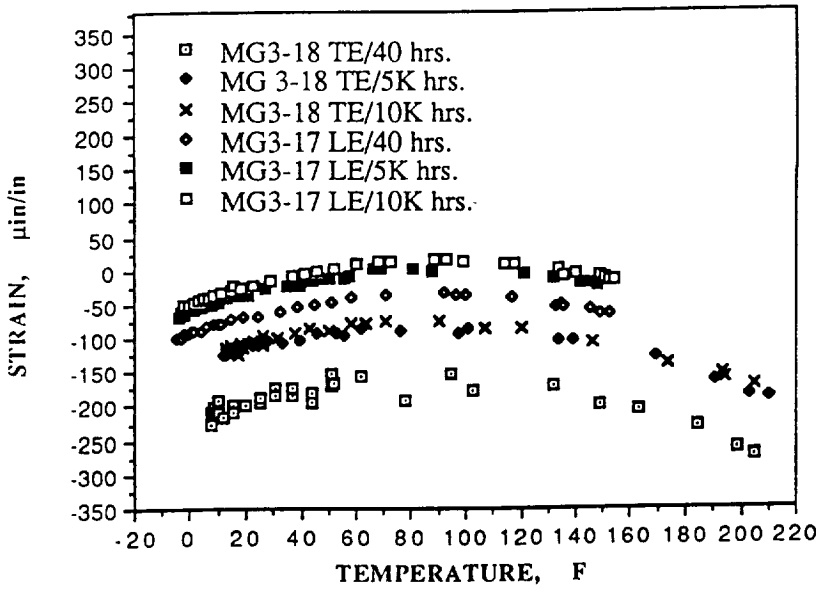

Figure 12. Flight data showing the change in strain as a function of temperature for P100/EZ33A/AZ31B Gr/Mg composites for three different orbits on the leading and trailing edges.

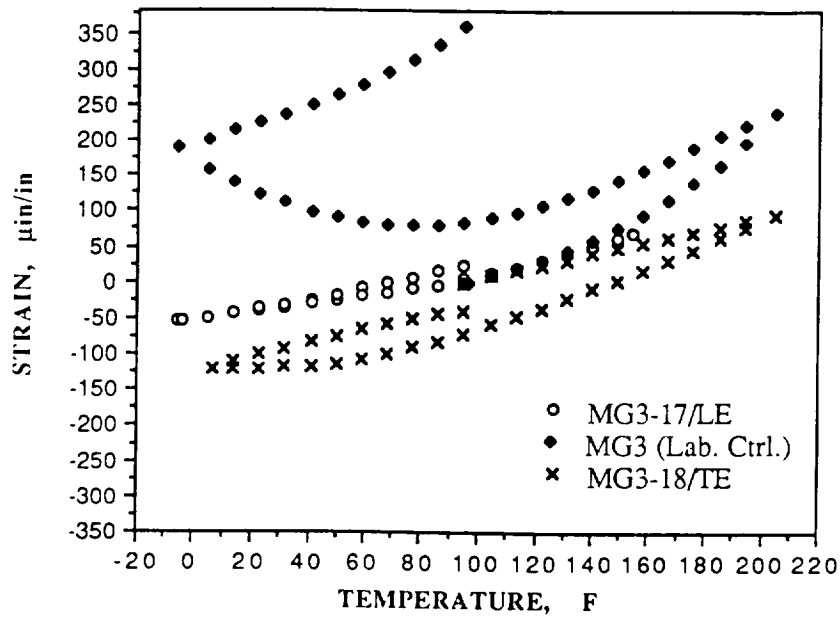

Figure 13. Postplight laser interferometer thermal expansion curves for leading and trailing edge and laboratory control P100/EZ33A/AZ31B Gr/Mg composites.

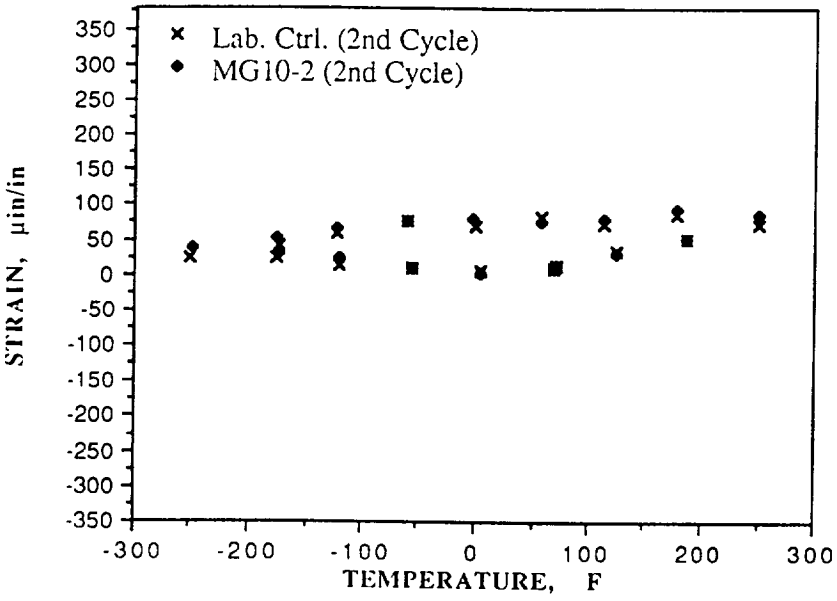

Figure 14. Postflight laser interferometer thermal expansion curves for leading edge and laboratory control P100/AZ91C/AZ61A $(\pm 10°)_S$ Gr/Mg composites.

SPACE ENVIRONMENTAL EFFECTS ON POLYMER COMPOSITES: RESEARCH NEEDS AND OPPORTUNITIES

Bor Z. Jang, J. Bianchi, Y.M. Liu, and C.P. Chang
Materials Engineering Program
202 Ross Hall
Auburn University, AL 36849
Phone (205) 844–3324, FAX (205) 844–3400

SUMMARY

The long-term performance of polymer-based composites in the space environment is discussed. Both thermoset and thermoplastic matrix composites are included in this discussion. Previous efforts on the space environmental effects on composites are briefly reviewed. Focus of this review is placed on the effects of hygrothermal stresses, atomic oxygen, ultraviolet (UV), and space debris/micrometeoroid impacts along with the potential synergism. Potential approaches to estimating the residual strength of polymer composites after exposures to atomic oxygen erosion or space debris/micrometeoroid impact are evaluated. New ground-based data are then utilized to illustrate the effects of atomic oxygen and thermal cycling on the failure behavior of polymer composites. Finally, research needs, challenges, and opportunities in the field of space environmental effects on composite materials are highlighted.

INTRODUCTION

Many structural materials, including polymer matrix composites, are being used or considered for space applications. Space-based structures (e.g., in the low-Earth orbit (LEO)) will experience an environment of very low pressure and temperature extremes, possibly subject to severe hygrothermal effect (moisture degassing and thermal cycling). The structures will also encounter the attack of various atomic species, charged particles, radiation, micrometeoroids, and man-made debris. For instance, atomic oxygen has been found to cause severe erosion of materials (refs. 1–8). The impacts of micrometeoroids can cause local cratering, cracking, and possible fracture of structural components (ref. 9).

Very limited data base existed on the interaction between the polymeric composites and the space environment. This situation is improving since an increasing amount of data are becoming available from the Long Duration Exposure Facility (LDEF) mission. At the present time, the long-term behavior and reliability of polymeric composites in space remains poorly understood. The changes in the properties and structure of composite materials after exposure to the space environment can be better understood when these changes are compared to the predictions based on the ground-based laboratory experiments. This would require much more laboratory evaluation of composites and, equally importantly, a comprehensive model that would allow for the prediction of material durability in the space environment.

Effective solutions to the space material degradation problems are practically nonexistent. Maintenance strategy and repair methodology of future space structures have yet to be identified. The potential of utilizing the space environmental agents to polymerize the protection/maintenance materials for space structures has not been explored. These represent some of the challenging research opportunities in the field of space materials.

BRIEF REVIEW OF RELATED LITERATURE

Surface degradation of space materials has been initially attributed to neutral atomic oxygen, which has a translational kinetic energy of approximately 5 eV by virtue of the spacecraft velocity of 8 km/s (refs. 1,2,4,6,7). However, various observed orbital effects on materials have been duplicated by Whitaker and co-workers (e.g., ref. 10) in plasma reactors where translational energy is low. This observation suggests that the high kinetic energy may not be the primary cause for atomic oxygen erosion. An alternative explanation offered by spacecraft glow investigators is that the recombination energy of oxygen atoms on surfaces is responsible for the observed degradation (ref. 11). The studies conducted by Whitaker and Jang (ref. 10) also includes the development of an equation relating exposure area, atomic oxygen flux, frequency factor, and activation energy to rate of polymer mass loss. Previous studies (refs. 1–10) have placed emphasis on the causes of atomic oxygen erosion and the changes of material surfaces. The effects of such erosion on the subsequent structural performance of materials have not been studied to any significant extent.

Several experiments conducted during the first LDEF mission contained polymer-based composites, which included different reinforcing fibers (graphite, boron, Kevlar, S-glass) and a variety of resin matrices (epoxies, polyimide, polysulfone) (ref. 9). This LDEF project also contained several other monolithic polymeric materials (without reinforcement). Additional information concerning the mass loss suffered by these materials due to atomic oxygen erosion, the material darkening effect caused by UV, and the space debris/micrometeoroid impact-induced damage has just become available (refs. 12,13). These two conference proceedings contain the preliminary data obtained from the various LDEF composite experiments (refs. 14–26). Some preliminary conclusions have been drawn from these experiment (refs. 27,28). The following are considered to be more important observations from these studies:

Atomic oxygen (AO) effect: Matrix resins were found to erode at a higher rate than the reinforcement fibers in composites (ref. 14). The AO erosion depth was inversely proportional to the fiber content for graphite/polymer composites; fiber content was more important than fiber type in dictating the erosion rate (ref. 14). The erosion features may be a function of fiber modulus and structure (ref. 24), but no controlled experiments were designed to assess the roles that the various material factors play. The erosion depths of the uncoated polymer composites were much less than for matrix resins alone (ref. 14).

Based on a very small sampling space, a 20- to 30-percent reduction in the flexural strength and modulus for uncoated graphite/epoxy composites was observed on the leading edge of LDEF (ref. 24). An uncoated graphite/bismaleimide composite suffered a 60-percent reduction in flexural strength. The short beam shear strength of these same materials was reduced by 10 percent (ref. 24). These effects were presumably due to AO erosion; but why AO erosion on a composite surface would result in modulus or shear strength reduction remains unclear. These property degradation results were reported by the General Dynamics Space System Division (GDSSD). In contrast, the LDEF polymer composites investigated by the Lockheed Missiles and Space Company (LMSC) did not exhibit any reduction in flexural strength, modulus, or short beam shear strength (ref. 24). The preliminary data further confirmed the notion that polymer composites for long-duration-mission spacecraft in LEO would require protection from AO attack (ref. 28). All the LDEF composite experiments on the effect of AO can only be considered qualitative in nature. No study was directed toward elucidating the AO erosion kinetics or mechanisms of polymer composites, with or without surface protection. Without such a study, design against AO erosion can only be accomplished by a trial-and-error basis.

Thermal cycling and moisture loss effect: Boeing Defense and Space Group (ref. 19,25) estimated that the leading edge exposed (unshielded) composites had experienced thermal cycling between

–53 °F (–47 °C) and 183 °F (84 °C) while the trailing edge exposed composites between –27 °F (–33 °C) and 170 °F (76 °C) for approximately 3,400 cycles during the 69 months in space. Extensive microcracking was observed with the leading edge exposed materials, including graphite/PMR-15 polyimide and graphite/polysulfone, and with the trailing edge exposed materials, although to a slightly smaller extent. Microcracking was only observed in the multidirectional (nonunidirectional) laminates. Microcracking was believed to be caused by thermal cycling (refs. 17,19,25), but moisture content variations could have been a significant factor. Moisture induced residual stresses (or strains) may be no less important than those caused by the mismatch in coefficient of thermal expansion (CTE). This factor appears to have been neglected in the interpretation of the microcracking phenomenon.

Space debris/micrometeoroid impact effect: The space debris/micrometeoroid impact damaged polymer composite samples did not show the typical hemispherical craters found on metallic structures (refs. 16,26). The damage patterns are characterized by the formation of penetration holes with adjacent surface damage, some internal delaminations, and local fiber fracture. For composites containing brittle graphite fibers, the exit and impact holes exhibited cleaner fiber fractures. In contrast, aramid fiber composites failed in a "brush or broom" mode surrounding the impact damage region (ref. 26). These damage morphologies of polymer composites are very similar to what was observed in the composites subjected to low-velocity impact (refs. 29,30). Determination of post-damage residual properties of advanced polymer composites has been an active area of composites research. However, so far no data of this nature have been reported from the LDEF community.

The effect of UV radiation: Optical property changes on the composite surfaces were considered to be an indication of polymer degradation due to UV radiation exposure. These changes were not present where graphite fibers could have prevented penetration of UV radiation into the material. Although synergistic effects between UV and AO were speculated, no direct evidence was available for or against this speculation.

The small number of specimens recovered from the first LDEF mission has severely limited the scientists' ability to investigate the residual properties of polymer composites exposed to the real space environment. Future space-structure design would require additional knowledge on the degree of microcracking and the changes in such critical properties as the CTE, strength, stiffness, fracture toughness, and vibrational characteristics. A better understanding of these property changes can only be achieved by conducting more ground-based simulation tests to supplement the long-duration exposure data.

SOME GROUND-BASED SIMULATION RESULTS

Thermal Cycling of Polymer Composites

Thermal cycle induced microcracking phenomena were observed on carbon fiber reinforced polymer matrix composites (epoxy-, poly(phenylene sulfide)-, and PEEK-based). One or two minute intraply cracks were observed on thermoplastic matrix composites after a single thermal cycle between –45 °C and +85 °C. Microcracks were initiated at the fiber-matrix interface, preferentially in fiber-rich (or resin-deficient) zones (Fig. 1). Microcracking appeared more severe in PPS than in PEEK composites. Microcracking was not observed in epoxy composites for the first 200 cycles. Judging from the fact that thermoplastic composites tend to have weak fiber-matrix interfacial bonding, these observations suggest that interfacial bond plays a critical role in initiating microcracks in carbon fiber reinforced thermoplastic composites. Intraply cracks are known to be the precursors to delamination cracks, the most serious life-limiting failure mode in laminated composites.

Thermal cycle cracks are caused by the hygrothermal stresses (temperature and moisture variations) present in a laminate. The residual thermal stresses in a fibrous composite may be analyzed at different levels of complexity. First, the differential thermal stresses established between a single fiber and the matrix may be estimated either analytically or numerically. Second, the residual stress fields developed within a group of regularly arrayed fibers may also be determined either theoretically or experimentally. Third, the thermal stresses that occur between laminae with different effective thermal expansion coefficients (CTE) (e.g., due to different fiber orientations) and that caused by moisture content variations may also be calculated using, for example, the classical lamination theory. In each level of study, certain assumptions have to be made to render the problem more tractable.

As a first approach (levels 1 and 2), a "thick cylinder model" (fig. 2) (ref. 31) was developed to simulate the thermomechanical behavior near a fiber in a group of fibers with a given fiber volume fraction. In this model, the stress and strain fields in a thick cylinder under uniform pressure were derived based on the classical elasticity theory. Using such a thick cylinder model, the residual stresses established in a model single fiber-matrix system representing various polymer composites were calculated.

In practically all advanced polymer composites, the matrix has a greater CTE than the fiber, which subjects the fiber to a compressive stress. For most practical volume fractions of fibers, the matrix will generally be subjected to a radial compression at the fiber-matrix interface and a tangential tensile stress. Even in the absence of a good chemical bond, this radial compression against the interface provides friction forces to assist in the load transfer process between the fiber and the matrix. These mechanical bonds are particularly important for thermoplastic composites in which chemical bonds are difficult to form. The magnitudes of such residual thermal stresses at the microscopic level have been calculated for the composite systems being considered for space applications. Equation (1) was utilized in these calculations, which were meant to estimate the orders of magnitudes of these microscopic-level stresses:

$$P = \frac{(\alpha_m - \alpha_f)\,\Delta T}{\frac{1}{E_m}\left(\frac{r_f^2 + r_m^2}{r_m^2 - r_f^2} + \nu_m\right) + \frac{1-\nu_f}{E_f}} \quad . \tag{1}$$

In this equation, α, E, r, and ν are, respectively, the CTE, elastic modulus, effective radius, and volume fraction of the fiber (f) or the matrix (m). Derivation of this equation was based on a single-fiber system, but did include the effect of fiber volume fraction (ref. 31). In the case of $V_f = 0.6$, $r_f^2/r_m^2 = 0.6$ and equation (1) may be further simplified to estimate the magnitudes of $P/\Delta T$ for a variety of composites. The results of such calculations are given in Table 1.

The TCM analysis indicates that, at the microscopic level, the matrix generally is subjected to a radial compression and a tangential tensile stress at the fiber-matrix interface when the end-use temperature (T_e) is lower than the curing temperature or crystallization temperature (T_c). The lower the end-use temperature, the greater the magnitudes of these residual stresses. When good chemical bonding is absent, this radial compression against the interface provides a mechanical bond between the fiber and the matrix. The magnitudes of such residual thermal stresses at the microscopic level for high modulus carbon fiber-PPS composites are of approximately 83×10^3 Pa/K (Table 1). With T_c = 175 °C and T_e = 25 °C, we have p = 12.5 MPa. The magnitude of this interfacial compressive stress will drop to 7.47 MPa when the C/PPS specimen is heated to 85 °C. The fact that microcracks in C/PPS were observed after the second-half (heating) cycle, but not after the first-half (cooling) cycle, may be ascribed to the reduced interfacial adhesion (compressive stress) when the composite was raised to a higher temperature. Although the residual stress magnitudes caused by differential CTE's between layers would also be reduced with a higher T_e, these magnitudes were obviously sufficient to overcome the weak interfacial

adhesion between carbon fibers and the PPS matrix, leading to interfacial debonding and, thus, the observed microcracking.

At the more macroscopic scale (between laminas), a change in temperature (ΔT) or moisture content of a laminated composite structure causes a variation in its dimensions proportional to the change in temperature (ΔT) or moisture content (ΔC) and its initial dimensions. This leads to the development of a thermal strain (ε^T) or hygroscopic strain (ε^H). However, thermal deformation of a lamina is constrained by its neighboring laminae, leading to the development of residual stresses. the magnitudes of these macroscopic residual stresses in each layer of a composite for several composite systems may be estimated using the classical lamination theory. These stresses will produce additional stresses at the fiber-matrix interface and must be added to or subtracted from the microscopic interface thermal stresses mentioned earlier.

The magnitudes of the macroscopic residual thermal stresses in each layer of a composite for several composite systems (not including C/PPS system) have been estimated. The residual stresses in individual plies of a C/PPS laminate are being computed. Their values are expected to be of the same order of magnitude as obtained with the C/epoxy system. The results (Table 2) indicate that the transverse stress (σ_{xx} in the 90° layers) is approximately 12.9 MPa at room temperature and reduced to 8.1 MPa at ~80 °C. This stress will yield a local tensile stress at the fiber-matrix interface. The interfacial compressive stress magnitudes (caused by the difference in CTE between the fiber and the matrix) for a typical C/epoxy will drop from 5.7 MPa at room temperature to 3.6 MPa at ~80 °C. This microlevel stress is not sufficient to compensate for the corresponding macrolevel contribution. Fortunately, relatively strong chemical bonds are present between carbon fibers and the epoxy resin. Thus, much higher stresses are required to induce interfacial debonding in epoxy systems. This is why the C/epoxy composite did not exhibit microcracking even after several hundred thermal cycles between –45 °C and 85 °C. The moisture effect has yet to be analyzed.

Atomic Oxygen Erosion of Polymer Composites (Residual Properties)

The response of four types of fiber-epoxy composites to atomic oxygen was investigated by Bianchi (ref. 32): carbon fiber-, aramid (Kevlar) fiber-, glass fiber-, and glass/carbon/glass hybrid composites. In terms of mass loss, the carbon fiber-epoxy composite suffered the greatest rate of degradation among this group of materials (Fig. 3). This was followed by the Kevlar, hybrid (not shown) and glass fiber systems. That the glass fiber-epoxy and the hybrid composite (with the top and bottom layers being glass fiber-epoxy laminas) suggested the glass fiber to be relatively more resistant to the AO attack. In light of flexural modulus and strength retention, the Kevlar fiber composite stood out to be the best against AO degradation for long-term exposures. Again, the carbon fiber system exhibited the highest rate of strength reduction (Fig. 4).

Surface morphology studies by optical microscopy and SEM indicated that the AO degradation process in a composite followed a two-step process. In general, the matrix resin appeared to be less resistant to AO. This observation is consistent with the LDEF findings (refs. 17,24,25). Where accessible by AO, the resin located within the interstices between fibers tended to get eroded away first (Fig. 5). This resin erosion step typically proceeded to one or two fiber diameters deep prior to any significant fiber degradation was observed. The fiber erosion step was characterized by the formation of surface pores, some larger and deeper holes, nonuniform diameter reduction (necking) and, when a long exposure time was imposed, some fiber breakages (Fig. 6). Thinner (Fig. 7) and weaker fibers appeared to be the preferential initiation sites of damaging cracks that were responsible for the reduction in mechanical properties.

RESEARCH NEEDS AND OPPORTUNITIES

Previous research efforts concerning environmental effects on polymer composites were largely limited to the observations of the chemical and physical changes taking place on the surface of materials. No systematic efforts have been made in elucidating the AO erosion mechanisms and kinetics of polymer composites. Little endeavor has been directed to assessing the subsequent (residual) performance of polymer and composite materials after various degrees of space environment exposure. With a better understanding of erosion chemistry and performance-space environment relationship, we would be better prepared to study the maintainability and repairability of space materials and structures. Also lacking is a predictive model for material durability that incorporates both material and space environmental parameters. These efforts are essential to the establishment of improved guidelines for choosing composites for space applications.

Space Environment Effects on the Material Performance

Future ground-based simulation studies should include determination of the mechanical properties of various aerospace-grade composites in relation to the space environmental factors. These properties include the resistance to foreign object impacts, CTE, strength, stiffness, fracture toughness, and damping response.

As an example, composites may be exposed to a varying but controlled degree of AO attack in a simulated space environment. Various thermomechanical properties may then be measured and correlated with the chemical and physical changes of the material surface. This effort should be aimed at identifying the most critical morphological or microstructural features of material surfaces that would govern the degradation effect. Micromechanics models may then be developed to allow for prediction of the key mechanical properties of composites.

Extensive and indepth studies on the response of various polymer composites subjected to low-velocity impacts by foreign objects have been conducted by many researchers (e.g., refs. 29,30). Many key material parameters have been identified that dictate the impact resistance of polymer composites. Studies should be extended to include high-velocity impacts, simulating the interaction between micrometeoroids and structural components. Since the data on the velocity and dimensions of space debris/micrometeoroids are becoming increasingly available, we are now in a better position to predict the impact damage state and the residual properties of polymer composites. Information acquired through these future studies will help establish scientific guidelines, based on which one judge if, when, and how to service or repair the space structures.

Model Development

The LDEF community perhaps should collaborate to develop a model having some predictive value for material durability. The development of the model may begin by considering the mass loss and surface structural changes caused by the simulated attacks of AO, radiation, and micrometeoroids/debris under the conditions of hygrothermal variations. The effect of mass loss can be related to the parameters of microstructural or morphological changes (which may generate stress concentrations, e.g.) must also be considered perhaps from the statistical fracture mechanics perspectives. This suggestion originates from the observation that characteristic AO eroded and debris impact damaged surfaces of materials contain many defects of differing severity (varying defect size and crack tip radius of curvature). All these effects should be incorporated in the model and compared with the material's intended service

function (e.g., structural integrity) to predict the residual properties (e.g., strength) and durability of the material.

Maintenance of Space Structures

Future space missions may require development of a reliable maintenance methodology. this may be accomplished by first evaluating the surface chemical and physical states (surface functional groups and roughness profile) of potential space-bound polymers/composites exposed to AO, UV radiation, and hypervelocity impacts. These surface-eroded or damaged materials may then be coated with fresh layers of identical material or other chemically compatible materials. Different degrees of surface treatment (e.g., grit blasting or chemical cleaning) may be applied to the eroded structures prior to coating/repairing. The mechanical integrity (strength, stiffness, and impact resistance) of the repaired structures must then be measured as a function of the surface conditions. This task will produce desirable knowledge on the candidate protection/repair materials and the surface treatments required.

Future space missions may also demand development of effective techniques to cure or polymerize the protection or repair materials in a space environment. Conventional aerospace techniques such as press molding of polymers and autoclave curing of composites require a high temperature to active the reaction and a high pressure to consolidate the microstructure. Application of a high temperature and high pressure to the structures in space is not a straightforward task. A better alternative is to take advantage of the resources in the space environment to activate and accelerate the polymerization reaction. The potential resources that can be utilized to initiate polymerization include gamma radiation, electrons, protons, other charged particles, AO, and visible/UV light. The feasibility of utilizing atomic oxygen to initiate or accelerate polymerization reactions of silicon-, epoxide-, and imide-based resins should be established.

CONCLUDING REMARKS

The spacecraft or the components placed in orbit will be subjected to constant attacks by the various space environmental agents. The degradation mechanisms and kinetics of polymer composites in the space environment must be addressed. Further evaluations of structural changes and property degradation will allow us to gain a better understanding of the material-space environment interactions. The space components may require protection, maintenance, and repair to ensure long-term reliability and survivability. One goal of future research will be the establishment of an effective methodology to maintain or service the space structures. Efforts should also be made in the future to develop a durability predictive model that incorporates both material and space environmental parameters, and hopefully to suggest improved guidelines for choosing polymer composites for space applications.

ACKNOWLEDGMENTS

This project is partially supported by the 1992 ASEE/NASA Summer Faculty Fellowship Program. B.Z. Jang would like to thank his NASA host, Mr. Roger Linton, for technical assistance and encouragement. J. Bianchi is supported by the Engineering Physics Division of Marshall Space Flight Center through a NASA Graduate Researcher Fellowship, with Dr. A.F. Whitaker being the technical monitor.

REFERENCES

1. Leger, L.J.: "Oxygen Atomic Reaction With Materials at Orbital Altitudes." NASA Technical Memorandum 58246, May 1982.

2. Leger, L.J.: "Oxygen Atomic Reaction With Shuttle Materials at Orbital Altitudes—Data and Experimental Status." AIAA 21st Aerospace Sciences Meeting, Reno, NV, June 10–13, 1983.

3. Whitaker, A.F., Little, S.A., Harwell, R.J., Griner, D.B., DeHaye, R.F., and Fromhold, A.T., Jr.: "Orbital Atomic Oxygen Effects on Thermal Control and Optical Materials—STS-8 Results." AIAA-850416, 1985.

4. Leger, L.J., Spiker, I.K., Kuninecz, J.F., Ballentine, T.J., and Visentine, J.T.: "STS Flight 5 LEO Effects Experiment—Background Description and Thin Film Results." AIAA-8302631-CP, 1983.

5. Whitaker, A.F.: "LEO Atomic Oxygen Effects on Spacecraft Materials." AIAA Shuttle Environment and Operations Conference, Washington, DC, October–November 1983.

6. Stuckey, W.K., Borson, E.N., Meshishnek, M., Xehns, E., Arnold, G.S., Bertrand, P.A., Hall, D.F., Leung, M.S., Peplinski, D.R., and Tolentano, L.V.: "Effects on Optical and Metallic Surfaces: Results of Aerospace Trays A51 and A53 on the Oxygen Interaction With Materials (EOIM) Experiment." AIAA Shuttle Environment and Operations Meeting, October–November 1983.

7. Worley, S.D., Dai, C.H., Graham, J.L., Fromhold, A.T., Daneshvar, K., Whitaker, A.F., and Little, S.A.: "Analysis of Spacecraft Polymeric Materials." Journal of Spacecraft and Rockets, vol. 23, 1986, pp. 350–352.

8. Whitaker, A.F., Burka, J.A., Coster, J.E., Dalius, I., Little, S.A., DeHaye, R.F.: "Protective Coatings for Atomic Oxygen Susceptible Spacecraft Materials—STS-41G Results." AIAA Shuttle Environment and Operations II Conference, Houston, TX, November 13–15, 1985.

9. Tennyson, R.C.: "Composite Materials for Space." SAMPE J., vol. 26, No. 2, 1990, p. 7.

10. Whitaker, A.F., and Jang, B.Z.: "RF Oxygen Plasma Effects on Polymeric Materials." Accepted by J. Applied Polymer Sci.

11. Green, B.D.: "Atomic Recombination Into Excited Molecular—A Possible Mechanism for Shuttle Glow." Geophysical Res. Letters, vol. 11, 1984, p. 576.

12. NASA CP-3134: "LDEF—69 Months in Space." First Post-Retrieval Symposium, Kissimmee, FL, June 1991.

13. NASA CP-3162: "LDEF Materials Workshop '91." NASA Langley Research Center, Hampton, VA, November 1991.

14. Steckel, G.L., and Le, T.D.: "M0003-10, LDEF Advanced Composites Experiment." NASA CP-3134 (ref. 12), pp. 1041–1054.

15. Petri, B.C.: "LDEF—Space Environmental Effects on Materials: Composites and Silicone Coatings." NASA CP-3134 (ref. 12) (abstract only), p. 1055.

16. Tennyson, R.C., Mabson, G.E., Morison, W.D., and Kleiman, J.: "Preliminary Results From the LDEF/UTIAS Composite Materials Experiments." NASA CP-3134 (ref. 12), pp. 1057–1072.

17. Meshishnek, M.J., Gyetvay, S.R., and Jaggers, C.H.: "LDEF Experiment M0003 Deintegration: Findings and Impacts." NASA CP-3134 (ref. 12), pp. 1073–1109.

18. Pippin, H.G., Mulkey, O., Verzemnieks, J., Miller, E., Hill, S., and Dursh, H.: "Survey of Results From the Boeing Modules on the M0003 Experiment on LDEF." NASA CP-3134 (ref. 12), pp. 1109–1114.

19. George, P.E., and Hill, S.G.: "Results From Analysis of Boeing Composite Specimens Flown on LDEF Experiment M0003." NASA CP-3134 (ref. 12), pp. 1115–1142.

20. Felbeck, D.K.: "High-Toughness Graphite/Epoxy Composite Material Experiment." NASA CP-3134, pp. 1143–1148.

21. Slemp, W.S., Young, P.R., Witte, W.G., Jr., Shen, J.Y.: "Effects of LDEF Flight Exposure on Selected Polymer Matrix Composites." NASA CP-3134 (ref. 12), pp. 1149–1162.

22. Parcelier, M., and Assie, J. Pierre: "Effect of Space Environment on Composite Materials and Thermal Coatings." NASA CP-3134 (ref. 12), pp. 1163–1174.

23. Jabs, H.: "Effect of Space Exposure of Some Epoxy Matrix Composites on Their Thermal Expansion and Mechanical Properties (AO138-8)." NASA CP-3134 (ref. 12), pp. 1175–1186.

24. Steckel, G.L., Cookson, T., and Blair, C.: "Polymer Matrix Composites on LDEF Experiment M0003-9 and 10." NASA CP-3162 (ref. 13), pp. 515–542.

25. George, P.: "Space Environmental Effects of LDEF Low Earth Orbit Exposed Graphite Reinforced Polymer Matrix Composites." NASA CP-3162 (ref. 13), pp. 543–570.

26. Tennyson, R.C.: "Additional Results on Space Environmental Effects on Polymer Matrix Composites—Experiment AO180." NASA CP-3162 (ref. 13), pp. 571–592.

27. Steckel, G., Tennyson, R., and George, P.: "LDEF Panel Discussion Summary: Polymer Matrix Composites." NASA CP-3162 (ref. 13), pp. 727–736.

28. Whitaker, A.F.: "Coatings Could Protect Composites From Hostile Space Environment." Advanced Materials and Processes, April 1991, pp. 30–32.

29. Jang, B.Z., et al.: "Impact Resistance and Energy Absorption Mechanisms in Hybrid Composites." Composite Sci. and Technology, vol. 34, 1989, pp. 305–335.

30. Jang, B.Z., et al.: "Response of Polymer Composites on Low-Velocity Impact." Polymer Composites, vol. 11, 1990, pp. 144–157.

31. Jang, B.Z., Liu, Y.K., and Chang, Y.S.: "Cryogenic Failure Mechanisms of Fiber-Epoxy Composites." The Second International Conference on Post Failure Analysis Techniques for Fiber Reinforced Composites." Dayton, OH, July 1985, pp. 22-1 to 22-41.

32. Biachi, J.B.: "Evaluation of Epoxy-Matrix Composites and Polymeric Films Exposed to Atomic Oxygen." M.S. Thesis, Materials Engineering Program, Auburn University, AL, December 1992.

Table 1. The values of $P/\Delta T$ for several fiber-resin combinations.

Fiber	Matrix	Ef (GPa)	αf (E-6/K)	Em (GPa)	αm (E-6/K)	$P/\Delta T$ (KPa/K)
High-modulus carbon fiber	Toughened epoxy	340	7	3.0	60	36
Intermediate modulus carbon	Epoxy	270	8	3.5	55	37
High-modulus carbon	PPS	340	7	4.0	99	83
High-modulus carbon	PEEK	340	7	4.0		
E-glass	Epoxy			3.5	55	
Kevlar-49	Epoxy			3.5	55	

Table 2. Residual thermal stresses in a carbon/epoxy composite, $[0/45/90/-45]_{2s}$.

Layer Number	$\Delta T = -97$ °C			$\Delta T = -154$ °C			$\Delta T = -222$ °C		
	σ_{xx}	σ_{yy}	σ_{xy}	σ_{xx}	σ_{yy}	σ_{xy}	σ_{xx}	σ_{yy}	σ_{xy}
1(0°)	–195	8.12	0	–310	12.9	0	–446	18.6	0
2(45°)	93.5	93.5	102	148	148	161	214	214	233
3(90°)	8.12	–195	0	12.9	–310	0	18.6	–446	0
4(–45°)	93.5	93.5	102	148	148	–161	214	214	–233

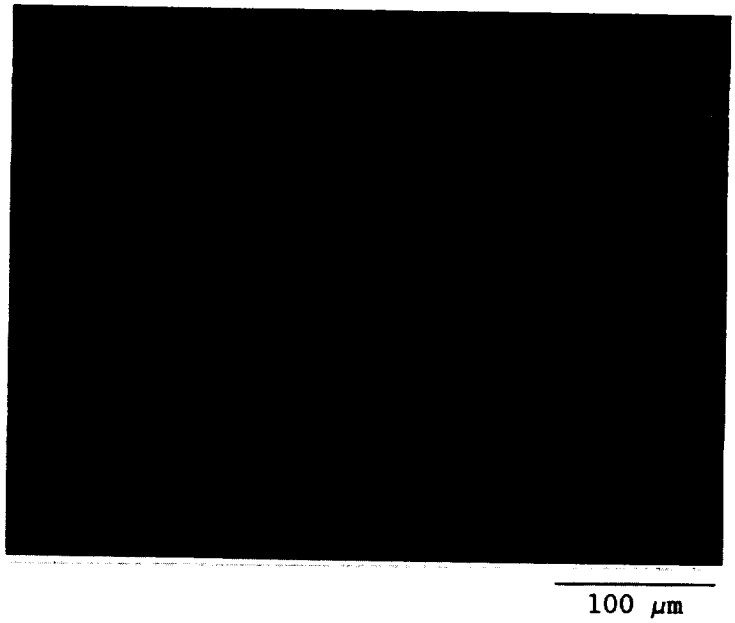

(a)

(b)

Figure 1. Microcracks in carbon fiber/PPS composites due to thermal cycling, (a) optical micrograph and (b) SEM micrograph.

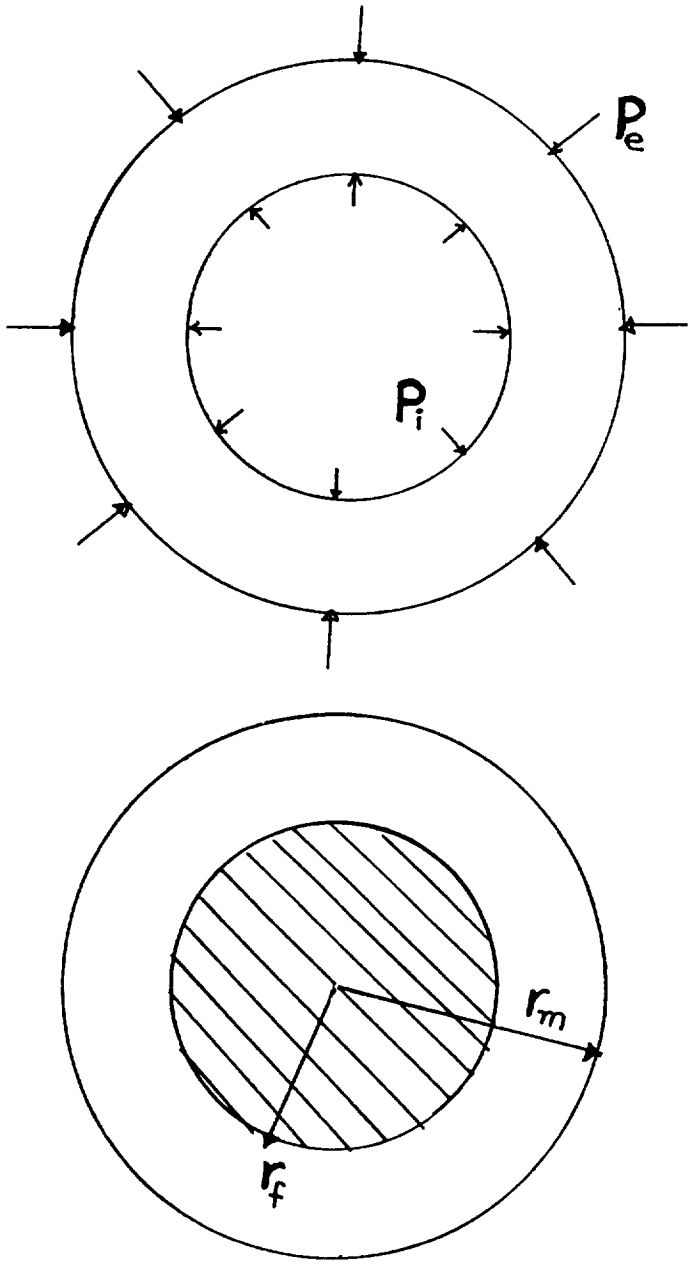

Figure 2. Schematic of thick-cylinder model (TCM).

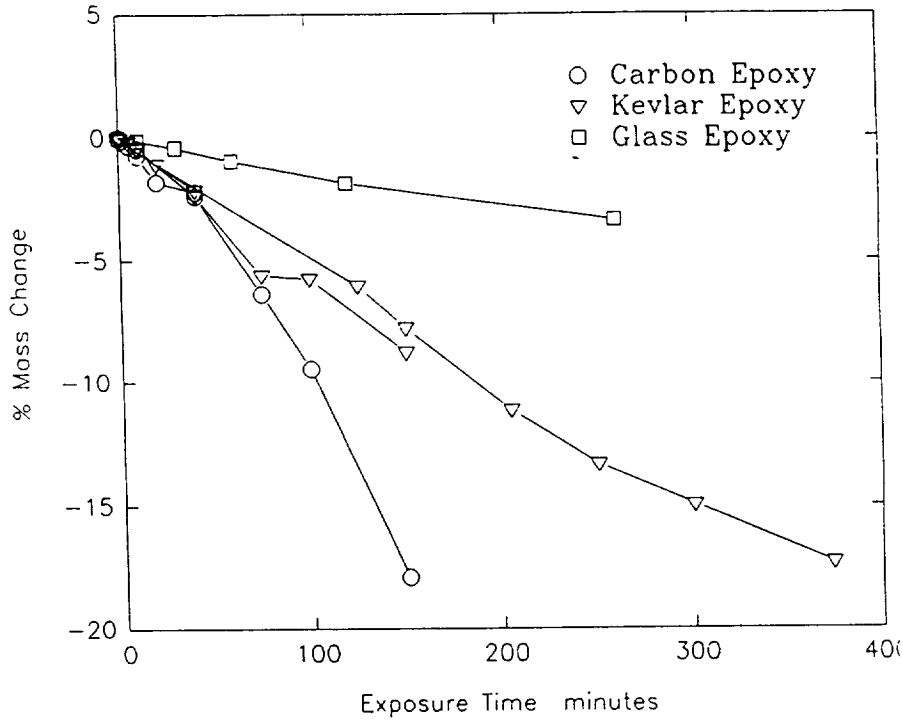

Figure 3. Mass loss per surface area exposed to AO for carbon-, Kevlar, and glass-fiber reinforced epoxy composites.

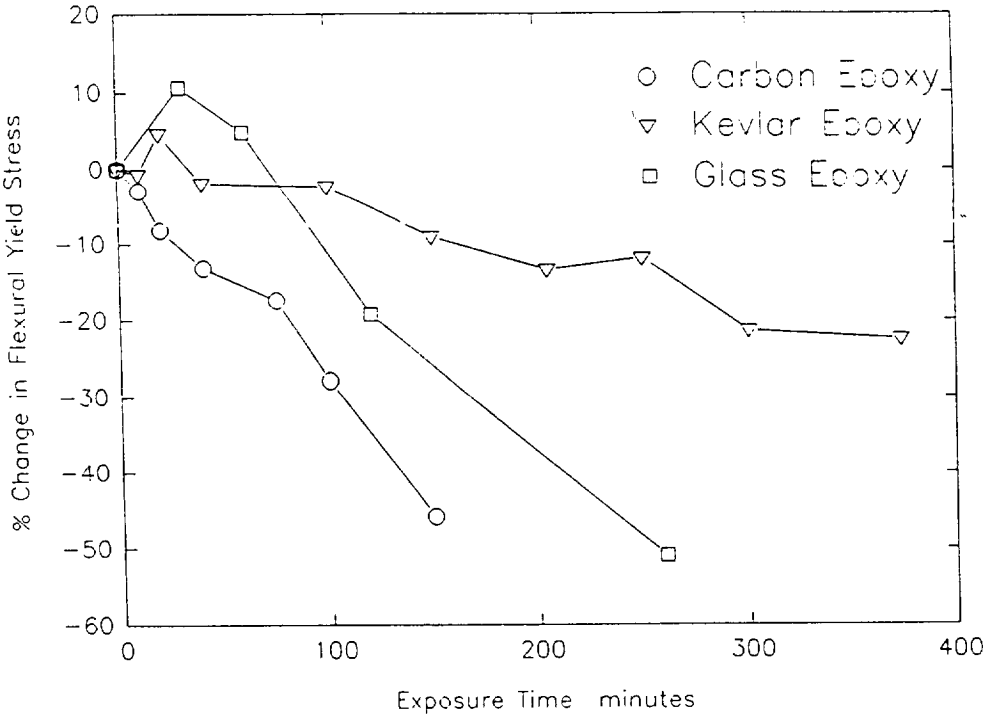

Figure 4. Flexural strength reduction of composites due to AO exposure.

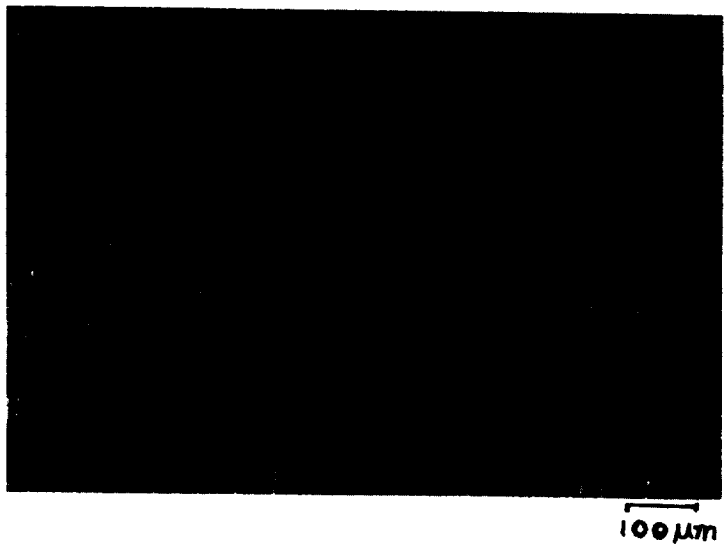

Figure 5. An atomic oxygen eroded surface of the glass-epoxy composite.

Figure 6. Kevlar fiber/epoxy composite surface after a long exposure to AO.

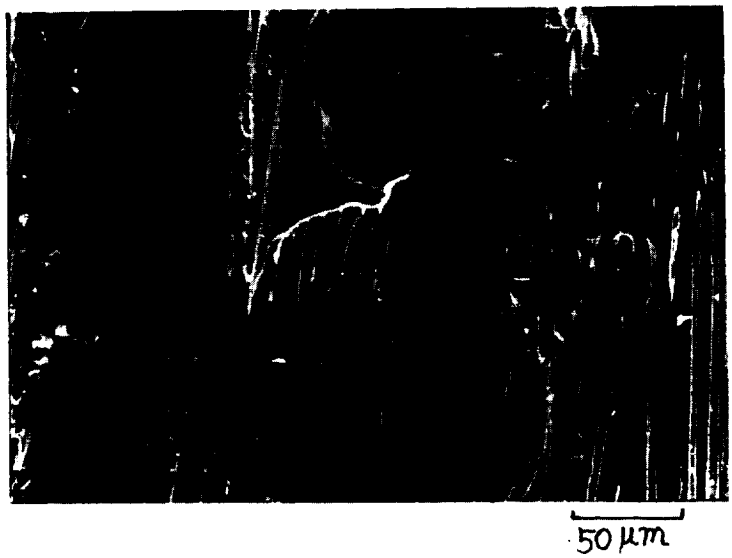

Figure 7. Postflexural test examination of an AO-eroded carbon/epoxy composite indicates necked fibers being the preferential sizes of crack initiation.

LOW-EARTH ORBIT EFFECTS ON ORGANIC COMPOSITE MATERIALS FLOWN ON LDEF*

Pete E. George
Boeing Defense & Space Group
Seattle, WA 98124–2499 M/S 73–09
Phone: 206/234–2679, Fax: 206/237–0052

Harry W. Dursch
Boeing Defense & Space Group
Seattle, WA 98124–2499 M/S 82–32
Phone: 206/773–0527, Fax: 206/773–4946

SUMMARY

Over 35 different types of organic matrix composites were flown as part of 11 different experiments onboard the NASA Long Duration Exposure Facility (LDEF) satellite. This materials and systems experiment satellite flew in low-Earth orbit (LEO) for 69 months. For that period, the experiments were subjected to the LEO environment including atomic oxygen (AO), ultraviolet (UV) radiation, thermal cycling, microvacuum, meteoroid and space debris (M&D), and particle radiation. Since retrieval of the satellite in January of 1990, the principal experiment investigators have been deintegrating, examining, and testing the materials specimens flown.

The most detrimental environmental effect on all organic matrix composites was material loss due to AO erosion. AO erosion of uncoated organic matrix composites (OMC) facing the satellite ram direction was responsible for significant mechanical property degradations. Also, thermal cycling-induced microcracking was observed in some nonunidirectional reinforced OMC's. Thermal cycling and outgassing caused significant but predictable dimensional changes as measured in situ on one experiment.

Some metal and metal oxide-based coatings were found to be very effective at preventing AO erosion of OMC's. However, M&D impacts and coating fractures which compromised these coatings allowed AO erosion of the underlying OMC substrates.

This paper summarizes the findings for organic matrix composites flown on the LDEF and identifies the LEO environmental factors, their effects, and the influence on space hardware design factors for LEO applications.

BACKGROUND

The benefits of OMC's in spacecraft applications include: (1) significant weight savings, which result in lower launch costs or increased payload; (2) the ability to tailor the coefficient of

* Testing of Boeing composites flown on LDEF was funded by Boeing IR&D. All other Boeing activities were supported by NASA Langley Research Center contracts NAS1-18224 and NAS1-19247.

thermal expansion, thereby providing a structure with dimensional stability; and (3) high stiffness. Because composite laminate properties can be varied by altering the fiber, resin, and laminate layup, a wide range of mechanical and thermal properties can be achieved. Some of the more promising space applications for OMC's include truss structures, frames, booms, solar arrays, and monocoque shell structures.

OMC's have been used in many space applications, but only with extreme caution and a conservative design approach as required with relatively new materials in a space environment. Therefore, the full advantages of OMC's in spacecraft applications have not yet been realized. Because of these advantages, many OMC's were included in both active and passive experiments on LDEF.

LDEF was deployed on April 7, 1984, in LEO at an altitude of 482 km and retrieved January 12, 1990, at an altitude of 340 km. During the 5.8-year mission, the LDEF experienced the following LEO environments:

Atomic Oxygen—ram facing fluence of 9E+21 atoms/cm^2. The higher AO concentrations at lower altitudes resulted in roughly 50 percent of the AO fluence occurring in the last 6 months of the mission.

Solar UV—Cumulative equivalent Sun hours ranged from 4,500 h at LDEF's Earth end to 11,000 h at leading and trailing edges to 14,500 h at the space end.

Thermal Cycling—32,422 ninety-minute cycles. Actual on-orbit measured LDEF structure temperatures ranged from +35 °F to +134 °F. Composite specimen temperatures were a function of both location on LDEF and optical properties. For example, bare composites on the leading edge had a predicted temperature range of –70 °F to +235 °F, while nearby coated composite specimens had a predicted range of –75 °F to +60 °F.

Meteoroid and Space Debris—LDEF had ≈35,000 impact craters with over 3,100 craters >0.5 mm in diameter. The largest crater on LDEF had a diameter of 5.25 mm.

Particle Radiation—The total exposure of LDEF was below the threshold for observable radiation effects in composites. The predicted surface electron dose was ≈300,000 rads.

Figure 1 is a photo of one of The Aerospace Corporation's trays that contained numerous composite specimens provided by several principal investigators. Table 1 lists all the OMC specimens flown, along with their position on the satellite, environment, experiment number, and principal investigator.

POSTRETRIEVAL EXPERIMENT INVESTIGATION

Since the retrieval of LDEF, experiment investigators have been extracting useful design data and observations from the material specimens. Figure 2 shows the general flow for the phases of postretrieval materials experiment investigations. Currently, most OMC specimen testing has been completed, and the results are being reported in relation to the environmental exposures received.

Deintegration and initial observations revealed the significant effects of AO erosion on leading-edge-located OMC's. Trailing edge specimens appeared relatively unchanged with the exception of occasional discolorations due to nearby contamination sources. As a whole, OMC's appeared to have survived relatively intact.

More detailed observations and nondestructive testing revealed that non-AO-exposed graphite-reinforced-OMC specimens were in excellent condition. Non-AO-exposed, glass-reinforced organic matrix composite specimens displayed heavy discoloration due to UV exposure. AO-exposed, graphite-reinforced specimens displayed significant loss of material due to AO erosion up to 0.005 inch for ram facing specimens. AO-exposed, glass-reinforced specimens displayed erosion only through the surface resin layer. The glass fibers then shielded the underlying material, whereas the graphite fibers, due to their AO erosion, provided minimal shielding.

Analysis of dimensional stability data collected on-orbit revealed dimensional changes as a result of both outgassing and thermal cycling (ref. 1). Results for on-orbit measurements of 90° direction strain versus temperature of unidirectional fiber-reinforced organic composited revealed a 40-day period of changing coefficient of thermal expansion (CTE) as the specimen outgassed. The CTE asymptotically approached and reached the preflight value during these 40 days. Moisture desorption was cited as the most likely cause of the shrinkage and changing CTE. On-orbit measurement of 0° CTE did not reveal any significant changes. These results verified the investigators' ground-based simulation predictions. These dimensional changes must be factored into the design of low distortion OMC laminates.

Destructive mechanical testing of non-AO-exposed graphite reinforced materials revealed no significant property changes. AO-exposed specimens displayed reductions in mechanical properties commensurate with the loss of material due to AO erosion. No bulk chemical changes were found for the matrix resins, implying that the environmental effects were only skin deep for the remaining material.

Various coatings were found to be effective at preventing AO erosion of the OMC substrates. Thermal control coatings may have also prevented microcracking by reducing temperature extremes and thermal shocks during thermal cycling. All coatings were subjected to compromise by micrometeoroid and debris impacts which, in addition to allowing AO attack of the OMC substrate, also created delaminations and interply cracking.

ENVIRONMENTAL EFFECT—DESIGN FACTOR RELATIONSHIPS

The hardware designer for spacecraft applications must think in terms of key parameters to design an efficient and reliable structure. Factors such as stiffness and strength can be subject to change due to environmental effects in LEO. Figure 3 is a nonprioritized list of the more significant space hardware design parameters, potential environmental effects, and the LEO environments responsible for those effects. A great deal has been learned about the relationships between these factors and the magnitude of the relationships.

LEO environments for OMC's depend a great deal on hardware location onboard the spacecraft. These environments can be divided into five categories: (1) manned spacecraft interiors; (2) AO- and UV-shielded spacecraft exteriors; (3) AO-shielded, UV-exposed spacecraft exteriors (trailing edge environment); (4) UV-shielded, AO-exposed spacecraft exteriors (backside of solar array panels, Sun tracking satellites); and (5) AO- and UV-exposed spacecraft exteriors (ram

facing environments). The first category is not addressed here as no LDEF specimens were flown in such an environment. Also, this is a relatively benign environment as required for human life support. The last three categories also include effects from the micrometeoroid and debris environment. No specimens were flown with AO exposure and UV shielding. Therefore, category 4 is not addressed except for possible future work to look for synergistic AO and UV effects.

Both the thermal and microvacuum environments exist to some extent in each of the four exterior categories. The synergistic effects of these two environments result in significant, but predictable, dimensional stability concerns for LEO-exposed OMC's. Dimensional changes can occur as a result of outgassing and thermal expansion. Figure 4 shows the dimensional changes as measured on orbit as a function of temperature as part of experiment A0180 by Tennyson et al (ref. 1). Dr. Tennyson and company have shown that these changes are predictable (ref. 2). These two environments also result in outgassing which can be a concern for contamination reasons. OMC specimens on a number of experiments were subjected to outgassing tests which revealed similar values for pre- and postflight testing of epoxies, polysulfones, and polyimides. This suggests that outgassing occurring in space is due to absorbed moisture and not solvents or low-molecular-weight prepolymer species.

AO- and UV-Shielded Environments

Figure 5 lists the predominant environments, effects, and influenced design parameters along with their relationships for AO- and UV-shielded locations. The LDEF specimens shielded from AO and UV were either mounted on the interior of LDEF or as witness specimens on the backside of trays holding exposed specimens. The two predominant environments for these shielded specimens is thermal cycling and microvacuum. Due to LDEF's nonpolar LEO orbit, the particle radiation environment seen by both shielded and exposed specimens was below the observable threshold for composites. While not as extreme as if exposed directly to the LEO environment, the thermal cycling seen by shielded OMC's combined with the microvacuum conditions can result in the following design conditions: (1) microcracking resulting in changes in thermal and mechanical properties and (2) outgasssing resulting in significant, but predictable, dimensional changes. Results from testing of LDEF specimens exposed to this environment showed no mechanical property changes.

AO-Shielded, UV-Exposed Environments

The LDEF satellite flew in a gravity-gradient stabilized orientation, maintaining the same position relative to the direction of motion. As the atmosphere at mission altitudes consists primarily of AO with a mean free path on the order of meters, the satellite swept a clean path through the AO. Therefore, the backside of the satellite received virtually no AO exposure. OMC specimens located on the backside of LDEF were in an AO-shielded, UV-exposed environment.

Figure 6 lists the predominant environments, effects, and influenced design parameters along with their relationships for AO-shielded and UV-exposed locations. These factors and relationships include those discussed previously (identified as grey in Figure 6) and new ones (black) associated with UV exposure and micrometeoroid and space debris. Dimensional stability and outgassing concerns still exist for OMC materials used in this type of environment.

The effects of meteoroid and debris impacts can be devastating for any material depending on the size and velocity of the impactor. However, for OMC specimens flown on LDEF, no specific mechanical property reductions were attributable to impacts. Although fiber breakage and minor delaminations were reported by a number of investigators (refs. 2,3), Whittaker et al. reported no tensile test breakage initiated or culminated on any impact site. It appears that no direct mechanical property influence data from impacts will be available from LDEF OMC specimens. However, documentation of impact damage patterns will allow ground-based testing to simulate these and larger impacts.

No mechanical property changes were attributed to UV exposure effects. Figure 7 shows the flexural strength and modulus results for both control and flight specimens (ref. 4). No significant changes were found for these materials as well as other graphite-reinforced OMC's. Glass-reinforced OMC's flown in AO-shielded, UV-exposed positions did display visible signs of UV degradation.

Optical property changes were observed for AO-shielded, UV-exposed OMC specimens. Table 2 shows pre- and postflight values for absorption and emittance properties for three different OMC materials (ref. 4). Sets of these materials were flown at both the leading and trailing edge of the satellite. The trailing edge specimens which received UV radiation only (no AO) displayed significant increases in emittance (ε). Figure 8 is a thin section photomicrograph of one of the trailing edge specimens. This section, which is illuminated by transmitted light, clearly shows some surface discoloration in the matrix resin with the fibers shielding underlying material. These findings explain the change in optical properties with no measured change in mechanical properties.

Based on LDEF results, exposure to the LEO UV environment without AO exposure does not significantly alter the functionality of graphite-reinforced OMC's. The only possible UV effects are on optical properties. However, provisions must be made for the other environments present in these locations, such as meteoroid and debris, thermal cycling, etc.

AO- and UV-Exposed Environments

The most severe combination of environmental effects for LDEF specimens existed on the leading edge or front side of the satellite. This area received all the environments discussed so far plus highly reactive AO. Figure 9 shows the predominant environments, effects, and influenced design parameters along with their relationships for AO- and UV-exposed locations. Previously discussed factors and relationships are shown in grey, with the additional factors and relationships shown in black. AO erosion was found to be the most severe of all environmental effects for OMC's.

Table 2 lists the optical properties for leading edge exposed graphite-reinforced OMC's. All specimens showed a significant increase in emittance from preflight values, most likely due to surface texturing caused by the AO erosion. Some specimens displayed a thin layer of "ash" while others did not. The C6000 graphite/ PMR-15 polyimide specimens listed in Table 2 did not have this "ash" and displayed significant increases in absorption. Further discussion on the origin of this ash is available elsewhere (refs. 1,6).

Figure 10 shows a photomicrograph of the typical level of AO erosion for leading edge exposed OMC's. The actual erosion level for various OMC specimens distributed around the front side of the satellite varied with angle of exposure to the direction of motion. Reactivity has been calculated at 0.9 to 1.2×10^{-24} cm^3/atom based on recession measurements for graphite/epoxy

specimens by a number of investigators. This resulted in a loss of up to 0.005 inches of material, the equivalent of approximately one ply of laminate.

For unidirectionally reinforced specimens, the reduction in mechanical properties was found to be proportional to the reduction in specimen cross-sectional area. Therefore, as shown in Figure 11 for the AO and UV exposed T300 graphite /934 epoxy specimens flown on M0003-8, there was little change in modulus based on postflight specimen cross-sectional area. Strength values may have been effected by AO erosion-created stress concentration sites. Although useful for determination of lamina properties, unidirectional layups are rarely used in real applications due to the highly isotropic nature of the material.

A better indication of OMC mechanical property performance in AO environments is given by the test values from nonunidirectionally reinforced specimens. The results shown for C6000 graphite/PMR 15 epoxy in Figure 11 reveal a significant drop in both strength and modulus. These reductions are based on a postflight specimen cross section indicating losses due to more than thickness reduction. The loss of a surface 0° oriented ply greatly reduces stiffness and strength properties as only a portion of the plies are in the 0° direction for typical layup. Also, for optimization of bending stiffness, 0° plies are often placed at or near the surface of a laminate. For AO-eroded specimens, this will result in greater reduction in bending stiffness and an imbalanced layup with bending-stiffness coupling during loading. These specimens also displayed minor warpage due to the erosion of the surface 0° direction ply.

In most exterior spacecraft applications which require the high stiffness and dimensional stability of graphite-reinforced OMC's, the type of environmental effect experienced by AO-exposed LDEF OMC's is clearly unacceptable. In addition, expected AO fluences for future long-term LEO missions such as Space Station *Freedom* are many times that experienced by LDEF. OMC's used in these applications will require protective coatings.

AO- and UV-Exposed OMC's with Protective Coatings

Figure 12 shows the predominant environments, effects, and influenced design parameters along with their relationships for effectively coated OMC's in AO- and UV-exposed locations. If fully effective against AO and UV attack, the influence of environmental factors on design concerns is reduced to those discussed in the previous section on AO and UV shielded OMC's.

The full impact of the LEO AO environment on organic materials became evident during early shuttle missions and LDEF integration occurred before this realization. Fortunately, a number of OMC specimens were flown on LDEF with various coatings. These coatings were primarily intended for thermal control but many of them offered excellent protection against AO erosion.

Experiment A0134 contained T300 graphite/ 934 epoxy specimens coated with a thin sputtered coating of 600 Å of SiO_2 over 1,000 Å of nickel (ref. 5). This coating was effective in preventing AO caused erosion of the composite substrate. Figure 13 shows the large 11.75- by 16.75-inch T300 graphite/ 934 epoxy specimen flown as part of M0003-8. This panel was divided into four quadrants with one quadrant uncoated and the other three quadrants coated with A-276 white polyurethane, Boeing Materials Standard (BMS) 10-60 white polyurethane, or Z-306 black polyurethane. Although some coating thickness loss was observed for the white polyurethane coatings, the TiO_2 and talc pigments and fillers accumulated on the surface, providing an effective

AO barrier. The Z-306 coating with organic carbon filler underwent AO caused degradation resulting in loss of composite material.

Figure 14 is a three-dimensional plot of the data collected during a laser profilometry raster scan of a portion of the panel shown in Figure 13. The data are plotted as a 0.0005-inch grid for the x-y plane and 0.001-inch line segments of various thicknesses for the z-direction (depth). The approximately 1-in^2 area contains a circular region shielded from AO attack by a mounting washer on the surface. An A276 white polyurethane coating covers the rear left half of the panel segment. The A276 coating was clearly effective at preventing AO erosion of the underlying OMC substrate. However, AO erosion was observed by different investigators in areas where the protective coatings had been breached by impacts or cracks.

Figure 15 shows the effectiveness of coatings possessing optimum optical properties for the minimization of thermally induced microcracking of the composite substrate. This is accomplished by passively controlling the thermal cycling extremes and thermal shock seen by the underlying composite substrate. This figure shows the postflight measured microcrack density versus thermal cycling conditions for the coated composite panel shown in Figure 13 (ref. 3). Crack density is measured from polished cross sections at $\times$ 200 magnification. Thermal cycling conditions were estimated using LDEF environmental data (ref. 6), physical and optical properties, and recorded flight data for an underlying structure. The increased crack density for the more severely cycled material is most likely due to the thermal shock as the energy input was into one side of the specimens in the form of solar exposure. No inflight measurement of dimensional stability versus microcracking data is yet available. However, the impact of microcracking on dimensionally critical spacecraft hardware has been a design issue in past experiences such as the Hubble space telescope optical truss assembly.

The significance of these findings is that microcracking was prevented by reducing the thermal cycling extremes and shock, in this case through the use of reflective optical coatings.

AO- and UV-Exposed OMC's with Breached Protective Coatings

While a number of coatings were found to be effective at preventing AO attack, micrometeoroid and debris impacts along with thermal-stress-induced cracks did expose OMC substrates allowing AO erosion. Figure 16 shows the factors and relationships for AO- and UV-exposed coated OMC's with a coating breach. Compromising the coating brings back the concerns with unprotected OMC materials in this type of environment. The level of concern is tied to the severity of expected coating removal due to impacts and/or cracking.

Figure 17 shows a cross-section photomicrograph of an LDEF A-276 coated graphite/epoxy specimen taken from a large panel with a meteoroid or debris impact. Near the sides of the photomicrograph the coating has effectively prevented AO erosion of the substrate. However, at the impact site, in addition to the impact damage, the jagged pattern of AO erosion is plainly visible on exposed OMC surfaces.

The area of the panel effected by these impacts was less than 0.01 percent, and the total volume of the OMC material effected by the impacts and erosion was less than 0.000001 percent. This suggests that OMC's can be adequately protected with coatings for many LEO applications. Straightforward design calculations, based on anticipated meteoroid and debris environments and

AO fluences combined with AO reactivity data, can be performed by the space hardware designer to determine if coated OMC's can be used.

CONCLUSIONS

The data and observations generated from LDEF organic matrix composite experiments will greatly increase the spacecraft hardware designers confidence for using these materials in LEO applications. OMC's used in high atomic-oxygen exposure environments will require protective coatings. However, LDEF results show that adequate coatings are available. OMC's used in low or zero AO-exposure environments may not require coatings or shielding based on AO erosion rates, meteoroid and debris protection, and thermal control requirements.

The main design considerations for AO exposed coated OMC's relative to the LEO environment include (1) outgassing/ microcracking-induced dimensional changes, (2) coating optical properties and AO/UV resistance, (3) impact damage and subsequent AO erosion effects on mechanical properties, and (4) contamination from outgassing. No detectable mechanical or chemical property changes have been reported for AO-shielded composites. Glass-reinforced OMC's may not require protective coatings as the surface layer of glass fibers protects underlying material. However, UV degradation is more significant with glass reinforced OMC's.

The main design considerations relative to low or zero AO-exposed uncoated OMC's relative to the LEO environment include (1) AO erosion rate (0.9 to 1.2×10^{-24} cm^3/atom for graphite/ epoxy at 60-percent fiber volume, similar for other graphite OMC's); (2) impact damage; (3) outgassing/ microcracking-induced dimensional changes; (4) AO- and UV-induced optical property changes, and (5) contamination from outgassing. Graphite-reinforced OMC's were found to have some inherent UV resistance. No bulk chemical changes have been reported for both AO- and UV-exposed, graphite-reinforced OMC's.

FUTURE WORK

The largest potential payoff for LDEF data relative to all materials may not be in directly applied design information but in verification of simulation and modeling techniques. This will allow ground-based evaluation of new materials developed since the integration of LDEF.

Future OMC materials development efforts based on LDEF results should focus on microcrack resistance, low outgassing, and AO resistance along with dimensional stability modeling. Also, increased matrix polymer AO resistance would reduce post-impact substrate erosion of coated OMC's in high AO-fluence, long-term missions.

REFERENCES

1. Tennyson, R. et al: "Preliminary Results From the LDEF UTIAS Composite Materials Experiment." First LDEF Post Retrieval Symposium, NASA CP-3134, February 1992.

2. Tennyson, R., and Manuelpillai, G.: "Analysis of LDEF Micrometeoroid/Debris Data and Damage to Composite Materials, LDEF Materials Results For Spacecraft Applications." Printed elsewhere in this publication, October 1992.

3. George, P.E., Dursch, H.W., and Hill, S.G.: "Space Environmental Effects on LDEF Composites: A Leading Edge Coated Graphite Epoxy Panel." Second LDEF Post Retrieval Symposium, NASA CP-3194, June 1992.

4. George, P.E., and Hill, S.G.: "Results from Analysis of Boeing Composite Specimens Flown on LDEF Experiment M0003-8." First LDEF Post Retrieval Symposium, NASA CP-3134, February 1992.

5. Slemp, W. S. et al.: "Effects of LDEF Flight Exposure on Selected Polymer Matrix Composite Materials." First LDEF Post Retrieval Symposium, NASA CP-3134, February 1992.

6. Bourassa, R.J., and Gillis, J.R.: "Solar Exposure of LDEF Experiment Trays." NASA Contractor Report No. 189554, February 1992.

Table 1. Organic matrix composites flown on LDEF.

ROW #	ANGLE OFF RAM	AO FLUX x10^21a/sq.cm.	UV ESHx10^3	EXP. NUMBER	PRINCIPAL INVESTIGATOR	MATERIALS
9	8°	8.32	11.1	A0134	Wayne Slemp - NASA La RC (804) 864-1334	5208/T300,934/T300,P1700/C6000,P1700/C3000 930/GY70
				M0003-9	Brian Petrie - Lockeed (408) 742-8244	CE-339/GY70, F263/T50, 934/T50, X904B/T50 E788/T50, 3501-5A/HMS, E788/C6000 934/HMF176, CE-339/E-Glass,F593/P75,934/P75
				M0003-8	Pete George - Boeing (206) 234-2679	934/T300, P1700/T300, PMR15/C6000
10	22°	7.78	10.7	A0054	TRW	Epoxy/Fiberglass
8	-38°	6.63	9.4	A0171	Ann Whitaker - NASA MSFC (205) 544-2510	934/HMS, 934/P75S, P1700/HMF, Epoxy/ S-Glass
				MOOO3-10 **	Brian Petrie - Lockeed (408) 742-8244	X904B/GY70, 3501-5A/HMS, X904B/E-Glass
				MOOO3-10 **	Thomas Cookson - General Dynamics (619)547-5081	X-30/GY70*,CE-339/GY70, CE-339/P75S 934/P75S, 934/GY70, P1700/W722*, V378A/T300
				M0003-10 **	Charles Smith - McDonnell Douglas (714) 896-4015	5208/T300*, P1700/T300*, PES/T300* Polyimide/C6000*
				M0003-10 **	Pete George - Boeing (206) 234-2679	934/T300, 3501-6/AS, P1700/T300, PMR15/C6000 LARC 160/Graphite
7	-68°	3.16	7.2	A0175	Dick Vyhnal - Rockwell (918) 835-3111 x2252	F178/T300, PMR15/C6000
12	82°	1.2	6.9	A0180	Rod Tennyson - U of Toronto (416) 667-7710	934/T300, 5208/T300, SP288T300 SP328 Kevlar/Epoxy, SP290 Boron/Epoxy
				A0019	David Felbeck - U of Mich. (313) 994-6662	5208/T300 interleafed w/ Kapton
1	112°	0.06	7.5	A0175	Dick Vyhnal - Rockwell (918) 835-3111 x2252	934/T300, LARC 160/C6000
5	-128°	0	8.2	P0005	Dean Lester - Morton Thiokol (801) 863-6809	carbon/carbon, Epoxy/graphite, Epoxy/Kevlar Epoxy/Glass (all mounted internally)
4	-158°	0	10.4	A0054	TRW	Epoxy/Fiberglass
				M0003-10	(See Row 8 List for M0003-10)	
3	172°	0	11.1	MOO03-9	(See Row 9 List for M0003-9)	
				M0003-8	(See Row 9 List for M0003-8)	
				A0138	Heinrich Jabs - Matra Espace France (33)-1-61-39-72-73	934/GY70,V-108/Kevlar, V108/T300, V108/GY70 V108/G837

* Some specimens flown with protective coating

** Part of Advanced Composites experimet integrated by Aerospace corp. Gary Steckel (213) 336-7116

Table 2. Typical optical property changes for UV-exposed LDEF graphite-reinforced OMC's.

Material	Property	Preflight values	Postflight values Exposed side	
			Trailing	Leading
934 Epoxy/	α =	0.90	0.87	0.93
T300 Graphite	ε =	0.73	0.82	0.93
P1700 Polysulfone/	α =	0.90	0.88	0.93
T300 Graphite	ε =	0.73	0.82	0.93
PMR-15 Polyimide/	α =	0.90	0.90	0.98
C6000 Graphite	ε =	0.73	0.79	0.93

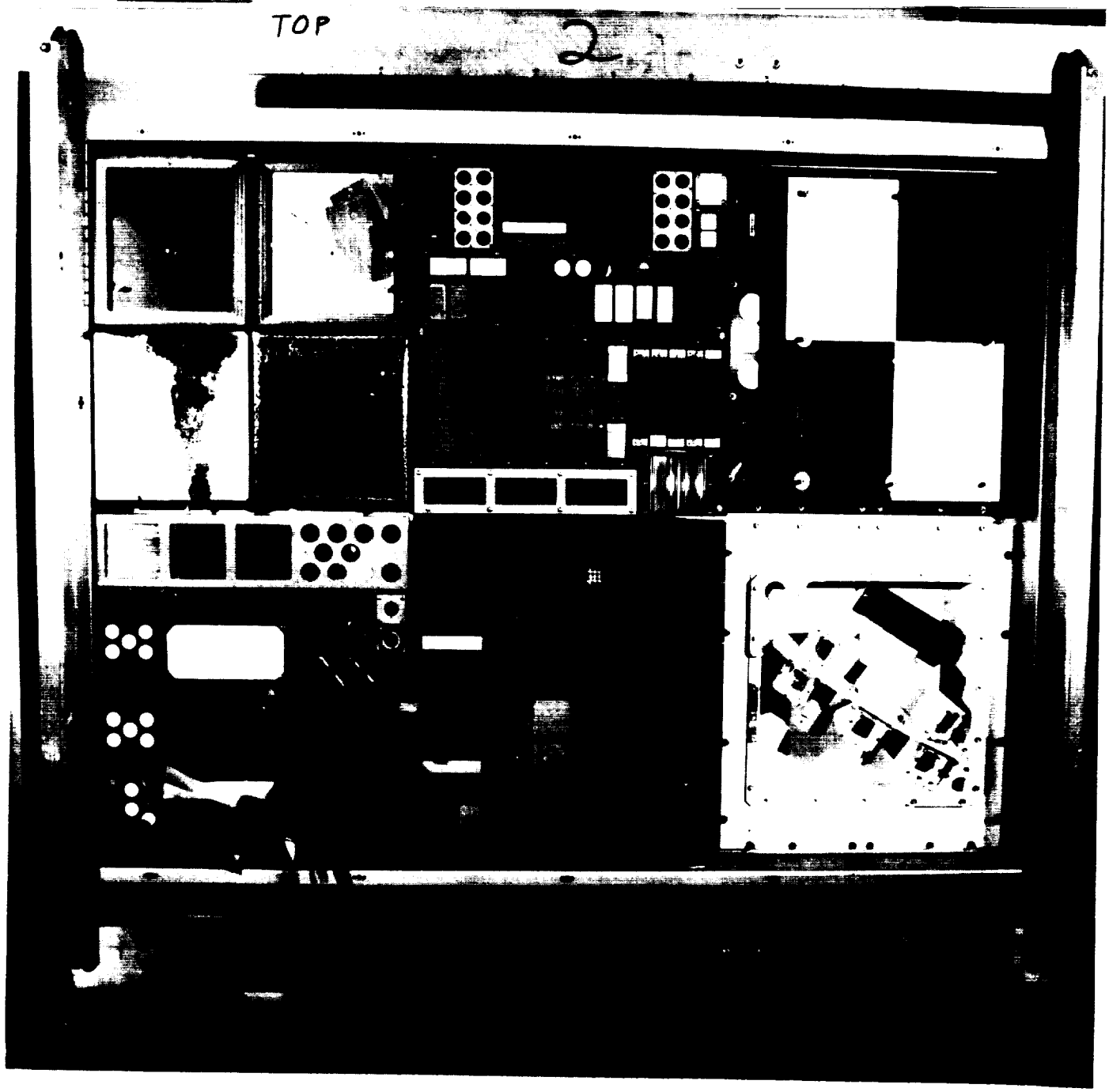

Figure 1. Postflight photograph of experiment M0003 taken by NASA photographers at Kennedy Space Center.

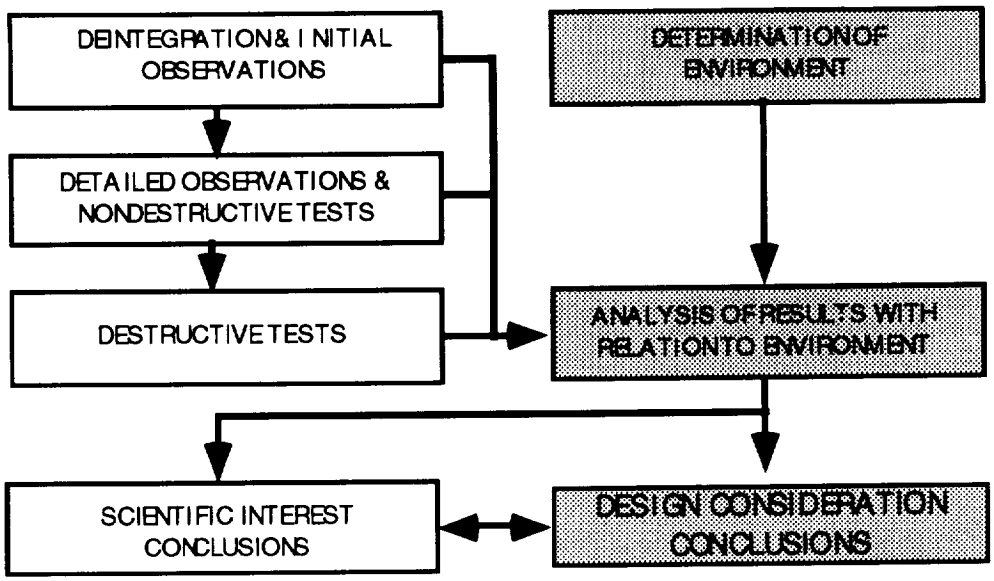

Figure 2. Flow of LDEF materials experiment investigation process.

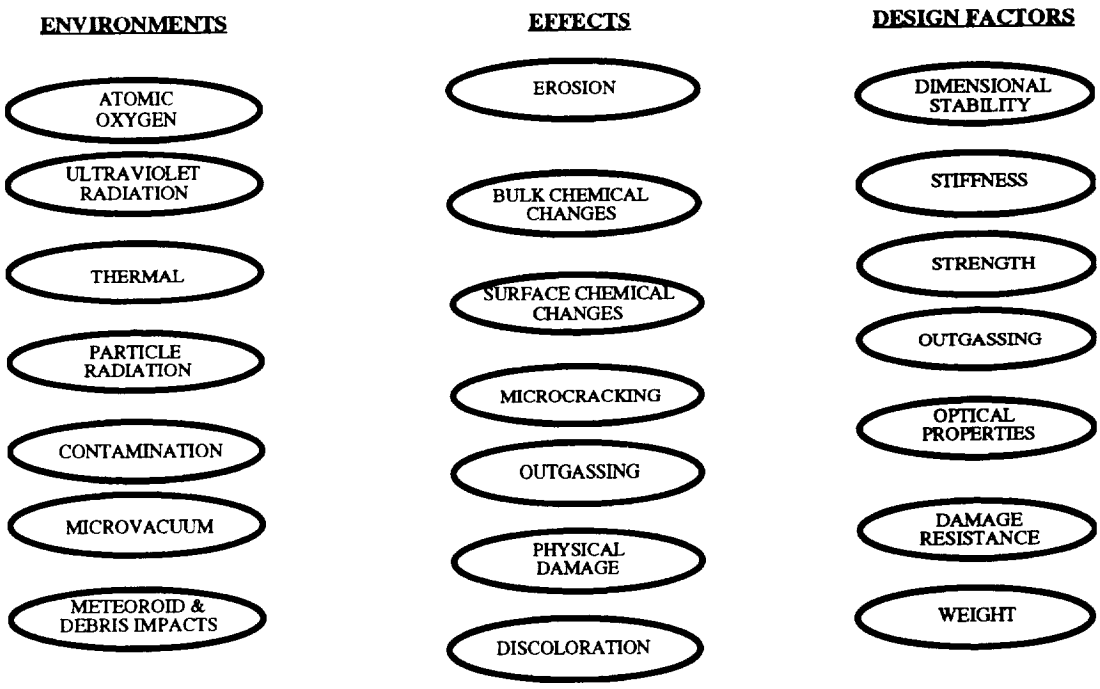

Figure 3. Environments, effects, and design factors for organic matrix composite materials in LEO applications.

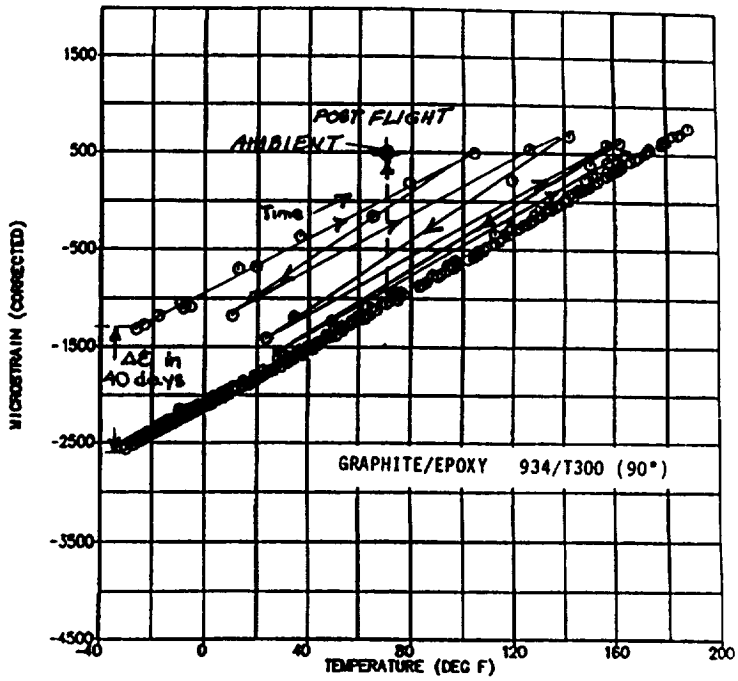

Figure 4. Effects of outgassing and thermal cycling on dimensional stability for an LDEF graphite-reinforced OMC.

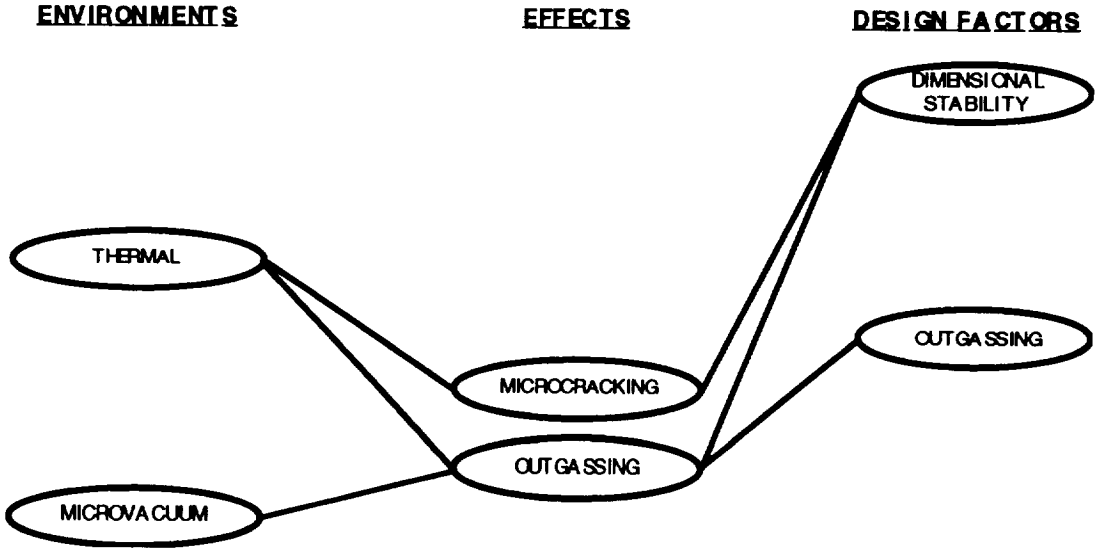

Figure 5. Environmental design factors and relationships for AO- and UV-shielded OMC's in LEO.

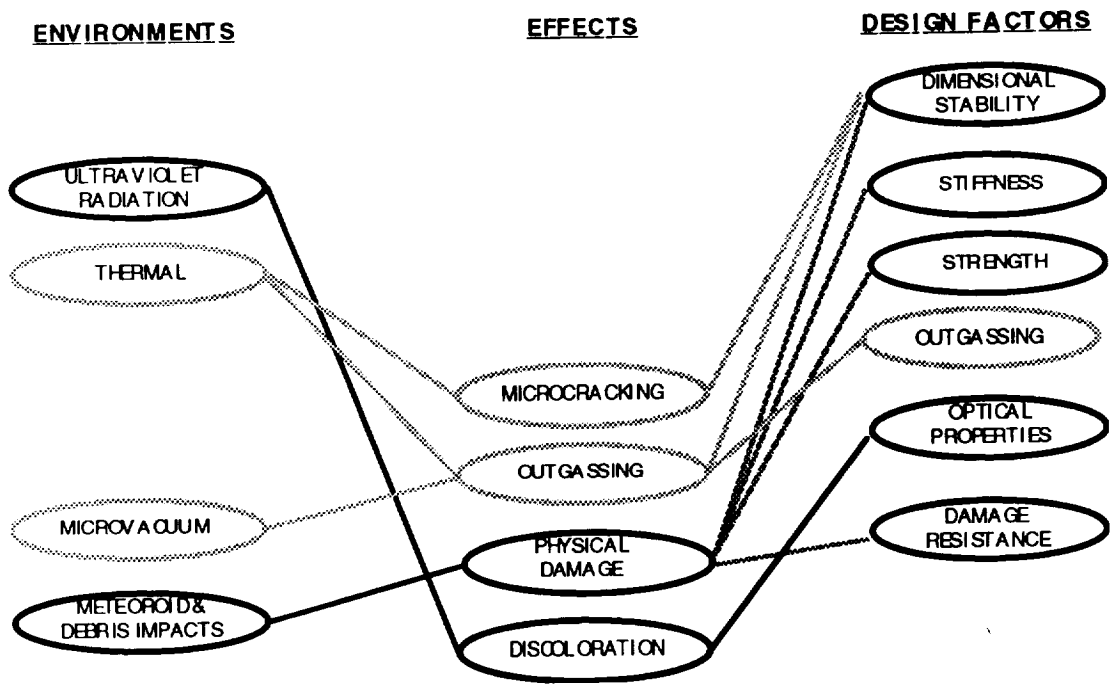

Figure 6. Environmental design factors and relationships for AO-shielded and UV-exposed OMC's in LEO.

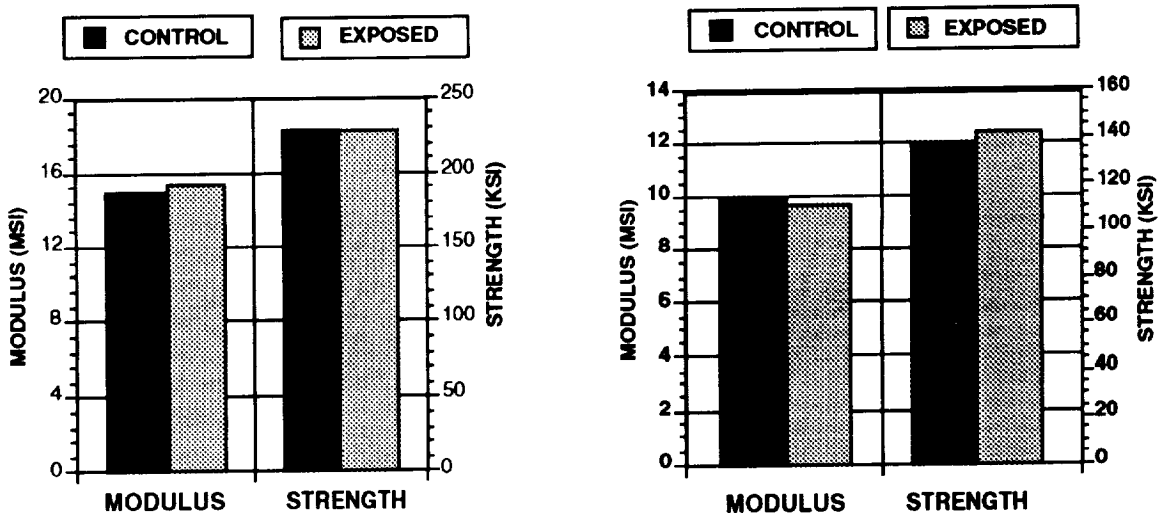

Figure 7. Typical flexural mechanical property changes for AO-shielded, UV-exposed LDEF graphite-reinforced OMC's.

Figure 8. Cross-sectional photomicrograph of UV-exposed LDEF graphite-reinforced OMC showing limited UV degradation.

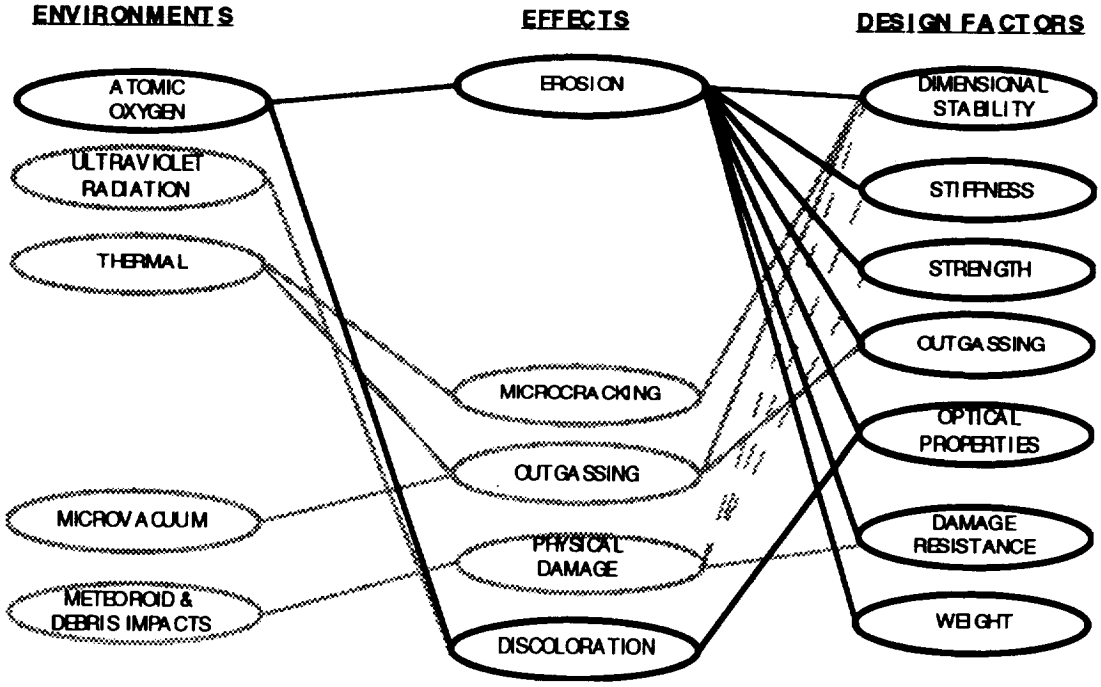

Figure 9. Environmental design factors and relationships for AO- and UV-exposed OMC's in LEO.

Figure 10. Cross-sectional photomicrograph of UV-exposed LDEF graphite-reinforced OMC showing AO erosion.

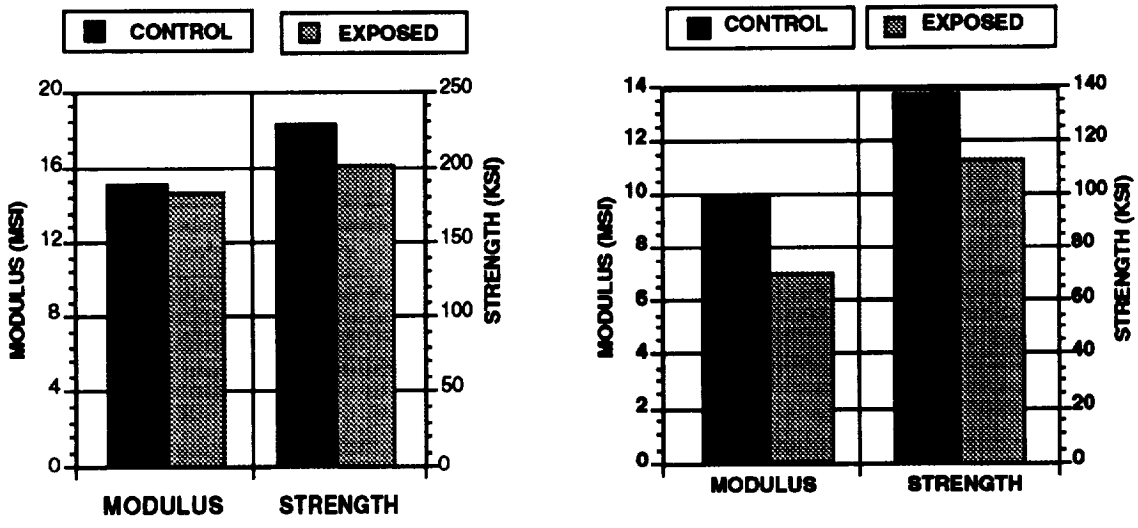

Figure 11. Typical flexural mechanical property changes for AO- and UV-exposed LDEF graphite-reinforced OMC's.

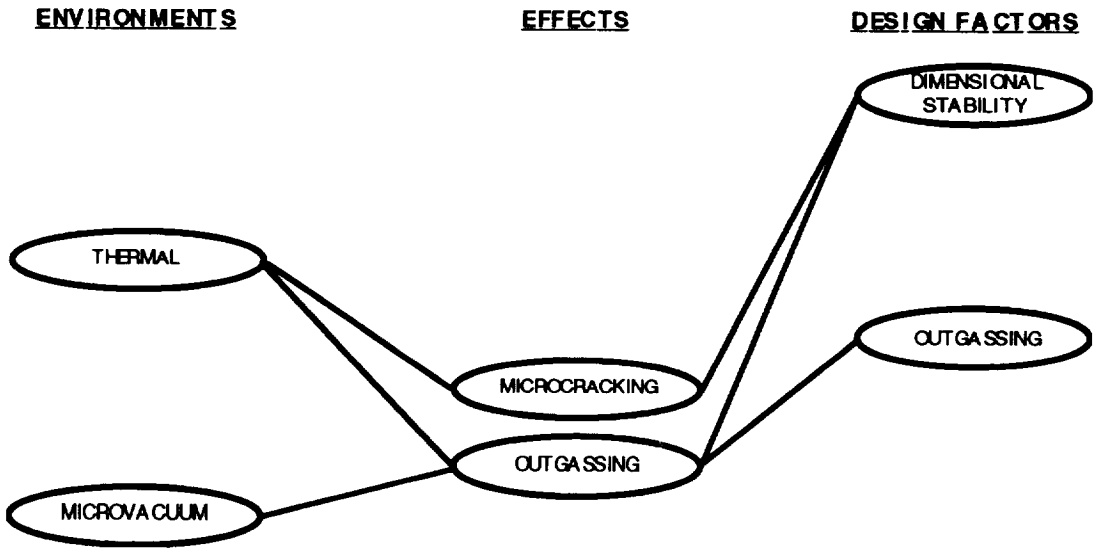

Figure 12. Environmental design factors and relationships for AO- and UV-exposed OMC's with protective coatings in LEO.

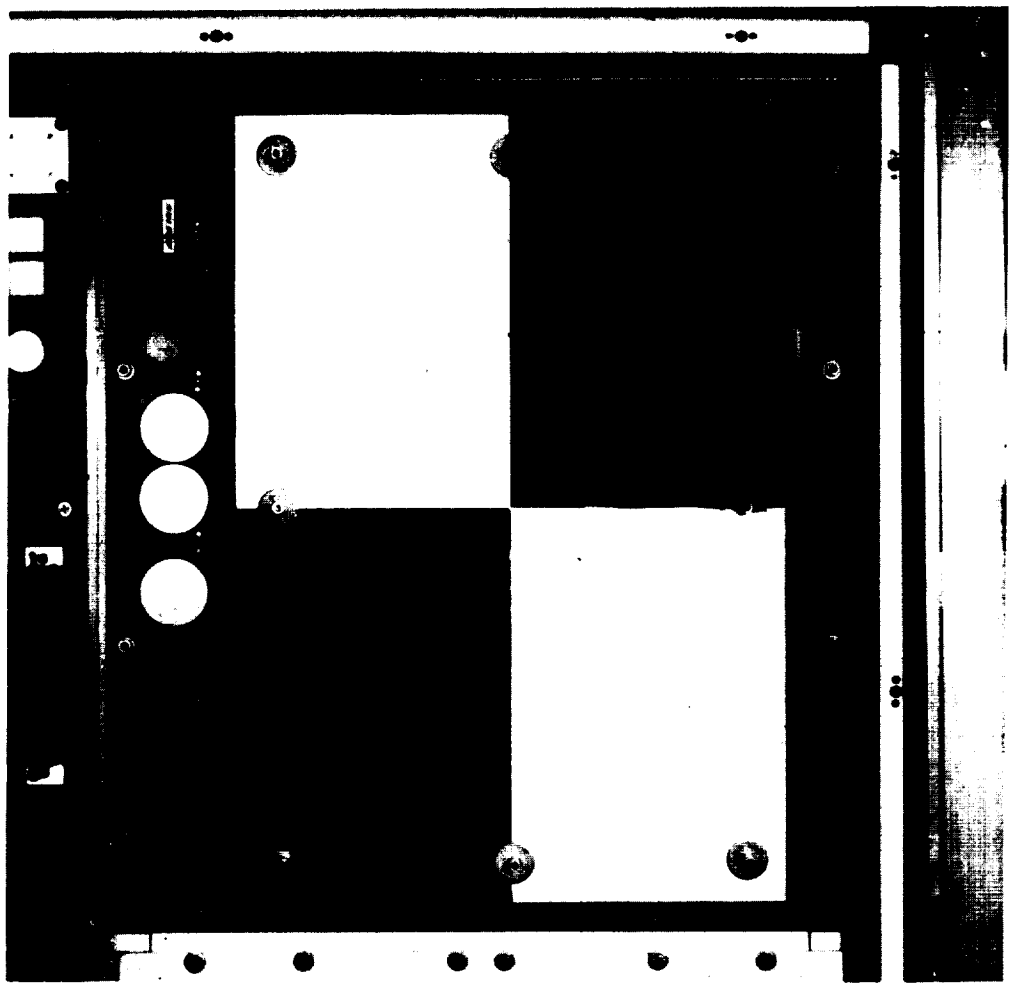

Figure 13. Coated T300 graphite/934 epoxy composite panel.

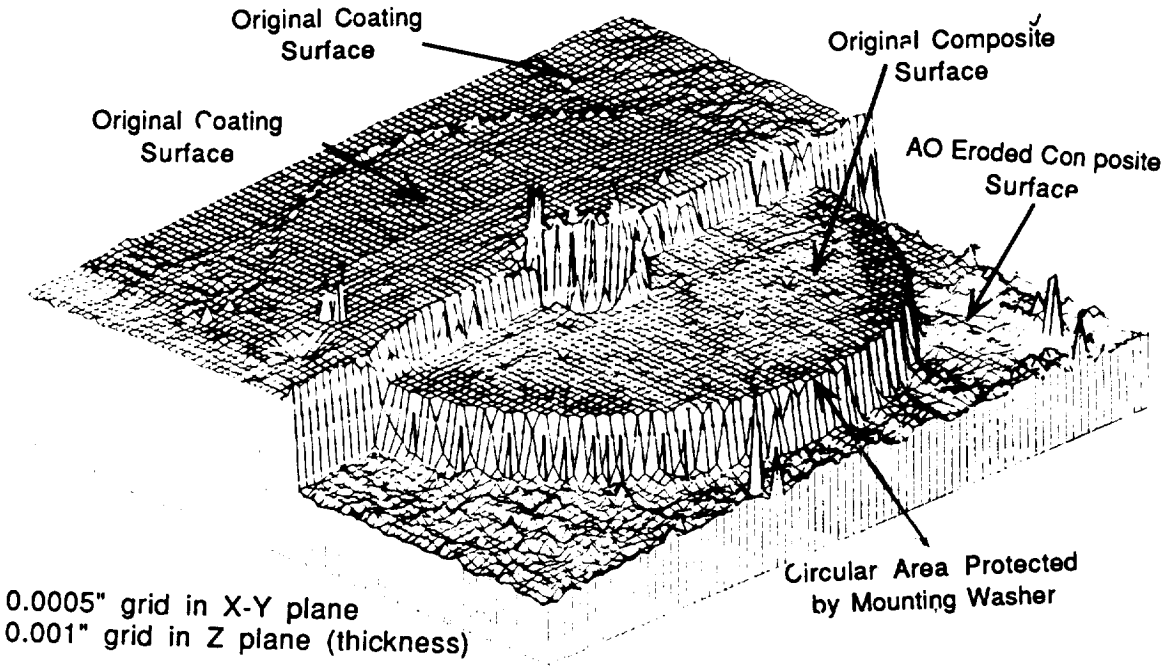

Figure 14. Three-dimensional plot of profilometry measurements taken from a partially coated graphite-reinforced OMC.

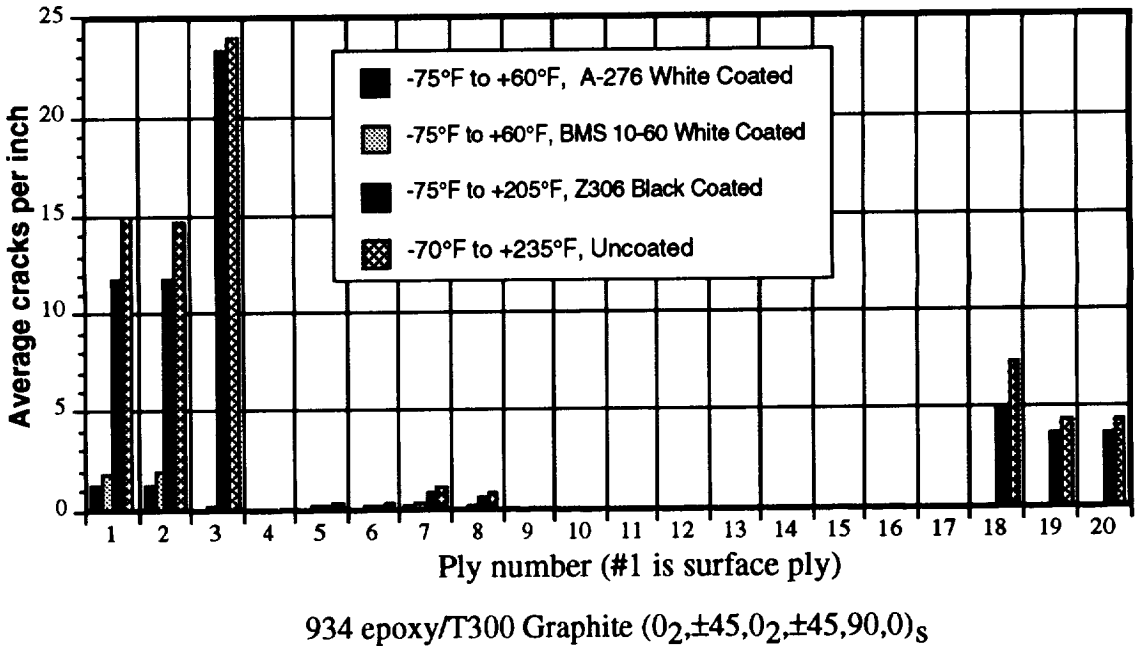

Figure 15. Microcrack density and distribution in an LDEF OMC for various thermal environments.

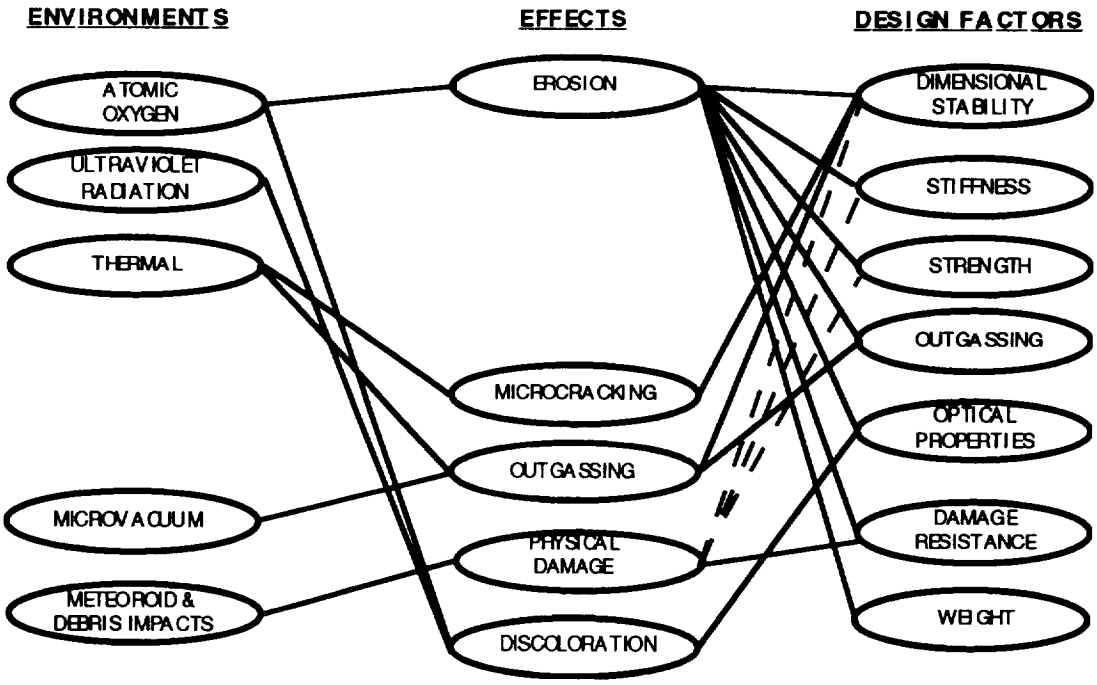

Figure 16. Environmental design factors and relationships for AO- and UV-exposed coated OMC's in LEO with protective coating breach.

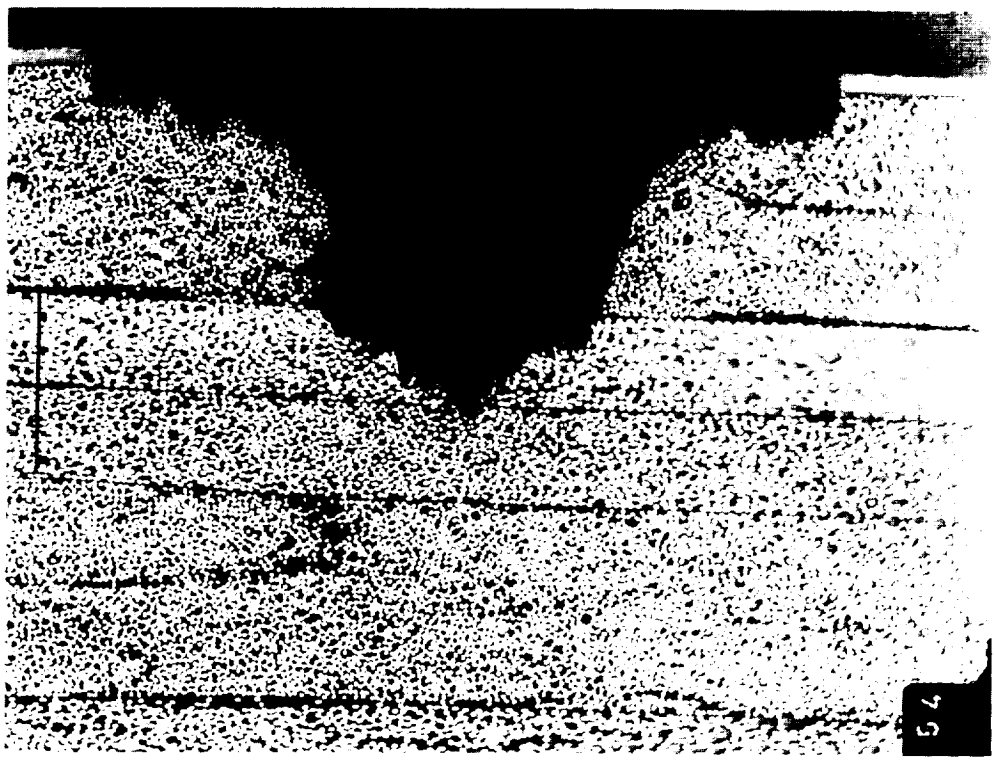

Figure 17. Cross-sectional photomicrograph of coated graphite-reinforced OMC showing impact damage and post-impact AO erosion.

SUMMARY OF MATERIALS AND HARDWARE PERFORMANCE ON LDEF*

Harry Dursch
Dr. Gary Pippin
Boeing Defense & Space Group
Seattle, WA 98124
Phone: 206/773-0527, Fax 206/773-4946

Lou Teichman
NASA Langley Research Center
Hampton, VA 23665

ABSTRACT

A wide variety of materials and experiment support hardware were flown on the Long Duration Exposure Facility (LDEF). Postflight testing has determined the effects of the almost 6 years of low-Earth orbit (LEO) exposure on this hardware, and this paper is an overview of the results. Hardware discussed includes adhesives, fasteners, lubricants, data storage systems, solar cells, seals, and the LDEF structure. Lessons learned from the testing and analysis of LDEF hardware will also be presented.

INTRODUCTION

The extended duration of the LDEF mission presented a unique opportunity to learn more about the effects of long-term exposure to LEO on both materials and systems. Hardware discussed in this paper ranges from the Velcro™ used to fasten thermal blankets to the LDEF structure, to solar arrays used to actively charge a nickel-cadmium (NiCd) battery used to power a heat pipe experiment, to the LDEF structure itself. Testing results were assembled from the following sources: individual experimenters; the Materials, Systems, Induced Radiation, and Meteoroid and Debris Special Investigation Groups (SIG); the LDEF Science Office; the Boeing Material SIG and the Boeing Systems SIG Support Contracts; and from the hardware flown on the Boeing LDEF experiment and then tested at Boeing.

The discussion of these material and hardware investigations is divided into the four major engineering disciplines represented by the LDEF hardware: electrical, mechanical, thermal, and optical systems. Within each discipline there will be a brief description of the hardware, followed by an overview of the pertinent testing and analysis results and lessons learned. Because of the number of papers already presented that discuss findings within the optics and thermal disciplines, this paper focuses on mechanical and electrical hardware.

A detailed discussion of LDEF, its mission, and the environment seen by LDEF during its 69-month mission is presented in reference 1.

* All Boeing activities were supported by NASA Langley Research Center contracts NAS1-18224 and NAS1-19247.

MECHANICAL HARDWARE

This section discusses the effects of the 69-month LEO exposure on the LDEF primary structure, grapples, viscous damper, fasteners, adhesives, lubricants, seals, and composites.

Primary Structure

The LDEF primary structure is a framework constructed of welded and bolted aluminum 6061-T6 rings, longerons, and intercostals. The structure is approximately 30-ft long and 14 ft in diameter. A fusion welding process developed by NASA Langley Research Center (LaRC) for 6061 aluminum was used to fabricate the center ring. The remainder of the structure was mechanically fastened together. Figure 1 is a preflight photo of the structure prior to installation of experiments.

The welds were inspected postflight by dye penetrant and eddy current techniques following deintegration of the experiment trays. The welds were found to be nominal, with no evidence of any launch or flight-related degradation.

The potential for space exposure effects on the microstructural or mechanical properties of the aluminum primary structure was investigated by metallurgical analysis of the 6061-T6 aluminum experiment tray clamps. The tray clamps are representative of the primary structure (same aluminum alloy) and were distributed uniformly around the exterior of LDEF. Clamps from near leading edge (LE) and near trailing edge (TE) were cross sectioned and examined. The microstructures were found to be normal for 6061-T6 aluminum. *The lack of any differences between the samples and control specimens illustrates that LEO space exposure has no discernible effect on the bulk microstructures of typical structural metals.* Mechanical property changes are precluded in the absence of microstructural changes.

Primary Structure Fasteners

Following removal of the experiments, all primary structure fastener assemblies were retorqued to preflight values. The fastener assemblies consist of stainless steel bolts ranging in diameter from 1/4 to 7/8 inch with silver-plated locking nuts. Results showed that only 4 percent of the 2,928 assemblies had relaxed. Nut rotations, required to reestablish preflight torque levels for those that relaxed, ranged from 5° to 120°. The small number of relaxed fastener assemblies indicates that the reliability of bolted joints in space applications is very high. This conclusion must be tempered by the fact that LDEF was exposed to a rather benign thermal environment with minimal thermal swings. *Examination of the primary structure, the welds, and fasteners shows that the concept of a reusable bolted and welded spacecraft is a viable concept.*

Viscous Damper

Located on the center line of the space-end internal structure, the viscous damper provided attitude stabilization of LDEF from oscillations resulting from deployment. Postflight testing indicated that the damper performed flawlessly over the almost 6-year flight, even though the design life

was 1 year. It was concluded that the damper suffered no discernible degradation from long-duration space exposure and that it can be flown again. The damper has been returned to NASA LaRC in a flight-ready condition.

Grapples

Both the rigidize-sensing (active) and the flight-releasable (passive) grapple fixtures have undergone postflight evaluation. The rigidize-sensing grapple was designed to activate the LDEF experiment initiate system (EIS) on or off via the remote manipulator system (RMS) with the LDEF still in the shuttle bay. The flight-releasable grapple was used to deploy and retrieve LDEF via the RMS. Both grapples performed as designed during deployment, and the passive grapple performed as designed during the retrieval of LDEF. Due to the extended mission length and consequent uncertain state of batteries, and the desire not to disturb the final state of certain experiments, it was decided not to reset the systems. Therefore, the rigidize-sensing grapple was not used during retrieval. Postflight testing of grapple components has shown nominal performance. However, postflight functional testing has yet to be performed.

Fasteners—Tray Clamp Fasteners

The experiment trays were held in the structure openings in the primary structure by aluminum clamps. The clamps consisted of flat 0.25-in thick rectangular or "L" shaped plates with three mounting holes in them. They were attached to the structure with 0.25-28 A286 heat-resistant steel bolts. The bolts, with alodined aluminum washers under the head, were inserted into self-locking thread inserts installed in the primary structure. The bolts were cleaned with alcohol and installed with a preflight torque of 75 ±5 in-lb.

During deintegration of LDEF, unseating (breakaway) torque values were recorded for all 2,232 tray clamp fasteners, and prevailing (running) torque values were obtained for every third bolt (the middle of the three bolts in each clamp). The unseating torques averaged 72 in-lb, ranged between 10 and 205 in-lb, and the average values were similar throughout LDEF, indicating no pronounced effect of varying space exposure conditions on bolt torque behavior. The prevailing torques averaged 17 in-lb and ranged between 2 and 132 in-lb. Prevailing torque specifications for these threaded inserts called for torques ≤30 in-lb. Almost 10 percent of the 720 prevailing torques exceeded these specification.

The range in unseating torques is not surprising considering the unpredictable nature of fatigue, bolt stretching, corrosion, and particulate contamination. However, the amount of bolts exceeding the prevailing torque specifications was unexpected. Further testing and analysis was performed to determine why. Several causes were found, such as bolt shank contact with the clamp and shim holes during removal and the relative softness of these bolts. No clear correlation was made between thread condition, washer condition, and unseating torques. *No evidence of cold welding was observed.* All thread damage was consistent with galling damage.

Fasteners—Experimenter Fasteners

The LDEF Science Office suggested that experimenters use type 303 stainless steel bolts combined with self-locking nuts (AN, MS types). In fact, a wide variety of fastener assemblies and lubrication schemes were used. The following paragraph highlights some of the fastener removal difficulties encountered by experimenters during postflight hardware removal.

The most extensive fastener damage is shown in Figure 2. This photo shows both a sheared fastener and a severely damaged nut plate. It was reported that the majority of nut plates had the original MoS_2 dry-film lubricant removed by acid stripping prior to installation because of concerns with possible volatilization and contamination while in orbit. The MoS_2 was then replaced with cetyl alcohol. Initial speculation was that the A286 fasteners may have cold welded on orbit because of insufficient lubrication provided by the cetyl alcohol. However, testing and analysis of the fastener assemblies has shown that all removal difficulties were caused by galling (from lack of MoS_2) which had begun during installation.

Fasteners—Velcro™

Velcro™ was used to attach a variety of thermal blankets used on LDEF. In one instance, Velcro™ was stitched to the blankets with NOMEX thread. This thread, which was directly exposed to ultraviolet (UV), turned yellow. Tensile testing of the thread showed a 10-percent reduction. The mating side of the Velcro™ was successfully bonded to the tray structure using 3M's EC2216 adhesive. Qualitative tests carried out during disassembly showed a high level of separation resistance. On another experiment, the Dacron™ thread used to stitch the Velcro™ to thermal blankets failed.

Velcro™ was also used to fasten the 3- by 4-ft silverized Teflon™ thermal blankets used on 16 exterior surfaces throughout LDEF. Approximately 54 one-inch strips of Velcro™ were used for each thermal blanket. One surface of the Velcro™ was bonded to the backside of the blanket, and the other surface was bonded to aluminum surfaces on the tray. The experimenter responsible for the experiment deintegration reported that the Velcro™ retained its preflight disassembly parameters.

Velcro™ proved to be an excellent form of fastening low stressed hardware in space. However, it is critical to keep the adhesive or threads used to fasten the Velcro™ shielded from the LEO environment.

Adhesives

A variety of adhesives and adhesive-like materials were flown on LDEF. These included epoxies, silicones, conformal coatings, potting compounds, and several tapes and transfer films. Six different adhesive systems were evaluated using lap shear specimens exposed to leading and TE environments. All other adhesives were used in assembly of various experiments. Typically, these materials were shielded from exposure to the external spacecraft environment. *In most experiments, these adhesives were of secondary interest and were only investigated by visual examination and a "Did failure occur?" criteria. These adhesives performed as expected, holding the hardware*

together. Several experimenters noted that the adhesives had darkened in areas that were exposed to UV. The following paragraphs document the results from testing epoxy lap shear specimens.

3M's EC 2216 (Boeing Materials Standard 5-92) along with 3M's AF 143 (BMS 5-104) epoxy adhesive lap shear specimens were flown on the TE. The EC 2216 is a room-temperature cure and the AF 143 is a 350F cure system. Both titanium-composite and composite-composite adherents were evaluated. The lap shear specimens were mounted such that one surface was exposed to the exterior environment. Visual examination of the specimens showed the exposed bondline to have become dark brown when compared to the shielded bondline on the backside of the specimens. Five specimens for each of the two epoxy systems were flown. The ultimate shear stress increased from 7 to 28 percent over preflight values. No control specimens were tested. The reason for the increase in strength compared to preflight values is speculated to be related to continued cure advancement.

Two separate experiments evaluated a third epoxy system, Hysol EA 9628 250F cure, using composite-composite and aluminum-aluminum adherents, respectively. A total of seven specimens were located on the LE with four shielded specimens located on the backside of the tray acting as in-flight controls. A similar arrangement was flown on the TE for a total of 22 specimens. In addition, eight ground control specimens existed. Postflight testing showed both the LE and TE in-flight control and the ground control specimens to possess equivalent shear values. However, the LE exposed specimens had decreased an average of 8 percent and the TE exposed specimens had a 28-percent decrease in shear when compared to the controls. These results were identical for both the composite and aluminum specimens. The reason for the decreases is unknown as the vast majority of the adhesive is between the adherents mating surfaces and, therefore, shielded from the detrimental effects of the atomic oxygen (AO) and UV. The only two LEO environments that could affect the adhesive strength are radiation and thermal cycling. While the temperature extremes seen by the exposed specimens were greater than the in-flight controls, the actual temperatures were well within the adhesive specifications. Also, the charged particle radiation environment seen by LDEF was minimal. While almost all other adhesives and tapes flown on LDEF showed no degradation and, in a significant number of cases, actually increased in mechanical properties, it is currently unknown why these particular adhesive shear properties degraded and why the TE specimens showed a much greater decrease than the LE specimens.

Lubricants

A variety of lubricants and greases were flown on LDEF. With the exception of three lubricants, all were components of functioning hardware and not the principal item of the investigation. The current status and test results of all lubricants flown on LDEF are listed in Figure 3. *The majority of the lubricants were shielded from direct exposure to space and performed their design function as anticipated.*

Seals

A variety of seals were also used on LDEF. These were generally O-rings, although sheet rubber was also used. All seals were shielded from direct exposure to the exterior environment. *These materials performed as designed, sustaining little or no degradation caused by exposure to the LEO environment.*

Composites

The most significant findings for fiber-reinforced organic composites were AO erosion and dimensional changes. Composites directly exposed to the LE environment exhibited erosion of up to one ply of material along with reduction of mechanical properties. *The following thin protective coatings were successfully used to prevent this erosion: 1,000 Å of sputtered nickel with a 600 Å sputtered SiO_2 overcoat; two white polyurethane coatings, BMS 10-60 and A276; and a carbon black polyurethane coating, Z306.* Composites located on the TE and on the LDEF's interior exhibited no erosion and did not display any reduction in mechanical properties. Chemical changes to composite systems were only a few microns deep on composites mounted on exterior surfaces and had no impact on the bulk performance properties of the materials. Microcracking has been reported for several nonunidirectional reinforced polymer matrix composites on both the leading and TE's.

ELECTRICAL HARDWARE

LDEF also carried a variety of electrical and electronic systems which were the result of the diversity in experiments. NASA provided certain guidelines and design review requirements, but responsibility for success (or failure) rested solely with the experimenters. The authors know of no LDEF components that were "space rated," i.e., they had not been subjected to the rigorous testing and inspections normally required of spacecraft system components (e.g., MIL-STD-883, Class S). Some were off-the-shelf, commercial quality parts, while most were MIL-STD-883, Class B or equivalent. LDEF provided a unique opportunity for evaluation of such components.

On-Orbit Data Storage Systems

LDEF was a passive satellite with no telemetry of data to Earth during the mission. However, several experiments required on-orbit collection of data. Seven Experiment Power and Data Systems (EPDS's) were supplied by NASA, and two other experiments used data storage systems of their own design and construction. All EPDS units were similar, consisting of a Data Processor and Control Assembly (DPCA), a tape recorder (the Magnetic Tape Module (MTM)), and two lithium sulfur dioxide ($LiSO_2$) batteries, all of which were attached to a mounting plate designed to fit into the backside of the experiment tray. The EPDS components were not directly exposed to the exterior environment, being protected by their mounting plate and by external thermal shields. Although simple compared with today's data systems, the EPDS contained many elements common to most such systems, including various control and "handshake" lines, programmable data formats and timing, and a data storage system. EPDS electronic components were procured to MIL-SPEC-883, Class B standards, and were not rescreened prior to installation. Data analysis and postflight functional testing showed that all EPDS functioned normally during and after the LDEF flight.

During postflight inspections, it was noted that the magnetic tape on all but one MTM unit had taken a "set" where it was wrapped around the phenolic capstan. The exception was the single unit which had operated periodically throughout the flight (experiment S0014). The MTM's were backfilled with dry nitrogen prior to flight. During postflight deintegration at Lockheed, the tapes were exposed to a controlled humidity, and the mechanical set gradually disappeared. Evidently

some level of humidity is necessary in the sealed units to avoid this problem under long-term, inactive storage. Interestingly, it has been reported that a different type of tape (a ruggedized cassette) used in experiment A0180 did not encounter this problem even though it too had been backfilled with dry nitrogen. It has been speculated that outgassing of some other material in that tape recorder housing prevented excessive drying of the tape (ref. 2).

The University of Toronto used a custom-designed and built data storage system also based on the magnetic tape cassette concept. This unit performed as designed. *All magnetic tape cassette recorders worked well. They are simple, well proven, and reliable.*

The remaining data storage system was based on semiconductor technology using an Electrically Alterable Read Only Memory (EAROM)-based storage system. During postflight inspection, it was determined that on-orbit data did not exist. The resulting failure analysis showed that data had been stored on the EAROM at one time, but failed to identify the cause of data loss. However, this particular EAROM is thought to be radiation sensitive.

Solar Cells

Nine experiments involved solar cells, solar cell components, and/or solar array materials. The complexity of the experiments ranged from active on-orbit monitoring of solar cells, to recharging a NiCd battery used to power a heat pipe experiment, to passive exposure of cells and solar array materials. A total of over 350 cells representative of the late 1970's and early 1980's technology were flown. Eleven of these cells were gallium-arsenide and the remaining cells were silicon. A majority of these were actively monitored while on orbit. The following four major LEO environments, operating individually or synergistically, caused the vast majority of performance losses seen in the solar cells: meteoroid and debris impacts, AO, UV, and charged particle radiation.

The most extensive electrical degradation of the cells was caused by impacts and the resulting cratering. The extent of damage to the solar cells was largely dependent upon the size and energy of the impactors. Figure 4 shows the postflight current-voltage (IV) curves for three impacted cells (ref. 3). The first cell, M-3, has a small impact crater in the coverglass, but not penetrating the cell itself. From the curve, it is apparent that there is little change. The second cell, NA-9, has a large (about 1.8-mm diameter) impact crater which penetrated into the silicon cell. The cell was apparently shunted by this damage, resulting in a decrease in a open-circuit voltage (Voc) of approximately 100 mV. The third cell, M-9, has an impact crater in the coverglass which cracked the coverglass and the cell. The cell crack does not go all the way across the cell, but the resulting discontinuity in many of the current collection busbars on the front has caused an increase in series resistance and a drop in fill factor. The fill factor is a measure of how close to ideal (100 percent) the cell is performing. It is the ratio of the product of max-power-current and max-power-voltage divided by the product of short-circuit-current and open-circuit-voltage $(Imp \times Vmp)/(Isc \times Voc)$.

The other cause of cell degradation was reduced light reaching the cells. This was caused by contamination, UV degradation of the coverglass adhesive, and/or AO/UV degradation of the antireflection coating.

A variety of changes were reported by the various experimenters including silver oxidation on grid lines, some broken silver interconnects, and voltage and current drops. However, the fill factors were approximately the same as preflight and there was no delamination or loss of covers.

In general, the solar cells flown on LDEF proved to be robust. There were no significant changes in the performances of solar cells that had not undergone micrometeoroid or space debris impacts. Solar array designers need to account for individual cell loss caused by impacts. Results from some low-cost solar array materials such as silicone, Teflon™, and polyimide indicated that these materials will require additional research before full-scale replacement of the conventional encapsulants (fused silica coverglass and Dow Corning DC 93500 adhesive) is justified.

Wire Harnesses

The LDEF wire harness was essential to the success of all active experiments, as it carried the experiment initiate signals. It was assembled in-place on the LDEF frame, using Teflon™ insulated wire and nylon cable ties. Much of the harness also was protected by shielded braid and an outer Teflon™ jacket. The majority of the harness was well shielded from direct exposure to the external environment. Extensive testing included in-place visual inspection, connector disconnect torques, continuity measurements, and 500 Vdc insulation resistance. *All tests were nominal. There were no reported instances of experimenter-provided harnessing exhibiting deterioration of electrical properties.*

Batteries

Three different types of batteries were used on LDEF: $LiSO_2$, lithium carbon monofluoride (LiCF), and NiCd batteries. NASA provided a total of 92 $LiSO_2$ batteries that were used to power all but three of the active experiments. Ten LiCF batteries were used by the two active NASA Marshall Space Flight Center (MSFC) experiments. One NiCd battery, continuously charged by a four-array panel of solar cells, was used to power an active experiment from NASA Goddard Space Flight Center. A loss of overcharge protection resulted in the development of internal pressures which caused bulging of the NiCd cell cases. However, postflight testing showed that the battery still had the capability to provide output current in excess of the cell manufacturer's rated capacity of 12.0 ampere-hours. All the LiCF and $LiSO_2$ batteries met or exceeded expected lifetimes.

Relays

Electrical/mechanical relays continue to be a design concern. Two of the most significant LDEF active system failures involved relay failures. The Interstellar Gas Experiment was one of the more complex experiments on LDEF, with seven "cameras" located on four trays. Each camera contained five copper-beryllium foil platens, which were to sequentially rotate out of their exposed position at predetermined intervals. This experiment was never initiated due to a failure of the experiment's master initiate relay. The Thermal Control Surfaces Experiment recorded on-orbit optical properties of various thermal control coatings using a four-track MTM (the other six MTM's were two track). The latching relay which switched track sets failed to operate when switching from track 3 to track 4. Consequently, portions of the early flight data on track 1 were overwritten and lost.

Electronic Support Hardware

Most of the electronics carried on LDEF were used to support active experiments, rather than being flown as part of an experiment. An exception was the Boeing Electronics Experiment, which was an investigation of the effects of LEO on inexpensive, commercial quality components. These included a number of plastic packaged integrated circuits and discrete components such as transistors, resistors, capacitors, and diodes. A total of over 400 components were mounted on a pair of circuit boards with half the components conformally coated with Hysol PC18. All hardware was mounted such that they were protected from direct exposure to the external environment, and many were powered up periodically during data collection periods. Postflight data were compared against preflight data. No failures or significant degradation were observed.

Many low cost, nonspace-qualified components performed quite well, without any measurable degradation. The question of whether to permit use of commercial or Class B parts in space applications is beyond the scope of this paper. However, it is evident that such components can survive long-term exposure to LEO and their use may often be justified for low cost systems when failures would not result in safety concerns or other major mission costs.

THERMAL HARDWARE

Thermal hardware flown on LDEF included a broad array of materials consisting of both experiment specimens and experiment support hardware. The largest component within the thermal discipline was the thermal control coatings. Also flown were three heat pipe experiments to evaluate a total of four different types of heat pipes.

Thermal Control Coatings

Over 50 percent of LDEF's exterior surfaces were chromic acid anodized (CAA). Extensive testing of these surfaces and several CAA test specimens was completed by numerous investigators, including the LDEF deintegration team. *Results show that for CAA with low to medium emissivities (0.2 to 0.7), any differences between pre- and postflight optical values were attributable to contamination, manufacturing, and/or measurement variations.* However, two high emissivity CAA test specimens showed signs of coating degradation (ref. 4).

S13G and S13G/LO white coatings had darkened significantly with UV exposure, but were partially "scrubbed" by AO to near original optical properties (ref. 5). Specimens of Z93 and YB71 white coatings were significantly less effected. The silicate-based coatings, even those containing carbon black pigments, indicate excellent stability in the AO environment. Silicone-based materials were also observed to be resistant to AO.

The loss of specularity of silverized Teflon™ thermal blankets, one of the earliest observations noted at the time of retrieval, was determined to have had no significant effect on the thermal performance. The increase in diffuse reflectance was greatest for materials closest to the LE. This loss of specularity is the result of first surface erosion and roughening caused by AO.

Analysis of thermal control coatings flown on LDEF greatly refined our knowledge of recession rates and changes in solar absorptance and thermal emittance due to long-term exposure to the LEO environment. The data showed that AO modifies and/or removes molecular contamination and UV degraded material.

Heat Pipes

Initial functional tests were successfully performed on all heat pipe experiments. All heat pipe experiments were found to be intact and were not degraded by the long-term LEO exposure.

OPTICS HARDWARE

In general, optical components showed some effects related to the space environment, unless well protected. The effects were often small, but sometimes had a significant effect on the respective hardware.

Four experiments flew fiber optics and a fifth experiment evaluated fiber optic connectors. Four of these five experiments recorded on-orbit data. Overall, the fiber optics performed well, with little or no degradation to performance. Most environmental effects were confined to the protective sheathing. However, one fiber optic bundle was struck by a meteoroid or debris particle causing discontinuity in the optical fiber. Preliminary data have indicated the need for additional study of the temperature effects on fiber optical performance. Postflight testing performed on fiber optics flown on the Fiber Optic Exposure Experiment showed an increase in loss with decreasing temperature, becoming much steeper near the lower end of their temperature range.

Dr. Don Blue (ref. 6) has listed general characteristics for both "weak" optical materials (susceptible to environmental effects) and "strong" optical materials.

Weak	Strong
Contains ionic bonds (halides) Potential for bond breaking (plastics) Thin precision layers degraded by - thermal cycling - oxidation - bond breaking (multilayer dielectric coatings)	Covalently bonded (silicon) Hard and brittle (Li NbO_3) Contains no plastic packaging, coatings, or filters

An LDEF Optical Experiment Data Base was created (using Claris™ Filemaker Pro data base software) that provides for quick and easy access to available experimenter's optics related findings. The data base contains a file for each of the LDEF experiments that possessed optical hardware (data base currently contains 29 files). Each file contains various fields that identify the optical hardware flown, describe the environment seen by that hardware, summarize experimenter findings, and list references for additional information. A paper copy of this data base is contained in reference 1.

CONCLUSIONS

LDEF carried a remarkable variety of mechanical, electrical, thermal, and optical hardware. The extended mission length provided a unique potential to refine our knowledge about the effects of long-term exposure to the LEO environment. No anomalies occurred that indicate any new fundamental limitations to extended mission lifetimes in LEO. To date, the data from LDEF have refined the knowledge of the LEO environment and serves as the benchmark for ground-based testing.

Shielding from the effects of AO, micrometeoroids, space debris, and UV radiation must be considered. If shielding is impossible, a thorough understanding of the surrounding environment and the materials response to that environment is necessary. Without this knowledge, it is impossible to accurately predict the material's lifetime.

There were several major system anomalies. However, the analysis to date has indicated that none of these can be solely attributed to the long-term exposure to LEO. Design, workmanship, and lack of preflight testing have been identified as the primary causes of all system failures.

The combination of any of the individual LEO environmental factors, such as UV, AO, thermal cycling, meteoroid and/or debris impacts, and contamination, can produce conditions that may accelerate the onset and rate of degradation of space-exposed systems and materials.

LDEF greatly refined our understanding regarding the possibility of on-orbit cold welding occurring. If the correct materials, tolerances, and lubricants are used such that galling does not develop during preflight fastener installation or removal, or during the launch environment, and the fastener remains undisturbed while on-orbit, no difficulty will be encountered during postflight removal. This also applies to an on-orbit replacement. No difficulty due to cold welding will be encountered if a nongalled fastener assembly is removed on orbit. However, repeated on-orbit removals and installations will require the use of appropriate lubrication schemes, shielding, and an understanding of the microenvironment to ensure that no thread or lubricant damage occurs.

This paper has been an overview of representative findings from the testing of LDEF material and hardware. References 1, 6, 7, and 8 provide additional detailed information on both hardware covered and not covered within this paper (ref. 8 is expected to be released in April 1993).

REFERENCES

1. Analysis of Systems Hardware Flown on LDEF—Results of the Systems Special Investigation Group, NASA Contract Report 189628, April 1992.

2. Tennyson, R.L., and Mabson, G.E.: "Thermal-Vacuum Effects on Polymer Matrix Composite Materials." LDEF 69 Months in Space; First LDEF Post-Retrieval Conference, NASA CP-3134, February 1992.

3. Brinker, D.J., Hickey, J.R., and Scheiman, D.A.: "Advanced Photovoltaic Experiment, S0014: Preliminary Flight Results and Postflight Findings." LDEF 69 Months in Space; First LDEF Post-Retrieval Conference, NASA CP-3134, February 1992.

4. Wilkes, D.R., Miller, E.R., Zwiener, J.M., and Mell, R.J.: "Thermal Control Surfaces Experiment Materials Analysis." Second LDEF Post-Retrieval Symposium, NASA CP-3194, April 1993.

5. Linton, R.C., Kamenetzky, R.R., Reynolds, J.M., and Burris, C.L.: "LDEF Experiment A0034: Atomic Oxygen Stimulated Outgassing." LDEF 69 Months in Space; First LDEF Post-Retrieval Conference, NASA CP-3134, February 1992.

6. Blue, M.D.: "Degradation of Electro-Optical Components Aboard LDEF." Second LDEF Post-Retrieval Symposium, NASA CP-3194, April 1993.

7. LDEF 69 Months in Space; First LDEF Post-Retrieval Conference, NASA CP-3134, February 1992.

8. LDEF Materials Workshop 1991, NASA CP-3162, November 1991.

9. Second LDEF Post-Retrieval Symposium, NASA CP-3194, April 1993.

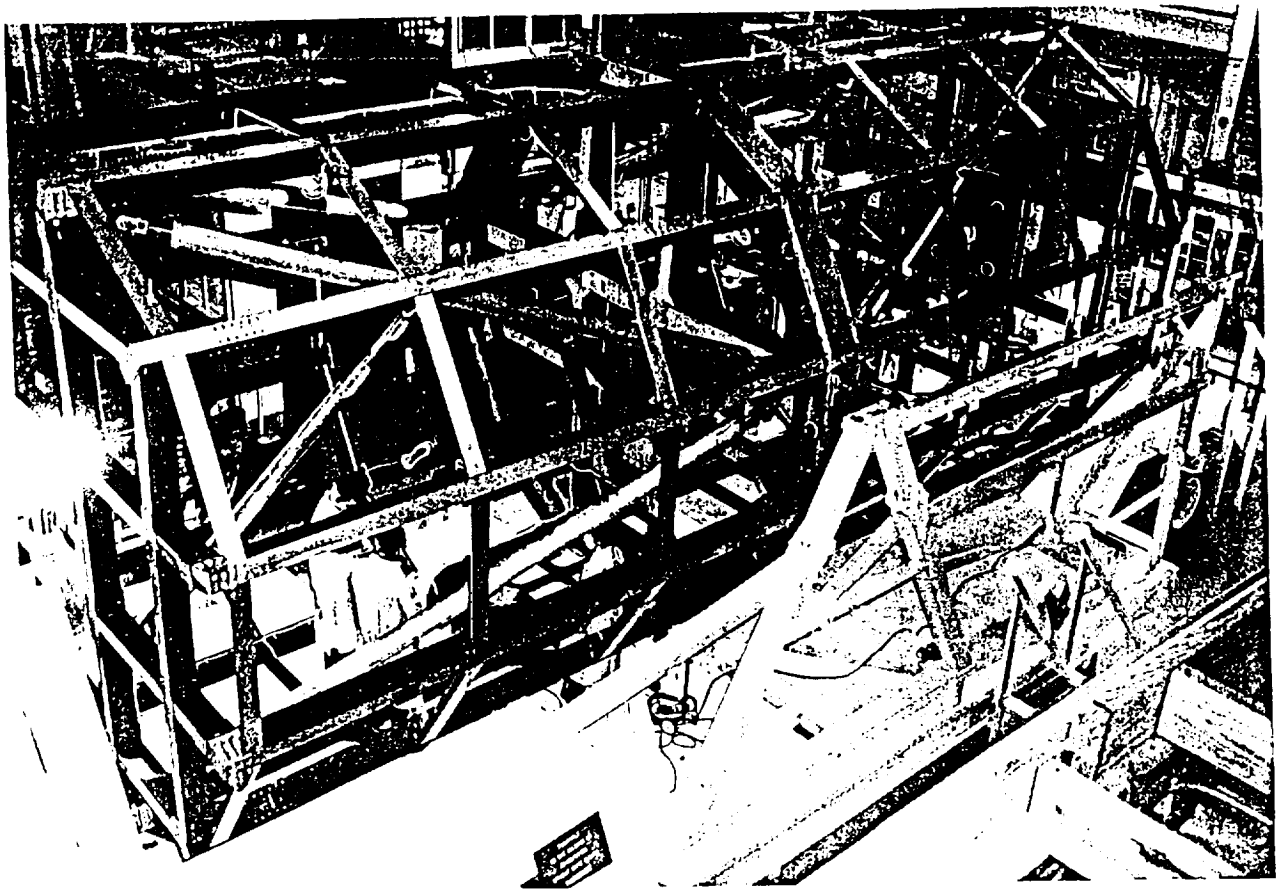

Figure 1. LDEF primary structure.

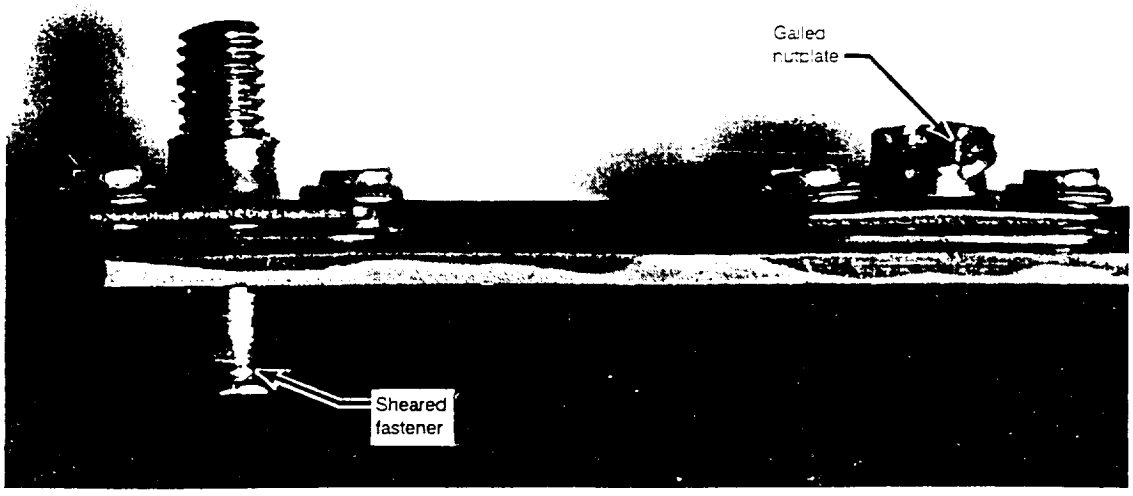

Figure 2. Sheared fasteners and galled nutplates.

LUBRICANTS

MATERIAL - DESCRIPTION	LOCATION	FINDINGS
Cetyl alcohol	A1 & A7	Failed
MoS_2	A1 & A7	Used on nut plates, appears to be nominal
MoS_2 – Air-cured dry film lubricant (MIL-L-23398)	EECCs (shielded and exposed)	Nominal, further testing required
MoS_2	B3 (shielded)	Not tested
WS_2 (tungsten disulfide)	Grapples	Bulk properties nominal
Apiezon H – thermal grease	F9 (shielded)	Outgassing tests nominal
Apiezon L – lubricant	D12	Not tested
Apiezon T – lubricant	H3 & H12 (space end)	Slight separation of oil from filler, some migration
Ball Aerospace VacKote 18.07 – MoS2 with polyimide binder	A9 (shielded)	Not tested
Ball Brothers 44177 – Hydrocarbon oil w lead naphthanate & clay thickener	EECCs (shielded)	Not tested, extensive outgassing
Castrol Braycote 601 – PTFE filled perfluoronated polyether lubricant	A3	Extensive testing, results nominal
Dow Corning 340 – Silicone heat sink compound	Shielded	IR spectra unchanged
Dow Corning 1102 – Mineral oil based heat sink compound	Shielded	Visual examination nominal
Dow Corning Molykote Z – MoS_2	Shielded	Not tested
DuPont Vespel 21 – Graphite filled polyimide	D3	Optical, EDX and friction tests nominal
DuPont Vespel bushings – polyimide	Various	Nominal
E/M Lubricants Everlube 620C – MoS2 with modified phenolic binder	D3	Complete binder failure
Exxon Andok C – Petroleum grease	Shielded	System test results nominal, lubricant not evaluated
Mobil Grease 28 – Silicone grease	MTM's (shielded)	System test results nominal, lubricant not evaluated
Rod end bearings with PTFE coated Nomex liner	D3	Extensive test results nominal

Figure 3. Lubricants and greases flown on LDEF.

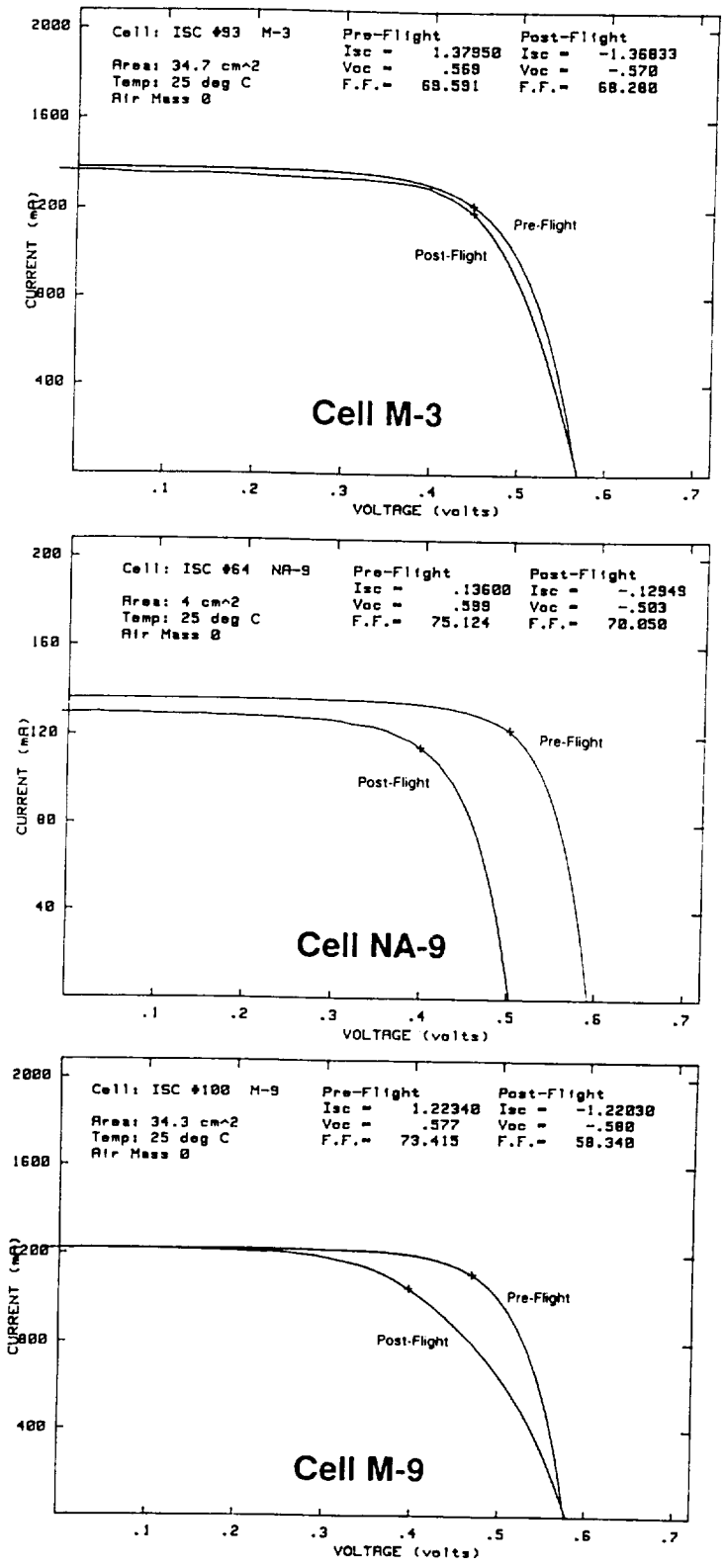

Figure 4. IV curves of cells impacted by micrometeoroids or space debris (courtesy of Dr. Dave Brinker).

N94-31038

LDEF MATERIALS SPECIAL INVESTIGATION GROUP'S DATA BASES

John W. Strickland
BAMSI, Inc.
150 West Park Loop Suite 107
Huntsville, AL 35806
Phone: (205) 544-7375, Fax: (205) 544-7372

Joan G. Funk
NASA Langley Research Center, M/S 188B
Hampton, VA 23681
Phone: (804) 864-3092, Fax: (804) 864-7893

John M. Davis
NASA Marshall Space Flight Center, EH44
Huntsville, AL 35812
Phone: (205) 544-2494, Fax: (205) 544-5786

SUMMARY

The Long Duration Exposure Facility (LDEF) was composed of and contained a wide array of materials, representing the largest collection of materials flown for space exposure and returned for ground-based analyses to date. The results and implications of the data from these materials are the foundation on which future space missions will be built. The LDEF Materials Special Investigation Group (MSIG) has been tasked with establishing and developing data bases to document these materials and their performance to assure not only that the data are archived for future generations but also that the data are available to the space user community in an easily accessed, user-friendly form. This paper discusses the format and content of the data bases developed or being developed to accomplish this task. The hardware and software requirements for each of the three data bases are discussed along with current availability of the data bases.

INTRODUCTION

The LDEF MSIG was charged with the task of establishing and developing electronic data bases which could eventually contain the wide variety and vast quantity of materials data being generated by the MSIG members and other LDEF investigators (ref. 1, 2). The MSIG chose to accomplish this task by a three-pronged approach. The first approach utilized a preexisting global-access data base system, the Materials and Processes Technical Information System (MAPTIS), as the host for the LDEF Materials Data Base. The second approach was to build on the Optical Materials Data Base developed by the Boeing Defense and Space Group under the auspices of the Systems Special Investigation Group (SSIG) (ref. 3). The Optical Materials Data Base was expanded and four other PC/Macintosh (MAC) software-based data bases, commonly referred to as "minidata bases," were developed by the Langley Research Center. The third approach was to

develop a version of the LDEF Materials Data Base for use with PDA Engineering's M/VISION™ software. An overview of the capabilities and requirements of the M/VISION™ software and this version of the LDEF Materials Data Base will be discussed. Information on availability and how to access these data bases are given. The future plans for developing these data bases are discussed.

MAPTIS LDEF MATERIALS DATA BASE

The Materials and Processes Laboratory management at NASA/Marshall Space Flight Center agreed to incorporate the LDEF Materials Data Base as a part of their automated storage, retrieval, and display data base system. The preliminary version of the LDEF Materials Data Base was released to the user community in June of 1992, and an updated version is currently available to all interested parties in the International Space Materials Community. The goal of MAPTIS is to provide an efficient, reliable means of supplying the information needed for the selection and application of materials and processes to produce the hardware required for NASA's and industry's current and future space missions. MAPTIS uses an ORACLE Corporation Relational Data Base Management System and can be accessed via a modem and a 1-800 telephone number or via Telnet. Users can access MAPTIS using hardware that emulates a Digital Equipment Corporation (DEC) VT100 terminal. The LDEF Materials Data Base is one of several different data bases in MAPTIS.

After reviewing comments and suggestions from the LDEF user community, the main menu of the LDEF Materials Data Base was restructured to make the data base more flexible in terms of format. A number of new types of searches and report formats is now available. New main menu options are now divided into six categories as listed below:

- LDEF Materials Listing—returns a list of all known materials flown on or as part of LDEF that meet the user's search criteria, detailing which experiment(s) it was flown on and whether property data on that material are currently in the data base. Search options include materials code, use type designation, composition, specification(s), manufacturer/supplier, and experiment number.

- Basic Data Search—returns all basic data (material code, manufacturer, designation and composition, etc.) on all materials meeting the user's search criteria. Search options include material code, use type, designation, composition, specification, and manufacturer/supplier.

- Property/Value Search—searches by property and user specified property value regardless of other data. Search options include 26 different properties currently on the data base, and this list will expand as new properties are added.

- All Data Search—returns all available data on materials that meet the user's search criteria, including property and value, location, atomic oxygen (AO) flux and fluence values, estimated Sun hours, etc. Search options include all available properties, material code, use type, designation, composition, specification, manufacturer/supplier, experiment number, location on the satellite, estimated Sun hours, AO flux exposure, angle of AO incidence values, and sources from which the data have been taken.

- Data Source Searches—searches for a source by data source number, primary facility or organization conducting the testing, author(s) of the published paper or principal investigators, or by the document title of the published paper.

There are slight differences in search criteria options from one area to the next, but the user is allowed to enter from three to five search criteria options in most areas of the data base. This helps maintain the data base's search flexibility. On-line help screens are now available throughout the LDEF Materials Data Base. These screens show the input information required for a specific option and the information included in the output.

This data base is a growing entity. As more published and unpublished data become available it will be incorporated. Feedback from the user community is appreciated so that this data base will become an indispensable tool for both space researcher and spacecraft designer. The primary purpose of this data base is to become the central storage point for the vast amount of data so that its results will not be lost to future researchers, engineers, and designers in the aerospace industry.

M/VISION™

M/VISION™ is a materials software system that allows for the capture, organization, and visualization of materials engineering data. M/VISION™ allows the user to reduce, manipulate, query, and graph materials data. The software includes graphics, spreadsheet, imaging, and modeling capabilities as well as data basing capabilities. Multiple data types, such as tabular data, graphs, and raster images can be stored in a single data base. M/VISION™ is a hybrid hierarchical/relational data base with both hierarchical and standard Structure Query Language interfaces. An integrated engineering spreadsheet is included in the software that allows the user more efficient means to manipulate and visualize the information in the data base. Data bases can be manipulated via user written FORTRAN and C codes.

The M/VISION™ software is configured to run on UNIX workstation computers by Hewlett-Packard, Silicon Graphics, SUN, and IBM. It is also configured to run on DEC computers running VMS and ULTRIX™. The software operates in the X-Windows environment with any networked X device such as a PC or MAC using X emulation software. In the VMS environment, the software supports both DEC Windows/Motif and TEK devices.

M/VISION™ LDEF MATERIALS DATA BASE

In the late spring of 1993, the LDEF Materials Data Base that runs on the M/VISION™ software will be available to users in the International Space Materials Community to run on their own licensed M/VISION™ software. A very preliminary version of the data base in the M/VISION™ format was demonstrated at the LDEF Materials Results for Spacecraft Conference. Figure 1 is a depiction of the M/VISION™ data base window overlaid with a spread-sheet window. In the data base display, the user has already made several choices such as the materials, environment, descriptors, and experiment, which are shown at the far right of the display. The main portion of the data base window displays the source and reference of the data. The actual data are displayed on a previous screen. The spreadsheet illustrates the direct connection between the spreadsheet and the data base. In this example spreadsheet, the user requested that all materials with "*934*" in the designation, which had mass loss data in terms of percent total loss and had an AO value, be displayed along with the property name, qualifier, postflight value of the total mass loss, and AO flux. The spreadsheet automatically calculated the log of the AO flux and displayed it in column F. The data shown in the spreadsheet can then be plotted for a variety of materials, which would allow visualization of data trends. This is one example of data in the data base being manipulated by the

spreadsheet and then plotted for the user's easier visualization of the data and data trends. The spreadsheet can be stored and used as a template for future comparisons.

COMPARISON OF THE MAPTIS AND M/VISION™ VERSION OF THE LDEF MATERIALS DATA BASE

The users of the LDEF Materials Data Base have a wide range of computer hardware, software, and expertise. The two versions of the LDEF Materials Data Base require different hardware and software with accompanying levels of computer expertise. By offering the user a choice of these two versions of the data base, users may tailor their investment in hardware, software and time. The MAPTIS™ version of the data base requires relatively inexpensive computer hardware and software and allows the user to search and retrieve tabular data. The M/VISION™ version of the LDEF Materials Data Base requires the user to have more sophisticated hardware and software allowing the user to manipulate and analyze the data. Once the M/VISION™ version of the data base is transferred to the user's local machine, the data base requires only local access by the user and is available to any local networked X device. The user can incorporate in-house data or data from other sources into the data base. Both versions of the LDEF Materials Data Base are available at no charge.

MINIDATA BASES

The Boeing Defense and Space Group, which is under contract to the SSIG and MSIG, has developed a series of data bases containing results from LDEF. These data bases were developed to provide the user community with early access to LDEF data. The data bases were developed for use with PC and MAC versions of the Claris Corporation's Filemaker Pro™ software. Filemaker Pro™ is a flat file data base which allows the user to retrieve multiple data types such as tabular data, test, graphs, diagrams, and/or picture files. The data bases' simple interface allows for easy use by novice users. The individual data bases are password protected, allowing the user full access privileges to read, print, or download the data but not allowing the user to edit the data files. The software allows the user to search and retrieve specific information in a variety of layouts. Data can be exported to a variety of formats including ASCII. As with other data bases, all data are traced back to their original data source. A more detailed report of the capabilities of these minidata bases can be found in reference 3.

The minidata bases cover the optical materials, silverized Teflon™ thermal blankets, treated aluminum hardware, thermal control paints, and the LDEF environments areas of interest. The Optical Materials Data Base is a compilation of the results on the optical materials flown on LDEF and was originally developed by the SSIG. The silverized Teflon™ thermal blankets data base covers the results from the silverized Teflon™ thermal blankets utilized on LDEF. The treated aluminum hardware data base is a compilation of data from the various types of aluminum hardware flown on LDEF including different alloys, surface conditions, etc. The thermal control paints data base contains information on the wide variety of paints flown on LDEF. The LDEF environments data base contains information on the environment that LDEF was exposed to, including thermal profiles, solar UV irradiation, and AO exposure levels. Final versions of these data bases will be available by October 1993.

AVAILABILITY OF THE DATA BASES

For those parties interested in accessing the MAPTIS™ version or the M/VISION™ version of the LDEF Materials Data Base, contacts should be made with the second author, Joan Funk, or the third author, John M. Davis. Free copies of the LDEF minidata bases will be available through December 1994 by sending a written request including which format (PC or MAC) is being requested with a blank 3.5-in floppy disk for each data base to: Gary Pippin, Technical Lead LDEF Materials Data Analysis, Boeing Defense and Space Group, P. O. Box 3999, M/S 82-32, Seattle, WA 98124-24999. After that time the data bases will be available from NASA.

ACKNOWLEDGMENTS

The authors wish to thank Jon Coulter of PDA Engineering and Dr. Gary Pippin of Boeing Defense and Space Group who presented the M/VISION and "minidata bases" portions of this presentation. The authors also thank the aforementioned and Curt Loomis of PDA Engineering and Gail Bohnhoff-Hlavacek of Boeing Defense and Space Group for their help in writing those portions of the text.

REFERENCES

1. Stein, B.A.: "An Interim Overview of LDEF Materials Findings." NASA TM-107664, August 1992.

2. Levine, A.S.: "LDEF—69 Months in Space: First Post-Retrieval Symposium." NASA CP-3134, June 1991.

3. Bonhoff-Hlavacek, G.: "Data Bases for LDEF Results." Second LDEF Post-Retrieval Symposium, NASA CP-3194, 1993.

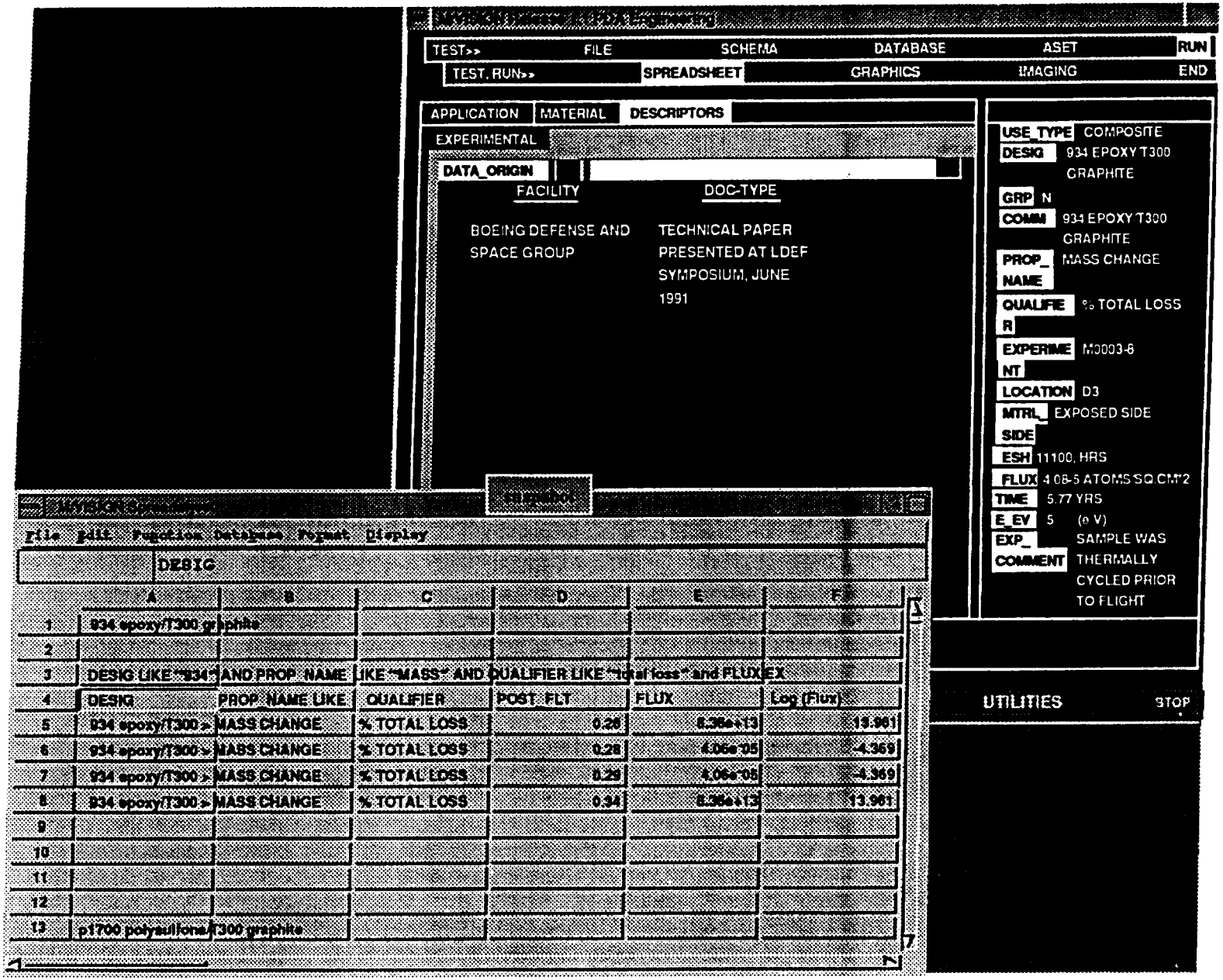

Figure 1. An example of the data base and spreadsheet screens of the M/VISION™ version.

ADVANCED APPROACHES TO SPACECRAFT MATERIALS ISSUES

GROUND-BASED SIMULATION OF LEO ENVIRONMENT: INVESTIGATIONS OF A SELECT LDEF MATERIAL—FEP TEFLON™

Dr. Jon B. Cross
Chemical and Laser Sciences Division
Los Alamos National Laboratory
Los Alamos, NM 87545
Phone: 505/667-0511, Fax: 505/665-4631

Dr. Steven L. Koontz
National Aeronautics and Space Administration
Johnson Space Center
Houston, TX 77058
Phone: 713/483-5906, Fax: 713/483-2162

SUMMARY

The Long Duration Exposure Facility (LDEF) has produced a wealth of data on materials degradation in the low-Earth orbit (LEO) space environment and has conclusively shown that surface chemistry (as opposed to surface physics-sputtering) is the key to understanding and predicting the degradation of materials in the LEO environment. It is also clear that materials degradation and spacecraft contamination are closely linked and that the fundamental mechanisms responsible for this linking are in general not well understood especially in the area of synergistic effects. The study of the fundamental mechanisms underlying materials degradation in LEO is hampered by the fact that the degradation process itself is not observed during the actual exposure to the environment. Rather the aftermath of the degradation process is studied, i.e., the material that remains after exposure is observed and mechanisms are proposed to explain the observed results. The EOIM-3 flight experiment is an attempt to bring sophisticated diagnostic equipment into the space environment and monitor the degradation process in real time through the use of mass spectrometry. More experiments of this nature which would include surface sensitive diagnostics (Auger and photoelectron spectroscopes) are needed to truly unravel the basic chemical mechanisms involved in the materials degradation process. Since these in-space capabilities will most likely not be available in the near future, ground-based LEO simulation facilities employing sophisticated diagnostics are needed to further advance the basic understanding of the materials degradation mechanisms. The LEO simulation facility developed at Los Alamos National Laboratory has been used to investigate the atomic oxygen/vacuum ultraviolet (AO/VUV) enhanced degradation of FEP Teflon® (®E.O. Du Pont de Nemours, Inc.). The results show that photo-ejection of polymer fragments occur at elevated temperature (200 °C), that VUV synergistic rare gas sputtering of polymer fragments occur even at 25 °C, and that combined AO/VUV interaction produces a wide variety of gas phase reaction products.

INTRODUCTION

The results of polymer material degradation studies in the LEO environment (refs. 1,2) and ground-based LEO simulation environments (refs. 3,4,5) have shown a strong synergistic interaction between AO and VUV radiation when interacting with fluorocarbon polymers: fluorinated ethylene

propylene-FEP Teflon™ and polytetrafluoroethylene-PTFE). The degradation effects are of great practical importance since FEP Teflon™-coated silvered thermal blanketing material is routinely used on spacecraft and is being considered for use on large permanent space platforms (Space Station *Freedom* (S.S. *Freedom*), etc.). These future missions call for long-lived materials, requiring little servicing or replacement—thus the importance of determining materials service life from accelerated testing and fundamental degradation mechanism studies.

Early extensive investigations of γ-radiation damage to FEP and PTFE fluorocarbon polymers have been reported (refs. 5,6,7) with electron spin resonance (ESR) detecting surface absorbed free radicals such as ($-CF_2\bullet$) and ($-CF_2CF\bullet CF_2-$) (ref. 8) and mass spectrometer detection of CF_4 liberation (ref. 9) into the gas phase. The conclusions presented in reference 9 show that for photons having an energy below the F(1s) binding energy (≈690 eV), the total energy deposited in PTFE (per photon) is roughly constant at 2 percent/Å up to a depth of several microns. The primary gas phase reaction product was CF_4 as detected by CF_3^+ and that extensive cross linking occurred which resulted in an increase in resistance to chemical etching by sodium hydroxide. The cross linking reaction is initiated by low-energy valence excitations resulting from direct absorption of VUV radiation or the production of low-energy secondary electrons. While these studies were undertaken to investigate the primary photolysis degradation, other investigations (ref. 10) undertook studies of the subsequent reactions of the surface absorbed free radicals with O_2. In this study mass spectrometric probing of high pressure (10^4 Pa) oxygen flowing over the irradiated PTFE sample showed a wide range of complex reaction products some of which contained oxygen and others not containing oxygen: CO_2, CF_2O and CF_4, C_2F_6, C_3F_6, C_3F_8, C_4F_8, C_4F_{10}, C_5F_{14}, etc. This study also found that irradiation of PTFE in the absence of O_2 resulted in a similar nonoxygen containing reaction products but with intensities ≈50 time less than with O_2 present. It was also concluded that free fluorine was produced which resulted in the formation of unsaturated COF_2 when O_2 was present and CF_4 when oxygen was not present. The general conclusions drawn from information found in the literature are that all formulations of fluorinated polymer (FEP, PTFE, etc.) give similar results in terms of the types of gas phase products and surface absorbed products produced, that the extent of damage extends deep (several microns) into the polymer bulk, that there are large changes in mechanical properties after exposure to radiation and oxidants, and the surface becomes cracked and rough.

Exposure of these polymers to the LEO space environment results in similar effects except that polymers exposed to the direction of travel (ram) have the cross-linked material removed through AO oxidation, while material facing the direction opposite to ram (wake) retains the cracked cross-linked layer. The effect of the LEO environment on spacecraft materials has been well documented (ref. 11) and results from the high collision energy (5 eV) and flux of atomic oxygen on the ram facing surfaces. In the case of polymers containing only C, O, H, and N, the effect of collision energy is very severe, with oxidation reactivities increasing three to four orders of magnitude in going from thermal energy (0.05 eV) AO to 5 eV AO. Fluorocarbon polymer oxidation rate dependence on collision energy has not been as extensively studied as with polyimides, but indeed does show a high anisotropic reaction rate when AO is combined with VUV radiation indicative of a strong collision energy dependence. There is indeed evidence that fluorocarbons can exhibit reactivities as high as polyimides (≈10 percent of the AO flux results in volatile reaction products) when VUV radiation intensities are high. The purpose of this paper is to present a preliminary investigation of the mechanism of the synergistic degradation effects between VUV radiation and hypervelocity atomic oxygen on FEP Teflon™.

EXPERIMENTAL

The LEO simulation facility has been described in detail elsewhere (ref. 12), thus only a short description will be given here. A cw laser sustained discharge is employed to form a high intensity beam of AO. Since the source uses a rare gas/oxygen mixture, samples are exposed to a cw beam of rare gas and oxygen atoms (percent dissociation of O_2 into AO ≈ 90 to 100 percent) along with roughly 2 suns of VUV radiation in the wavelength range of 3,000 to 1,000 Å. Figure 1 shows the VUV spectrum produced using a 50-percent mixture of O_2 and argon. The AO flux in position closest to the nozzle is $\approx 5\text{-}10\times10^{16}$ AO/cm^2-s, whereas the experiments reported in this paper were performed in a position where fluxes are $5\text{-}10\times10^{14}$ AO/cm^2-s. In situ Auger and XPS surface sensitive diagnostics have also been recently added though not used in this investigation. The following equipment has been incorporated into the turbomolecular/liquid nitrogen cryoshroud pumped experimental station shown in Figure 2—a VUV krypton low pressure resonance lamp having a MgF_2 window which produces $\approx 10^{14}$ VUV photons/cm^2-s at 1,236 Å and a quadrupole residual gas mass spectrometer operated in the pulse counting mode which can be swung into the primary AO beam to measure composition and modulation spectra. When the residual gas analyzer is out of the beam, a sample can be positioned in the AO beam with the analyzer ion source ≈1.5 cm from the surface at 45° to the surface normal. These configurations allow measurements to be taken of the primary beam velocity distribution and prompt photon signal and then modulated gas phase reaction product spectra with the detector positioned out of the beam. The time delays seen in the product spectra compared to the direct beam are due primarily to surface desorption kinetics and not time-or-flight effects (short flight path from surface to detector). The primary AO beam is modulated near the source by a four sector 50-percent duty cycle (378 Hz) chopper wheel driven by a hysteresis motor and variable frequency power source. A photocell/light detector is used to provide a timing signal to drive a pulse counting multichannel scalar which is used to record the modulation spectra. The cw krypton resonance lamp is positioned on the opposite side of the beam with respect to the mass spectrometer. A sample manipulator is employed to position the material under study in the AO beam and to heat the sample above room temperature. A pressure of 8×10^{-10} torr is obtained with the AO beam off and a background pressure of 2×10^{-6} torr when the beam is on. Tests were conducted to ensure that the average background pressure was not modulated at 378 Hz by removing the sample from the beam while keeping the mass spectrometer out of the direct beam. Integration times of 10-min duration on masses 40, 32, 16, 28, and 44 showed no discernible modulation. Reaction product integration times were all less than 10 min.

RESULTS

We report results for three different experimental conditions: VUV lamp on and hypervelocity beam off, VUV lamp off and hypervelocity pure argon beam on, and finally VUV lamp off and hypervelocity AO/Ar beam on. The beam source is not yet configured to eliminate the photon component using a slotted disk velocity selector. A photomultiplier was employed to detect the photon modulation reference signal.

VUV 1,236 Å Photodesorption Results

Mass spectra results were obtained with the FEP Teflon™ sample at three temperatures: 60 °C, 148 °C, and 248 °C by taking spectra with the lamp on and then subtracting spectra taken with the lamp off. The summary spectra are shown in Figure 3 as a function of sample temperature. Note that at the

low temperature, no gas phase products are seen while at higher temperatures CF_3^+ along with lower molecular weight ion radicals are observed. The CF^+ ion is produced primarily (ref. 13) from dissociative ionization of C_2F_4 in the mass spectrometer ion source where as the CF_4^+ ion can be produced from dissociative ionization of CF_4, C_2F_6, C_3F_8, and C_4F_{10}. The large change in the ratios of CF_3^+/CF^+, and the fact that no ions of mass greater than 100 amu were observed is indicative that at the highest temperature only CF_4 and C_2F_4 are being desorbed. An Arrhenius plot of the data gives a thermal activation energy of ≈0.2 eV for thermal assisted ejection of photo-produced radicals. There was no evidence for C or F atom release from the surface probably because these species are tightly bound and recombine to form high molecular weight fragments, i.e., CF_4 is not part of the polymer chain and must be formed by recombination of CF_3 and F.

Figure 4 shows the time history of the rate of emission of CF_4 product into the gas phase. The data were taken by turning the krypton lamp on and off while recording the mass 69 intensity. Signal averaging techniques were not employed for this particular data set. Note the very long times (10's of seconds) associated with the photo-induced desorption. From data presented in the literature it is known that photodissociation in Teflon™ occurs over a depth of 1 to 2 μm with ≈2 percent/Å of the photon energy being deposited. The data shown in Figure 4 therefore are interpreted as exhibiting diffusion limited release of photoproducts, i.e. upon lamp turn-on ≈2-percent photon energy eV/Å is deposited in the near surface region. Upon lamp turn off, diffusion and recombination of radical occurs resulting in long-term release of gas phase products. From these data, it is concluded that modulation of VUV photon intensity on the millisecond time scale would not produce observable modulated photo-produced gas phase products. As will be shown this indeed is the case.

Neat Hyperthermal Argon Beam Results

Gas phase products produced by the interaction of hyperthermal argon and its associated VUV spectral component with FEP Teflon™ are shown in Figure 5 at three temperatures. Note that at the low temperature CF_4 is observed in the mass spectrum in contrast to the data in Figure 3 where VUV alone does not release CF_4 at low temperature. The presence of hypervelocity (≈2 to 3 eV) argon appears to produce sputtering of the weakly bound CF_4 which therefore must reside on the Teflon™ surface. No CF is observed indicating that C_2F_4 must reside in the subsurface region where sputtering release will not occur. At the higher surface temperature of 255 °C, both CF_4 and C_2F_4 are produced. Modulated beam spectra in Figure 6 shows the results from the interaction of hyperthermal argon (3 eV) and VUV radiation with FEP Teflon™ held at a temperature of 60 °C. The curves labeled photons and direct Ar are the direct beam photon component and neutral argon, respectively, while the resulting gas phase product CF_4 is represented by the CF_3^+. Note that the CF_4 product correlates with the neutral argon beam component and not the photon component, i.e., the CF_3^+ intensity does not begin to rise before the arrival of the modulated argon. The direct photon modulation produced species is damped out by diffusional effects but does prepare the surface and subsurface regions with low concentrations of free radicals. The high kinetic energy (≈3 eV) argon arrives later in time and produces sputtering of low binding energy surface absorbed species. Free radicals are most likely chemisorbed with binding energies greater than 3 eV while CF_4 with fully occupied orbitals is physisorbed with a binding energy <3 eV. Note that the CF_3^+ signal is complex. The initial rate of CF_4 ejection just after the argon arrives is much higher than later in the argon pulse, i.e., the surface absorbed CF_4 concentration is high resulting in a high removal rate compared to later times when the surface concentration is replenished by diffusion of CF_3 and F on the surface or from the Teflon™ interior to form CF_4. The diffusion is slower than the initial CF_4 removal rate thus producing a diffusion limited removal. After the beam is turned off, a

slowly decreasing intensity of CF_4 is observed which is nearly linear with log(t) indicating a diffusion controlled release.

AO/Argon/VUV Combined Interaction Results

The gas phase reaction product relative intensities for the interaction of hyperthermal AO and argon along with the associated VUV component from the beam source are shown in Figure 7. The mass spectral intensities are 20 to 50 times that produced by hyperthermal argon alone. It is evident from the spectrum that there are two classes of reaction products, ones containing oxygen and those that do not. The oxygen containing molecules are CO, CO_2, and COF_2 (COF comes from cracking of COF_2 in the ion source and O_2F_2 represents a minor channel). The methane equivalent, CF_4, appears to be a major fraction of the nonoxygen containing molecules although a substantial amount of high molecular weight polymer fragments must also be present and may crack to form CF_3^+ in the ion source. Fragments with molecular weight above 131 amu were not observed and are most likely not present as the signal to noise was especially favorable to observe high molecular weight species if they were present. It appears that C_3F_8 or C_2F_6 are the highest molecular weight gas phase fragments desorbed into the gas phase. Modulated mass spectra (not shown) give the same qualitative diffusion effects shown for hyperthermal argon interaction.

DISCUSSION AND CONCLUSION

Fluorocarbon polymers appear to exhibit a complex response to the LEO environment. The results presented here indicate that surface recession of FEP Teflon™ can occur in the presence of VUV radiation alone even without the presence of AO. VUV radiation forms free radicals over a wide depth range (several microns) which at low temperatures (<50 °C) remain on the material surface and bulk forming crosslinked material. The crosslinked material is chemically different from the virgin material but is susceptible to removal by hypervelocity AO. At high surface temperature (>100 °C) VUV produced reaction products are thermally desorbed as fully bonded stable saturated and unsaturated fluorocarbon gases, i.e., CF_4, C_2F_4, C_2F_6, etc. The results presented here also indicate that hypervelocity nonreactive species such as argon can produce sputtering of surface absorbed fluorocarbon gases which would normally only desorb at higher temperatures. The interaction of VUV and hypervelocity AO produces a wealth of gas phase reaction products which can be classed as oxygen and nonoxygen containing species. The most abundant oxygen containing products are low molecular weight species such as CO and CO_2. The gas phase products not containing oxygen are high molecular weight fluorocarbon gases up to C_3F_8 and C_2F_6. All gas phase products irrespective of their oxygen content appear to desorb in at least two steps. The first step being prompt, is most likely due to desorption of surface absorbed gas while the second, extending over a much longer period of time, is produced by diffusion limited desorption. This second long time step appears to be diffusion controlled either from surface mediated diffusion or diffusion from deep (several microns) within the material.

The preliminary mechanism of fluorocarbon polymer oxidation by combined VUV and hypervelocity AO indicates that diffusion mediated steps are active and that care must be given to the development of accelerated testing methodologies. It remains to be seen whether fluorocarbon polymer reactivity is linear with VUV and/or AO flux. Under low flux conditions and suitable temperatures where diffusion rates are fast compared to oxidation, the oxidation rate may appear first order in AO flux. There may be other regimes at high flux and low temperatures where the oxidation rate may be diffusion

limited and relatively insensitive to changes in AO flux when the flux is high. We are presently investigating this parameter space in order to develop guidelines for the development of accelerated testing strategies.

REFERENCES

1. Santos-Mason, B.: "Preliminary Results of Solar Maximum Mission Exposed Aluminized Kapton and Silver Teflon™." Proceedings of Solar Maximum Recovery Mission Degradation Study Work-shop, 408-SMRM-79-0001, May 1985, pp. 273–286.

2. Rousslang, K., Crutcher, E., and Pippin, G.: "Results of Examination of Silvered Teflon™ From the Long Duration Exposure Facility." Boeing Aerospace and Electronics Co., Seattle, WA, NASA. Langley Research Center, LDEF: 69 Months in Space. First Post-Retrieval Symposium, Part 2, pp. 847–859 (See N92-24806 15-99) Publication Date: January 1992.

3. Koontz, S., Leger, L, Albyn, K, and Cross, J.: "Vacuum Ultraviolet Radiation/Atomic Oxygen Synergism in Materials Reactivity." Journal of Spacecraft and Rockets, vol. 27, No. 3, 1990, pp. 346–348.

4. Stiegman, A., Brinza, D., Laue, E., Anderson, M., and Liang, R.: "Vacuum Ultraviolet Radiation/ Atomic Oxygen Synergism in Fluorinated Ethylene Propylene Teflon™ Erosion." Journal of Spacecraft and Rockets, vol. 29, No. 1, 1992, pp. 150–151.

5. Kim, W. and Lian, R.: "Effects of UV and VUV Irradiation on Fluorinated Ethylene Propylene Copolymer: An EPR Study." Polymer Preprints, American Chemical Society Division of Polymer Chemistry, vol. 31, No. 2, 1990, pp. 389–390.

6. Siegel, S., and Hedgpeth, H.: "Chemistry of Irradiation Induced Polytetrafluoroethylene Radicals: I. Re-examination of the EPR Spectra." Journal of Chemical Physics, vol. 46, No. 10, 1967, pp. 3904–3912.

7. Iwasaki, M., Toriyama, K., Wasaki, T., and Inoue, M.: "Electron Spin Resonance of γ-Irradiated Tetrafluoroethylene-Hexafluoropropylene Copolymers." Journal of Chemical Physics, vol. 47, No. 2, 1967, pp. 554–559.

8. Iwasaki, M., and Toriyama, K.: "Photoinduced and Thermal Radical Conversions in γ-Irradiated Copolymers of Tetrafluoroethylene and Hexafluoropropylene as Studied by Electron Spin Resonance." Journal of Chemical Physics, vol. 47, No. 2, 1967, pp. 559–563.

9. Rye, R., and Shinn, B.: "Synchrotron Radiation Studies of Poly(tetrafluoroethylene) Photochemistry." Langmuir, vol. 6, No. 1, 1990, pp. 142–146.

10. Khrushch, B., Ershov, Y., Lyulichev, A., Udovenko, V., Pshisukha, A., and Strizho, G.: "Degradation of Polytetrafluoroethylene by Vacuum Ultraviolet Radiation." Khimiya Vysokikh Energii, vol. 15, No. 6, 1981, pp. 415–419.

11. Leger, L., Visentine, J., and Santos-Mason, B.: "Selected Materials Issues Associated With Space Station." 18th International SAMPE Technical Conference, vol. 18, October 1986, pp. 1015–1026.

12. Cross, J.B., and Blaise, N.C.: "High Energy/Intensity Atom Beam Source for Low Earth Orbit Materials Degradation Studies, Rarefied Gas Dynamics: Space-Related Studies." E.P. Muntz, D.P. Weaver, and K.H. Campbell (editors), Progress in Astronautics and Aeronautics, vol. 116, AIAA, Washington, DC, 1989, pp. 143–155.

13. Wheeler, D.R. and Pepper, S.V.: "Effect of X-Ray Flux on Polytetrafluoroethylene in X-Ray Photoelectron Spectroscopy." J.Vac. Sci. Technol., vol. 20(2), February 1982, pp. 226–232.

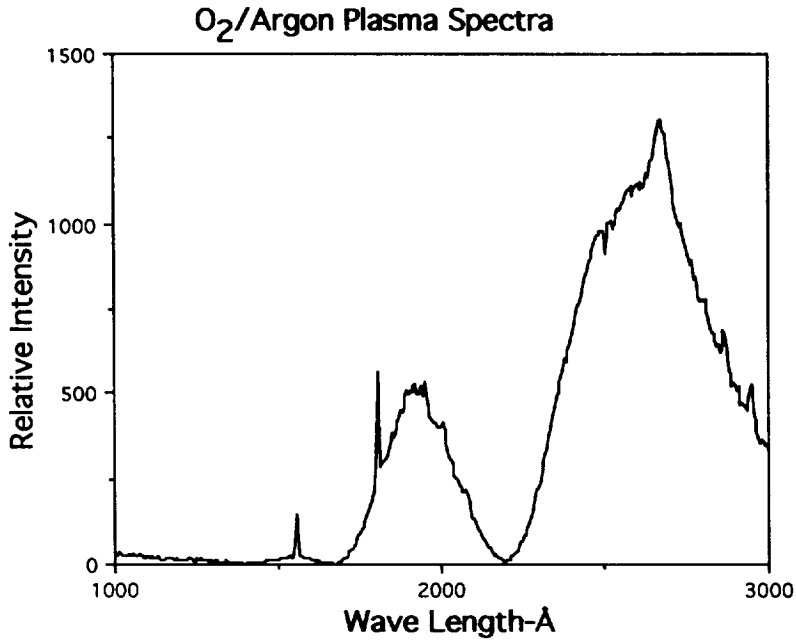

Figure 1. O_2/argon plasma spectrum. Intensity is ≈1-2 UV suns.

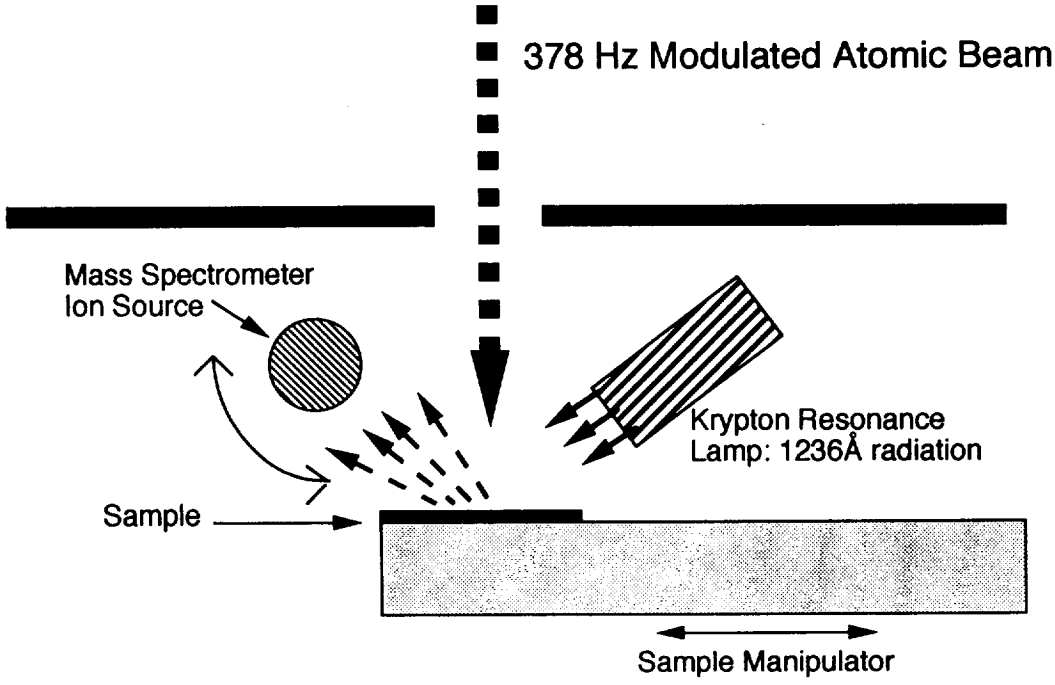

Figure 2. Experimental configuration. Modulated atomic beam scatters from sample and is detected by a residual gas analyzer in line-of-sight pulse counting mode. Source to sample distance is 1.25 meters. Krypton resonance lamp (1236Å) is ≈2 cm from the sample and is operated in cw mode. Photon flux from lamp is ≈ 10^{14} photons/s-cm^2.

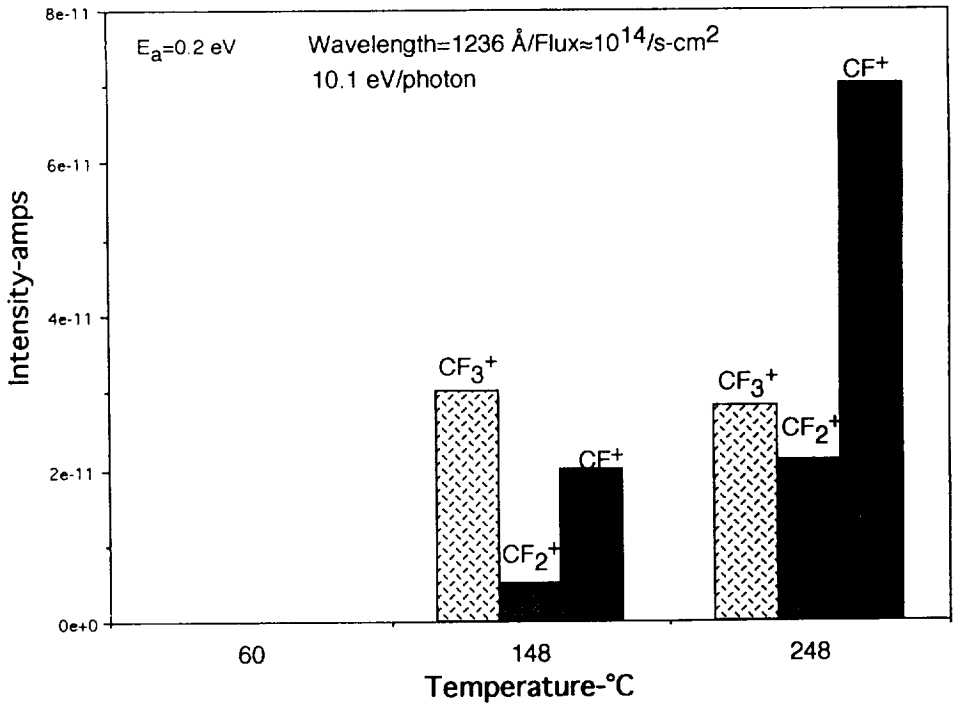

Figure 3. Temperature dependence of VUV photo produced reaction products from FEP Teflon™. Thermal activation energy is ≈0.2 eV and CF_4 and C_2F_4 are the major products. Note no measurable mass signals at low temperature.

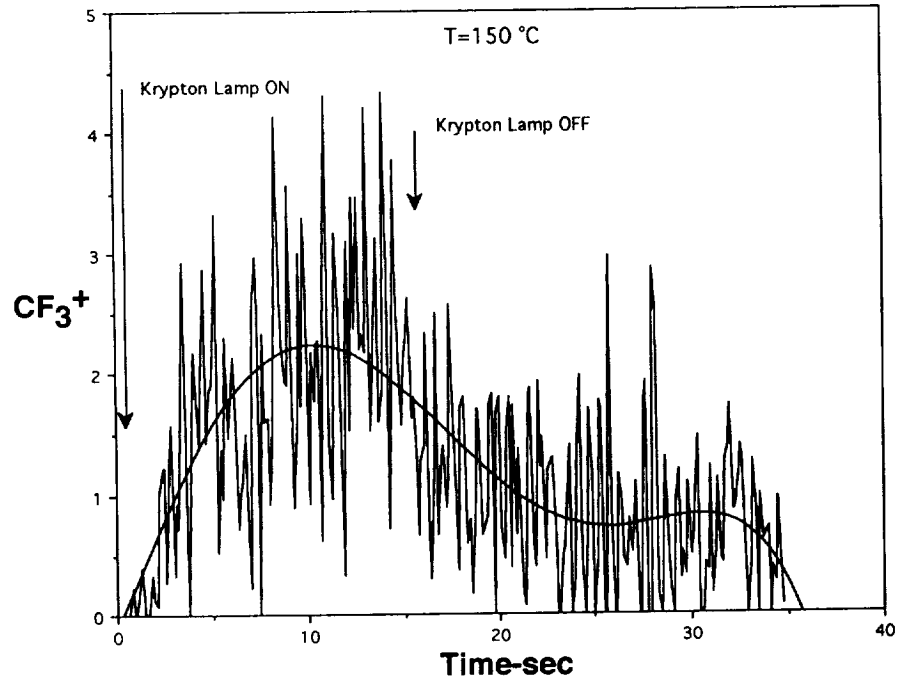

Figure 4. Time history of CF_4 VUV (1,236 Å) photo-produced product from FEP Teflon™. The time scale indicates the products are desorbing through a diffusion limited mechanism.

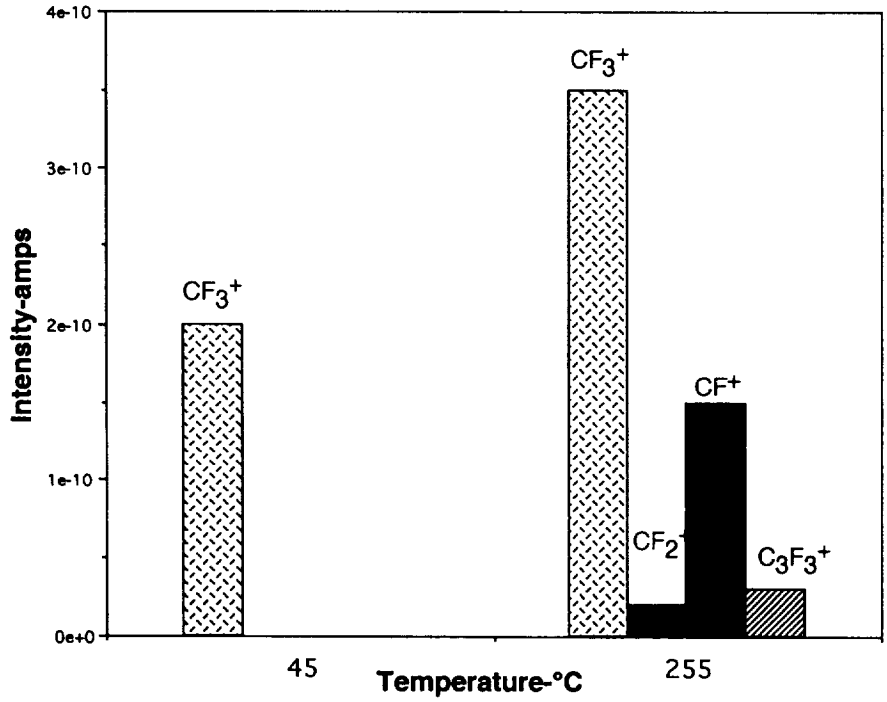

Figure 5. Temperature dependence of VUV/hyperthermal argon produced reaction products from FEP Teflon™. The CF_4 product observed at low temperature is due to hyperthermal argon sputtering. At higher temperature a mixture of CF_4 and C_2F_4 is observed.

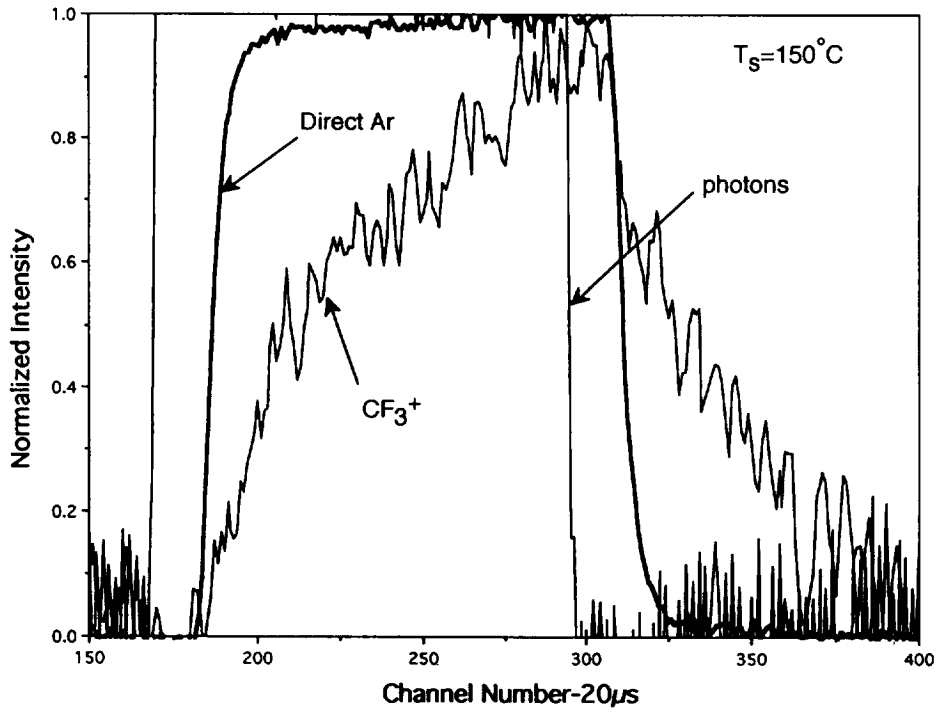

Figure 6. Modulation spectra of VUV/hyperthermal argon produced CF_4 gas phase product from FEP Teflon™. The CF_4 product correlates with the hypervelocity argon and not VUV radiation and is released in a two step process.

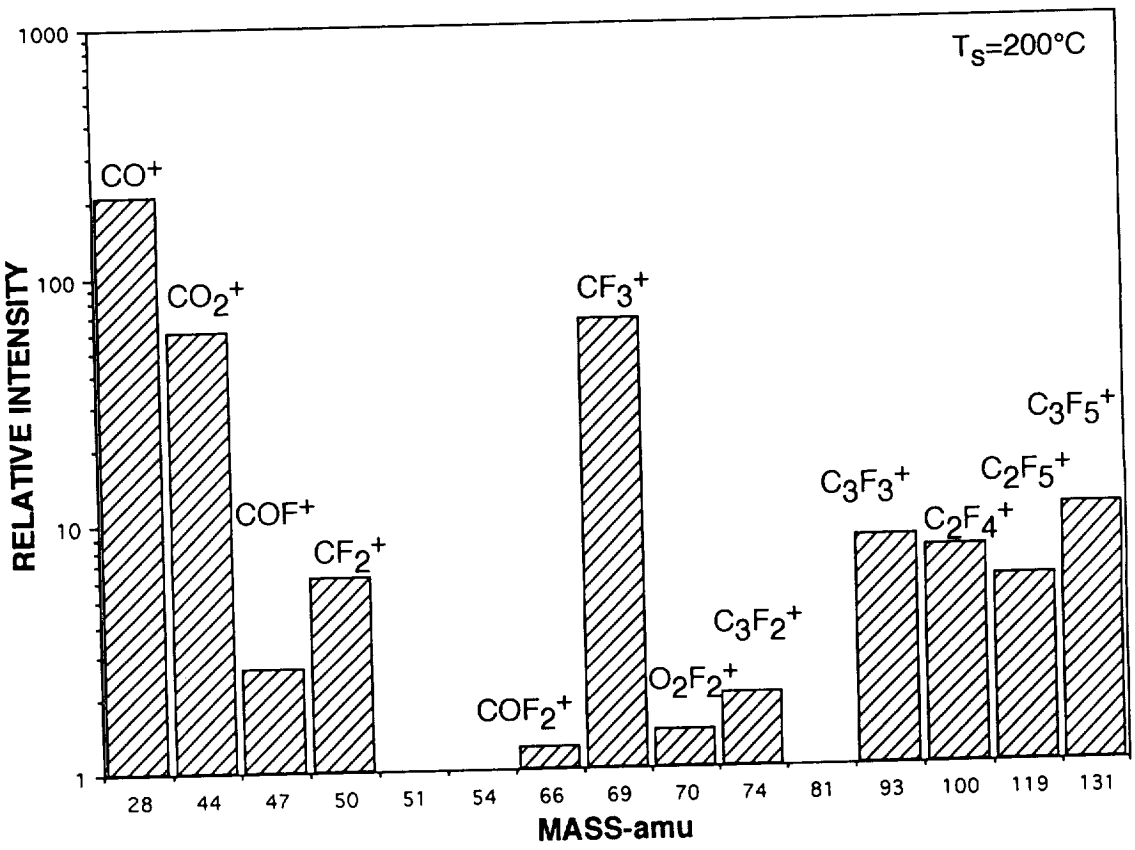

Figure 7. AO/VUV produced gas phase products from FEP Teflon™. Products are classed as oxygen containing and nonoxygen containing. Note high molecular weight products are produced when AO is present.

AN OVERVIEW OF THE EVALUATION OF OXYGEN INTERACTION WITH MATERIALS—THIRD PHASE (EOIM-III) EXPERIMENT: SPACE SHUTTLE MISSION 46

Lubert J. Leger, Steven L. Koontz, James T. Visentine and Donald Hunton

ABSTRACT

The interaction of the atomic oxygen (AO) component of the low-Earth orbit (LEO) environment with spacecraft materials has been the subject of several flight experiments over the past 11 years. The effect of AO interactions with materials has been shown to be significant for long-lived spacecraft such as Space Station *Freedom* (S.S. *Freedom*) and has resulted in materials changes for externally exposed surfaces. The data obtained from previous flight experiments, augmented by limited ground-based evaluations, have been used to evaluate hardware performance and select materials. Questions pertaining to the accuracy of this data base remain, resulting from the use of long-term ambient density models to estimate the O-atom fluxes and fluences needed to calculate materials reactivity in short-term flight experiments. The EOIM-III flight experiment was designed to produce benchmark AO reactivity data and was carried out during STS-46. Ambient density measurements were made with a quadrupole mass spectrometer which was calibrated for AO measurements in a unique ground-based test facility. The combination of these data with the predictions of ambient density models allows an assessment of the accuracy of measured reaction rates on a wide variety of materials, many of which had never been tested in LEO before. The mass spectrometer is also used to obtain a better definition of the local neutral and plasma environments resulting from interaction of the ambient atmosphere with various spacecraft surfaces. In addition, the EOIM-III experiment was designed to produce information on the effects of temperature, mechanical stress, and solar exposure on the AO reactivity of a wide range of materials. An overview of EOIM-III methods and results are presented in this paper.

INTRODUCTION

The external surfaces of spacecraft in the LEO (200 to 500 km) environment are exposed to a number of natural environmental factors capable of degrading spacecraft materials and spacecraft performance. AO, solar ultraviolet (UV) and vacuum ultraviolet (VUV) radiation, ionizing radiation, plasma interactions, thermal cycling, and micrometeoroids/debris can all contribute to spacecraft performance degradation to varying degrees depending on spacecraft orientation, orbital inclination, orbital altitude, and state of the solar cycle (refs. 1–3). AO is the major constituent of the natural atmospheric environment in LEO and has been shown to be one of the most important factors in the environmental degradation of several important classes of spacecraft materials in a series of flight experiments and laboratory studies conducted over the past 11 years (refs. 4–8). The data from these experiments have, along with 10- to 30-year life requirements, driven a number of materials selections for S.S. *Freedom* such as: (1) SiO_x protective coatings for Kapton™ solar array blankets, (2) O-atom/UV resistant multilayer insulation blankets, and (3) anodized aluminum coatings.

In addition, the interaction of the natural environment with spacecraft surfaces creates local induced environments which can have an impact on vehicle performance and mission success.

Examples include spacecraft glow and the ram-density or bow wave effect. Spacecraft in LEO travel through the ambient environment at high velocity so that forward-facing surfaces receive a constant flux of high-velocity atoms and molecules which lose kinetic energy on inelastic collision with those surfaces. The result is a buildup of thermalized ambient species and surface reaction products ahead of the spacecraft and especially around any ram-oriented spacecraft surfaces (ram surfaces are oriented perpendicular to the velocity vector, facing forward). Spacecraft glow (refs. 9,10) and ram density (ref. 11) are examples of local induced environment effects which can influence Earth observation and astrophysical measurements.

An understanding of the surface chemistry which gives rise to materials degradation and induced environment effects in LEO is essential for the design of reliable long-lived LEO spacecraft such as S.S. *Freedom*. The LEO AO reactivities of materials measured before EOIM-III are based on AO fluences calculated using the MSIS-86 model of the thermosphere (ref. 12). Predictions made using MSIS-86 can have errors of up to ±25 percent because the inputs used in the calculations are averages taken over various time periods rather than instantaneous values (ref. 13). As a result, the uncertainty in the O-atom fluence propagates directly to become uncertainty in measured reactivities. Similar limitations apply to modeling and prediction of induced environments.

The primary objective of the EOIM-III flight experiment is to produce benchmark AO reactivity and induced environment data. The AO flux and fluence measured during the period of materials exposure is compared with MSIS-86-based calculations (ref. 13). The secondary objectives of EOIM-III include: (1) characterization of the induced microenvironment near several surfaces; (2) acquisition of basic chemistry data related to reaction mechanism; (3) determining the effects of surface temperature, mechanical stress, atom fluence, and solar UV/VUV radiation exposure on materials reactivity; and (4) characterization of the induced environment in the space shuttle cargo bay in a variety of flight orientations.

Our approach to achieving the EOIM-III objectives employed developing a ground-based mass spectrometer calibration facility which reproduces both the chemistry and rarefied gas dynamics of the LEO environment so that the mass spectrometer could be calibrated accurately before flight. As a result, quantitative measurements of both natural and induced environments could be made with confidence, satisfying the primary objective and many of the secondary objectives. The remaining secondary objectives were achieved using a physical organic chemistry approach, i.e., a number of polymeric materials were exposed to the same O-atom environment in LEO to determine O-atom reactivity as a function of temperature, solar UV/VUV radiation dose, mechanical stress, polymer molecular structure, and formulation. While the Johnson Space Center (JSC) portion of EOIM-III emphasized polymers and S.S. *Freedom* materials candidates, other investigator teams selected inorganic, metallic, or composite materials. However, the same reasoning, i.e. reactivity as a function of material structure, composition, and temperature for a single well-defined O-atom dose, still applies.

The EIOM-III experiment was carried out during STS-46 (late August 1992) in the Space Shuttle *Atlantis* at an orbital altitude of 123 to 124 nmi to maximize the O-atom fluence obtained in a 42-h exposure. The inclination of the orbit was 28.5°. The shuttle was oriented so that the cargo bay normal was within ±2° of the velocity vector so that the experiment was in AO ram for 42 h. A standard air-to-ground telemetry link combined with a telemetry work station permitted the display and analysis of data during the mission.

EOIM-III was a team effort involving not only NASA Centers but also the U.S. Air Force Phillips Laboratories, the Aerospace Corporation, the University of Alabama in Huntsville, and the S.S. *Freedom* contractor team. International participation included the National Space Agency of

Japan, the European Space Agency (ESA), and the Canadian Space Agency. This paper reports only the preliminary results from the JSC and Air Force Phillips Laboratory portion of the experiment.

EOIM-III FLIGHT EXPERIMENT HARDWARE

Photographs of the EOIM-III experiment hardware after installation in the Space Shuttle *Atlantis* are shown in Figures 1 and 2. The cargo bay aft bulkhead is visible at the top of Figures 1 and 2. EOIM-III is on the left and Thermal Energy Management Processes 2A3 (TEMP-2A3) on the right of the supporting white framework (IMPESS structure) as viewed in the photographs. The payload at the bottom of Figure 1 is the ESA Retrievable Carrier (EURECA) satellite. EOIM-III is in flight configuration with all protective covers removed. Figure 3 is a line drawing of the EOIM-III payload which identifies the various subexperiments and assemblies and should be used as a key to identify the various features in Figures 1 and 2. Figure 4 is a line drawing showing the cargo bay configuration of *Atlantis* for STS-46.

The passive sample carriers, rectangular trays with circular openings, are visible on the left hand, forward side of Figure 2, with composite stress fixtures, a polymer film stress fixture, and a scatterometer assembly toward the back. In the center portion of the experiment, moving from fore to aft (away from the viewer), we have a S.S. *Freedom* Solar Array Materials Experiment (SSFAME, the brown rectangle), the mass spectrometer carousel, and finally the mass spectrometer itself, the metallic cylinder pointing along the cargo bay normal (-Z axis in space shuttle orbiter coordinates). The right-hand side of the experiment holds three heated trays, rectangular trays with small openings, which were thermostated at 200 °C (fore), 120 °C (center), and 60 °C (aft) during the 42-h AO ram exposure period. Also on the right-hand side are additional polymer film stress fixtures, scatterometers, the AO Monitor (AOM), the temperature-controlled quartz crystal microbalances (TQCM's) in the Environmental Monitoring Package (EMP), the Variable Exposure Tray (VET) assembly and the Solar UV Tray (SUV) assembly. The temperatures of specific locations on the passive and heated tray sets as well as the payload pallet and the mass spectrometer were measured throughout the mission.

Samples in the passive carriers, the heated trays, and the SUV and VET were characterized before and after the EOIM-III exposure; and oxygen reactivity was calculated from sample property change and total atom fluence. The relationship between property change and atom fluence is not linear in all cases. Specific characterization techniques and data interpretation vary with the materials and the choices of the investigator teams. The polymeric materials selected by the JSC team were characterized by: (1) mass loss measured by weighing the AO samples and controls before and after flight, (2) surface recession as determined by profilometry and/or scanning electron microscopy, and (3) bulk and surface chemistry changes as determined by Fourier transform infrared spectroscopy and x-ray photoelectron spectroscopy. All AO samples and controls were baked in a vacuum of 10^{-7} torr or better for at least 48 h at the expected on-orbit temperature. Sample surfaces were then cleaned by rinsing with Optisolv (QClean Systems, Monrovia, CA), a low-nonvolatile residue solvent, and air drying in a desiccator prior to installation in the sample trays. Samples were tested for compatibility with Optisolv. A high-transparency, stainless-steel, electroetched grid (Interconics, St. Paul, MN) was placed over each polymer sample to serve as an etch mask. The resulting periodic O-atom etch pattern made accurate profilometry possible despite the presence of natural surface irregularities. The preflight vacuum bakeout procedure was repeated before the postflight weighings, albeit without the solvent rinse.

The VET and SUV trays were equipped with movable covers. The VET tray was designed to progressively uncover a series of sample trays during the 42-h exposure period so that each tray experienced a different O-atom fluence. As described in the results section, the VET cover failed to operate properly during the mission and all sample trays received nearly identical exposures. The cover on the SUV tray covered one sample tray whenever solar UV/VUV radiation was present, so that one tray received O-atoms with UV/VUV, the other received O-atoms only, and a control tray was subjected to the same exposure as the passive trays.

The AOM and EMP subexperiments were designed to monitor both AO flux and molecular contamination by reporting near real time O-atom reaction rates with various materials or rate of mass deposition. The EMP consisted of five TQCM sensors, one of which had no reactive coating while the remaining three were coated with amorphous carbon, TFE Teflon™, a polyurethane, and a polyimide respectively. The AOM consisted of several vapor deposited carbon resistors. AO reaction with the carbon resistors produces a decrease in conductance as carbon is removed.

The mass spectrometer/carousel assembly was the key component of the EOIM-III flight experiment. The Air Force quadrupole mass spectrometer (ref. 14) was capable of sampling either the local neutral environment while rejecting naturally occurring ionic species (MODE-2) or measuring ionic species while rejecting the neutrals (MODE-1). The mass scan range was 2 to 80 amu and was scanned every 5 s. The mass spectrometer was equipped with a copper/beryllium dynode secondary electron multiplier having a gain of about 10^6 for detection of mass analyzed ions. The output current of the secondary electron amplifier was fed into a logarithmic amplifier which compressed 7 orders of magnitude of multiplier current into a 0 to 5 V output voltage which was digitized as an 8 bit binary integer, MS02 (0 to 256 = 0 to 5 V). The binary integer voltage (MS02) was converted to a linear multiplier current display using the formula,

$$I_{amps} = 10^{(-12.372+1.386*MS02*5/256)}.$$

The mission team could display mass spectra with either linear or logarithmic scales using the telemetry workstation.

The quardupole mass spectrometer was flown on a rotating mount so that the mass spectrometer sampling aperture could be pointed either directly out of the cargo bay (-Z direction as shown in Figures 1 to 4) or, after rotating 90° (+X direction), directly at one of the carousel sectors. When pointed in the -Z direction, the mass spectrometer is configured to make ambient density measurements whenever the cargo bay normal is ram oriented (-Z into the velocity vector). When pointed at a carousel sector, measurements of local induced environment were made. During the 42-h EOIM cycle the mass spectrometer and carousel assembly were operated according to a preprogrammed time sequence in which measurements of ambient neutrals, ambient ions, and the local induced environment in several carousel sectors were made in sequence during every 8-h EOIM cycle. Local induced environment effects measurements were made both with the carousel sector directly exposed to incoming ambient ram flux and with a movable baffle covering the sector being observed. The surfaces of each carousel sector were coated with a different material: (1) Z-306 black paint, (2) anodized aluminum, (3) ^{13}C Kapton™ polyimide, (4) Parylene-C, and (5) FEP Teflon™. Anodized aluminum and Teflon™ are common external surface types on S.S. *Freedom* as presently configured. Z-306 black paint is known to produce significant amounts of spacecraft glow when interacting with the ambient atmosphere (ram orientation) in LEO. Both ^{13}C Kapton™ Polyimide and Parylene-C are reactive organic polymers containing mass labels that permit easy mass spectrometric detection of gaseous reaction products in the presence of natural

orbiter and instrument background gases; ^{13}CO and $^{13}CO_2$ in the case of the labeled Kapton™ and Cl, COCl, and other chlorine containing in the case of Parylene-C.

Preflight calibration of the EOIM-III mass spectrometer was conducted at Los Alamos National Laboratories using techniques which have been previously reported (ref. 15). It should be noted that the calibration factors reported in reference 15 were not those used during the mission. The Air Force mass spectrometer was cleaned, refurbished, and recalibrated prior to EOIM-III, and small changes in the calibration factors were noted. Postflight calibration is in progress at Los Alamos, and a complete description of calibration and mass spectrometer performance will be published separately. Briefly, the flight mass spectrometer was calibrated for thermalized gases using a spinning rotor gauge (molecular drag gauge) which had been subjected to a National Institutes of Science and Technology traceable calibration. The same spinning rotor gauge was used to support quantitative calculation of the flux of oxygen atoms in the high-velocity neutral O-atom beam, permitting calibration for ram flux measurements on orbit. Preliminary postflight calibration of the Air Force mass spectrometer has shown no significant change in calibration factors thus far. It should be noted that mass peak areas, not peak heights, were used for all measurements. Also, mass 16 peak areas (AO) were corrected for contributions resulting from mass 16 fragments produced by higher mass species such as H_2O, O_2,and CO_2.

EOIM-III FLIGHT EXPERIMENT PROCEDURES AND ENVIRONMENTS

The EOIM-III payload was activated in stages. Primary electrical power was applied about 2 h after opening the cargo bay doors. Telemetry was then enabled so that temperature and EMP data were transmitted for the rest of the mission. The mass spectrometer was operated intermittently before EOIM-III was initiated to obtain natural and induced environment data for selected vehicle attitudes and altitudes. Ambient neutral and ionic density measurements were conducted at altitudes of 231, 160, and 124 nmi. The mass spectrometer was pointed in the -Z direction for all measurements made prior to EOIM-III with MODE-1 (ambient ions) and MODE-2 (ambient neutrals) measurements made during alternate 1-min time periods.

EOIM-III was performed toward the end of the STS-46 mission, after the orbital altitude was reduced to 123 to 124 nmi and the inclination ramained fixed at 28.5°. Data were collected and telemetered continuously for several preprogrammed measurement cycles. Just prior to powering down the EOIM-III payload, *Atlantis* was put through a roll around the orbiter X-axis, moving the mass spectrometer from ram to deep wake and back into ram again to obtain data on the induced environment at various angles of attack. Mass spectrometer data were collected continuously during the roll maneuver, with the mass spectrometer taking neutral mass spectra (MODE-2) while pointed in the -Z direction. The EOIM-III vehicle orientation and orbital path are illustrated in Figure 5. Orbital inclination was 28.5°, with a beta angle (the angle between the Earth-Sun vector and the plane of the orbit) between 17.5° and 24.3°.

EOIM-III environmental exposure is summarized in Table 1. AO fluences were calculated using the MSIS-86 model of the thermosphere combined with an orbital mechanics package (Runflux) developed at JSC (ref. 16). The O-atom fluence values reported in Table 1 are provisional in that a significant increase in solar activity was observed during the EOIM-III experiment so that the usual monthly average values of the solar activity parameters are probably inappropriate. In addition, there is evidence of geomagnetic storm activity during STS-46 which suggests that the version of MSIS-86, capable of accounting for the enhanced nitrogen and argon densities which occur

during such storms, should be used. Final O-atom fluence values will be reported at a later date, although the increase in fluence should be less than 10 percent of the values reported in Table 1. An important feature of Table 1 is the 11.27-h period of solar inertial exposure associated with Eureka deployment and checkout. Solar inertial (cargo bay to the sun) is a high temperature attitude which also results in a significant solar UV/VUV radiation dose. The EOIM-III samples which were not covered during this time period (all samples except VET and SUV tray specimens which were under movable covers at the time) received a UV/VUV radiation dose greater than that received during the rest of the mission. Figures 6 and 7 show O-atom density (calculated using the methods of reference 16) as a function of time during the post EURECA deployment and EOIM-III portions of STS-46, respectively.

RESULTS AND DISCUSSION

Flight instrumentation generally performed well during EOIM-III. The Air Force mass spectrometer generated approximately 48,000 neutral and ion spectra. Mass spectra were collected at three different altitudes (124, 160, and 231 nmi), and included both ram and wake orientations of the orbiter cargo bay, vehicle roll maneuvers, shuttle engine firings, and support of Tethered Satellite System-1 operations. The EMP measured large deposition rates which correlated with ambient ram incident of the TQCM sensor. Postflight analysis shows thick deposits of SiO_x on the sensor surfaces which are not consistent with the low levels of contamination measured in an x-ray photoelectron spectroscopy survey of the EOIM-III payload (Table 2). The AOM functioned properly, showing a linear decrease in electrical conductance with increasing O-atom fluence and no evidence of increasing contamination levels. The cover on the VET experiment did not function as programmed; all three covered trays received the same O-atom fluence. The SUV and heated trays both functioned correctly. Finally, two switching problems were encountered which have not been explained. First, the mass spectrometer did not power-off properly after first power-on early in the mission resulting in an unplanned 13.6-h operation period. Second, the preprogrammed mass spectrometer/carousel cycle failed to initiate properly so that the first series of carousel measurements were delayed by about 6 h.

Mass Spectrometer/Carousel

As of this writing, only a limited amount of the mass spectral data has been reduced. As shown in Table 1, agreement between the calculated atom fluence and the mass spectrometer data from a limited number of orbits is satisfactory, confirming, at least qualitatively, the accuracy of the methods of reference 16 for this application and, therefore, the existing space shuttle AO reactivity data base.

Typical mass spectrometric measurements (MODE-2, neutrals) of ram flux taken at 231, 160, and 124 nmi altitudes are shown in Figures 8, 9, and 10, respectively. Several features of these spectra are a result of the induced environment in the ram oriented shuttle cargo bay and the mass spectrometer itself. The close proximity of the cargo bay aft bulkhead and the mass spectrometer (Figures 1 to 4) means that thermalized cargo bay gases can easily reach the mass spectrometer sampling aperture or the carousel sectors simply by scattering off (or desorbing from) the aft bulkhead. Water is not a significant component of the natural environment at 231 nmi but is the base peak in Figure 8. The water is not related to a specific dump event and is most likely due to cargo

bay and/or mass spectrometer outgassing. The molecular nitrogen and oxygen peaks become increasingly important in Figures 9 and 10, implying higher ambient densities for these species than are predicted by the ambient density model of reference 16. High molecular oxygen values were also observed during preflight calibration of the mass spectrometer in the high velocity O-atom beam at Los Alamos National Laboratories and is attributed to O-atom recombination in the ion source. O/O_2 peak area ratios were very nearly the same on orbit and at Los Alamos.

Mass spectra corresponding to deep wake orientation at the same altitudes are shown in Figures 11 and 12. Water vapor is the only prominent peak in all spectra and the total pressure is obviously much lower (see scale on vertical axis). No significant amount of AO, molecular nitrogen or molecular oxygen is apparent.

Mass spectrometers measure the density of gas in the ion source, so we can calculate the density of various species in the ram and wake spectra (using the thermal gas calibrations of the mass spectrometer, not the high velocity neutral beam calibration) and compare with the values calculated by Runflux (ref. 16) (Table 3). As inspection of Table 3 shows the ram spectra contain higher N_2 and O_2 than is predicted by the MSIS-86 model. The high O_2 levels result from recombination of AO in the instrument, and the orbital data show the same O_2/O peak area ratios that were observed in the preflight calibration with the high velocity neutral O-atom beam at Los Alamos.

The most important discrepancy between the MSIS-86 model and the mass spectrometer measurements is found in the N_2/O partial pressure ratio which is too large to account for with either the well-known dependence of vacuum pumping speed on atomic or molecular mass (ref. 17). Replacing the partial pressure of O with $O+O_2$ still leaves a big discrepancy. Argon, however, shows a similar excess while nitrogen to argon ratios appear normal. Simultaneous and nearly equal enhancements of argon and nitrogen suggest the occurrence of magnetic storm conditions during EOIM-III (personal communication, Dr. Alan Hedin). Data from the National Oceanics and Atmospherics Administration Space Environment Services Center show that the daily A_p index changed from 5 to 43 during STS-46 while the daily F10.7 increased from 103 to 141. A modified version of the Runflux method (ref. 16) which employs 3-h average values of geomagnetic indices, should be able to calculate the observed nitrogen and argon levels. The results of calculations with the modified Runflux model will be reported in a subsequent publication.

Mass spectrometric measurements of the induced environments in the carousel sectors contain evidence of gas scattering off cargo bay and experiment surfaces, though the primary objectives of the carousel measurements could be achieved nonetheless. A comparison of the mass spectra taken with and without the carousel baffle over the ^{13}C Kapton coated sector shows the clear presence of $^{13}CO_2$ and ^{13}C ions in the carousel spectra as shown in Figures 13 and 14. ^{12}CO is probably also present but cannot be resolved the N_2 peak as both are at mass 28.

The effects of engine firings were often apparent in the ambient ram mass spectra. Especially interesting was the appearance of a mass peak corresponding to NO after Primary Reaction Control System (PRCS) engine firings which decayed in intensity with a characteristic time of about a minute. The NO appears to be desorbing from orbiter surfaces long after the 80-ms engine pulse has been terminated. A typical mass spectrum taken shortly after a pulsed PRCS firing in the -Z direction is shown in Figure 15.

It should be obvious from the preceding paragraphs that quantitative interpretation of the EOIM-III mass spectrometer data, including final high accuracy estimates of the oxygen atom

fluence, will require more detailed modeling of both the ambient and the induced environment in the space shuttle cargo bay. That modeling effort is in progress and results will be published at a later date.

Polymeric Materials Reactivity

The measured reaction efficiencies (cm^3 of material removed per O-atom) of the JSC polymeric materials samples from the EOIM-III passive trays are shown in Table 4 (hydrocarbons and inorganics) and Table 5 (halocarbons), along with reaction efficiencies produced by previous flight experiments if the data exist. The passive tray reaction efficiencies produced by EOIM-III are in reasonable agreement with the results of earlier in-space experiments. Reaction efficiencies were calculated using the Runflux (ref. 16) with monthly average values (July, 1992) of A_p and F10.7 to estimate O-atom fluence in all cases. We believe these values are about 10 to 20 percent too low as a result of the large change in solar activity parameters which occurred during the 42-h exposure period. More accurate atom fluences and reaction efficiencies will be reported as they become available. No previous in-space data were available for many of the polymers flown on EOIM-III.

Scanning electron photomicrographs of Kapton-HN™ samples from STS-41 (INTELSAT Solar Array Coupon, 1.1×10^{20} O-atoms/cm^2) (ref. 6) and STS-46 (EOIM-III, 2.07×10^{20} O-atoms/cm^2) are compared in Figures 16 and 17, respectively. The familiar carpet or grass morphology produced by high velocity O-atom attack is evident in both photomicrographs (Kapton-HN™ itself is relatively smooth and featureless at these magnifications). The measured reaction efficiencies were 3.3×10^{-24} cm^3/atom for STS-41 and 3.5×10^{-24} cm^3/atom for STS-46, demonstrating the near equivalence of the cargo bay exposure of EOIM-III and the remote manipulator system (RMS) exposure (samples were exposed to ram about 10 m away from the cargo bay) of STS-41.

The effects of the long solar inertial period prior to EURECA deployment (Table 1) is apparent in the reactivity of the FEP and TFE Teflon™ samples (Table 5). While considerably lower than the reaction efficiencies measured on Solar Max satellite repair samples or on the LDEF, the EOIM-III reaction efficiencies of FEP and TFE Teflon™ are significantly higher than those measured on STS-8 (EOIM-II) or on STS-41. It is likely that the differences in the reactivity of the Teflons™ in these missions is due to differences in the net solar UV/VUV dose as has been suggested by both ground based testing (ref. 18) and detailed analysis of LDEF materials (ref.19).

Tables 4 and 5 show some interesting general trends in the reactivity of polymers as a function of molecular structure. Eymyd-F™, a polyimide similar to Kapton-HN™ but with all hydrogen atoms replaced by fluorine atoms (during synthesis, not as a result of surface fluorination after synthesis), shows the same reaction efficiency as Kapton™, demonstrating that the same reactivity is obtained in these aromatic systems whether hydrogen or fluorine is bonded to the aromatic ring carbons. It is also the case that the saturated hydrocarbons, as a group, (polyethylene, polypropylene, polymethylpentene) show significantly higher reaction efficiencies than the aromatic polymers with the notable exception of polycarbonate. The unusually high reaction efficiency of polycarbonate may be related to the well-known radiation sensitivity of that material though the mechanistic details are unclear at this time. Radiation sensitivity and O-atom reactivity may be related mechanistically. We do not, however, mean to suggest that the high reaction efficiency was necessarily caused by the space radiation dose received during STS-8 or STS-46.

As shown in Table 4, passive tray reaction efficiencies of a wide variety of polymer types fall within a factor of 1.5 of the average value for the group. Changes in polymer molecular structure which produce enormous changes in general physical and chemical properties produce only small changes in O-atom reactivity in LEO for this set of polymers. It should be noted that polystyrene, polybenzimidazole, and polysulfone showed reaction efficiencies somewhat lower than this group during STS-8, but still within a factor of 2 of the mean value of the EOIM-III group reported above.

In contrast, comparison of the simple saturated hydrocarbons, i.e. polyethylene, polypropylene, and polymethylpentene, with FEP Teflon™, TFE Teflon™, Tefzel™, and Kynar™ show that the presence of C-H bonds determines the reactivity of these saturated systems in which hydrogen atom abstraction is an important step in the overall mass loss reaction. Tefzel™ and Kynar™, which contain equal numbers of C-H and C-F bonds in the polymer repeat unit, show reactivity intermediate between polyethylene and the Teflons™. It should be noted that the C-H bond is much stronger in Tefzel™ and Kynar™ than it is in polyethylene suggesting that H-atom abstraction will be correspondingly more difficult. In addition, Tefzel™ and Kynar™ have only half as many C-H bonds available for direct O-atom attack.

The saturated chain hydrocarbon polymers, polyethylene, polypropylene, and polymethylpentene have the highest observed reaction efficiencies (except for polycarbonate). An important feature of the O-atom chemistry of these polymers is the production of highly reactive gas phase reaction products such as O-H radical which have been observed to produce much higher rates for the saturated hydrocarbon polymers than for aromatic polymers such as Kapton™ and Mylar™ in thermal atom systems (ref. 20). The carpet morphology produced by high velocity O-atom attack on polymers results in a higher probability that any reactive gas phase product can recontact the polymer surface and react. This may be the best explanation for the relatively high O-atom reaction rates observed for the saturated hydrocarbon polymers both on-orbit and in the laboratory.

There is no definitive kinetic isotope shift between the fully deuterated polyethylene and the other polyethylenes as predicted for high by Koontz et al. (ref. 20) for the case of orbital velocity oxygen atoms. A deuterium kinetic isotope shift has been observed for thermal energy oxygen atoms(0.04 eV) reacting with polyethylene (ref. 20). The presence of a kinetic isotope shift at thermal energies combined with the disappearance of that shift at orbital energies (5 eV) suggests that much of the atom kinetic energy is directly available to overcome the activation barriers to O-atom reactions with polyethylene and suggests that H atom abstraction is the rate limiting step of the reaction at thermal atom energies.

It is interesting to note that one previously untested (in-space) polymer, the poly(bistrifluoropropylphosphazene), shows little or no mass loss or other signs of degradation either in the passive trays or in the heated trays (see below), verifying the predictions of ground based testing (ref. 21). This polymer may have value as an elastic protective coating or as a durable elastomer for use in O-atom environments.

Temperature dependence of the O-atom reactivity of polymeric materials was an important secondary objective of EOIM-III. The results of the heated tray subexperiment are summarized in Table 6, where the data are expressed as parameters of the Arrhenius equation,

$$R = A \times e^{-(E_a/kT)}$$

where R is the rate of reaction expressed as reaction efficiency at constant atom flux, A, the pre-exponential factor, is equal to the absolute rate at high temperatures ($kT>E_a$), E_a is the activation

energy or activation barrier size, k is the Boltzman constant, and T is the temperature, the heated tray temperature in this case. The kinetic energy of the high velocity ram oxygen atoms (5 eV) does not appear in this expression and, significantly, the activation energies measured in a number of thermal atom (0.04 eV) systems are on the order of 10 times larger (ref. 20) implying that some portion of the atom kinetic energy is available for overcoming activation barriers in the rate limiting step of the process, as was suggested in the discussion of kinetic isotope shifts in polyethylene discussed above.

SUMMARY AND CONCLUSIONS

The primary and secondary data objectives of the EOIM-III flight experiment were achieved during STS-46. The preliminary data analysis and interpretation presented in this paper demonstrate that the overall objectives of EOIM-III can be achieved with more detailed analysis of the flight data and flight samples. In a qualitative sense, those overall objectives have already been achieved and demonstrated. More accurate Runflux calculations combined with a complete postflight calibration check of the mass spectrometer will be completed in the near future, permitting quantitative completion of the EOIM-III objectives.

The EOIM-III materials reactivity measurements have, in combination with the mass spectrometer data, increased our confidence in the existing materials reactivity data base as well as expanding that data base significantly by producing: (1) reaction efficiency data on previously untested polymers showing remarkable durability, (2) activation energy (temperature dependence) data on a range of polymers, and (3) new reaction mechanism data which confirms the fundamental importance of chemistry in understanding the reactivity of materials in the LEO environment. These results suggest that thermal energy O-atom Arrhenias parameters can be used to estimate orbital energy O-atom reactivities in some cases, thereby improving our confidence in low cost thermal atom screening tests. In addition, the EOIM-III data provide a foundation for validating high quality laboratory simulations of the LEO environment as well as supporting materials test method development.

In addition, the mass spectrometer data provide a unique resource for improving our understanding of vehicle-environment interactions in the LEO environment. Direct measurements of ambient neutral and ionic species sampled with various vehicle attitudes and mass spectrometer orientations permit direct verification of induced environment models. More complete results of EOIM-III will be published as data reduction and analysis is completed.

REFERENCES

1. Jursa, A.S., editor: "Handbook of Geophysics and the Space Environment." Air Force Geophysics Laboratory, United States Air Force, 1985 (National Technical Information Service).

2. Griffin, M.D., and French, J.R.: "Space Vehicle Design." Chapter 3, Environment; AIAA, Washington, DC, 1991.

3. Hedin, A.E.: "A Revised Thermospheric Model Based on Mass Spectrometer and Incoherent Scatter Data: MSIS-83." J. Geophys. Res., vol. 88, No. 10, 1983, pp. 170–188.

4. Visentine, J.T., Leger, L.J., Kuminecz, J.F., and Spiker, I.K.: "STS-8 Atomic Oxygen Effects Experiment." AIAA paper AIAA-85-0415, 23rd Aerospace Sciences Meeting, January 14–17, 1985, Reno, NV.

5. Zimcik, D.G., and Magg, C.R.: "Results of Apparent Oxygen Reactions with Spacecraft Materials During STS-41G." J. Spacecraft, vol. 25, No. 2, March–April 1988.

6. Koontz, S., King, G., Dunnet, A., Kirkendahl, T., Linton, R., and Vaughn, J.: "The International Telecommunications Satellite (INTELSAT) Solar Array Coupon (ISAC) Atomic Oxygen Flight Experiment: Techniques, Results and Summary." Materials in a Space Environment, September 1991, Tolouse, France, Publisher, Centre National D'Etudes Spatiales, Tolouse, 1992.

7. Visentine, J.T., comp.: "Atomic Oxygen Effects Measurements for Shuttle Missions STS-8 and STS-41G, Volumes I to III." NASA Technical Memorandum 100459.

8. Leger, L.J., Visentine, J.T., and Santos-Mason, B.: "Selected Materials Issues Associated With Space Station *Freedom.*" SAMPE Quarterly, vol. 18, No. 2, January 1987, pp. 48–54.

9. Mende, S.B., Swenson, G.R., Clifton, K.S., Gause, R., Leger, L. J., and Garriot, O. K.: "Space Vehicle Glow Measurements on STS-41D." J. Spacecraft, vol. 23, No. 2, March–April, 1986, pp. 189–193.

10. Banks, P.M., and Williamson, P.R.: "Space Shuttle Glow Observations." Geophys. Res. Lett., vol. 10, 118, 1983.

11. Swenson, G.R., and Meyerott, R.E.: "Spacecraft Ramcloud Atom Exchange and N_2 LBH Glow," Geophys. Res. Lett., vol. 15, No. 3, pp. 245–248.

12. Hedin, A.E.: "MSIS-86 Thermospheric Model." J. Geophys. Res., vol. 92, No. A5, May 1987, pp. 4649–4662.

13. Visentine, J.T., and Leger, L.J.: "Materials Interactions With the Low-Earth Orbit Environment: Accurate Reaction Rate Measurements." AIAA paper AIAA 85-7019, AIAA Shuttle Environments and Operations II Conference, November 1985, p. 168.

14. Hunton, D.E., Trzcinski, E., Wlodyka, L., Federico, G., and Dorian, J. 1Lt, USAF: "Quadrupole Ion-Neutral Mass Spectrometer for Space Shuttle Applications." AFGL-TR-86-0084, Environmental Engineering Paper No. 953.

15. Koontz, S.L., Cross, J.B., and Lan, E.: "Characterization and Calibration of the EOIM-III Flight Mass Spectrometer in a High Velocity Atom Beam." Materials Degradation in Low-Earth Orbit (LEO), Srinivasan, V., and Banks, B. A., eds., The Materials, Metals and Minerals Society, 1990.

16. Leger, L.J., Visentine, J.T., and Schleising, J.A.: "A Consideration of Atomic Oxygen Interactions with Space Station." AIAA-85-0476, AIAA 23rd Aerospace Sciences Meeting, January 14–17, 1985, Reno, NV.

17. Santeler, D., and Warren, D.: "Computer Solution to Chamber-Gas Fractionation During Pumpdown." J. Vac. Sci. Technol. A11(1), January–February 1993, pp. 231–239.

18. Koontz, S.L., Leger, L.J., Albyn, K.A., and Cross, J.: "Ultraviolet Radiation/Atomic Oxygen Synergism in Materials Reactivity." J. Spacecraft, vol. 27, No. 5, May–June 1990, pp. 346–348.

19. Steigman, A.E., Brinza, D.E., Anderson, M.S., Minton, T.K., Laue, E.G., and Liang, R.H.: "An Investigation of the Degradation of Fluorinated Ethylene Propylene (FEP) Copolymer Thermal Blanketing Materials Aboard LDEF and in the Laboratory." JPL publication 91-10, May 15, 1991, Jet Propulsion Laboratory, Pasadena, CA.

20. Koontz, S.L., Albyn, K., and Leger, L.J.: "Atomic Oxygen Testing with Thermal Atom Systems: A Critical Evaluation." J. Spacecraft, vol. 28, No. 3, May–June 1991, pp. 315–323.

21. Fewell, L., and Fenney, L.: Polymer Comm., vol. 32, No. 13, 1991, pp. 393–396.

Table 1. STS-46 AO fluence summary.

	Orbiter Altitude, Nmi	Exposure Attitude	Exposure Duration, (H)	AO Fluence, Atoms/cm^2
• EURECA Deployment & Checkout	231	-ZSI	11.27	3.29×10^{17}
• EURECA Release & Station Keep	231	-ZVV	5.28	6.45×10^{17}
• EOIM-3 Flight Operations	124	-ZVV	42.25	2.06×10^{20}
AO Total Fluence:			58.80	2.07×10^{20}

Table 2. EOIM-III XPS survey results.

- X-ray photoelectron spectroscopy: Pre- and postflight surface contamination measurements
  - Payload hardware and some sample materials were analyzed by XPS (KSC/Dr. Orlando Melendez)
  - No evidence of fluorocarbon contamination (<0.5 atom percent fluorine) on nonfluorocarbon samples tested
  - Surface silicon was detected as silicate
  - Polymer samples: O atom percent on covered portions; 0.8 to 2.39 atom percent on AO exposed surfaces
  - For exposed hardware, average is 5.95 (±3.8) atom percent SI, pure SiO_2 is 30 atom percent Si. Exposed hardware samples not corrected for natural Si content.
- Conclusion: Surface contamination nominal.

Table 3. RUNFLUX ambient versus mass spec. ram/wake densities.

Gas	alt. (nmi.)	Mass spec. ram (atoms or molecules per cc)	Mass spec. wake (atoms or molecules per cc)	Ave. MSIS-86 (atoms or molecules per cc)
O	231	3.2×10E9	———	5.0×10E7
H_2O		2.8×10E9	———	0.0
N_2		3.0×10E9	———	2.3×10E6
O_2		9.3×10E8	———	5.5×10E4
CO_2		8.7×10E8	———	0.0
O	160	6.3×10E10	5.0×10E8	3.6×10E8
H_2O		5.4×10E9	3.9×10E8	0.0
N_2		5.7×10E10	6.4×10E8	1.6×10E7
O_2		3.9×10E10	1.8×10E8	3.9×10E5
CO_2		7.8×10E9	2.1×10E8	0.0
O	124	1.7×10E11	4.5×10E8	2.2×10E9
H_2O		2.2×10E9	3.6×10E8	0.0
N_2		3.6×10E11	0.0	4.9×10E8
O_2		2.5×10E11	0.0	6.3×10E7
CO_2		3.3×10E9	0.0	0.0

Table 4. Reaction efficiencies* (RE) ($\times 10^{24} cm^3$ /atom)
1-inch samples: passive trays.

POLYMER	RE (EOIM-III)	RE (STS-8)
Eymyd-F Polyimide (Ethyl Corp.)	3.0	
CR-39 Polycarbonate	7.0	6.0
LCP 4100 (liquid crystal, DuPont)	3.7	
XYDAR (liquid crystal, Amoco Chemical)	3.3	
VICTRIX PEEK (ICI)	3.9	
POLYMETHYLPENTENE	6.1	
HDPE EMH6606 (Phillips)	4.3	3.7
"ROUND ROBIN" POLYETHYLENE	5.1	
DEUTERATED (D4) POLYETHYLENE	4.3	
MYLAR A (DuPont)	4.4	3.9
"ROUND ROBIN" KAPTON (DuPont)	3.5	3.0
POLYPHOSPHAZENE; X-221 (Ethyl Corp.)	$<5\times10^{-2}$	
EYPEL (R) – F GUM; X-222 (Ethyl Corp.)	$<5\times10^{-2}$	

* Reaction efficiencies calculated from sample weight loss and preliminary MSIS-86 AO fluence. Samples were vacuum-baked for 48 h prior to weighing both before and after flight.

Table 5. Reaction efficiencies* (RE) ($\times 10^{24} cm^3$ /atom)
1-inch samples: passive trays.

HALOCARBON POLYMER	RE (EOIM-III)	RE (STS-8)
TEFZEL BLUE (SSF WP-4, Raychem))	1.3	
TEFZEL WHITE (SSF WP-4, Raychem)	1.0	
POLYCHLOROTRIFLUOROETHYLENE	1.0	
"ROUND ROBIN" FEP TEFLON	5.6×10^{-2}	$<3\times10^{-2}$
PTFE	6.5×10^{-2}	
KYNAR (Penwalt)	1.4	
TEFZEL (DuPont)	1.0	
TEDLAR (DuPont)	4.3	3.2
ACLAR 33C (Allied)	1.1	
HALAR (Allied)	2.2	

* Reaction efficiencies calculated from sample weight loss and preliminary MSIS-86 AO fluence. Samples were vacuum-baked for 48 h prior to weighing both before and after flight.

Table 6. Polymer arrhenius activation parameters.

POLYMER	A (cm^3/atom$\times 10^{24}$)	E_a (eV)
Kapton (polyimide)	7	0.02
XYDAR (liq. crystal)	22	0.05
CR-39 polycarbonate	30	0.04
LCP 4100 (liq. crystal)	20	0.04
EYMIDE-F (fluroine substituted polyimide)	9	0.03
Mylar	7	0.05
Tefzel	2	0.04
HDPE (polyethylene)	13	0.06

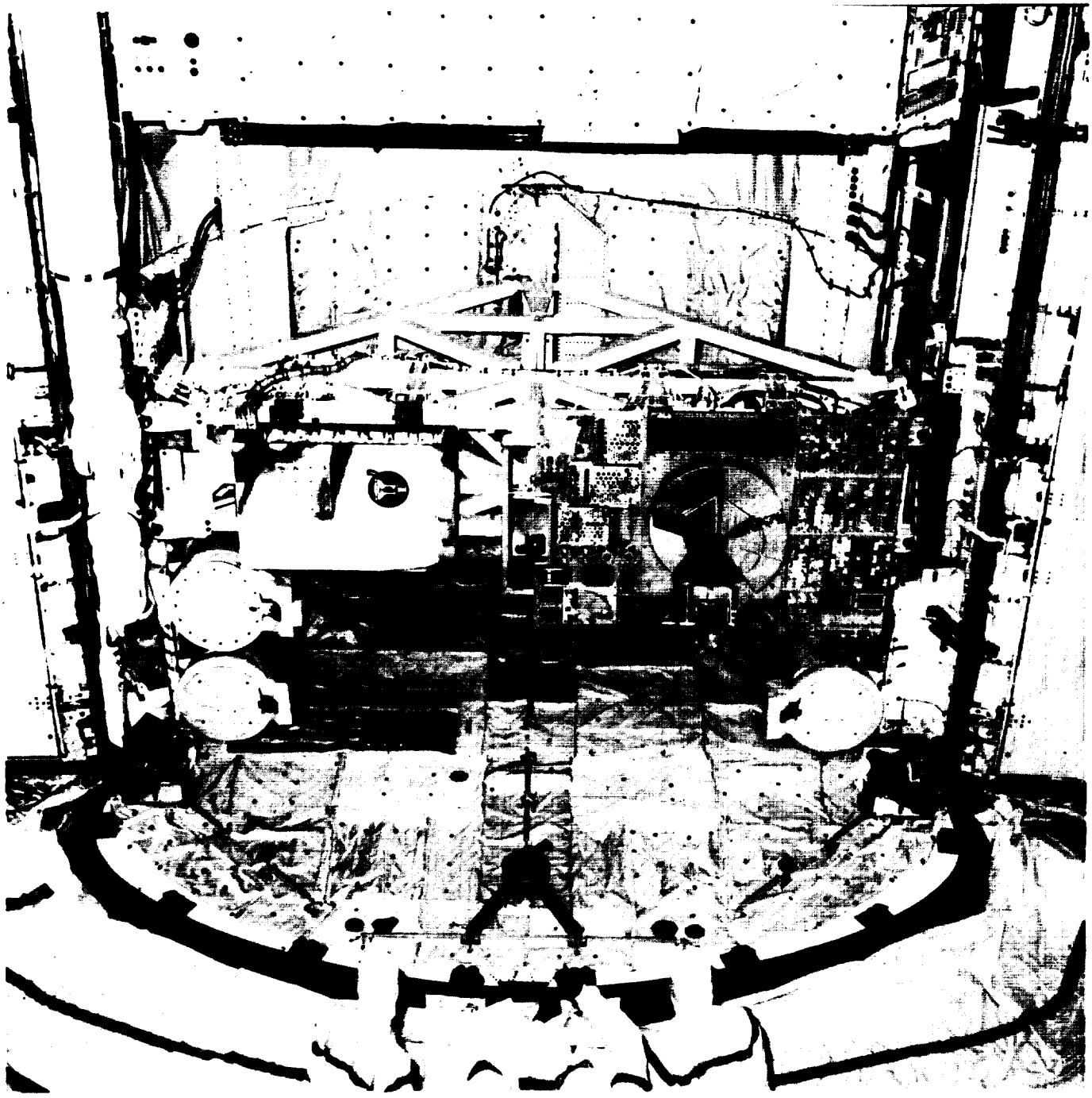

Figure 1. Launch pad close-out photo of EOIM-III (left) and TEMP-2A (right). The aft cargo bay bulkhead is visible at the top of the photo.

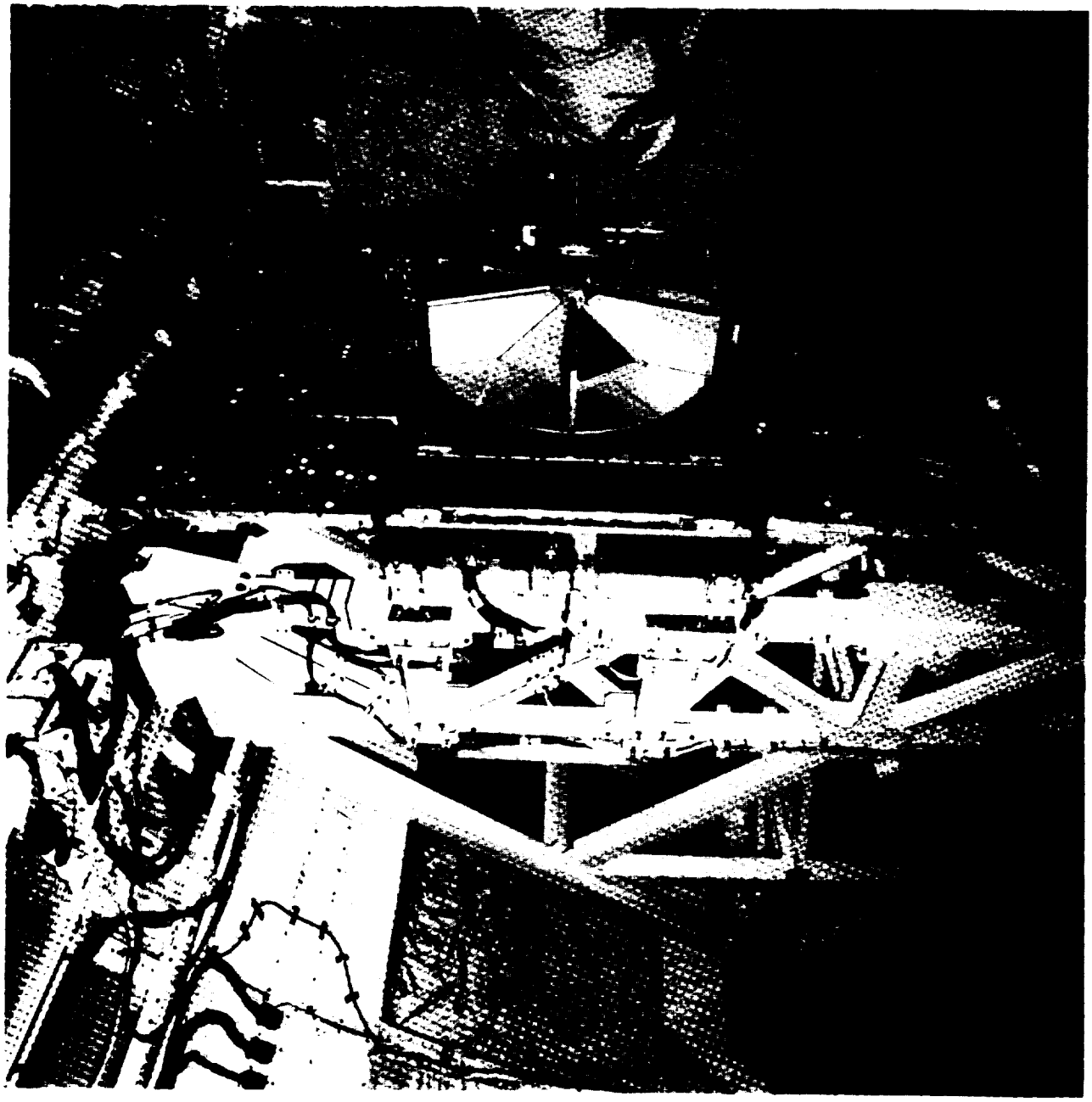

Figure 2. Launch pad close-out photo of EOIM-III payload looking toward the aft cargo bay bulkhead, i.e. the forward edge of the payload nearest the viewer in this photo.

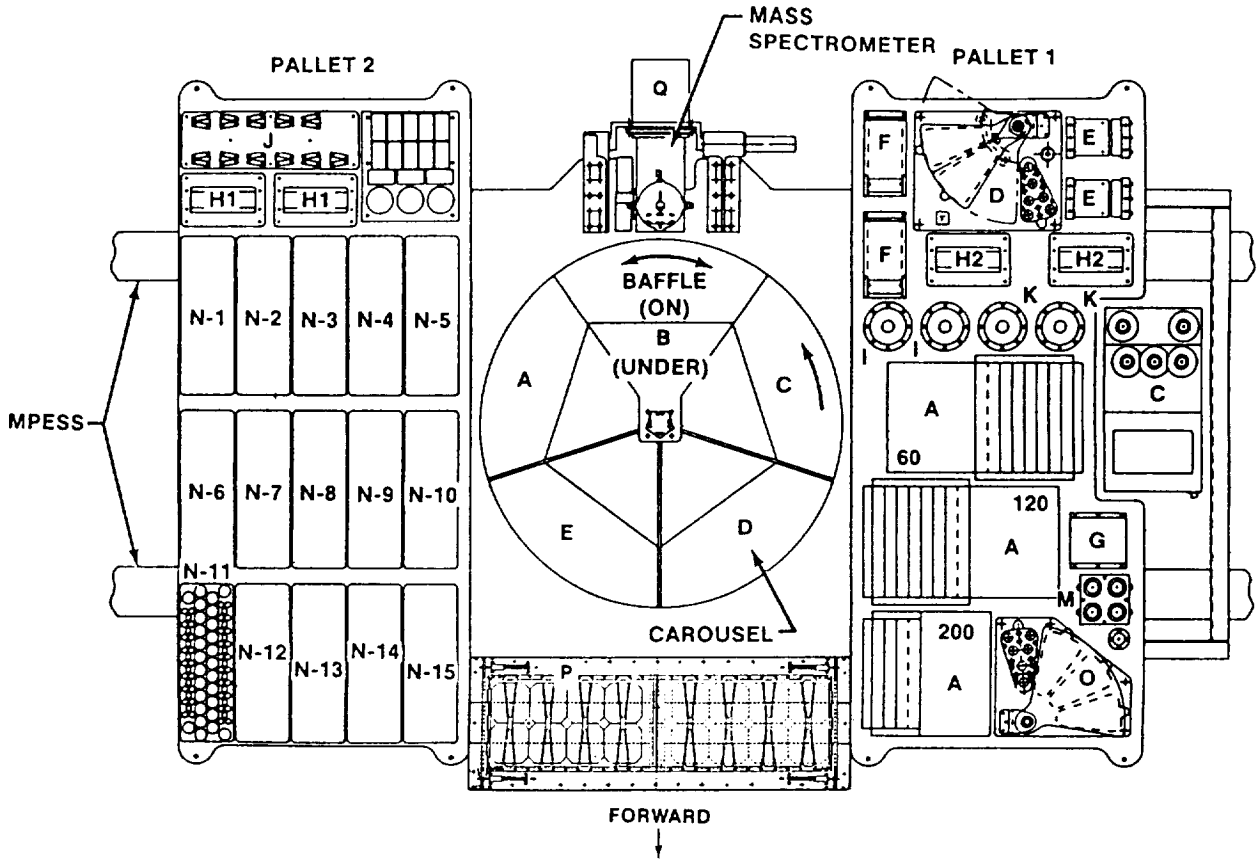

ATOMIC INTERACTION EXPERIMENTS:

A - HEATED PLATE (JSC), 3EA
B - ATOM SCATTERING EXPERIMENT (UAH), 1EA
C - ENVIRONMENT MONITOR PACKAGE (GSFC), 1EA
D - SOLAR UV EXPERIMENT (JSC), 1EA
E - STATIC STRESS FIXTURE (MSFC), 2 EA
F - UNIFORM STRESS FIXTURE (MSFC), 2 EA
G - ATOMIC OXYGEN MONITOR (MSFC), 1 EA
H1 - COMPOSITE STRESS FIXTURE(LaRC), 2EA
H2 - COMPOSITE STRESS FIXTURE (JSC), 2 EA
I - SCATTEROMETER (JPL), 2 EA
J - MECHANICAL STRESS FIXTURE (LeRC), 11 EA
K - REFLECTOMETER (LeRC), 2 EA
L - PINHOLE CAMERA (LeRC), 1 EA
M - SCATEROMETER(AEROSPACE CORP.), 1EA
N - PASSIVE SAMPLE CARRIERS, 15 EA
O - VARIABLE EXPOSURE TRAY, 1EA
P - FREEDOM ARRAY MATERIALS EXPOSURE EXPERIMENT(LeRC), 1 EA
Q - QUADRUPLE MASS SPECTROMETER, 1 EA

Figure 3. A line drawing of the EIOM-III payload identifying the various features in Figures 1 and 2. The forward edge of the payload is at the bottom of the line drawing.

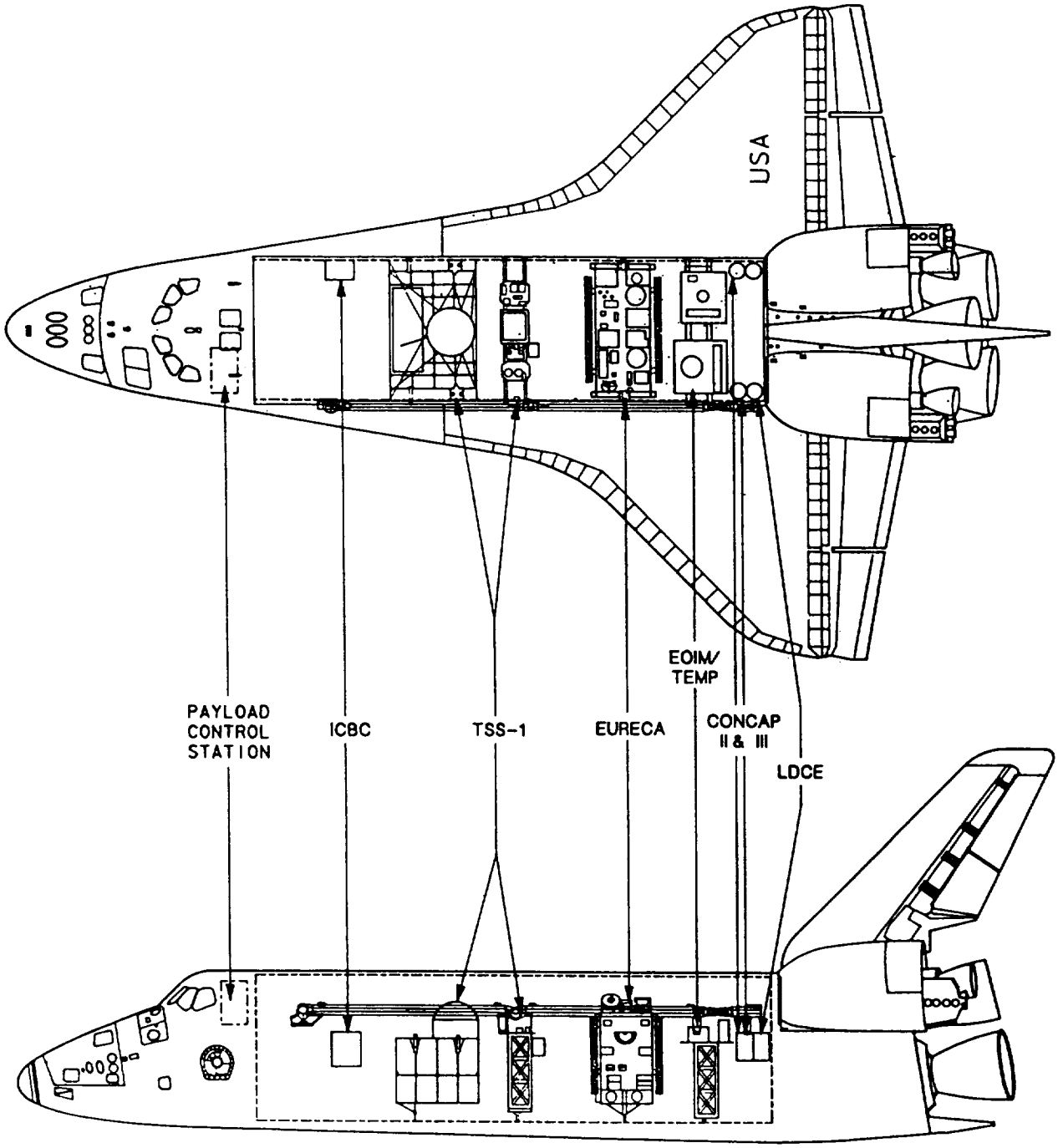

Figure 4. Cargo bay configuration of *Atlantis* for STS-46.

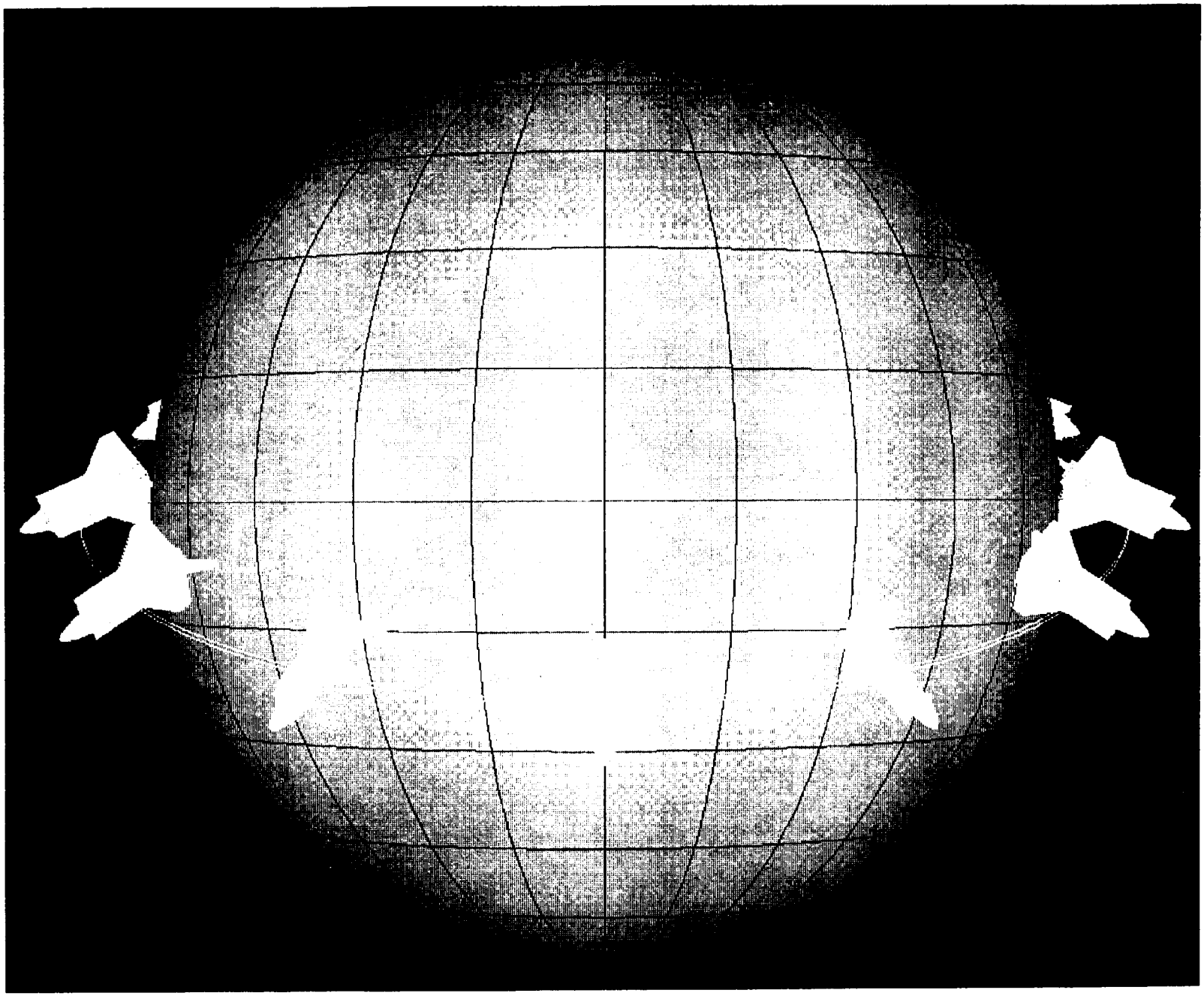

Figure 5. Orbital path and attitude of *Atlantis* during the 42-h EOIM-III period. The Sun-Earth vector is perpendicular to the center of the figure.

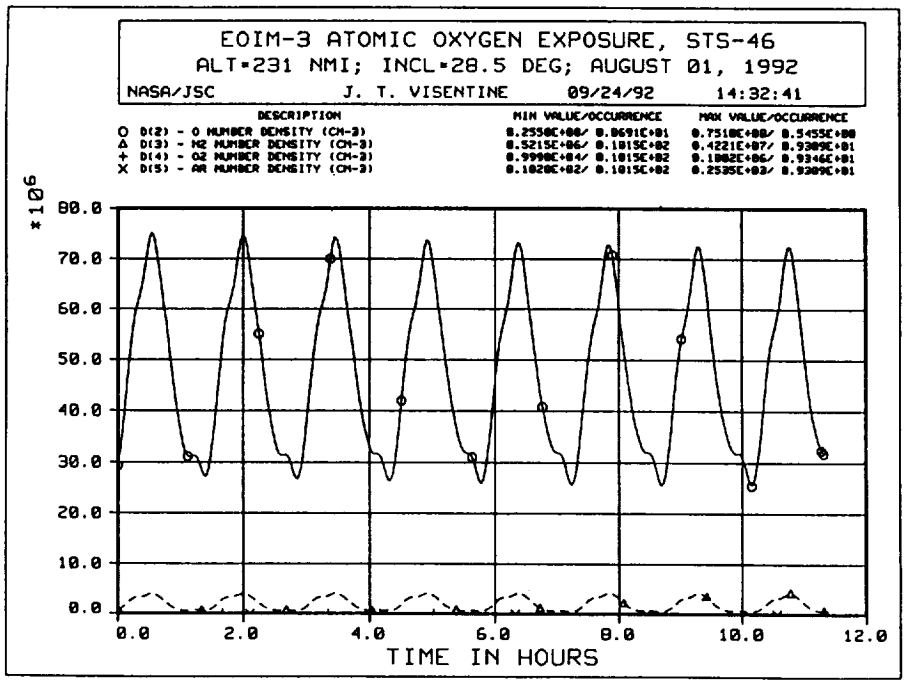

Figure 6. MSIS-86 predictions of O-atom density at 221 nmi.

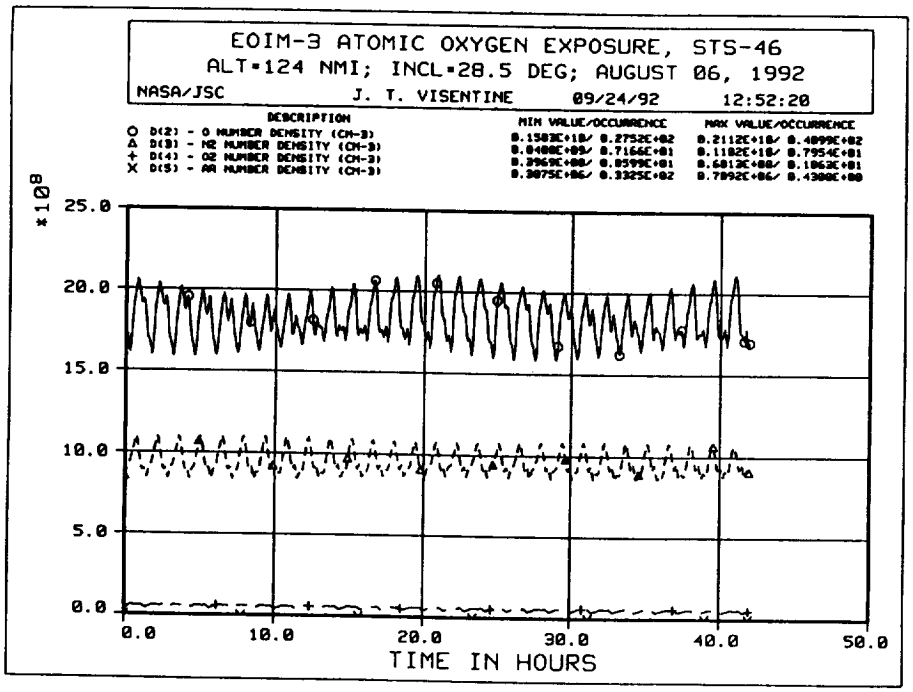

Figure 7. MSIS-86 predictions of O-atom density at 123 nmi.

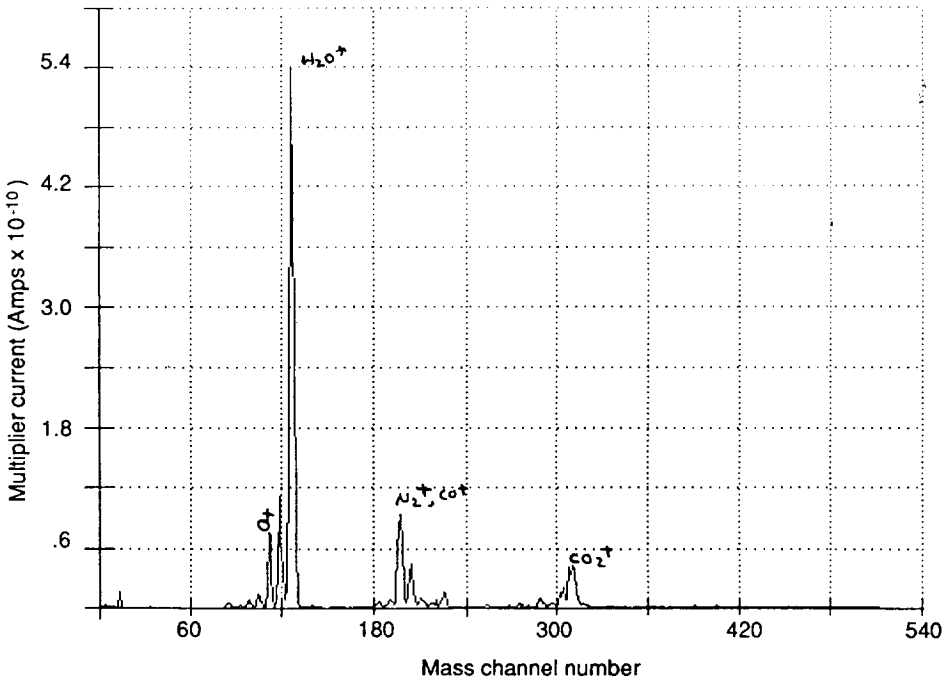

Figure 8. A typical neutral (mode 2) ram-flux mass spectrum taken at 231 nmi as part of the ambient density data set shown in Figure 6. *Atlantis* is in the -ZVV attitude; the mass spectrometer orientation is -Z, as in Figure 2.

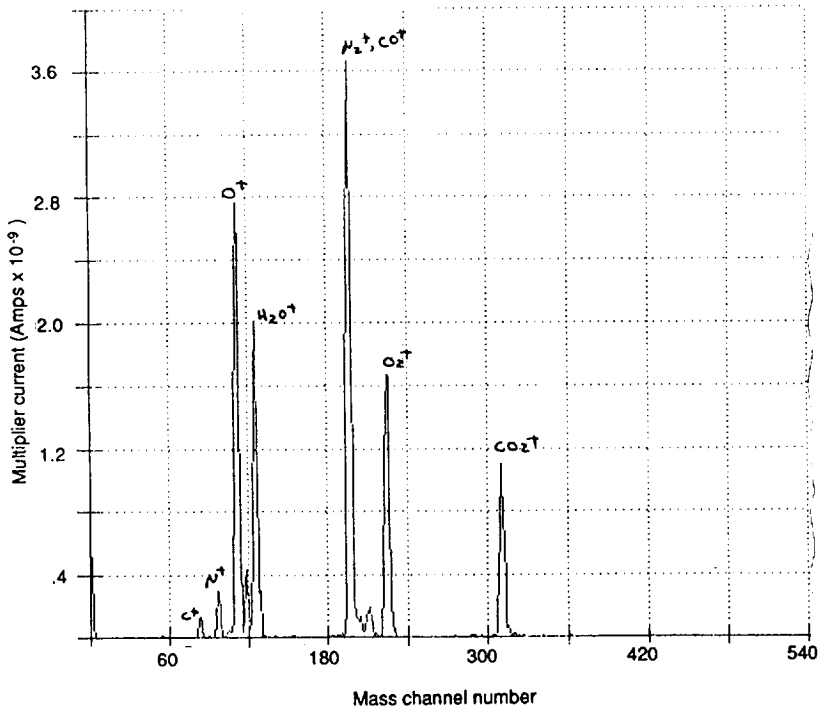

Figure 9. A typical neutral (mode 2) ram-flux mass spectrum taken at 160 nmi. *Atlantis* is in the -ZVV attitude; the mass spectrometer orientation is -Z, as in Figure 2.

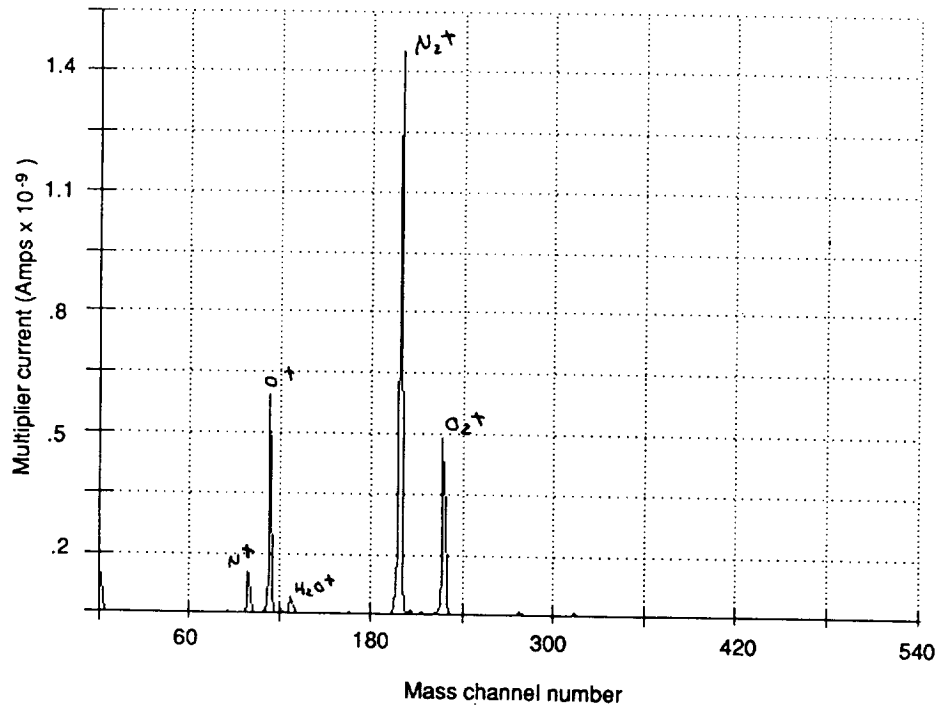

Figure 10. A typical neutral (mode 2) ram-flux mass spectrum taken at 123 nmi as part of the AO measurement sequence of the second preprogramming EOIM cycle. *Atlantis* is in the -ZVV attitude and the mass spectrometer is -Z oriented, as in Figure 2.

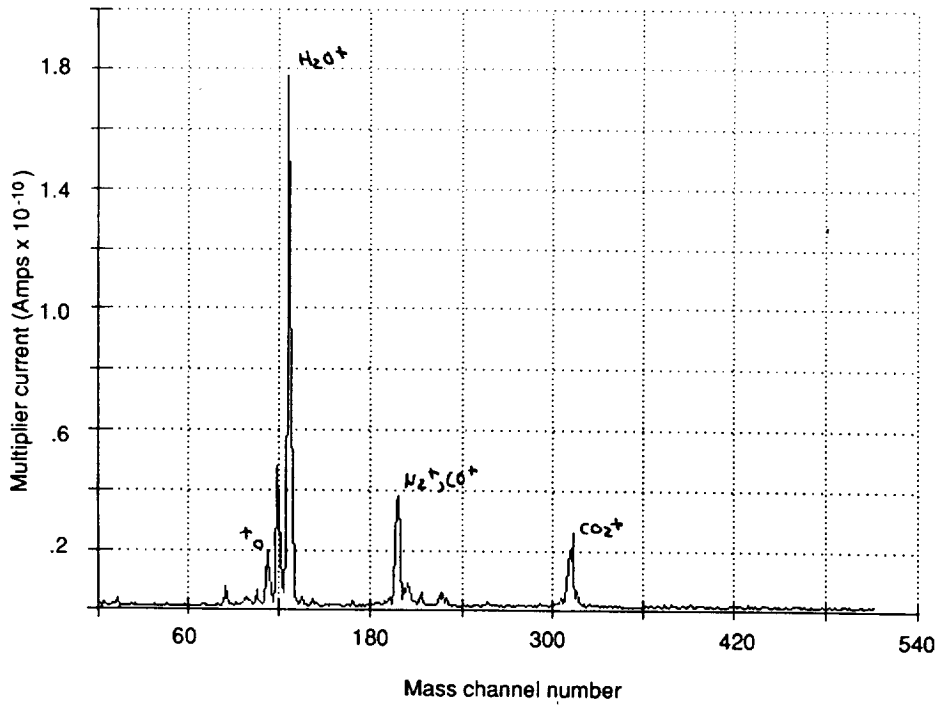

Figure 11. Deep wake mass spectrum taken with the same conditions as in Figure 9 except *Atlantis* is now +ZVV attitude (cargo bay in wake). The total pressure indicated is much lower than in the ram attitude, and the dominant mass peaks have changed.

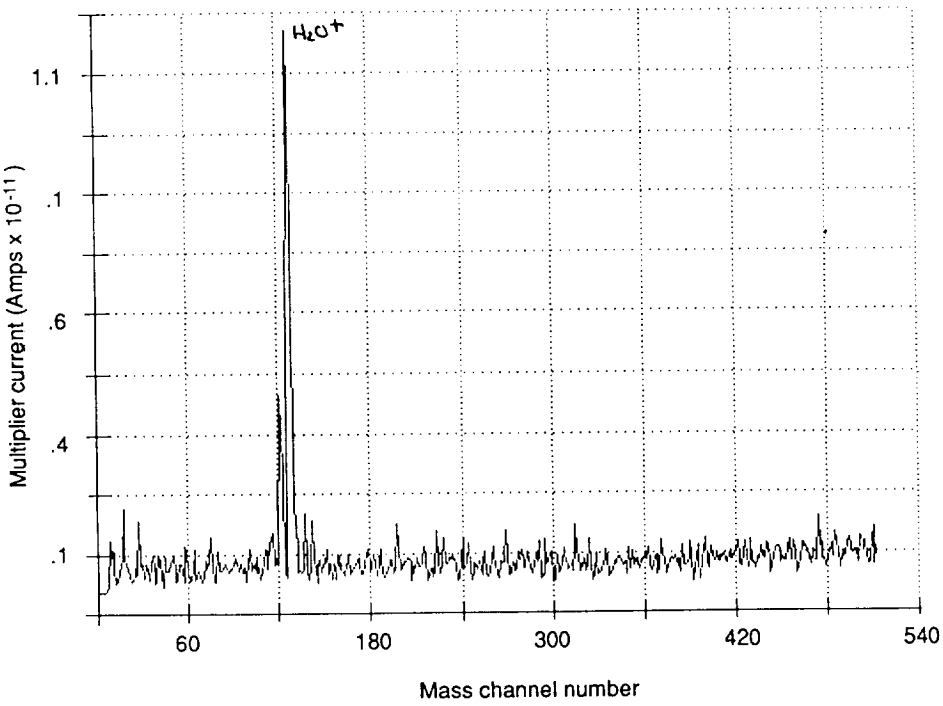

Figure 12. Deep wake mass spectrum taken with the same conditions as in Figure 10 except *Atlantis* is now +ZVV attitude (cargo bay in wake). The total pressure indicated is much lower than in the ram attitude, and the dominant mass peaks have changed.

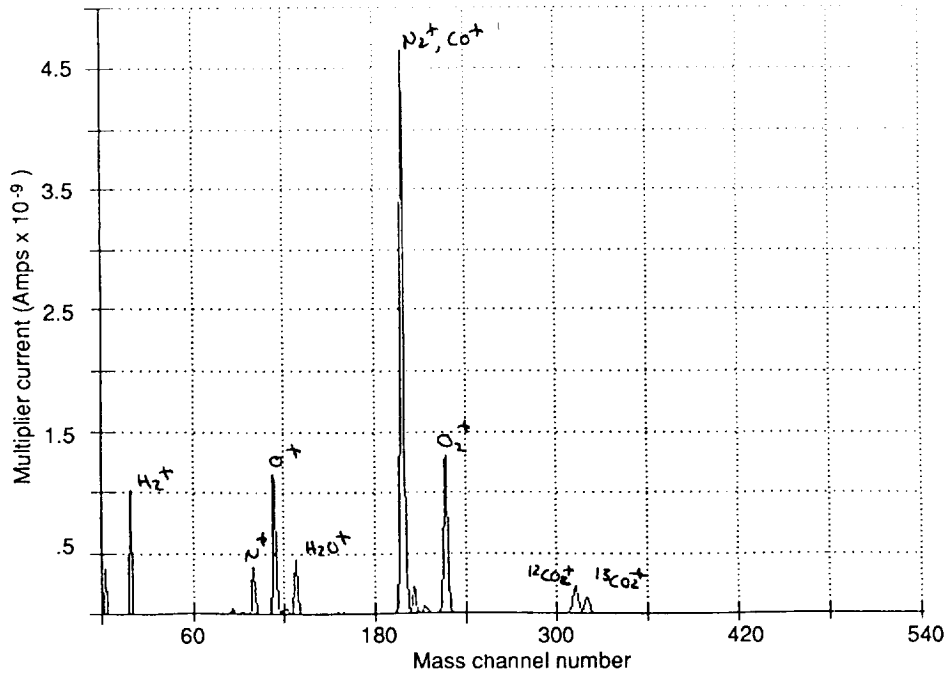

Figure 13. Mass spectrum of the gaseous induced environment above the carousel sector lined with ^{13}C Kapton. *Atlantis* is in the -ZVV attitude and the mass spectrometer is +X oriented. Direct ram ambient is incident on the carousel sector (baffle off). Isotopes labeled CO_2 and CO are both visible.

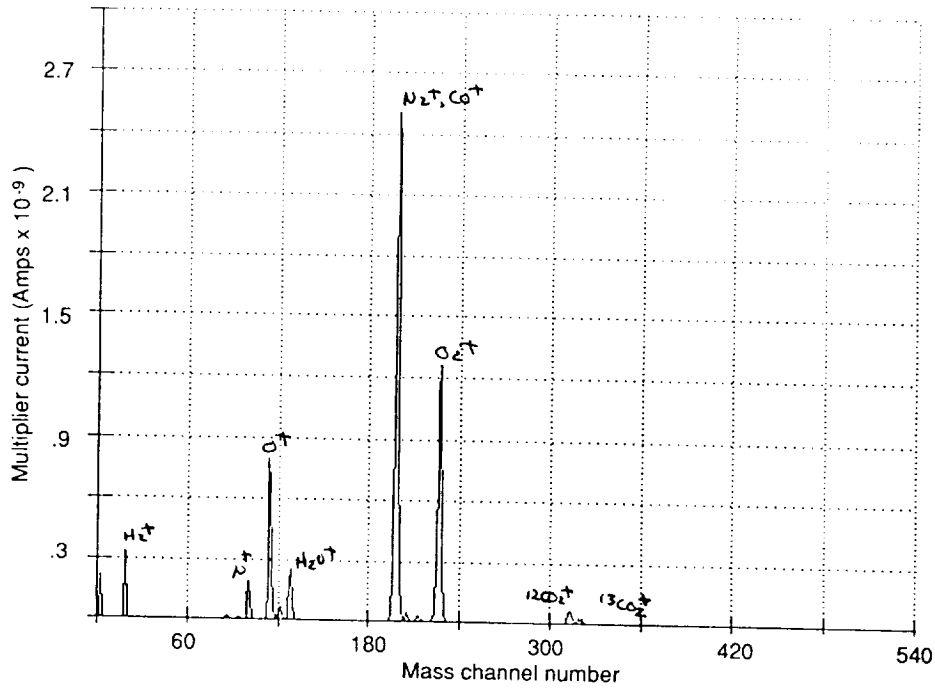

Figure 14. Mass spectrum of the induced environment in the carousel sector lined with ^{13}C Kapton™. Same conditions as Figure 13, except the baffle now covers the carousel sector under observation (baffle on). Some isotopes labeled CO and CO_2 are still visible, though the intensity is reduced.

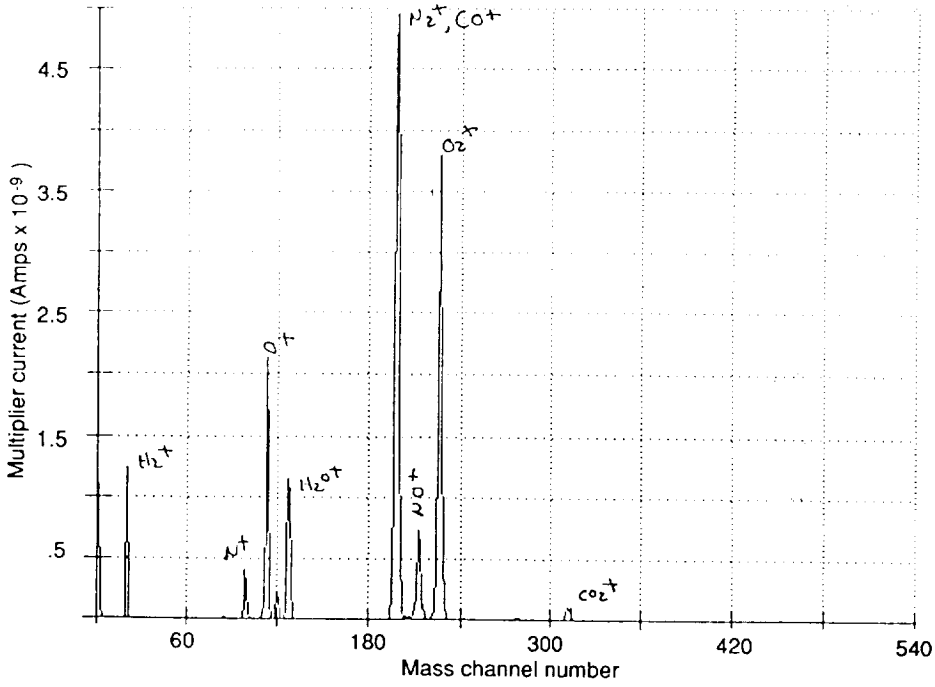

Figure 15. A typical mass spectrum taken shortly after an 80-ms pulsed firing of a -Z directed Primary Reaction Control System engine. The mass peak at 30 is believed to be NO and decays steadily after the engine pulse. This is an ambient ram mass flux spectrum, as in Figures 8 to 10.

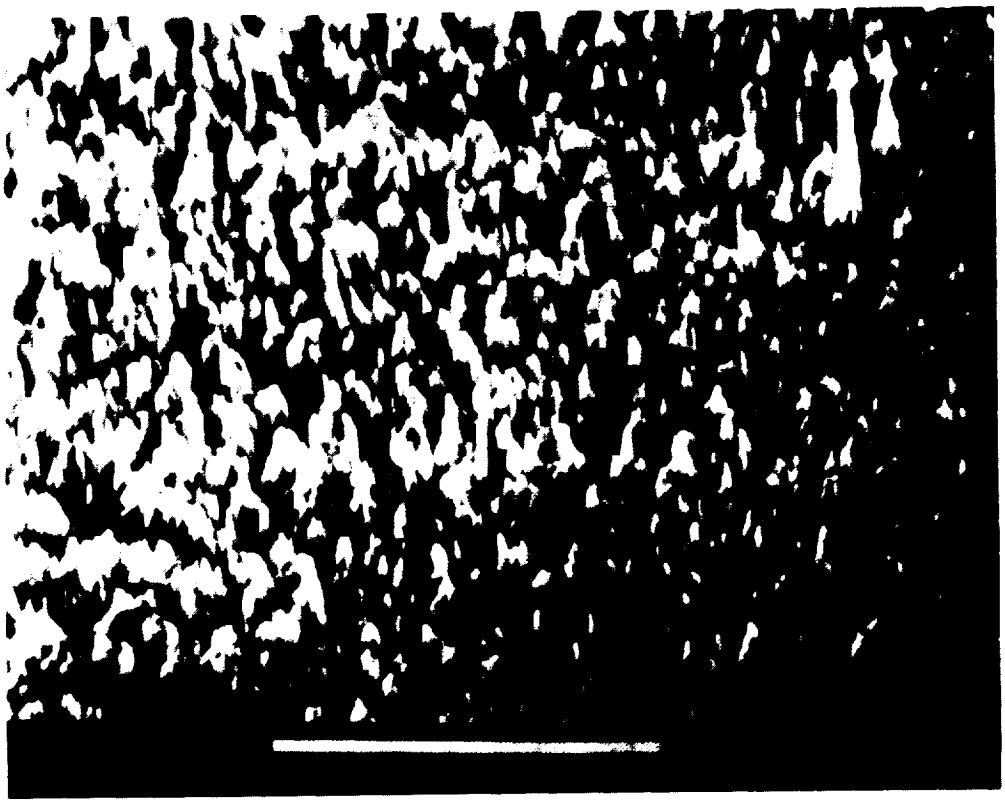

Figure 16. SEM photomicrograph of Kapton™ HN from EOIM-III passive sample tray.

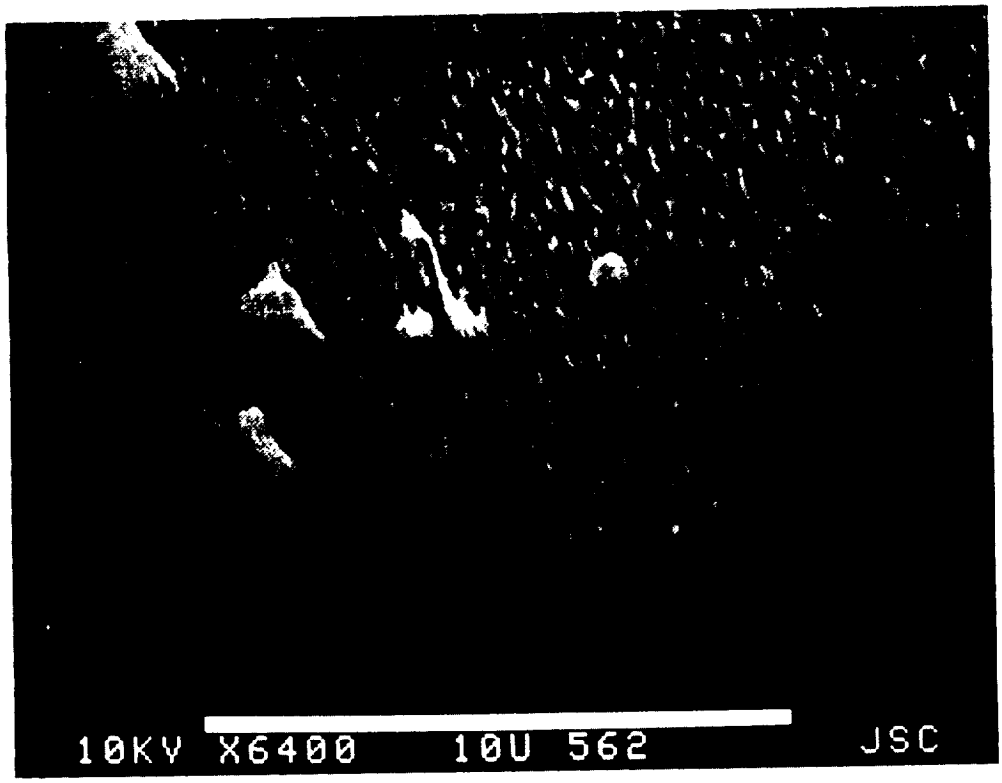

Figure 17. SEM photomicrograph of Kapton™ HN from ISAC sample tray (STS-41).

ANALYSIS OF LEADING EDGE AND TRAILING EDGE COVER GLASS SAMPLES BEFORE AND AFTER TREATMENT WITH ADVANCED SATELLITE CONTAMINATION REMOVAL TECHNIQUES

S.P. Hotaling
Rome Laboratory, OCPC
Griffiss Air Force Base, New York 13441-5700

ABSTRACT

Two samples from Long Duration Exposure Facility (LDEF) experiment M0003-4 were analyzed for molecular and particulate contamination prior to and following treatment with advanced satellite contamination removal techniques (CO_2 gas/solid jet spray and oxygen ion beam). The pre- and post-cleaning measurements and analyses will be presented. The jet spray removed particulates in seconds. The low-energy reactive oxygen ion beam removed 5,000 Å of photo polymerized organic hydrocarbon contamination in less than 1 hour. Spectroscopic analytical techniques were applied to the analysis of cleaning efficiency including: Fourier transform infrared, Auger, x-ray photoemission, energy dispersive x ray, and ultraviolet/visible. The results of this work suggest that the contamination studied here was due to spacecraft self contamination enhanced by atomic oxygen plasma dynamics and solar UV radiation. These results also suggest the efficacy for the jet spray and ion beam contamination control technologies for spacecraft optical surfaces.

INTRODUCTION

Today, satellite contamination is kept within specification during production, assembly, and storage by clean rooms, solvent wipes, inert gas/air purges, and vacuum bakeout. Although these techniques have proven acceptable for launching "clean" satellites (level 1000 typical), the combined effects of the space environment lead to increased contamination levels once deployed (ref. 1,2). LDEF was initially launched with MIL-STD-1246B Level 2000C cleanliness. This is considered clean by industry standards today, but post-recovery LDEF analysis showed over 1 lb of molecular contaminants notwithstanding particulates (ref. 3). LDEF experiments provide a unique window into the contamination effects on a large variety of spacecraft materials, all exposed to the same low-Earth orbit (LEO) environment for the same amount of time. Thus, LDEF really is a "treasure trove of data" as described by S.A. Little in 1991 (ref. 4).

In this paper, the results of utilizing the CO_2 jet spray and oxygen ion beam contamination removal techniques for the cleaning of LDEF contaminant species will be discussed. The overall conclusion of the paper is as follows: Indeed the proper choice of spacecraft materials and prelaunch cleanliness is important, but the physical realities of the space environment necessitate an on-orbit contamination mitigation philosophy which is potentially implementable using the contamination control techniques described herein.

PRECLEANING SAMPLE ANALYSIS

Optical microscopy was used to obtain sample morphological features. EDX, Auger, ESCA, and FT-IR were used to obtain chemical and compositional information. UV/Vis spectrophotometry provided the optical properties for the samples. Computer image analysis was utilized to analyze the microscopy data. After contamination removal, the same techniques were applied to the samples (ref. 5).

Two solar cell cover glass samples from the LDEF experiment M0003-4 were analyzed in this study. Sample No. L3-IV-4-14-52 was positioned on LDEF tray D9 on the leading edge of the spacecraft. Sample No. T3-IV-4-14-54 was positioned on the trailing edge of the spacecraft in tray D3. The leading edge sample (henceforth, sample L) was visually different in appearance than the trailing edge sample (henceforth, sample T).

Sample L collected 5,000 Å of an organic contaminant film, scattered particulate debris, and two micrometeorite craters. Circular polarized optical microscopy showed the presence of many orders of brightly colored Newton's interference rings on sample L, as shown in Figure 1 (magnification = 13×). This figure is a montage of micrographs pasted together in a jigsaw puzzle fashion since the field of view for one micrograph at 13× was too small to contain the entire sample. Seen here are the two halves of the sample placed together. The cover glass sample was stuck to the silicon backing plate by the contaminant film which acted like an adhesive. This afforded the opportunity to analyze the effects of this photo-polymerized contaminant and contamination removal techniques on both the cover glass and crystalline silicon materials. Subsequent microscopic analysis revealed the presence of a subsurface fracture running across the crystalline silicon sample. This defect was deemed responsible for the sample becoming severed in the analysis procedure.

Sample T on the other hand collected only 50 Å of a light brown contaminant film and scattered particulate debris. This sample was not "glued" to its silicon backing plate. Sample L was in two parts, as can be seen from close examination of Figure 1. As discussed above, sample T was not found to be as heavily contaminated as sample L, and was not fixed to its crystalline silicon backing plate. In Figure 2, sample T is positioned above square graph paper (20 squares per inch). From this figure, the thin brown contaminant film is clearly seen as a contrast difference.

The physical condition of these samples was anti-intuitive. Since the leading edge sample experienced a higher atomic oxygen (AO) fluence than the trailing edge of the spacecraft (ref. 6), one would expect a fairly clean-contaminant free surface. It is possible that such a surface would even be slightly eroded due to interaction with the reactive flux. During recovery, the AO fluence for sample L was 8.74×10^{21} atoms-cm^{-2}. The trailing edge sample was somewhat shielded from this AO flux, having an AO fluence of 1.3×10^{17} atoms-cm^{-2}. Intuitively, the author expects this to imply a thicker contaminant deposition on the trailing edge relative to the leading edges, which was not the case for the two samples examined in this work. The author is still speculating as to the reasons for this contamination density inversion.

FT-IR spectroscopy was performed with a Biorad FTS-40 spectrophotometer. The FT-IR spectrum of the contaminant film taken from sample L's interferences fringes on the silicon side of the sample is shown in Figure 3. Figures 4a and 4b show that the FT-IR spectrum of nylon 6:6 is present in

the contaminant film. Another expansion of the hydrocarbon region for the sample is shown in Figure 5a. In Figure 5b, the FT-IR spectrum of polyacetal Delrin 500 plastic is shown. Figures 4 and 5, when correlated with Figure 3, indicated that the major constituents of the contaminant film are nylon 6:6 and Delrin 500.

ESCA and Auger microprobe analyses were performed at several points in and around the micrometeorite crater shown in Figure 6. The seven numbered positions in Figure 6 indicate the Auger microprobe beam positions. The Auger electron spectrum for the crater is shown in Figure 7. The seven sampling positions did not offer strikingly different data for chemical proportion. The chemical composition of the film is given in Table 2.1 as atomic percentages. The atomic percentage values calculated from the Auger spectra were commensurate with those calculated from ESCA, giving confidence in the identification of the chemical composition of the contaminant.

A lower magnification view of the micrometeorite crater of Figure 6 is shown in the SEM photo of Figure 8. In Figure 8, the interference fringes are clearly visible as dark bands. The SEM photo of Figure 8 indicates that some of the contaminant film is starting to peel off the substrate, as can be seen by the small area of film at about 2 o'clock referenced from center, the position of the micrometeorite crater (see arrow). Also clear in this figure are several pieces of particulate ranging in size from 0.2 mm down to probably the tens of microns spatial dimension. EDX analysis of these particles identified them as mostly metallic: copper, zinc, tin, aluminum, and silicon.

CONTAMINATION REMOVAL

Gas/Solid Jet Spray Technique

The gas/solid jet spray was used to remove particulate contamination. The CO_2 jet spray is shown in Figure 9. The jet spray has been described in the literature (ref. 1, 2), but may be simply described as a particle removal process which exploits momentum transfer from incident snow flakes to particulates adhering to the surface through van der Waal's forces (first and second order). The energy/momentum transferred to the adhered particle breaks these surface potential forces, and the "free" particle is entrained in the gas stream and carried away from the surface. The mixture of solid/gas in this process is very important for the removal of submicron particles (ref. 1), which are not removed by high pressure gas and liquid streams due to the gas/surface boundary layer's "insulating" action.

Ion Beam Technique

The molecular film was removed by reactive ion etching using a beam of oxygen ions and electrons from a Hughes helicon wave source (HWS) shown in Figure 10. The output beam contains oxygen ions and neutral atoms as well as electrons. The HWS also has a UV radiation component. The effects of these species upon contaminant removal is under investigation. The ion cleaning experimental parameters are as follows. The ion energy was varied between 12 and 45 eV (average). The ion flux densities varied between 550 and 1,300 $\mu A/cm^2$ (average) as measured by a Faraday cup. The plasma was operated at 165 mHz with a power of 10 to 20 W. The oxygen flow rate was measured to be 10 sccm using an Omega Engineering gas flow meter (FMA-5601). Chamber partial pressures were monitored by

a VG Scientific Micromass 560 mass spectrometer to be: oxygen, 3×10^{-5} torr; water, 3×10^{-5} torr; and nitrogen, 5×10^{-5} torr. Other species were present in the chamber registering partial pressures of less than 1×10^{-8} torr, and, as such, were of no consequence to this work.

POSTCLEANING SAMPLE ANALYSIS

Figure 11 shows a circular polarized light micrograph of a heavily contaminated region of sample L. The region of the sample to the left of the circular arc (AB) was masked while the region to the right of the arc was exposed to 1 hour of reactive oxygen ions. Comparison with Figure 1 shows that the sample was cleaned by the reactive oxygen ion beam. Figure 12 is a Nomarski photomicrograph (200×) of the region surrounding the crater before ion beam treatment. The same region at the same microscopic settings is shown in Figure 12 after ion cleaning. Note that only the outline of the crater remains and that the contaminant film has been completely removed. The jet spray removed the particular debris, including the particles of glass chips on glass substrate.*

In 1 hour of total treatment time, the sample went from being contaminated at levels that the unaided eye could easily discern, to having a contamination level at the Nomarski microscopy threshold of detection.

Figure 14 is a fluorescence light micrograph of a masked and unmasked section of sample L after 21 minutes of ion beam cleaning. The dark (nonfluorescing) side of the micrograph shows the result of removal of 1,760 Å of molecular film. There is evidence of residual contamination (brightly fluorescing yellow matter) near the mask boundary.

The brown film of sample T (see Fig. 2) was removed with 5 minutes of reactive oxygen ions. The UV/Vis spectra for the sample before and after ion cleaning are shown in Figure 15. A UV/Vis spectrum of the very edge of the sample, which was masked during the LDEF flight and ion cleaning operations, was taken. Comparison of the spectra corresponding to this protected edge and the ion cleaned area of the sample showed conclusively that the sample was completely cleaned, within optical detection limits.

CONTAMINATION COLLECTION

The above contamination removal techniques have been shown to successfully remove spacecraft contamination, and development is underway to build small, lightweight flight qualifiable contamination removal systems. However, there remains the problem of preventing the removed contaminants

*It is well known that removal of glass chips from glass substrates after long periods of time is a most difficult problem. Additionally, there is evidence of variations in humidity of the LDEF environment during the (post STS-landing) ferry flights (ref. 3). This implies that not only did the glass chips fall on a glass surface, but that the presence of post-flight humidity enhances the probability for a very strong glass to water chemical bond which would be a very tenacious particle to remove. Of course, the interfacial geometry is very important for the removal, but it is noteworthy that not only metallic and fibrous particulates were removed by the jet spray, but also glass chips from a glass surface.

from redepositing onto the cleaned surfaces. In response to this, Rome Laboratory developed a contamination collection device. This contamination collector is capable of collecting and containing both molecular and particular contaminants throughout the spacecraft operational parameter space (temperature, vibration, radiation, vacuum, and micrometeorite environments). One embodiment of this device, the Aerogel Mesh Contamination Collector (AMCC, patent pending) is shown in the SEM of Figure 16. In the figure is shown a cross section of the AMCC with collected particulate contaminants of various sizes. In a system, the AMCC would work in conjunction with the jet spray and ion beam removal devices as shown in Figure 17. Here, the reactive ion beam removes organic particles and molecular films as the jet spray removes particles and entrails the removed species into the AMCC's waiting pores (ref. 1, 2).

CONTAMINATION CONTROL FOR SPACECRAFT APPLICATIONS

The above contamination removal techniques are being developed for autonomous operation in spacecraft applications. These data present the first results of the application of these contamination mitigation technologies to long-duration spacecraft exterior surface materials. The cleaning rates and efficiencies obtained are optimistic. This suggests further contamination control experimentation in orbital systems such as the retrievable payload carrier (RPC), as shown in Figure 18 (ref. 7). In such an experiment, small jet spray and ion beam sources would be mounted in a pallet which could be reused for both leading edge and trailing edge missions, and/or several low-cost contamination control pallets could be fabricated and flown on several RPC missions in various locations. RPC contamination experiment data would fuel a contamination control system for Space Station *Freedom.*

ACKNOWLEDGMENT

The author wishes to thank Barry Lippey and Dan Demeo of Hughes Aircraft Corporation for their kind hospitality and research collaboration on the contamination removal phase of this work. The author also wishes to thank Maurice Dumais of USAF/Rome Laboratory (Hanscom AFB) for his hospitality in the performance of the electron microscopy work. The hospitality and expertise of N.T. Castello of Oneida Research Corporation are greatly appreciated. The effort could not have been funded without the ardent support of Capt. Deidra A. Dykeman, Rome Laboratory Contamination Control Program Manager. The author wishes to thank Terry Trumble of USAF/Wright Laboratory for providing the samples used for the experiment.

REFERENCES

1. Hotaling, S.P., and Dykeman, D.A.: "An Advanced Particle Removal and Collection System." To appear in *Particles on Surfaces IV*, K. Mittal (ed.), Plenum Press, 1993.

2. Hotaling, S.P., and Dykeman, D.A.: "An Introduction to Rome Laboratory Contamination Control Technology," RL-TM-92-18, 1992.

3. Crutcher, E.R., et al.: Proceedings of the First LDEF Post-Retrieval Symposium, A.S. Levine (ed.), NSA CP-3134, 1991, pp. 101, 121, 141, 155, 847, and 861.

4. Little, S.A.: "The Role of the LDEF in the Development of Space Systems," p. 1687.

5. Hotaling, S.P.: "The Application of Jet Spray and Ion Beam Contamination Removal Techniques to Samples From the LDEF Spacecraft." To appear in Proc. High Power Optical Components Conf., NIST, 1993.

6. Bourassa, R.J., and Gillis, J.R.: "LDEF Atomic Oxygen Flux and Fluence Calculations." Boeing LDEF task NAS1-18224, Task 12 Report, January 1991.

7. Perry, A.T.: "Retrievable Payload Carrier—Next Generation LDEF." In Proc. First LDEF Post-Retrieval Symposium, A.S. Levine (ed.), NASA CP-3134, 1991, p. 1698.

Figure 1. Montage of photomicrographs (magnification: 13×) taken with circular polarized light. The thick contaminant film is indicated by the presence of several orders of Newtonian interference rings. The area defined by the "crescent moon" shape on the left side of the circle is the cover glass on top of a crystalline silicon backing plate. The contaminant film is on the top surface of the cover glass and also deposited between the cover glass and the silicon backing plate. The region to the right of the glass is the crystalline backing plate with associated contamination. It is also noteworthy that the center of the sample shows indication of a micrometeorite impact. The white rectangular area in the upper left of the figure is a "missing piece" which somehow was not photo-documented.

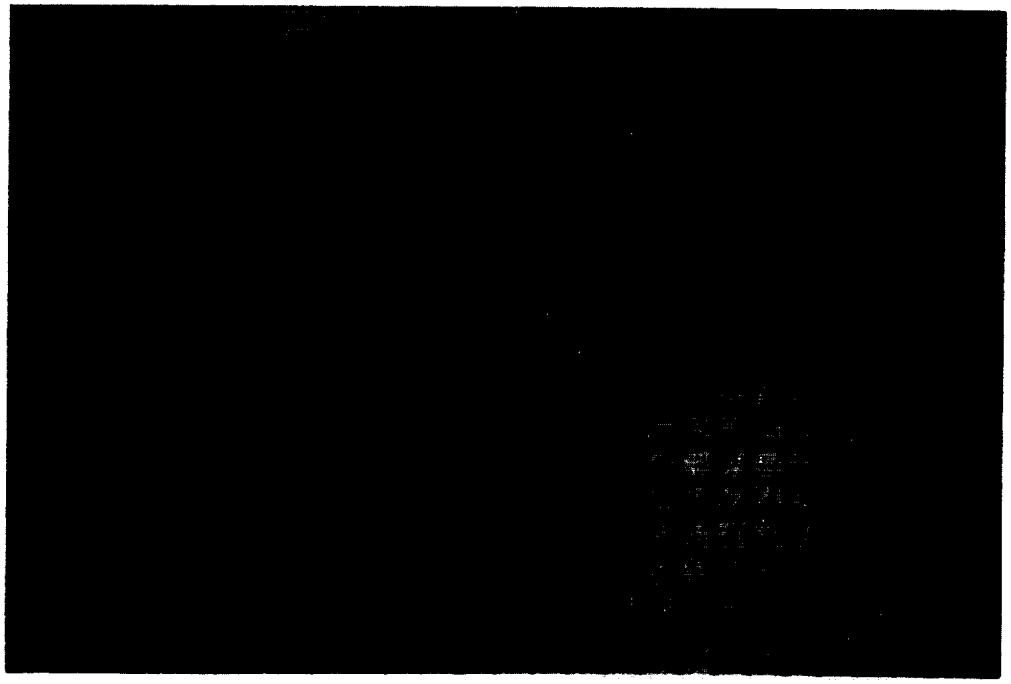

Figure 2. The trailing edge sample viewed with circular polarized light at a magnification of 3×. The sample is positioned over a piece of graph paper (20×20 squares/inch). The contaminant film on this sample is apparent as a brown stain which is not uniform in thickness. Note the vast difference in appearance of the contaminant films in Figures 1 and 2.

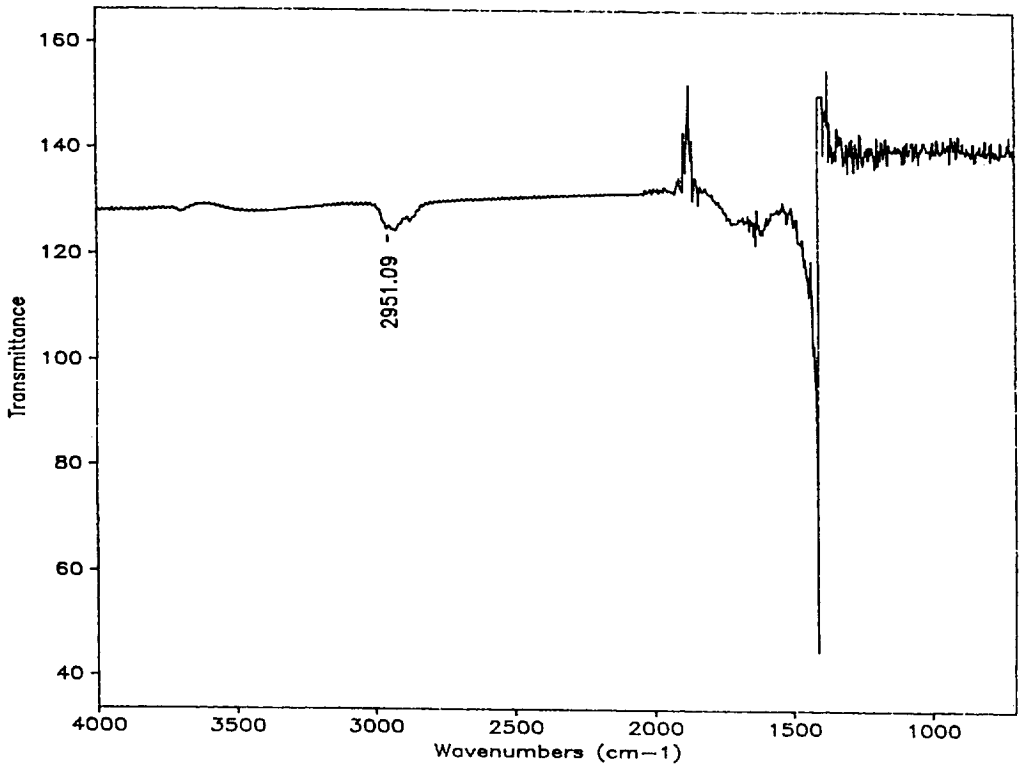

Figure 3. The FT-IR spectrum (reflection mode) of the contaminant film of Figure 1. The figure indicates the absorption region which was associated with aliphatic hydrocarbons.

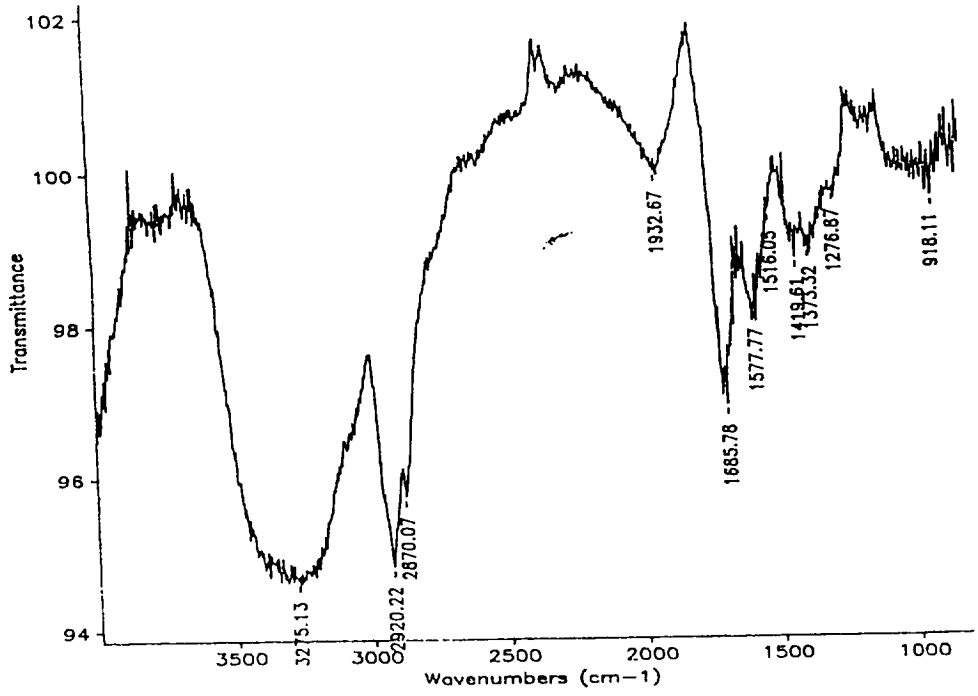

Figure 4*a*. An expansion of the hydrocarbon region of the FT-IR spectrum of Figure 3.

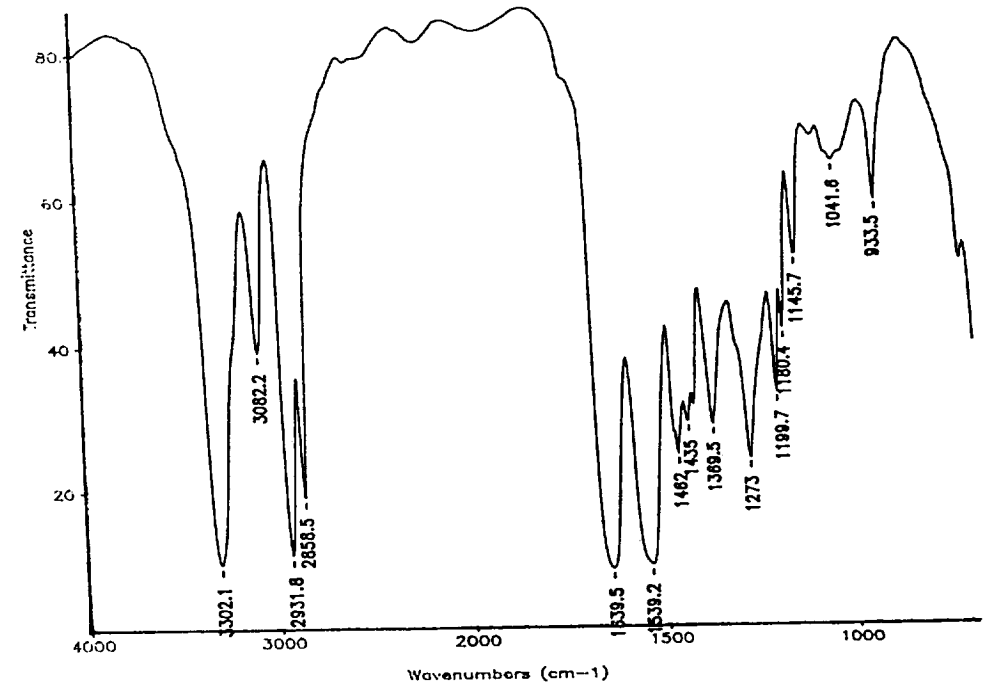

Figure 4*b*. The FT-IR spectrum of nylon 6:6 which is correlated with Figure 4*a*.

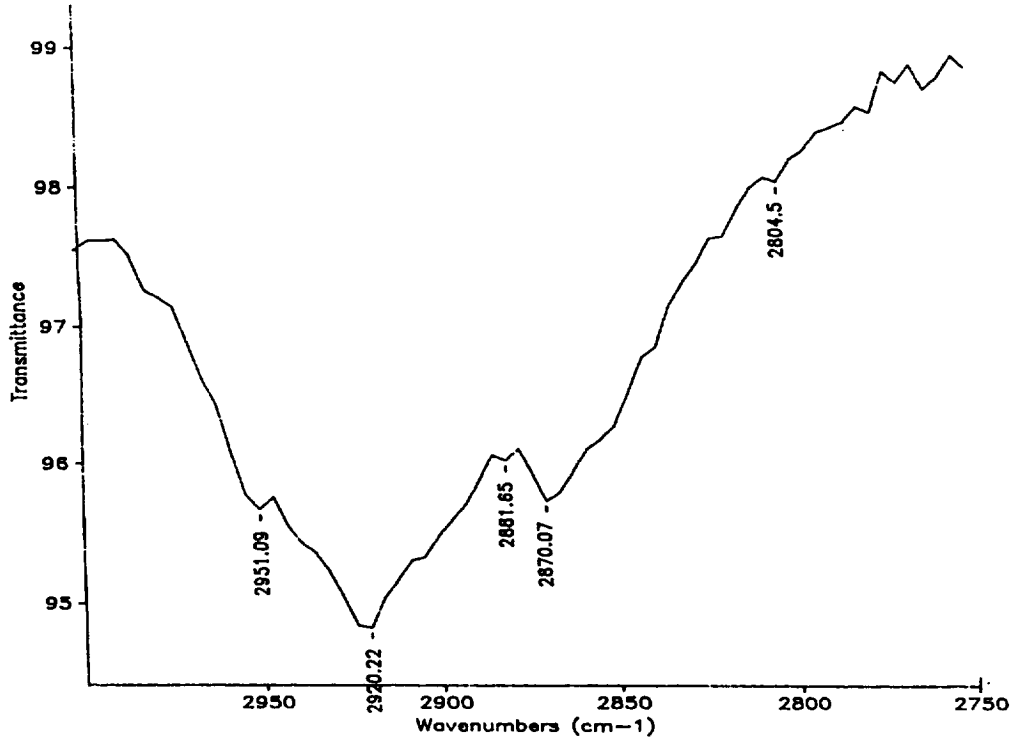

Figure 5*a*. An expansion of the hydrocarbon spectrum of Figure 3.

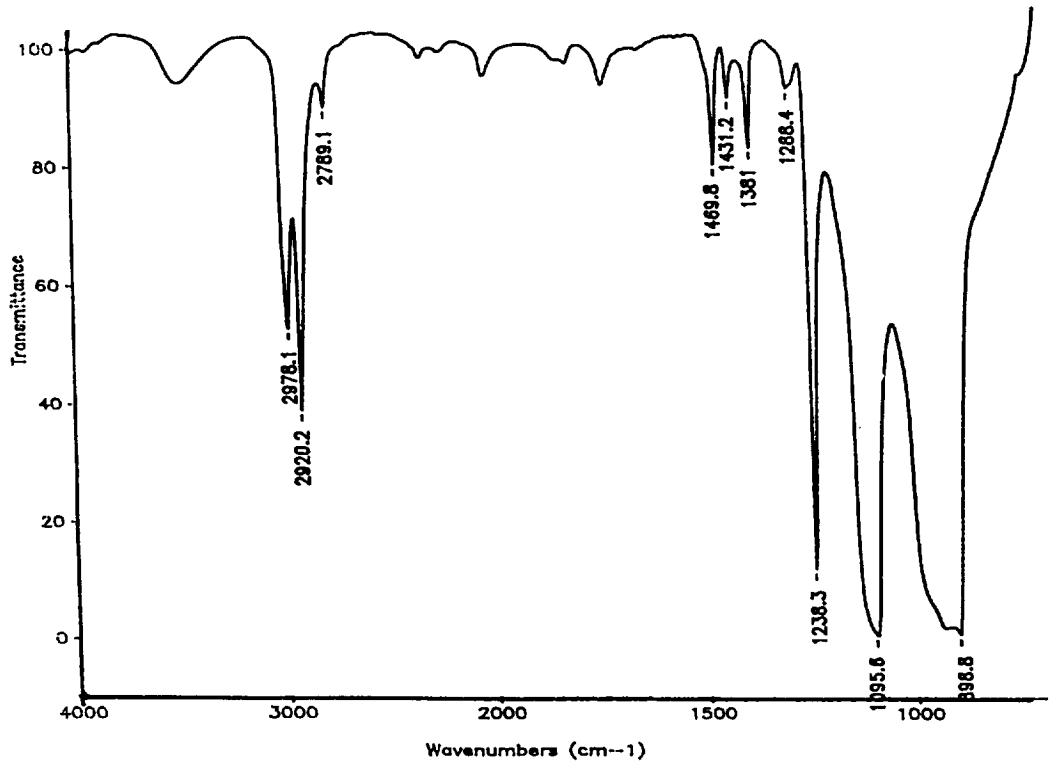

Figure 5*b*. The FT-IR spectrum of polyacetal Delrin plastic which correlates with Figure 5*a*.

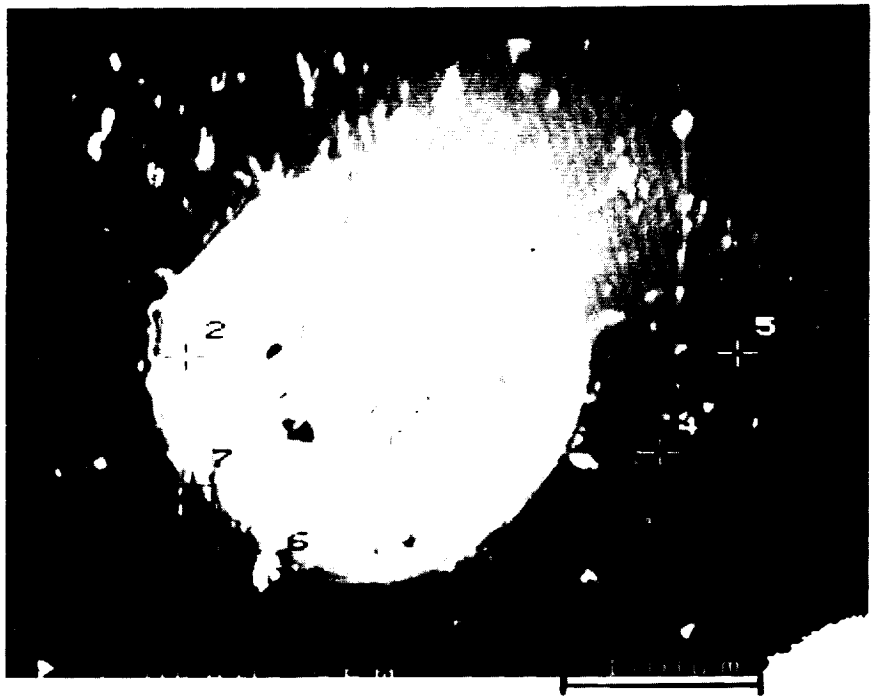

Figure 6. A SEM photo of the micrometeorite (or artificial space debris) impact site in the center of Figure 1. The seven numbered sites indicate positions of the Auger microprobe analysis.

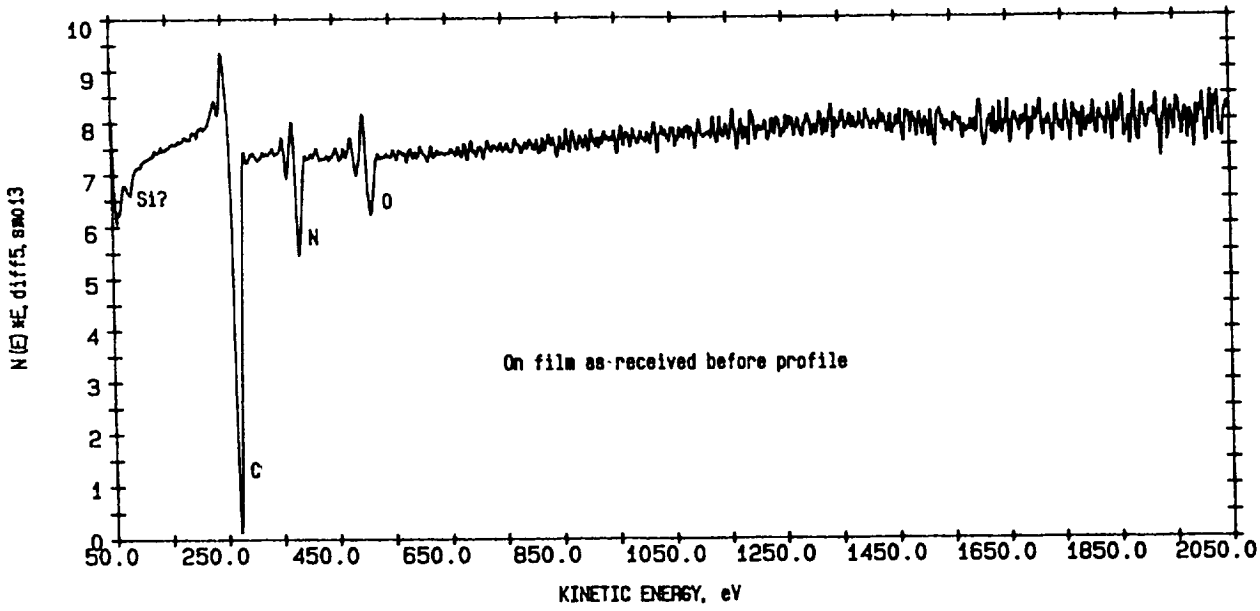

Figure 7. The Auger electron spectrum (AES) from location number 1 of Figure 6. These AES data were typical of those of Figure 6 locations; differences were in magnitude of the Auger peaks only.

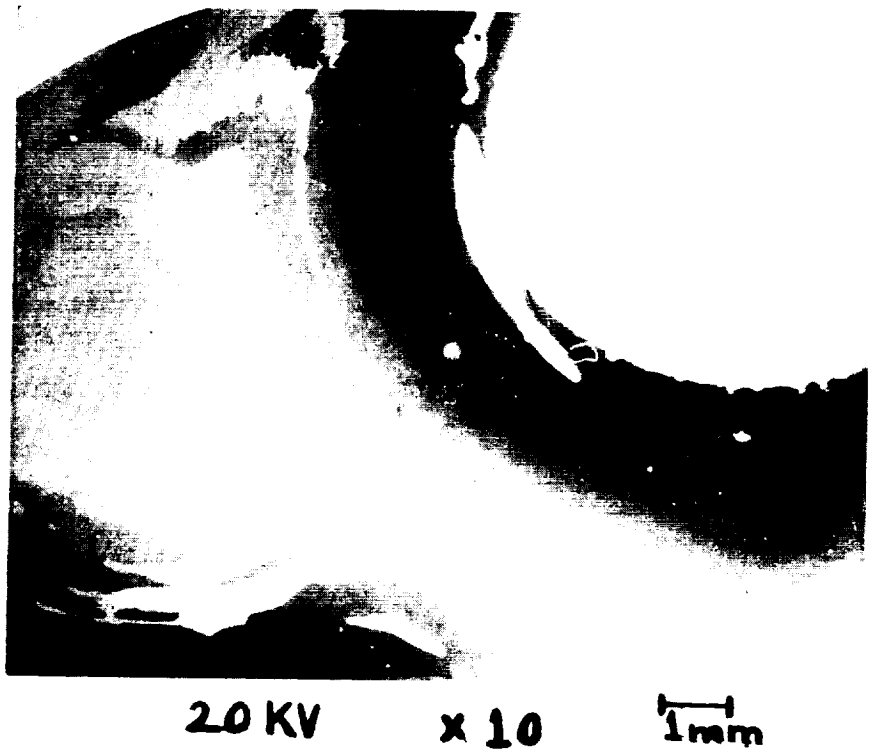

Figure 8. A low magnification (10×) SEM photo of the leading edge sample showing the central micrometeorite crater illustrated in Figures 1 and 8. Note the scattered particulate debris and shadowing of one of the areas of the contaminant film. This shadow is believed to be the start of film delamination.

Figure 9. A 35-mm photograph of a research model CO_2 gas/solid jet spray in operation. Newer designs are much smaller and more compact. Flight units have been designed and are awaiting production.

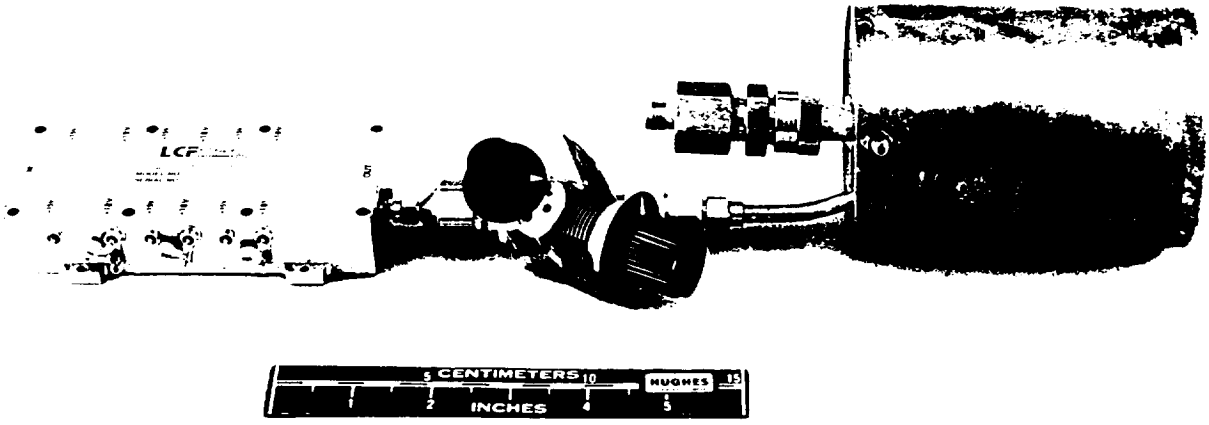

Figure 10. A 35-mm photograph of an old research model HWS ion beam cleaner. The newer designs are inductively coupled, obviating the variable capacitors between the RF amp and cavity, and is much smaller and more lightweight.

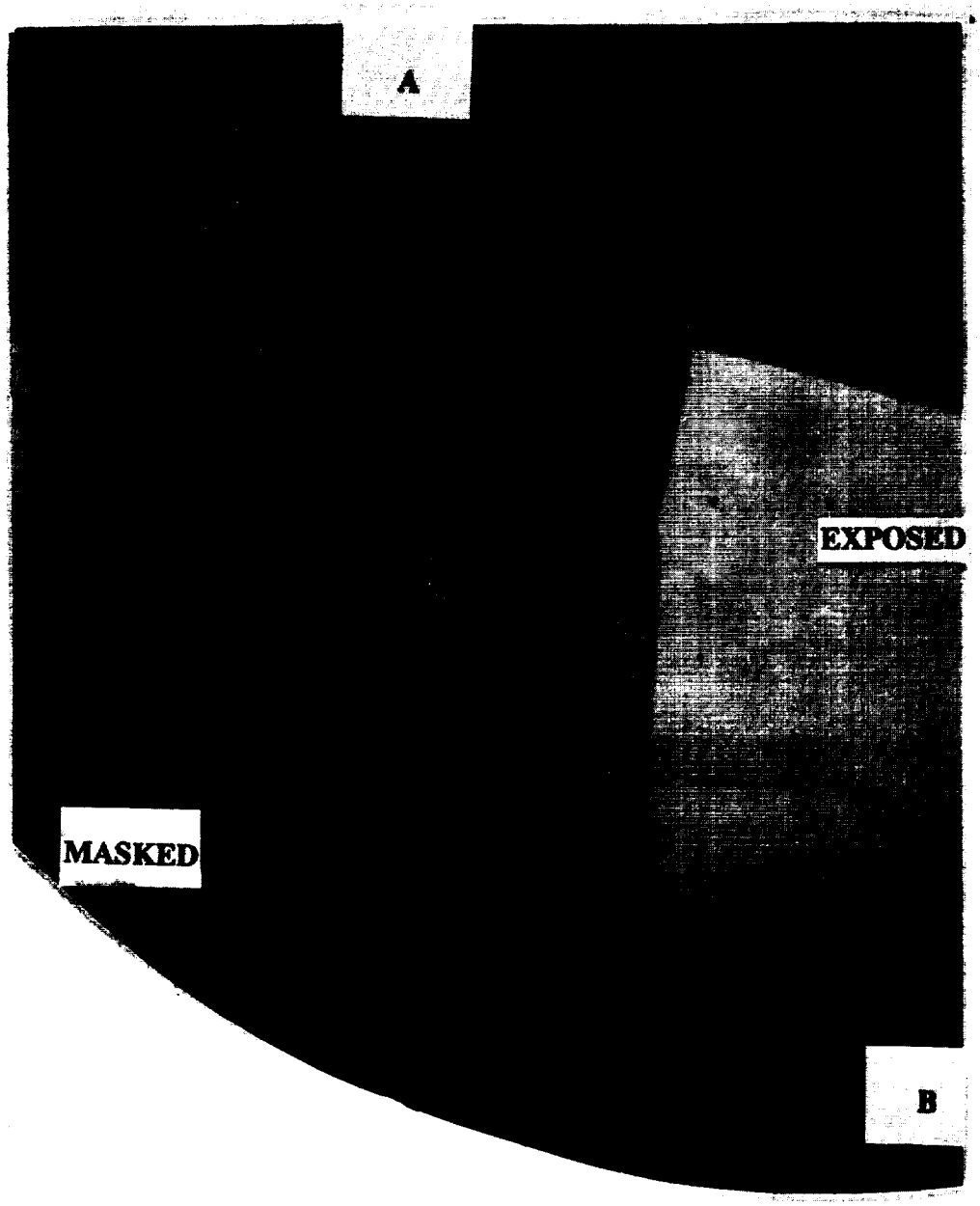

Figure 11. A circular polarized light micrograph (13×) of a section of the leading edge sample after treatment with the ion beam and jet spray contamination removal devices. The region to the left of the circular arc was also exposed to the cleaning treatments while the glass coverslip masked (protected) the contamination. This Figure thus illustrates a before/after type comparison for the cleaning techniques. The sample was treated with 1 hour of reactive oxygen ion cleaning.

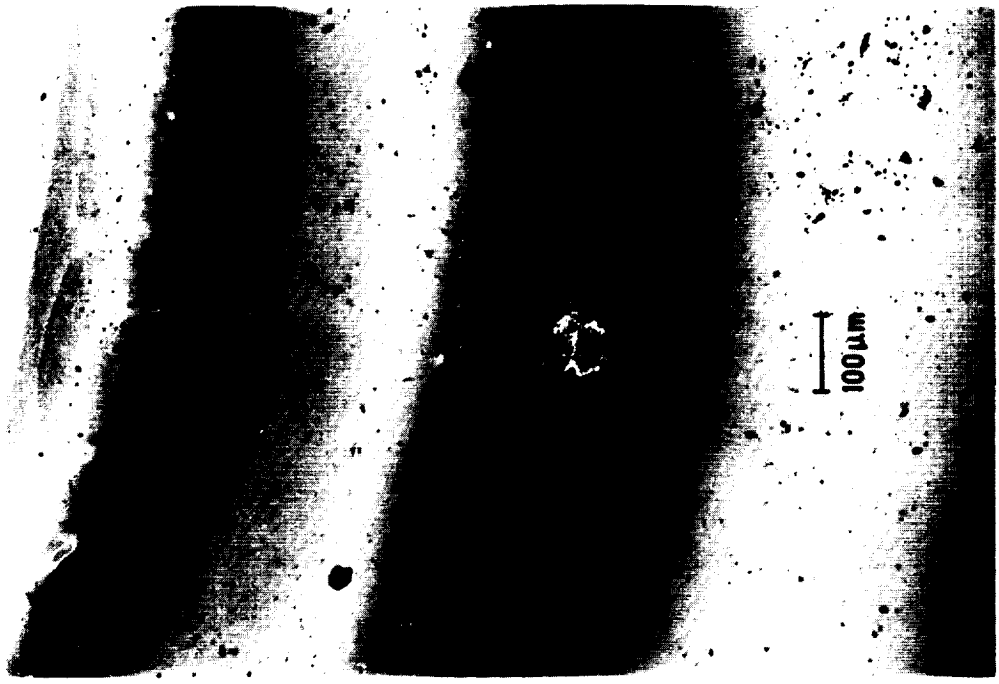

Figure 12. A Nomarski light micrograph (magnification: 200×) of the leading edge sample prior to treatment with contamination removal techniques. The brightly colored interference rings indicate a thickness of 4,500 Å of contaminant film. Notice also the presence of scattered secondary debris and other particular contamination absorbed onto the sample surface.

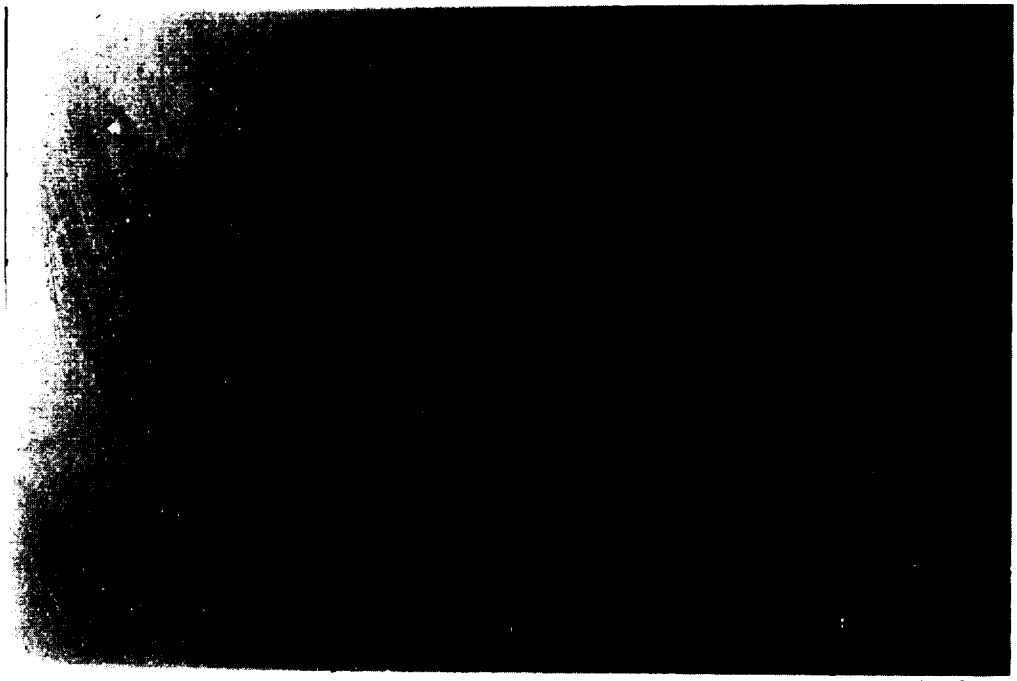

Figure 13. A Nomarski photomicrograph (magnification: 200×) of the micrometeorite impact region of Figure 12 after treatment with the gas/solid jet spray and ion beam cleaners. There is only a faint indication of the presence of residual film. Nomarski gives an approximate thickness less than 15 Å. Note also that most of the particular debris has been removed.

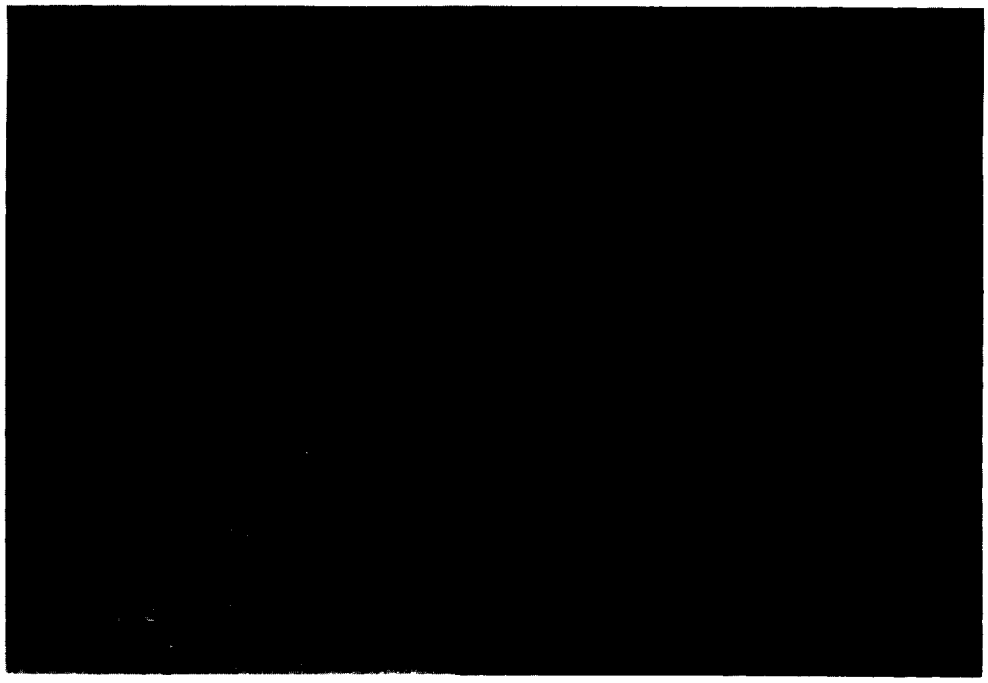

Figure 14. A blue light fluorescence light micrograph of the cleaned (dark)/uncleaned (bright yellow and green) section of the leading edge sample. As in Figure 11, the cover glass masked (protected) part of the sample from cleaning treatments. This sample was treated with 21 minutes of reactive oxygen cleaning.

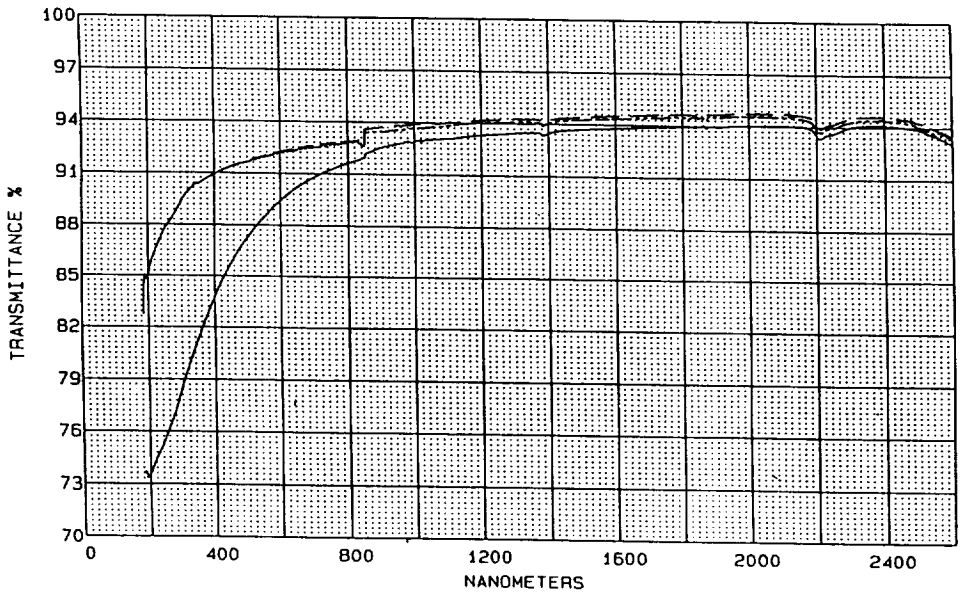

Figure 15. The ultraviolet/visible (UV/Vis) transmission spectra for the trailing edge sample before (solid) and after (dashed) treatment with the ion cleaner. The after cleaning spectrum of a section of the sample which was protected from direct interaction with the space environment was compared to that of the sample after ion cleaning. No difference was discernible, indicating that the cleaning was highly efficient.

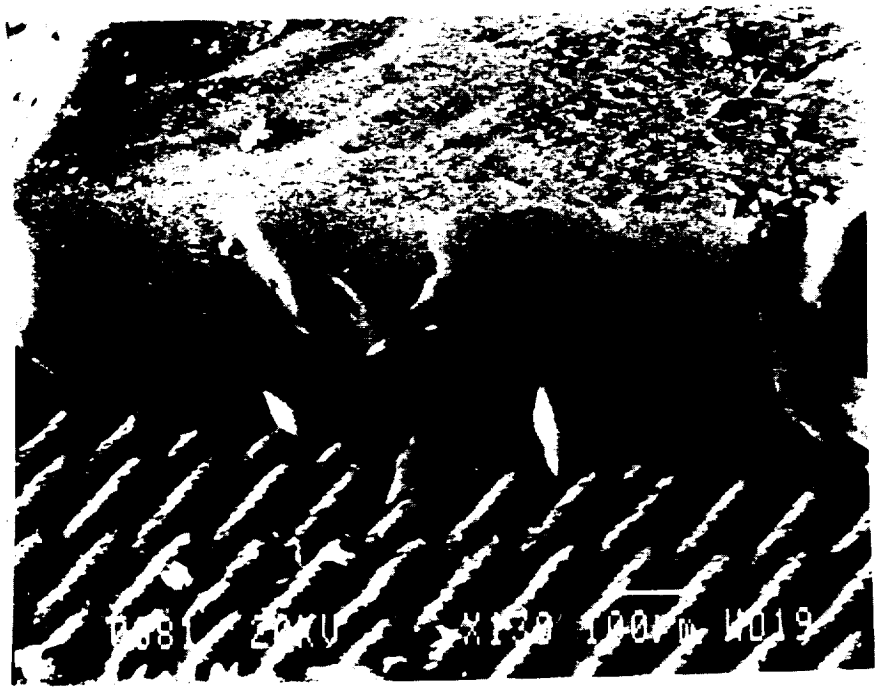

Figure 16. A SEM photo of the Aerogel Mesh Contamination Collector (AMCC, patent pending) showing captured particles.

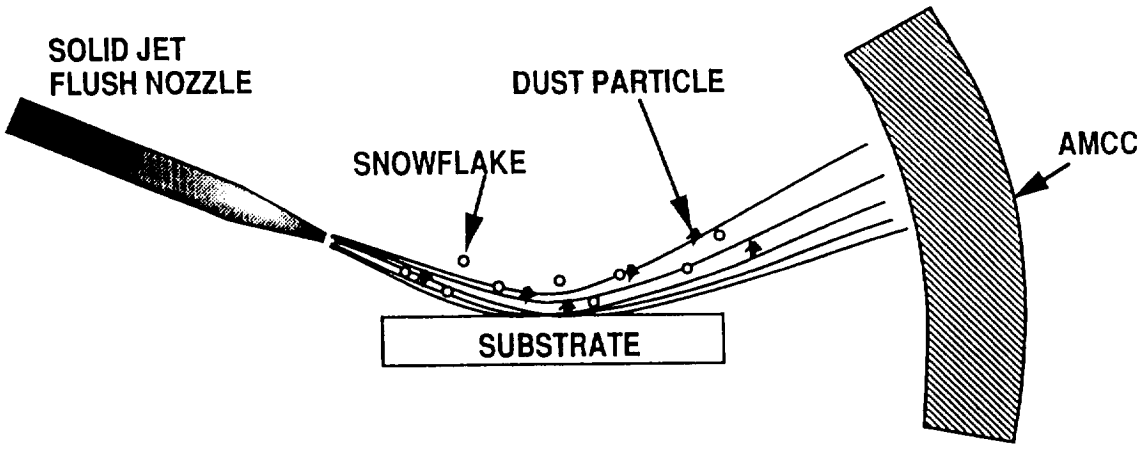

Figure 17. A system concept level diagram of the jet spray and AMCC in operation.

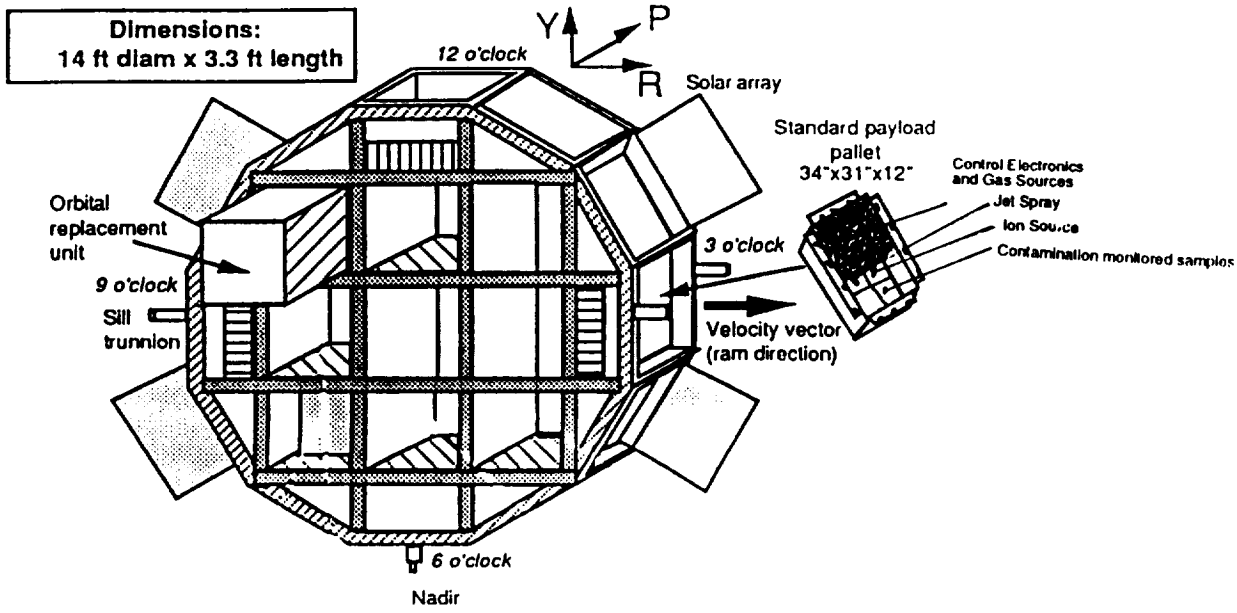

Figure 18. A concept-level diagram of the RPC with a leading edge contamination control experiment. The experiment includes sample materials, contamination detection, jet spray and ion contamination removal devices and the AMCC to collect removed species. The experiment could be run autonomously or under remote control by shuttle or ground-based experimenters. The compactness, limited scope, simple design, and palletized nature of the experiment make it attractive for multiple RPC missions. (This Figure is an adaptation from reference 8.)

POSTER SESSION

PRELIMINARY RESULTS FROM THE CONCAP-II-01 AND EOIM-3 EXPERIMENTS ON STS-46

John C. Gregory and Ganesh N. Raikar
Surface Science Laboratories
The University of Alabama in Huntsville
Huntsville, AL 35899
Tel: (205) 895–6076 Fax: (205) 895–6061

SUMMARY

CONCAP-II-01 (Complex Autonomous Payload, first flight) was the maiden flight of "CONCAP-II," a secondary payload, utilizing the Get-Away Special (GAS) carrier system, sponsored by the Consortium for Materials Development in Space (CMDS), at the University of Alabama in Huntsville (UAH). A host of materials such as high-T_c superconductor samples, metal films, polymers, carbons, and semiconducting materials were exposed to a low-Earth orbit (LEO) environment. We have also measured on orbit the changes in the electrical resistance of some of the high-T_c materials plus carbon and silver dosimeters exposed to the space environment. The preliminary results of this experiment are compared with those from EOIM-3, both of which flew on STS-46 and are presented here.

INTRODUCTION

Both CONCAP-II-01 and EOIM-3 (Evaluation of Oxygen Interactions with Materials—third series) payloads flew on Space Shuttle *Atlantis*, STS-46, on July 31, 1992.

The CMDS is one of the Centers for the Commercial Development in Space funded jointly by NASA and private sector companies interested in promoting the commercialization of space. UAH serves as the integrator of CONCAP-II. The EOIM-3 experiment was managed by Johnson Space Center.

The first flight of the facility carried three thin film experiments which investigated high-temperature superconducting materials improvement and materials preparation and longevity in hyperthermal oxygen. The payload contained an electronic controller and data system which monitored and recorded electrical resistance of 24 material samples of diverse composition. The system also controlled a hot-plate at 320 °C, the highest temperature at which materials studies of this kind have been conducted in space. Figure 1 shows a layout of experiment insert plate. The experiments that were flown on the first flight of the facility are briefly described below.

Experiment 1: High-T_c Superconductors

This experiment addresses the improvement and survivability of high-T_c superconductors (HTSC's) in space. In 1987 at UAH, a ceramic material, $YBa_2Cu_3O_{7-x}$, was discovered which attained zero electrical resistance above the normal boiling point of liquid nitrogen (0 K) (ref. 1).

For optimum performance, these materials must be fully oxygenated. With normal methods, this is achieved by sintering at 600 to 700 °C which severely limits the kind of substrates on which thin-film HTSC devices may be deposited. Further, exposure to heat and vacuum causes loss of oxygen, and thus, performance.

Based on recent experiments at Los Alamos Laboratory (ref. 2), it is believed that HTSC's prepared with mediocre superconducting properties may be converted to high-performance materials by processing in hyperthermal atomic oxygen (AO) (1.5 eV) at considerably lower substrate temperatures. The aim of the CONCAP experiment was to process a variety of thin film HTSC materials in the intense 5 eV AO flow encountered by the space shuttle in LEO.

In order to differentiate changes in HTSC film properties which occur during short ambient AO exposure (~10 h) from those produced by 3 to 4 months of environmental exposure, we have measured the electrical resistance of the devices during the flight exposure, using a 4-point contact technique. All devices, which included HTSC thin films and carbon and silver dosimeters, were exposed both at 320 °C and ambient temperatures to determine the effect of temperature on the oxygen-uptake process. These objectives have been satisfactorily achieved on this maiden flight. The hot plate and the controller performed efficiently and we have some interesting results. We are still in the process of analyzing these data.

Experiment 2: Longevity of Materials in Space

This experiment was concerned with the longevity of materials in space. We have exposed a large number of samples (metals, carbons, polymers, semiconductors, and high-T_c superconductors) to the 5 eV AO flow on the ambient plate and are in the process of measuring the degradation, contamination, and changes in the chemical, mechanical, and optical properties using a variety of techniques. We also had 16 samples on the 320 °C hot plate to evaluate the temperature dependence of AO surface reactions. There were identical samples on the EOIM-3 experiment, both on the ambient plate and three different hot plates (60, 120, and 200 °C). The CONCAP-II samples received one-half of the oxygen fluence of those on EOIM-3, and were covered and protected from contamination during all other flight operations by the motorized door assembly (MDA).

SAMPLE PREPARATION

The majority of the metallic longevity samples were deposited using planar diode sputtering and e-beam evaporation on fused silica optical flats, 1 inch and also 1/2 inch in diameter, supplied by Acton Research Inc. These metal films were optically thin in many cases, with thickness in the range of 20 to 230 nm. Polymer and some semiconductor samples were obtained from various sources. Some of the polymer thin films flown on CONCAP-II were prepared by the spin-coating technique. Some of the vitreous carbon samples were prepared in-house and the rest were manufactured by Union Carbide.

The high-T_c superconducting films, typically of the 1-2-3 type, were provided by our co-investigators, Dr. Tony Mogro (General Electric), Dr. Ian Raistrick (Los Alamos), Dr. Hoi Kwok (SUNY), and Dr. C. Y. Huang (Lockheed). These were mounted with AREMCO 569 and 571 epoxy glue in flatpax™ holders supplied by AIRPAX, MD as shown in the figure and the connections were made by thermoacoustic bonding.

Carbon and silver films for oxygen dosimeters were provided by Dr. Renchler (Los Alamos) and Dr. Smith/Ms. Lan (McDonnell Douglas), respectively. Additional films were obtained from Metech, PA. These were mounted in flatpaxes™ using AREMCO 569 epoxy and were bonded thermoacoustically at SCI, Huntsville.

MEASUREMENT TECHNIQUES

X-ray photoelectron spectroscopy and scanning profilometry are used to obtain preliminary results and are described in detail elsewhere (refs. 3 and 4). We intend to use other techniques such as scanning electron microscopy, scanning Auger microscopy, scanning tunneling microscopy/ atomic force microscopy, thin film x-ray diffraction, fourier transform infrared spectroscopy, Raman spectroscopy, and ultraviolet- (UV-)visible reflectance measurements.

RESULTS AND DISCUSSION

Onflight resistance data from carbon and silver dosimeters measured using 4-point technique is presented here briefly. The data on HTSC samples are being analyzed and will be published separately. Figure 2 shows the resistance (Ω) versus mission elapsed time (MET) (in minutes) data measured on the carbon thin film (~5,000 Å) which was mounted on the ambient plate. It is evident from this figure that most of the material was eroded away within ~400 min of exposure to AO in the RAM direction. Figure 3 shows the Ω versus MET data measured on silver thin film (220 Å thick) mounted on the ambient plate. As can be seen from this figure, most of the silver was attacked by AO, forming nonconducting silver oxides. These data indicate that the controller and associated electronics worked as designed.

Postflight visual inspection of the CONCAP-II samples suggested they were cleaner than the EOIM-3 samples which had a whitish appearance at the mask boundary on some samples. It is apparent that CONCAP-II samples were exposed only in orbit and were subsequently covered by the motorized door assembly (MDA) after ~21 h of exposure to AO, unlike EOIM-3 samples which remained exposed to the ambient environment of the shuttle after the mission. The relative levels of contamination on EOIM-3 and CONCAP-II will be compared.

X-ray photoelectron spectroscopy is one of the most surface-sensitive analytical techniques. This technique probes <100 Å at the surface, and it is easy to extract information about surface atomic concentration and chemical states of the constituents from the details of changes in shape and binding energy shifts of the core level peaks. The surface composition information for Cu, Ni, and Cu samples from CONCAP-II and EOIM-3 is tabulated in Tables 1, 2, and 3. Examination of the data in these tables shows that all the longevity samples that are analyzed have Si contamination in the range of 2 to 11 percent. In addition, other contaminants such as Na, Cl, and F plus some N are observed. Carbon content due to ambient hydrocarbon contamination was similar on all the metallic samples. Oxygen is present on all the samples, in the form of oxides on metallic samples and in adsorbed form due to moisture and or CO and CO_2 species on carbon samples.

Figures 4, 6, and 8 compare the X-Ray Photoelectron Spectroscopy (XPS) survey scans measured on Cu, Ni, and C samples from CONCAP-II and EOIM-3. In addition to the substrate peaks, we can clearly see the peaks due to oxygen, carbon, and silicon. Figure 5 compares the high resolution Cu 2p scans measured from the Cu samples. The peak shape and the appearance of "shake-up satellites" suggest the presence of CuO (Cu^{2+}) species in the exposed area of the flight samples (ref. 3). Figure 7 compares the high resolution Ni 2p peaks from Ni samples, the binding energy, and the shape of Ni 2p peaks suggest that Ni at this interface is in NiO (Ni^{2+}) form (ref. 5). Detailed analysis will be presented in a separate paper. There is hardly any difference in the shape of the carbon peaks measured from the CONCAP-II and EOIM-3 samples (Figure 9). It is difficult to differentiate between the carbon from the bulk and the contamination due to residues from extraneous hydrocarbons. Some portion of the measured carbon 1s peaks may be due to this contamination.

The advantage of using stylus profilometry to measure the erosion characteristics on polymers and metals has been amply demonstrated previously (ref. 4). Here we present profilometry results on Cu and carbon samples. Figure 10 shows the stylus profile of the exposed region of Cu thin film from the ambient plate of CONCAP-II. Based on the initial thickness of 570 Å, this film shows an increase in thickness of ~90 Å in the exposed area. Similar increase in thickness was observed on the Cu thin film exposed on the ambient plate of EOIM-3. The Cu thin film exposed to the AO on the 320 °C hotplate on CONCAP-II showed an increase in thickness of ~900 Å (Figure 11). Similarly there was an erosion of ~2 μm on the highly polished vitreous (glassy) carbons exposed on the ambient plate of CONCAP-II as shown in Figure 12. More measurements on EOIM-3 samples are underway.

CONCLUSION

A comparison was made of contamination on samples from CONCAP-II and EOIM-3. The XPS results measured on samples from these two experiments agree reasonably well. Silicon contamination on samples from both the experiments is similar. Similar contaminant levels were observed on samples from the STS-8 flight. The origin of this contamination may be attributed to siloxanes/silicones which converts to silica on being exposed to AO. From XPS data we can deduce that the oxide formed on Cu thin film samples mounted on both the experiments is predominantly CuO in nature. Similarly, we have observed the presence of NiO species on Ni samples.

Scanning profilometry results show that there is an increase in the thickness of ~90 Å on the Cu samples from the ambient plates of CONCAP-II and EOIM-3. However, we observed a step height of ~900 Å on the Cu sample exposed on 320 °C hot plate of CONCAP-II. It would be interesting to compare this result with those from samples on three different hot plates (60 °C, 120 °C, and 200 ° C) of EOIM-3. We have observed an erosion of ~2 mm on the highly polished samples of vitreous carbon from CONCAP-II. Other samples are being currently analyzed.

The operation of the flight experiment facility CONCAP-II on STS-46 has demonstrated its flexibility and usefulness as a rapidly deployable system for obtaining active measurements on materials in orbit. Resistance measurements from HTSC and oxygen-dosimetry devices were recorded during oxygen atom exposure. It is surprising that the Si levels on CONCAP-II samples are, within the scatter of the data, the same as these on EOIM samples, which were exposed to the shuttle bay environment throughout all orbital operations. These included deployment of EURECA and the tethered satellite. It is noted that adsorption of silicon molecules onto surfaces is dependent

on surface temperature and perhaps on surface chemical nature. Large amounts of silicones are used in the treatment of shuttle external surfaces before launch, and it appears that a volatile fraction of these is present in the shuttle gas cloud on orbit. It may be that the ram-beam of AO striking the surfaces of the shuttle bay actively contributes to the silicone molecular density by desorbing bound molecules. We have observed similar effects in terrestrial AO beam facilities.

REFERENCES

1. Wu, M.K., Ashburn, J.R., Torang, C.J., Hor, P.H., Meng, R.L., Gao, L., Huang, Y.Q., Wang, Y.Q., and Chu, C.W.: Phys. Rev. Lett. 58, 1987, p. 908.

2. Cross, J.C. (Private Communication).

3. Raikar, G.N., Gregory, J.C., Christl, L.C., and Peters, P.N.: "Interaction of Atomic Oxygen With Thin Film and Solid Copper: An XPS, AES, XRD, and Profilometer Study." Proceedings of the Second LDEF Post-Retrieval Symposium, San Diego, CA, June 1–5,1992.

4. Christl, L.C., Gregory, J.C., and Peters, P.N.: "Measurements of Characteristics for Metal and Polymer Surfaces Using Profilometry." Proceedings of the First LDEF Post-Retrieval Symposium, Kissimee, FL, June 2–8, NASA Conference Publication 3134.

5. Matienzo, L.J., Yin, L.I., Grim, S.A., and Swartz, W.E.: Inorg. Chem. 12, 1973, p. 2762.

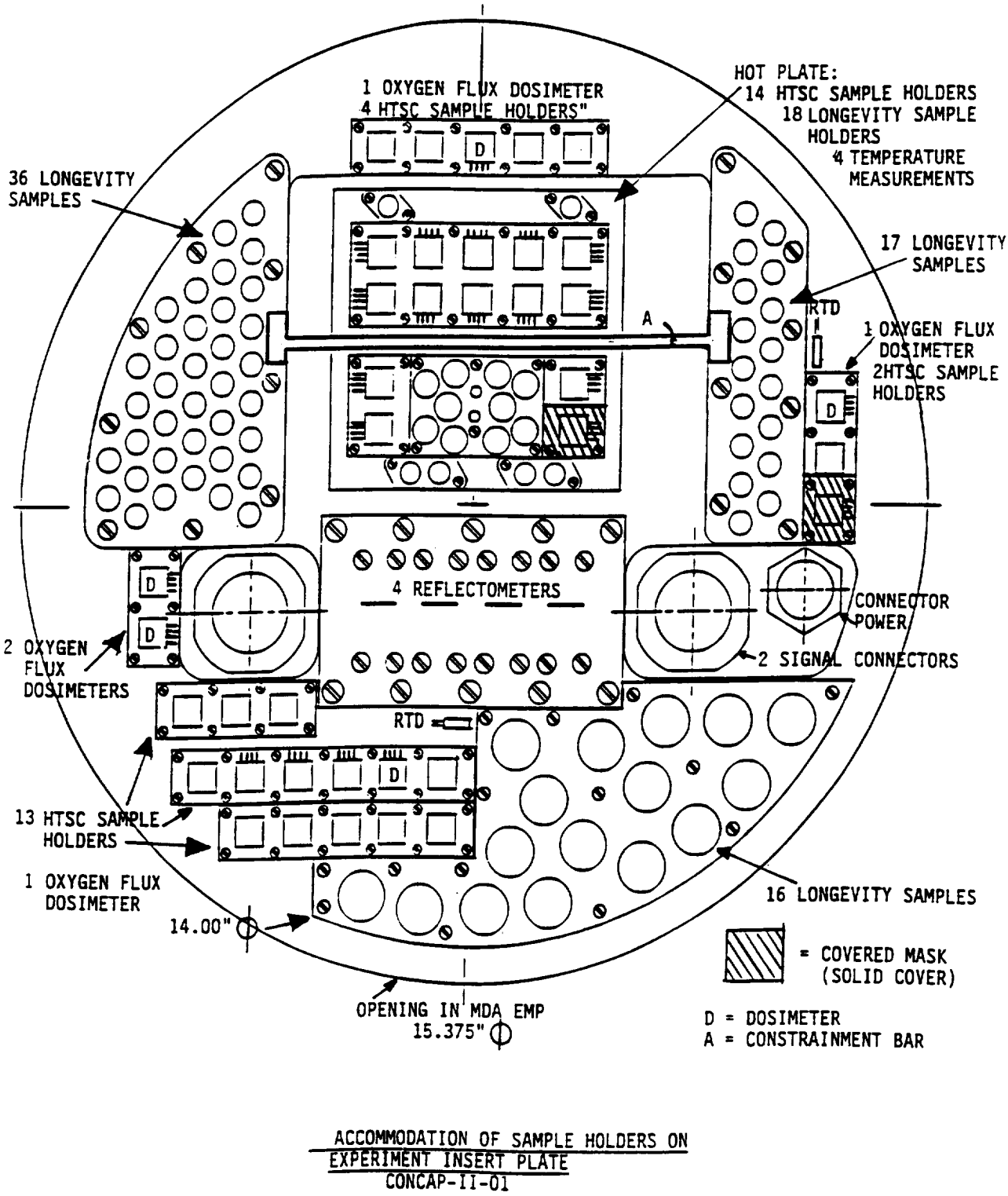

ACCOMMODATION OF SAMPLE HOLDERS ON EXPERIMENT INSERT PLATE
CONCAP-II-01

Figure 1. Layout of CONCAP-II.01 experiment insert plate.

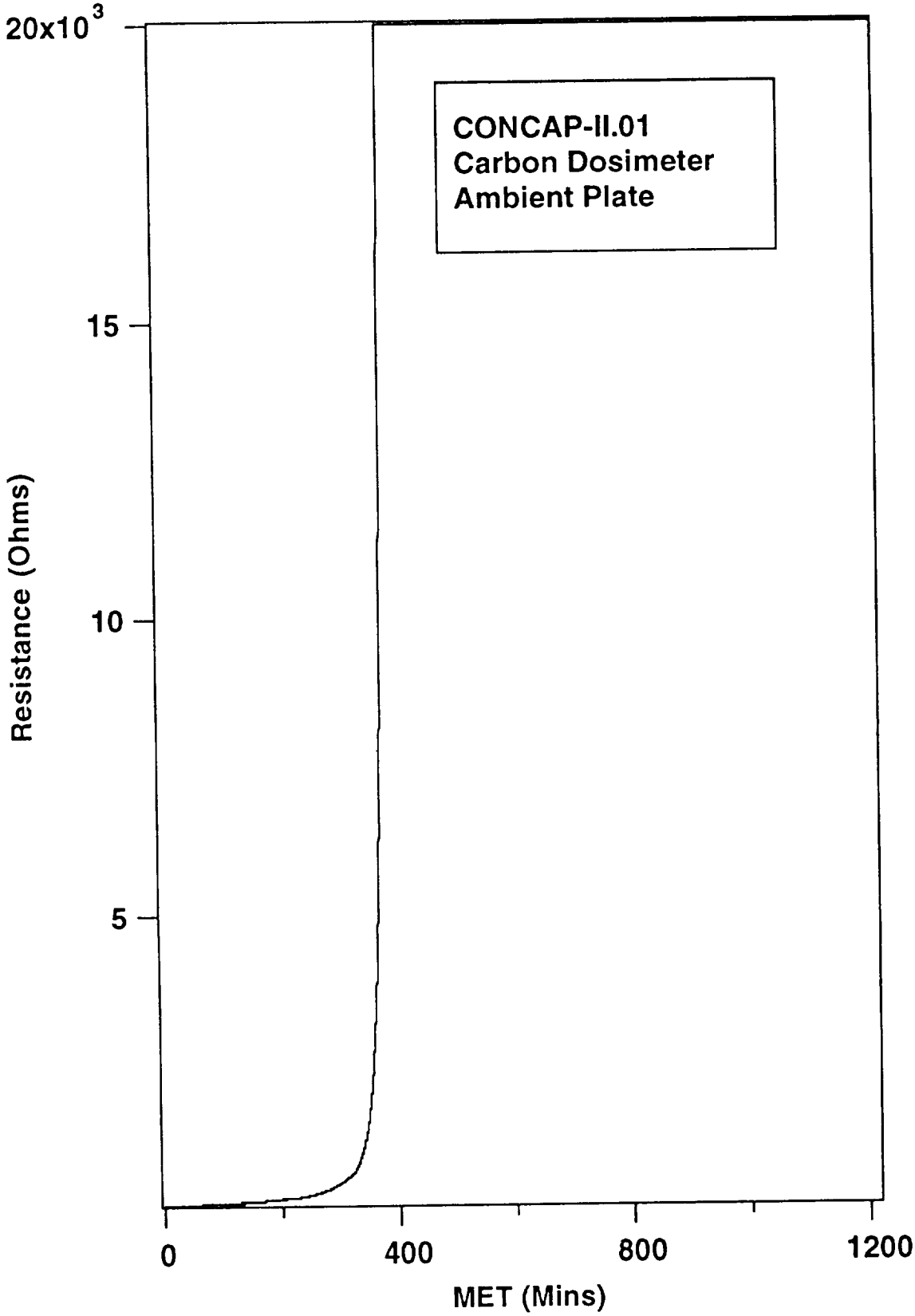

Figure 2. The resistance versus MET time plot of carbon dosimeter from the ambient plate.

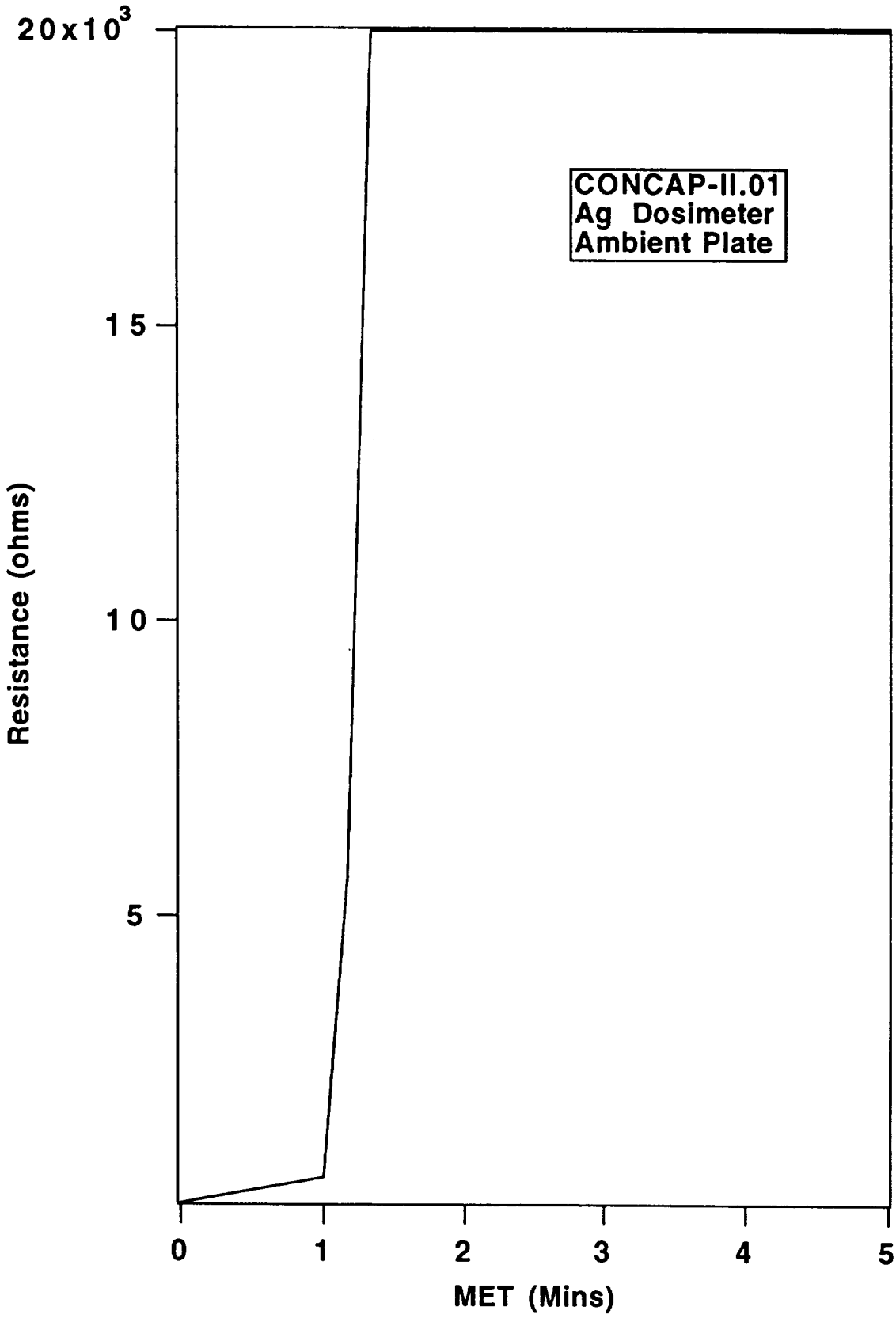

Figure 3. The resistance versus MET plot of silver dosimeter from the ambient plate.

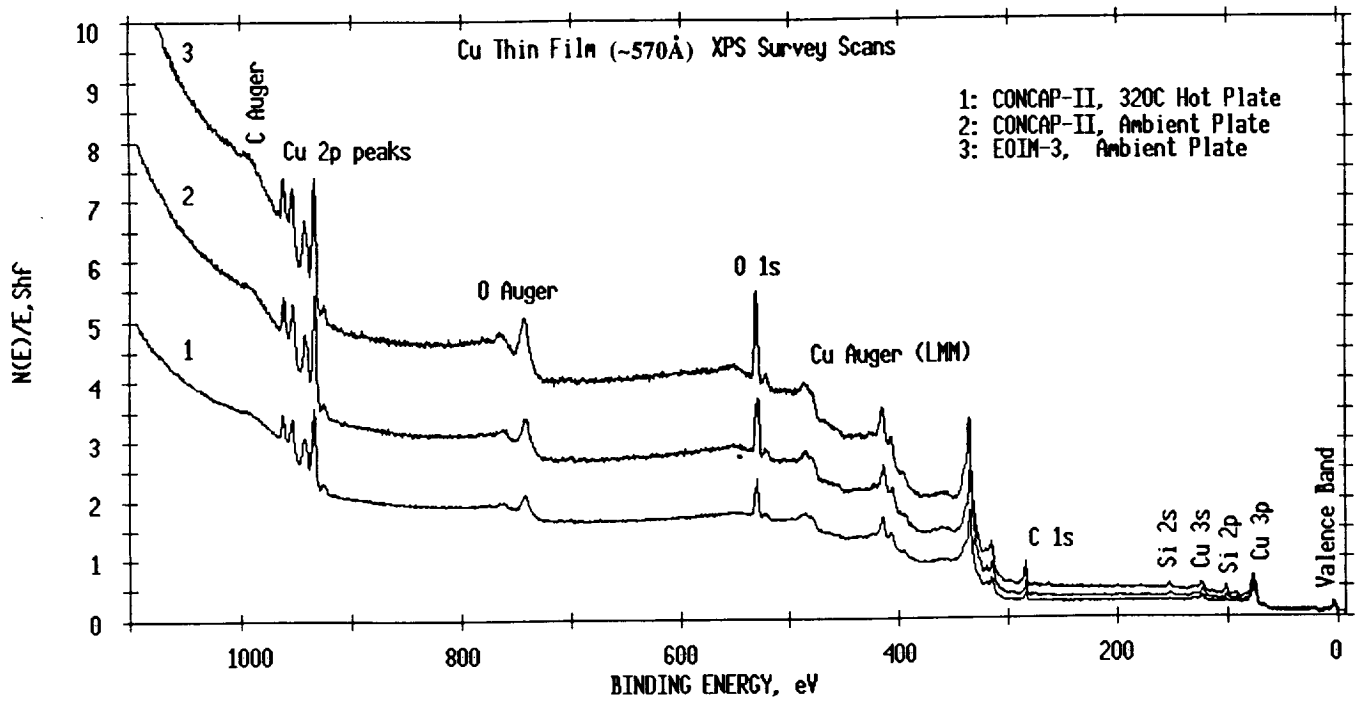

Figure 4. Comparison of XPS survey scans from Cu thin films from CONCAP-II and EOIM-3.

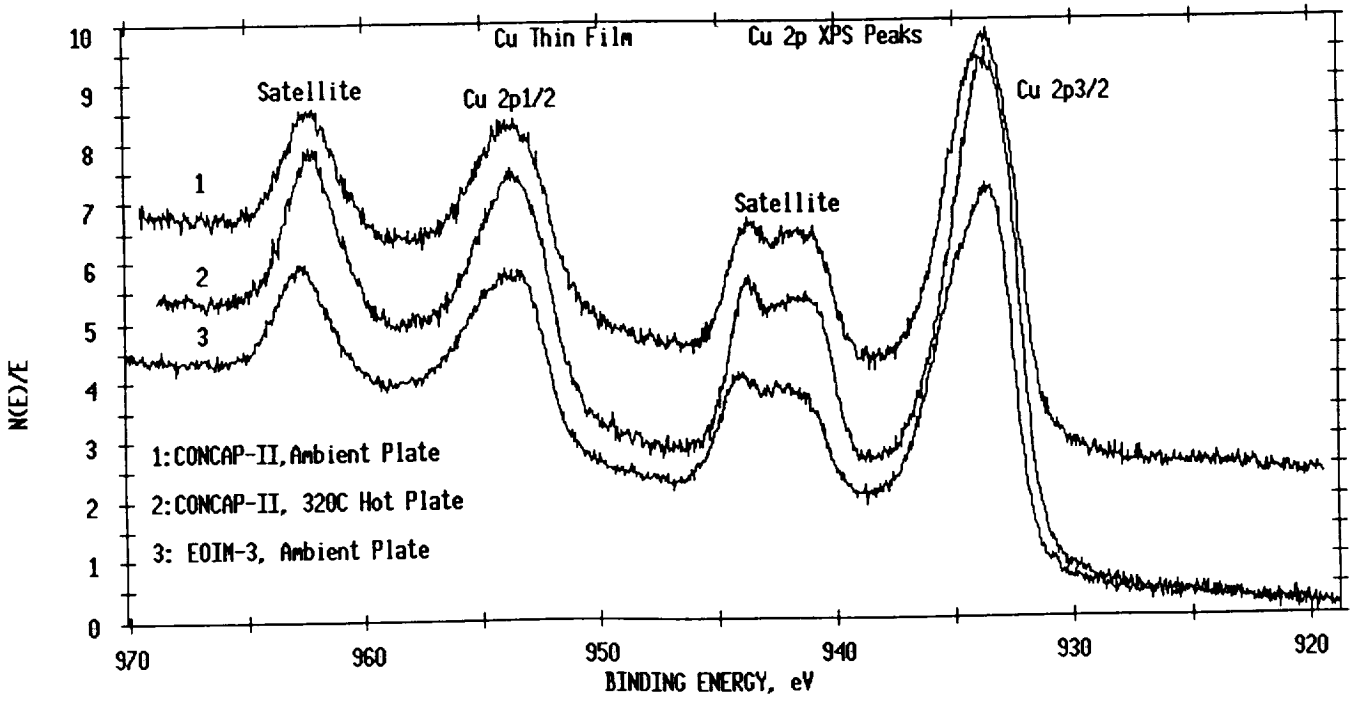

Figure 5. Comparison of Cu 2p core lines from Cu thin films (~570 Å).

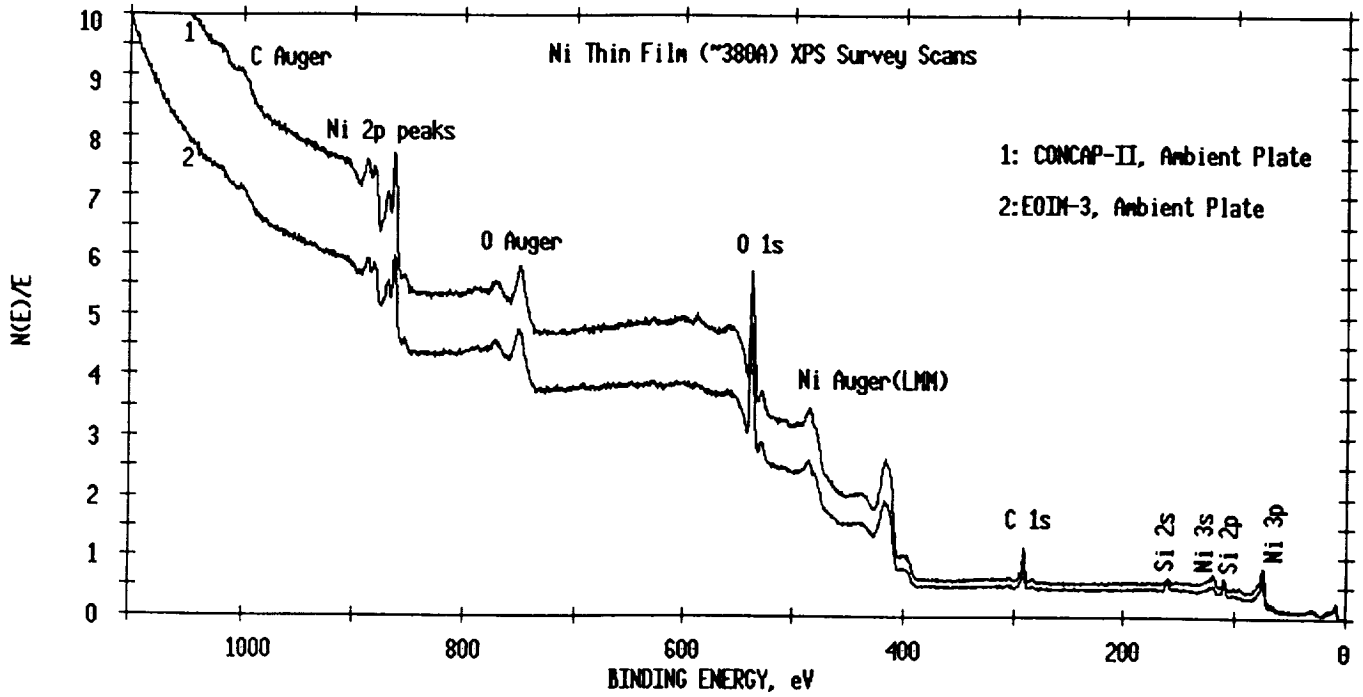

Figure 6. Comparison of XPS survey scans from Ni thin films from CONCAP-II and EOIM-3.

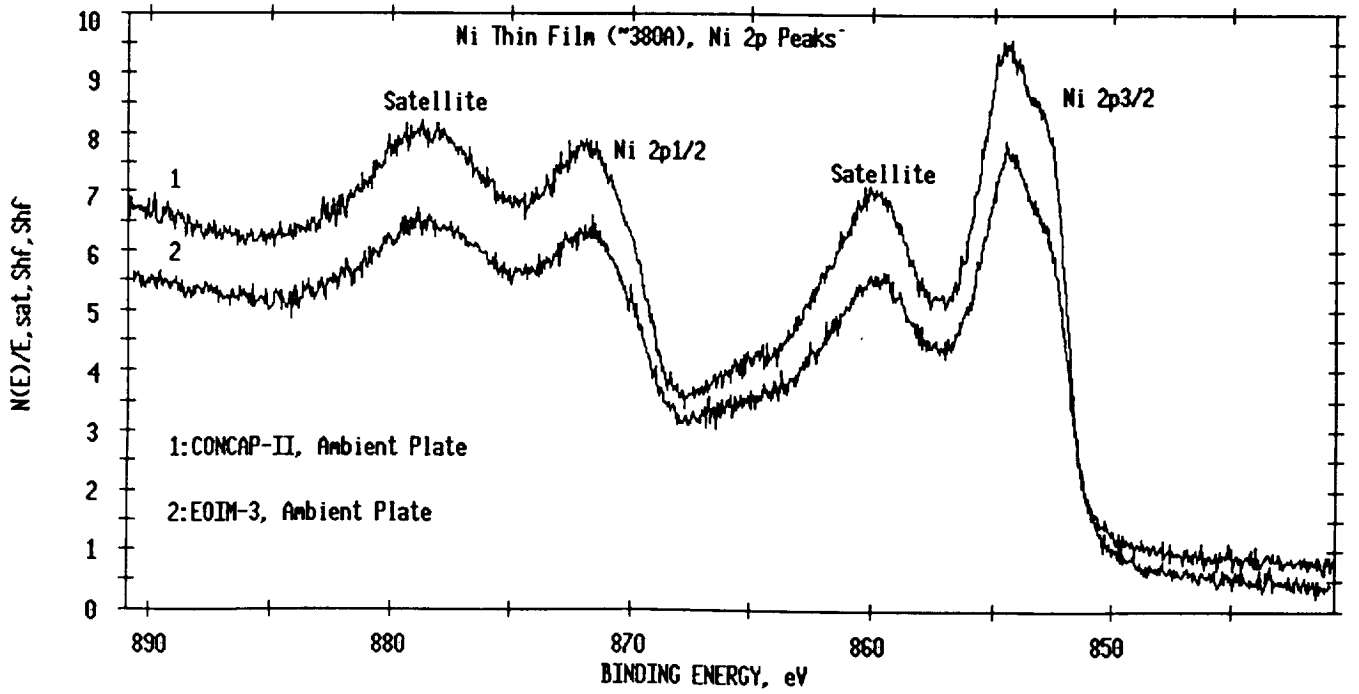

Figure 7. Comparison of Ni 2p core lines from Ni thin films (~380 Å).

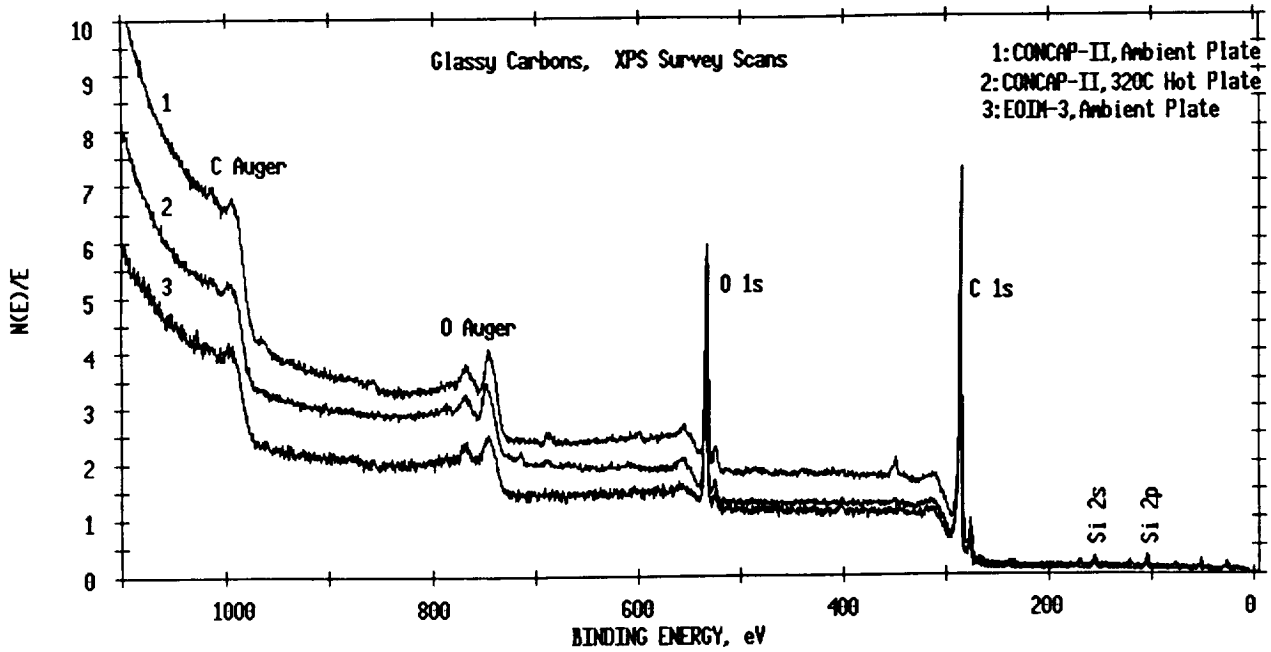

Figure 8. Comparison of XPS survey scans from glassy carbons from CONCAP-II and EOIM-3.

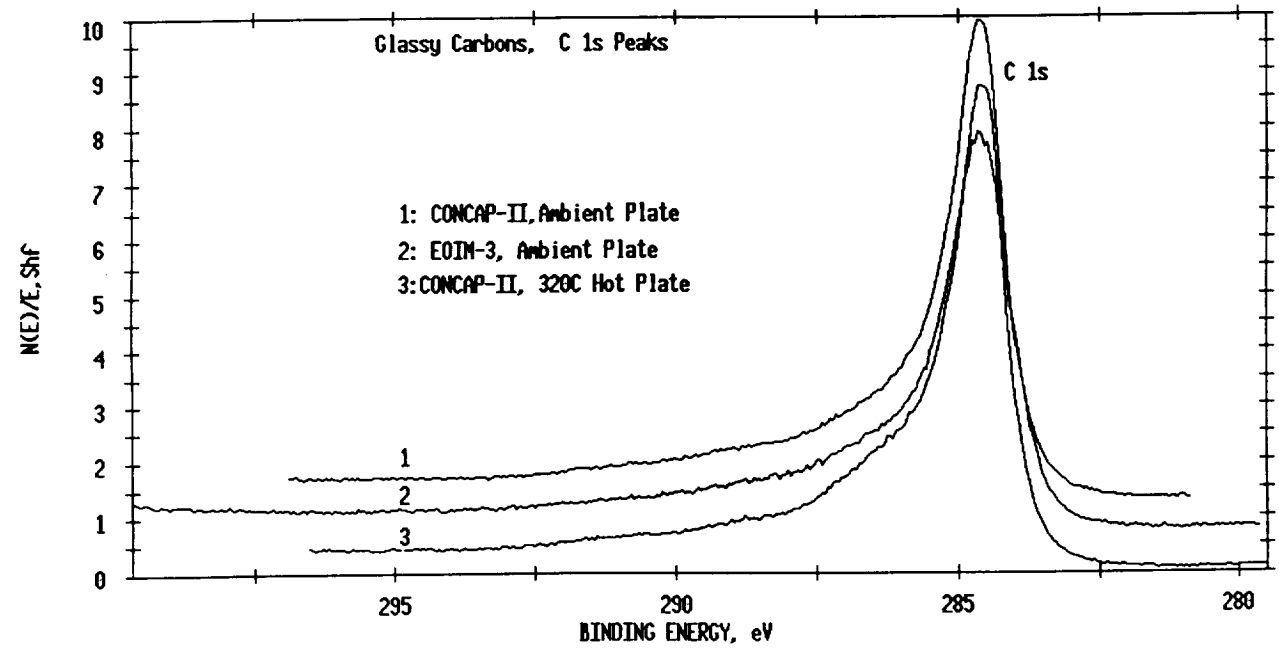

Figure 9. Comparison of C 1s core lines from glassy carbons.

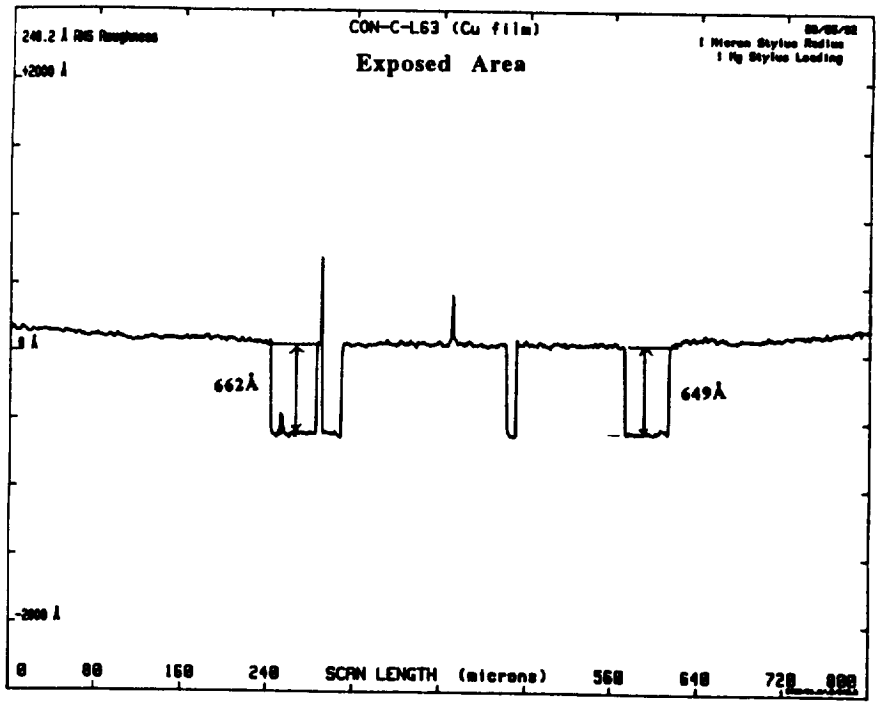

Figure 10. Surface profile of the exposed region of Cu thin film from the ambient plate of CONCAP-II.

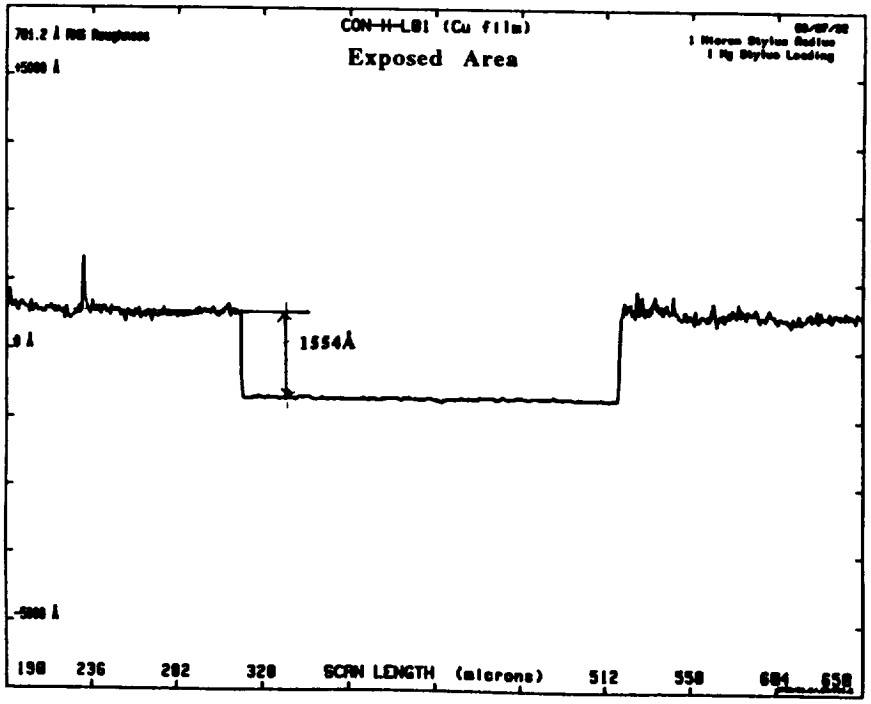

Figure 11. Surface profile of the exposed region of Cu thin film from the 320 °C hot plate of CONCAP-II.

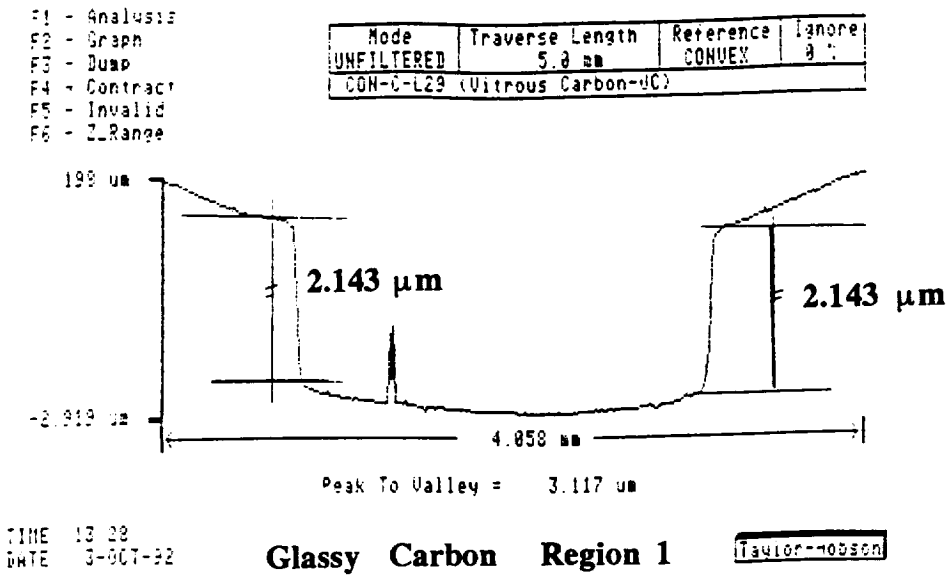

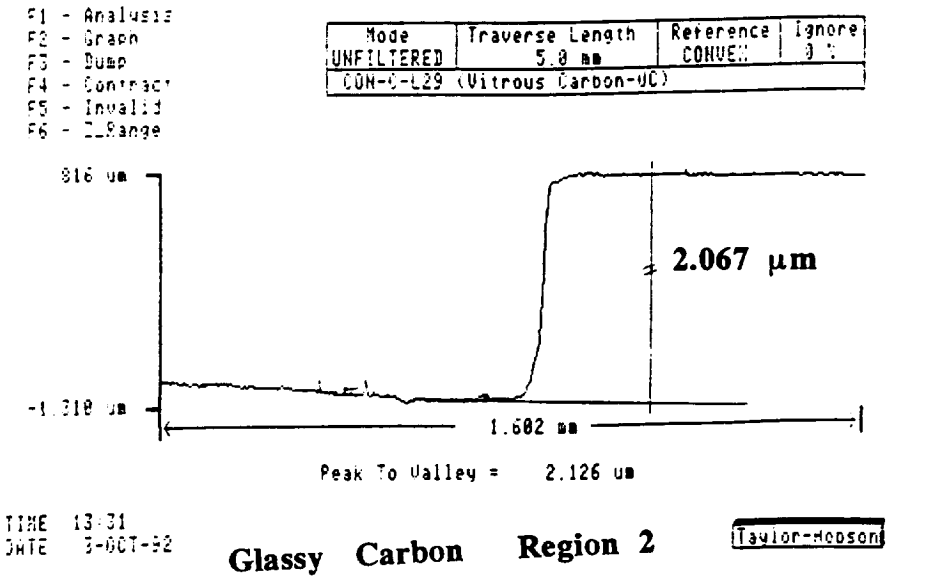

Figure 12. Surface profile of the exposed region of glassy carbon from the ambient plate of CONCAP-II.

Table 1. Atomic concentrations of Cu thin film samples from CONCAP-II and EOIM-3.

XPS Photo Peak	CONCAP-II Ambient Plate (~300 Å)	CONCAP-II Ambient Plate (~700 Å)	CONCAP-II 320 °C Hot Plate (~700 Å)	EOIM-3 Ambient Plate (~300 Å)
Cu 2p A.C in %	12.4	12.8	14.6	21.2
O 1s A.C in %	46.5	47.5	54.3	43.8
C 1s A.C in %	26.5	26.6	22.4	22.4
Si 2p A.C in %	11.4	9.2	6.4	9.9
Na 1s A.C in %	2.0	1.7	1.1	1.0
Cl 2p A.C in %	1.2	2.1	1.2	1.3
F 1s A.C in %	0.0	0.0	0.0	1.3
N 1s A.C in %	0.0	0.0	0.0	0.0

Table 2. Atomic concentrations of Ni thin film samples from CONCAP-II and EOIM-3.

XPS Photo Peak	CONCAP-II Ambient Plate (~380 Å)	EOIM-3 Ambient Plate (~300 Å)
Ni 2p A.C in %	21.0	17.0
O 1s A.C in %	44.2	48.3
C 1s A.C in %	25.3	21.8
Si 2p A.C in %	7.2	10.9
Na 1s A.C in %	0.3	0.0
Cl 2p A.C in %	6.0	0.6
F 1s A.C in %	1.4	1.7
N 1s A.C in %	0.0	0.0

Table 3. Atomic concentrations of glassy carbons from CONCAP-II and EOIM-3.

XPS Photo Peak	CONCAP-II Ambient Plate (1/2-inch Disk)	CONCAP-II 320 °C Hot Plate (1/2-inch Disk)	EOIM-3 Ambient Plate (1-inch Disk)
C 1s A.C in %	71.0	62.8	84.0
O 1s A.C in %	16.0	23.6	12.0
Si 2p A.C in %	2.7	4.7	1.8
Na 1s A.C in %	9.1	0.4	0.2
Cl 2p A.C in %	0.3	0.4	trace
F 1s A.C in %	0.9	0.6	0.3
N 1s A.C in %	1.4	1.1	1.7
Al 2p A.C in %	nd	6.4	nd

EFFECTS OF ORBITAL EXPOSURE ON RTV DURING THE LDEF MISSION

William E. Brower, Jr., S.V. Golub, and Robert A. Bauer
Department of Mechanical and Industrial Engineering
Marquette University
1515 W. Wisconsin Avenue
Milwaukee, Wisconsin 53233

ABSTRACT

Thermomechanical analysis (TMA), differential scanning calorimetry (DSC), and thermogravimetric analysis (TGA) were performed on samples of RTV 511 exposed on the Long Duration Exposure Facility (LDEF) mission for 6 years in orbit and unexposed RTV 511 control samples. Slices 20- to 400-microns thick were removed from the exposed surface down to a depth of 1,500 microns through the 3-mm thick samples. The TMA and DSC results, which arise from the entire slice and not just its surface, showed no significant differences between the LDEF exposed and the control samples. TMA scans were run from ambient to 500 °C; results were compared by a tabulation of the onset temperatures for flow. DSC scans were run from ambient to 600 °C; no endotherms or exotherms occurred over the range observed. What appear to be glass transition temperatures were compared for the samples as a function of section depth within the sample and between the exposed and control samples. The TGA scans from 25 to 900 °C, which arise from the surface of the sample initially, showed a slight increase in the top most 105-micron slice (the exposed, discolored side) in the weight loss at 600 °C in oxygen. This weight loss dropped to bulk values at the next slice below the top section, a mean depth of 258 microns. The control sample also showed an increase in weight loss as the top surface was approached, but the 600 °C weight losses were very inconsistent. The LDEF RTV sample appears to be mechanically undamaged, with a surface layer which oxidizes slightly faster as a result of orbital exposure.

INTRODUCTION

Early results of LDEF exposure on polymeric materials showed varying degrees of degradation, discoloration, and weight loss (refs. 1–4). Young and Slemp (ref. 5) reported no differences in DSC thermograms of FEP Teflon between exposed and control samples. They also reported no difference in TGA curves for Kapton films between the exposed and control samples. Brower, Holla, and Bauer (ref. 6) reported some difference among sections taken through the thickness of exposed Halar samples. The top 50 microns of the exposed Halar sample exhibited a significantly higher weight loss in oxygen than the bulk. Such a top surface effect was not observed in the Halar control sample. Brower et al. (ref. 6) found no difference between the control and exposed samples of Halar in DSC and TMA, in agreement with Young and Slemp's DSC and TGA results on Teflon and Kapton. Possibly, the surface effect in TGA reported by Brower et al. (ref. 6) on Halar was detectable due to the sectioning through the thickness of the film, which concentrated the surface damaged layer with respect to the bulk. Hurley and Jones (ref. 7) reported reflectance changes as a result of LDEF exposure on a number of polymer films. They also observed RTV 560 + 12 percent graphite adhesive bonds to fail in all cases.

RTV 511 in 3-mm thick film form was studied in the work reported here. The thrust of this investigation was to determine the depth profile of the LDEF orbital damage to the RTV 511 samples. TMA, TGA, and DSC were performed on slices of the RTV exposed and control samples to assess the depth of damage (if any) due to orbital exposure during the LDEF mission.

EXPERIMENTAL PROCEDURE

The procedure for preparing samples from the pieces of RTV 511 exposed and control samples was the same as that for the Halar samples as described previously (ref. 6). The measured areas of the pieces and their densities calculated from their measured weights and thicknesses are given in Table 1. From the measured weight of each microtomed slice from the given RTV piece, the measured density of the RTV piece, and the measured cross-sectional area of the slice, the mean thickness of each slice was calculated and is given in Table 1. This calculated thickness value was used instead of a measured thickness, due to the irregular thickness of each microtomed slice. The mean depth of each slice is given by the total thicknesses of the previous slices plus the half thickness of the present slice.

The test conditions during the various thermal analyses are given in Table 2. The heating rates were all the same, whereas the temperature range varied with the technique. TGA and DSC could be performed well above the glass transition temperature, but TMA could not. The TGA atmosphere was oxygen to measure the relative oxidation rates of the exposed and control RTV 511 slices.

RESULTS AND DISCUSSION

As opposed to the previous results with Halar (ref. 6), the density of the exposed RTV 511 was about 6 percent higher than the RTV 511 control (Table 1). If outgassing occurred during the LDEF exposure, the reverse should occur, unless shrinkage also occurred and volume contraction more than offset the mass loss.

The results are presented for each thermal analysis technique by showing typical thermograms in the figures included here and tables of peak temperatures or baseline shifts (weight changes and penetrations). The information from the TMA, DSC, and TGA thermograms of all the slices of the exposed and control RTV 511 is given in Tables 3, 4, and 5, respectively.

The penetration versus temperature TMA output plot is shown in Figure 1 for a section of the RTV 511 control sample. This plot was typical of all the TMA plots for both the exposed and control slices, showing thermal expansion upon heating giving way to contraction due to flow at the high temperatures. The temperature for the onset of flow is calculated by the method of intersecting tangents by the TMA software, and is shown in Figure 1. The onset temperatures are listed versus mean section depth in Table 3. Although visible discoloration was present in the top slice of the exposed RTV 511 piece, the onset temperatures showed no significant variation with slice depth in either the exposed or the control slices, Table 3. The average onset temperature for flow for the exposed slices of 401 °C is slightly higher than the average of the control slices of 393 °C. This agrees with the slightly higher density of the exposed piece.

A typical DSC thermogram is shown in Figure 2 for the top-most slice of the LDEF exposed RTV 511 sample. An apparent glass transition temperature onset calculated by the DSC software is shown at 309 °C. This shift was observable only after expanding the ordinate sensitivity such that significant noise is evident. Other slices of the exposed and control samples either exhibited similar shifts to that shown in Figure 2, or exhibited no shifts or peaks at all over the 25 to 600 °C temperature range scanned. The transition temperatures reported in Table 4 for all the DSC scans of all the slices are too few to identify any effect of slice depth or any significant difference between the exposed and control slices.

Figures 3 and 4 are typical TGA output plots for weight loss while heating in oxygen for the top-most LDEF exposed RTV sample slice and a slice 597-microns deep, respectively. Cumulative weight losses at 420 and 600 °C are given in Table 5. As can be seen by comparing Figures 3 and 4, the weight loss at 600 °C is 54 percent of the top-most exposed RTV slice, and only 40 percent for the 597-micron deep slice of the RTV 511 exposed sample. As shown in Table 5, the LDEF exposed RTV shows an increase in weight loss in the top slice, 54 percent, as compared to the average weight loss of 46 percent for all the slices. The control sample slices showed irregular TGA weight losses, Table 5. The top slice of the control sample, three other control slices, and one exposed slice showed anomalous step function drops in weight at around 525 °C, preventing a measurement of the 600 °C weight loss. Either an unexplainable TGA system error occurred, or these samples oxidized completely at 525 °C.

The TMA and DSC techniques measure the response of the whole sample section which is placed in the analyzer. Near surface effects that are truncated in several atom layers would not be resolvable in the roughly 50- to 200-micron thick sections. The TGA, however, measures the oxidation rate at the surface of the section placed in the analyzer. The top-most slice of the exposed RTV 511 had as its top surface the actual discolored top surface given the orbital exposure. The other side of the section was produced by the microtome. Thus, the TGA is the most surface sensitive of the three techniques employed, and it is the only technique to sense damage from orbital exposure in the RTV 511. The measured difference between top and bulk slices for the RTV 511 in TGA is much less pronounced than that observed for the Halar slices in TGA (ref. 6). However, due to the uncontrolled section depth produced by the microtome, the top Halar slice was 12-microns thick, while the top RTV 511 slice was 210-microns thick. The thicker RTV 511 slice would tend to mask surface damage detected by TGA.

CONCLUSIONS

In general, little difference between the LDEF exposed and control samples of RTV 511 was detected by thermal analysis. Some subtle differences are listed below.

1. A small difference between the top section of the LDEF exposed sample as compared to the lower sections appeared in TGA. The top section lost 54 percent of its weight by 600 °C, while the average section loss was 46 percent.

2. In TMA, the exposed sections had slightly higher flow temperatures than the control sections. There appeared to be no surface effect in either sample.

3. In DSC, no endotherms or exotherms were observed in either the sections of the exposed or the control samples. A glass transition like shift occurred in about half of the sections of each sample. There were no significant differences among the shifts in the samples.

4. The density of the RTV 511 exposed sample is 6 percent higher than the control sample.

REFERENCES

1. Whitaker, A.F.: "Coatings Could Protect Composites From Hostile Space Environments." Adv. Materials and Processes, vol. 4, 1991, pp. 30–32.

2. Tennyson, R.C., Mabson, G.E., Morison, W.D., and Kleinman, J.: "LDEF Mission Update: Composites in Space." Adv. Materials and Processes, vol. 5, 1991, pp. 33–36.

3. Dunbar, B.J.: "A Materials Scientist in Space." MRS Bulletin, May 1991, pp. 36–41.

4. Steckel, G.L., and Le, T.D.: "LDEF Mission Update: Composites Survive Space Exposure." Adv. Materials and Processes, vol. 8, 1991, pp. 35–38.

5. Young, P.R., and Slemp, W.S.: "Characterization of Selected LDEF-Exposed Polymer Films and Resins." LDEF Materials Workshop '91, NASA CP-3162, Part 1, 1991, pp. 357–389.

6. Brower, W.E. Jr., Holla, H., and Bauer, R.A.: "Effects of Orbital Exposure on Halar During the LDEF Mission." LDEF Materials Workshop '91, NASA CP-3162, Part 1, 1991, pp. 390–415.

7. Hurley, C.J., and Jones, M.: "Long Duration Exposure Facility M0003-5, Recent Results on Polymeric Films." LDEF Materials Workshop '91, NASA CP-3162, Part 1, 1991, pp. 417–447.

Table 1. Weight and density measurements for cut sections of RTV 511 LDEF and control samples. Thicknesses are calculated from the measured weight, density, and areas of the slices. The mean depth is reported at half the section thickness.

RTV in TGA

Control Piece No. 1

Area = 0.7971 cm^2
Density = 1.2646 gr/cm^3

Sample II	Wt (gr)	Thick (μm)	Mean Depth
R1C1	0.0020	19.8	9.9
R1C2	0.0023	22.8	32.3
R1C3	0.0056	55.6	70.4
R1C4	0.0051	50.6	123.5
R1C5	0.0125	124.0	210.8
R1C6	0.0016	15.9	280.8
R1C7	0.0027	26.8	302.1
R1C8	0.0286	283.7	457.3
R1C9	0.0345	342.3	770.3
R1C10	0.0283	280.8	1,081.8
51C11	0.0029	28.8	1,236.6
51C12	0.0392	388.9	1,445.4
Cutoff	0.4454	4,418.6	
Total	0.6107	6,058.5	
Original	0.6120	6,071	

RTV in TGA

Exposed Piece No. 2

Area = 0.6032 cm^2
Density = 1.3356 gr/cm^3

Sample ID	Wt (gr)	Thick (μm)	Mean Depth
R2C1	0.0169	209.8	104.9
R2C2	0.0077	95.6	257.6
R2C3	0.0149	184.9	397.8
R2C3A	0.0149	184.9	397.8
R2C4	0.0064	79.4	530.0
R2C5	0.0044	54.6	597.0
R2C6	0.0171	212.3	730.5
Cutoff	0.4135	5,132.6	
Total	0.4809	5,969.2	
Original	0.4931	6,121	

Table 2. Test conditions for RTV 511 samples for thermal analysis.

Technique	Test Atmosphere	Heating Rate (°C/min)	Temperature Range (°C)
TMA	Flowing Ar	10	25 to 500
TGA	Flowing O_2	10	25 to 900
DSC	Flowing Ar	10	25 to 600

Table 3. Thermomechanical analysis results on RTV 511.
Onset temperatures for flow over the range 320 to 430 °C.

Sample Number		Depth (microns)	Onset Temperature (°C)
Exposed	R2C1	105 (top)	402
	R2C2	258	394
	R2C3	398	402
	R2C4	530	403
	R2C6	730	403
			Avg = 401
Control	R1C5A	210	399
	R1C8	457	396
	R1C9B	770	398
	R1C12	1,445	397
			Avg = 393

Table 4. Differential scanning calorimetry results for RTV 511.
Glass transition temperatures over the range 3,275 to 350 °C.

			Glass Transition Temperature (°C)	
Sample Number		Depth (microns)	Onset	Midpoint
Exposed	R2C1	105 (top)	309	283
	R2C2	258	286	288
	R2C3	398	None	
	R2C4	530	None	
	R2C6	730	None	
Control	R1C3	70	None	
	R1C4	124	None	
	R1C5	211	330	330
	R1C6	281	293	305

Table 5. Thermogravimetric analysis results on RTV 511.

Sample Number		Mean Depth (microns)	Percent Weight Loss 25 to 420 °C	Percent Weight Loss 25 to 600 °C
Exposed	R2C1	105 (top)	5	54
	R2C2	258	3	44
	R2C3A	398	3	50
	R2C4	530	4	44
	R2C5	597	1	40
	R2C6	730	2	46
				Avg = 46
Control	R1C1	9.9 (top)	2	–
	R1C2	31.2	2	53
	R1C4A	123	2	32
	R1C6	280	2	30
	R1C8A	457	5	49
	R1C10	1,081	5	44
	R1C12	1,445	6	57
				Avg = 42

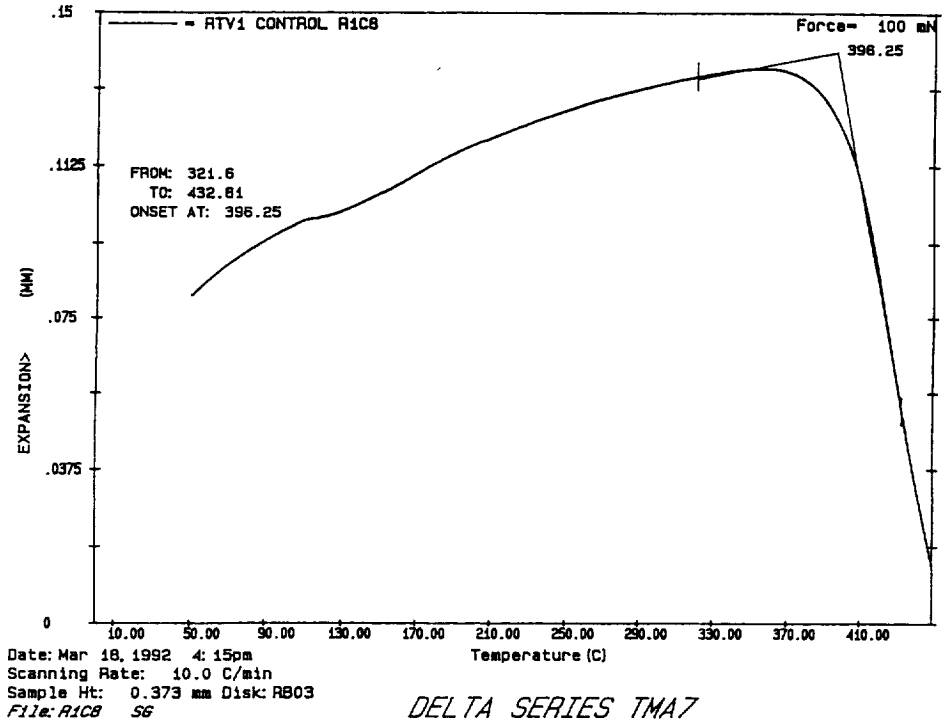

Figure 1. Typical TMA plot for a section of the RTV 511 LDEF sample showing the determination of onset temperature by the intersection of tangents.

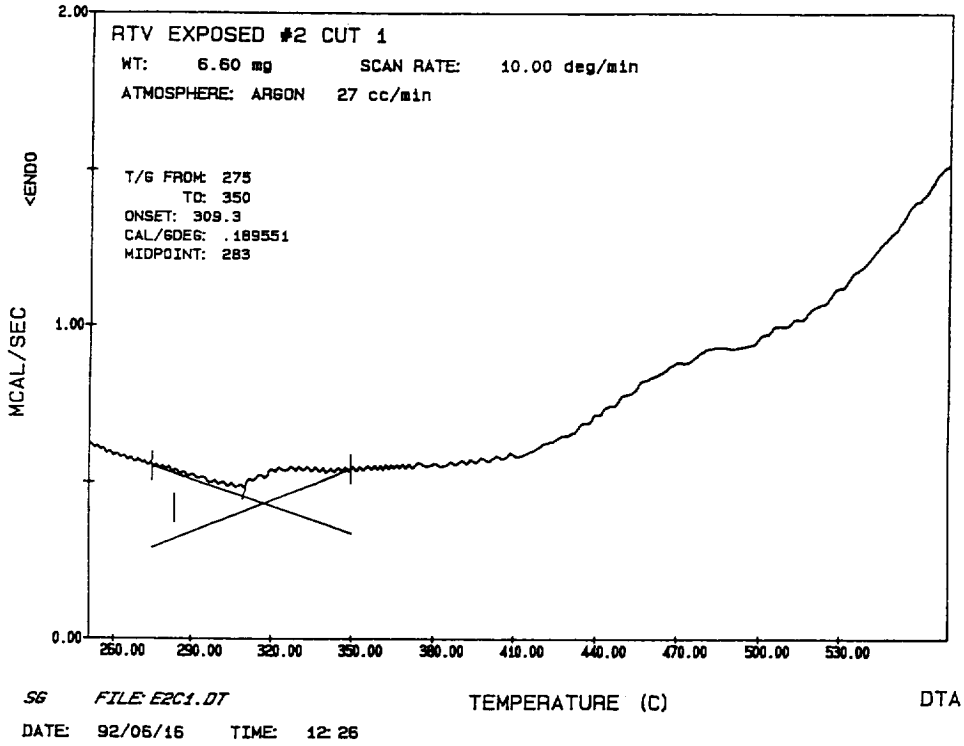

Figure 2. DSC plot for the top section of the RTV 511 LDEF exposed sample showing an apparent glass transition temperature with an onset of 309 °C and a midpoint of 283 °C.

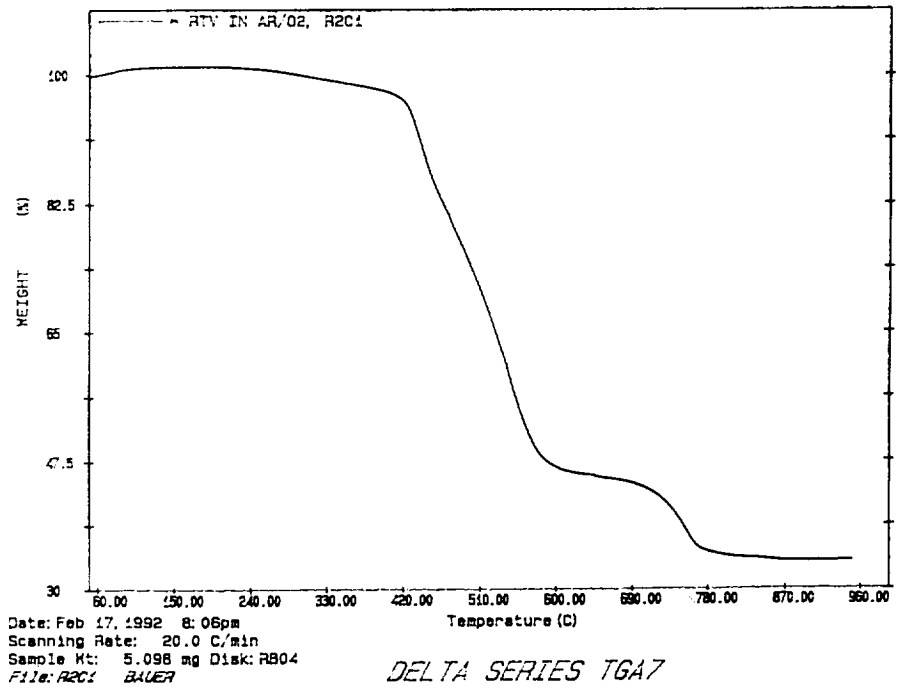

Figure 3. TGA plot for the top section of the RTV 511 LDEF exposed sample showing a 54-percent weight loss by 600 °C.

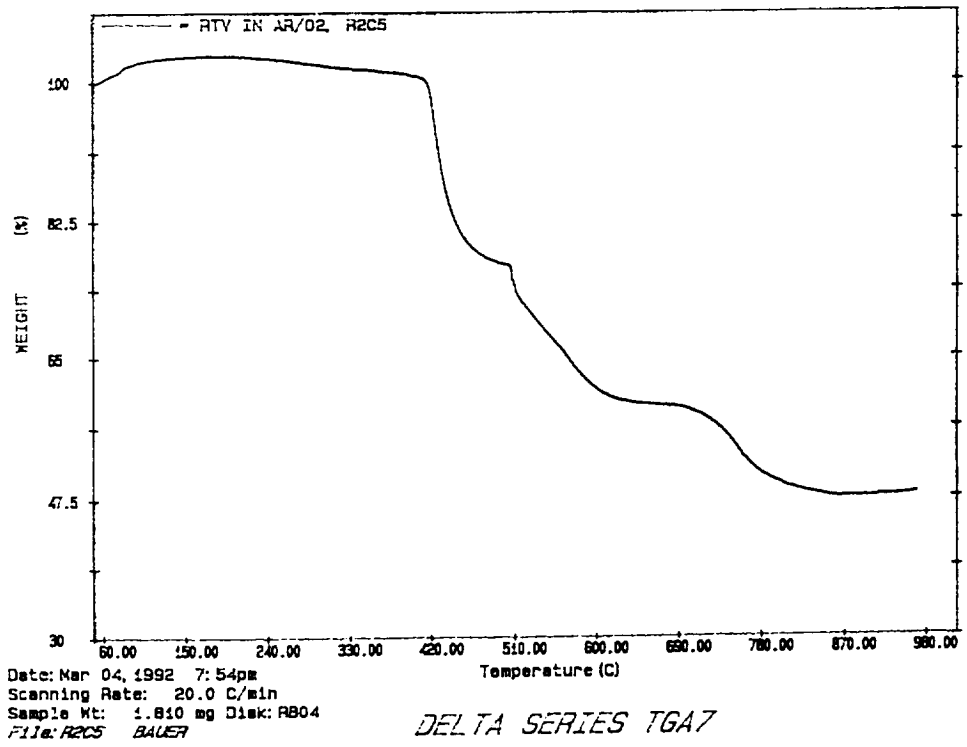

Figure 4. TGA plot for the section of the RTV 511 exposed at a mean depth of 597 microns showing a 40-percent weight loss by 600 °C.

MISCELLANEOUS

NASA's SPACE PLATFORM TECHNOLOGY PROGRAM AND PLANNING

Gary L. Bennett
National Aeronautics and Space Administration
Washington, DC 20546
Phone: 202/453-2858, Fax: 202-426-0001

Russell C. Cykoski
General Research Corporation
Washington, DC 20024
Phone: 702/506-4908, Fax: 202/488-3292

SUMMARY

As part of the Civil Space Technology Initiative, NASA has established a space platform technology program which encompasses two ongoing programs as well as active planning for new platform initiatives in such areas as advanced heat rejection technologies, advanced space suits, advanced life support, and better support equipment (refrigerators, furnaces, etc.). Platform technology is extremely important because it provides both the basis for future missions and enhanced national competitiveness in space.

INTRODUCTION

The space platform is the foundation of any space mission whether manned or unmanned. The space platform encompasses essentially everything outside the payload, including (as appropriate) structure, power, propulsion, thermal management, life support, space suits, and guidance, navigation, and control. The space platform has to be light weight to minimize the launch weight (and the launch cost), but it must be strong enough to withstand launch loads. The space platform has to maintain its attitude and orbit in a stable manner. The space platform serves in a sense as a utility by supplying, for example, power and, in some cases, life support to the payloads and crew (ref. 1). In many ways, space platform technology is generic in that the technology can be applied to many different kinds of missions. For example, a light-weight solar array technology could be applied to Space Station *Freedom* (S.S. *Freedom*), commercial satellites, space science missions, or human exploration of the Moon and Mars. Thus, investment in space platform technology can benefit the U.S. space program across the board.

OBJECTIVES

NASA's Office of Advanced Concepts and Technology (OACT) has a space technology program composed of two principal elements: Base Research and Technology (R&T) program and the focused Civil Space Technology Initiative (CSTI). Within the CSTI program, OACT has established a Space Platforms Technology program to develop the technologies to increase on-orbit mission efficiency and decrease life cycle costs for future manned and unmanned science, exploration, and commercial

missions (ref. 1). Within NASA the space platforms program is primarily designed to respond to the identified needs of NASA's space science program and NASA's S.S. *Freedom* program; however, there is a strong focus on developing technologies of use to the broader U.S. space community, both government and commercial. Additional objectives include:

- Developing technologies that will decrease launch weight and increase the efficiency of space platform functional capabilities
- Developing technologies that will increase human productivity and safety of manned missions
- Developing technologies that will increase maintainability and reduce logistics resupply of long-duration missions
- Identifying and developing flight experiments in all technology and thrust areas that will benefit from the utilization of S.S. *Freedom* facilities.

The "vision" of the Space Platform Technology Program includes:

- World leadership in space platform technology
- Development to enable better, lower cost missions
- Improving the American competitive position.

The Space Platform Technology Program currently has two funded elements: controls-structures integration (CSI) and a ground test of a 2-kilowatt (kW) solar dynamic (SD) power system. Looking 10 years into the future, the specific objectives of the Space Platform Technology Program include:

- Developing solar dynamic receiver units with specific powers of 25 W/kg and a 50-percent mass reduction
- Developing technology to support high-performance integrated control/structure systems design

as well as these objectives for planned programs:

- Developing advanced heat rejection technologies to accommodate growth S.S. *Freedom*
- Developing an advanced, light-weight concentrator array with twice the efficiency of existing arrays
- Developing advanced batteries with a performance of 60 W-h/kg and a design life greater than or equal to 5 years
- Developing advanced extravehicular mobility unit (EMU) technologies to support an increase in demand for S.S. *Freedom* extravehicular activity (EVA) operations while reducing cost and ensuring health and safety

- Upgrading the S.S. *Freedom* environmental control and life support system (ECLSS) to reduce logistics requirements, increase crew safety, and to match projected increases in crew size in the post 2000 period

- Developing reliable user support systems (such as refrigerators and furnaces) to enable the conduct of experiments on S.S. *Freedom*

- Developing advanced deep-space power management and distribution (PMAD) components to reduce the mass by a factor of 2, the parts count by 75 percent, and to increase the low-voltage power conservation efficiency to greater than 90 percent

- Reducing radioisotope power source fuel requirements by increasing thermal-to-electric conversion efficiency by up to 3 times.

BACKGROUND

Contributions of Base R&T to Space Platforms

NASA-sponsored R&T has already contributed to the improvement of space platforms. Some recent examples include (refs. 1, 2, and 3):

- Nickel-hydrogen battery technology—Improved specific energy lifetime (including for low-Earth orbit (LEO) applications) which will benefit S.S. *Freedom* and which provided support to the decision to change to nickel-hydrogen batteries for the Hubble space telescope (HST).

- NASCAP (NASA Charging Analysis Program) spacecraft charging model—This model has been used to modify the design of the S.S. *Freedom* electrical system to overcome potential electrical arcing and sputtering problems.

- Long Duration Exposure Facility (LDEF)—This experiment has provided a wealth of data on space environmental effects (as amply demonstrated by these proceedings and earlier proceedings).

- Life support technologies—Regenerative technologies for water recovery and recycling for crew consumption and for recovery of oxygen for crew consumption have been developed. Thermal control system technology has also been developed. Models and chemical sensors are being developed.

- Multipropellant resistojets—This propulsion technology offers improved performance over standard chemical propulsion systems for attitude control and maneuvering, and it can run on waste water from the life support system on S.S. *Freedom.*

- Large area solar cells—Early work has led to the use of large area solar cells (maximized active area) on S.S. *Freedom.*

- Arcjet thruster—Low-power arcjet technology has been taken to the point where it is now being baselined on commercial satellites (e.g., Telstar IV) to improve station keeping while reducing propellant mass.

Technology Trends

Figure 1 illustrates the breakout of the deployment mass of S.S. *Freedom*. This represents a "fixed" mass, but the resupply mass breakout shown in Figure 1 illustrates the benefits to be achieved by reducing the resupply (in such areas as spares, ECLSS, propulsion, and crew support) and, hence, the cost of maintaining S.S. *Freedom*. Figure 2 illustrates the S.S. *Freedom* resupply needs and the technologies which could reduce the resupply. Eventually over the lifetime of S.S. *Freedom*, the equivalent of several space shuttle launches could be saved with improved technologies. NASA's Office of Space Systems Development (OSSD), which is responsible for the overall management of the S.S. *Freedom* program, has identified many of these space platform technologies to OACT as being of high priority to the S.S. *Freedom* program.

Figure 3 shows the trends in launch masses for 195 robotic NASA spacecraft, indicating some recent upward movement. Figure 4 shows a typical mass breakout for today's robotic spacecraft. Currently, NASA is emphasizing smaller, cheaper, and quicker missions. The goals are to reduce the total launched mass to under 1,000 kg and to increase the payload fraction (ideally to 0.5). As shown in Figure 5, platform technologies such as power, propulsion, thermal management, structure, and guidance, navigation, and control (GN&C) can play critical roles in achieving these goals. Many of these space platform technologies have been identified as high priority to OACT by NASA's Office of Space Science and Applications (OSSA), which is responsible for the robotic science missions. In several cases there is an overlap between OSSA and OSSD technology development requests which indicates the generic nature of space platform technology.

OVERVIEW OF THE CURRENT SPACE PLATFORM TECHNOLOGY PROGRAM

Fiscal Year 1993 Program

Working within overall budget guidance, the Fiscal Year (FY) 1993 Space Platform Technology Program consists of only two ongoing elements: (1) power and thermal management (specifically a 2-kWe solar dynamic power system ground test) and (2) structures and dynamics (specifically the CSI program). These two programs are discussed in the following two sections.

Solar Dynamic Test Program

Growth in S.S. *Freedom* will be limited by available power. While the baseline S.S. *Freedom* design will use photovoltaic (PV) planar arrays (~14 percent efficient), such arrays are not feasible for meeting the power requirements anticipated for S.S. *Freedom* evolution because of their high atmospheric drag characteristics and the associated mass penalties related to reboost and propellant resupply. One option to increase the power of S.S. *Freedom* while minimizing mass and drag area is to

C-6.

use the more efficient solar dynamic power system technology. In the past, concerns have been expressed over the long-term performance of rotating machinery and thermal energy storage (TES) systems. The solar dynamic power system program will address many of these concerns by ground testing, in a space vacuum chamber with a solar simulator, the essential components of a solar dynamic power system. (A related flight experiment will address the thawing and freezing of TES material in a microgravity environment.) The testing and analysis will be conducted to support scaling the models up to at least 20 kWe. In FY 1992, the SD program, which is being managed by Lewis Research Center (LeRC), awarded a contract to design, fabricate, and test a 2-kWe solar dynamic space power system. In addition, the program completed the system requirements review for the 2-kWe solar dynamic space power system. In FY 1993, the program will complete the preliminary design review and the critical design review. In addition, the refurbishment of the government-furnished equipment (turbine-alternator-compressor and the recuperator) will be completed, and fabrication of the new hardware will be initiated. More information can be found in Reference 4.

Controls-Structures Integration Program

CSI brings together, in a unified manner, the control and structural aspects of space platforms to reduce spacecraft dynamic response and to improve the control and pointing capabilities of spacecraft. Out of the CSI program will come unified controls-structures modeling, analysis, and design methods which will allow a complete iteration on all critical design variables in a single integrated computational framework. CSI will enable increased pointing precision; increased flight path control; increased use of articulated components; increased use of multipayload platforms with multiple interacting control systems; and (as needed) increased platform sizes and lower frequencies (ref. 1). One source of information on CSI may be found in the papers presented at the annual AIAA/ASME/ASCE/AHS/ASC Structures, Structural Dynamics, and Materials Conferences.

The CSI program is being conducted at three NASA Centers (Jet Propulsion Laboratory (JPL), Langley Research Center (LaRC), and the Marshall Space Flight Center (MSFC)) in a coordinated effort involving space science technology, space platform technology, and the Base R&T program. In FY 1992, the CSI program completed the CSI benefits study for Upper Atmospheric Research Satellite (UARS) and Earth Observing System (EOS) class missions and identified an approach to decrease the jitter by a factor of 5. A NASA Research Announcement (NRA) was issued for the Phase III guest investigator program at five cooperating ground test facilities (JPL, LaRC, MSFC, Edwards Air Force Base, and Kirtland Air Force Base). The Class I integration design methodology was validated by means of a rebuilt (Phase I) evolutionary model. Tests run on the space shuttle remote manipulator system (RMS) using a LaRC-developed control algorithm have shown substantial improvements in instrument pointing jitter and reduction of the settling time.

In FY 1993, the CSI program will focus on:

- S.S. *Freedom*/Space Transportation System (STS) assembly simulations
- Phase I evolutionary ground testbed model ground test results
- Middeck Active Control Experiment (MACE) critical design review
- Follow-on shuttle engineering simulator testing of RMS active damping for payloads of large mass

- Initial control tests for multipayload pointing
- Structural system identification testing of Phase II CEM
- Integrated design of GOES-I spacecraft
- Integrated design methodology for Class-II-type mission
- Advanced control laws for Class II experimentally evaluated
- Modal testing of hybrid-scale erectable components, major subassemblies, and full assembly of MB-5 configuration.

The future focus of CSI will include:

- Space shuttle RMS
- S.S. *Freedom*
- Earth observing platforms
- "Flagship" missions.

Contribution and Relationship of Current Program

The two ongoing programs will contribute to the nation's space capabilities.

Solar Dynamic Power Program

The solar dynamic power program will provide proof-of-concept through ground testing. This information is directly relevant to the original S.S. *Freedom* solar dynamic power module design. The test hardware will be flight configured and, through analysis and testing, the results will be scalable to 20 kWe. Again, the importance relates to the reduced area and reduced mass compared to the existing S.S. *Freedom* PV/battery system. The solar dynamic ground test program builds on the ongoing solar dynamic component technology program being conducted in the Base R&T program.

CSI Program. The CSI program has already demonstrated the following benefits:

- An increase of 4× in the maximum antenna diameter for a large geostationary platform that meets pointing and jitter requirements
- A decrease of 5× in the amount of settling time for the shuttle RMS during S.S. *Freedom* assembly operations
- A decrease of 5× in the pointing jitter error for a multipayload spacecraft similar to UARS.

The CSI also benefits from and is related to ongoing CSI technology development in the Base R&T program.

SPACE PLATFORMS TECHNOLOGY PROGRAM STRATEGIC PLANNING

Planning Process

As part of the OACT Integrated Technology Plan (ITP), the user organizations (such as OSSD and OSSA) provided OACT in 1992 with a formal set of technology needs. Those related to space platforms are listed below:

Office of Space Systems Development

- Advanced heat rejection for growth S.S. *Freedom*
- ECLSS for S.S. *Freedom* (in particular closing the oxygen and water loops)
- High-efficiency space power (better batteries and solar cells)
- Advanced EMU (to reduce the resupply and refurbishment time)
- Orbital debris protection (to protect S.S. *Freedom*).

Office of Space Science and Applications

- Efficient/quiet/safe/reliable refrigerator for science experiments on S.S. *Freedom* or STS
- Improved GN&C for science spacecraft
- Improved electric power (in particular a small radioisotope thermoelectric generator)
- Improved CSI for antennas
- Long-life, light-weight batteries
- Better thermal control on spacecraft
- Improved EMU for S.S. *Freedom*
- Regenerative life support for S.S. *Freedom*
- Improved solar array/cell technology for science spacecraft
- Improved furnaces for materials experiments on S.S. *Freedom.*

In response to these needs, OACT established a Space Platform Technology Thrust Team managed by OACT and with members from Ames Research Center (ARC) (EMU), GSFC (thermal management), JPL (power, propulsion, GN&C), Johnson Space Center (JSC) (advanced EMU, refrigerator), LaRC (CSI, materials, nondestructive examination, environmental effects), MSFC (ECLSS), OSSA, OSSD, and the Office of Exploration (OEXP). The Thrust Team developed a series of initiatives to meet the user needs. These initiatives included goals, objectives, milestones, deliverables, and funding profiles. This information was forwarded to OACT management as part of the FY 1994 budget deliberations.

Figure 6 shows the platform planning approach, and Figure 7 relates the user needs to the space platform program. All elements (except furnaces) are covered in the plan. Figure 8 shows the road map to meet OSSD needs, and Figure 9 shows the road map to meet OSSA needs.

Science Platform Initiative

A very recent initiative in support of future OSSA missions is the small spacecraft initiative. Specifically, in FY 1993, OACT will be funding an advanced technology insertion program to reduce the mass, improve the performance, and reduce the schedule for the proposed Pluto Fast Flyby mission and the Thermosphere-Ionosphere-Mesosphere Energetics and Dynamics (TIMED) mission. In addition, elements of the Base R&T program will be focused on technologies applicable in general to "microspacecraft" or "lightsats."

Future Directions in Platforms

In looking to the future, the Space Platform Technology Program will be focusing on:

- Commercial spacecraft (to enhance U.S. competitiveness)
- Changing Earth observing systems
- Microspacecraft for science missions
- Cooperative programs with industry and other agencies (such as electric propulsion technology for station keeping or orbital maneuvering).

SUMMARY AND OBSERVATIONS

Enhancing U.S. competitiveness in space and expanding scientific knowledge of Earth, the solar system, and the universe represents a tremendous technological challenge requiring a significant, long-term investment in space platform technologies. Space platform technology has the advantage of applying to a wide range of space systems and can benefit all types of users. Based on studies of existing platforms and estimating future costs for planned missions, it is clear that there is significant room for improvement. OACT has established a Space Platform Technology Program which, if implemented, will develop the necessary technologies to meet this challenge.

REFERENCES

1. Office of Aeronautics and Space Technology, *Space Platforms Focused Program Plan, Integrated Technology Plan*. National Aeronautics and Space Administration, Washington, DC, July 1991.

2. Bennett, G.L.: "The OAST Space Power Program." Space Photovoltaic Research and Technology–1989, proceedings of a conference held at NASA Lewis Research Center, Cleveland, OH, November 7–9, 1989, NASA Conference Publication 3107, 1991.

3. Bennett, G.L., Watkins, M.A., Byers, D.C., and Barnett, J.W.: "Enhancing Space Transportation: The NASA Program to Develop Electric Propulsion." NASA Technical Memorandum 4244, National Aeronautics and Space Administration, Washington, DC, October 1990.

4. Calogeras, J.E., and Dustin, M.O.: "The Ground Testing of a 2-kWe Solar Dynamic Space Power System." Proceedings of the 27th Intersociety Energy Conversion Engineering Conference, vol. 1, p. 1455, proceedings of a conference held in San Diego, CA, August 3–7, 1992.

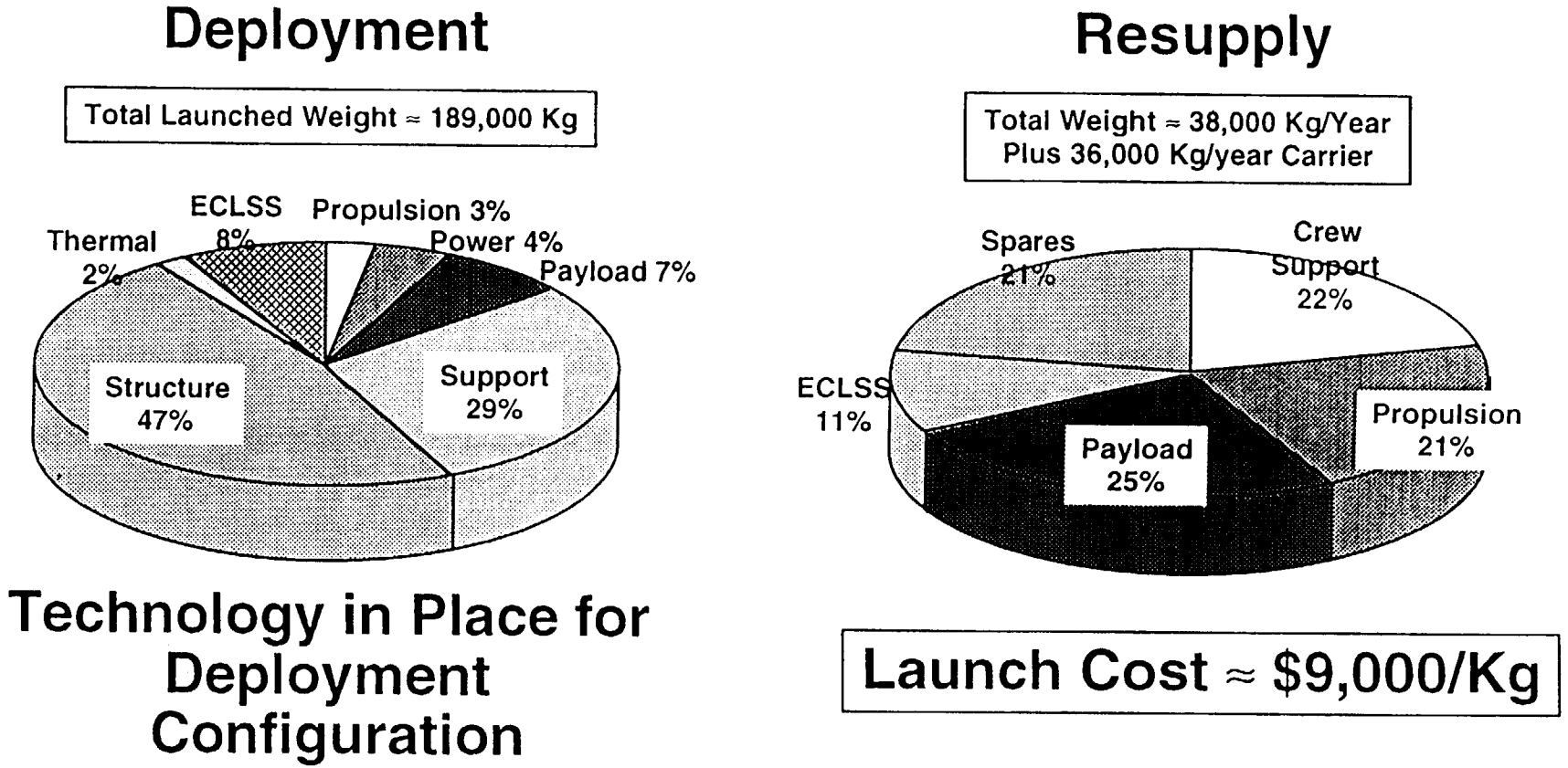

Figure 1. Technology evolution of S.S. *Freedom*.

Specific Technologies Requested by NASA User Codes	Resupply Reduction
High Efficiency Space Power Systems (OSSD)	Spares/Propulsion
Thermal Control System (OSSA/OSSD)	Spares
Improved Solar Arrays/Cells/Batteries (OSSA)	Propulsion
Advanced Heat Rejection Devices (OSSA/OSSD)	Spares
Advanced Furnace Technology (OSSA)	Payload
Efficient, Quiet Refrigerator/Freezer (OSSA)	Payload
Advanced Extravehicular Mobility Unit Technologies (OSSA/OSSD)	Crew Support
Advanced Environmental Control & Life Support System (OSSA/OSSD)	ECLSS

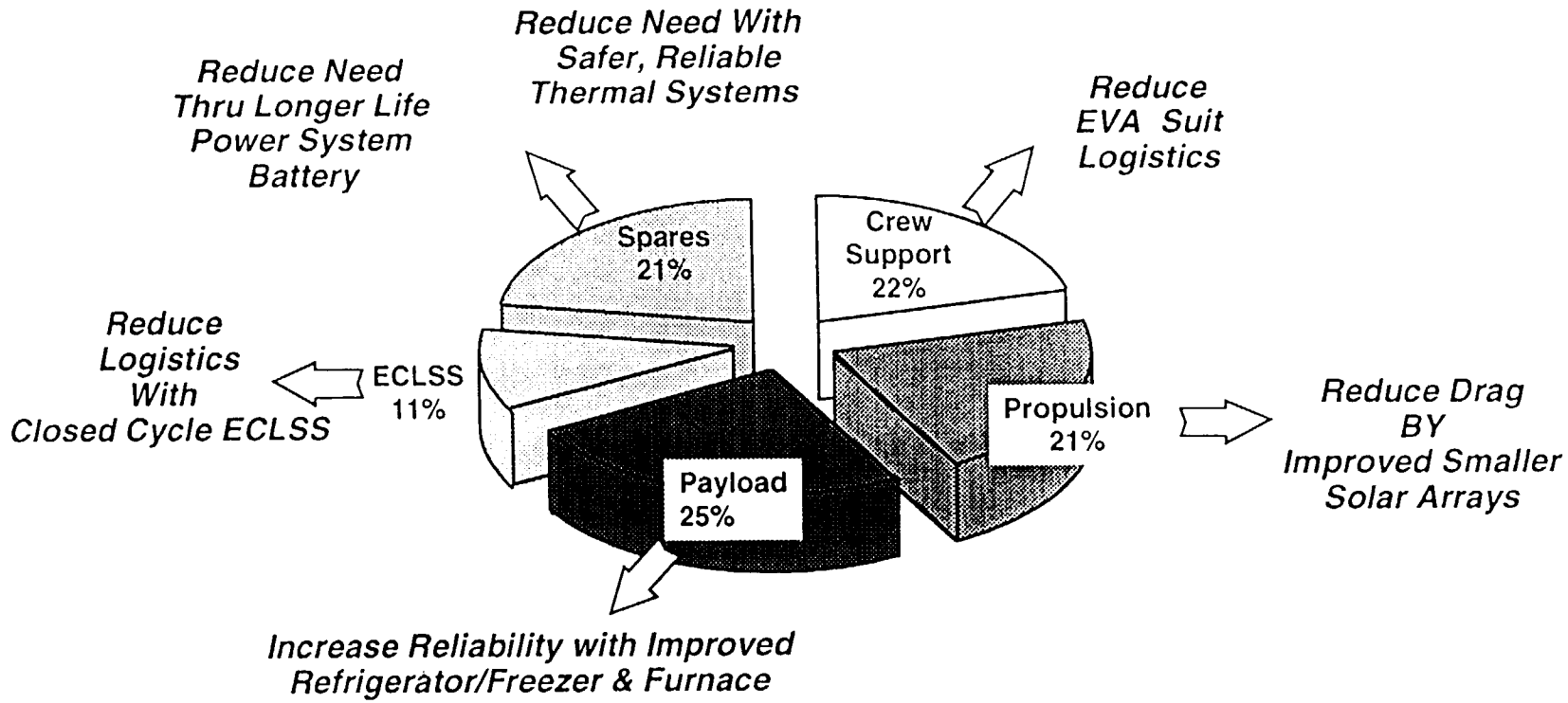

Figure 2. S.S. *Freedom* resupply needs.

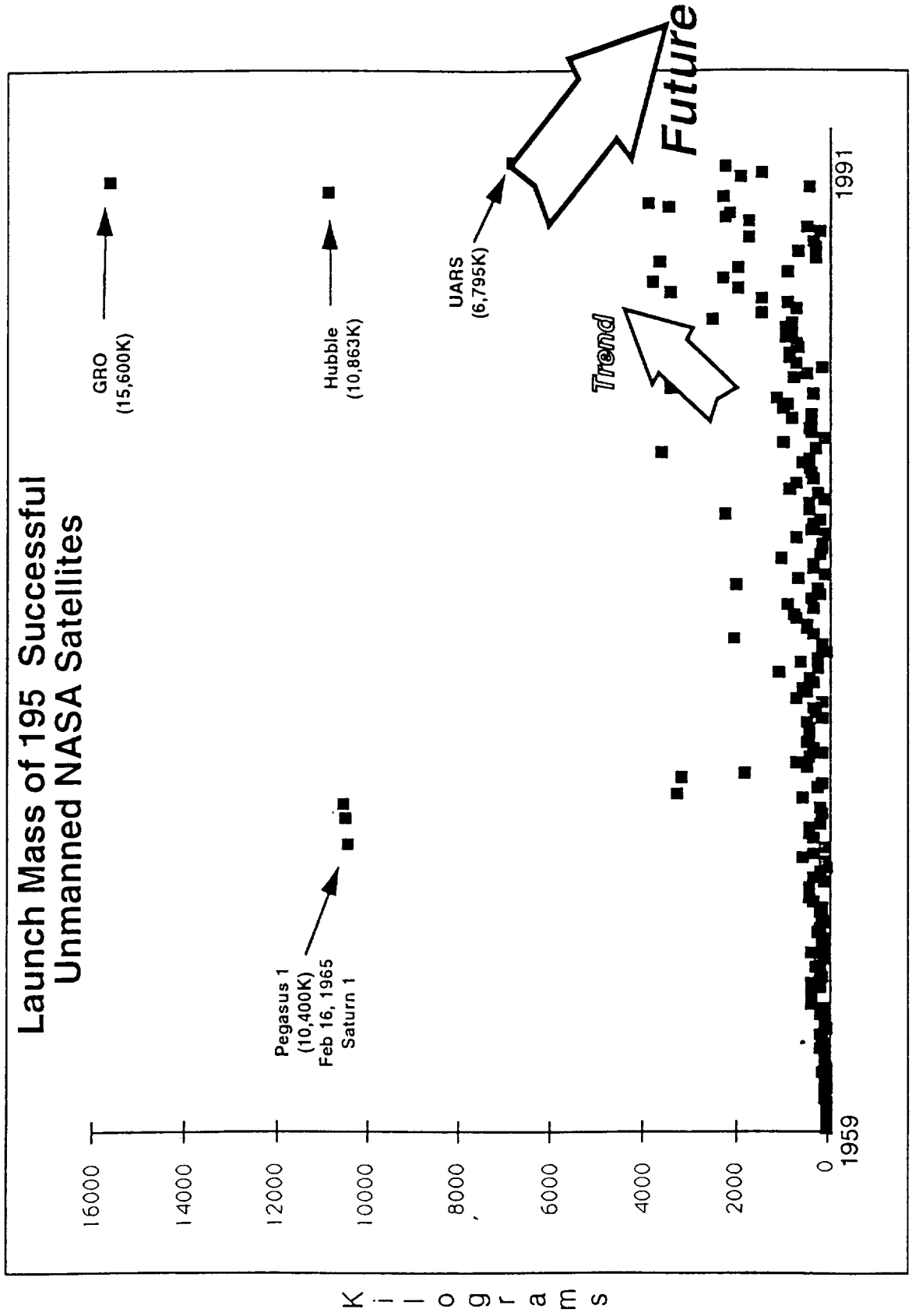

Figure 3. NASA unmanned missions.

Unmanned Systems

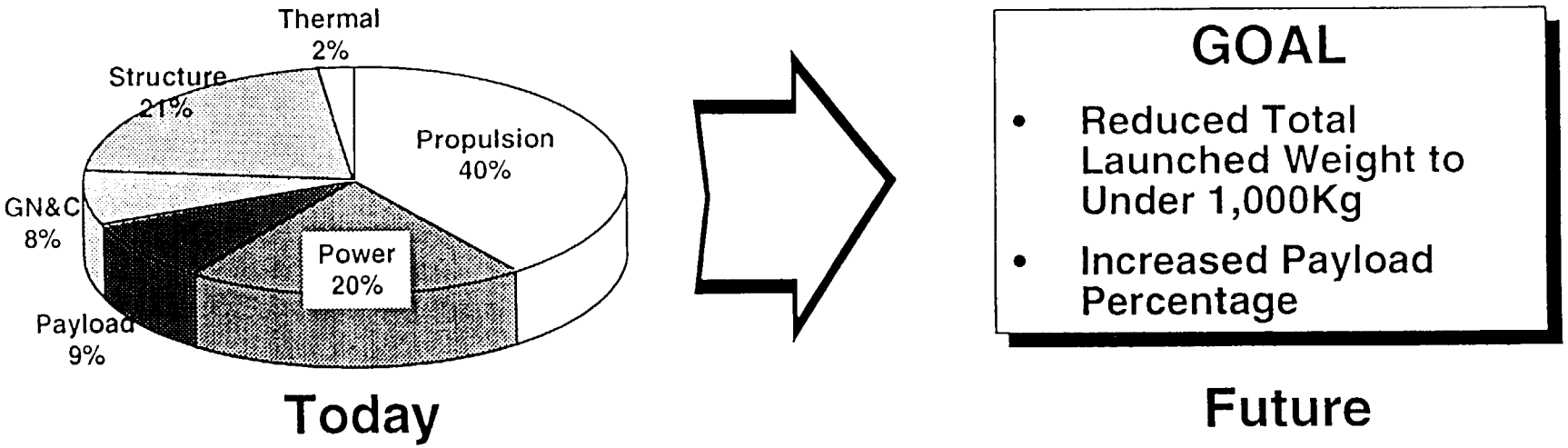

Figure 4. Technology evolution of platforms.

Specific Technologies Requested by NASA User Codes	Cost Reduction
High Efficiency Space Power Systems (OSSA/OSSD)	Power System
Thermal Control System (OSSA/OSSD)	Thermal System
Improved Solar Arrays/Cells/Batteries (OSSA/OSSD)	Power System
Advanced Heat Rejection Devices (OSSA/OSSD)	Thermal System
Microsystems / Deep Space GN&C / Deep Space Power (OSSA)	All Systems
Controlled Structures/Large Antenna Structure/Area (OSSA)	Structure Systems

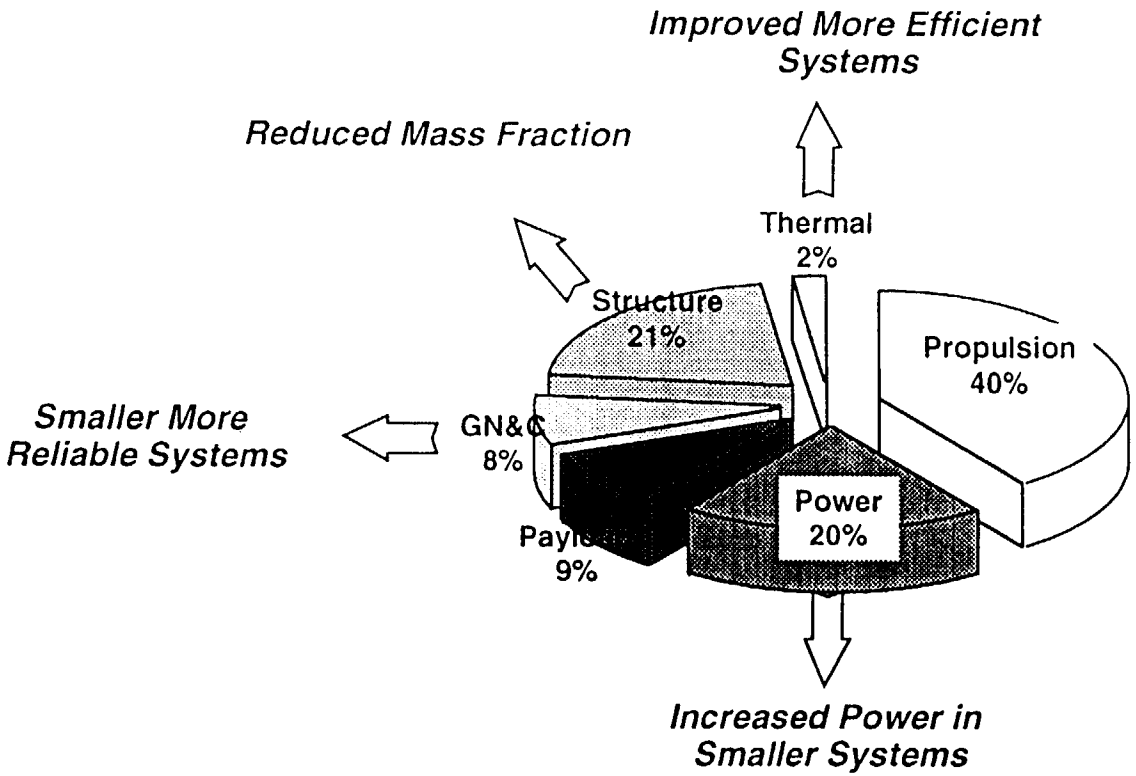

Figure 5. Science platform needs.

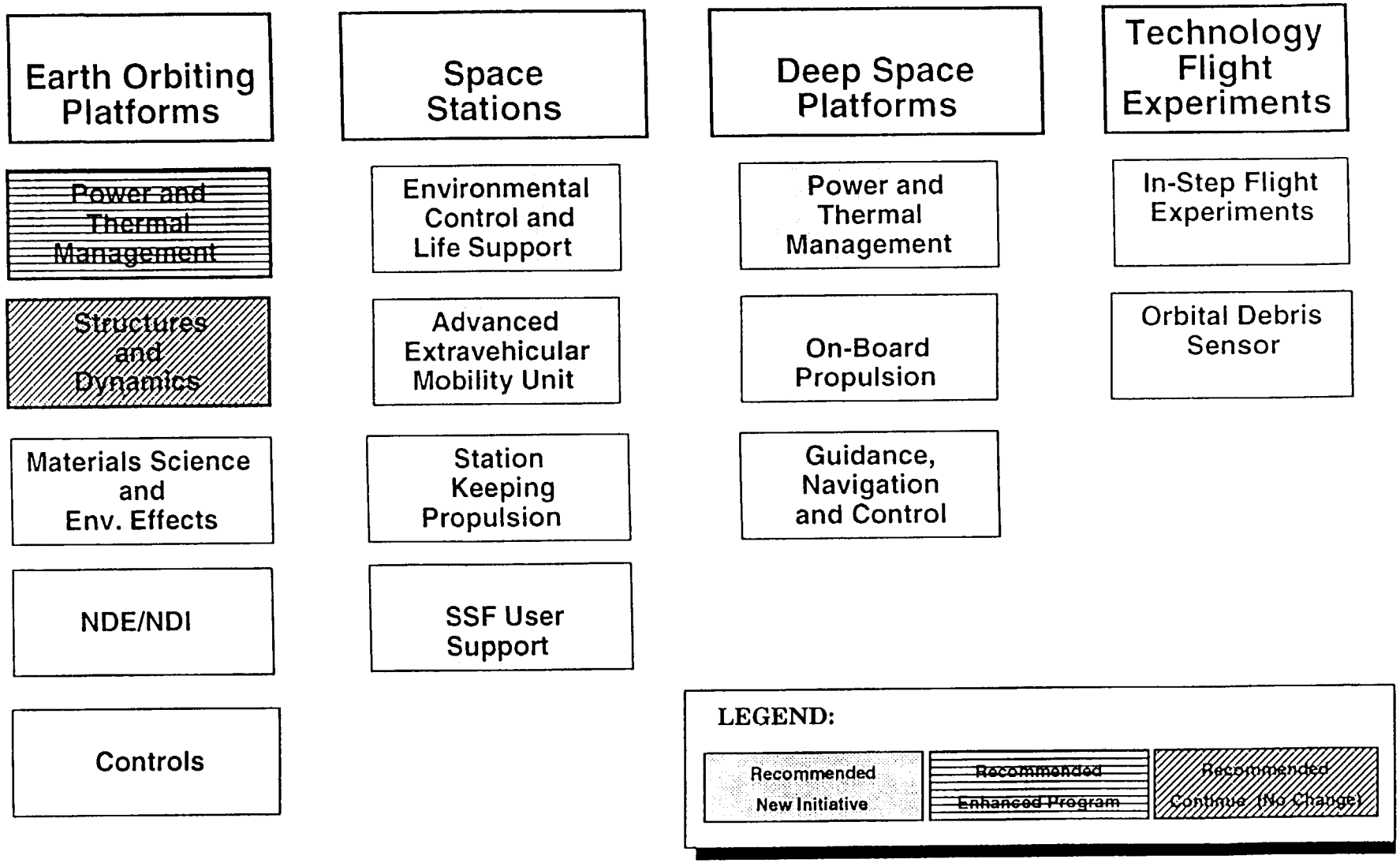

Figure 6. Platform thrust planning approach.

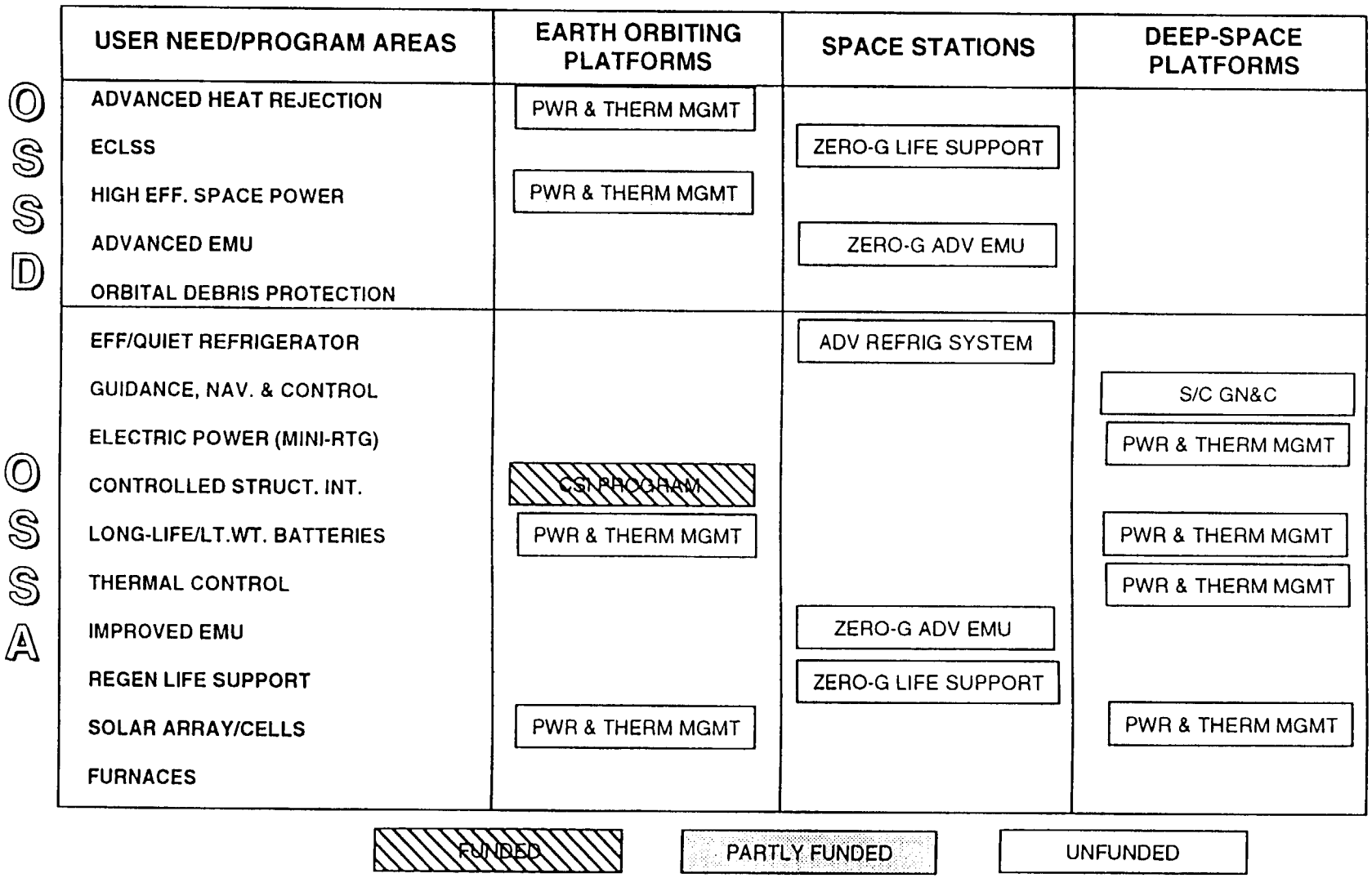

Figure 7. User needs/space platform matrix.

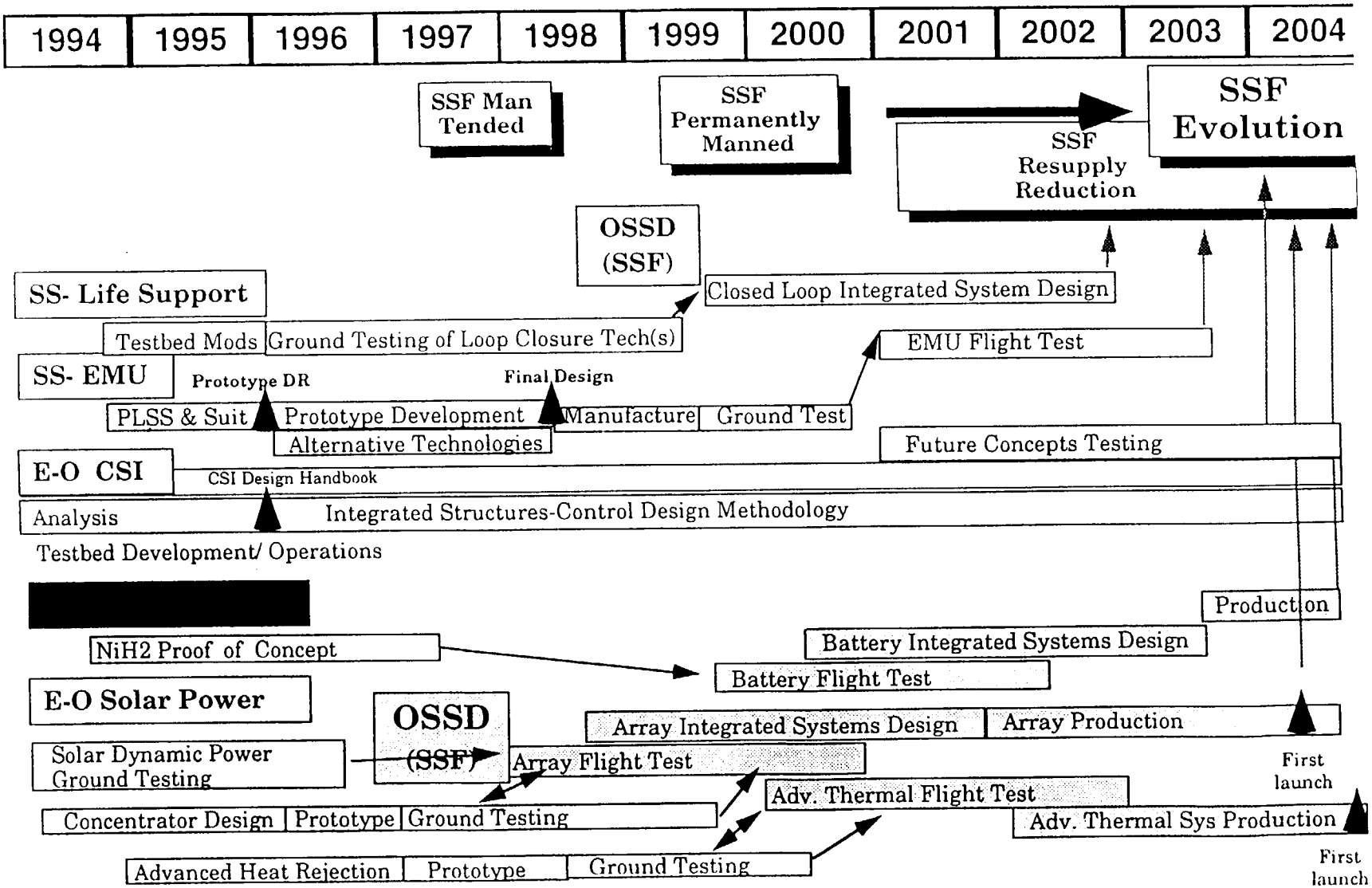

Figure 8. Road map to OSSD needs.

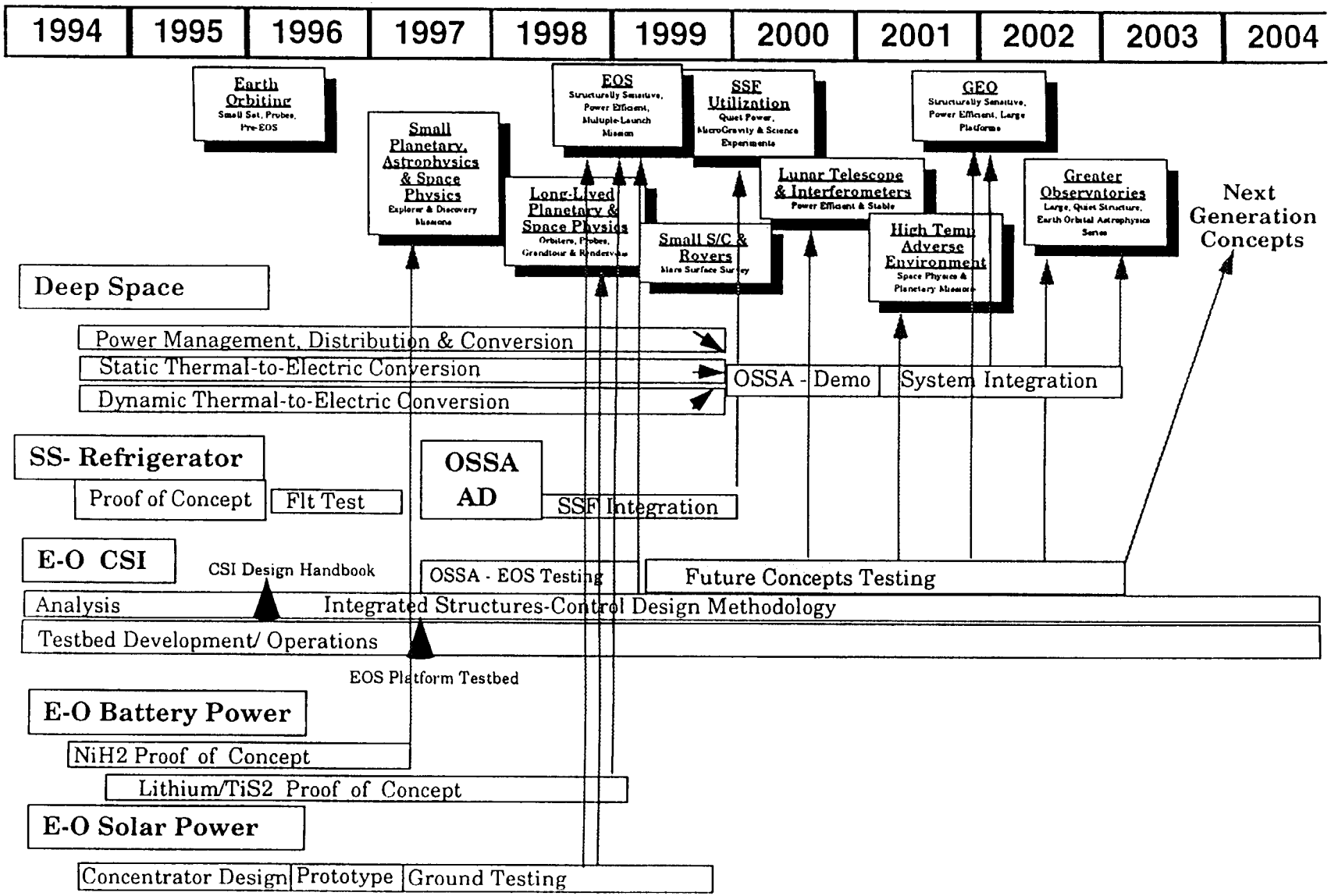

Figure 9. Road map to OSSA needs.

SPACECRAFT MATERIALS: COMPARISON BETWEEN FLIGHT RESULTS OBTAINED ON LDEF AND MIR

Jean-Claude Guillaumon
CNES CT/TE/AE/MT/TH
18 Avenue E. Belin, 31055 Toulouse cedex (France)
Phone: (33) 61 27 39 53, Fax (33) 61 27 40 99

Alain Paillous
ONERA / CERT / DERTS
2 Avenue E. Belin, 31055 Toulouse cedex (France)
Phone: (33) 61 55 71 19, Fax (33) 61 55 71 69

SUMMARY

Two flight experiments dedicated to the study of the performance of materials in space have been carried out. Material samples have been exposed passively to low-Earth orbit (LEO) environment, then retrieved for laboratory study. The first experiment was conducted in the framework of the FRECOPA project and was flown on the trailing edge of the Long Duration Exposure Facility (LDEF) (exposure to vacuum and ultraviolet (UV) radiation for 5.5 years). The experiment COMES was installed outside of the MIR space station during an extravehicular activity; it was exposed to vacuum, O-atoms, and UV radiation for 1.1 year; and it was brought back to Earth by cosmonauts. The difference in exposure conditions and the use of transparent filters protecting some samples of COMES enable to differentiate the effects of UV radiation and oxygen atoms. The degradations of several thermal control coatings (paints, metalized polymeric films with and without ITO), structural materials, and optical components have been observed, measured, and compared after these two flight experiments. This paper summarizes various "lessons learned" that can be used to identify aspects of space aging, to orientate future research in this field, and to assist in spacecraft design.

INTRODUCTION

Various types of materials are used on satellites and space stations: structural materials (polymeric films, bulk polymers, composites), thermal control coatings (paints, second surface mirrors), optical components (windows, mirrors, lenses), etc. For all of them, there exists the problem of stability in a space environment and, more precisely, an understanding of the mechanisms involved in their degradation and of the long-term evolution of their properties.

The space environment is complex. Spacecraft materials are subjected to the effects of its different components which sometimes act alone but usually simultaneously. The space environment parameters met on low orbit are vacuum, solar UV radiation, micrometeoroids and space debris, atomic oxygen (AO), and deep thermal cycles.

In practical terms, research for material selection and qualification always makes use of space environment simulations which usually involve setting up very expensive, highly specialized equipment in the laboratory. The opportunities of retrieving materials which have really sojourned in space are rare, but they should always be taken as they provide invaluable data on effective degradations in space. Materials retrieved from space highlight the effects of synergy between the different environmental components and enable the researcher to evaluate the validity of the ground simulations.

The CERT/ONERA and the CNES were associated in two onboard experiments where a large number of specimens were exposed to a space environment in an LEO and then brought back to Earth for a laboratory study of their degradation. One of the experiments was carried by the NASA's LDEF satellite; the other was placed on the outer surface of the MIR space station during the Franco-Russian ARAGATZ flight. The resulting data have been used to identify aspects of space aging, to orientate future research in this field, and to assist in spacecraft design.

DESCRIPTION OF THE EXPERIMENTS

The AO 138-6 FRECOPA Experiment on LDEF

A part of the experiment was located directly at the surface of the FRECOPA tray and was exposed to the LDEF environment during all stages of the mission. It consisted of a total of 24 samples, 20 by 20 mm each. The other part of the experiment (Figure 1) was located inside a vacuum tight canister which was opened 15 days after placing in orbit and then closed again in space after 9 months; 30 samples were mounted in the canister. The AO 138-6 Experiment has been described in several reports (ref. 1–3).

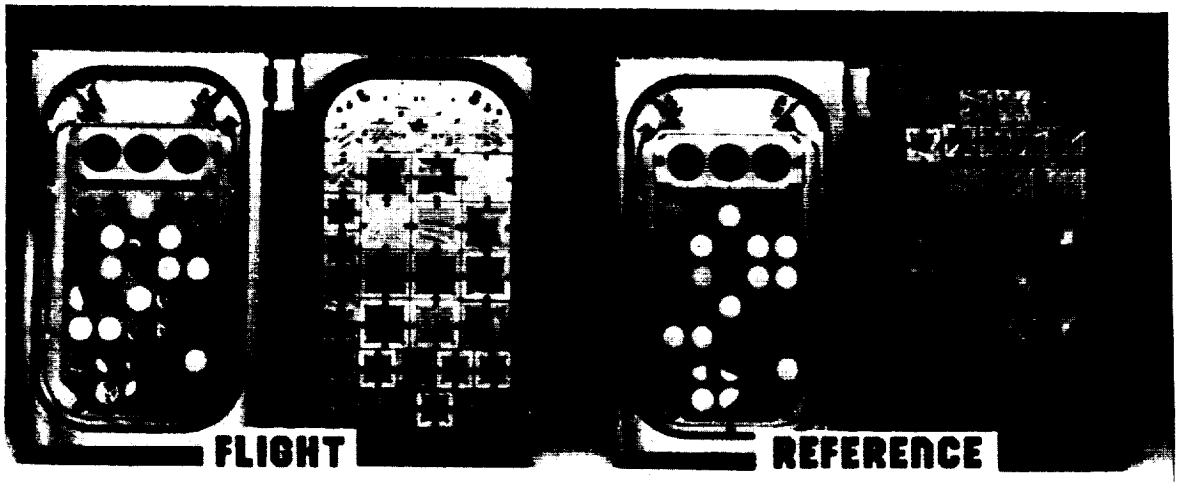

Figure 1. Sample-holder of Experiment AO 138-6 in the FRECOPA canister; comparison of the samples after flight to reference samples.

LDEF was a three-axis satellite, stabilized by gravity gradient. It had a circular orbit with an inclination of 28°; the initial altitude was 426 km and during capture 330 km. The total mission duration was 2,015 days. Because of its position on side three of the LDEF, the AO 138-6 experiment did not receive any oxygen atoms during the mission, with the exception of a short period during the

capture when it received a fluence evaluated at 1.32 10^{17} atoms cm^{-2}. The solar illumination was 11,110 equivalent Sun hours (esh) for the samples located on the tray and only 1,448 esh for the samples inside the canister. The particular irradiation dose (mainly due to the electron flux) was weak: 3×10^5 rads. The number of temperature cycles was 34,000 with temperatures within the ranges shown in Table 1.

Table 1. Range of estimated sample temperatures in typical lighting conditions.

Position	Conditions	Maximum temperature (°C)	Minimum temperature (°C)
Tray		49 to 63	–43 to –52
Canister	open	67 to 85	–33 to –40
Canister	closed	65 to 82	–20 to –26

The COMES Experiment on MIR

The COMES experiment (Figure 2) consisted of four panels which were deployed by an astronaut in space outside of MIR with the possibility of exposing samples on both sides, conventionally identified as "V" and "R." It included several modules on both sides.

V Side:

A total of 113 samples (20- by 20-mm squares or circles of 25 mm in diameter) had their central areas exposed to the space environment, without mechanical stress (20 mm in diameter). Among them, eight groups consisting of four identical samples of the same material were used to distinguish the effects of different space environment constituents, i.e.:

- exposure to all of the parameters (UV, AO, vacuum, temperature)
- exposure behind a 1-mm thick silica filter transmitting solar radiation with a wavelength greater than 190 nm (thus including most of the solar UV radiation)
- exposure behind a 1-mm thick optical filter only transmitting wavelengths greater than 360 nm
- exposure behind a metal disk, painted white and protecting the sample against the effects of AO and UV radiation.

In addition, six samples of polymeric films were exposed to the space environment while maintained under traction by a spring, and six samples of composite materials with an organic matrix underwent bending stress.

R Side:

Thirty-two samples were exposed without mechanical stress.

COMES is described in references 3 to 5. A total of 85 different materials were exposed on this experiment.

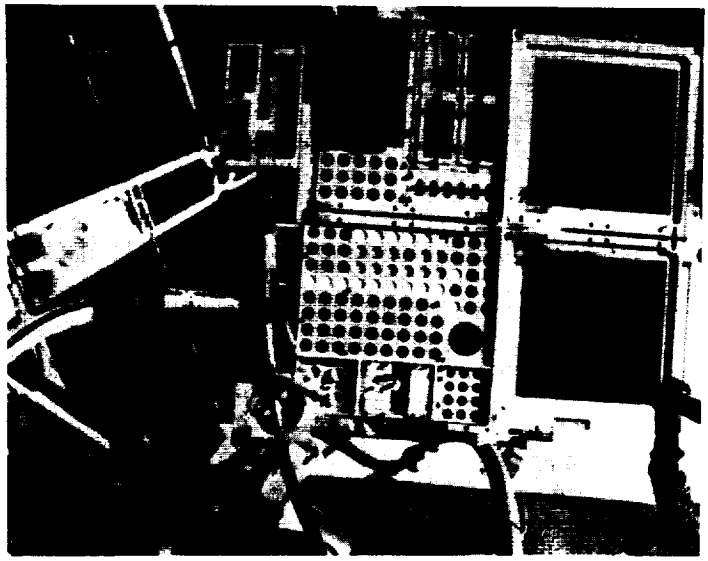

Figure 2. The COMES ARAGATZ experiment on board MIR; the photograph shows the face V.

During the flight, the MIR station followed an orbit located between 350 and 425 km in altitude, inclined at 51.6°. It should be noted that the orbit was transferred to more than 400 km in altitude from October 4, 1990, on, in order to continue the MIR flight in an automatic mode since there was no longer a crew aboard. On January 11, 1990, after having spent 392 days in space outside of the MIR, the COMES experiment unit was refolded during an extravehicular activity of cosmonauts; then it was stored aboard the station until October 2, 1990, at which date it was returned to Earth.

As the Russian team of the experiment had not provided much information on the attitude of the station during exposure of the COMES experiment, it is difficult to ascertain exactly the amount of sunlight received by each side of the experimental unit. However, after analysis of the data from the "Microcalorimeter" experiment, also mounted on the COMES panels, it may be estimated (ref. 6) that the V side received a solar UV dose of 2,850 esh and the R side 1,900 esh. For the same reasons, it was not possible to calculate, by means of the MSIS-86 environment model, the fluence of oxygen atoms accumulated by each of the two sides of COMES during the mission. Nor was it possible to determine whether the oxygen atoms had been received more for a particular inclination to the surfaces. On the basis of the erosion measured on samples of Kapton™ polyimide and Terphane™ polyethylene terephtalate arranged over the surface, it may be estimated that the fluences received were probably between 3.6 10^{20} and 5.9 10^{20} atoms cm^{-2} on the R side,* and between 3.7 10^{18} and 7.3 10^{19} atoms cm^{-2} on the V side.† It should however be pointed out that: (a) whereas the fluences appear to be rather uniform on R, this is probably not the case on V; and (b) these values have probably been underestimated, since a strong contamination, in particular by silicones, was detected on the samples on both sides. This must have protected the surfaces, at least partially, against AO. The temperature estimates of the sample holders on COMES, which may be made using thermal modeling, indicate that, in the case of the hottest exposure, the average temperature of the sample holders on the V side is probably of the order of +10 to +30 °C and that of the R side of the order of +50 to +60 °C. In the case of the coldest exposure (experiment unit in the shadow of the station), the temperature was determined for both sides to be between –60 and –70 °C.

---

* On the basis of the measurement of the decrease in mass of five samples, taking a reactivity of 3.0 10^{-24} cm^3 $atom^{-1}$ for the Kapton™, and 3.4 10^{-24} cm^3 $atom^{-1}$ for the Terphane™.

† On the basis of the measurement of the decrease in mass of eight different samples.

LESSONS FURNISHED BY THESE EXPERIMENTS

Validity of the Results

These experiments on LDEF and MIR are complementary: FRECOPA on LDEF gave an exposition to UV only; COMES on MIR gave an exposition where UV and AO were present simultaneously. On the other hand, the conditions of exposure on MIR (in particular, the UV and AO doses) are less well defined and a high surface contamination was observed (see below). This must be taken into account when comparing the results.

It is important to point out that they are based on measurements made after modification of the optical and mechanical degradations during the inevitable return of the specimens. More or less complete recovery of degradations caused by irradiation in a vacuum were noted when most of the polymers or white paints were returned to the air. An example of the importance of this phenomenon can be seen in Figure 3. On the other hand, there may be a postirradiation evolution following a peroxidation of the free radicals which are still trapped at the end of irradations, which helps to understand the progressive deterioration on the ground of samples recovered after the STS flights. This problem must, therefore, always be born in mind when using the data from these onboard experiments to forecast material behavior during an eventual future mission.

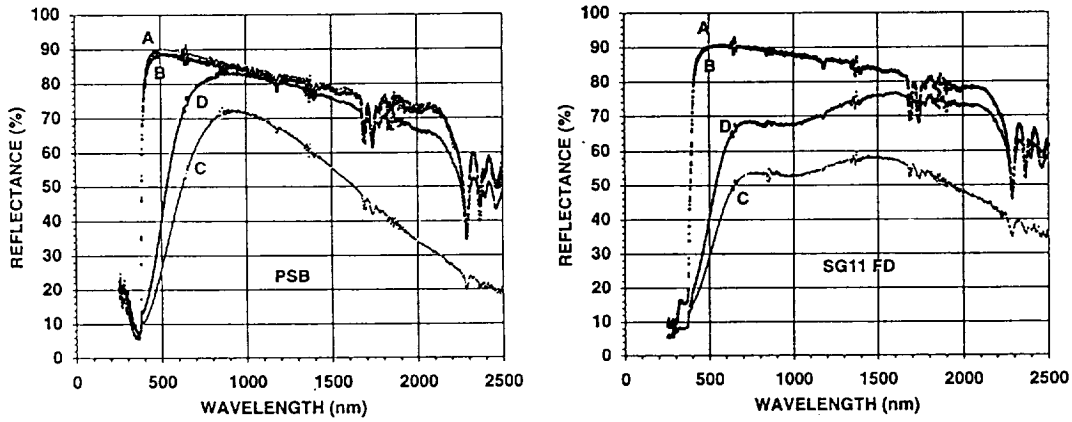

(A) in air, before irradiation,
(B) in vacuum, before irradiation,
(C) in vacuum, after combined irradiation with UV (6,250 esh), electrons (2.5 10^{15} electrons cm^{-2} s^{-1} of 400 keV) and protons (5 10^{15} protons cm^{-2} s^{-1} of 45 keV, 5 10^{14} protons cm^{-2} s^{-1} of 240 keV),
(D) after 5 days in air, postirradiation.

Figure 3. In air recovery of the white paints PSB and SG11 FD after combined irradiation with UV and particles in vacuum.

Synergy

Generally, in LEO it was found that there was much synergy of action of the different parameters of the natural and induced environments (UV, AO, thermal cycles, micrometeorites and

debris, and contamination). This is shown, for example, by the results of tests to separate the effects of different environmental components which were carried out on MIR.

For the COMES experiment, Table 2 shows the deteriorations in the solar reflectance of different samples exposed to different environments (see above), i.e. for the same samples:

- an exposure to all of the parameters: UV solar radiation (including far UV), AO, vacuum, and the temperature
- an exposure to UV radiation with a wavelength greater than 190 nm, to the vacuum and to the temperature
- an exposure to radiations with a wavelength greater than 360 nm, to the vacuum and to the temperature
- an exposure to the vacuum and to the temperature.

Table 2. Solar reflectance degradation ΔR_s of coatings on the V side of COMES, for different space environment conditions ΔR_s = final R_s – initial R_s.

Material	UV + At. Ox.+ vacuum ΔR_s	UV (λ >190 nm) ΔR_s	UV (λ>360 nm) ΔR_s	Vacuum ΔR_s
PCBZ	–0.01	–0.01	–0.01	+0.01
PSG 120 FD	–0.04	–0.03	0.00	0.00
A 276	–0.01	–0.14	0.00	+0.01
PCB 119	–0.01	0.00	+0.01	+0.01
SG 11 FD	–0.04	–0.01	0.00	0.00
PSB	0.00	0.00	+0.01	0.00
Kapton™ HN 50 µm	–0.03(*)	0.00(*)	0.00(*)	0.00(*)
FEP 25 µm	–0.05(*)	0.00(*)	0.00(*)	0.00(*)
FEP/Al 50 µm	–0.03	0.00	+0.01	+0.02

(*) ΔT_s: Variation of solar transmittance.

The Kapton™ HN and the Teflon™ FEP suffer deterioration under the combined effect of AO and UV radiation. As may be observed, the deterioration generally found on the white paints is relatively low, whether submitted to the complete environment or under UV.†† The A 276 paint is an exception. It suffers very strong deterioration under UV with a wavelength greater than 190 nm, but on the other hand its solar reflectance is stable under UV + AO. In the case of this paint, it has been confirmed that the AO decreases the extent of damage which would be experienced under UV radiation acting alone, as had been clearly shown by many observations on LDEF. On the R side of COMES which received the most oxygen atoms, the solar reflectances of the A276 paint and the PCB 119 even seem to have increased following the flight (Table 3). The PSG 120 FD and SG 11 FD paints, on the other hand, appear to deteriorate more under UV + AO than under UV radiation alone.

In certain cases, AO may counterbalance certain effects of UV irradiation acting alone. This is confirmed on MIR by the fact that exposition to space cured damage caused to specimens of PCB-Z and PCB-119 by preflight UV preirradiation on the ground (Table 4). This behavior is not general.

†† It should be remembered that the degradations considered here are those recorded after the samples have been returned to the air; those which might have been observed in orbit would have been different.

Table 3. Variations of solar reflectance and emissivity of various samples after their flight on FRECOPA/LDEF and COMES/MIR with $\Delta R_s = R_{s\ final} - R_{s\ initial}$ and $\Delta\varepsilon = \varepsilon_{final} - \varepsilon_{initial}$.

				AO 138-6 FRECOPA		AO 138-6 FRECOPA		COMES-ARAGATZ		COMES-ARAGATZ	
Type	Material	R_s initial	$\varepsilon_{initial}$	Canister ΔR_s	Tray ΔR_s	Canister $\Delta\varepsilon$	Tray $\Delta\varepsilon$	Face V ΔR_s	Face R ΔR_s	Face V $\Delta\varepsilon$	Face R $\Delta\varepsilon$
White paint	A276	0,75	0,877	-0,24		-0,005		-0,01	+0,03	+0,005	+0,036
White paint	S36	0,81	0,856	-0,04	-0,08	-0,001	-0,001				
White paint	PV100	0,78	0,865	-0,08		-0,001					
White paint	PSB	0,83	0,895	-0,05	-0,01	-0,001	-0,003	-0,01		-0,003	
White paint	SG11 FD	0,82	0,854					-0,04	-0,01	-0,005	-0,005
White paint	PSG 120 FD	0,80	0,876	-0,07		-0,002		-0,04	-0,02	0,000	-0,002
White paint (conductive)	PCB-Z	0,78	0,872	-0,04		0,000		-0,01	-0,02	+0,006	+0,003
White paint (conductive)	PCB-T	0,72	0,815	-0,10		0,000					
White paint (conductive)	PCB 119	0,79	0,861					-0,01	0,01	+0,008	+0,006
Black paint	PU1	0,03	0,885	+0,04		-0,002		+0,06	+0,06	+0,032	+0,032
Black paint	Z306	0,04	0,906	+0,035				+0,06		+0,026	
Black paint	Cuvertin 306	0,03	0,910					+0,03		+0,025	
Black paint	VHT SP102	0,05	0,860	+0,013		+0,001					
Black paint	HT650	0,03	0,873	0,01		-0,001					
Black paint	Electrodag 501	0,04	0,791					+0,02		+0,014	
Black paint	L300	0,05	0,843	+0,035		-0,013					
Black paint	PNC	0,08	0,796	+0,02		-0,040					
Black paint (conductive)	PUC	0,07	0,757					+0,03	+0,01	+0,127	+0,119
Aluminum paint	PSG173	0,69	0,317	-0,08		-0,006		-0,06		-0,009	
Aluminum paint (conductive)	PAC	0,73	0,275					-0,21		-0,024	
Coating	Alodine	061	0,050					+0,01		+0,020	
Black anodisation	PSS-703	0,09	0,874					+0,01		0,000	

Curiously, the solar reflectance of paint A276, preirradiated on the ground, continues to degrade in a LEO environment containing atomic oxygen.

Table 4. Effects of the MIR LEO environment on solar reflectance R_s of paints preirradiated with UV to 2,200 esh under vacuum in laboratory ΔR_s = final R_s – initial R_s.

Material	Preirradiation with UV	Initial R_s	ΔR_s
PCB-Z	no	0.77	–0.01
	yes	0.72	+0.03
PCB119	no	0.79	–0.01
	yes	0.74	+0.03
A276	no	0.75	–0.01
	yes	0.55	–0.03

Moreover, the LDEF and the STS flights results show generally that degradation of Teflon™ FEP depends on the relation between the quantities of AO and UV radiation received. On MIR, it was seen that on face V of COMES, the reactivity of FEP seems to have been very close to that of polyimide Kapton™ (FEP erosion exceeding 1 μm compared to a maximum Kapton™ erosion of 2.2 μm and an average of 0.7). On the other face, R, it seems to conform to that measured on LDEF** or STS flights (FEP erosion between 1.1 and 1.8 μm compared with a Kapton™ erosion of 11 to 17 μm). A similar anomaly was also noted for the black polyurethane paints PU1 and PUC which, on the two faces of COMES on MIR, were eroded by 3 to 4 μm whereas it is estimated that AO fluence was 10 times less on face V. The high level of contamination on MIR prevents us, perhaps, from drawing a definitive conclusion about these anomalies but they seem to indicate that precise, local ambient conditions greatly influence degradation.

Table 5. Erosion of FEP, polyimide, and PET films after exposure to LEO on MIR.

Position	Material	Number of samples	Minimum erosion (μm)	Maximum erosion (μm)	Average erosion (μm)
Side R	Polyimide	3	10.7	16.7	14.6
	PET	2	18.8	20.0	19.4
	FEP	3	1.1	1.8	1.5
Side V	Polyimide	9	0.11	2.2	0.5
	PET	4	0.18	1.3	0.5
	FEP	4	0.8	1.1	1.0

The exact synergy of the observed effects is difficult to understand. It may depend on the relative intensity of the elements involved (UV radiation, oxygen atoms, and contamination) and also on whether they are or are not simultaneous. We do not know how important is the fact that LDEF

** 10 to 13 percent of that of the Kapton™ polyimide.

received AO essentially during the last days of the flight. Damage kinetics during the flights is unknown for most of the LDEF and COMES experiments. We must, therefore, bear in mind that variations in solar activity, attitude, and orientation may influence the importance and nature of damage.

Temperature

With respect to the samples used in the FRECOPA AO 138-6 experiment, it may, however, be observed (Table 6) that almost all of the degradations measured following the flight on samples contained in the canister were greater than what might have been predicted on the basis of ground simulation of solar UV irradiation, with ex situ measurements. In addition, the differences between the degradations recorded for the samples located in the canister and those located on the external tray were relatively slight in spite of a much greater solar illumination on the tray (11,100 esh) than for the canister samples (1,450 esh).

Table 6. Ratio between solar reflectance changes in the FRECOPA canister and those after UV-irradiation at laboratory (ex situ measurements after 1,450 esh in vacuum).

Material	Ratio
PSB	1.8
S36	2.0
PSG 120	2.5
A-276	0.9
PCB-T	1.2
FEP	1.2
Aluminized Kapton™	3.0
Conductive aluminized Kapton™	1.1
Beta cloth	1.0

There are three possible interpretations for the excessive deterioration of the samples contained in the canister:

(1) A more significant contamination of the samples in the FRECOPA canister: measurements made by SIMS or RBS show a very slight contamination of these samples by a contaminant containing silicium, with a layer thickness probably less than 50 Å. Tests carried out at DERTS (ref. 7) on materials precontaminated by VCM products of silicon origin before their irradiation with UV and particles at room temperature indicate that the increased solar absorption due such thicknesses of pollutant is less than 0.01. This means that contamination cannot be the main cause of the observed differences.

(2) A deficiency in the quality of solar simulation applied, especially in the case of radiation with wavelength less than 200 nm. If this were the case, the deterioration would have been much more significant for the tray samples compared to those placed in the canister.

(3) An influence of temperature cycles undergone in space. This interpretation is the most likely according to thermal-vacuum tests undertaken on the ground which show (Table 1) that the maximum temperatures were almost 20 °C greater for the samples in the canister, and that they might thus reach +85 °C. The irradiation on the ground was carried out under standard conditions close to the ambient temperature. Deterioration under the effects of radiation is most likely greatly increased for the highest temperatures.

It is not, however, possible to know if the influence of a higher temperature on the specimens in the canister was felt more during the period when it was open than during the 4 years it was kept closed. There is little published literature in this field, and it does not permit a correlation between the importance of the degradation of the thermal control coatings and their irradiation or postirradiation temperature. In these conditions, laboratory studies seem indispensable in order to clarify this point for material irradiated by UV radiation and/or AO. This would probably permit a better choice of the conditions for simulation tests designed to predict behavior in a mission for a given thermal cycle profile.

Contamination

As was mentioned above, the samples retrieved after the FRECOPA flight on the trailing edge of LDEF seem to have been submitted to a rather low level of contamination (about 50 Å for a product containing silicon) compared with what has been published about other experiments on LDEF. This is probably due to the preconditioning in vacuum to which the specimens were subjected in the laboratory before their integration, to the conditions selected for this treatment, and to the design chosen for the whole FRECOPA experiment. The same precautions were taken for the COMES specimens on MIR. Nevertheless, a high degree of contamination by various products was noted on the surfaces of this experiment. Figure 4 shows at least three different types of contaminants on a silica surface. Through the microscope, we can see circular marks, probably droplets, on different types of specimens and various types of defects which are branching out. It should be noted that these defects, whose size varies between a few micrometers and several hundred micrometers, were observed only on electrical insulating material on COMES. Some certainly correspond to crystalline growth forms (Figure 5). Other defects (Figure 6) seem to resemble the arboresences known as Lichtenberg figures which are caused by an electrical breakdown resulting from charged particle irradiation of the dielectrics. Other causes could be imagined as an explanation for these ramified defects which are still being studied.

Figure 4. Surface contamination on silica after flight on MIR.

Figure 5. SEM study of crystal growth figures on a polyimide surface after flight on MIR.

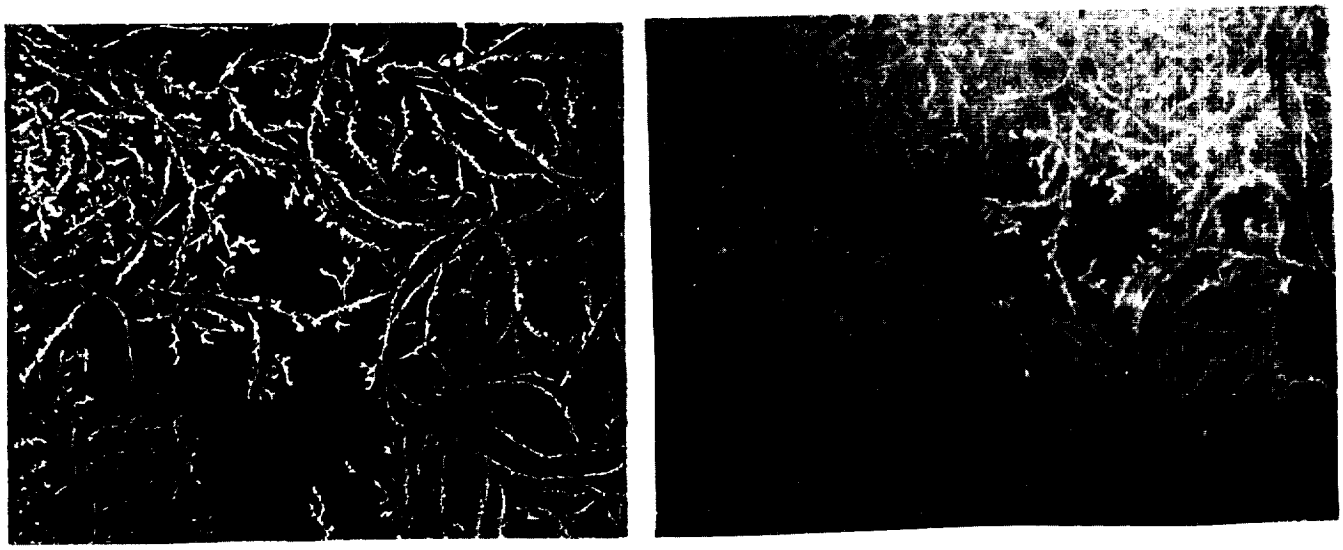

Figure 6. Unidentified defect on surface of a PES film after flight on MIR.

For these contaminants, it is difficult to define the origin, the moment at which they appeared, and the length of application. We must not forget that the experiment was also stored in the humid interior atmosphere of the MIR after exposure to space, with possible consequences for the samples. This leads us to think that the contamination observed on LDEF is very certainly much lower and less varied than that which will be obtained on a larger manned space station, subject to extravehicular and internal activity and serviced by regular visits by space shuttles.

Effects of an LEO Environment on Different Classes of Materials

Detailed results of the COMES and FRECOPA experiments have been published in various reports (ref. 1–5) giving details of variations in mass, optical reflection or transmission (spectral and solar), and emissivity. In this paper, we shall examine a few major facts.

A certain number of materials (aluminum, gold, and, above all, silver, OSR, alumina, or MgF_2 coatings) present slight but significant increases in weight after exposure on MIR—typically between 0.05 and 0.2 mg. This may correspond to oxidation but also, at least in part, to an accretion of contaminants. For example, a coating of silicon oxide (coming from AO oxidation of silicone products) with a specific mass approximately equal to 2.1 g cm^{-3} could correspond to an increase in mass of 0.10 mg if it were 1,500 Å deep on the surface of the exposed part of the specimens.

Contrary to a widely-held idea, according to which exposure to a space environment does not cause a variation in surface emissivity ε, many specimens presented quite clear changes[§] in this property. The erosion noted has been relatively low; as a result, the emissivity values did not decrease because of a reduction in the thickness of the emissive layer of an SSM, for example. In the case of conductive SSM's, polymer films, polyurethane, or carbon paints, an increase of ε was noted as a consequence of an irregular attack of the surface on a microscopic scale. An increase can also be noted for metallic materials which may oxidize; silver (included in the PAC conductive paint) and, to a much lower degree, gold and anodizations. As surface temperature depends on the relation α/ε, it is essential to know, for the thermal control coatings, the variations in both parameters α and ε in function of the time spent in LEO.

Even though no systematic measurements were made, the diffuse component of the optical reflection or transmission of the materials studied had visibly increased. This may have an important consequence on, for example, the design of optical equipments and baffles.

As already mentioned, it seems that the presence of AO sometimes (but not always, however) brings about a decrease in the damage caused by UV irradiation on solar reflectance. However, the behavior of the different classes of white paint in an environment which includes simultaneously UV radiation and AO is not the same. In order of decreasing stability, we find paints with a silicate binder, with a silicone binder, and finally those with a polyurethane binder. These latter should be proscribed for LEO usage.

All black paints have been undoubtedly bleached by exposure to LEO, more on MIR than on the trailing edge of LDEF (perhaps because of a synergistic action of UV radiation and oxygen atoms).

Aluminum paints deteriorated badly in a low orbit environment, as was proved by data from FRECOPA on LDEF (where they were subjected to UV only) and from COMES on MIR (where they were subjected to UV and AO). This result is surprising, bearing in mind the excellent stability of these paints noted during ground irradiation tests with UV radiation. It seems obvious that the reflectance spectrum of aluminum paints exposed on MIR was greatly modified. As analogous spectral modifications were also noted on solid aluminum and on VDA layers, it would seem that the aluminum underwent some sort of superficial chemical attack during the mission on MIR.

[§] Emissivity measurements were made with a Gier & Dunkle DB100 reflectometer.

Unlike the thermo-optical properties, the mechanical properties (elastic modulus and damping, T_g) measured after the mission on face V of the COMES experiment, using a Polymer Lab DMTA1 thermomechanical dynamic analyzer, do not seem to have been greatly modified on the FEP and Kapton™ films. It would seem, therefore, that there is no mechanical degradation due to UV irradiation in the bulk of the film even though it must be remembered that these measurements were made during exposure to air and that there may have been some form of degradation recovery because of this. Only a residual elongation was noticed on all films which had been exposed in mechanical tension.

Generally, polymer films and organic matrix composites exposed on COMES were eroded and, for prolonged exposition in LEO, in conditions where they are exposed to AO, need to be protected by a thin superficial layer of a stable material. According to our measurements, it is possible to say that the ITO and VDA layers, and the silicone overcoatings, have proved to be effective in this role (providing they were uniform in thickness and without holes).

On the organic matrix composites exposed on COMES, an important weight loss (0.12 to 1.2 percent of the initial mass in the exposed zone) was noted. This does not correspond to the real erosion, which was observed by optical means and remains low. It is the result of long-term outgassing in space vacuum, despite the preconditioning in a dry atmosphere carried out before integration.

If the silica or cerium glass OSR and the FK52 glass presented good stability, it must be mentioned that an antireflection optical coating showed signs of considerable spectral changes; this was also true for the MgF_2 coatings on aluminum which have already been mentioned. On the other hand, the anodizations resisted well.

CONCLUSION

To summarize, the important alterations in properties noted in LEO for very varied materials confirm the need for great care to be taken during their selection for use in a given mission.

In-flight results should not be used indiscriminately and, even if they indicate good behavior, should not be considered as a qualification for general use in a space environment or even, more particularly, in a LEO environment.

Most of the degradation observed in space is the result of a synergistic action between various parameters which define a space environment. HEO and GEO environments possess their own specific conditions due to fluxes of charged particles. Even in LEO, degradation depends on precise local conditions of exposure (intensity, simultaneity and proportion of UV radiation and AO) and use (thermal cycles). The problems must, therefore, be studied for each individual case.

Moreover, the data obtained after exposure of the specimens to vacuum and their return to the air (which is the case for most data at present available) are to be used with the greatest possible precaution as they do not take possible air recoveries into account. They can be used only if they are supported by simulation experiments carried out in the laboratory. In any case, simulations using UV irradiation and oxygen atoms simultaneously, in controlled conditions, are needed for an evaluation of the performance of a new material or one which is destined for a particular function, and also to determine the exact mechanisms of damage.

Contamination has been observed to be very general on a satellite. Associated with various environmental parameters, it affects the behavior of surfaces and the nature and extent of damage. It has very varied origins and can appear at practically any stage of a mission. In most cases, it plays an important part in the degradations which have been observed in surface properties. Bearing in mind the oxidation caused to many substances by AO, standardized VCM criteria are obviously no longer enough to be representative of the outgassing of materials in LEO and to allow their selection for use in a space environment. Some serious thought is required in this field.

REFERENCES

1. Guillaumon, J.C., and Paillous, A.: "Experiment AO 138-6, Spacecraft Thermal Control Coatings." Proceedings of the First LDEF Post-Retrieval Symposium, Kissimmee, FL, June 2–6, 1991.

2. Guillaumon, J.C., and Paillous, A.: "Project FRECOPA, Experience AO 138-6, Revetments de Control Thermique." Note CERT-ONERA-DERTS CR/LDEF/06, July 1991.

3. Guillaumon, J.C., Marco, J., and Paillous, A.: "Flight and Laboratory Testing of Materials in Low Earth Orbit." Proceedings of the Fifth International Symposium on Materials in a Space Environment, Mandelieu, France, September 16–20, 1991, pp. 27–42.

4. Guillaumon, J.C., and Paillous, A.: "ARAGATZ. Rapport final sur l'Expérience COMES-Echantillons." Note CNES, July 1992.

5. Paillous, A., and Oscar. H.: "ARAGATZ. Expérience COMES-Echantillons: étude des échantillons exposés à l'espace en traction." Note DERTS-CERT-ONERA, CR ARAGATZ COMES/05, August 1992.

6. Subias, M.: "Expérience Microcalorimètres, Compte-Rendu des mesures effectuées en vol. Note CNES 90/TE/AE/MT/TH n° NT118.

7. Marco, J., and Paillous, A.: "Long-Term Tests of Contaminated OSR's Under Combined Environment." Proceedings of the Third European Symposium on Spacecraft Materials in Space Environment, ESTEC Noordwijk, The Netherlands, October 1–4, 1985, p. 245.

N94-31046

CHARACTERIZATION OF POLYMER DECOMPOSITION PRODUCTS BY LASER DESORPTION MASS SPECTROMETRY

Joan B. Pallix and Kenneth A. Lincoln
Eloret Institute
NASA Ames Research Center
Moffett Field, CA 94087
Phone: 415/604-0332, Fax: 415/604-0487

Charles J. Miglionico, Robert E. Roybal and Charles Stein
Phillips Laboratory
Kirtland AFB, NM 87177-6008
Phone: 505/846-4798, Fax: 505/846-1926

Jon H. Shively
California State University
Northridge, CA 91330
Phone: 818/885-2166

SUMMARY

Laser desorption mass spectrometry has been used to characterize the ash-like substances formed on the surfaces of polymer matrix composites (PMC's) during exposure on LDEF. In an effort to minimize fragmentation, material was removed from the sample surfaces by laser desorption and desorbed neutrals were ionized by electron impact. Ions were detected in a time-of-flight mass analyzer which allows the entire mass spectrum to be collected for each laser shot. The method is ideal for these studies because only a small amount of ash is available for analysis. Three sets of samples were studied including C/polysulfone, C/polyimide and C/phenolic. Each set contains leading and trailing edge LDEF samples and their respective controls. In each case, the mass spectrum of the ash shows a number of high mass peaks which can be assigned to fragments of the associated polymer. These high mass peaks are not observed in the spectra of the control samples. In general, the results indicate that the ash is formed from decomposition of the polymer matrix.

INTRODUCTION

Materials retrieved from the long duration exposure facility (LDEF) have exhibited a wide variety of exposure induced chemical and physical surface modifications. Numerous investigations are underway to characterize the behavior of the various materials exposed from different locations on the satellite in order to identify the processes responsible for the observed effects. These processes may include complex interactions between the surface and atomic oxygen, UV or thermal radiation and/or chemical reactions with the products of outgassing. Surface properties were also affected by micrometeorite impacts and other contaminating particles.

The work presented here focuses on studies of several graphite/polymer matrix composites retrieved from leading edge and trailing edge positions on LDEF. A schematic diagram of the satellite is shown in Figure 1. The composite materials examined in this work were located in row 9, bay D (D09) on the leading edge and in row 3, bay D (D03) on the trailing edge of the satellite. While leading and trailing edge materials experienced similar exposure to solar radiation, there was a dramatic difference in exposure to atomic oxygen (AO) for panels in different locations on LDEF. The maximum total dose of AO received by the leading edge was on the order of 10^{22} atoms/cm^2 while the minimum on the trailing edge was only about 10^4 atoms/cm^2.

The long term goal of this particular study is to determine the origin of the ash-like substance found on the surfaces of polymer matrix composites (PMC's) exposed on the leading edge of LDEF. The preliminary work presented here involves the initial characterization of the surfaces of several leading and trailing edge PMC's by laser desorption mass spectrometry and by electron microscopy (SEM and TEM). The three composite materials of interest C/polysulfone, C/polyimide and C/phenolic, are considered dark body composites because of their black carbon fiber matrices. Initial inspection of PMC's indicated that the dark body composites placed on the leading edge of LDEF experienced erosion as well as an "ashing" effect of the excess resin layer on the sample surfaces. Samples placed on the trailing edge of LDEF did not experience the ashing effect but did show slight surface blistering. Light body composites, such as 3D-quartz phenolic placed on the leading edge displayed no ashing behavior but did experience erosion of the surface resin. The silica reinforcement fibers underwent no noticeable erosion. Trailing edge 3D-quartz phenolic produced no observable erosion or blisters.

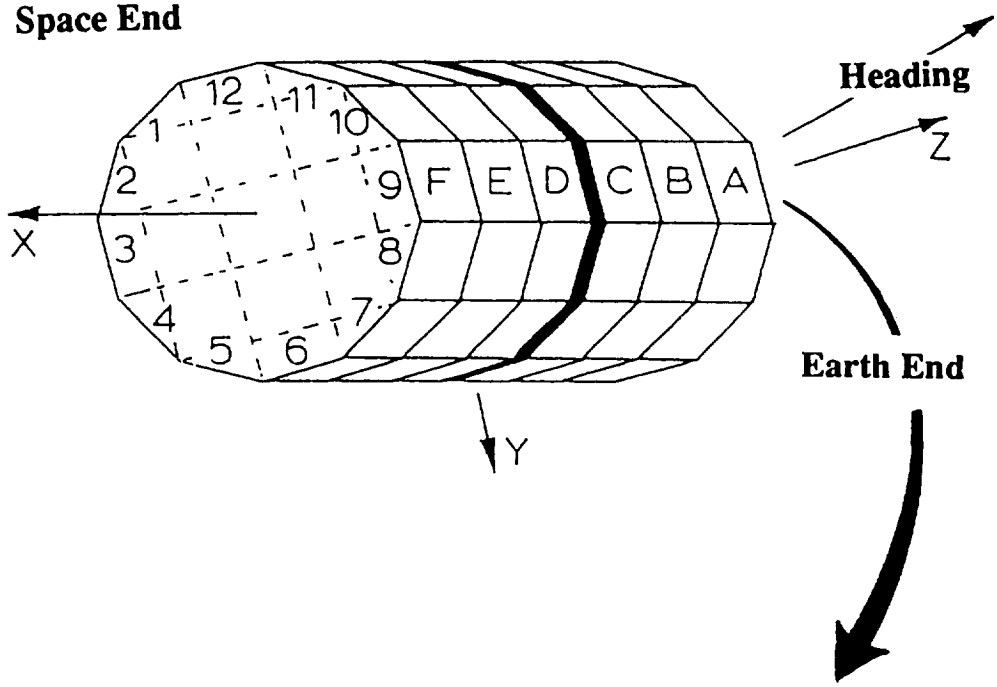

Figure 1. Schematic view of LDEF showing orientation and tray notations.

SEM images of the carbon reinforced composites were typical of those reported previously by other research groups (refs.1–4). The erosion process has caused cone type formation on the surfaces of leading edge samples and the ash appears in clumps that have a "cobweb"-like appearance. The level of ash on the C/polyimide was much higher than on the C/polysulfone. As reported in other work, there is erosion of both resin and top ply fibers in many areas of the C/polysulfone composite and in a few isolated areas of the C/polyimide. The observed differences in fiber damage may be due to differences in thickness of the surface resin layer on the two composites and/or the differences in polymer erosion rates. The SEM cross-sections show that the erosion does not extend deeper than ~80 microns into the carbon fabric of the C/polysulfone and ~35 microns into the top ply of the C/polyimide.

It is not clear why the delicate ash-like material remains on the surfaces of leading edge composites rather than being removed by AO erosion. It is also unclear why the silica reinforced materials with the same matrix polymers experience erosion but no ash is found on the surfaces. Possibly, the extreme differences in emissivity (and resulting temperature differences) of the different reinforcement materials plays a role in formation and/or removal of the ash. Surface impurities may also play a role.

Preliminary studies of three graphite reinforced PMC's have been made using time-of-flight mass spectrometry to help determine the composition of the surface ash. The many advantages of time-of-flight (TOF) mass spectrometry for surface analysis are well known. For this work, the technique is particularly useful due to the small amount of material available for analysis and the fact that no sample preparation (or modification) is required. In our instrument, surface material is removed directly by laser desorption. With laser desorption, electrically insulating materials are much less susceptible to surface charging which can cause detection problems when using ion beam or electron stimulated desorption. Desorbed neutral species are subsequently ionized by electron impact and accelerated into the TOF analyzer. The entire mass spectrum is collected for each laser pulse which minimizes sample volume requirements. Another advantage of this method is that electron impact is a nonresonant ionization process which means that no one species will be selectively ionized leading to ambiguous data interpretation.

Energy dispersive x-ray (EDX) and electron diffraction techniques have been used in conjunction with the mass spectra to identify inorganic contaminants. Because of the relatively large number of peaks observed mass spectra of organic materials, it is often difficult to identify inorganic contamination due to mass interferences (i.e., Si and CO at mass 28 or S and O_2 at mass 32). In addition, using laser desorption, some inorganic species may not be removed from the surface as efficiently as the organic material. As will be discussed later, EDX results have revealed a number of surface contaminants that were not apparent in the mass spectra. Macroscopic and scanning microscopy results have been presented elsewhere and will be published in the Journal of the International Metallographic Society in January 1993.

EXPERIMENTAL

The laser desorption mass spectrometer used for this work is shown in Figure 2 (ref. 5). The instrument was developed around a Bendix TOF analyzer at NASA Ames Research Center (Thermal Protection Materials Branch). The desorption laser is an non-Q-switched Nd:YAG with a pulse width of ~300 microseconds (μs). The neutral portion of the vapor cloud produced by the laser travels in a line-of-sight path directly into the region of 70 eV electron impact where ions are formed.

Any ions emitted directly from the surface are deflected in a 1000 V field before they are able to reach the electron interaction region. The extractor of the TOF spectrometer can be pulsed at a repetition rate of up to 50 kHz so that a complete spectrum of the transient vapor cloud is collected every 25 to 100 μs resulting in a mass spectral array. In this work, 15 mass spectra are obtained for each laser pulse and these are averaged for the final plots. The data collection system consists of an 8 bit, 100 MHz Transiac transient digitizer with averaging memory (CAMAC system).

The laser beam is focused to a spot size of ~4-mm diameter in order to keep the photon flux relatively low to minimize production of small organic fragments during desorption. Spectra containing only low mass generic fragment peaks are not very useful when trying to characterize organic materials. SEM images were obtained before and after desorption to ensure that the ash was being removed. Desorption of ash is observed using pulse energies as low as 100 mJ/pulse (<1.3 kW/cm^2) but no signal was observed from the bulk C/polymers at energies below ~250 mJ/pulse. In order to carry out all experiments under the same conditions it was necessary to use the higher laser power. Note that due to cross linking and/or intertwining of high molecular weight polymer chains, it is difficult to remove material from the surfaces of bulk polymers without also causing significant fragmentation. This is a general problem for any surface sensitive technique used to generate characteristic mass spectra of bulk polymers. While characteristic spectra can be obtained, they typically contain peaks at masses below 500 amu. Also note that the ionization process itself can cause additional fragmentation of the desorbed species. In future work we will use a CO_2 laser for desorption and the postionization will be accomplished using vacuum ultraviolet laser radiation at 118 nm. Ionization with VUV has proven to be an effective method for providing efficient ionization while avoiding further fragmentation of desorbed organic polymer species (ref. 6).

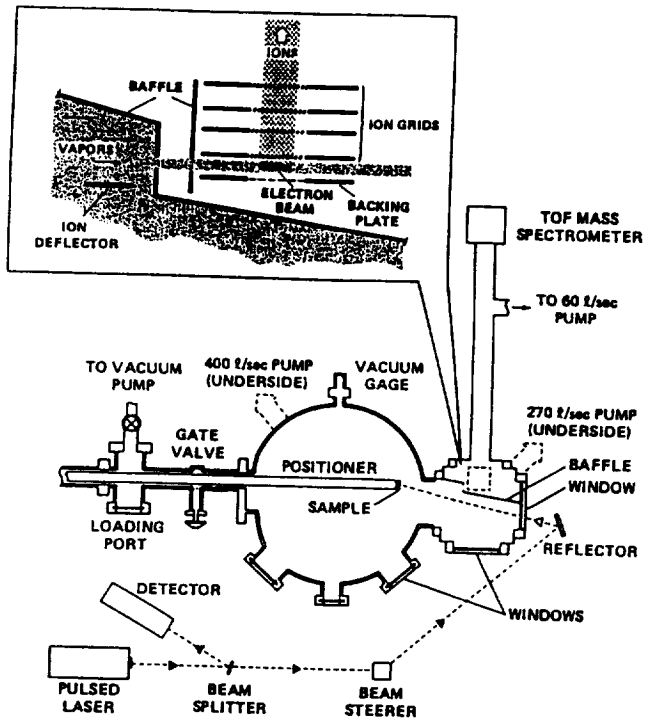

Figure 2. Schematic representation of the laser desorption time-of-flight mass spectrometer.

RESULTS AND DISCUSSION

The first step in understanding the origin of the surface ash observed on the three leading edge PMC's was to determine if the ash was different for each sample. If it had the same composition on all three samples it would clearly have resulted from the deposition and/or reaction with some general contaminant (i.e., species outgassing from the satellite). Mass spectra of the surface ash observed on the C/polysulfone, C/polyimide and C/phenolic are shown in Figure 3. The mass peaks above ~100 m/z units are the most useful for making a comparison. A cursory comparison of the three spectra indicates that all of the surfaces have different compositions and this could not result from the same source of contamination.

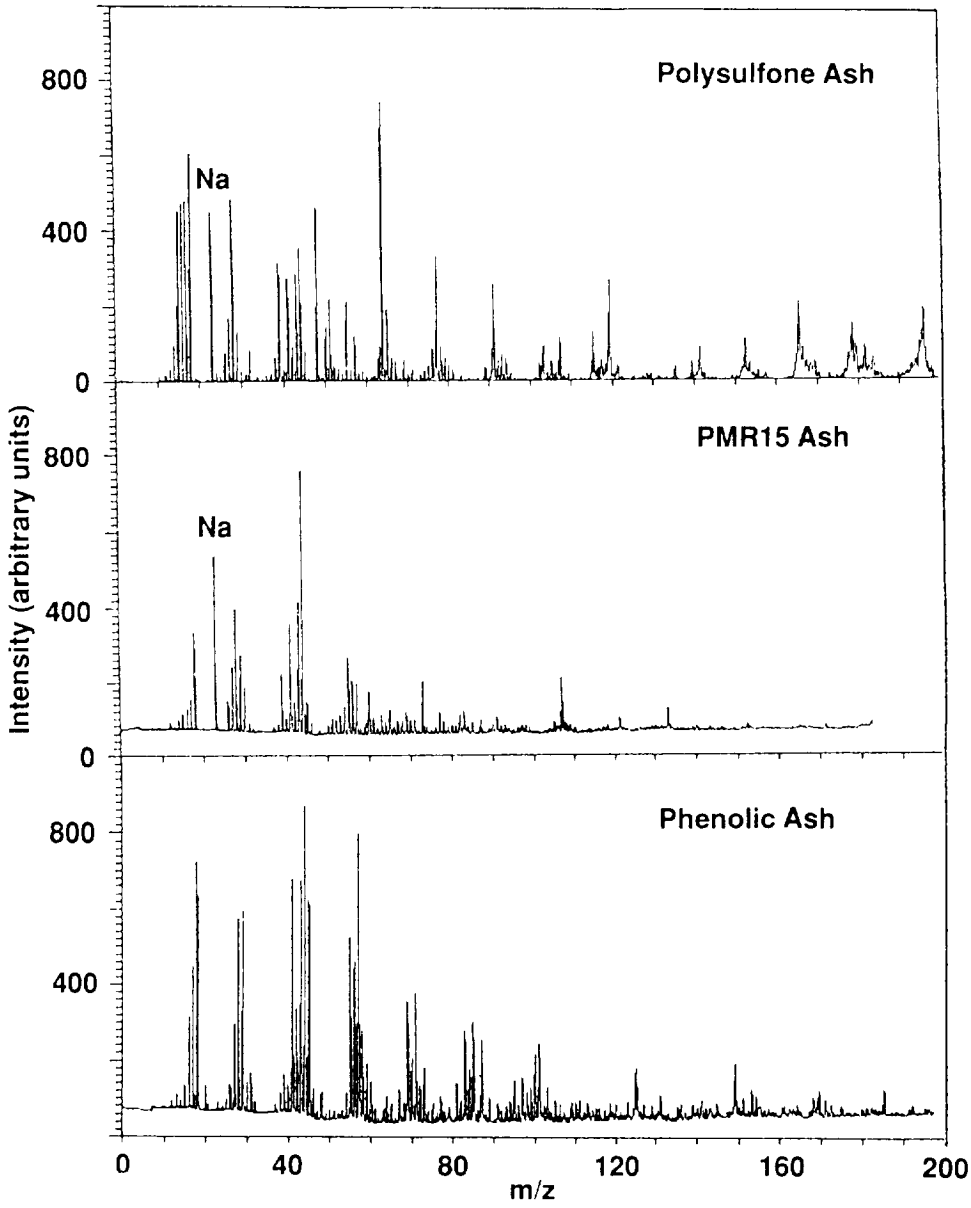

Figure 3. Comparison of mass spectra obtained from three leading edge polymer matrix composites.

Note that no significant peaks are present in the ash spectrum that are characteristic of graphitic carbon (i.e., C_2 or C_3). Electron diffraction studies also show that the ash consists only of amorphous C. No crystalline forms of carbon are found in the surface ash. There is a large Na peak in the surface ash spectrum of both C/polysulfone and C/polyimide which was not observed on the C/phenolic. EDX analysis of all the control samples show a very low level of Na and Si. However, these contaminants observed on exposed samples appear to have come from some source external to the sample because they are observed at much higher average surface concentrations than on the controls. Other inorganic contaminants were detected in the EDX spectra of both leading and trailing edge samples. These include F, Mg, Al, Si, S, Cl, Ca, K, Ti, Cr, Fe and Ni which were not necessarily distributed uniformly over the surfaces. In addition to these contaminants, the leading edge samples were also contaminated with P, Zn, Ga, As, Mo, Ag, Au, and Pb. The sources of most of the contamination particles can be attributed to scattered debris from nearby materials on the tray (i.e. Ga-As, Ag coated Teflon) and outgassing of lubricants and adhesives on the satellite. General discussions of contamination (organic and inorganic) on LDEF and other spacecraft have been presented elsewhere (refs. 7–9).

Figures 4 and 5 give structures for the components of the polysulfone and the PMR15 (polyimide) respectively. The Figures also compare the mass spectra of the bulk control samples with those of the leading edge LDEF samples in the surface ash and the bulk. The top frame shows the mass spectrum of the ash which, in both cases, contains high mass peaks that can be assigned to fragments of the respective matrix polymers. Although all of the high mass peaks have been assigned, only some of them are shown in the polysulfone spectra. The other tentative peak assignments are given in Table 1 for the polysulfone ash. Note that for both samples, the total intensity of the ash spectrum is at least 5 times higher than in the layer beneath the ash or in the control. A high desorption yield is typical for species that are not strongly bound to the surface. Although the surface coverage of the ash is not uniform and some of the pure polymer may be exposed on the surface, the majority of the signal observed in the "ash" spectrum is due to the ash and not the pure polymer. As mentioned previously, it is difficult to remove intact high molecular weight polymer chains from a bulk sample by any means (laser desorption, ion or electron stimulated desorption). The fragmentation resulting from desorption and ionization processes are responsible for most of the peak intensity being observed at masses below 100 m/z units.

SEM images show that the "ash-like" material has been removed from the surface after one or two laser shots. On the polyimide composite, 15 to 20 additional laser shots were required to remove the remaining surface resin and fully expose the bulk material. The mass spectra shown in the center frames of Figures 4 and 5 are obtained in the bulk of the PMC's. These spectra show characteristic carbon fiber peaks at m/z = 12, 24 and 36 as well as peaks characteristic of the polymers. This is clearly obtained from the bulk C/polymer and compares well with the bulk of the control sample. For these experiments, the surfaces of the control samples were scraped with a clean razor blade to be sure that a spectrum of the bulk material was obtained. This is common practice for studies of bulk polymers and is important in order to avoid collecting spectra of surface reaction products which will not be characteristic of the bulk polymer itself. In general, the peak assignments for C/polysulfone and C/polyimide suggest that the ash formation results from exposure induced decomposition of the matrix polymer.

Table 1. Tentative assignments of notable mass peaks in the polysulfone ash spectrum.

15	CH_3	77	C_6H_5
18	H_2O	91	C_6H_5-CH_2
23	Na	107	O-C_6H_4-CH_3
28	CO	119	C_6H_5-$C(CH_3)_2$
32	S	141	C_6H_5-SO_2
44	CO_2	166	C_6H_5-C-C_6H_5
48	SO	170	C_6H_5-O-C_6H_5
64	SO_2	181	C_6H_5-$C(CH_3)$-C_6H_5
		196	C_6H_5-$C(CH_3)_2$-C_6H_5

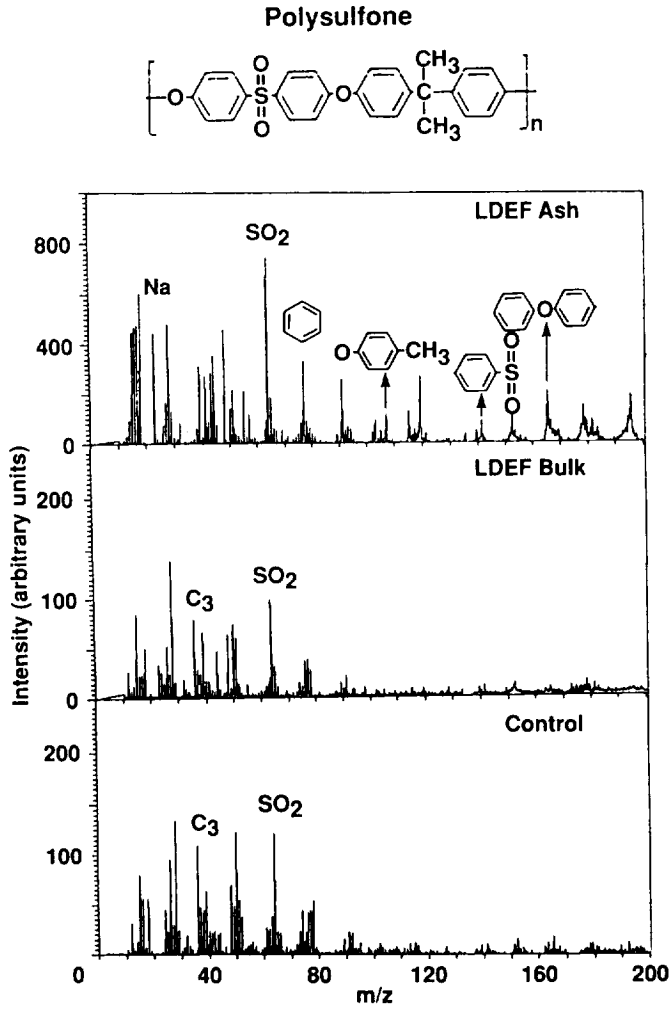

Figure 4. Comparison of mass spectra of polysulfone control sample (bottom) to the leading edge LDEF sample in the ash (top) and in the bulk (center).

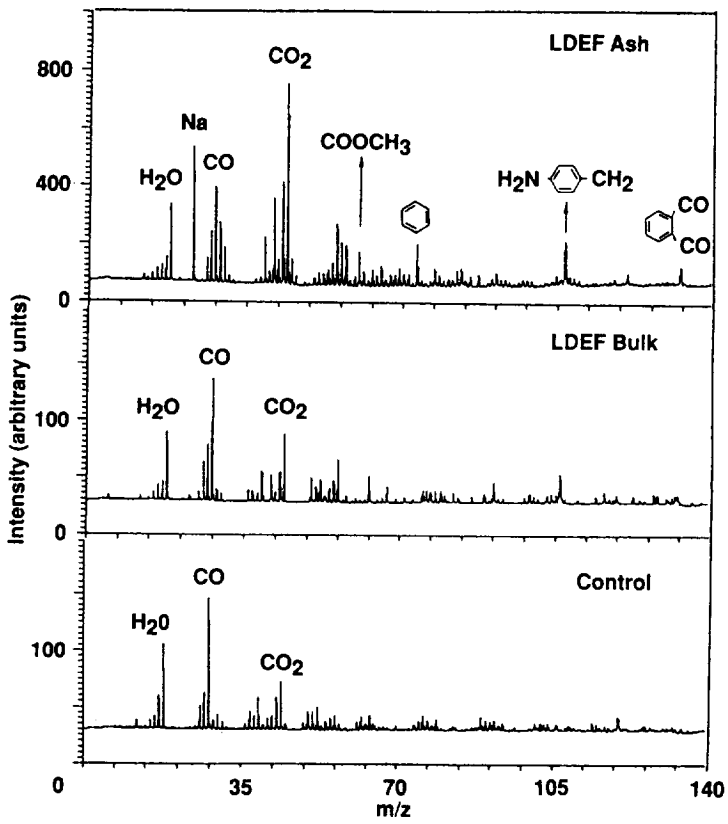

PMR15 - Polyimide Monomers

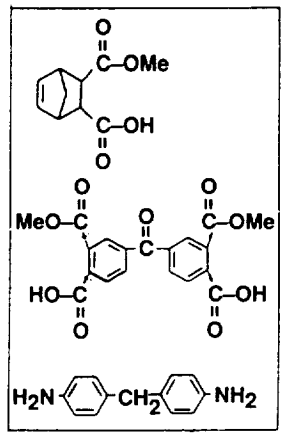

Figure 5. Comparison of mass spectra of polyimide (PMR15) control sample (bottom) to the leading edge LDEF sample in the ash (top) and in the bulk (center).

One important experimental question to answer is : How do we know that the optical properties of the ash (which is dull black) are not different than the control sample (which is shiny black) at 1.06 microns? If the leading edge samples absorb significantly more photons than the control samples then surface heating or energy redistribution effects might cause decomposition of the polymer under the ash giving rise to some of the observed mass peaks. To confirm that this is not occurring, two experiments were done. First, the infrared reflectance spectra were obtained for the C/polysulfone leading edge and the control sample. The samples showed similar reflectance (within 1 percent) at 1.06 microns. In the second experiment, mass spectra were obtained from the control samples at a higher laser power (factor of 3) than that used for the previous measurements. This was done to see if the resulting spectrum was similar to the spectrum of the ash. This was not the case as shown in Figure 6. As expected, the high laser power caused extensive fragmentation for polysulfone and phenolic and the strongest signals were produced from species below m/z = 100. Surprisingly, the PMR15 spectrum obtained at high power shows four very intense high mass peaks. Three of these peaks are also observed in the ash spectrum but at very different relative intensities. It is interesting to note the different fragmentation patterns resulting from the two different methods of fragmentation (i.e., exposure on LDEF vs. laser ablation at 1.06 microns). The results of the IR analysis and the high power study indicate that peaks observed in the ash spectra (above ~100 m/z) are not due to desorption of the intact bulk polymers.

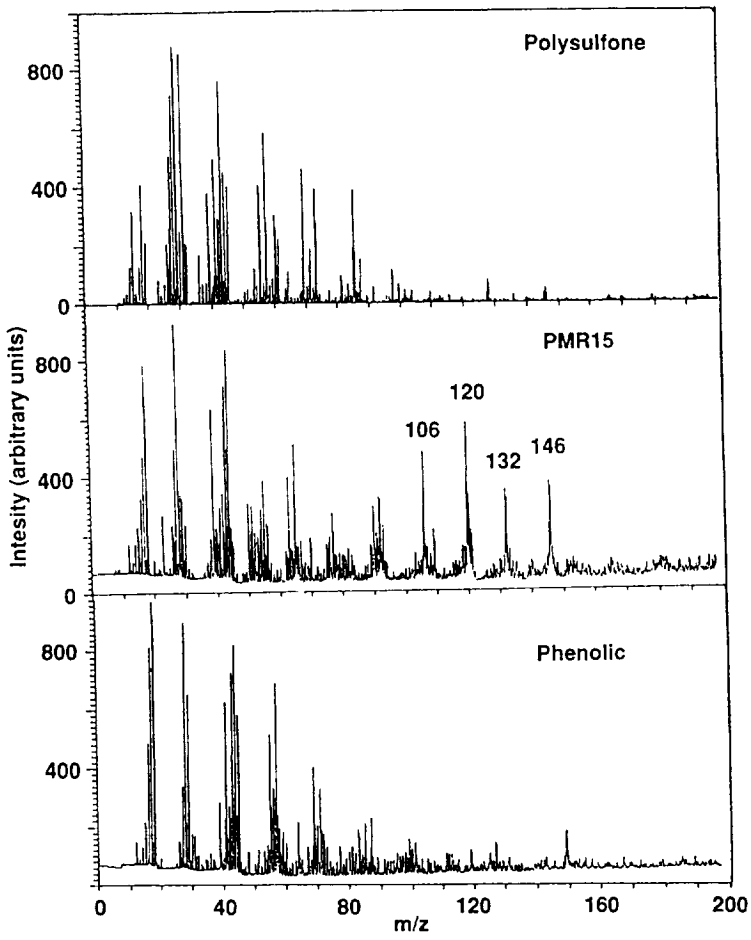

Figure 6. Mass spectra of control samples obtained at high laser power (800 mJ/pulse).

In the final study, a comparison was made of the mass spectra obtained from the surfaces of the control samples and the LDEF trailing edge composites. Although the control samples were essentially "unexposed," surface reactions can occur in any environment and even the control resins may have a different composition at the surface than in the bulk. The trailing edge mass spectra appear very similar to the control samples indicating that no extensive polymer degradation other than blistering occurred on the trailing edge as a result of exposure on LDEF. This indicates that the ash formation depends on the dose of AO (and/or other particle bombardment) and possibly on synergistic effects.

CONCLUSION

This preliminary study has shown that the ash observed on leading edge graphite reinforced PMC's contains both organic and inorganic contaminants. For the PMC's studied, a significant effect of exposure on LDEF was the erosion and decomposition of the surface resin. Erosion of both the resin and the reinforcement fiber was observed in the C/polysulfone, but for the C/polyimide it was primarily the surface resin that was affected and not the bulk material underneath. The ashing effect occurred only on leading edge samples while trailing edge samples underwent no observable

changes in surface composition relative to the control samples (although there was evidence of surface blistering on graphite reinforced composites).

It has not been the goal of this preliminary work to identify the causes of the observed material behavior but to simply make a preliminary characterization of the effects of prolonged exposure in low Earth orbit. This initial empirical evaluation is essential for determination of long-term material performance. A complete surface characterization would include studies of optical, compositional, crystallographic, morphological, and mechanical properties. This information alone cannot lead to definitive mechanistic conclusions but could aid in the development of laboratory experiments designed to reproduce the observed material dependent effects. Determination of the synergistic mechanisms responsible for material modifications will require a much more extensive future effort. In future work, experimental attempts to reproduce the erosion and ashing effects on these PMC's will include sample exposure to a source of low energy AO and other particles in conjunction with UV, VUV and/or IR radiation. The general need for these studies has long been recognized and this type of work is currently underway in other laboratories (ref. 10). Subsequent to ground-based exposure, mass analysis of polymer decomposition products may be helpful in the elucidation of erosion and depolymerization mechanisms. If mechanistic information is to be extracted from the mass spectra, the peaks of parent fragments existing on the composite surface must be observable. To achieve this goal, a CO_2 laser will be used for desorption and VUV laser radiation for "soft" ionization. In addition, efforts will be made to understand why the ash is not eroded from the surface by AO and why no ash is observed on silica reinforced composites.

REFERENCES

1. Young, P.R., Slemp, W.S., Siochi, E.J. and Davis, J.R.J.: 24th Int'l. SAMPE Tech. Conf., 24(3), 1992, pp. T174.

2. Steckel, G.L., Cookson, T., and Blair, C.: "LDEF Materials Workshop '91." NASA CP 3162, Part 2, 1991 pp. 515.

3. George, P.: "LDEF Materials Workshop '91." NASA CP 3162, Part 2, 1991 pp. 543.

4. Young, P.R. and Slemp, W.S.: "LDEF Materials Workshop '91." NASA CP 3162, Part I, 1991, pp. 357.

5. Lincoln, K.A.: Int. J. Mass Spectrom. Ion Processes, vol. 99, 1990, pp. 41.

6. Pallix, J.B., Schuhle, U., Becker, C.H. and Huestis, D.L.: J. Anal. Chem., vol. 61, No. 8, 1989, pp. 805 and references therein.

7. Borson, E.N.: "Environmental Effects on Materials Workshop." NASA CP 3035, Part I, 1989, pp. 331 and references therein.

8. Gordon, T. and Rantanen, R.: "LDEF Materials Workshop '91." NASA CP 3162, Part I, 1991, pp. 141.

9. Hemminger, C.S.: "LDEF Materials Workshop '91." NASA CP 3162, Part I, 1991, pp. 159.

10. Koontz, S.L.: "Environmental Effects on Materials Workshop." NASA CP 3035, Part I, 1989, pp. 241 and references therein.

DESIGN APPLICATION AND DEVELOPMENT OF SPACECRAFT IN LEO UTILIZING LDEF RESULTS

George B. Rauch, Jr.
Boeing Defense and Space Group
P.O. Box 240002, MS JR-36
Huntsville, Al. 35824-6402
Phone 205-461-5755, Fax 205-461-5600

Richard D. Sudduth
Boeing Defense and Space Group
P.O. Box 240002, MS JR-36
Huntsville, Al. 35824-6402
Phone 205-461-5787, Fax 205-461-5600

SUMMARY

In general, the results from the Long Duration Exposure Facility (LDEF) have provided much useful information on material sensitivity in the low-Earth orbit (LEO) environment. This is particularly true for selected materials such as thermal control coatings, composites, polymers, fasteners and solar cells. However, LDEF material sensitivity data for other materials like glasses, glass coatings, lubricants, adhesives and seal materials were limited. Some of this important LDEF material sensitivity data has not yet been addressed in detail at the LDEF meetings.

The type of material information needed in the design and development of an new spacecraft in LEO depends to a large extent on program phase. In early program phases it is only necessary to have material sensitivity data to determine what materials may or may not work. Later program phases require details on the material strength, optical properties, and/or other long term survivability requirements for materials in LEO.

Unfortunately, documentation of exposure results for many materials sensitivity experiments that flew on LDEF has not yet been summarized in a convenient form for use by multiple users. Documentation of this data in a form convenient for scientists, engineers as well as technicians remains a significant area of concern for the Aerospace industry.

Many of the material experiments that flew on LDEF were only designed to measure material sensitivity for one year in an LEO environment. However, some materials expected to survive one year simply did not survive the 5.8 years that LDEF eventually remained in orbit. Therefore the survivability of several materials in an LEO environment was determined by default. Most of the LDEF materials experiments were not designed to establish long term material survivability data. This long term material survivability data is particularly useful in later program phases of Spacecraft development. The lack of more controlled materials experiments to determine long term material survivability was one of the major limitation of many LDEF experiments. The identified need for this critical information on the long term material survivability offers a challenge to possible future LDEF type experiments.

INTRODUCTION

The LDEF was deployed into LEO in April of 1984 and retrieved by the space shuttle in January of 1990. Some 10,000 plus materials and samples were on board (ref. 1). It also contained 57 experiments (ref. 1) for further defining the space environments and effect on materials. Two LDEF conferences in '91 and two in '92 have given principal investigators several opportunities to present their LDEF results and findings. Several summaries of LDEF materials have appeared in the literature (refs. 2,3) that attempted to combine the results from several principal investigators.

The design and development of new spacecraft is expected to be strongly dependent on the utilization of LDEF results. The successful application of LDEF materials results to new spacecraft will at some point require that they be in a form that can meet several needs including:

- Multiple users must be considered including; scientists, engineers, technicians and operators.
- Different components of LDEF results will need to be addressed when considering different mission types including; short duration in LEO, long duration in LEO, intermediate orbital altitude, GEO applications, and translunar and planetary space applications.
- Material life analysis detail needed from LDEF results will depend on the program phase i.e., concept, design, verification.
- LDEF data will need to be accessible and user friendly

In general, the results from LDEF have provided much useful information on material sensitivity in the LEO environment. This is particularly true for selected materials such as thermal control coatings, composites, polymers, fasteners, solar cells, etc. However, LDEF material sensitivity data for other materials like glasses, glass coatings, lubricants, adhesives and seal materials was limited. Many of the material experiments that flew on LDEF were only designed to measure material sensitivity for one year in an LEO environment. However, some materials expected to survive one year simply did not survive the 5.8 years that LDEF eventually remained in orbit. Therefore the survivability of several materials in an LEO environment was determined by default. However, most of the LDEF materials experiments were not designed to establish long term material survivability data.

Unfortunately, documentation of exposure results for many materials sensitivity experiments that flew on LDEF has not yet been summarized in a convenient form for use by multiple users. LDEF results will be used by a broad spectrum of users within the aerospace companies, academic institutions and our society in general. The completion of the documentation of LDEF materials results is critical to insure maximum utility to the many people expected to use this information.

LDEF DOCUMENTATION

A comprehensive data base for LDEF experiments and LDEF materials that would be most useful to multiple users is described in Figure 1. Documentation in this form would allow several ways to cross reference LDEF results to survey information for a potential material application. If the desired information was not available, then all LDEF experiments with the material of interest

could be identified along with their LDEF location. Information on the principal investigators for these experiments would also identify valuable contacts that could potentially provide additional material data.

Unfortunately, it has been found that the documentation of LDEF results is significantly incomplete. In discussions with various coordinators involved in the documentation of LDEF results at NASA Langley Research Center and elsewhere, the estimated status of incomplete LDEF results has been approximated by the summary in Table 1. It is clear that the reporting of materials results by principal investigators is significantly incomplete. It is also apparent that the documentation of LDEF materials results has not resulted in the kind of data base that would be useful in the design and development of new spacecraft.

LDEF RESULTS REQUIRED AT SELECTED SPACECRAFT PROGRAM PHASES

The three principal program phases in the development of a new spacecraft are shown in Figure 2 along with the typical time allotted for these phases. The type of material information needed in the design and development of an new spacecraft in LEO depends to a large extent on program phase. In early program phases it is only necessary to have material sensitivity data to determine what materials may or may not work. Some typical evaluations that would be considered for the concept phase of a space craft program are shown in Table 2. Also included in this table are the materials requirements for the Concept phase. As indicated only materials screening results are required for the concept phase since many materials are being considered.

Long term material survivability data is particularly useful in later program phases of Spacecraft development. For both the Design and Verification phases of a spacecraft program as described in Tables 3 and 4 additional information on material life is required. Later program phases require details on the material strength, optical properties, and/or other long term survivability considerations for materials in LEO. The most detailed material life considerations are usually addressed in the Verification phase when maintenance and replacement times are needed for specific material applications.

The lack of more sequenced time phased measurements on LDEF to estimate long term material survivability was one of the major limitations of most material experiments on LDEF.

EVALUATION OF MATERIAL LIFE ON LDEF

Several approaches were used to evaluate material life for the experiments on LDEF. These approaches are summarized in Table 5. The first approach is the pass/fail approach. An example of this approach was the single aluminized Kapton layer that was used as the outer layer of the McDonnell Douglas MLI experiment A0076 (ref. 4). Since the uncoated side of this film was exposed to atomic oxygen in a near ram direction, it was degraded to the point of complete decomposition during the 5.8 years LDEF was in orbit. For this example, it is known that the single aluminized Kapton failed on orbit but it is not known how long it survived before failure. There were no intermediate measurements.

The second type of life failure analysis in Table 5 can be illustrated using the evaluation of the chromic acid anodized tray clamps. For this case, the optical properties of these clamps have been evaluated for all the trays on LDEF. The absorptance and emittance were plotted by Plagemann (ref. 5) as a function of the tray position. Plagemann (ref. 5) also plotted the absorptance and emittance as a function of the solar radiation and atomic oxygen fluence found for chromic acid anodized clamps at each tray position. He found that there was a correlation for the absorptance measurements with atomic oxygen fluence but not with solar radiation fluence. This result turned out to be related to the accumulation of contamination. This result could have also been related to the accumulation of either atomic oxygen or solar radiation to estimate life of a material in space. Here the higher fluence would be considered the longer time in space. However, there are some complications with this type of life analysis. To better understand these complications, some significant details of these fluence calculations will be described.

Bourassa et al. (ref. 6) developed computer programs that were used to predict the total fluence of atomic oxygen and solar radiation received by each tray on LDEF. The LDEF satellite was a 12 sided polygon structure with two additional sides; one facing Earth (Nadir) and the other facing space (Zenith) respectively. If the LDEF satellite could be simplified as a six sided box structure with one side always facing the ram direction, then the total 5.8 year fluences for atomic oxygen and solar radiation calculated by Bourassa et al. (ref. 6) can be described as a percentage of the largest fluence as summarized in Table 6. These results show that the largest solar radiation fluence is in the zenith direction and the maximum atomic oxygen fluence is in the ram direction. By contrast the proton radiation fluence established from measurements on LDEF itself have determined that the maximum fluence occurs in the aft direction (refs. 7,8). Electron radiation appears to be more uniform in all directions (ref. 7). It is apparent from the calculations summarized in Table 6 that the space environment for LDEF or any spacecraft in LEO will not be the same in all directions. The space environment will also not be proportional from one position to another since each component of the LEO environment has a different direction for its maximum fluence. As a result, life analyses determined from different locations on LDEF cannot be used directly to extrapolate to an estimated material life. However, such a material life analysis would be possible if only one component of the LEO environment was important and all other components were negligible. An even better life analysis approach would involve the development of some technique that weights the importance of the different components of the LEO environment as one evaluates materials from different locations on LDEF.

The third approach to evaluate material life from LDEF results indicated in Table 5 involves the evaluation of material measurement made at periodic but specified times at the same location on LDEF. Wilkes et al. (ref. 9) had such a carousel on LDEF as indicated in Figure 3. A schematic of this carousel shown in Figure 4 describes the way samples were rotated periodically from the exposed condition to a position where optical measurements for the samples could be made. Periodic time measurements made for the material S13B/LO are shown in Figures 5. In this instance, Wilkes et al. (ref. 9) were able to estimate a projected life for this material using the log-log plot of the data in Figure 5 as shown in Figure 6. While the approach of Wilkes et al. to estimate material life it is not recommended for all material applications these results do illustrate one potentially successful approach.

The fourth and last approach to evaluate material life from LDEF results indicated in Table 5 involves a modification of the approach used by Wilkes et al. For this case Meshishnek et al. (ref. 9) developed a tray, shown in Figure 7, that provided different sample exposure times at the same

location on LDEF but without the capability of making sample measurements on orbit. For this case, the samples had to be returned to earth to make the measurements necessary to estimate material life.

It is apparent that some approaches to estimate material life from LDEF results will be more successful than others. The identified need for information on the long term material survivability offers a challenge to possible future LDEF type experiments to find new and improved approaches to estimate material life.

WHAT'S NEXT?

Based on the available results from LDEF, it would appear that improved methods to obtain environmental exposure data for use in extrapolating material life are needed. Future flight experiments similar to LDEF that might be pursued in the near future should also extend the LDEF knowledge base in such areas as:

- Additional data on seal materials, glasses, glass coatings, lubricants and adhesives exposed to the space environment are needed
- New materials with expectations of improved performance and durability need to be tested.
- Polar and elliptical orbit data with high particulate radiation would prove useful.
- Effects of active versus passive solar cells should be evaluated
- Improved understanding of synergistic environmental phenomena (UV, atomic oxygen, etc.) on materials degradation needs to be addressed.

In addition to the generation of new data for samples exposed to the LEO environment, it is also important to continue further development of effective ground based simulations to correlate with space based experiments. Good ground based simulation techniques and procedures could help minimize material life evaluation requirements.

CONCLUDING REMARKS

Well documented LDEF results are very much needed by those engineers associated with spacecraft "Design." Where possible the LDEF data should be organized at different levels of detail consistent with the information required at different phases of a spacecraft program. It is also expected that LDEF results will be used by a broad spectrum of users within the aerospace companies, academic institutions and our society in general. It is very important that LDEF information be available and easily obtainable by all that might want access to it. In particular, this information needs to be provided in a user friendly data base. Unfortunately, it is also apparent the much work still needs to be done to obtain, analyze, and document basic information from unreported LDEF experimental results. Where possible a maximum effort should be made to estimate projected life from LDEF materials data. The completion of a comprehensive LDEF materials data base is critical to insure maximum utility to the many people expected to use this information.

Any new LDEF type materials experiments will need to build on the experience obtained from the current LDEF results. In particular, new and novel ways to predict the long term survivability of materials exposed to the LEO environment are needed. Improved ground based verification techniques are also needed to predict and correlate with LEO materials degradation.

REFERENCES

1. "69 Months in Space: A History of the First LDEF (Long Duration Exposure Facility)." NASA NMP 149, Langley Research Center.

2. Dursch, H.W., Spear, W.S., Miller, E.A., Bohnhoff-Hlavacek, G.L., and Edelman, J.: "Analysis of Systems Hardware Flown on LDEF—Results of the Systems Special Investigation Group." Boeing Defense and Space Group, Contract NAS1-19247, NASA Contractor Report 189628, April 1992.

3. Stein, B.: "LDEF Materials: An Overview of the Interim Findings." LDEF Materials Workshop '91, NASA Conference Publication 3162, Proceedings of a Workshop held at NASA Langley Research Center, pp. 1–56, November 19–22, 1991.

4. Smith, C.A., Hasegawa, M.M., and Jones, C.A.: "Space Station WP-2 Application of LDEF MLI Results." LDEF Materials Results for Spacecraft Applications Conference, Huntsville, Alabama, October 27–29, 1992.

5. Plagemann, W.L.: "Space Environmental Effects on the Integrity of Chromic Acid Anodized Coatings." LDEF—69 Months in Space, First Post-Retrieval Symposium, NASA Conference Publication 3134, Proceedings of a Symposium Held in Kissimmee, Florida, pp. 1023–1040, June 2–8, 1991.

6. Bourassa, R., Gillis, J.R., and Rousslang, K.W.: "Atomic Oxygen and Ultraviolet Radiation Mission Total Exposure for LDEF Experiments." LDEF—69 Months in Space, First Post-Retrieval Symposium, Arlene S. Lavine, ed., NASA Conference Publication 3134, Part 2, June 2–8, 1991.

7. Armstrong, T.W., Colborn, B.L., and Watts, J.W.: "Ionizing Radiation Calculations and Comparisons With LDEF Data." LDEF—69 Months in Space, First Post-Retrieval Symposium, Arlene S. Lavine, ed., NASA Conference Publication 3134, pp. 347–357, June 2–8, 1991.

8. Harmon, A., (Based on Sodium 22 Measurements), Personal Communication, October 19, 1992.

9. Wilkes, D., Brown, M.J., Hummer, L.L., and Zwiener, J.M.: "Initial Materials Evaluation of the Thermal Control Surfaces Experiment (S0069)." LDEF—69 Months in Space, First Post-Retrieval Symposium, Arlene S. Lavine, ed., NASA Conference Publication 3134, pp. 899–917, June 2–8, 1991.

10. Meshishnek, J.J., Gyetvay, S.R., and Jagers, C.H.: "Long Duration Exposure Facility Experiment M0003 Deintegration/Findings and Impacts." LDEF—69 Months in Space, First Post-Retrieval Symposium, Arlene S. Lavine, ed., NASA Conference Publication 3134, pp. 1073–1107, June 2–8, 1991.

Table 1. Status summary of materials data base for LDEF.

	Percent Materials Identified	Percent Materials Results reported	Percent Materials Documented in Data Base
Adhesives	90	<50	0
Seals	90	<50	0
Solar Cells	100	<<50	25
Lubricants	90	<50	0
Optical Fibers	100	<50	25
Optical Glasses	75	<50	25
Optical Coatings	75	<50	25
Batteries	100	<50	0
Composites	95	<50	0
Plastics	90	<50	0
Velcro	90	<<50	0
Fasteners	90	<<50	10
Thermal control Coatings	90	<<50	25
Paints	90	<<50	20
Multilayer Insulation	90	<<50	0
Thermal Blankets	90	<<50	25

Table 2. Concept phase mission profile evaluation and materials requirements.

Mission Profile

- **Application Altitude (i.e. LEO, GEO, etc.)**
- **Environment (Atomic Oxygen, UV Radiation, Electron/Proton Radiation, etc.)**
- **Reboost Schedule**
- **Hardware Function**

Materials Screening

- **Operational Scenario for each Material**
- **Potential Materials for Application**
- **Literature Review of Available Materials Data Described by Mission Profile**
  - **Materials Susceptibility Data**
  - **Materials Projected Life Data**

Table 3. Design phase materials requirements.

Hardware Analysis and Testing

- **Stress/Strain Evaluations**
  - **Environmental Impact Analysis**
    - * **Model Spacecraft Microenvironments**
- **Materials Protection Guidelines**
  - **Optical Properties Changes to Exterior and Interior Coatings**
  - **Bumpers, Shields, Thermal Isolators Design Guidelines**
  - **Single Event Upset Guidelines**
  - **End of Life Performance of Solar Cells and Batteries**

Materials Selection from Analysis and Testing

- **Correlate Space Test Results to New Spacecraft Design**
- **Evaluate Materials as Described by Operational Scenarios**
  - **Materials Environmental Susceptibility Data**
  - **Materials Projected Life Data**

Table 4. Verification phase materials requirements.

Hardware Function for Life of Spacecraft

- **Materials Replacement Schedule**
  - **Materials Projected Life Evaluation**
    - * **Accelerated Life Testing**
    - * **Combined Environmental Testing**
    - * **Validation of Laboratory Environmental Testing to on Orbit Performance**

Table 5. Approaches to evaluation of expected life for materials on LDEF.

(1) Expected Life < 5.8 years ------- material failed on orbit

- Single aluminized Kapton film removal on leading edge experiment A0076

(2) Identical material experiments at various locations around LDEF allowed utilization of different LDEF environments to extrapolate life

- Chromic acid anodized plates on all LDEF experiment trays

(3) Material experiment periodic measurements on orbit at one location on LDEF allowed life extrapolation

- Rotating sample carousel with periodic optical measurements on experiment S0069

(4) Material experiment provided moveable canisters to provide several exposure times to identical samples on orbit at one LDEF location to extrapolate life

- Aerospace Corporation sample canisters that opened in three stages on experiment M0003 (trays D4 and D8)

Table 6. Calculated levels of environmental components for sides of orbiting box structure.

Orbiting Box Side	Percent Total LDEF Fluence			
	Solar Radiation*	Atomic Oxygen*	Electron Radiation**	Proton Radiation**
Zenith Side	100.	4.4	100.	56.
Ram Side	77.	100.0	100.	61.
Aft Side	77.	5.7×10^{-13}	100.	100.
Starboard Side	46.	4.4	100.	90.
Port Side	46.	4.4	100.	67.
Nadir Side	31.	4.4	100.	56.

References

* Roger Bourassa, J.R. Gillis, and K.W.Rousslang, "Atomic Oxygen and Ultraviolet Radiation Mission Total Exposure for LDEF Experiments", LDEF -69 Months in Space, First Post -Retrieval Symposium, Arlene S. Lavine -Editor, NASA Conference Publication 3134, Part 2, June 2-8, 1991

** T.W. Armstrong, B.L. Colborn, & J.W. Watts, " Ionizing Radiation Calculations and Comparisons with LDEF Data", NASA Conf. Publication 3134, LDEF 69 Months in Space, First Retrieval Symposium, June 2-8, 1991, Page 347-357----- And personal communication with Allen Harmon (10/19/92) and based on Sodium 22 measurements

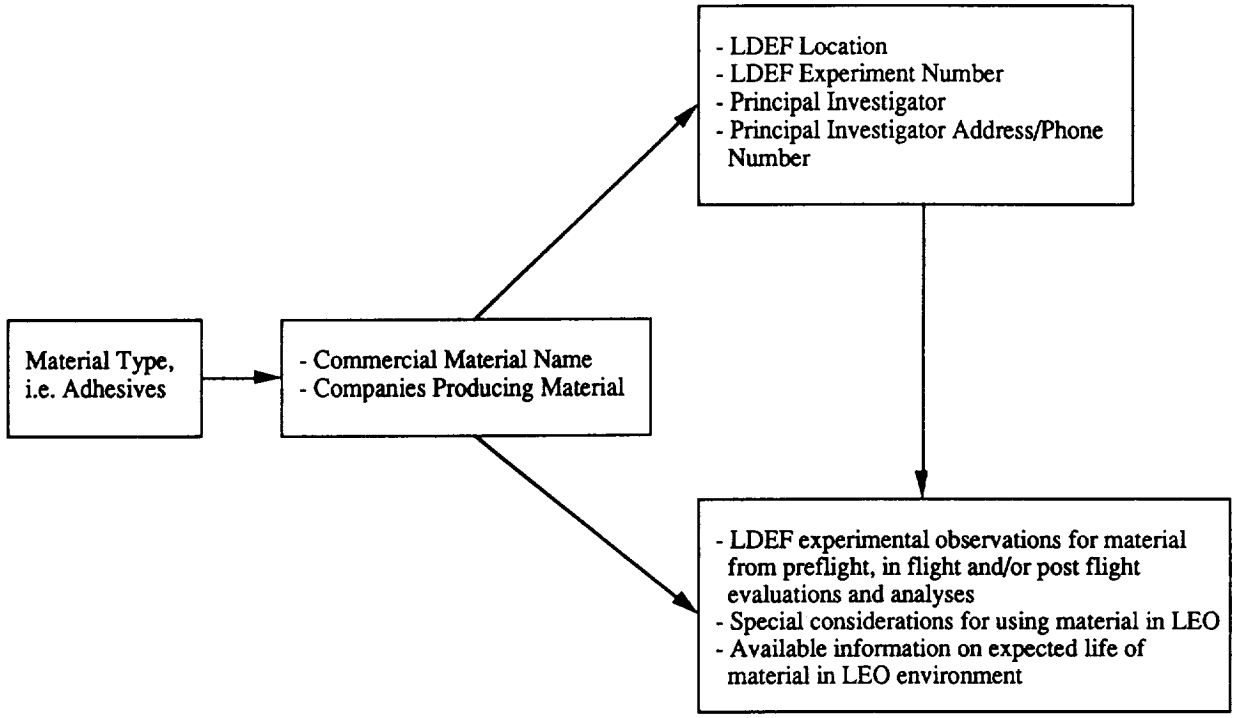

Figure 1. Preferred data base for LDEF experiments and materials.

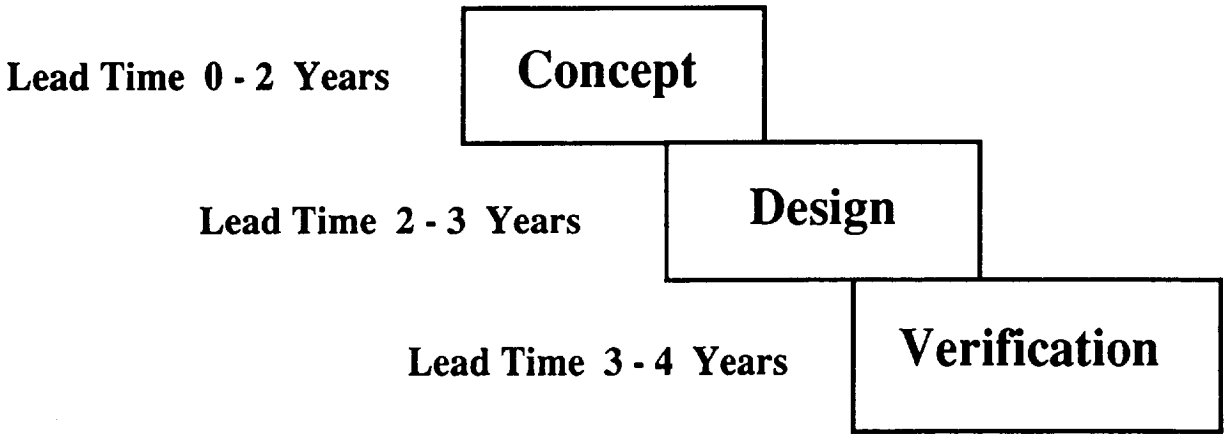

Figure 2. Spacecraft program phases.

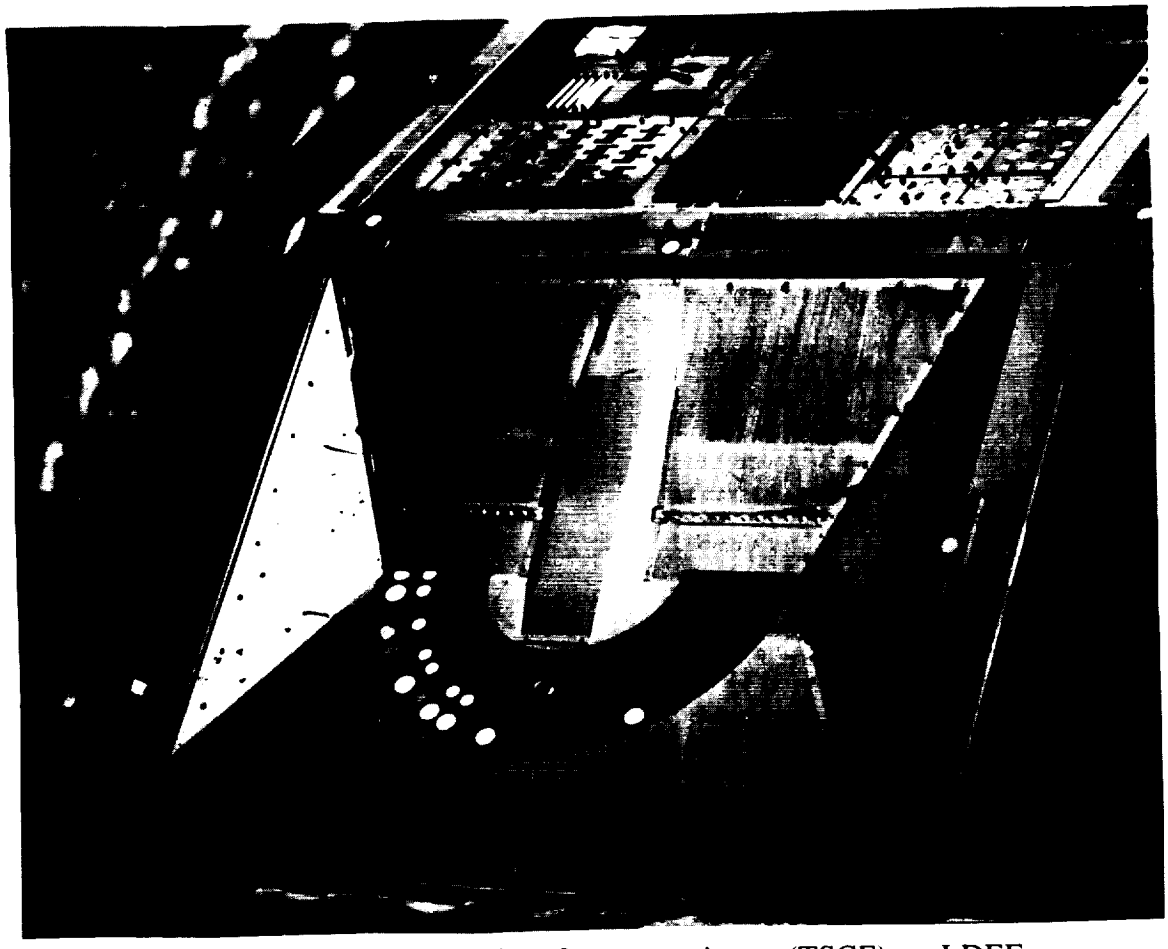

Figure 3. Thermal control surfaces experiment (TSCE) on LDEF.
(Photo courtesy of AZ Tech and NASA Marshall.)

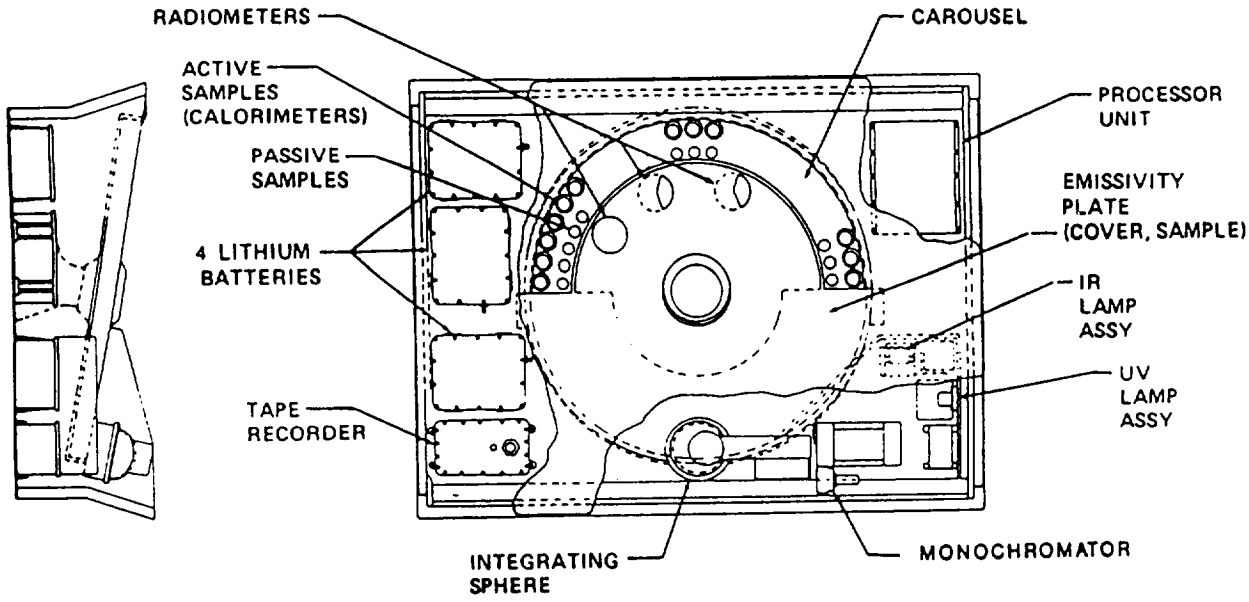

Figure 4. Schematic of TCSE on LDEF.
(Schematic courtesy of AZ Tech and NASA Marshall.)

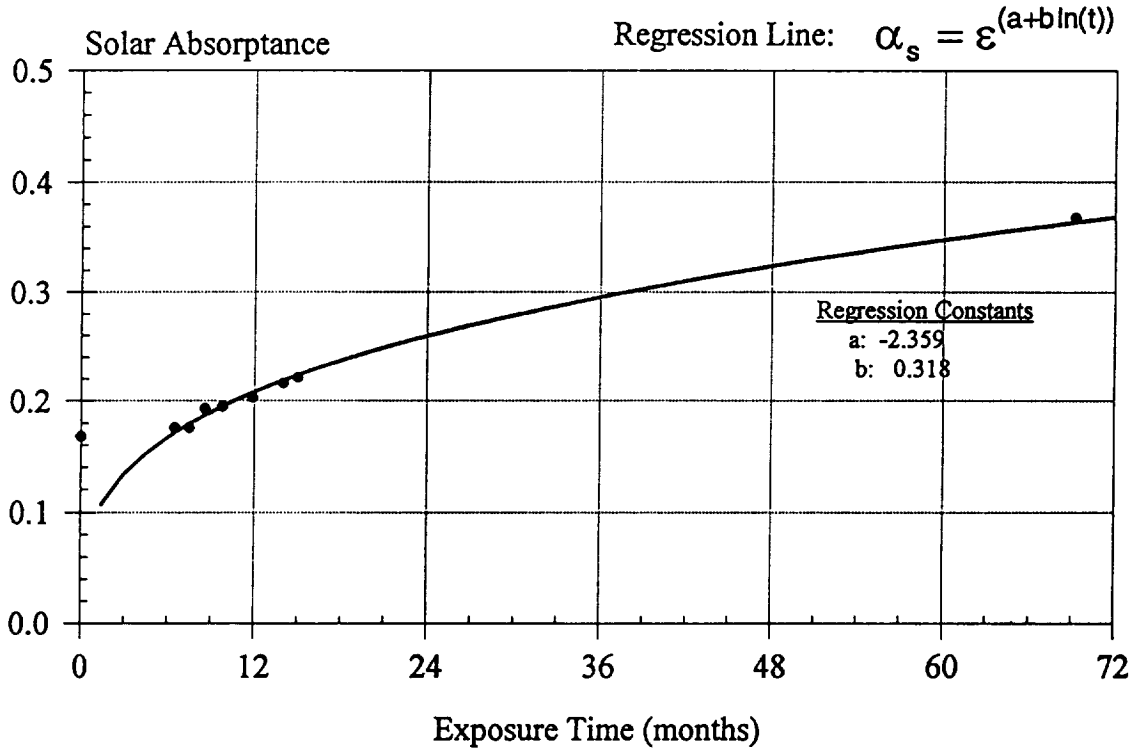

Figure 5. Power regression analysis of S13G/LO LDEF results.
(Courtesy of AZ Tech and NASA Marshall.)

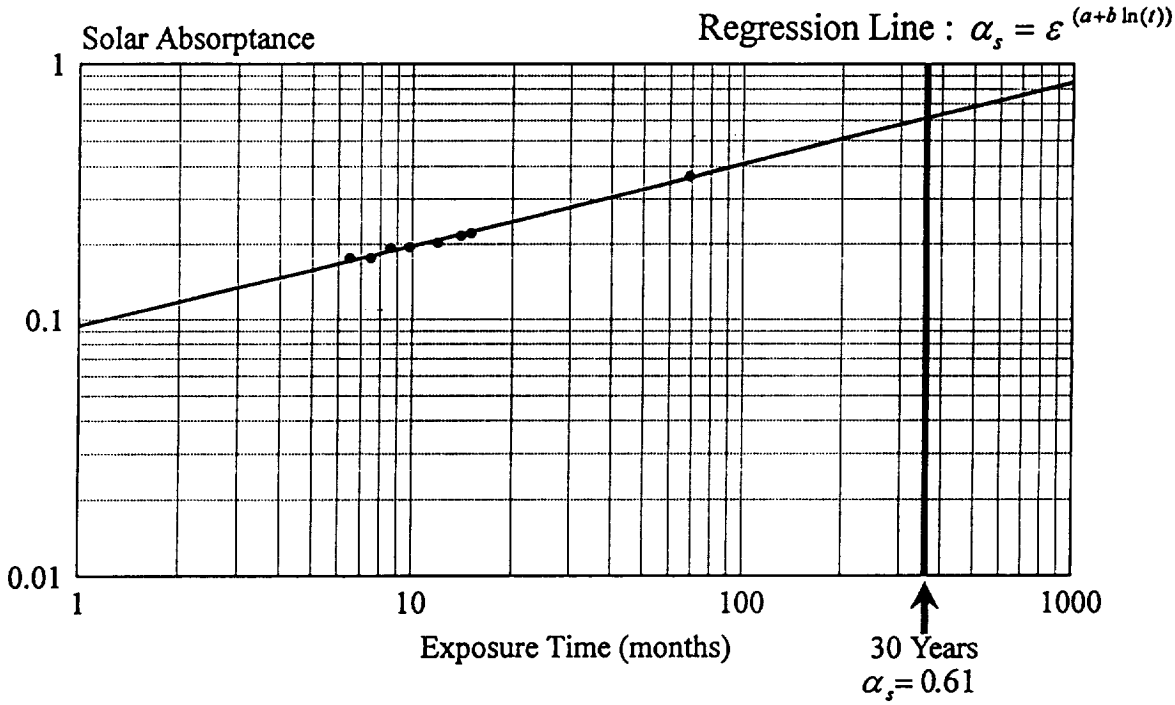

Figure 6. Log/log plot of S13G/LO LDEF data.
(Courtesy of AZ Tech and NASA Marshall.)

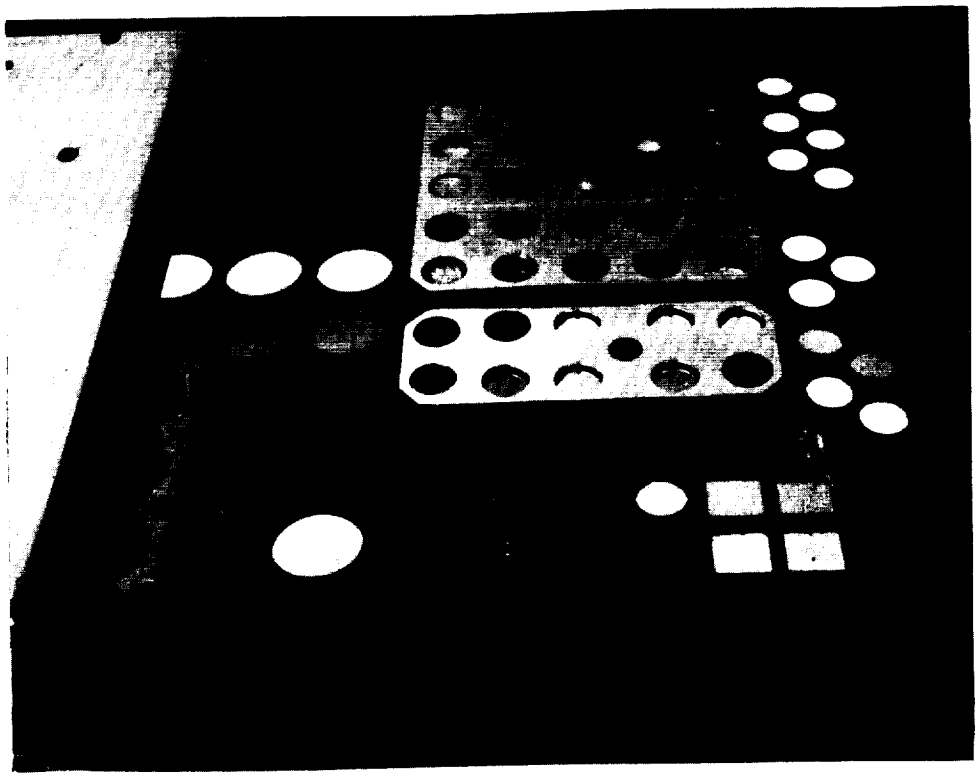

Figure 7. Aerospace Corporation LDEF canister. Identical samples exposed 9, 19, and 40 weeks with adjustable tray. (Courtesy of Aerospace Corporation.)

N94-31048

MSFC ORBITAL SPACECRAFT DEVELOPMENT EMPHASES FOR THIS DECADE

Robert J. Schwinghamer
Deputy Director for Space Transportation Systems
NASA George C. Marshall Space Flight Center
Marshall Space Flight Center, AL 35812

SUMMARY

Historically, the Marshall Space Flight Center (MSFC) has been responsible for significant accomplishments in the area of developing both manned and unmanned spacecraft. MSFC is presently involved in many of NASA's largest and most prominent programs, with some operational, others being readied for flight, and still others in various stages of design and development. Examples of MSFC programs being designed or developed are Space Station *Freedom* (S.S. *Freedom*), the Advanced X-Ray Astrophysics Facility (AXAF) which includes imaging and spectroscopy facilities, the Laser Atmospheric Wind Sounder (LAWS), and the Lunar Ultraviolet Telescope Experiment (LUTE), with Spacelab and Tethered Satellite System (TSS) as examples of current operational MSFC spacecraft. The information obtained from the Long Duration Exposure Facility (LDEF) will aid the design process and life predictions for these and all future spacecraft. A second LDEF is presently being considered. All of these projects will be briefly described in this paper.

INTRODUCTION

MSFC, with a long reputation as a center of excellence for propulsion research and development, has been responsible for numerous scientifically significant manned and unmanned missions. Many orbital missions of the future are much larger, more complex, and require longer life than those of the past. As a result, the consequences of the space environmental effects on materials and systems are becoming increasingly important. Missions such as LDEF provide information that will benefit these future programs through improved definition of performance degradation and life predictions while in orbit. S.S. *Freedom* is being designed for a 30-year lifetime and will be much larger and provide higher power levels than any previously flown spacecraft. The AXAF will be the next of the great observatories to be placed in orbit above the distorting atmosphere of the Earth. Satellites, such as LAWS, will operate in low-Earth orbit (LEO) in the future to provide information to help us understand the planet on which we live. Some missions, such as LUTE, will require a return to the Moon. There are many other projects under development at MSFC, including numerous payloads. The Marshall Center's role in development of orbital spacecraft will be significant in the upcoming decade.

SPACE STATION FREEDOM

S.S. *Freedom* is to be a permanently manned facility in LEO. The station, as shown in Figure 1, is 353 feet long and will have one habitation module for astronaut living quarters and three laboratory modules for life sciences, microgravity, and crystal growth research. S.S. *Freedom* will be

an observation post for Earth and the universe and a facility to assemble, operate, and maintain large spacecraft for future endeavors, including the manned mission to Mars. It also provides for peaceful international cooperation, with other nations working with the United States and NASA to develop an international space station. Japan is providing the Japanese Experiment Module, the European Space Agency is providing the Columbus Laboratory Module, and Canada is providing the Canadian Mobile Servicing System which will allow robotic arms to move payloads and equipment around the station. Assembly of S.S. *Freedom* will begin in 1996, with manned tended capability (MTC) by mid-1997 and permanently manned capability (PMC) by 2000. During the buildup to PMC, there will be many stages of integrated assembly making S.S. *Freedom* a useful space platform and laboratory much earlier.

MSFC is responsible for the design and manufacture of life support systems, composite equipment racks, habitation and laboratory modules, including environmental control and other support systems. The solar arrays, with a length of 112 feet, contain 198,600 solar cells to provide 56 kW of power. The LDEF has proven to be a wealth of information on how these solar arrays should be designed, as well as long-term space environment effects on other materials. For example, anodized aluminum had excellent performance for the 5.8 years exposure and anodized aluminum, tailored to provide passive thermal control, is planned for the micrometeoroid/space debris shielding on S.S. *Freedom.*

ADVANCED X-RAY ASTROPHYSICS FACILITY

AXAF will be a two-part orbiting observatory to study neutron stars, black hole candidates, debris from supernova explosions, quasars, and active galaxies. AXAF will succeed the Einstein X-ray Observatory with significantly improved sensitivity. AXAF-I's mission will consist of high-resolution imaging and grating spectroscopy. AXAF-S will use a cryogenically cooled x-ray spectrometer for high-energy, high-spectral resolution spectroscopy. With both observatories, scientists can obtain images and characterization of the x rays emanating from astronomical objects. AXAF-I will be built by TRW and launched in 1998 from the space shuttle into a high-Earth orbit. AXAF-S will be designed and built by MSFC with a planned launch in 1999 by a Delta II rocket into a low-Earth, Sun-synchronous polar orbit. AXAF-I and -S whose configurations are shown in Figure 2 will operate for 5 and 3 years, respectively. Cleanliness of optics and contamination control are primary concerns due to the grazing incidence optics and the performance requirements.

TETHERED SATELLITE SYSTEM

The TSS, a joint project of the United States and Italy under an agreement signed in 1984, consists of a satellite, a $^1/_{10}$th inch diameter tether, and a deployer in the shuttle's cargo bay. This satellite system can demonstrate the feasibility of using a tether to generate electricity, as a propulsion system to power spacecraft, and for studying the Earth's magnetic field and ionosphere.

The conducting tether generated electrical currents using the same principle as a standard electrical generator, converting the mechanical energy of the shuttle's 17,000 mph orbital motion into electrical energy by passing a conductor through the Earth's magnetic field lines. The TSS-1 scientific instruments, mounted in the shuttle cargo bay, the middeck, and on the satellite, allows scientists to examine the electrodynamics of the conducting tether system, as well as clarify the understanding of physical processes in the ionized plasma of LEO.

One possible future application of the tethered satellite would be to use long conductive tethers to generate electricity for S.S. *Freedom* or other orbiting bodies. Conversely, by expending electrical power to reverse the current flow into a tether, the system could be placed in an "electric motor" mode to generate thrust for orbit maintenance. Tethers may also be used to raise or lower spacecraft orbits by releasing a tethered body from a primary spacecraft, thereby transferring momentum and imparting motion to the spacecraft. Another potential application is the creation of artificial gravity by rotating two or more masses on a tether. Downward deployment could place a satellite in regions of the atmosphere that are currently difficult to study since they lie above the range of high-altitude balloons and below the minimum altitude of free-flying satellites. Deploying a tethered satellite towards Earth from the shuttle would also make possible aerodynamic and wind tunnel type testing in the region 50 to 75 nautical miles above the Earth.

The Tethered Satellite (Figure 3) first flew on the space shuttle *Atlantis* in August 1992. The satellite did not fully deploy due to mechanical problems, but the tether did generate 40 V of electricity. In addition, the mission provided data on the dynamics of deployment and retrieval. A possibility for reflight of the experiment on a future shuttle mission is being studied. MSFC was responsible for the U.S. portion of the project, as well as the rapid development, qualification, and application of the electrically conductive paint used on the satellite sphere.

EARTH OBSERVATIONS

The Earth Observing System includes LAWS. This instrument addresses the problem of ozone depletion and pollution. LAWS consists of a carbon dioxide coherent laser system, common transmit and receive optics, and a scanning telescope system for off-track coverage. It will provide real-time measurement of global atmospheric winds, circulation, and climate dynamics. LAWS will be capable of measuring the magnitude of ozone depletion, global warming, and the nature of the threat to the Earth environment, in addition to monitoring man's effects on the atmosphere. LAWS can be flown as either a space station payload or attached to a polar platform. MSFC is presently managing the development of this project.

PAYLOADS

MSFC is also leading the development and flight of several Spacelab and space station payloads. On S.S. *Freedom*, the Material Sciences Glovebox is capable of fluids handling and wet chemistry, particulate generating procedures, and equipment servicing or repair in a clean environment. The internal atmosphere is recycled and filtered to remove dust particles and fluid droplets. Also, a portable glovebox will be available as part of the laboratory support equipment.

A furnace facility is being developed to include a crystal growth furnace, with configurations to include high and low gradients directional solidification processing, vapor crystal growth, and a programmable multizone. Also included are a metals and alloys solidification apparatus, a visibly transparent furnace, a large bore Bridgman furnace, and a high pressure furnace module. These facilities will provide for investigations of the solidification of metals and alloys, crystal growth of electronic and photonic materials, and oxide/glass formation.

Also under development is a electronic still camera laboratory for high-resolution digital imaging systems and processing systems. It is equipped to measure and analyze analog and digital

circuit parameters of electronic digital systems and video cameras, as well as perform extensive digital processing of images from video resolution up to 16 million pixel true color resolution. The current design first flew on STS-48, with the downlink from the space shuttle in near real time.

The Optical Properties Monitor Satellite is a multifunction, in-flight laboratory for the study of space environment effects on materials. It is scheduled to fly on the space shuttle in 1997. A very similar project is the LDEF II. LDEF II would be a more compact version of LDEF so as to fit in the current shuttle manifest. It would contain about a dozen experiments with optics, polymers, thermal control coatings, and composites. It would study the space environment, particularly atomic oxygen, and its effects on materials.

In recent years, consideration of science outposts on the Moon and subsequent mission to Mars has increased. The LUTE is part of the planned lunar base of the Space Exploration Initiative (SEI). Because the Moon has no atmosphere, it is an excellent place for telescopic observations. Also part of SEI is the Laser Power Beaming Experiment. This would transfer energy from Earth to Moon, Earth to orbit, or orbit to orbit using phased laser light. Photovoltaic cells would convert the light into electricity. Efficient energy transfer is achieved since very little attenuation of the laser beam would occur due to atmospheric interference.

CONCLUSION

There are many other space-based hardware projects being planned at MSFC, such as space platforms and other Earth-orbiting systems. There are also smaller projects that are in various stages of development here. Whatever the size spacecraft or length of stay in the space environment, it is essential to have a data base of knowledge about atomic oxygen, thermal vacuum, micrometeoroids, space debris, ultraviolet and particle radiation. We will continue to study the environment and its effects on materials in order to develop and build qualified space hardware.

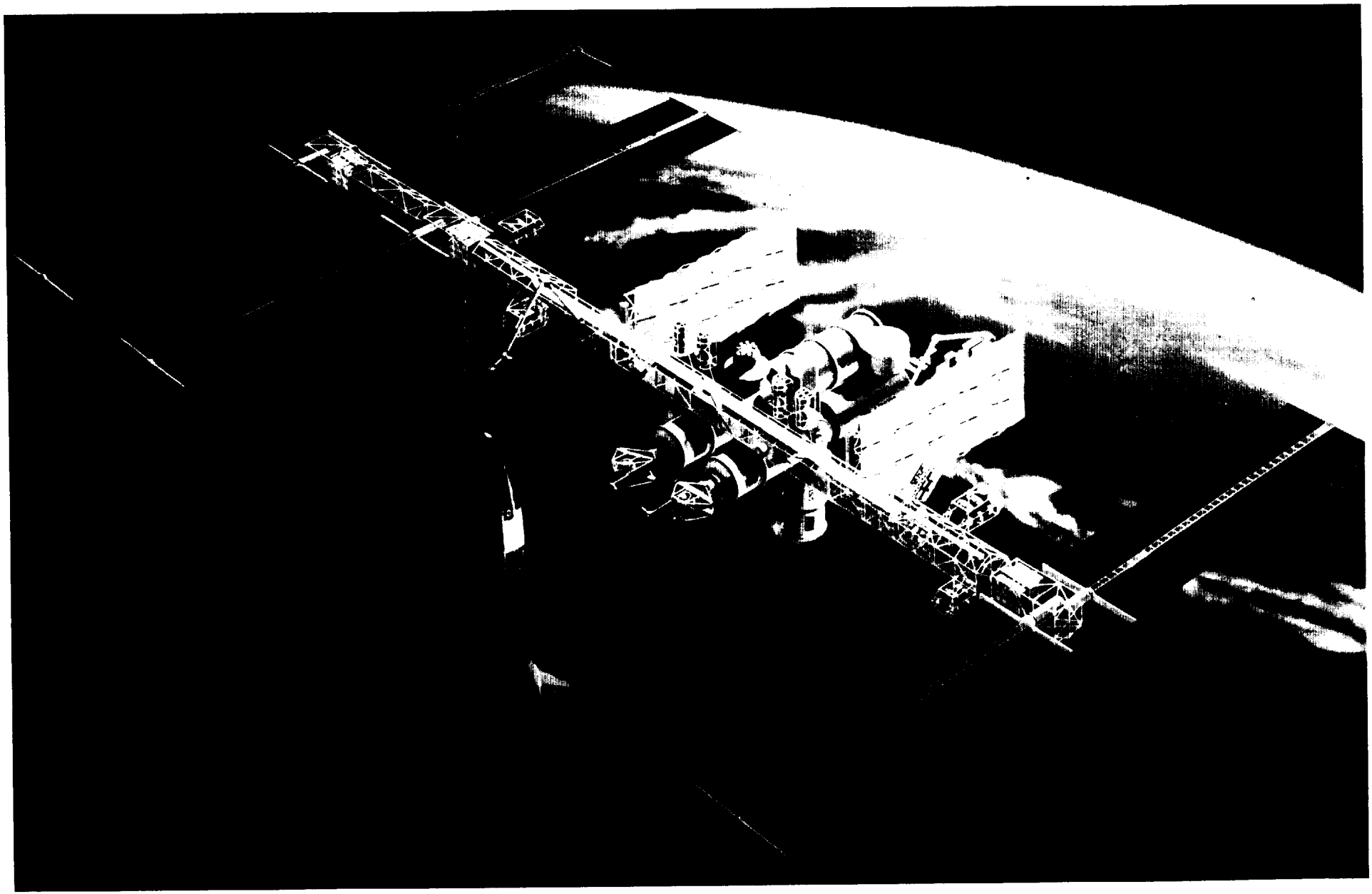

Figure 1. S.S. *Freedom* concept.

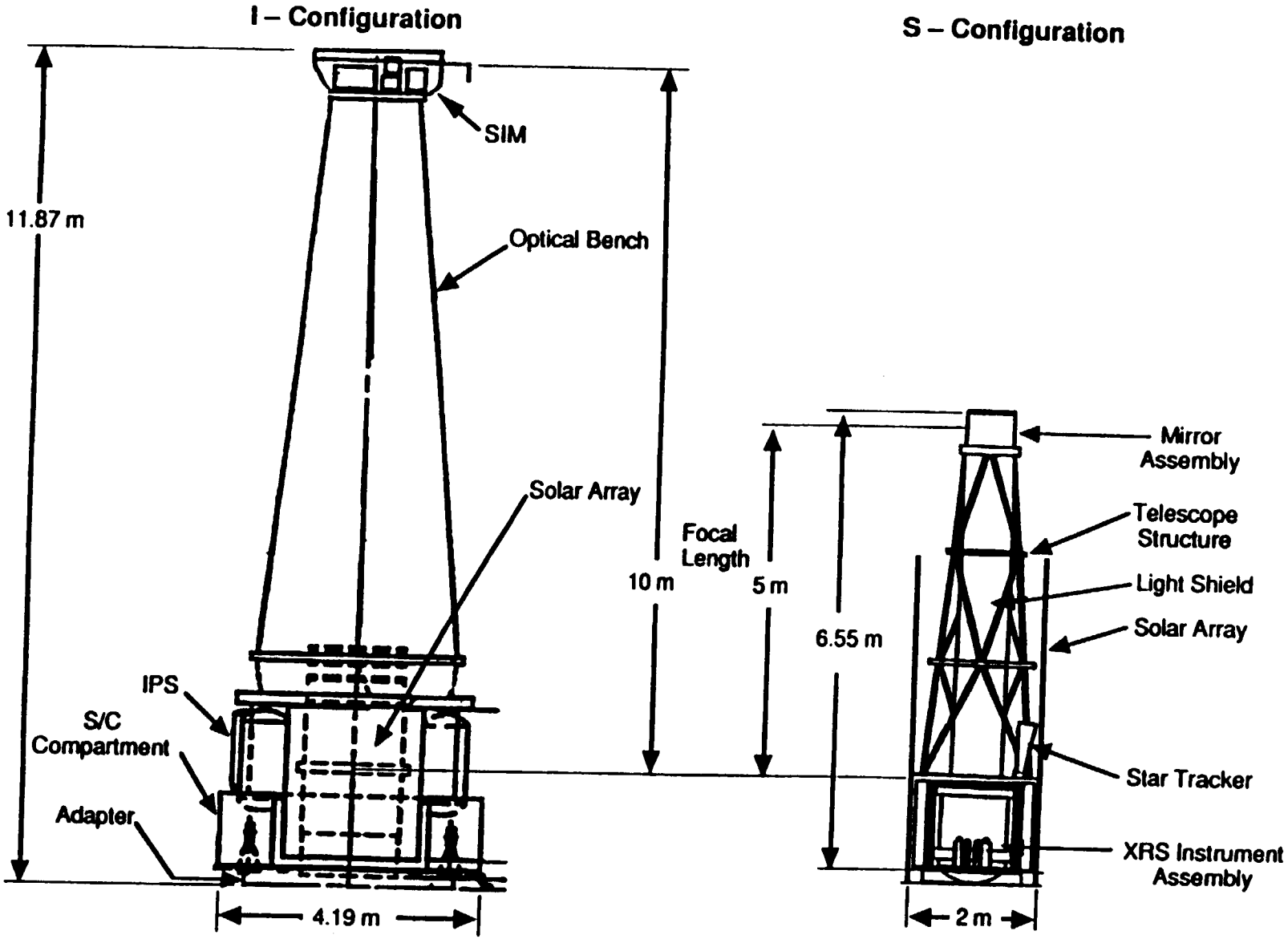

Figure 2. Configurations of the AXAF imaging and spectroscopy spcecrafts.

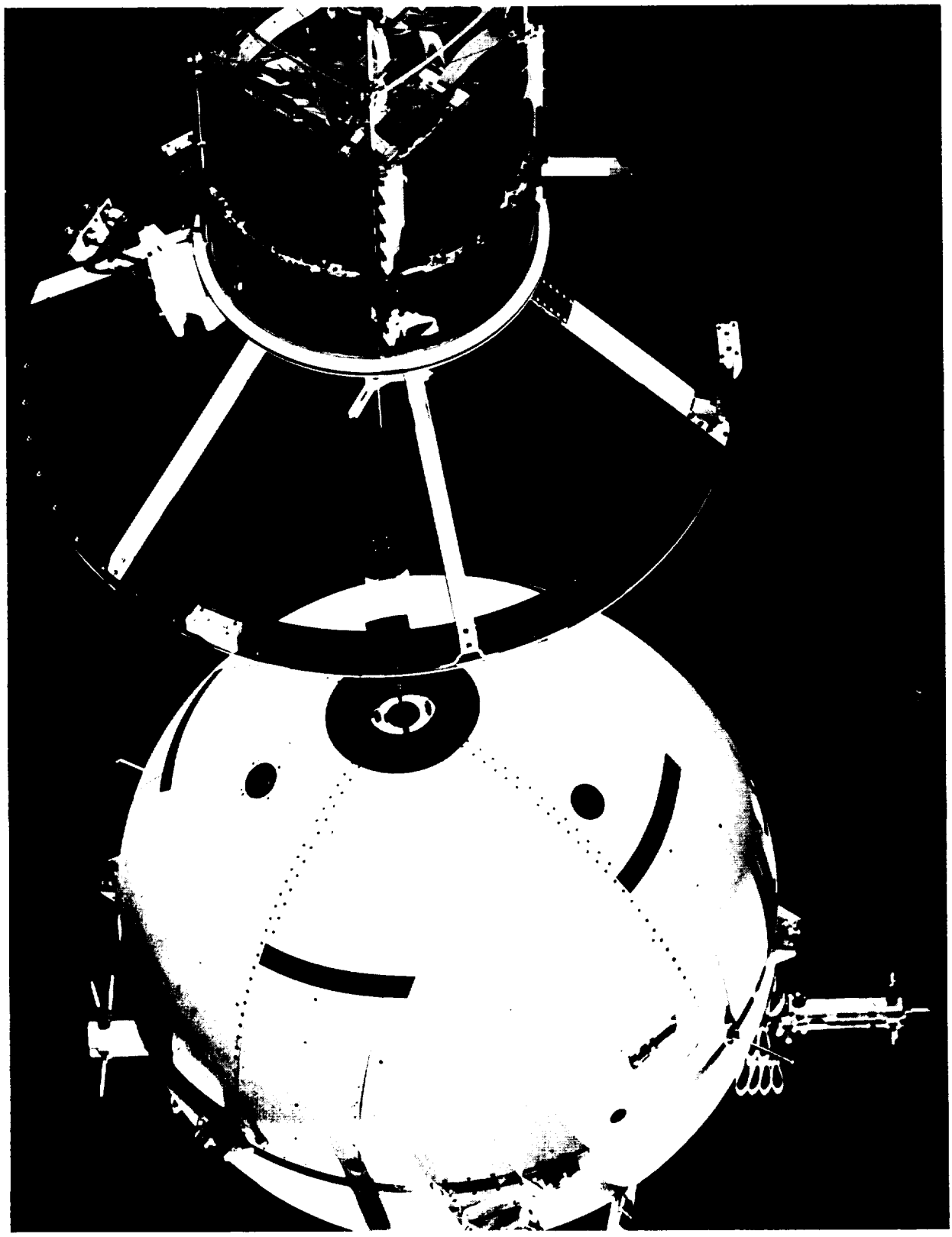

Figure 3. Tethered Satellite during deployment.

AN OVERVIEW OF THE ON-ORBIT CONTAMINATION OF THE LONG DURATION EXPOSURE FACILITY (LDEF)

W. K. Stuckey
The Aerospace Corporation
2350 East El Segundo Blvd.
El Segundo, CA 90245
Phone: 310/336-7389, FAX: 310/336-5846

SUMMARY

Contamination that leads to degradation of critical surfaces becomes a vital design issue for many spacecraft programs. One of the processes that must be considered is the on-orbit accumulation of contaminants. The Long Duration Exposure Facility (LDEF) has presented an opportunity to examine the deposits on surfaces returned from orbit in order to help in understanding the deposition processes and the current models used to predict spacecraft contamination levels. The results from various investigators on the contamination of LDEF have implications for material selection, contamination models, and contamination control plans for the design of future spacecraft.

INTRODUCTION

The control of contamination is very important for critical surfaces of satellite systems since contamination can lead to the degradation of optical or thermal properties. Contaminants can be accumulated during assembly, ground operations, launch, deployment, or flight, and all of these must be considered to control undesirable contaminant deposition on a spacecraft surface. Many investigations have addressed deposition mechanisms, predictive models, and measurements of contamination deposition under various conditions. However, LDEF represents the first opportunity for a laboratory examination of the contamination accumulated during nearly 6 years on orbit. This contamination represents the result of the combined environments experienced by LDEF in low Earth orbit. The characteristics of the deposits, their composition, and their effect on properties provide valuable information that will aid our understanding of the process of contaminant deposition on spacecraft surfaces. In this discussion, the contamination accumulated during the time LDEF was on orbit will be emphasized, rather than that occurring during assembly, ground operations, launch, etc., which can be studied by other means.

CONTAMINATION OBSERVATIONS

Contamination was immediately observable upon the retrieval of LDEF. Photographs were taken of the D9 tray from the M0003 experiment on the leading edge of LDEF while still in orbit. These photographs (ref. 1) clearly show debris on the D9 tray generated from atomic oxygen erosion of the Kapton from aluminized Kapton material. It is interesting that this debris had apparently migrated to adjacent areas while on orbit. Evidence for particulate migration was observed in other investigations of contamination after retrieval (ref. 2). The particulate contamination was reported to have been approximately Level 2000 on LDEF surfaces examined at the Kennedy Space Center (KSC). Most particulate contamination is not accumulated on orbit but comes from ground-based sources.

Molecular contamination was clearly evident in the initial observations of the LDEF vehicle upon return to KSC. There were multiple areas on LDEF having very heavy brown deposits (such as those on the space end of LDEF) that can be attributed to the outgassing from connectors. This kind of deposit would severely impact a critical component in the field of view of such a high outgassing source. Significant deposits were also observed on many other surfaces of LDEF (ref. 3). There were easily visible deposits associated with venting paths, particularly from the interior of the LDEF structure. The location of these deposits confirms the importance of the role of solar ultraviolet (UV) radiation and the photoenhanced deposition of contaminants, which was known to be important prior to the LDEF retrieval. Similarly, the ability of atomic oxygen to remove or alter contaminants was known. Deposits that were clearly associated with the atomic oxygen exposures were observed on many LDEF surfaces. Clearly, the selection of materials, the venting paths, the temperature, the UV interactions, and the atomic oxygen interactions are of utmost importance to control contamination and must be included in spacecraft design if a critical surface requires contamination control. Contamination control was not consistent on the LDEF experiments.

In addition to the visible deposits on LDEF, contamination was present on many surfaces not necessarily associated with line-of-sight deposition from an outgassing source(ref. 4). Infrared analyses identified this contamination as a mixture of silicones and hydrocarbons, with most contamination being typical of materials intentionally used on LDEF. This contamination, while not always sufficient for visible detection, is nevertheless significant for many optical components and has been an interference in many analyses of LDEF surfaces and studies of the impact residue in craters.

CONTAMINATION INVESTIGATIONS

Quartz-crystal microbalances (QCM's) were flown on the Long Duration Exposure Facility (LDEF M0003-14) by QCM Research, Laguna Beach, California, as contamination monitors. This subexperiment was one of 19 subexperiments that comprised the M0003 experiment assembled by The Aerospace Corporation. The QCM's used quartz crystals with two types of coatings. One set of leading- and trailing-edge QCM's consisted of crystals with 9,000 Å of aluminum and aluminum oxide (Al + Al_2-O_3) and a top layer of 150 Å of indium oxide (In_2-O_3). The second set of crystals on the leading and trailing edges consisted of 9,000 Å (Al + Al_2-O_3) and a top layer of 150 Å zinc sulfide (Zn-S). The crystals with the In_2-O_3 coating were selected for the on-orbit data acquisition. The QCM's consists of a pair of crystals, one that was exposed to the environment and termed the "sense" crystal, and one that remained unexposed and hence termed the "reference" crystal. The beat frequency monitored between the "sense" and "reference" crystal represents a change in mass of the "sense" crystal as a result of exposure, relative to the unexposed "reference" crystal.

The QCM response was recorded for about 14 months, the lifetime of the data acquisition batteries. The crystals continued to be exposed to the Low Earth Environment on Row 9 on the leading edge of LDEF and Row 3 on the trailing edge for the entire LDEF mission, even though the response was no longer recorded. Data were recorded in bursts lasting a period of 111.7 min (about one LDEF orbit). During this 111.7-min period, each data channel was scanned 32 times, producing a profile for the entire orbit. After the burst period, the data system rested for 93.16 h before start of the next burst period. Data were taken in this manner until the end of the recording media was reached, 424 days after launch. The maxima and minima frequencies were recorded for the leading- and trailing-edge QCM's during each period. The data corresponding to the minimal temperature during each orbit are shown in Figures 1 and 2 (ref. 5). Note that the trailing-edge QCM shows an increase in weight that continues for the entire 424-day data acquisition period, while the leading edge shows an apparent weight loss.

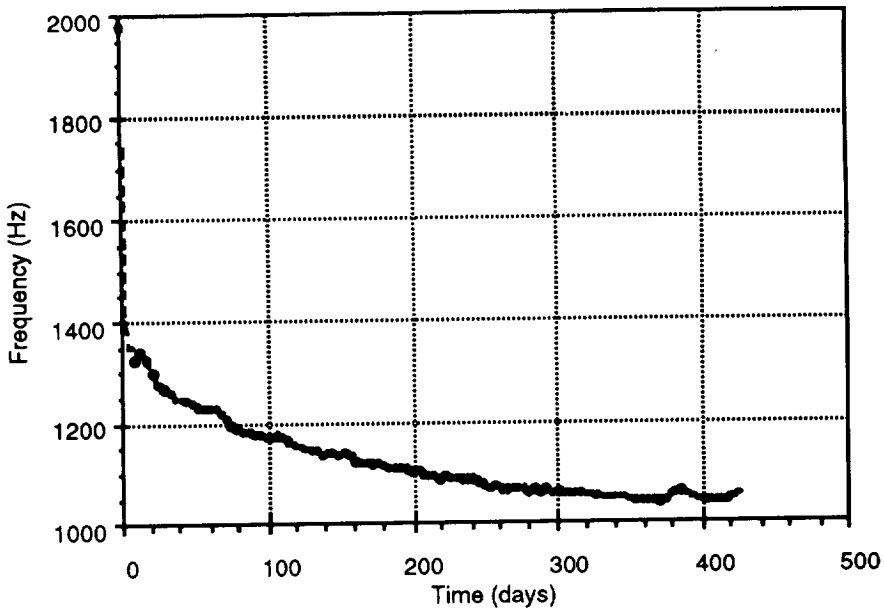

Figure 1. Leading-edge quartz-crystal microbalance frequency change.

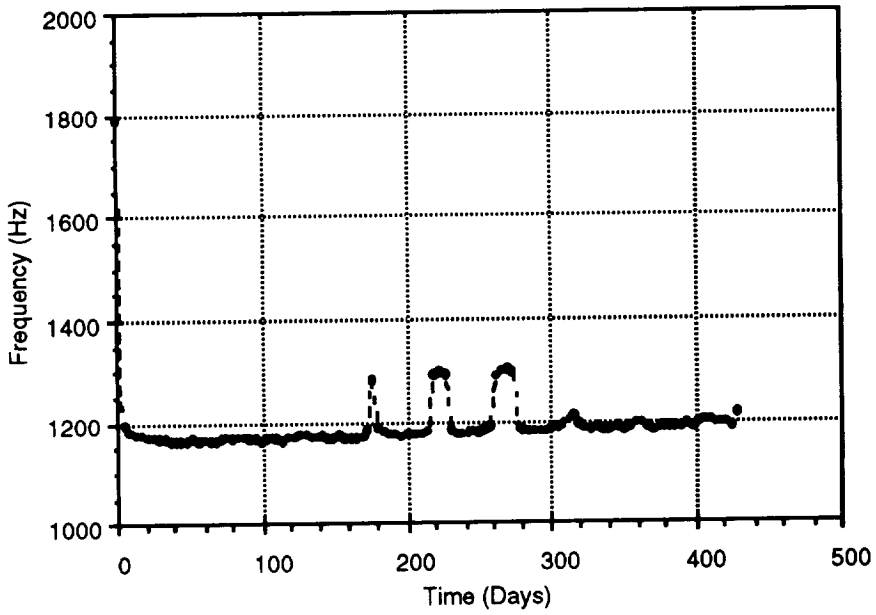

Figure 2. Trailing-edge quartz-crystal microbalance frequency change.

One of the most sensitive means to analyze material surfaces is by x-ray photoelectron spectroscopy. This technique probes ~50 to 100 Å at the surface and can reveal chemical information about the constituents. Both In_2-O_3 and Zn-S surfaces from the QCM's have been analyzed with similar results with respect to contamination (ref. 6). The data in Table 1 show that silicon is detected on both leading-edge and trailing-edge surfaces, with the silicon higher on the leading edge. The detection of substrate signals indicates an incomplete coverage or a coverage less than the electron escape depth (50 to 100 Å). Atomic oxygen erosion would explain the decrease in carbon species on the leading edge while the silicon would tend to form nonvolatile oxides and still be present. Note that the oxygen is also higher on the leading edge as expected. The trailing edge

shows higher levels of carbon and lower levels of silicon. These observations of differences between leading edge and trailing edge are confirmed by other analytical techniques. Results from the Secondary Ion Mass Spectrometry (SIMS) studies of the quartz crystals are shown in Table 2. About an order of magnitude higher level of silicon is detected for these crystals on the leading edge as compared to the trailing edge (ref. 5).

Silver Teflon samples have been studied from 11 of the 12 rows of samples around the perimeter of LDEF. The contamination of the Teflon surfaces varies according to the location on leading or trailing edge of LDEF. On the trailing edge, surface analysis shows that contaminants are present at levels similar to that found on the QCM surfaces discussed earlier. Some areas were more heavily contaminated with easily visible contaminants (ref. 7). However, on the leading edge, where erosion of ~1 mil of the Teflon has occurred, the Teflon surface is "clean," similar to representative control samples. Other eroded polymers were also found to have been cleaned (ref. 6). Since the contaminant films on LDEF typically contain silicon, which forms a nonvolatile oxide that should not be eroded, there appears to be a mechanical removal that accompanies the erosion of the polymers that results in a cleaning of the surface.

The accumulation of molecular contamination can increase solar absorptance. One of the experiments on M0003 was designed to measure the effects of contamination on material properties (ref. 8). Samples were placed on both the leading and trailing edges of LDEF in canisters where the samples were exposed for only 300 days during the first year on orbit and on the trays outside the canister where the samples were exposed for the entire mission. Results for the Si-O_2/Al second-surface mirrors in Table 3 show that some degradation in solar absorptance was observed on the samples with the 300-day exposure. The samples with the full 69-month exposure showed even further degradation. The degradation is slightly higher on the trailing edge in both cases. The x-ray photoelectron spectroscopy analysis of nickel mirrors in the same locations also indicates that the silicon contamination continued to accumulate after the first year in orbit. Note that for both the

Table 1. X-ray photoelectron spectroscopy analyses of quartz-crystal surfaces.

Sample	Surface Mole Percent (Normalized)						
	C	O	Si	In	Sn	Zn	S
In_2-O_3 Leading Edge	17	58	23	0.7	0.2	n.d.	0.1
Zn-S Leading Edge	48	35	10	n.d.	0.2	0.9	0.5
In_2-O_3 Trailing Edge	68	25	1.5	n.d.	0.3	n.d.	0.1
ZnS Trailing Edge	67	25	2.3	n.d.	0.4	0.1	0.1

(n.d. = not detected)

Table 2. Ion ratios on quartz-crystal surfaces detected by SIMS analysis.

Sample	Ion Ratios	
	Si^+/In^+	Si^+/Zn^+
In_2-O_3 Leading Edge	0.27	
In_2-O_3 Trailing Edge	0.036	
ZnS Leading Edge		63
ZnS Trailing Edge		6.8

leading-edge and trailing-edge specimens, the silicon levels are significantly higher for the full mission exposure compared to the 300-day exposure (see Table 4). The full mission exposures again indicate higher silicon levels on the leading edge. However, the 300-day exposure during the first year in orbit indicates a slightly higher level of silicon on the trailing edge. The carbon level is observed to be lower on both leading-edge samples where atomic oxygen has reduced the carbon level for the full mission exposure and for the 300-day exposure.

Table 3. Molecular contamination effects on Si-O_2/Al second surface mirrors.

Exposure		Solar Absorptance
Si-O_2/Al Lab Control		0.103
Si-O_2/Al Leading Edge	300 Days	0.107
Si-O_2/Al Leading Edge	Full Mission	0.112
Si-O_2/Al Trailing Edge	300 Days	0.113
Si-O_2/Al Trailing Edge	Full Mission	0.136

Table 4. X-ray photoelectron spectroscopy results on nickel mirror surfaces.

Sample		Surface Mole Percent (Normalized)							
		C	O	Si	Ni	F	Cl	S	P
Nickel Leading Edge	300 Days	19	43	2,5	34	1.7	0.2	0.1	0.3
Nickel Leading Edge Mission	Full	15	59	16	7.8	0.3	1.8	0.1	n.d.
Nickel Trailing Edge	300 Days	51	36	6.8	2.4	0.2	trace	0.1	2.9
Nickel Trailing Edge Mission	Full	40	43	12	n.d.	3.4	0.1	n.d.	n.d.

(n.d. = not detected)

CONTAMINATION LESSONS LEARNED

Contamination may degrade the optical and thermal properties of spacecraft materials. The effects on optical materials are documented in the LDEF literature and the Optical Materials Data Base. In fact, contamination is one of the dominant effects on optical materials on LDEF documented by other investigators. Contamination will increase the scatter of reflective optics and may decrease the transmission of filters and other external optics.

Surface analysis results have shown that the levels of contaminants such as silicon depend on the underlying material. For materials that have been eroded, the remaining material is contamination free. However, in nearby areas on materials that do not erode, the silicon is observed to remain in an oxidized form. Since the silicon is not expected to erode by chemical reaction, its absence on eroded material must indicate that a mechanical process is involved that results in a clean surface. The influence of UV radiation to enhance contaminant deposition is well known, and

contamination was observed on LDEF consistent with this mechanism. Most deposits were non-soluble and many heavier deposits were removed by physical means for analysis. However, some investigators have commented that the contaminants could be easily removed by solvent wipes of optical components.

The effects on the absorptance of solar energy are another type of concern. Contamination will increase the solar alpha and, as a consequence, the temperature of spacecraft surfaces. The degradation of second-surface mirrors is a good indication of an effect of contamination since the surface is expected to be stable to atomic oxygen and UV radiation. The observed degradation was less than 0.05 in solar alpha. This would generally be considered acceptable and is representative of cleaner satellites for which data is available (see Figure 3). Obviously, there are areas on LDEF with noticeable contamination where high values of solar alpha have been measured. These appear to be from localized sources that should be controlled to avoid undesirable increases in equilibrium temperatures.

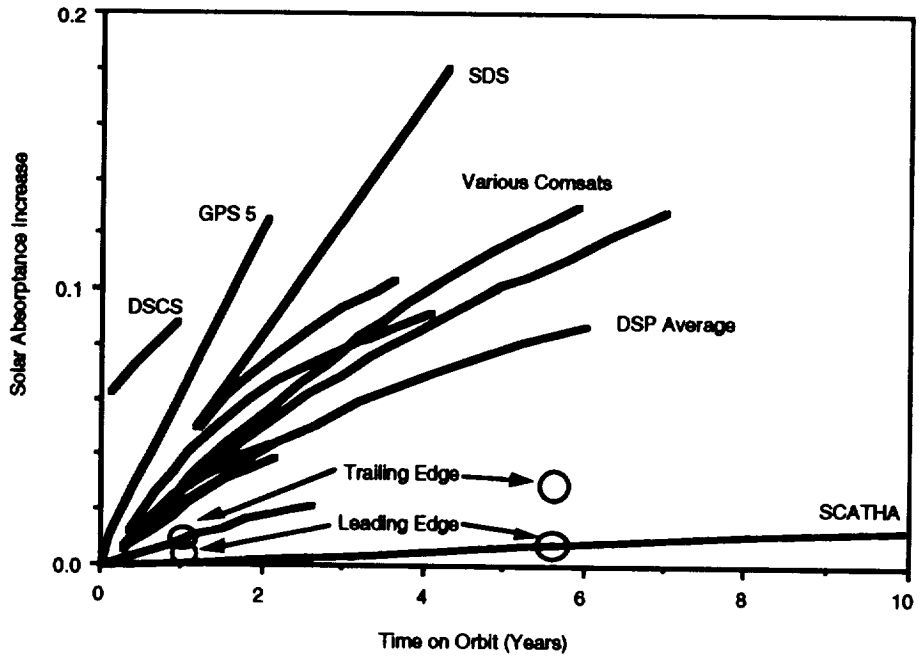

Figure 3. Fused-silica mirror degradation.

SUMMARY

There were many observations of contamination that occurred during the flight of LDEF. While the cleaner areas of LDEF had less than 100 Å of contaminant deposition, other areas were heavily contaminated. The most obvious include the large pieces of debris generated by atomic oxygen erosion that occurred while LDEF was still in orbit and the molecular deposits around tray vents from the LDEF interior or the trays themselves. The role of UV and atomic oxygen fixing of deposits on surfaces could be easily seen from the very noticeable brown stains attributed to atomic oxygen flow patterns or exposure to UV. The quartz-crystal microbalances show that the accumulation was still measurable after a year on orbit. The leading edge had higher contamination levels in some cases, apparently due to the return flux of contaminants. However, the atomic oxygen erosion could result in removal of the contaminants, leaving a "clean" surface. Silicones were known before the flight to result in oxidized, nonvolatile forms of deposits due to the removal of the hydrocarbon

portions of the silicones, but the high level of silicon is a concern for future spacecraft. A number of possible sources of silicones on LDEF have been suggested.

Examples of all of these various mechanisms affecting the level of contamination were observed on LDEF. The impact of the contamination depends on the material, its desired property, and the planned measurements. In order to minimize the impacts of contamination on a surface where the level of contamination is critical, contamination control plans and procedures should to be developed that cover all possible sources of contamination. The level of contamination may necessitate the establishment of contamination budgets or goals and the use of models for prediction of levels from outgassing sources, vents, and the return flux. Material selection is always a critical issue. A material that is acceptable by the ASTM E595 testing procedure does not necessarily eliminate contamination concerns or mean that it is not a potential contamination source. It only means that the material has a 1 percent or less total mass loss (TML) in 24 h at 125 °C and a 0.1 percent collected volatile condensable material (CVCM) at 25 °C. Similarly, a material that has been flown previously does not imply that it is not a potential contamination source. The acceptability of a material is dictated by its contamination potential and the requirements of each individual application.

REFERENCES

1. Meshishnek, M.J.; Gyetvay, S.R.; and Jaggers, C.H.: "Long Duration Exposure Facility Experiment Deintegration/Findings and Impacts." *LDEF-69 Months in Space First Post-Retrieval Symposium*, pp. 1073–1107, ed. Arlene S. Levine, NASA Conference Publication 3134, 1992.

2. Crutcher, E.R.: "Materials SIG Quantification and Characterization of Surface Contaminants." *LDEF-69 Months in Space First Post-Retrieval Symposium*, pp. 155-177, ed. Arlene S. Levine, NASA Conference Publication 3134, 1992.

3. Crutcher, E.R.; and Warner, K.J.: "Molecular Films Associated with LDEF." LDEF Materials Workshop '91, NASA Conference Publication 3162, 1992.

4. Stuckey, W.K.; Koontz, S.; and Crutcher, R.: "LDEF Contamination." *Proceedings of LDEF Materials Workshop '91*, pp. 689–698, ed. Bland A. Stein and Philip R. Young, NASA Conference Publication 3162, 1992.

5. Stuckey, W.K.; Radhakrishnan, G.; and Wallace, D.: "Post-Flight Analyses of the Crystals from the M0003-14 Quartz Crystal Microbalance Experiment." Second LDEF Post-Retrieval Symposium, San Diego, CA, June 4, 1992.

6. Hemminger, C.S.: "Surface Contamination on LDEF Exposed Materials." *Proceedings of LDEF Materials Workshop '91*, pp. 159–174, ed. Bland A. Stein and Philip R. Young, NASA Conference Publication 3162, 1992.

7. Pippin, G.L.; Hemminger, C.S.; and Stuckey, W.S.: "Performance of Silvered Teflon Thermal Control Blankets on Spacecraft." LDEF Materials Results for Spacecraft Applications Conference, NASA CP- , 1993.

8. Borson, E.N.; and Sinsheimer, F.B.: "Contamination Measurements on M0003." Second LDEF Post-Retrieval Symposium, San Diego, CA, June 4, 1992.

N94-31050

WHAT LDEF MEANS FOR DEVELOPMENT AND TESTING OF MATERIALS

Ann F. Whitaker
NASA/Marshall Space Flight Center
Marshall Space Flight Center, AL 35812
Phone: (205) 544-2510, Fax: (205) 544-5786

Wayne K. Stuckey
The Aerospace Corporation
El Segundo, CA 90009-2957
Phone: (310) 336-7389, Fax: (310) 336-5846

Bland A. Stein
NASA/Langley Research Center
Hampton, VA 23665-5225
Phone: (804) 864-3499, Fax: (804) 864-7729

INTRODUCTION

The Long Duration Exposure Facility (LDEF) served as the ultimate laboratory to provide combined space environmental effects on materials. The LDEF structure and its 57 experiments contained an estimated 12,000 to 14,000 specimens of materials and materials processes. It not only provided information about the resistance of these materials to the space environment but gives us direction into future needs for spacecraft materials development and testing. This paper provides an overview of the materials effects observed on the satellite and suggests recommendations for the future work in space-qualified materials development and space environmental simulation.

A number of observations regarding space environmental effects was made for the first time from LDEF. The overall environmental response of the spacecraft and evaluations of materials at various experiment locations provided some insights into the relationship of spacecraft orientation and consequent environmental exposure. The contamination deposits on LDEF served to verify the pressure buildup from the return flux on the leading surfaces of the spacecraft and the resulting flow from the leading surface through 90°. New exposure phenomena and new synergistic effects in materials were noted; in some materials which were exposed to all environments, one dominant environmental effect determined the resultant material properties. Numerous micrometeoroid and small space debris "peppered" the spacecraft, creating some surface degradation. Complex contamination phenomena involving multiple environmental interactions were present. Surprisingly good performance was noted in a few space environmentally resistant materials and devices.

Space environments to which LDEF materials were exposed are shown in Table 1. The pressure level which was estimated would be expected to vary from the leading surface to the trailing surface. Material effects found on LDEF may have been influenced by the sequence of individual environmental exposures. LDEF was placed on orbit during a solar minimum, so that more space debris/micrometeoroid impacts would have occurred during that time and less atomic oxygen (AO) would have been present. During the last 10 percent of the mission, the spacecraft saw a higher flux of AO. Even though materials experience many thermal cycles, the temperature extremes would tend to be peculiar to materials, their optical properties, and their mounting configuration. From the standpoint of being a

verifying spacecraft for contamination effects, molecular contamination appeared to have four major sources: uncontrolled components on individual experiments, bicycle reflectors on both ends of the spacecraft, electrical connectors, and the unbaked black urethane paint on the structure interior. In the absence of moderate levels of AO on the trailing surfaces, darkening of material from ultraviolet (UV) irradiation was prominent. While we characteristically think of LDEF as addressing issues related only to the low-Earth orbit (LEO) environment, the trailing surfaces of the spacecraft to a large extent, except for e^-, p^+ radiation levels, are relevant to what occurs to materials exposed to the geosynchronous-Earth orbit (GEO) environment.

Table 1. LDEF environments.

High Vacuum	10^{-6} to 10^{-7} torr (estimated) on leading edge; $<<10^{-6}$ torr trailing edge
UV Radiation	<2,000 ESH Earth end to ~15,000 ESH space end
Proton Fluence	10^9 p^+/cm^2 (0.5 to 200 MeV)
Electron Fluence	10^{12} to 10^8 e^-/cm^2 (0.5 to 3.0 MeV)
AO	9×10^{21} atoms/cm^2 on forward surface with less exposure through 90°; $<10^{17}$ atoms/cm^2 on trailing surfaces
Micrometeoroid/ Space Debris	~34,000 impacts > 0.1 mm, impact density varying over spacecraft
Thermal Cycles	~32,000 cycles, temperature extremes peculiar to material, mounting configuration

LDEF made significant contributions to the understanding of spacecraft durability issues. It renewed the emphasis for thermal vacuum bakeout of materials and components by identifying major sources of contaminants and their resulting effects on the spacecraft. Space exposure of a large number of engineering and model materials allowed for comparative grading of the materials durability. LDEF further sensitized us to spacecraft orientation in the relative partitioning of environmental effects. The approximate 6 years of exposure effects have assisted in identifying the combination of space environments for testing and the sequencing of individual environments in the testing of materials. As such, it confirms and identifies approaches to ground-based testing.

SIGNIFICANT LDEF FINDINGS

Several groupings of materials and components showed reasonable resistance to the space environment. Table 2 gives a qualitative description of how they fared in the LDEF environment. Ceramic-based materials and the fully oxidized glassy ceramic coatings demonstrated good stability. No radiation degradation was observed in solar cell covers probably because LDEF surface temperature of glasses would have annealed out any radiation-induced darkening. The structural metals, aluminum and steel, had no problems, but oxidation was noted in copper and silver, as anticipated. Silicone overcoats appeared to provide AO protection for ductile material, but additional testing is required to sort out subtle issues which could have consequences for durability longer than the 5.8 years of LDEF.

Table 2. Important LDEF materials findings.

- Materials and Components Durable Under Long Space Exposure
  - Ceramic coatings on rigid substrates—good stability
  - Solar cells/cover slips—limited degradation
  - Structural metals—no problems
  - Silicone overcoats on ductile materials—good AO protection although some cracking occurred
  - Acrylic and silicone adhesives—performed well
  - Fully oxidized glassy ceramic coatings—best protection for mirrors/reflectors
  - Beta cloth—limited degradation
- Materials and Components Requiring Modifications to Increase Space Durability Long Term
  - Beta cloth thermal blankets—replace threading/extend Beta cloth over Velcro™ fastening
  - Solar cells—cover slip to mask N wraparound/utilize fully oxidized AR coatings
  - Carbon fiber composites—require metallized/other tape coating

Silicone and acrylic adhesives functioned well. They underwent some aging evidenced by increased bond strength, but their companion control specimens in the laboratory also aged. Degradation of Beta cloth-covered multilayer insulation (MLI) was limited to some erosion of the TFE Teflon™, thread, and Velcro™. With a changeout of the thread to another AO resistive type and overlap protection of the Velcro™ by the Beta cloth, this MLI configuration should be durable for long exposures in the space environment. The maintenance of nominal optical properties requires that any silicones incorporated in the manufacture of the Beta cloth be restricted. Carbon fiber composites, particularly if they are thin, require some protection from AO. The protection chosen must be coupled with required optical properties. The incorporation of wraparound contacts and the selection of an environmentally resistant antireflection (AR) coating for the cover slide should yield durable solar cells. Even though fluorine is lost from magnesium fluoride in the space environment, principally to AO, it may still retain sufficient fluorine to be an acceptable AR coating for periods longer than LDEF's 6 years. Additional testing is required for this assessment.

DEVELOPMENT OF MATERIALS

Two general categories of materials and materials components come readily to mind when we consider development needs in materials for external spacecraft applications. Coatings and special function materials comprise the majority of these materials. New coatings are needed for AO protection of high reflectivity mirrors, as antireflective coatings, as paints in passive thermal control systems, and as high optical absorptivity telescope baffle materials.

Special function materials comprise a gamut of applications—space debris protection systems, tether composites, flexible booms, and nonoptically transmissive tapes. Lubricants form a special class of materials where existing dry films, fluids, and self-lubricating composites have space durability limits. In many instances, we can design around lubricant properties in thin film usage but not in all

cases. Where a thin lubricating material is continually sheared during usage, it cannot afford additionally to lose mass in an AO environment.

LDEF CONTRIBUTIONS TO GROUND-BASED TESTING

While LDEF's principal contribution to the materials discipline has been the extensive and diverse materials exposure data, it has, further, contributed significantly to our approach to ground-based space environmental simulation. Table 3 describes the present approach to combined environments testing and the LDEF factors that contribute to update this approach.

Table 3. LDEF contributions to combined environments ground testing.

Present Approach To Ground-Based Combined Environments Testing	LDEF Contributed Testing Factors
• Generally, two parameters plus vacuum with configured materials	• Ground testing comparisons to LDEF results indicate qualitative damage can be reproduced in materials
• Sequential Environments Exposures – e.g., thermal vacuum cycling follows irradiation	• New synergistic effects
• Irradiation conducted as a series of parametric exposures at high intensities – Nonlinear response must be considered for accelerated exposures	• Fixing of contaminants by UV irradiation and/or AO
• Combining AO with UV irradiation and the sequencing/relative magnitudes of either yield different results	• Many materials specific results – e.g., densification of glass ceramics – e.g., optically transmissive materials yield complex response
• Space debris alone simulated to ~8 km/s	• All environmental parameters contributed to degradation – Dominant effect peculiar to material
	• Small particle/multiple velocity impacts of micrometeoroid/space debris must be considered; AO effects on impact areas

Historically, in our approach to combined environments testing, we utilize two parameters in a vacuum environment. We may also impose thermal cycle on our materials and/or either tension or compression on the test samples. In many cases, we tend to sequentially expose materials. For example, we thermal cycle materials after we irradiate with electrons or protons. Some testing, such as ground-based irradiation, is an accelerated process and, therefore, requires parametric exposures and data extrapolation.

We have noted more recently from LDEF and subsequent ground testing that when we combine AO and UV irradiation, the resulting properties obtained for the materials are dependent on the magnitude of the exposure parameters and also their sequencing. LDEF indicates to us that we can qualitatively reproduce the same kinds of damages with our laboratory test systems. We have observed new synergistic effects and phenomena not observed prior to LDEF such as the densification of ionic bonded

materials. This densification effect can be severe when the material of concern is a 300 to 400 Å optical coating. Where greater thicknesses of these materials are utilized, some change in optical properties will be observed. In addition, we see complex phenomena in optically transmissive materials. Other issues that must be dealt with are the multitude of small particle impacts and their separate effects on ductile and brittle materials. Combined environments testing must be tailored to materials and specific orbital environments, a fact which is well known and has been reinforced by LDEF. This is the major reason that there are no general detailed specifications related to the testing of materials in this area. LDEF promotes the notion that we must pay more attention to sequencing of environmental exposures since we cannot combine all of them with the relative magnitudes that exist on orbit.

Now let us examine the issues of simulating individual space environments. Vacuum simulation alone is traditionally associated with addressing materials-generated contamination phenomena in the materials discipline. Sufficient specifications exist to address outgassing issues associated with materials, and special instrumentation is available to investigate finer questions. There is some work required based on observed LDEF contamination levels and locations that involves updating current predictive models for spacecraft contamination assessment. Pressure buildup on leading surfaces, gaseous flow around the spacecraft, distribution of molecular and particulate contaminants, and local source behavior contributions from LDEF should yield significant inputs to update these existing contamination models.

Particle impacts on materials from space debris, AO, electrons, and protons require their own unique simulations and peculiar protocols for specific materials exposures. Similar considerations are necessary for electromagnetic simulations. Many laboratories use thermal AO for materials evaluations because of availability and for rationale based on peculiar material response in simulation of orbital effects. The ideal AO simulation facility would be a 5 eV, large area exposure source for materials evaluation that can produce moderate and high fluxes. Some adjustments are needed in space debris simulation to account for the multiple velocities of small particles, and to cover evaluations across the gaps in ballistic limit curves. From an optical and mechanical effect on materials standpoint, few contributions were made to charged particle simulations by LDEF. Charged particle simulation is, of course, an accelerated testing parameter. Table 4 provides a summary of these simulation considerations.

Probably the area requiring the most systematic examination is UV irradiation simulation. Sources are limited by wavelength range, reliability, life, and competitive effects induced in materials from the UV and infrared regions. Disagreement of absorptivity changes induced in materials between ground and LDEF results is complicated both by simulation source and synergistic effects with other environmental parameters. Considerable additional research is required in this area. Fluorescence phenomena observed on LDEF may provide a new sensitive technique for surface analyses. Another aspect of LDEF exposure to be noted is that thermally activated and suppressed phenomena in materials were not addressed in the form of controlled thermal experiments.

RECOMMENDATIONS

There are a number of LEO materials durability issues that were not resolved by or were discussed on LDEF which must be considered for future long duration exposures of materials in space. There is a need for active in situ measurement of degradation rates for various materials at selected temperatures. The materials flown on LDEF represent those developed up to and during the 1970's; a new generation of materials and components are available for exposure. Investigation of synergistic effects and the verification of the space debris environment and contamination models should have a high priority. Finally, LDEF has alerted us to degradation mechanisms in materials arising from space exposures

that must be understood—surface texturing, temperature dependence, involvement of stress, influence of microstructures, and the role of electrostatic interactions.

Table 4. Environmental simulations considerations for materials.

Single Environment	Present Approach	LDEF Generated Issues
Thermal Vacuum	10^{-5} to 10^{-9} torr; conventional and special tests and sensors for contamination	Pressure buildup on ram surfaces; localized source behavior; gaseous flow promoted distribution of contamination; contamination models update
AO	Thermal AO, small exposure areas for 5 eV at low fluxes	5 eV large area exposure required; long versus short exposures phenomena; competition of effects; synergism with contamination and incorporation of UV
UV Radiation	Sources: mercury xenon principally, hydrogen, krypton, deuterium	Conflict of absorptivity results between ground simulations and LDEF perhaps involving synergism; severity and dominance of effects
Particulate Radiation	e^- and p^+ (a few KeV to $2^1/_2$ MeV)	Little attention paid to effects although bulk polymers show free radical generation
Micrometeoroid/Space Debris	Space debris velocities to ~8 km/s for particle diameters to $^3/_8$ in	New simulation required for multiple velocities of small particles; brittle versus ductile materials behavior

BIBLIOGRAPHY

Proceedings of the First LDEF Post-Retrieval Symposium, Kissimmee, FL, June 2–8, 1991, NASA Conference Publication 3134, Parts 1 through 3.

Proceedings of a Workshop—LDEF Materials Workshop '91, NASA Langley Research Center, November 19–22, 1991, NASA Conference Publication 3162, Parts 1 and 2.

Proceedings of the Second LDEF Post-Retrieval Symposium, San Diego, CA, June 1–5, 1992, NASA Conference Publication 3194, Parts 1 through 4.

ATOMIC OXYGEN DAMAGE CHARACTERIZATION BY PHOTOTHERMAL SCANNING

N94-31051

A.W. Williams, N.J. Wood, and A.B. Zakaria
Department of Physics, University College of Swansea
University of Wales, Singleton Park, Swansea SA2 8PP U.K.

ABSTRACT

In this paper we use a photothermal imaging technique to characterize the damage caused to an imperfectly coated gold-coated Kapton sample exposed to successively increased fluences of atomic oxygen in a laboratory atomic source.

INTRODUCTION

One major problem associated with the flight of low Earth orbit (LEO) spacecraft is the damage caused to various materials by bombardment with atomic oxygen (AO). AO will readily oxidize materials with high erosion yield coefficients, such as polyimide Kapton, epoxy graphite, and Mylar. Materials with low erosion yield coefficients such as aluminum, gold, and SiO_2 may be used as barrier coatings to prevent damage to the more vulnerable underlying materials mentioned above (ref. 1). However, manufacturing defects in the barrier coatings such as scratches and pin holes act as sites where the AO can attack the substrate, and may cause undercutting of the protective layer (ref. 2).

Photothermal imaging of solids is a powerful technique which has been applied to numerous problems involving the characterization of surface and subsurface, cracks inclusions, and delamination in materials (ref. 3, 4). We have used this method to produce photothermal images of a gold-coated Kapton sample at various stages of its exposure to AO in a laboratory AO source. The gold layer was deliberately scratched prior to exposure of the sample, and the resultant damage around this site imaged photothermally.

PHOTOTHERMAL IMAGING APPARATUS

A diagram of the apparatus is given in Figure 1.

In order to produce a photothermal image, a modulated and localized heat source is required which is used to create thermal waves in the sample. In our system, we have used an argon ion laser as a heat source whose beam is focused by means of a microscope objective onto the sample to be scanned. The laser was operated on a wavelength of 488 nm in order to optimize the absorption in the gold (≈63 percent at this wavelength) and thus generates "thermal waves" within the sample being illuminated.

The depth to which the thermal waves penetrate the sample μ_s is given by:

$$\mu_s = \left(\frac{\alpha_s}{\pi f}\right)^{1/2},$$

where α_s is the thermal diffusivity of the material to be investigated, and f is the modulation frequency of the laser light.

The value of μ_s and, hence, the penetration depth may be changed by altering the modulation frequency.

Associated with the thermal waves are acoustic waves which are stresses generated in the sample due to the thermal waves and which penetrate the whole sample and are detected by a piezoelectric transducer coupled to the rear side of the sample. The voltage produced by the transducer, which depends on the magnitude of these waves, is then amplified and detected by a lock-in amplifier (Stanford SR530). The lock-in amplifier gives a reading of the magnitude of the photothermal signal detected, together with its phase shift with respect to the light modulation. The sample together with its piezodetector was mounted upon two orthogonal translation stages and raster scanned beneath the focused laser beam of diameter ≈2.5 μm in steps of 3 μm. The power density of the focused laser beam was kept below the damage threshold of the sample.

The thermal waves traveling into the bulk of the sample are reflected and scattered by regions of differing thermal properties within the sample. The photothermal signal, therefore, depends upon these imperfections, and hence gives the imaging capability of this technique.

In order to produce a subsurface image, the X–Y scans consisting of 75 by 75 data points for both the signal and its phase lag were recorded across a small area of the sample. The photothermal signal is sensitive to surface optical features which have differing optical absorption. However, the phase lag is much less sensitive to surface features and is a better measure of subsurface features especially delaminations (ref. 5). We have, therefore, concentrated upon the phase measurements in the results given in this paper.

SAMPLE EXPOSURE

A 1- by 3-cm, 130-μm thick Kapton sample was vacuum coated with 40 nm of gold and an area of 1 by 1 cm selected. A strip of the gold about 35-μm wide and extending from one side of the sample to the other was removed with a thin metal probe to expose the Kapton substrate beneath it. The sample was then mounted in a laboratory AO apparatus similar to the design described by Neely (ref. 6) and exposed to an AO flux of $\approx 1.5\times10^{17}$ atoms/cm^2/s at a temperature of 200 °C.

The sample was exposed to AO for four successive exposure times, with cumulative fluences of:

(i) 8.3×10^{20} atoms/cm^2

(ii) 17×10^{20} atoms/cm^2

(iii) 25×10^{20} atoms/cm^2

(iv) 50×10^{20} atoms/cm^2.

The sample was scanned photothermally before and after each exposure.

RESULTS

Five photothermal scans of the area containing the exposed Kapton, each comprising 75 by 75 data points were obtained giving a photothermal image 220 by 220 μm in area. The photothermal signal was detected by a piezotransducer on the Kapton surface remote from the gold. An imperfection in the gold/Kapton interface, such as delamination, which would introduce an air layer between the gold and Kapton substrate will scatter the thermal waves before they are detected, modifying the photothermal phase, since this is in effect the delay in generation of the photothermal signal with respect to the modulation frequency, hence making the scan sensitive to subsurface imperfections. The data were represented in false colors in the images of the scans, using Unimap 2000, Uniras A/S (ref. 7).

A modulation frequency of 3 kHz was chosen for all the scans which correspond to a thermal wave probe depth of ≈3.2 μm into the Kapton. Photothermal images of the phase lag of the signal are shown in Figure 2. These images show undercutting and delamination around the bare Kapton section of the sample. A greater phase lag is seen in the scans for the areas in which the gold is no longer in contact with the Kapton. As the sample becomes progressively more damaged, the area around the scratch area is seen to widen and the associated phase lag becomes greater.

Further photothermal analysis, performed in Swansea, will concentrate on coated samples that are scanned while inside the AO apparatus so that the progressive damage may be characterized in situ and in real time.

ACKNOWLEDGMENTS

The work was supported by the Strategic Defense Initiation Organization Office of Innovative Science and Technology (SDIO/IST) under contract number 60921-86-CA226 with the Naval Surface Warfare Center. ABZ wishes to thank the Public Service Department of Malaysia and the Universiti Pertanian Malaysia for the award of a postgraduate scholarship.

REFERENCES

1. Banks, B.A., Rutledge, S.K., Paulsen, P.E., and Streuber, T.J.: NASA Technical Memorandum 101971, 1989.

2. Pippin, H.G.: Surface Coatings Technology, vol. 39, No. 40, 1989, p. 595.

3. Wong, Y.H.: in *Scanned Image Microscopy*, Academic Press, London, 1980.

4. Sawada, T., and Kasai, M.: in *Photoacoustic and Thermal Wave Phenomena in Semiconductors*, vol. 3, A. Mandelis (ed.), North Holland, New York, 1987.

5. Zhang, S., and Chen, L.: in *Photoacoustic and Photothermal Phenomena in Semiconductors*, vol. 27, A. Mandelis (ed.), North Holland, New York, 1987.

6. Neely, W.C., Yang, T.C., Wey, J.P., Clothiaux, E.J., and Worley, S.D.: "Space Structures, Power, and Power Conditioning," SPIE, vol. 871, 1988, p. 313.

7. Unimap 2000 User Manual, Uniras A/S, Sϕborg, Denmark.

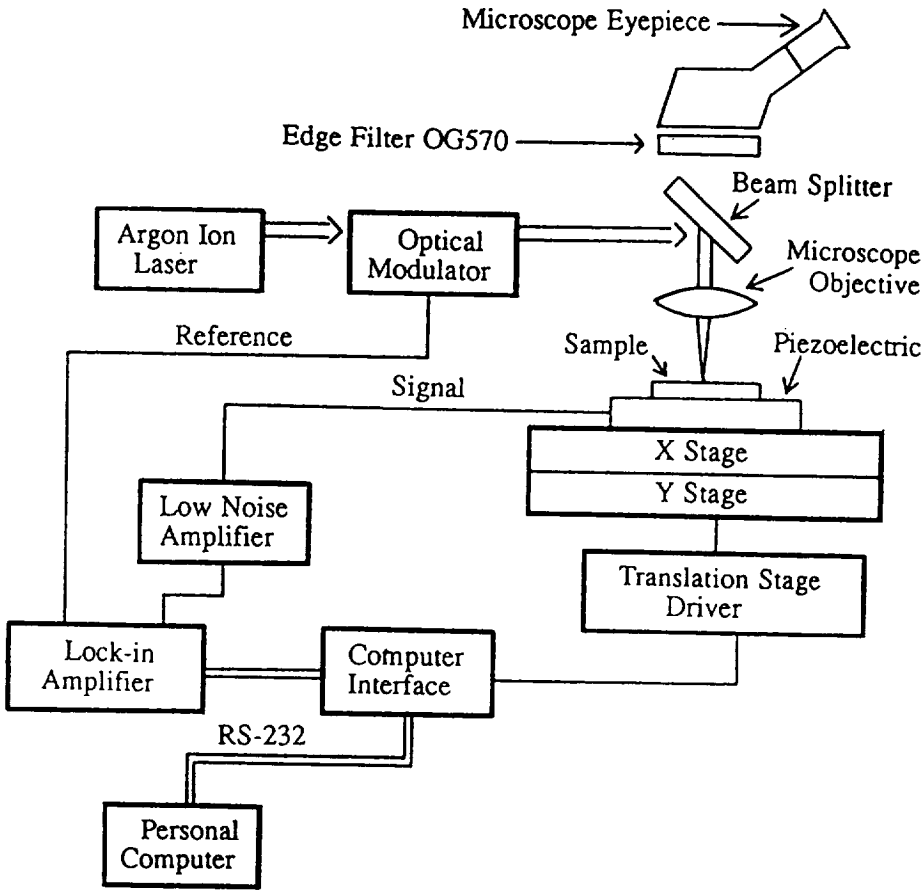

Figure 1. Diagram of photothermal imaging apparatus.

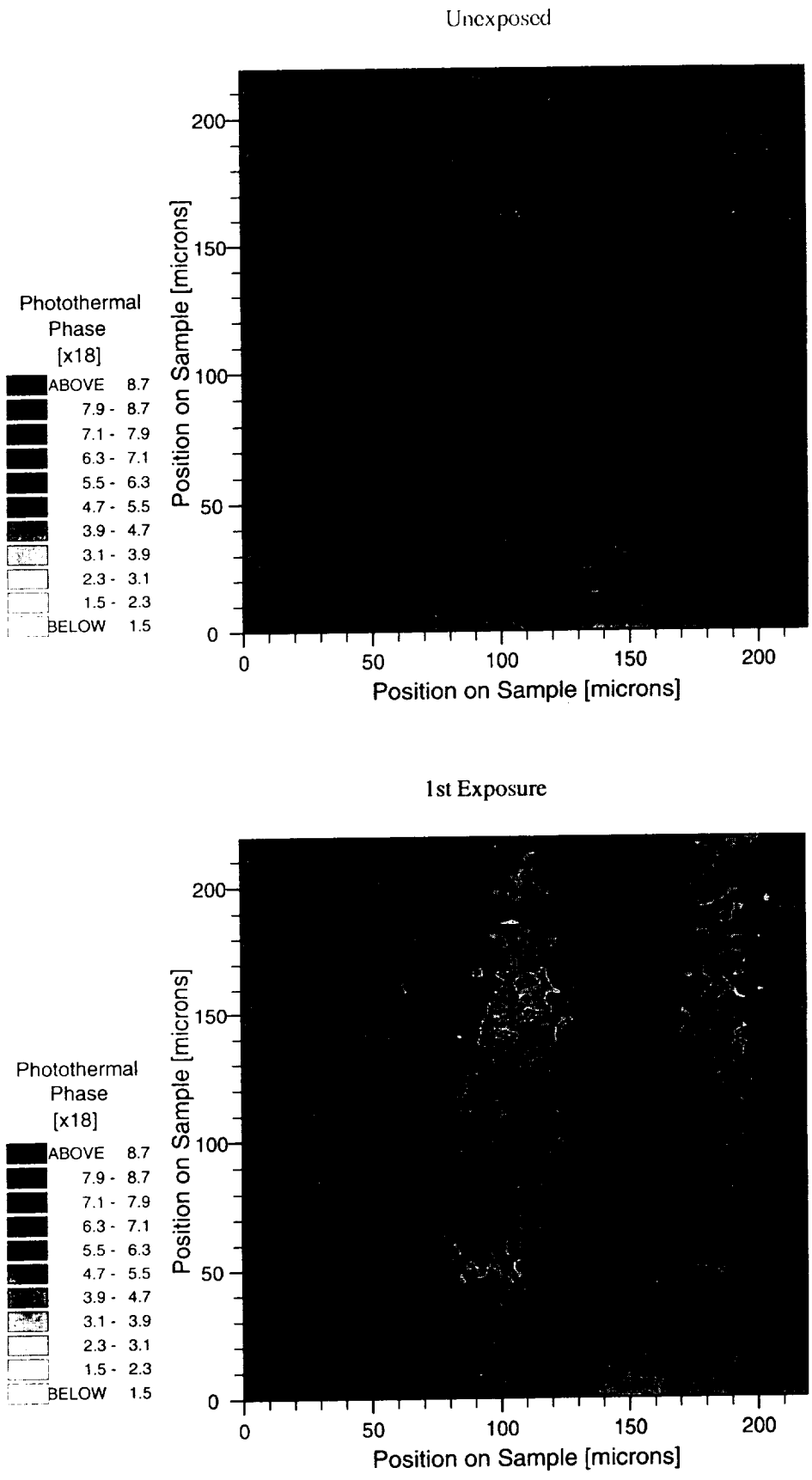

Figure 2. Photothermal phase images for cumulative AO exposures of gold-coated Kapton.

2nd Exposure

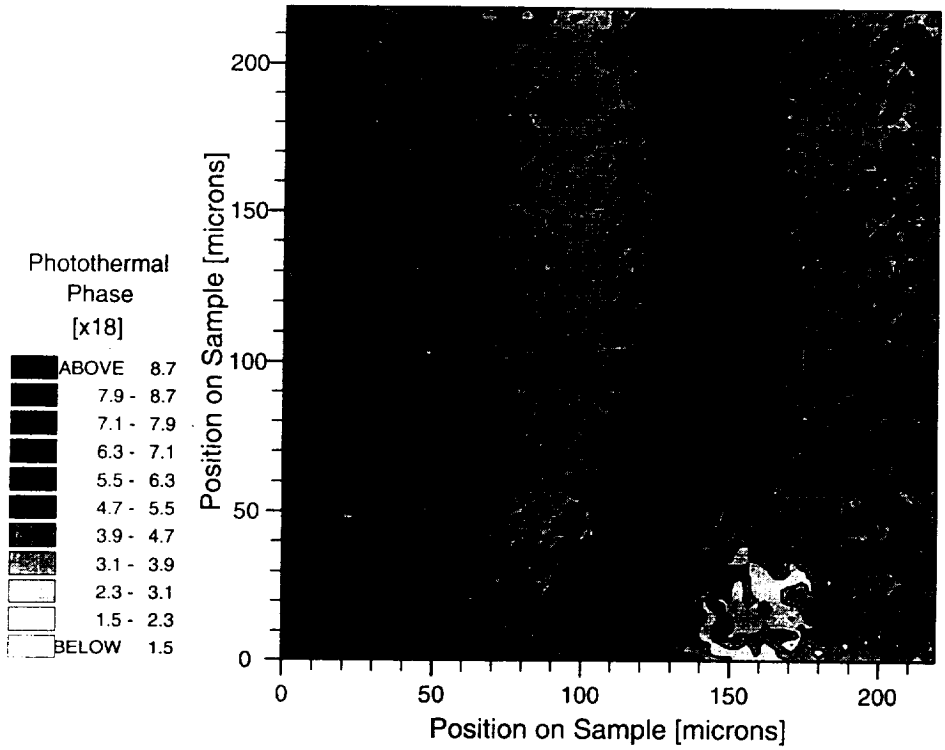

3rd Exposure

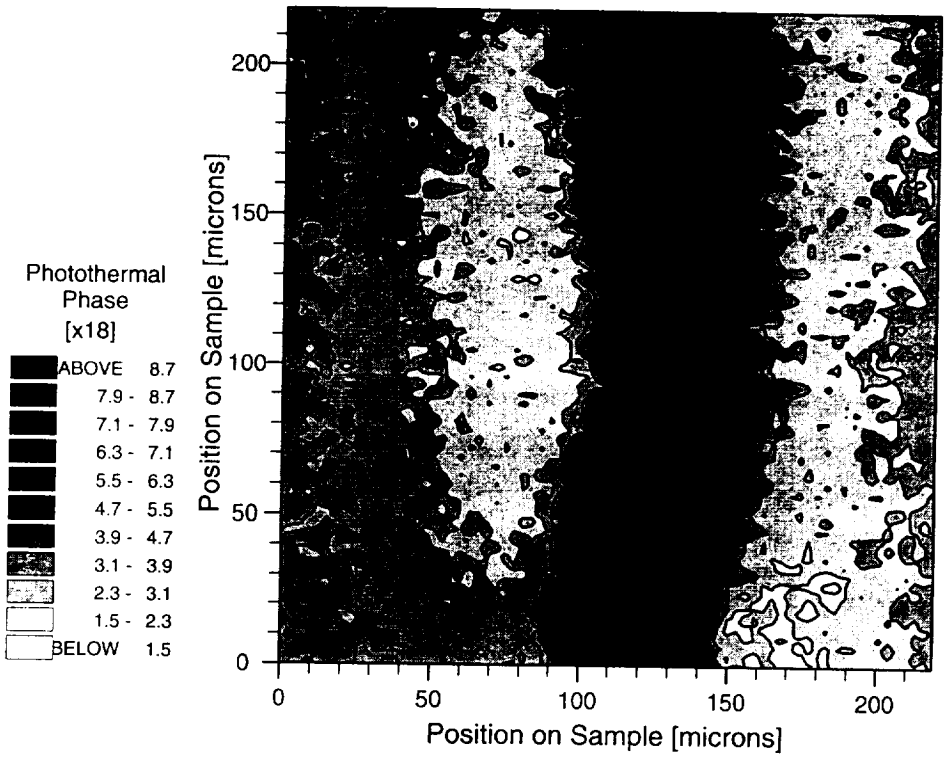

Figure 2. Photothermal phase images for cumulative AO exposures of gold-coated Kapton (continued).

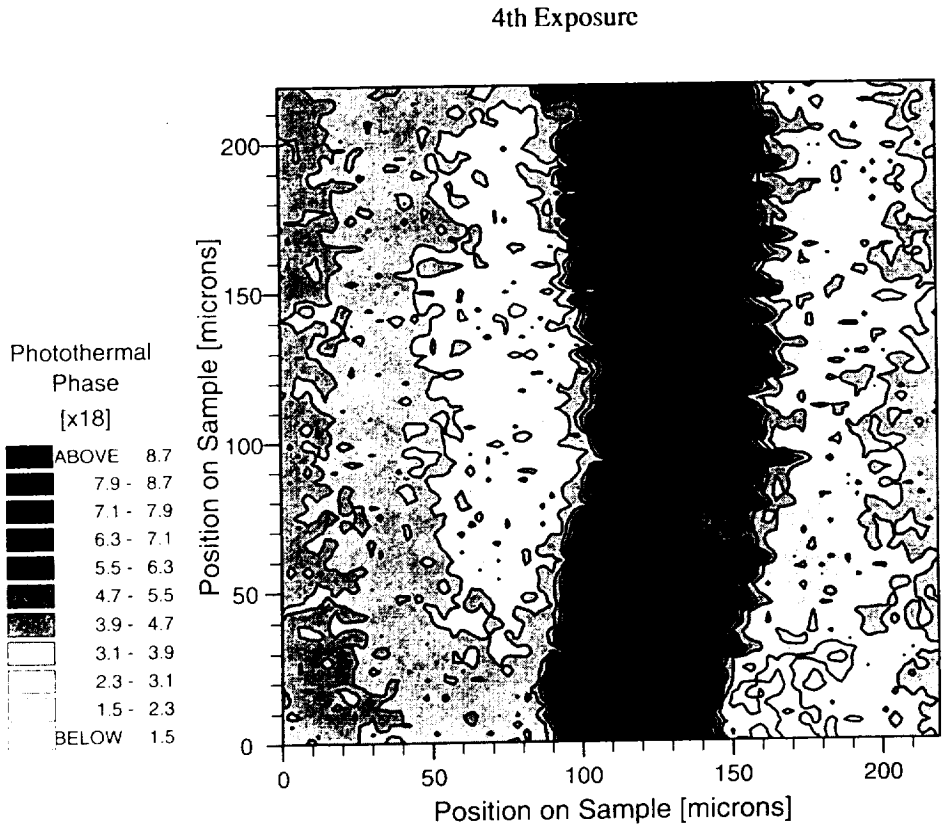

Figure 2. Photothermal phase images for cumulative AO exposures of gold-coated Kapton (continued).

☆U.S. GOVERNMENT PRINTING OFFICE 1994—533-108/00038

REPORT DOCUMENTATION PAGE

Form Approved
OMB No. 0704-0188

1. AGENCY USE ONLY (Leave blank)	2. REPORT DATE	3. REPORT TYPE AND DATES COVERED
	December 1993	Conference Publication

4. TITLE AND SUBTITLE

LDEF Materials Results for Spacecraft Applications

5. FUNDING NUMBERS

6. AUTHOR(S)

Ann Whitaker and John Gregory, Compilers

7. PERFORMING ORGANIZATION NAME(S) AND ADDRESS(ES)

George C. Marshall Space Flight Center
Marshall Space Flight Center, AL 35812

8. PERFORMING ORGANIZATION REPORT NUMBER

M-742

9. SPONSORING/MONITORING AGENCY NAME(S) AND ADDRESS(ES)

National Aeronautics and Space Administration
Washington, DC 20546-0001

10. SPONSORING/MONITORING AGENCY REPORT NUMBER

NASA CP-3257

11. SUPPLEMENTARY NOTES Proceedings of a conference sponsored by the National Aeronautics and Space Administration, Washington, DC, The University of Alabama in Huntsville, The Alabama Space Grant Consortium, and the Society of Advanced Materials and Process Engineers, and held in Huntsville, Alabama, October 27-28, 1992

12a. DISTRIBUTION/AVAILABILITY STATEMENT

Unclassified - Unlimited

Subject Category: 12

12b. DISTRIBUTION CODE

13. ABSTRACT *(Maximum 200 words)*

These proceedings describe the application of LDEF data to spacecraft and payload design, and emphasize where space environmental effects on materials research and development is needed as defined by LDEF data. The LDEF six years of exposure of materials has proven to be by far the most comprehensive source of information ever obtained on the long-term performance of materials in the space environment. The conference provided a forum for materials scientists and engineers to review and critically assess the LDEF results from the standpoint of their relevance, significance, and impact on spacecraft design practice. The impact of the LDEF findings on materials selection and qualification, and the needs and plans for further study, were addressed from the NASA, DoD, industry, and academic perspectives. Many timely and needed changes and modifications in external spacecraft materials selections have occurred as a result of LDEF investigations.

The Executive Summary of this conference is being printed as CP-3261.

14. SUBJECT TERMS

Materials, Environments, Spacecraft, Space Environment Effects

15. NUMBER OF PAGES
562

16. PRICE CODE
A24

17. SECURITY CLASSIFICATION OF REPORT	18. SECURITY CLASSIFICATION OF THIS PAGE	19. SECURITY CLASSIFICATION OF ABSTRACT	20. LIMITATION OF ABSTRACT
Unclassified	Unclassified	Unclassified	Unlimited